

Preface

The research field of robotics has been contributing widely and significantly to industrial applications for assembly, welding, painting, and transportation for a long time. Meanwhile, the last decades have seen an increasing interest in developing and employing mobile robots for industrial inspection, conducting surveillance, urban search and rescue, military reconnaissance and civil exploration.

As a special potential sub-group of mobile technology, climbing and walking robots can work in unstructured environments. They are useful devices adopted in a variety of applications such as reliable non-destructive evaluation (NDE) and diagnosis in hazardous environments, welding and manipulation in the construction industry especially of metallic structures, and cleaning and maintenance of high-rise buildings. The development of walking and climbing robots offers a novel solution to the above-mentioned problems, relieves human workers of their hazardous work and makes automatic manipulation possible, thus improving the technological level and productivity of the service industry.

Currently there are several different kinds of kinematics for motion on horizontal and vertical surfaces: multiple legs, sliding frames, wheeled and chain-track vehicles. All of the above kinematics modes have been presented in this book. For example, six-legged walking robots and humanoid robots are multiple-leg robots; the climbing cleaning robot features a sliding frame; while several other mobile prototypes are contained in a wheeled and chain-track vehicle.

Generally a light-weight structure and efficient manipulators are two important issues in designing climbing and walking robots. Even though significant progress has been made in this field, the technology of climbing and walking robots is still a challenging topic which should receive special attention by robotics research. For example, note that previous climbing robots are relatively large. The size and weight of these prototypes is the choke point. Additionally, the intelligent technology in these climbing robots is not well developed.

With the advancement of technology, new exciting approaches enable us to render mobile robotic systems more versatile, robust and cost-efficient. Some researchers combine climbing and walking techniques with a modular approach, a reconfigurable approach, or a swarm approach to realize novel prototypes as flexible mobile robotic platforms featuring all necessary locomotion capabilities.

The purpose of this book is to provide an overview of the latest wide-range achievements in climbing and walking robotic technology to researchers, scientists, and engineers throughout the world. Different aspects including control simulation, locomotion realization, methodology, and system integration are presented from the scientific and from the technical point of view.

This book consists of two main parts, one dealing with walking robots, the second with climbing robots. The content is also grouped by theoretical research and applicative realization. Every chapter offers a considerable amount of interesting and useful information. I hope it will prove valuable for your research in the related theoretical, experimental and applicative fields.

Editor

Dr. Houxiang Zhang
*University of Hamburg
Germany*

Mechanics and Simulation of Six-Legged Walking Robots

Giorgio Figliolini and Pierluigi Rea
*DiMSAT, University of Cassino
 Cassino (FR), Italy*

1. Introduction

Legged locomotion is used by biological systems since millions of years, but wheeled locomotion vehicles are so familiar in our modern life, that people have developed a sort of dependence on this form of locomotion and transportation. However, wheeled vehicles require paved surfaces, which are obtained through a suitable modification of the natural environment. Thus, walking machines are more suitable to move on irregular terrains, than wheeled vehicles, but their development started in long delay because of the difficulties to perform an active leg coordination.

In fact, as reported in (Song and Waldron, 1989), several research groups started to study and develop walking machines since 1950, but compactness and powerful of the existent computers were not yet suitable to run control algorithms for the leg coordination. Thus, ASV (Adaptive-Suspension-Vehicle) can be considered as the first comprehensive example of six-legged walking machine, which was built by taking into account main aspects, as control, gait analysis and mechanical design in terms of legs, actuation and vehicle structure. Moreover, ASV belongs to the class of "statically stable" walking machines because a static equilibrium is ensured at all times during the operation, while a second class is represented by the "dynamically stable" walking machines, as extensively presented in (Raibert, 1986).

Later, several prototypes of six-legged walking robots have been designed and built in the world by using mainly a "technical design" in the development of the mechanical design and control. In fact, a rudimentary locomotion of a six-legged walking robot can be achieved by simply switching the support of the robot between a set of legs that form a tripod. Moreover, in order to ensure a static walking, the coordination of the six legs can be carried out by imposing a suitable stability margin between the ground projection of the center of gravity of the robot and the polygon among the supporting feet.

A different approach in the design of six-legged walking robots can be obtained by referring to biological systems and, thus, developing a biologically inspired design of the robot. In fact, according to the "technical design", the biological inspiration can be only the trivial observation that some insects use six legs, which are useful to obtain a stable support during the walking, while a "biological design" means to emulate, in every detail, the locomotion of a particular species of insect. In general, insects walk at several speeds of locomotion with a

variety of different gaits, which have the property of static stability, but one of the key characteristics of the locomotion control is the distribution.

Thus, in contrast with the simple switching control of the “technical design”, a distributed gait control has to be considered according to a “biological design” of a six-legged walking robot, which tries to emulate the locomotion of a particular insect. In other words, rather than a centralized control system of the robot locomotion, different local leg controllers can be considered to give a distributed gait control.

Several researches have been developed in the world by referring to both “cockroach insect”, or *Periplaneta Americana*, as reported in (Delcomyn and Nelson, 2000; Quinn *et al.*, 2001; Espenschied *et al.*, 1996), and “stick insect”, or *Carausius Morosus*, as extensively reported in (Cruse, 1990; Cruse and Bartling, 1995; Frantsevich and Cruse, 1997; Cruse *et al.*, 1998; Cymbalyuk *et al.*, 1998; Cruse, 2002; Volker *et al.*, 2004; Dean, 1991 and 1992).

In particular, the results of the second biological research have been applied to the development of TUM (Technische-Universität-München) Hexapod Walking Robot in order to emulate the locomotion of the *Carausius Morosus*, also known as *stick insect*. In fact, a biological design for actuators, leg mechanism, coordination and control, is much more efficient than technical solutions.

Thus, TUM Hexapod Walking Robot has been designed as based on the stick insect and using a form of the Cruse control for the coordination of the six legs, which consists on distributed leg control so that each leg may be self-regulating with respect to adjacent legs. Nevertheless, this walking robot uses only Mechanism 1 from the Cruse model, *i.e.* “A leg is hindered from starting its return stroke, while its posterior leg is performing a return stroke”, and is applied to the ipsilateral and adjacent legs.

TUM Hexapod Walking Robot is one of several prototypes of six-legged walking robots, which have been built and tested in the world by using a distributed control according to the Cruse-based leg control system. The main goal of this research has been to build biologically inspired walking robots, which allow to navigate smooth and uneven terrains, and to autonomously explore and choose a suitable path to reach a pre-defined target position. The emulation of the stick insect locomotion should be performed through a straight walking at different speeds and walking in curves or in different directions.

Therefore, after some quick information on the Cruse-based leg controller, the present chapter of the book is addressed to describe extensively the main results in terms of mechanics and simulation of six-legged walking robots, which have been obtained by the authors in this research field, as reported in (Figliolini *et al.*, 2005, 2006, 2007). In particular, the formulation of the kinematic model of a six-legged walking robot that mimics the locomotion of the stick insect is presented by considering a biological design. The algorithm for the leg coordination is independent by the leg mechanism, but a three-revolute (3R) kinematic chain has been assumed to mimic the biological structure of the stick insect. Thus, the inverse kinematics of the 3R has been formulated by using an algebraic approach in order to reduce the computational time, while a direct kinematics of the robot has been formulated by using a matrix approach in order to simulate the absolute motion of the whole six-legged robot.

Finally, the gait analysis and simulation is presented by analyzing the results of suitable computer simulations in different walking conditions. Wave and tripod gaits can be observed and analyzed at low and high speeds of the robot body, respectively, while a transient behaviour is obtained between these two limit conditions.

2. Leg coordination

The gait analysis and optimization has been obtained by analyzing and implementing the algorithm proposed in (Cymbalyuk *et al.*, 1998), which was formulated by observing in depth the walking of the stick insect and it was found that the leg coordination for a six-legged walking robot can be considered as independent by the leg mechanism.

Referring to Fig. 1, a reference frame G' (x'_G y'_G z'_G) having the origin G' coinciding with the projection on the ground of the mass center G of the body of the stick insect and six reference frames O_{Si} (x_{Si} y_{Si} z_{Si}) for $i = 1, \dots, 6$, have been chosen in order to analyze and optimize the motion of each leg tip with the aim to ensure a suitable static stability during the walking.

Thus, in brief, the motion of each leg tip can be expressed as function of the parameters $s_i p_{ix}$ and s_i , where $s_i p_{ix}$ gives the position of the leg tip in O_{Si} (x_{Si} y_{Si} z_{Si}) along the x -axis for the stance phase and $s_i \in \{0; 1\}$ indicates the state of each leg tip, *i.e.* one has: $s_i = 0$ for the swing phase and $s_i = 1$ for the stance phase, which are both performed within the range $[PEP_i, AEP_i]$, where PEP_i is the Posterior-Extreme-Position and AEP_i is the Anterior-Extreme-Position of each tip leg. In particular, L is the nominal distance between PEP_0 and AEP_0 .

The trajectory of each leg tip during the swing phase is assigned by taking into account the starting and ending times of the stance phase.

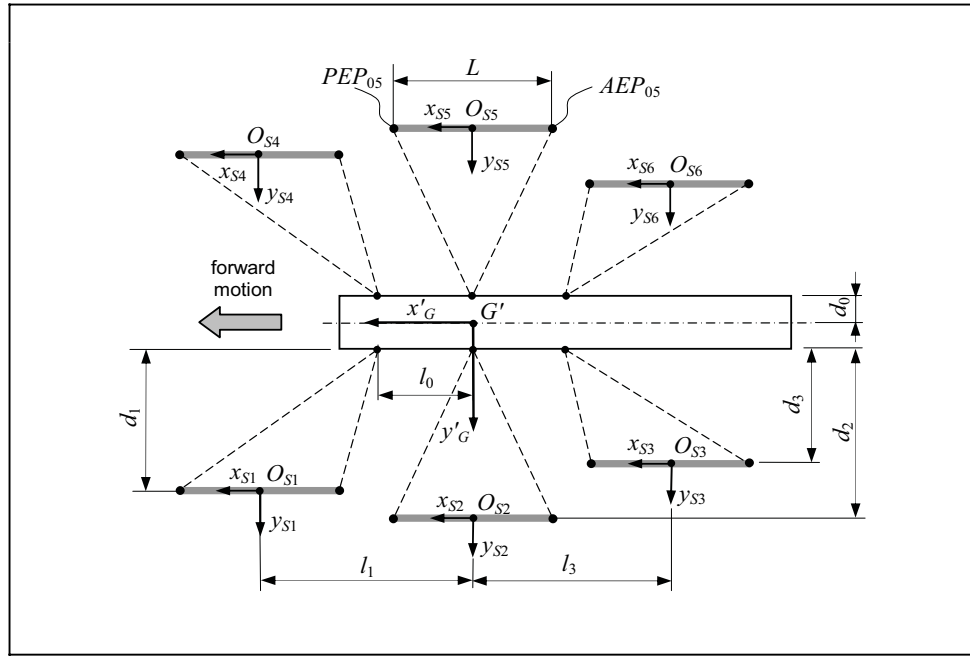


Fig. 1. Sketch and sizes of the stick insect: $d_1 = 18$ mm, $d_2 = 20$ mm, $d_3 = 15$ mm, $l_1 = l_3 = 24$ mm, $L = 20$ mm, $d_0 = 5$ mm, $l_0 = 20$ mm

3. Leg mechanism

A three-revolute (3R) kinematic chain has been chosen for each leg mechanism in order to mimic the leg structure of the stick insect through the coxa, femur and tibia links, as shown in Fig. 2.

A direct kinematic analysis of each leg mechanism is formulated between the moving frame O_{Ti} ($x_{Ti} \ y_{Ti} \ z_{Ti}$) of the tibia link and the frame O_{0i} ($x_{0i} \ y_{0i} \ z_{0i}$), which is considered as fixed frame before to be connected to the robot body, in order to formulate the overall kinematic model of the six-legged walking robot, as sketched in Fig. 3.

In particular, the overall transformation matrix \mathbf{M}_{Ti}^{0i} between the moving frame O_{Ti} ($x_{Ti} \ y_{Ti} \ z_{Ti}$) and the fixed frame O_{0i} ($x_{0i} \ y_{0i} \ z_{0i}$) is given by

$$\mathbf{M}_{Ti}^{0i}(\vartheta_{1i}, \vartheta_{2i}, \vartheta_{3i}) = \begin{bmatrix} r_{11} & r_{12} & r_{13} & {}^{0i}P_{ix} \\ r_{21} & r_{22} & r_{23} & {}^{0i}P_{iy} \\ r_{31} & r_{32} & r_{33} & {}^{0i}P_{iz} \\ 0 & 0 & 0 & 1 \end{bmatrix}. \quad (1)$$

This matrix is obtained as product between four transformation matrices, which relate the moving frame of the tibia link with the three typical reference frames on the revolute joints of the leg mechanism.

Thus, each entry r_{jk} of \mathbf{M}_{Ti}^{0i} for $j, k = 1, 2, 3$ and the Cartesian components of the position vector \mathbf{p}_i in frame O_{0i} ($x_{0i} \ y_{0i} \ z_{0i}$) are given by

$$\begin{aligned} r_{11} &= c\alpha_0 s\vartheta_{1i}; & r_{21} &= -c\vartheta_{1i}; & r_{31} &= -s\vartheta_{1i} s\alpha_0 \\ r_{12} &= s\vartheta_{3i} (s\alpha_0 s\vartheta_{2i} - c\alpha_0 c\vartheta_{1i} c\vartheta_{2i}) - c\vartheta_{3i} (c\alpha_0 c\vartheta_{1i} s\vartheta_{2i} + s\alpha_0 c\vartheta_{2i}) \\ r_{22} &= -s\vartheta_{1i} c\vartheta_{2i} s\vartheta_{3i} - s\vartheta_{1i} s\vartheta_{2i} c\vartheta_{3i} \\ r_{32} &= s\vartheta_{3i} (c\alpha_0 s\vartheta_{2i} + s\alpha_0 c\vartheta_{1i} c\vartheta_{2i}) + c\vartheta_{3i} (s\alpha_0 c\vartheta_{1i} s\vartheta_{2i} + c\alpha_0 c\vartheta_{2i}) \\ r_{13} &= c\vartheta_{3i} (c\alpha_0 c\vartheta_{1i} c\vartheta_{2i} - s\alpha_0 s\vartheta_{2i}) - s\vartheta_{3i} (c\alpha_0 c\vartheta_{1i} s\vartheta_{2i} + s\alpha_0 c\vartheta_{2i}) \\ r_{23} &= s\vartheta_{1i} c\vartheta_{2i} c\vartheta_{3i} - s\vartheta_{1i} s\vartheta_{2i} s\vartheta_{3i} \\ r_{33} &= -c\vartheta_{3i} (s\alpha_0 c\vartheta_{1i} c\vartheta_{2i} + c\alpha_0 s\vartheta_{2i}) + s\vartheta_{3i} (s\alpha_0 c\vartheta_{1i} s\vartheta_{2i} - c\alpha_0 c\vartheta_{2i}) \\ {}^{0i}P_{ix} &= [c\vartheta_{3i} (c\alpha_0 c\vartheta_{1i} c\vartheta_{2i} - s\alpha_0 s\vartheta_{2i}) - s\vartheta_{3i} (c\alpha_0 c\vartheta_{1i} s\vartheta_{2i} + s\alpha_0 c\vartheta_{2i})]a_3 + \\ &\quad +(c\alpha_0 c\vartheta_{1i} c\vartheta_{2i} - s\alpha_0 s\vartheta_{2i})a_2 + c\alpha_0 c\vartheta_{1i} a_1 \\ {}^{0i}P_{iy} &= a_3 (s\vartheta_{1i} c\vartheta_{2i} c\vartheta_{3i} - s\vartheta_{1i} s\vartheta_{2i} s\vartheta_{3i}) + (s\vartheta_{1i} c\vartheta_{2i})a_2 + s\vartheta_{1i} a_1 \\ {}^{0i}P_{iz} &= [-c\vartheta_{3i} (s\alpha_0 c\vartheta_{1i} c\vartheta_{2i} + c\alpha_0 s\vartheta_{2i}) + s\vartheta_{3i} (s\alpha_0 c\vartheta_{1i} s\vartheta_{2i} - c\alpha_0 c\vartheta_{2i})]a_3 + \\ &\quad -(s\alpha_0 c\vartheta_{1i} c\vartheta_{2i} - c\alpha_0 s\vartheta_{2i})a_2 - s\alpha_0 c\vartheta_{1i} a_1 \end{aligned} \quad (2)$$

where ϑ_{1i} , ϑ_{2i} and ϑ_{3i} are the variable joint angles of each leg mechanism ($i = 1, \dots, 6$), α_0 is the angle of the first joint axis with the axis z_{0i} , and a_1 , a_2 and a_3 are the lengths of the coxa, femur and tibia links, respectively.

The inverse kinematic analysis of the leg mechanism is formulated through an algebraic approach. Thus, when the Cartesian components of the position vector \mathbf{p}_i are given in the frame O_{Fi} ($x_{Fi} y_{Fi} z_{Fi}$), the variable joint angles ϑ_{1i} , ϑ_{2i} and ϑ_{3i} ($i = 1, \dots, 6$) can be expressed as

$$\vartheta_{1i} = \text{atan2}(\overset{F_i}{p}_{iy}, \overset{F_i}{p}_{ix}) \quad (3)$$

and

$$\vartheta_{3i} = \text{atan2}(s\vartheta_{3i}, c\vartheta_{3i}), \quad (4)$$

where

$$c\vartheta_{3i} = \frac{(\overset{F_i}{p}_{ix})^2 + (\overset{F_i}{p}_{iy})^2 + (\overset{F_i}{p}_{iz})^2 + a_1^2 - 2a_1\sqrt{(\overset{F_i}{p}_{ix})^2 + (\overset{F_i}{p}_{iy})^2} - a_2^2 - a_3^2}{2a_2a_3}, \quad (5)$$

$$s\vartheta_{3i} = \pm\sqrt{1 - c^2\vartheta_{3i}}$$

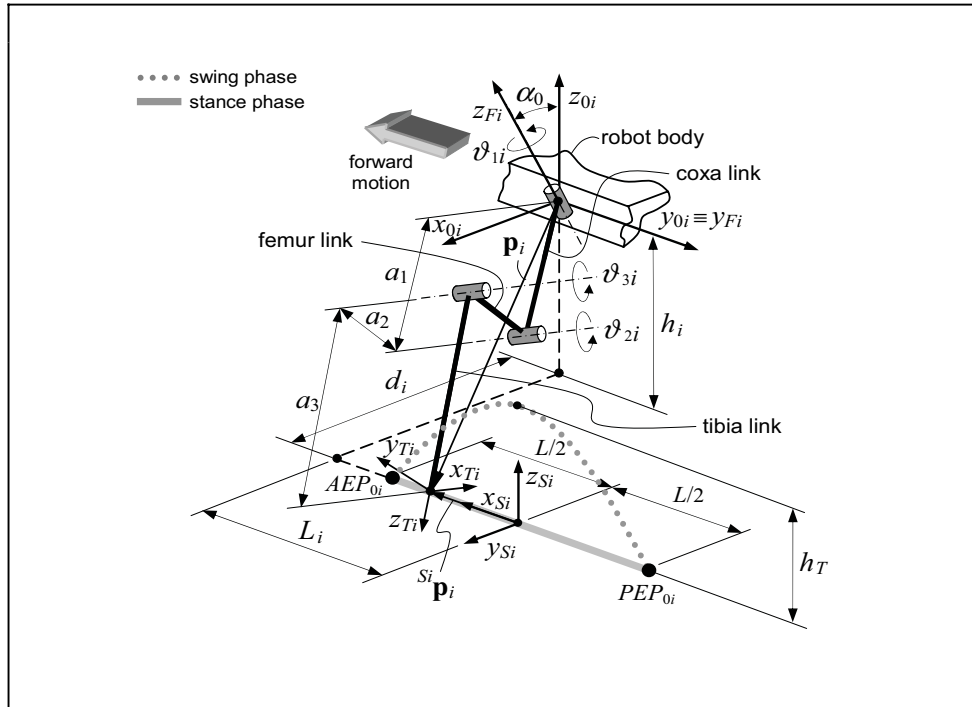


Fig. 2. A 3R leg mechanism of the six-legged walking robot

and, in turn, by

$$\vartheta_{2i} = \text{atan2}(\sin \vartheta_{2i}, \cos \vartheta_{2i}), \quad (6)$$

where

$$\begin{aligned} \sin \vartheta_{2i} &= -\frac{a_3 \sin \vartheta_{3i} \left(\sqrt{(\overset{F_i}{p}_{ix})^2 + (\overset{F_i}{p}_{iy})^2} \right) + \overset{F_i}{p}_{iz} (a_2 + a_3 \cos \vartheta_{3i})}{a_2^2 + a_3^2 + 2a_2 a_3 \cos \vartheta_{3i}}. \\ \cos \vartheta_{2i} &= -\frac{\overset{F_i}{p}_{iz} + \sin \vartheta_{2i} (a_2 + a_3 \cos \vartheta_{3i})}{a_3 \sin \vartheta_{3i}} \end{aligned} \quad (7)$$

Therefore, the Eqs. (1-7) let to formulate the overall kinematic model of the six-legged walking robot, as proposed in the following.

4. Kinematic model of the six-legged walking robot

Referring to Figs. 2 and 3, the kinematic model of a six-legged walking robot is formulated through a direct kinematic analysis between the moving frame O_{Ti} (x_{Ti} y_{Ti} z_{Ti}) of the tibia link and the inertia frame O (X Y Z).

In general, a six-legged walking robot has 24 d.o.f.s, where 18 d.o.f.s are given by ϑ_{1i} , ϑ_{2i} and ϑ_{3i} ($i = 1, \dots, 6$) for the six 3R leg mechanisms and 6 d.o.f.s are given by the robot body, which are reduced in this case at only 1 d.o.f. that is given by X_G in order to consider the pure translation of the robot body along the X -axis.

Thus, the equation of motion $X_G(t)$ of the robot body is assigned as input of the proposed algorithm, while $\vartheta_{1i}(t)$, $\vartheta_{2i}(t)$ and $\vartheta_{3i}(t)$ for $i = 1, \dots, 6$ are expressed through an inverse kinematic analysis of the six 3R leg mechanisms when the equation of motion of each leg tip is given and the trajectory shape of each leg tip during the swing phase is assigned.

In particular, the transformation matrix \mathbf{M}_G of the frame G (x_G y_G z_G) on the robot body with respect to the inertia frame O (X Y Z) is expressed as

$$\mathbf{M}_G(X_G) = \begin{bmatrix} 1 & 0 & 0 & p_{GX} \\ 0 & 1 & 0 & p_{GY} \\ 0 & 0 & 1 & p_{GZ} \\ 0 & 0 & 0 & 1 \end{bmatrix}, \quad (8)$$

where $p_{GX} = X_G$, $p_{GY} = 0$ and $p_{GZ} = h_G$.

The transformation matrix \mathbf{M}_{Bi}^G of the frame O_{Bi} (x_{Bi} y_{Bi} z_{Bi}) on the robot body with respect to the frame G (x_G y_G z_G) is expressed by

$$\mathbf{M}_{Bi}^G = \begin{cases} \begin{bmatrix} 0 & 1 & 0 & d_0 \\ -1 & 0 & 0 & l_i \\ 0 & 0 & 1 & 0 \\ 0 & 0 & 0 & 1 \end{bmatrix} & \text{for } i = 1, 2, 3 \\ \begin{bmatrix} 0 & -1 & 0 & d_0 \\ 1 & 0 & 0 & -l_i \\ 0 & 0 & 1 & 0 \\ 0 & 0 & 0 & 1 \end{bmatrix} & \text{for } i = 4, 5, 6 \end{cases} \quad (9)$$

where $l_1 = l_4 = -l_0$, $l_2 = l_5 = 0$, $l_3 = l_6 = l_0$.

Therefore, the direct kinematic function of the walking robot is given by

$$\mathbf{M}_{Ti}(X_G, \vartheta_{1i}, \vartheta_{2i}, \vartheta_{3i}) = \mathbf{M}_G(X_G) \mathbf{M}_{Bi}^G \mathbf{M}_{0i}^{Bi} \mathbf{M}_{Ti}^{0i}(\vartheta_{1i}, \vartheta_{2i}, \vartheta_{3i}) \quad (10)$$

where $\mathbf{M}_{0i}^{Bi} = \mathbf{I}$, being \mathbf{I} the identity matrix.

The joint angles of the leg mechanisms are obtained through an inverse kinematic analysis. In particular, the position vector ${}^{Si}\mathbf{p}_i(t)$ of each leg tip in the frame O_{Si} (x_{Si} y_{Si} z_{Si}), as shown in Fig.2, is expressed in the next section along with a detailed motion analysis of the leg tip. Moreover, the transformation matrix \mathbf{M}_{Si}^{Bi} is given by

$$\mathbf{M}_{Si}^{Bi} = \begin{cases} \begin{bmatrix} 0 & -1 & 0 & L_i \\ 1 & 0 & 0 & d_i \\ 0 & 0 & 1 & -h_i \\ 0 & 0 & 0 & 1 \end{bmatrix} & \text{for } i = 1, 2, 3 \\ \begin{bmatrix} 0 & 1 & 0 & L_{i-3} \\ -1 & 0 & 0 & -d_{i-3} \\ 0 & 0 & 1 & -h_i \\ 0 & 0 & 0 & 1 \end{bmatrix} & \text{for } i = 4, 5, 6 \end{cases} \quad (11)$$

where $L_1 = l_1 - l_0$, $L_2 = 0$ and $L_3 = l_3 - l_0$ with L_i shown in Fig.2.

Finally, the position of each leg tip in the frame O_{Fi} (x_{Fi} y_{Fi} z_{Fi}) is given by

$${}^{Fi}\mathbf{p}_i(t) = \mathbf{M}_{0i}^{Fi} \mathbf{M}_{Bi}^{0i} \mathbf{M}_{Si}^{Bi} {}^{Si}\mathbf{p}_i(t) \quad (12)$$

where the matrix \mathbf{M}_{0i}^{Fi} can be easily obtained by knowing the angle α_0 .

Therefore, substituting the Cartesian components of ${}^F_i \mathbf{p}_i(t)$ in Eqs. (3), (5) and (7), the joint angles ϑ_{1i} , ϑ_{2i} and ϑ_{3i} ($i = 1, \dots, 6$) can be obtained.

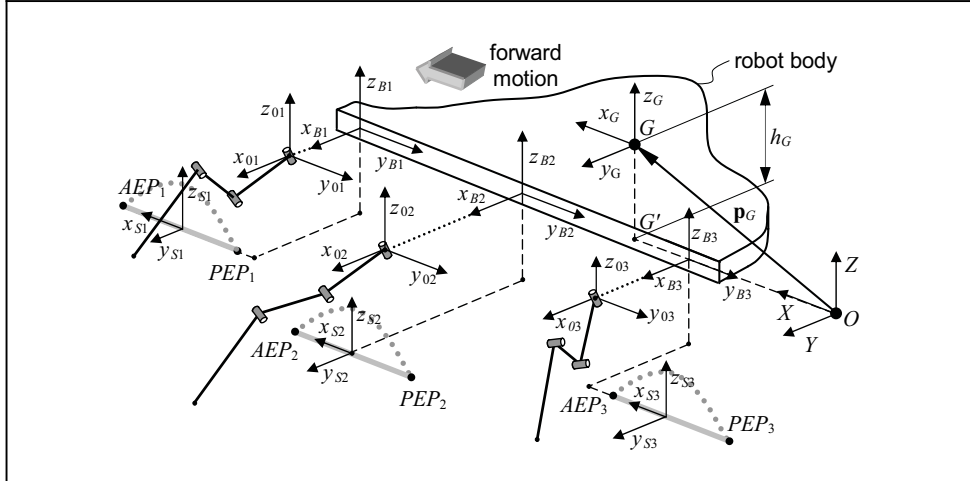


Fig. 3. Kinematic scheme of the six-legged walking robot

5. Motion analysis of the leg tip

The gait of the robot is obtained by a suitable coordination of each leg tip, which is fundamental to ensure the static stability of the robot during the walking. Thus, a typical motion of each leg tip has to be imposed through the position vector ${}^{Si} \mathbf{p}_i(t)$, even if a variable gait of the robot can be obtained according to the imposed speed of the robot body.

Referring to Figs. 2 to 4, the position vector ${}^{Si} \mathbf{p}_i(t)$ of each leg tip can be expressed as

$${}^{Si} \mathbf{p}_i(t) = \begin{bmatrix} {}^{Si} p_{ix} & {}^{Si} p_{iy} & {}^{Si} p_{iz} & 1 \end{bmatrix}^T \quad (13)$$

in the local frame O_{Si} (x_{Si} y_{Si} z_{Si}) for $i = 1, \dots, 6$, which is considered as attached and moving with the robot body.

Referring to Fig. 4, the x -coordinate ${}^{Si} p_{ix}$ of vector ${}^{Si} \mathbf{p}_i(t)$ is given by the following system of difference equations

$${}^{Si} p_{ix}(t + \Delta t) = \begin{cases} p_{ix}(t) - V_r \Delta t & \text{for } s_i(t) = 1 \\ p_{ix}(t) + V_p \Delta t & \text{for } s_i(t) = 0 \end{cases} \quad (14)$$

where V_r is the velocity of the tip of each leg mechanism during the retraction motion of the stance phase, even defined power stroke, since producing the motion of the robot body, and V_p is the velocity along the robot body of the tip of each leg mechanism during the protraction motion of the swing phase, even defined return stroke, since producing the forward motion of the leg mechanism.

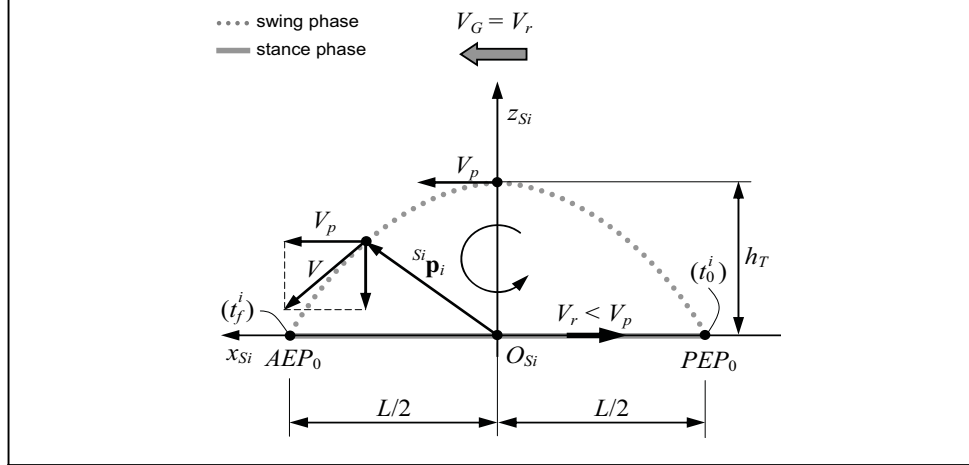


Fig. 4. Trajectory and velocities of the tip of each leg mechanism during the stance and swing phases

Parameter s_i defines the state of the i -th leg, which is equal to 1 for the retraction state, or stance phase, and equal to 0 for the protraction state, or swing phase.

Both velocities V_p and V_r are supposed to be constant and identical for all legs, for which the speed V_G of the center of mass of the robot body is equal to V_r because of the relative motion. In fact, during the stance phase (power stroke), each tip leg moves back with velocity V_r with respect to the robot body and, consequentially, this moves ahead with the same velocity. Thus, the function ${}^{S_i} p_{ix}(t)$ of Eq. (2) for $i = 1, \dots, 6$ is linear periodic function. Moreover, it is quite clear that the static stability of the six-legged walking robot is obtained only when $V_r (=V_G) < V_p$, because the robot body cannot move forward faster than its legs move in the same direction during the swing phase. Likewise, ${}^{S_i} p_{iy}$ is equal to zero in order to obtain a vertical planar trajectory, while ${}^{S_i} p_{iz}$ is given by

$${}^{S_i} p_{iz}(t) = \begin{cases} 0 & \text{for } s_i(t) = 1 \\ h_T \sin\left(\pi \frac{t - t_0^i}{t_f^i - t_0^i}\right) & \text{for } s_i(t) = 0 \end{cases} \quad (15)$$

where h_T is the amplitude of the sinusoid and time t is the general instant, while t_0^i and t_f^i are the starting and ending times of the swing phase, respectively.

Times t_0^i and t_f^i take into account the mechanism of the leg coordination, which give a suitable variation of AEP_i and PEP_i in order to ensure the static stability.

Thus, referring to the time diagrams of V_G in Fig. 5, the time diagrams of Figs. 6 to 8 have been obtained. In particular, Fig. 5 shows the time diagrams of the robot speeds $V_G = 0.05, 0.1, 0.5$ and 0.9 mm/s for the case of constant acceleration $a = 0.002$ mm/s². Thus, the transient periods $t = 25, 50, 250$ and 450 s for the speeds $V_G = 0.05, 0.1, 0.5$ and 0.9 mm/s of the robot body are obtained respectively before to reach the steady-state condition at

constant speed. The time diagrams of Figs. 6 to 8 show the horizontal x -displacement, the x -component of the velocity, the vertical z -displacement, the z -component of the velocity, the magnitude of the velocity and the trajectory of the leg tip 1 (front left leg) of the six-legged walking robot. Thus, before to analyze in depth the time diagrams of Figs. 6 to 8, it may be useful to refer to the motion analysis of the leg tip and to remind that the protraction speed V_p along the axis of the robot body has been assigned as constant and equal to 1 mm/s for the swing phase of the leg tip. In other words, only the retraction speed V_r can be changed since related and equal to the robot speed V_G , which is assigned as input data. Consequently, the range time during the stance phase between two consecutive steps of each leg can vary in significant way because of the different imposed speeds $V_r = V_G$, while the time range to perform the swing phase of each leg is almost the same because of the same speed V_p and similar overall x -displacements.

In particular, Fig. 6 show computer simulations between the time range 200 - 340 s, which is after the transient periods of 25 and 50 s for $V_G = 0.05$ and 0.1 mm/s, respectively.

Thus, both x -component of the velocity, protraction speed $V_p = 1$ mm/s and retraction speed $V_r = V_G = 0.05$ and 0.1 mm/s, are constant versus time. Instead, Figs. 7 and 8 show two computer simulations between the time ranges of 0 - 400 s and 200 - 600 s, which are greater than the transient periods of 250 and 450 s for the robot speeds V_G of 0.5 and 0.9 mm/s, respectively. Thus, the transient behavior of the velocities is also shown at the constant acceleration of 0.002 mm/s². In fact, during these time ranges of 250 and 450 s, the protraction speed V_p is always constant and equal to 1 mm/s, while the retraction speed V_r varies linearly according to the constant acceleration, before to reach the steady-state condition and to equalize the speed V_G of the robot body. The same effect is also shown by the time diagrams of Figs. 7e and 8e, which show the magnitude of the velocity.

Moreover, single loop trajectories are shown in the simulations of Figs. 6e and 6m, because one step only is performed by the leg mechanism 1, while multi-loop trajectories are shown in the simulations of Figs. 7f and 8f, because 3 (three) and 7 (seven) steps are performed by the leg mechanism 1, respectively. The variation of the step length is also evident in Figs. 7f and 8f because of the influence mechanisms for the leg coordination.

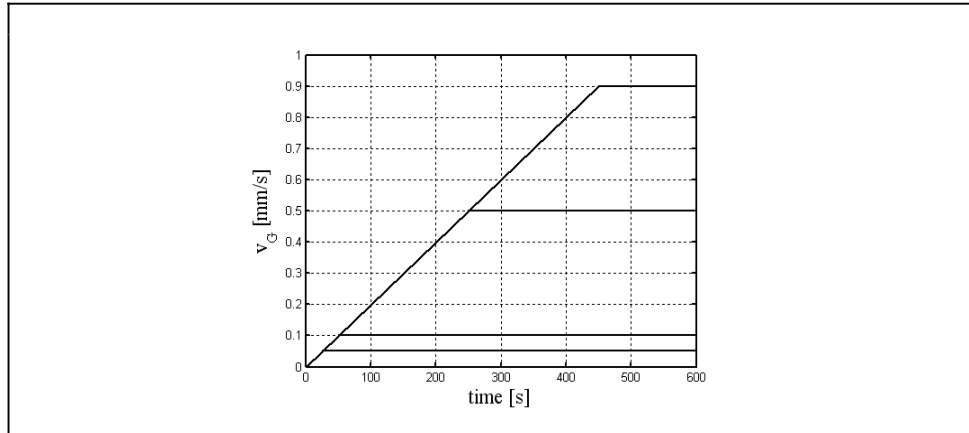


Fig. 5. Time diagrams of the robot body speed for a constant acceleration $a = 0.002$ mm/s² and $V_G = 0.05, 0.1, 0.5$ and 0.9 mm/s

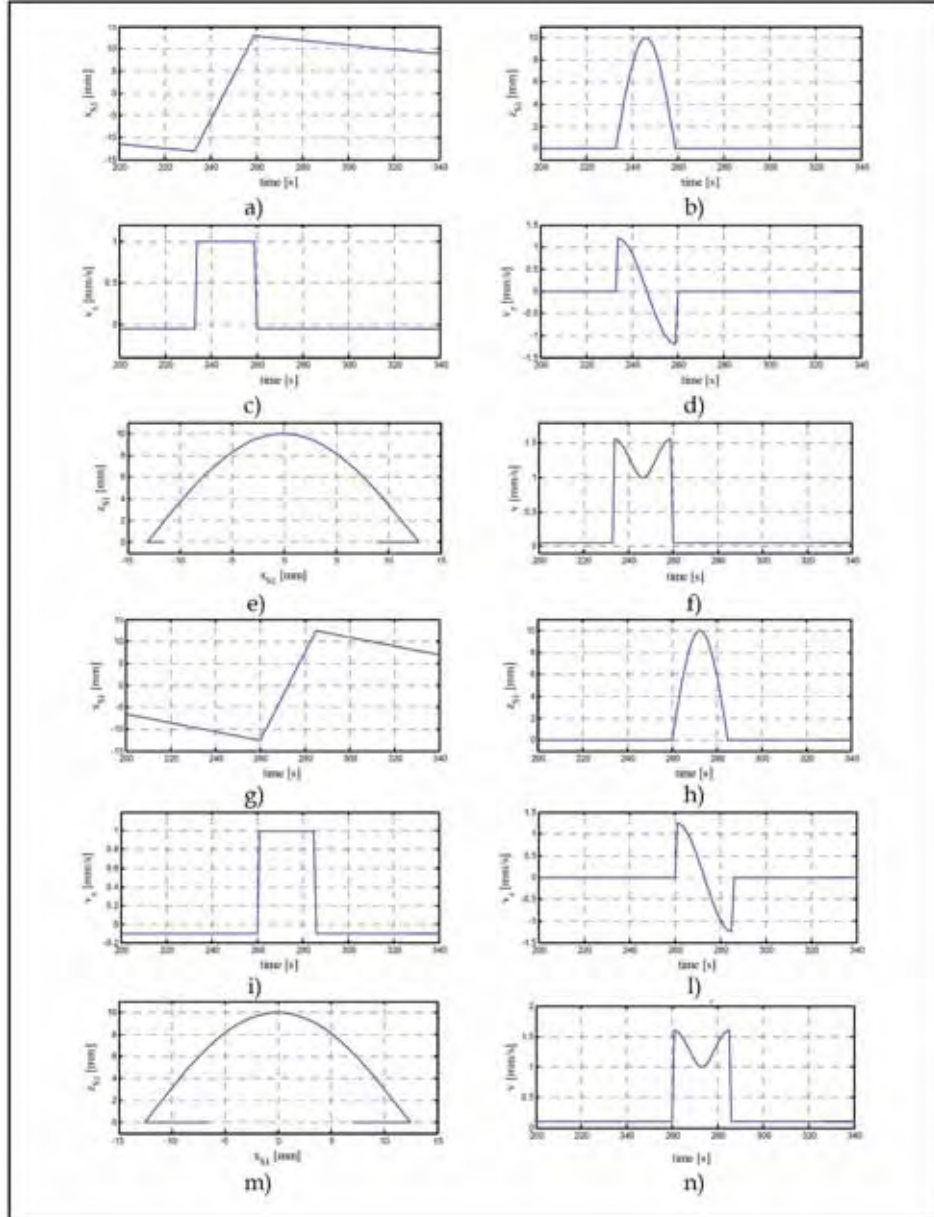


Fig. 6. Computer simulations for the motion analysis of the leg tip of a six-legged walking robot when $V_G = 0.05$ and 0.1 [mm/s]: a) and g) horizontal x -displacement; b) and h) vertical z -displacement; c) and i) x -component of the velocity; d) and l) z -component of the velocity; e) and m) planar trajectory in the xz -plane; f) and n) magnitude of the velocity

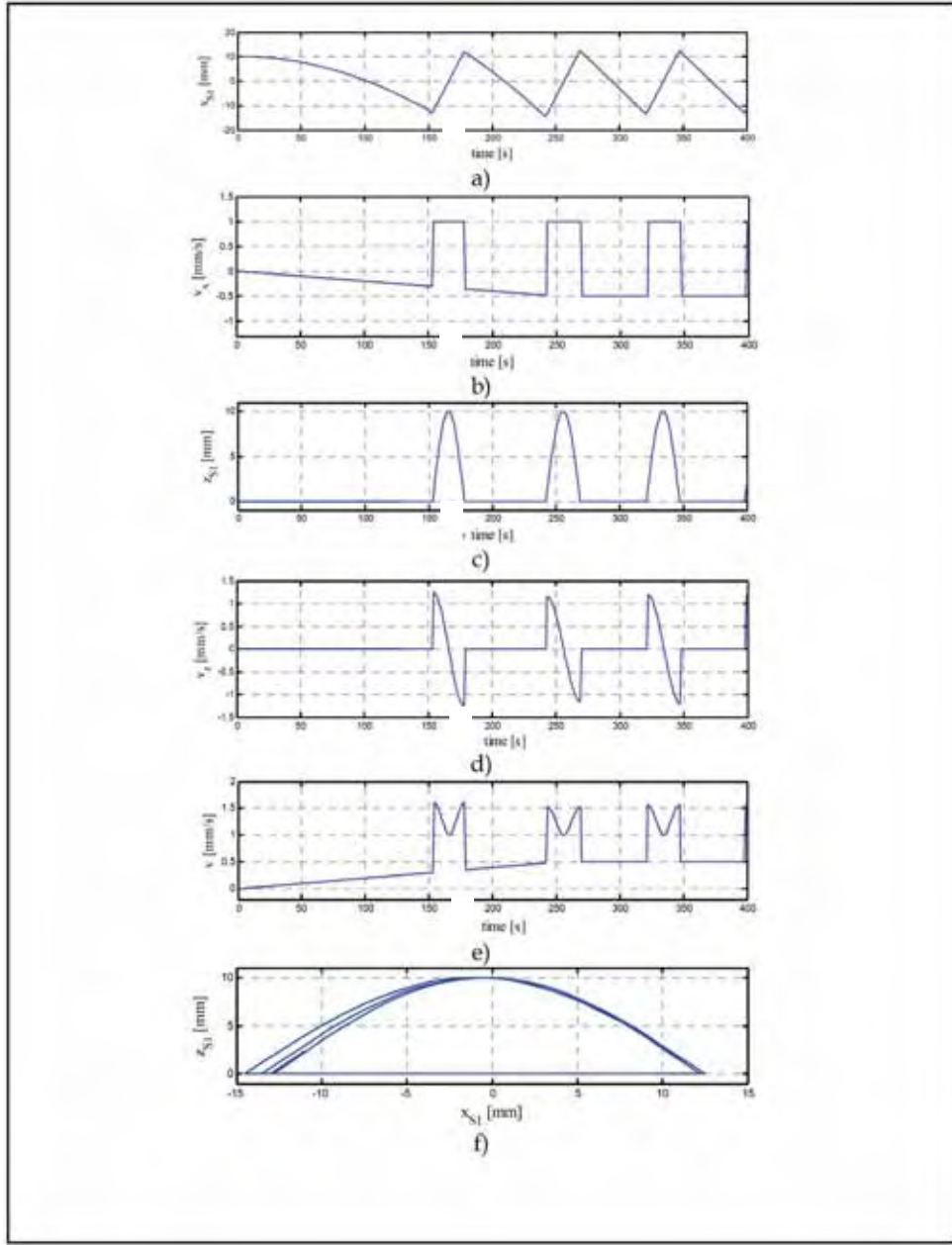


Fig. 7. Computer simulations within the time range 0 - 400 s for the motion analysis of the leg tip when $V_G = 0.5$ [mm/s]: a) horizontal x -displacement; b) x -component of the velocity; c) vertical z -displacement; d) z -component of the velocity; e) magnitude of the velocity; f) planar trajectory in the xz -plane

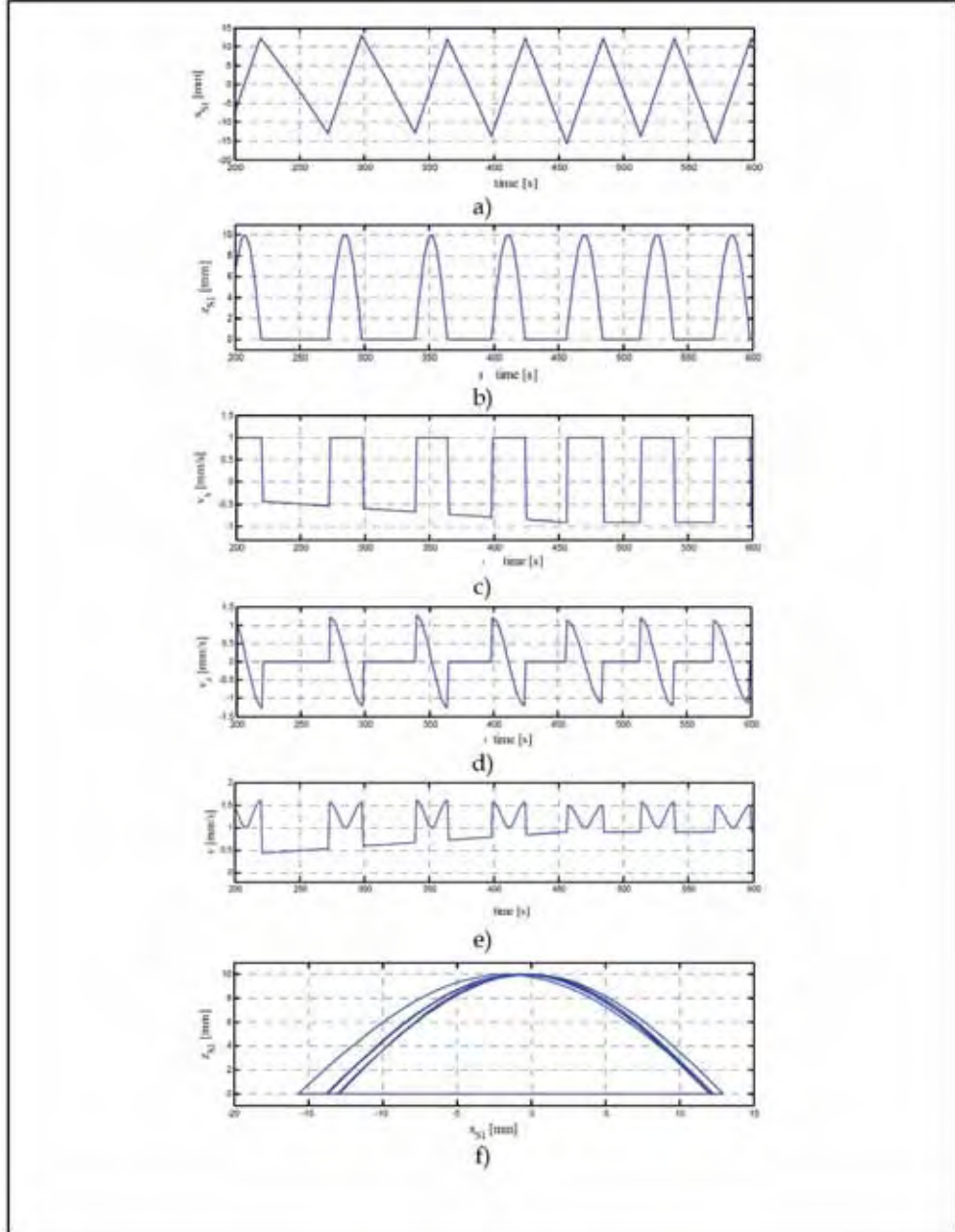


Fig. 8. Computer simulations within the time range 200-600 s for the motion analysis of the leg tip when $V_G = 0.9$ [mm/s]: a) horizontal x -displacement; b) x -component of the velocity; c) vertical z -displacement; d) z -component of the velocity; e) magnitude of the velocity; f) planar trajectory in the xz -plane

6. Gait analysis

A suitable overall algorithm has been formulated as based on the kinematic model of the six-legged walking robot and on the leg tip motion of each leg mechanism. This algorithm has been implemented in a Matlab program in order to analyze the absolute gait of the six-legged walking robot, which mimics the behavior of the stick insect, for different speeds of the robot body. Thus, the absolute gait of the robot is analyzed by referring to the results of suitable computer simulations, which have been obtained by running the proposed algorithm. In particular, the results of three computer simulations are reported in the following in the form of time diagrams of the z and x -displacements of the tip of each leg mechanism. These three computer simulations have been obtained for three different input parameters in terms of speed and acceleration of the robot body.

The same constant acceleration $a = 0.002 \text{ mm/s}^2$ has been considered along with three different speeds $V_G = 0.05, 0.1$ and 0.9 mm/s of the center of mass of the robot body, as shown in the time diagram of Fig. 5. Of course, the transient time before to reach the steady-state condition is different for the three simulations because of the same acceleration which has been imposed. Moreover, the protraction speed V_p along the axis of the robot body has been assigned equal to 1 mm/s for the swing phase. Thus, only the retraction speed V_r of the tip of each leg mechanism is changed since related and equal to the speed V_G of the center of mass of the robot body. Consequently, the range time during the stance phase between two consecutive steps of each leg varies in significant way because of the different imposed speeds $V_r = V_G$, while the time range to perform the swing phase of each leg is almost the same because of the same speed V_p and similar overall x -displacements.

The time diagrams of the z and x -displacements of each leg of the six-legged walking robot are shown in Figs. 9 to 11, as obtained for $a = 0.002 \text{ mm/s}^2$ and $V_G = 0.05 \text{ mm/s}$. It is noteworthy that the maximum vertical stroke of the tip of each leg mechanism is always equal to 10 mm , while the maximum horizontal stroke is variable and different for the tip of each leg mechanism according to the leg coordination, which takes into account the static stability of the six-legged walking robot. However, these horizontal strokes of the tip of each leg mechanism are quite centered around 0 mm and similar to the nominal stroke $L = 24 \text{ mm}$, which is considered between the extreme positions AEP_0 and PEP_0 .

Moreover, the horizontal x -displacements are represented through liner periodic functions, where the slope of the line for the swing phase is constant and equal to the speed $V_p = 1 \text{ mm/s}$, while the slope of the line for the stance phase is variable according to the assigned speed V_G , as shown in Figs. 9, 10 and 11 for $V_G = 0.05, 0.1$ and 0.9 mm/s , respectively.

In particular, referring to Fig. 11, the slopes of both linear parts of the linear periodic function of the x -displacement are almost the same, as expected, because the protraction speed of 1 mm/s is almost equal to the retraction speed of 0.9 mm/s .

Moreover, three different gait typologies of the six-legged walking robot can be observed in the three simulations, which are represented in the diagrams of Figs. 9 to 11.

In particular, the simulation of Fig. 9 show a wave gait of the robot, which is typical at low speeds and that can be understood with the aid of the sketch of Fig. 12a. In fact, referring to the first peak of the diagram of leg 1 of Fig. 9, which takes place after 400 s and, thus, after the transient time before to reach the steady-state condition of 0.05 mm/s , the second leg to move is leg 5 and, then, leg 3. Thus, observing in sequence the peaks of the z -displacements of the six legs, after leg 3, it is the time of the leg 4 and, then, leg 2 in order to finish with leg 6, as sketched in Fig. 12a, before to restart the wave gait.

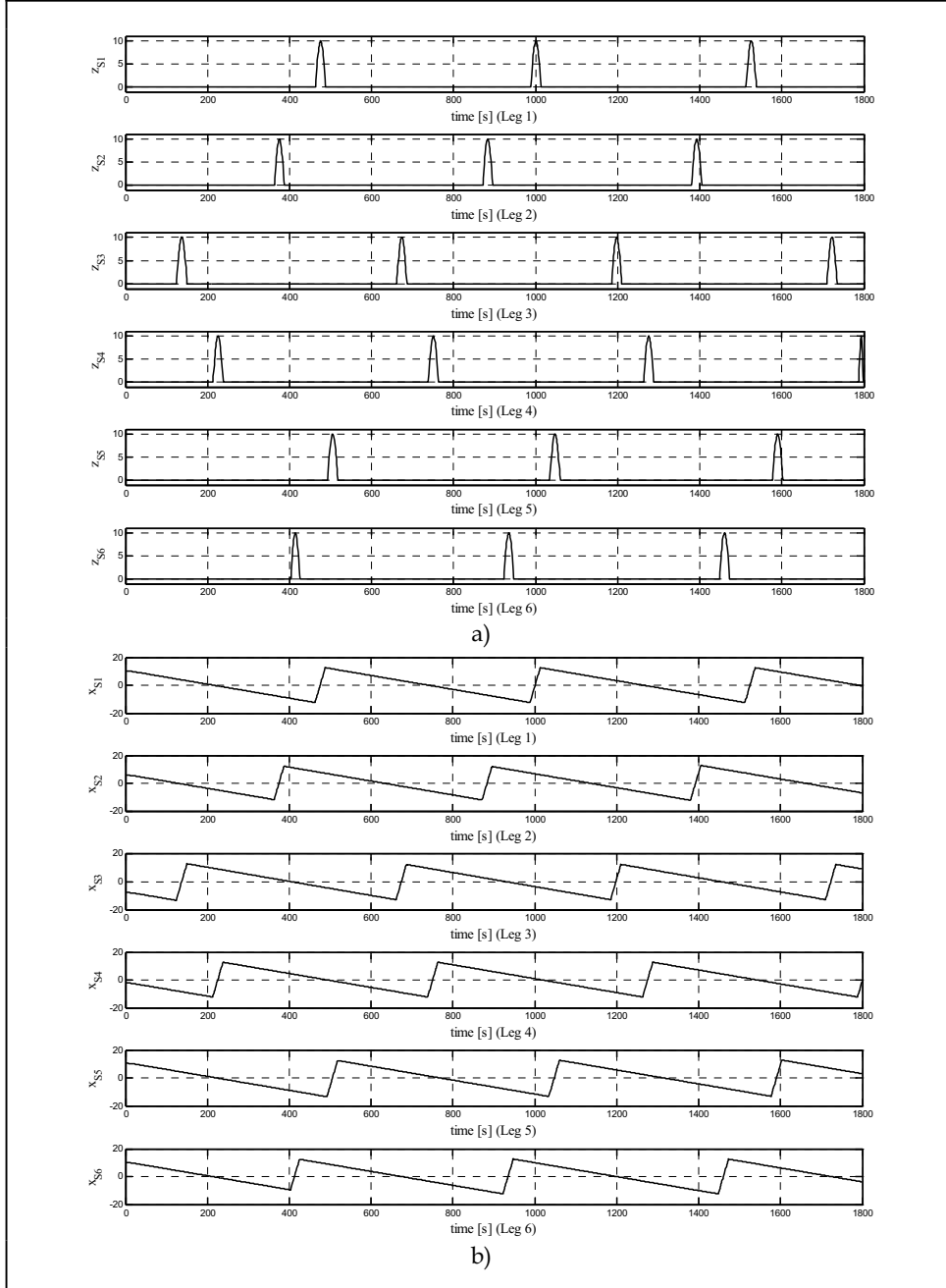


Fig. 9. Displacements of the leg tip for $V_G = 0.05 \text{ mm/s}$ and $a = 0.002 \text{ mm/s}^2$: a) vertical z -displacement; b) horizontal x -displacement

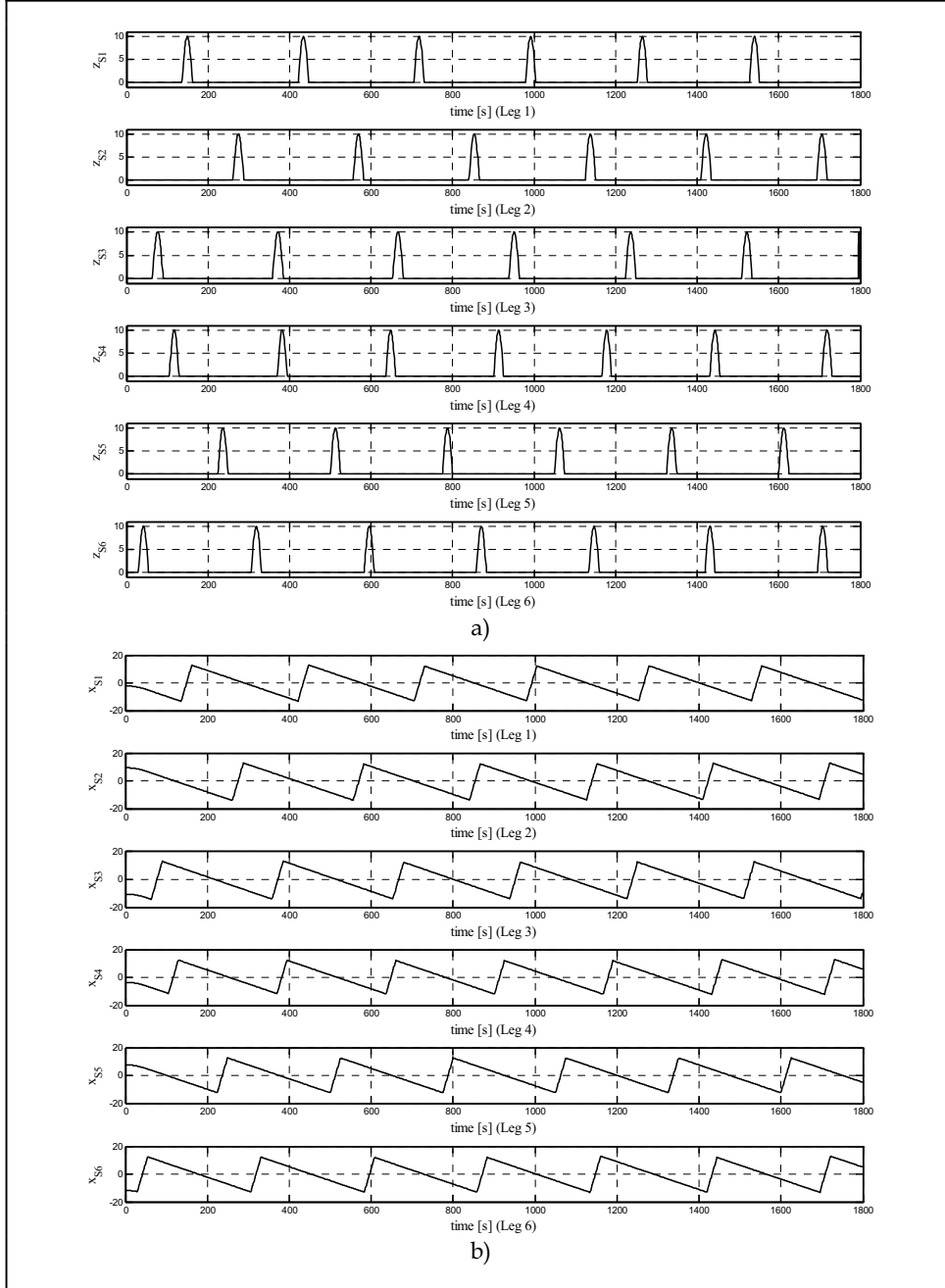


Fig. 10. Displacements of the leg tip for $V_G = 0.1 \text{ mm/s}$ and $a = 0.002 \text{ mm/s}^2$: a) vertical z -displacement; b) horizontal x -displacement

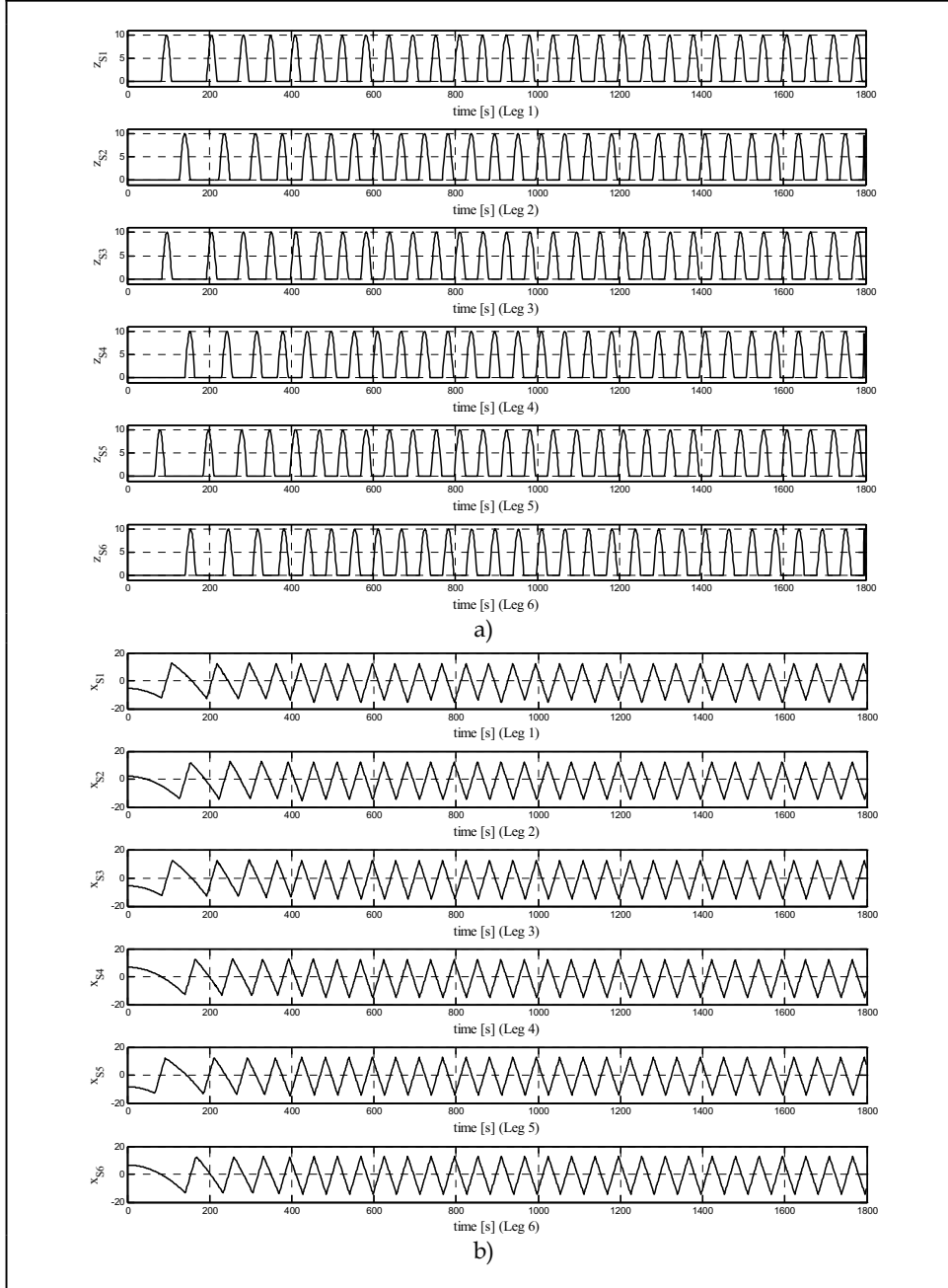


Fig. 11. Displacements of the leg tip for $V_G = 0.9 \text{ mm/s}$ and $a = 0.002 \text{ mm/s}^2$: a) vertical z -displacement; b) horizontal x -displacement

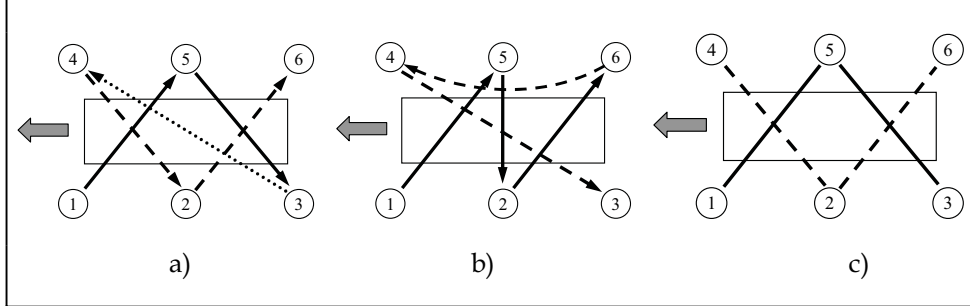


Fig. 12. Typical gaits of a six-legged walking robot: a) wave; b) transient gait; c) tripod

The simulation of Fig. 10 show the case of a particular gait of the robot, which is not wave and neither tripod, as it will be explained in the following. The sequence of the steps for this particular gait can be also understood with the aid of the sketch of Fig. 12b. This gait typology of the six-legged walking robot can be considered as a transient gait between the two extreme cases of wave and tripod gaits.

In fact, the tripod gait can be observed by referring to the time diagrams reported in Fig. 11. The tripod gait can be understood by analyzing the sequence of the peaks of the z -displacements for the tip of each leg mechanism and with the aid of the sketch of Fig. 12c. The tripod gait is typical at high speeds of the robot body. In fact, the simulation of Fig. 11 has been obtained for $V_G = 0.9$ mm/s, which is almost the maximum speed ($V_p = 1$ mm/s) reachable by the robot before to fall down because of the loss of the static stability. In particular, legs 1, 5 and 3 move together to perform a step and, then, legs 4, 2 and 6 move together to perform another step of the six-legged walking robot. Both steps are performed with a suitable phase shift according to the input speed.

7. Absolute gait simulation

This formulation has been implemented in a Matlab program in order to analyze the performances of a six-legged walking robot during the absolute gait along the X-axis of the inertia frame $O(XYZ)$.

Figures 13 and 14 show two significant simulations for the wave and tripod gaits, which have been obtained by running the proposed algorithm for $V_G = 0.05$ mm/s and $V_G = 0.9$ mm/s, respectively. In particular, six frames for each simulation are reported along with the inertia frame, which can be observed on the right side of each frame, as indicating the starting position of the robot. Thus, the robot moves toward the left side by performing a transient motion at constant acceleration $a = 0.002$ mm/ s^2 before to reach the steady-state condition with a constant speed.

In particular, for the wave gait cycle of Fig. 13, all leg tips are on the ground in Fig. 13a and leg tip 4 performs a swing phase in Fig. 13b before to touch the ground in Fig. 13c. Then, leg tip 2 performs a swing phase in Fig. 13d before to touch the ground in Fig. 13e and, finally, leg tip 6 performs a swing phase in Fig. 13f.

Similarly, for the tripod gait cycle of Fig. 14, all leg tips are on the ground in Figs. 14a, 14c and 14e. Leg tips 4-2-6 perform a swing phase in Fig. 14b and 14f between the swing phase performed by the leg tips 1-5-3 in Fig. 14d.

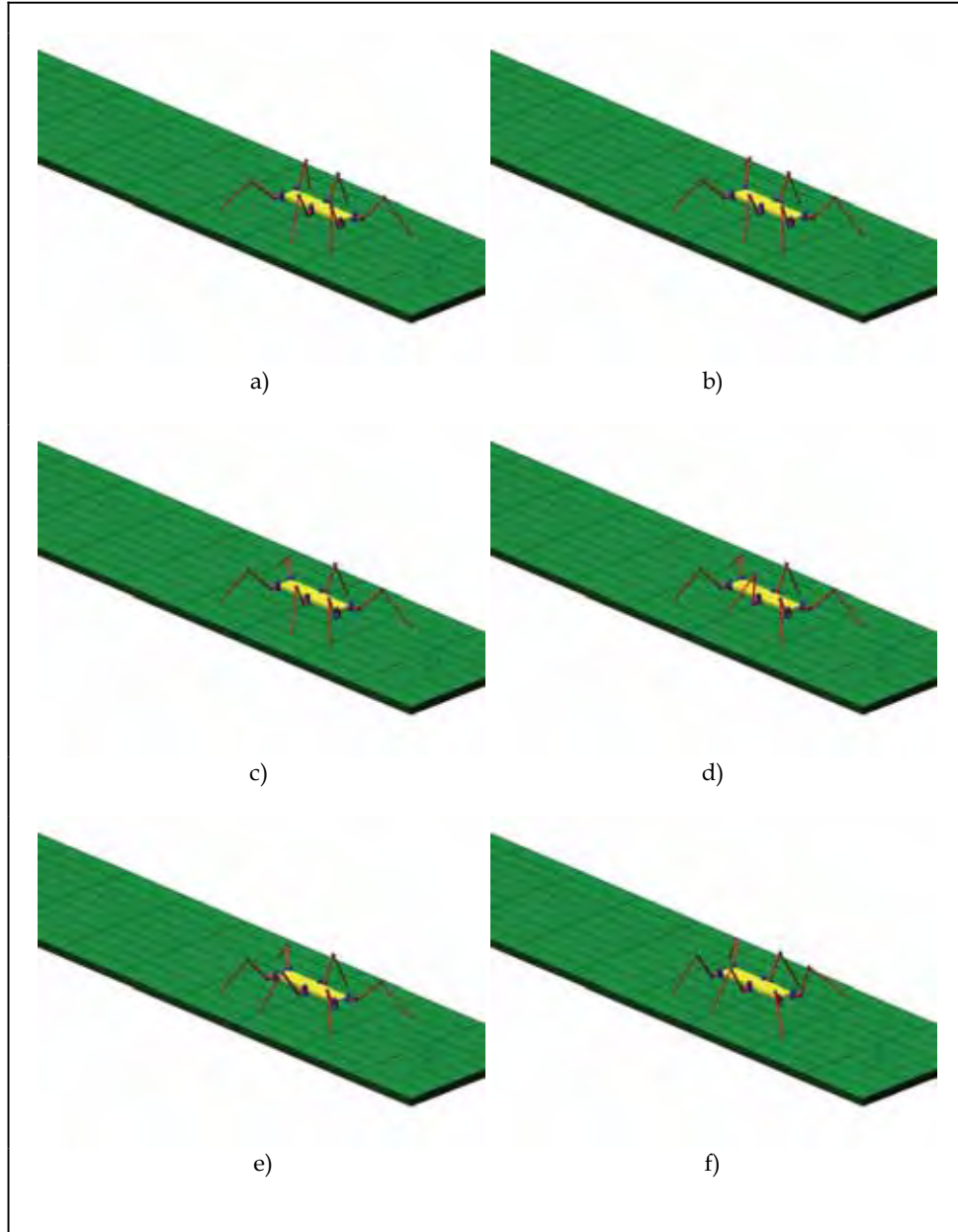


Fig. 13. Animation of a wave gait along the X-axis for $V_G = 0.05 \text{ mm/s}$ and $a = 0.002 \text{ mm/s}^2$:
a), c) and e), all leg tips are on the ground; b) leg tip 4 performs a swing phase; d) leg tip 2 performs a swing phase; f) leg tip 6 performs a swing phase

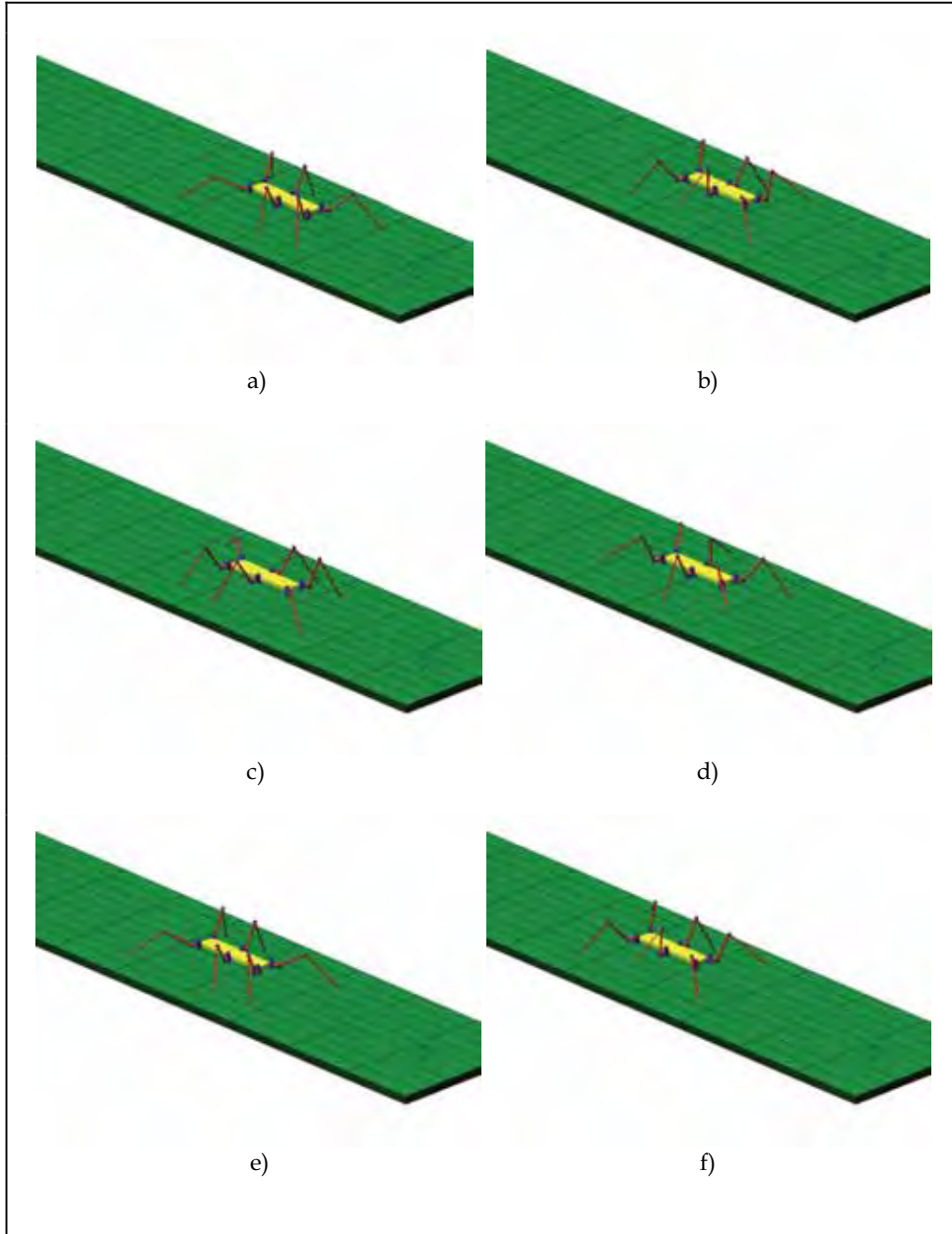


Fig. 14. Animation of a tripod gait along the X-axis for $V_G = 0.9 \text{ mm/s}$ and $a = 0.002 \text{ mm/s}^2$:
a), c) and e), all leg tips are on the ground; b) leg tips 4-2-6 perform a swing phase;
d) leg tips 1-5-3 perform a swing phase; f) leg tips 4-2-6 perform a swing phase

8. Conclusions

The mechanics and locomotion of six-legged walking robots has been analyzed by considering a simple "technical design", in which the biological inspiration is only given by the trivial observation that some insects use six legs to obtain a static walking, and considering a "biological design", in which we try to emulate, in every detail, the locomotion of a particular species of insect, as the "cockroach" or "stick" insects.

In particular, as example of the mathematical approach to analyze the mechanics and locomotion of six-legged walking robots, the kinematic model of a six-legged walking robot, which mimics the biological structure and locomotion of the stick insect, has been formulated according to the Cruse-based leg control system.

Thus, the direct kinematic analysis between the moving frame of the tibia link and the inertia frame that is fixed to the ground has been formulated for the six 3R leg mechanisms, where the joint angles have been expressed through an inverse kinematic analysis when the trajectory of each leg tip is given. This aspect has been considered in detail by analyzing the motion of each leg tip of the six-legged walking robot in the local frame, which is considered as attached and moving with the robot body.

Several computer simulations have been reported in the form of time diagrams of the horizontal and vertical displacements along with the horizontal and vertical components of the velocities for a chosen leg of the robot. Moreover, single and multi-loop trajectories of a leg tip have been shown for different speeds of the robot body, in order to put in evidence the effects of the Cruse-based leg control system, which ensures the static stability of the robot at different speeds by adjusting the step length of each leg during the walking.

Finally, the gait analysis and simulation of the six-legged walking robot, which mimics the locomotion of the stick insect, have been carried out by referring to suitable time diagrams of the z and x-displacements of the six legs, which have shown the extreme typologies of the wave and tripod gaits at low and high speeds of the robot body, respectively.

9. References

- Song, S.M. & Waldron, K.J., (1989). *Machines That Walk: the Adaptive Suspension Vehicle*, MIT Press, ISBN 0-262-19274-8, Cambridge, Massachusetts.
- Raibert, M.H., (1986). *Legged Robots That Balance*, MIT Press, ISBN 0-262-18117-7, Cambridge, Massachusetts.
- Delcomyn, F. & Nelson, M. E. (2000). Architectures for a biomimetic hexapod robot, *Robotics and Autonomous Systems*, Vol. 30, pp.5-15.
- Quinn, R. D., Nelson, G. M., Bachmann, R. J., Kingsley, D. A., Offi J. & Ritzmann R. E., (2001). Insect Designs for Improved Robot Mobility, *Proceedings of the 4th International Conference on Climbing and Walking Robots*, Berns and Dillmann (Eds), Professional Engineering Publisher, London, pp. 69-76.
- Espenschied, K.S., Quinn, R.D., Beer, R.D. & Chiel H.J., (1996). Biologically based distributed control and local reflexes improve rough terrain locomotion in a hexapod robot, *Robotics and Autonomous Systems*, Vol. 18, pp. 59-64.
- Cruse, H., (1990). What mechanisms coordinate leg movement in walking arthropods ?, *Trends in Neurosciences*, Vol. 13, pp. 15-21.
- Cruse, H. & Bartling, Ch., (1995). Movement of joint angles in the legs of a walking insect, *Carausius morosus*, *J. Insect Physiology*, Vol. 41 (9), pp.761-771.

- Frantsevich, F. & Cruse, H., (1997). The stick insect, *Obrimus asperrimus* (Phasmida, Bacillidae) walking on different surfaces, *J. of Insect Physiology*, Vol. 43 (5), pp.447-455.
- Cruse, H., Kindermann, T., Schumm, M., Dean, J. and Schmitz, J., (1998). Walknet - a biologically inspired network to control six-legged walking, *Neural Networks*, Vol.11, pp. 1435-1447.
- Cymbalyuk, G.S., Borisuk, R.M., Müller-Wilm, U. & Cruse, H., (1998). Oscillatory network controlling six-legged locomotion. Optimization of model parameters, *Neural Networks*, Vol. 11, pp. 1449-1460.
- Cruse, H., (2002). The functional sense of central oscillations in walking, *Biological Cybernetics*, Vol. 86, pp. 271-280.
- Volker, D., Schmitz, J. & Cruse, H., (2004). Behaviour-based modelling of hexapod locomotion: linking biology and technical application, *Arthropod Structure & Development*, Vol. 33, pp. 237-250.
- Dean, J., (1991). A model of leg coordination in the stick insect, *Carausius morosus*. I. Geometrical consideration of coordination mechanisms between adjacent legs. *Biological Cybernetics*, Vol. 64, pp. 393-402.
- Dean, J., (1991). A model of leg coordination in the stick insect, *Carausius morosus*. II. Description of the kinematic model and simulation of normal step patterns. *Biological Cybernetics*, Vol. 64, pp. 403-411.
- Dean, J., (1992). A model of leg coordination in the stick insect, *Carausius morosus*, III. Responses to perturbations of normal coordination, *Biological Cybernetics*, Vol. 66, pp. 335-343.
- Dean, J., (1992). A model of leg coordination in the stick insect, *Carausius morosus*, IV. Comparison of different forms of coordinating mechanisms, *Biological Cybernetics*, Vol. 66, pp. 345-355.
- Mueller-Wilm, U., Dean, J., Cruse, H., Weidermann, H.J., Eltze, J. & Pfeiffer, F., (1992). Kinematic model of a stick insect as an example of a six-legged walking system, *Adaptive Behavior*, Vol. 1 (2), pp. 155-169.
- Figliolini, G. & Ripa, V., (2005). Kinematic Model and Absolute Gait Simulation of a Six-Legged Walking Robot, In: *Climbing and Walking Robots*, Manuel A. Armada & Pablo González de Santos (Ed), pp. 889-896, Springer, ISBN 3-540-22992-6, Berlin.
- Figliolini, G., Rea, P. & Ripa, V., (2006). Analysis of the Wave and Tripod Gaits of a Six-Legged Walking Robot, *Proceedings of the 9th International Conference on Climbing and Walking Robots and Support Technologies for Mobile Machines*, pp. 115-122, Brussels, Belgium, September 2006.
- Figliolini, G., Rea, P. & Stan, S.D., (2006). Gait Analysis of a Six-Legged Walking Robot When a Leg Failure Occurs, *Proceedings of the 9th International Conference on Climbing and Walking Robots and Support Technologies for Mobile Machines*, pp. 276-283, Brussels, Belgium, September 2006.
- Figliolini, G., Stan, S.D. & Rea, P. (2007). Motion Analysis of the Leg Tip of a Six-Legged Walking Robot, *Proceedings of the 12th IFToMM World Congress*, Besançon (France), paper number 912.

Attitude and Steering Control of the Long Articulated Body Mobile Robot KORYU

Edwardo F. Fukushima and Shigeo Hirose
*Tokyo Institute of Technology
Tokyo, Japan*

1. Introduction

Many types of mobile robots have been considered so far in the robotics community, including wheeled, crawler track, and legged robots. Another class of robots composed of many articulations/segments connected in series, such as "Snake-like robots", "Train-like Robots" and "Multi-tailed vehicles/robots" has also been extensively studied. This configuration introduces advantageous characteristics such as high rough terrain adaptability and load capacity, among others. For instance, small articulated robots can tread through rubbles and be useful for inspection, search-and-rescue tasks, while larger and longer ones can be used for maintenance tasks and transportation of material, where normal vehicles cannot approach. Some ideas and proposal appeared in the literature, to build such big robots; many related studies concerning this configuration have been reported (Waldron, Kumar & Burkhardt, 1987; Commissariat A l'Energie Atomique, 1987; Burdick, Radford & Chirikjian, 1993; Tilbury, Sordalen & Bushnell, 1995; Shan and Koren, 1993; Nilsson, 1997; Migadis and Kyriakopoulos, 1997). However, very few real mechanical implementations have been reported.

An actual mechanical model of an "Articulated Body Mobile Robot" was introduced by Hirose & Morishima in 1988, and two mechanical models of articulated body mobile robot called KORYU (KR for short) have been developed and constructed, so far. KORYU was mainly developed for use in fire-fighting reconnaissance and inspection tasks inside nuclear reactors. However, highly terrain adaptive motions can also be achieved such as; 1) stair climbing, 2) passing over obstacles without touching them, 3) passing through meandering and narrow paths, 4) running over uneven terrain, and 5) using the body's degrees of freedom not only for "locomotion", but also for "manipulation". Hirose and Morishima (1990) performed some basic experimental evaluations using the first model KR-I (a 1/3 scale model compared to the second model KR-II, shown in Fig. 1(a)-(c)). Improved control strategies have been continuously studied in order to generate more energy efficient motions.

This chapter addresses two fundamental control strategies that are necessary for long articulated body mobile robots such as KORYU to perform the many inherent motion capabilities cited above. The control issue can be divided in two independent tasks, namely 1) Attitude Control and 2) Steering Control. The underlying concept for the presented

control methods are rather general and could be applied to different mechanical implementations. However, in order to give the reader better understanding of the control issues, the second mechanical model KR-II will be used as example for implementing such controls. For this reason, the mechanical implementation of KR-II will be first introduced, followed by the steering control and attitude control.

The authors believe that not only the financial issue, but the difficulty in the mechanical design and control has limited the progress in this area. However, the realization of this class of robots is still promising, so we expect this work to contribute to the understanding of the many control problems related to it.



Fig. 1. Articulated body mobile robot "KR-II", (first built in 1990, modified in 1997)

Total weight: 450kg, Height: 1.0m, Width: 0.48m, Wheel Diameter: 0.42m.

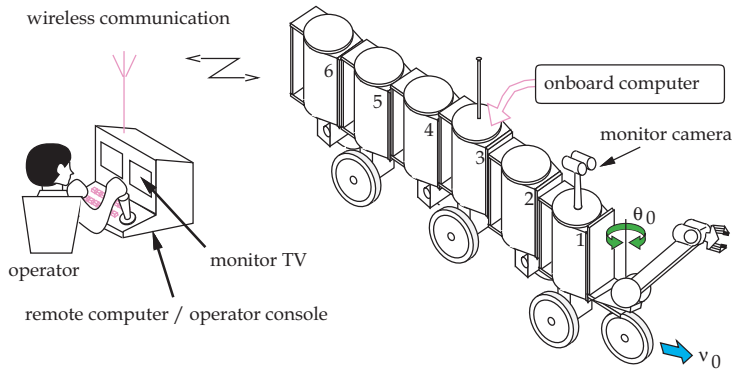


Fig. 2. KR-II is a totally self-contained system. A human operator commands only the foremost segment's steer angle and travelling velocity

2. Mechanical Configuration and Modelling of KR-II

KR-II is a totally self-contained robot, with batteries and controllers installed on-board, and remote controlled through a wireless modem. It is composed of cylindrical bodies numbered 1 to 6, and a manipulator in the foremost segment, numbered no. 0. The cylindrical bodies are in fact modular units we call a "unit segment" that can be easily detached mechanically and electrically from the adjacent segments, so the total system can be disassembled for transportation and easily assembled on-site.

The degrees of freedom (DOF) for these units can be divided in three distinct classes as shown in **Fig. 3**, say z axis, θ axis and s axis.

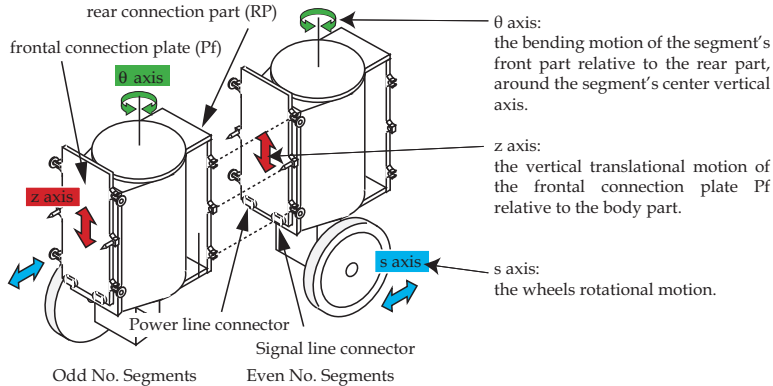


Fig. 3. KR-II's "unit segment" and its motion freedoms

2.1. Mechanical Details of the z axis

For a conventional translational motion mechanism, the output displacement developed at the front connection plate (P_f) is equal to the input displacement transmitted from the ball screw nut (B_N). A rack-and-pinion mechanism with two rack gears (G_R) and one pinion gear (G_T) as shown in Fig. (b), doubles the translational motion from the ball screw nut.

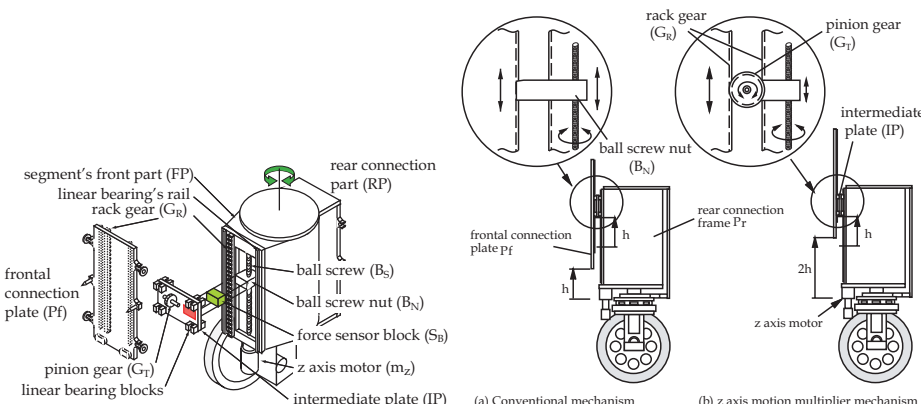


Fig. 4. KR-II's z axis mechanical details

2.2. Mechanical Details of the θ axis

The unit segments have another characteristic concerning the wheel's heading orientation. For mechanical simplification and weight reduction, a "1/2 angle mechanism" (**Fig. 5.**), which orients the wheel to half the bending angle of the θ axis was introduced. For this reason, wheel sideslips cannot be prevented during general manoeuvrings, but this

constraint does not degrade the steering motion of KR-II at all. In fact, previous work (Fukushima & Hirose, 1996) it has been shown that using the appropriate steering control method, the energy loss from wheel slippage can be minimized and good trajectory tracking performance achieved.

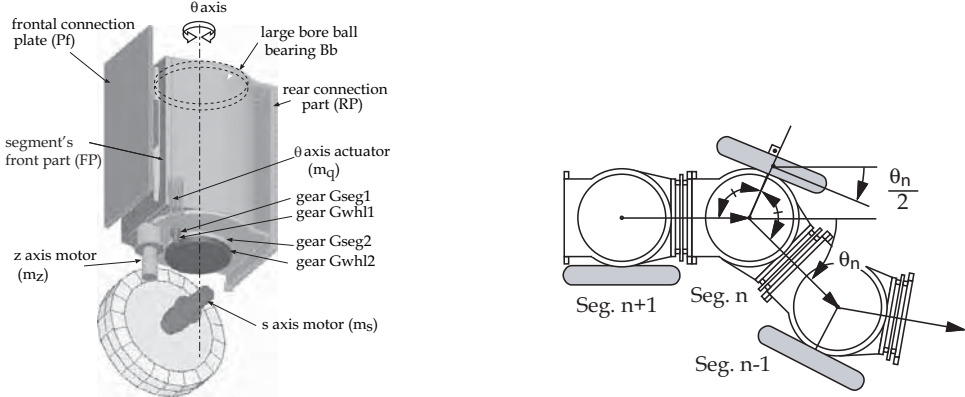


Fig. 5. KR-II's θ axis mechanical details. The "1/2 angle mechanism" orients the wheel to half the bending angle of the θ axis

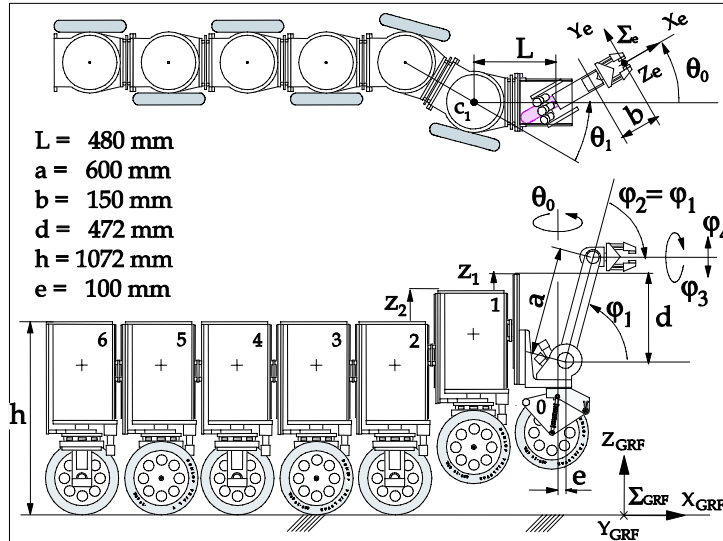


Fig. 6. Manipulator mechanism and degrees of freedom

2.3. Mechanical Details of the s axis

Each unit segment is equipped with one wheel, such that the odd numbered segments' wheels are arranged right-sided and the even segments' left-sided. This arrangement increases the rough terrain adaptability and decreases the total mechanical weight. As

mentioned in the Introduction, KR-II can pass over obstacles without touching them. In order to ensure static stability for these motions, we need a minimum of 6 basic unit segments connected in series, such that two segments can be lifted up at the same time without loosing stability and avoid contact with the obstacles.

2.4. Mechanical Details of the Front Manipulator

An extra connection plate Pf remains in the front part of the segment no. 1. We use it to connect a segment equipped with a manipulator and a wheel, aligned with the segment's center vertical axis, as shown in Fig. 6. The manipulator part is linked to the wheel so that the heading orientation coincides to it. This manipulator has only one independent degree of freedom in the arm part, say φ_1 . However, using the body's articulations and the motion of the wheels, a higher DOF manipulation tasks can be accomplished. Further details of manipulation are out of the scope of this chapter and will be omitted, but note that considering that the segment front part refers to the manipulator-wheel part, the segments no. 0's degrees of freedom that are used for steering control are the same as explained above, namely θ axis and s axis.

3. Steering Control Problem

3.1 Control variables

The segment's vertical axes (z-axes) are controlled to be always parallel to the gravitational force field, by an attitude control scheme that will be discussed later. As the attitude control works independently from the steering control, the control variables for the steering control can be modeled on the x-y plane as shown in Fig. 7. Nonetheless, this model is valid not only for locomotion on flat terrain, but also for locomotion on uneven terrain as well. The variables used to model KR-II are as follows:

- θ_n θ axis bending angle: the relative bending angle of segment no. n 's front part relative to the rear part.

$$\theta_n = \Theta_n - \Theta_{n+1}, \quad (n = 0 \sim 6) \quad (1)$$

- Θ_n Segment vector orientation: segment no. n 's front part orientation in the Global Reference Frame Σ_{GRF} . This orientation is the same as segment no. $(n-1)$'s rear part orientation. Note that Θ_7 is the orientation of segment no. 6's rear part.

- Φ_n Wheel heading orientation vector: segment no. n 's wheel heading orientation in the global reference frame. For the foremost segment $\Phi_0 = \Theta_0$.

$$\Phi_n = \Theta_n - \frac{\theta_n}{2} = \frac{\Theta_n + \Theta_{n+1}}{2}, \quad (n = 1 \sim 6) \quad (2)$$

- L Intersegment length: adjacent segments center to center distance. KR-II has constant length L = 0.48m for all segments.

- B Segment center to wheel distance: distance between the segment center to the wheel-ground contact point in the horizontal plane. For the basic unit segment of KR-II, $B=0.23m$, and for the segment no. 0, $B=0$.

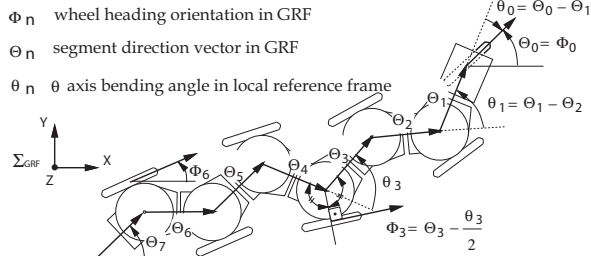


Fig. 7. KR's steering control variables

3.2 Steering Control Objectives

The main issue on KR's steering control is, given from a remote human operator the velocity and orientation commands for the foremost segment, to automatically generate joint commands for all the following segments, such that they follow the foremost segment's trajectory.

For KR's teleoperation scheme as shown in Fig. 2, a remote human operator sends steering control commands for the foremost segment only, namely velocity v_0 and heading orientation θ_0 , and the on-board computer calculates the joint commands for the following segments. Note that the bending angle of the manipulator-wheel part (segment no. 0) relative to the front part of the segment no. 1, i.e. θ_0 , is used as the command for changing the orientation of the foremost segment (i.e. segment no. 0). This is because θ_0 coincides with the angular displacement of the wheel displayed on the remote operator's monitor TV, having a camera set on segment no. 1's front part.

Concerning the control of KR-II's wheels (s -axes) and the bending angles between the segments (θ -axes), we have systematically investigated some basic steering control methods in previous work (Fukushima et al, 1995, 1996, 1998). The main criteria for evaluating the performance of each method were: i) trajectory tracking performance, ii) energy consumption performance and iii) amount of wheel sideslip. From these results, we demonstrated that for articulated body mobile robots with short intersegment lengths, e.g., the earlier snake-like robot ACM-III (Umetani & Hirose, 1974), a "Shift Control Method" which simply shifts the bending angle command from the foremost segment to the following segments, synchronized to the locomotion velocity can be effective.

However, for articulated mobile robots such as KR-II which has large intersegment length, this method introduces a large sideslip in the foremost segment's wheel, because the motion of the foremost segment is shifted to the next only after moving a certain distance, during which there is a difference between the foremost wheel's heading orientation and its actual motion direction. To attenuate this problem, two other methods were derived: 1) "Moving Average Shift Control", which takes the average value of the foremost segment's control angle θ_0 over the time to travel a distance L as the next segment command θ_1 and then shifts θ_1 to the following segments according to the moved distance, and 2) "Geometric

Trajectory Planning Method", which calculates all the θ axis bending angle commands from the geometric relationship that results when each segment center is considered to travel over a given desired trajectory. From the evaluation of these methods, the last one presented the best trajectory tracking performance and energy efficiency. This is because exact joint commands were calculated using equations in literal form. However, for a real-time implementation in the on-board computer, the second best method "Moving Average Shift Control" has been chosen. In reality, this method combined with a technique consisting of setting a small position control gain for each θ axis was considered the best steering control method for KR-II for some time.

For the s-axes, the so called "Body Velocity Control by Wheel Torque Compensation", in which the velocity of the body is controlled by equally distributed torques for all the wheels, presented the best performance in combination with any θ -axes steering method.

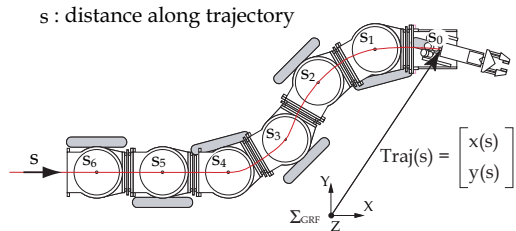


Fig. 8. Trajectory representation for the inertial reference frame method

3.3 The Inertial Reference Frame Steering Control Method

The "Inertial Reference Frame Method" introduced in this section can be considered as belonging to the same category as the "Geometric Trajectory Planning Method", in the way it is based on calculating the joint commands (θ -axes) from a trajectory described in an inertial reference frame. From a biomechanical point of view (Umetani and Hirose, 1974), the methods based on shift control that generate all the steering commands considering joint space variables only, are thought to be more suitable for controlling snake-like robots because it is improbable that joint commands generation in real snakes are performed considering inertial reference frame. However, as already demonstrated in previous work, the inertial reference frame based methods offers many advantages such as good trajectory tracking performance, energy efficiency and as will be demonstrated in the following sections, it can be easily extended for use in a "W-Shaped Configuration", which increases the stability of the robot for motion on uneven terrain. The only drawback of the method based on geometric calculation was the large computation time, which has been overcome by the method here explained. The basic algorithm is constructed by the following steps:

- Step 1.* Estimate the initial trajectory for the foremost segment (once at power-on)
- Step 2.* Update the trajectory moved by the foremost segment.
- Step 3.* Search each segment's center position over the trajectory.
- Step 4.* Calculate each segment's bending angle (θ_n)

Step 5. Repeat steps 2)~4).

This method is characterized by using the moved distance over the trajectory as a parameter for representing the trajectory in an inertial reference frame (as shown in Fig. 8), so that the position of the segments center s_{seg} can be tracked in a numerical fashion, by iteratively searching for the s_{seg} that satisfies the geometrical constraint between the segments (i.e., the intersegment length L is constant). Here are the details of each step.

- 1) *Initial Trajectory Generation* At the time the robot is powered-on, the trajectory between the last segment and the foremost segment is unknown. Therefore, the robot cannot initiate the steering motion because segments no. 1 to 6 does not have a trajectory to follow. This trajectory can be estimated by interpolating the segments center position at initialization time. For instance, a cubic spline interpolation function was implemented in the actual KR-II control.
- 2) *Trajectory Update* In case a trajectory is specified *a priori* or it is generated by an autonomous path planning algorithm, this step simply updates the position of the foremost segment s_0 over the known trajectory. However, as we assume that a human operator is manually maneuvering the robot, the trajectory must be calculated online. The natural choice is an odometric approach. This method calculates both the new position at time $t + \Delta t$ by estimating the moved distance δs , and the new orientation of the foremost segment from time t to $t + \Delta t$. Let $v_{0m}(t)$ be the actual velocity of the foremost segment measured from the wheel rotation velocity, the distance moved during the interval of one sampling time Δt is estimated by

$$\delta s = v_{0m}(t) \Delta t. \quad (3)$$

Next, from the measured bending angle of the foremost segment $\theta_{0m}(t)$, and the segment vector orientation of the segment no. 1 $\Theta_1(t)$, the foremost wheel heading orientation at time $(t + \Delta t)$ is estimated as follow.

$$\Theta_0(t + \Delta t) = \Theta_1(t) + \theta_{0m}(t) \quad (4)$$

With δs and $\Theta_0(t + \Delta t)$ estimated from real measurements, the position of the foremost segment at time $t + \Delta t$ can be calculate by

$$Traj(s_0(t + \Delta t)) = Traj(s_0(t)) + E^{\Theta_0(t + \Delta t)} \begin{bmatrix} \delta s \\ 0 \end{bmatrix}, \quad (5)$$

where

$$s_0(t + \Delta t) = s_0(t) + \delta s, \text{ and } E^\Theta = \begin{bmatrix} \cos(\Theta) & -\sin(\Theta) \\ \sin(\Theta) & \cos(\Theta) \end{bmatrix}.$$

Although the above computations are performed at each sampling time, for practical purposes the array $\text{Traj}(s_n) = (x(s_n), y(s_n))$ holds coordinates of the trajectory separated by a constant interval Δs . For the actual KR-II computation Δs is normally set to 1mm.

- 3) *Segments Center Position Search* By setting a condition that: "the minimum bending radius of the trajectory is greater than the intersegment length L for all intervals", the position of each segment center can be tracked by searching continuously in the forward direction of the trajectory. This means that for a forward movement, none of the following segments make a backward movement. The distance L_{calc} between two adjacent segment centers is calculated from equation (6).

$$L_{calc}^2 = [x(s_n) - x(s_{n-1})]^2 + [y(s_n) - y(s_{n-1})]^2 \quad (6)$$

Thus, considering a margin of error, the position s_n that satisfies equation (7) can be searched for, from segment no. 1 to no.6 ($n=1 \sim 6$).

$$(0.99L)^2 \leq L_{calc}^2 \leq (1.01L)^2 \quad (7)$$

- 4) *Segments Bending Angle Calculation* Knowing the coordinates of all segment center positions, the direction vectors between these segments, $\Theta_1 \sim \Theta_6$ are calculated by

$$\Theta_n = \tan^{-1} \frac{y(s_n) - y(s_{n-1})}{x(s_n) - x(s_{n-1})} \quad . \quad (8)$$

However, the direction vector of the last segment Θ_7 does not depend on the position of any segment center, so a direction that orients the last segment's wheel to the tangent of the trajectory is chosen to minimize energy loss due to wheel sideslips. The wheel orientation is calculated by

$$\Phi_6 = \tan^{-1} \frac{y(s_6) - y(s_6 - \delta s)}{x(s_6) - x(s_6 - \delta s)} \quad , \quad (9)$$

and Θ_7 by

$$\Theta_7 = 2\Phi_6 - \Theta_6 \quad . \quad (10)$$

Finally, the θ axis bending angles are calculated.

$$\theta_n = \Theta_n - \Theta_{n+1} \quad n = 1 \sim 6 \quad . \quad (11)$$

3.4 Validity of the Trajectory Updating Method

The actual robot KR-II does not have sensors to measure directly its position and orientation with respect to the inertial reference frame. For this reason, an odometric approach has been used to estimate the foremost segment's position and orientation at each new time step. In

order to verify the estimation accuracy a right angle cornering motion with a bending radius $R=500\text{mm}$ is simulated. First, the θ axis commands θ_0 to θ_6 (shown by the solid lines in **Fig. 9**) are generated from geometric relationship (i.e., analytically). Using the foremost segment's command θ_0 generated by this method as the input to equation (4), and considering velocity $v_{0m}(t) = 100 \text{ mm/s}$, and sampling time $\Delta t = 10 \text{ ms}$, results in the dashed lines in the same figure. These results, shows that the presented method generates joint commands extremely close to the analytical method's exact commands. The actual trajectories for both methods are also coincident.

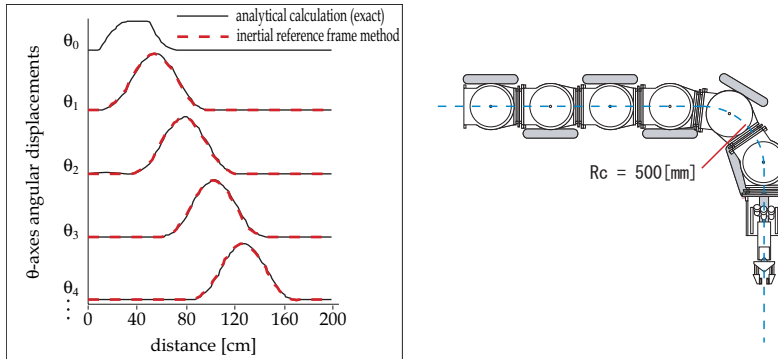


Fig. 9. Calculation of θ axis steering commands

3.4.1 Errors in the Odometric Approach

Note that the odometric approach introduces many errors in the position estimation, due to the terrain irregularities, tire pressure changes, and sensor offsets. These errors are cumulative. For this reason this position estimation is not well suited for autonomous navigation or for autonomous mapping of unknown environments. However, for the steering control purposes, the error introduced in the trajectory estimation affects only the interval from the foremost segment to the last segment (about 3.3 m). Moreover, as we consider teleoperation by a human operator and the motion of the foremost segment is controlled relative to the next segment, the difference between the estimated position and the actual position do not affect the overall steering control performance.

3.5 W-Shaped Configuration

The method discussed so far, was intended for the steering control in a "Straight-Line Configuration" (shown in **Fig. 11(a)**), i.e., when all the segment centers pass through the same trajectory travelled by the foremost segment. This configuration is very important for locomotion in narrow and meandering passes, but as KR-II has the wheels mounted right-sided for odd numbered segments and left-sided for even numbered segments, its stability becomes critical for locomotion over rough terrain. To overcome this problem, a "W-Shaped Configuration" as shown in **Fig. 11(b)**, which enlarges the wheel-to-wheel width by a W-shape width B_w is introduced. The "W-Shaped Configuration" is defined as:

"The configuration where the centers of the odd numbered segments follow a trajectory that is

continuous and “parallel” to the trajectory followed by the centers of the no. 0 and even numbered segments.”

Note that the word “parallel” is used with the same meaning as parallel rails of a rail-way where the rails do not cross and maintain a constant distance between them. For the “W-Shaped Configuration”, the distance between the rails (left and right trajectories), denoted as B_w , will be the parameter to be controlled, and for the particular case when $B_w = 0$, the two rails coincide and the configuration becomes the same as the “Straight-Line Configuration”.

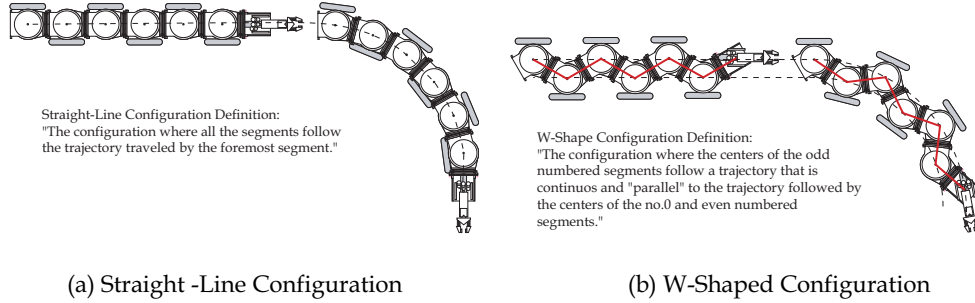


Fig. 10. Basic Steering formation for KR-II

3.5.1 Steering Control for the W-Shaped Configuration

The steering control for the “W-Shaped Configuration” is accomplished in a very straightforward way: the trajectory travelled by the foremost segment in the “Straight-Line Configuration” is set as the left trajectory $\mathbf{Traj}_L(s)$ to be followed by the even numbered segments. The odd numbered segments follow the right trajectory $\mathbf{Traj}_R(s)$, which is parallel to $\mathbf{Traj}_L(s)$.

The basic algorithm for the “Straight-Line Configuration” is extended to be used in the W-Shaped Configuration, as follows.

- 1) *Initial Trajectory Generation* In order to estimate the initial trajectory for a W-Shaped configuration, first the left trajectory $\mathbf{Traj}_L(s)$ is generated from a spline interpolation using the segments no. 0,2,4,6 center positions as control points, and the right trajectory $\mathbf{Traj}_R(s)$ from the segments no. 1,3,5. However, to generate more parallel left and right trajectories, auxiliary control points can also be used. The steps of this algorithm are detailed in Fig. 11. Note that the initial width is calculated by

$$Bw_{initial} = \frac{1}{5} \sum_{n=1}^5 L \sin\left(\frac{|\theta_n|}{2}\right). \quad (12)$$

- 2) *Trajectory Update* The left trajectory $\mathbf{Traj}_L(s)$ travelled by the foremost and the even numbered segments can be updated using the same equation (5) used for the line

configuration. And from the definition of W-Shaped configuration, the right trajectory $\mathbf{Traj}_R(s)$ is generated parallel to $\mathbf{Traj}_L(s)$.

$$\mathbf{Traj}_R(s_0(t + \Delta t)) = \mathbf{Traj}_L(s_0(t + \Delta t)) + \mathbf{E}^{\Theta_0(t + \Delta t)} \begin{bmatrix} 0 \\ -B_w \end{bmatrix} \quad (13)$$

- 3) *Segments Center Position Search* Given the correct left and right trajectories for each segment, equations (6)(7) can be used to calculate each segment center position.
- 4) *Segments Bending Angle Calculation* In this step, the line configuration's basic equations are also valid, given the correct trajectory for each segment.

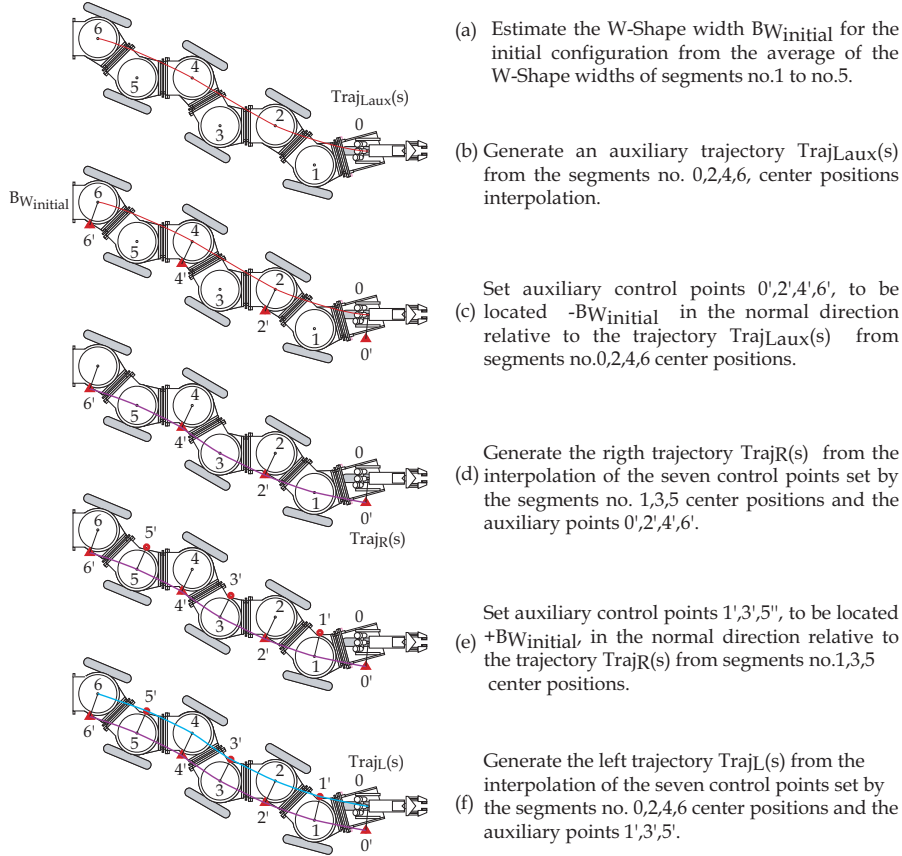


Fig. 11. Initial trajectory generation algorithm for the W-Shaped configuration

3.5.2 Foremost segment's control angle compensation

For the basic remote control scheme, the bending angle and velocity command for the

foremost segment is sent from a remote human operator controlling a joystick. For a straight forward motion the operator should hold the joystick θ axis command θ_{joy} at the zero (neutral) position. Furthermore, the operator should be relieved from the task of compensating for the change in cornering radius due to change in the W-Shaped width B_w , which changes the apparent intersegment length and results in smaller cornering radius. Taking in account these factors the bending angle θ_0 is compensated as:

$$\theta_0 = \theta_{joy} \cos(\theta_{0w}) - \theta_{0w}, \quad (14)$$

where θ_{0w} is an offset angle due to the W-Shaped configuration.

$$\theta_{0w} = \frac{\theta_w}{2} = \sin^{-1}\left(\frac{B_w}{L}\right) \quad (15)$$

3.5.3 Shift Between Straight-Line and W-Shaped Configurations

The shift between the configurations can be accomplished by smoothly changing the value of B_w according to the moved distance. The configuration shift algorithm must also take in account the trajectories of segments no. 0 and no. 1. There are several ways to perform this transition, and some examples are shown below.

3.6 Conclusions about Steering Control

For the real robot KR-II, the introduced method demonstrated good energy efficiency and trajectory tracking performance as well as real-time control feasibility. This method was successfully extended for use in the "W-Shaped Configuration", and it can be considered the best steering control scheme for articulated body mobile robots with long intersegment lengths. Some experimental results are shown in **Fig. 12, 13 and 14**.

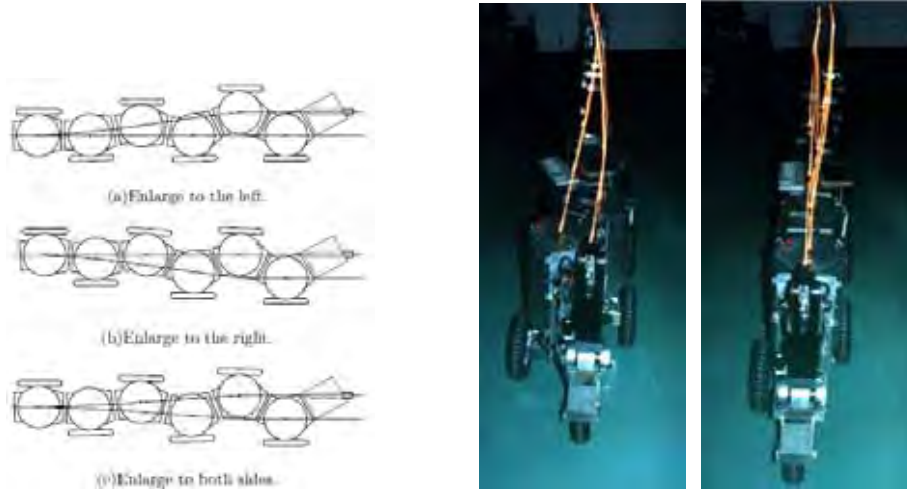


Fig. 12. Examples of configuration transition between Line and W-Shaped configurations



(a) Straight -Line Configuration

(b) W-Shaped Configuration

Fig. 13. Steering control experiments results



Fig. 14. Mailing a letter with cooperation of steering and manipulation control

4. Optimal Attitude Control

Optimal force distribution has been active field of research for multifingered hand grasping, cooperative manipulators and walking machines. The articulated body mobile robot "KORYU" composed of cylindrical segments linked in series and equipped with many wheels have a different mechanical topology, but it forms many closed kinematic chains through the ground and presents similar characteristics as the above systems. This section introduces an attitude control scheme for the actual mechanical model "Koryu-II (KR-II)", which consists of optimization of force distribution considering quadratic object functions, combined with attitude control based on computed torque method. The validity of the introduced method is verified by computer simulations and experiments using the actual mechanical model KR-II.

4.1 Attitude control problem description

KR-II is composed of cylindrical units linked in series by prismatic joints which generate vertical motion between adjacent segments. The simplest solution to control the vertical motion would be position control. However, as shown in Fig. 15(a), this method cannot be used for locomotion on uneven terrain. The vertical prismatic joints should be force

controlled so that each segment vertical position automatically adapts to the terrain irregularities, as shown in Fig.15(b). The simplest implementation of force control is to make these joints free to slide. However, in this case the system acts like a system of wheeled inverted pendulum carts connected in series and is unstable by nature, as shown in Fig.16(a) (b). Thus, an attitude control scheme to maintain the body in the vertical posture is demanded. This work introduces a new attitude control based in optimal force distribution calculation using quadratic programming for minimization of joint energy consumption.

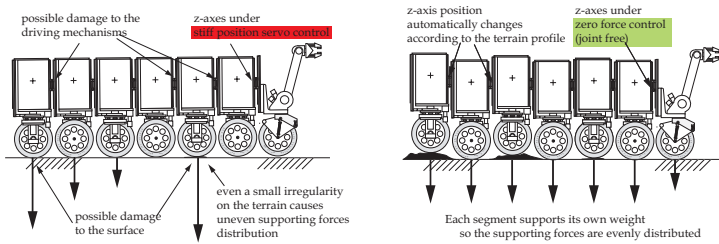


Fig. 15. Comparison between position and force control in the z axis

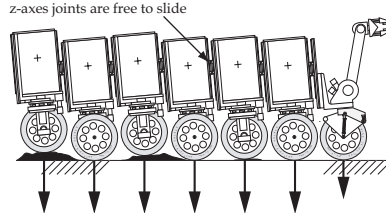


Fig. 16. Force control alone cannot maintain the posture of the robot, so an attitude control is needed

The presented method shares similarities with force distribution for multifingered hands, multiple coordinated manipulators and legged walking robots. In this section, the background on optimal force distribution problem is described, the optimal force distribution formulation and shows an efficient algorithm to solve this problem is introduced. Furthermore, the mechanical modelling of KR-II for the attitude control is presented and a feedback control is introduced.

4.2 Background on Optimal Force Distribution Problem

Many types of force distribution problems have been formulated for multifingered hands, multiple coordinated manipulators and legged walking robots. A brief review of the fundamental concepts and similarities with formulation of balance equation and equations of motion of multibody systems are hereafter described.

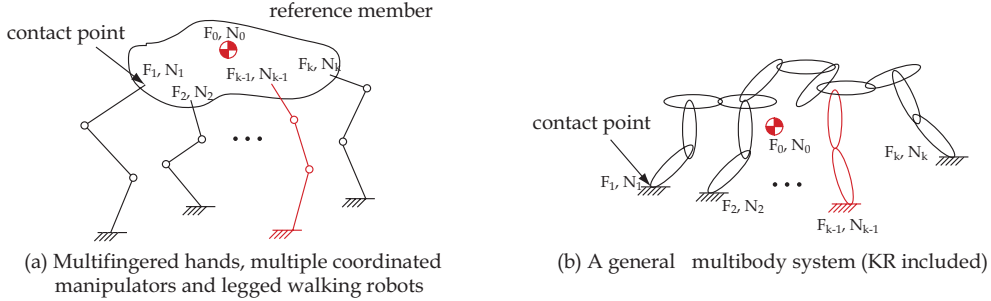


Fig. 17. Comparison of internal and external forces acting in a single and multibody systems

4.2.1 Balance Equations for Reference Member

Multifingered hands, multiple coordinated manipulators and legged walking robots can be modeled as one reference member with k external contact points as shown in Fig.17(a). Consider the reference member parameters given by: mass m_0 ; linear and angular acceleration at the center of mass $\alpha_0, \omega_0 \in \mathbf{R}^3$; inertia tensor at the center of mass coordinate $H_0 \in \mathbf{R}^{3 \times 3}$; force $F_i \in \mathbf{R}^3$ and moment $M_i \in \mathbf{R}^3$ acting on the i th contact point; position of the contact point with respect to the center of mass coordinate $p_i = [p_{i1} \ p_{i2} \ p_{i3}]^T \in \mathbf{R}^{3 \times 1}$. The resulting force and moment at the center of mass is given by $F_0 = \sum_{i=1}^k F_i \in \mathbf{R}^3$ and $M_0 = \sum_{i=1}^k (M_i + p_i \times F_i) \in \mathbf{R}^3$. The balance equations is given below, where the gravitational acceleration g which in principle is an external force, was included in the left term for simplicity of notation.

$$m_0 \alpha_0 = F_0 + m_0 g \quad (16)$$

$$H_0 \dot{\omega}_0 + \omega_0 \times (H_0 \omega_0) = M_0 \quad (17)$$

The inertial terms can be grouped as $Q \in \mathbf{R}^6$, and the external force terms into the matrix P and vector of contact points N .

$$P = \begin{bmatrix} I_3 & 0 & \cdots & I_3 & 0 \\ \tilde{p}_1 & I_3 & \cdots & \tilde{p}_k & I_3 \end{bmatrix} \in \mathbf{R}^{6 \times 6k} \quad (18)$$

$I_3 \in \mathbf{R}^{3 \times 3}$: identity matrix

$$\tilde{p}_i = \begin{bmatrix} 0 & -p_{i3} & p_{i2} \\ p_{i3} & 0 & -p_{i1} \\ -p_{i2} & p_{i1} & 0 \end{bmatrix} \in \mathbf{R}^{3 \times 3}$$

$$\mathbf{N} = \begin{bmatrix} \mathbf{F}_1^T & \mathbf{M}_1^T & \cdots & \mathbf{F}_k^T & \mathbf{M}_k^T \end{bmatrix}^T \in \mathbb{R}^{6k} \quad (19)$$

Thus the balance equations are described by the following linear relation.

$$\mathbf{Q} = \mathbf{P} \mathbf{N} \quad (20)$$

4.2.1.1 General solution

The general solution of equation (20) with respect to \mathbf{N} is given by

$$\mathbf{N} = \mathbf{P}^+ \mathbf{Q} + (\mathbf{I} - \mathbf{P}^+ \mathbf{P}) \boldsymbol{\lambda}, \quad (21)$$

as described in Walker et al., 1988, where \mathbf{P}^+ is a generalized pseudo-inverse matrix. Basic formulation of force distribution and description about internal forces concepts were first addressed by Kerr & Roth, 1986. The fundamental concepts are: i) the general solution can be divided in two orthogonal vectors $\mathbf{N} = \mathbf{N}_e + \mathbf{N}_i$; ii) the partial solution \mathbf{N}_e can be solved by $\mathbf{N}_e = \mathbf{P}^+ \mathbf{Q}$ using the pseudo-inverse matrix; iii) the partial solution \mathbf{N}_i resides in the null-space of \mathbf{P} and corresponds to the internal forces; iv) $(\mathbf{I} - \mathbf{P}^+ \mathbf{P})$ is a matrix formed by orthonormal basis vectors which span the null space of \mathbf{P} , and $\boldsymbol{\lambda}$ corresponds to the magnitude of the internal forces. Kerr and Roth used these concepts to formulate a linear programming problem which took in account friction forces at contact points and also joint driving forces.

Force distribution problem for gripper and hands usually results in searching optimal values for $\boldsymbol{\lambda}$. Nakamura et al., 1989, were the first to formulate a nonlinear problem using quadratic cost function $\|\mathbf{N}\|$ to solve the internal forces. Efficient solutions using linear programming were also analyzed by other authors (Cheng & Orin, 1991; Buss et al., 1996). Nahon & Angeles, 1992, showed that minimization of internal forces and joint torques can both be formulated in an efficient quadratic programming method, and Goldfarb and Idnami method (Goldfarb & Idnami, 1983) can be used to solve this problem. Other efficient formulations are also been investigated (Chen et al., 1998; Markefka & Orin, 1998).

4.2.2 Multibody systems

Multibody systems differ from multifingered hands as shown in Fig.17(a)(b) not only by the fact that in general they have no common reference member, but also because that forces and moments $\mathbf{F}_i, \mathbf{M}_i$ acting in the contact points arises from different physical natures. In system (a) the external forces are exerted from the fingers, manipulators or legs. However, system (b) can not have external forces exerted from the ground. Instead, the forces and moments at the contact points are originated from the gravitational acceleration and internal motion of the system itself. However, balance equations and equations of motion for these systems present similar characteristics as described next.

4.2.2.1 Balance equations

Let the variables $k, \mathbf{F}_i, \mathbf{M}_i, \mathbf{p}_i$ be defined the same in Fig.17(a)(b), the equations (18)(19) are valid for both systems, but equations (16)(17) due to inertial forces are not. However, the

total force acting on the system's center of mass can be derived as $\mathbf{Q}(\mathbf{q}, \dot{\mathbf{q}}, \ddot{\mathbf{q}})$, i.e., as function of generalized coordinate $\mathbf{q}, \dot{\mathbf{q}}, \ddot{\mathbf{q}}$. Hence, the balance equations can be described by

$$\mathbf{Q}(\mathbf{q}, \dot{\mathbf{q}}, \ddot{\mathbf{q}}) = \mathbf{P} \mathbf{N} . \quad (22)$$

Equations (22) and (20) are mathematically equivalent, and therefore the fundamental theory discussed for systems having common reference member, can be applied to multibody systems as well.

4.2.2.2 Equations of motion

For the system in Fig.17 (a), the problem of finding optimal values for contact forces \mathbf{N} and joint forces $\boldsymbol{\tau}$ can be independently formulated. However, the equations of motion can also be grouped as equation (23) for optimization of joint forces of the entire system (Walker et al., 1988).

$$\boldsymbol{\tau} = \mathbf{H}\ddot{\mathbf{q}} + \mathbf{C} + \mathbf{G}_g + \mathbf{J}^T \mathbf{N} \quad (23)$$

The above equation has the same structure for robot manipulators and multibody-systems where \mathbf{H} is the inertial term, \mathbf{C} the coriolis and centrifugal term, \mathbf{G}_g the gravitational term, and \mathbf{J} is the Jacobian matrix. Therefore, the equations of motion for systems in Fig.17 (a) and (b) are mathematically equivalent.

4.3 Efficient Algorithm for Solving Optimal Force Distribution Problem

4.3.1 Cost function

Electrical motor's energy consumption at low speed but high output torque operation can be estimated by the power loss in the armature resistance. Hence, the sum of squares of joint forces $\boldsymbol{\tau}$ can be used as the cost function to be minimized.

$$S(\boldsymbol{\tau}) = \boldsymbol{\tau}^T \mathbf{W} \boldsymbol{\tau} \quad (24)$$

Note that \mathbf{W} is a symmetric positive definite matrix. Now, let, $\mathbf{H}_q = \mathbf{H}\ddot{\mathbf{q}} + \mathbf{C} + \mathbf{G}_g$, $\mathbf{G} = 2\mathbf{J}\mathbf{W}\mathbf{J}^T$ and $\mathbf{d} = 2\mathbf{J}\mathbf{W}\mathbf{H}_q$ be defined as auxiliary variables. Substituting equation (23) into (24) results in a new cost function depending on the variable \mathbf{N} .

$$S(\boldsymbol{\tau}) = \mathbf{H}_q^T \mathbf{W} \mathbf{H}_q + \mathbf{d}^T \mathbf{N} + \frac{1}{2} \mathbf{N}^T \mathbf{G} \mathbf{N} , \quad (25)$$

4.3.2 Quadratic problem formulation

The first term in the right side of equation (25) does not depend on N , so the new cost function can be described by a new equation (26), and a general quadratic programming problem can now be formulated as equations (26) and (27).

$$\min_N : S(N) = \mathbf{d}^T N + \frac{1}{2} N^T \mathbf{G} N \quad (26)$$

$$\text{subject to : } \begin{cases} \mathbf{P}_e N = \mathbf{Q}_e \\ \mathbf{P}_i N \geq \mathbf{Q}_i \end{cases} \quad (27)$$

Equations (27) are linear constraint equations, with equality constraints given by equations (20) or (22), and inequality constraints given by the system's friction, contact and joint force limitations. A positive definite matrix \mathbf{W} guarantees this problem to be strictly convex, thus having efficient solution algorithms (Goldfarb & Idnami, 1983).

4.3.3 Solution considering equality constraints

The partial problem when considering only equality constraints can be solved as

$$\mathbf{N}_e = \mathbf{P}_e^+ \mathbf{Q}_e - \mathbf{H}_e \mathbf{d}, \quad (28)$$

where the generalized pseudo-inverse matrix \mathbf{P}_e^+ defined as

$$\mathbf{P}_e^+ = \mathbf{G}^{-1} \mathbf{P}_e^T (\mathbf{P}_e \mathbf{G}^{-1} \mathbf{P}_e^T)^{-1}, \quad (29)$$

and auxiliary matrix \mathbf{H}_e defined as

$$\mathbf{H}_e = (\mathbf{I} - \mathbf{P}_e^+ \mathbf{P}_e) \mathbf{G}^{-1} \quad (30)$$

From the observation that the first term of equation (28) corresponds to the norm of N , i.e., the solution which minimizes $N^T \mathbf{G} N$, the second term is the partial solution which minimizes the norm of τ . Note that although it resides in the null-space of \mathbf{P}_e an analytic solution is available.

4.3.4 Solution considering inequality constraints

Problems with inequality constraints usually do not have analytical solutions but use some kind of search algorithms (Nakamura et al., 1989; Nahon & Angeles, 1992; Goldfarb & Idnami, 1983). In order to achieve better real-time performance, only negative contact forces will be considered in this formulation. This is valid for hands, grippers, walking machines and mobile robots in general, that can exert positive forces, i.e., "push", but can not exert negative forces, i.e., "pull". The proposed method introduces a new equality constraints term $\mathbf{P}_d N = \mathbf{Q}_d \in \mathbf{R}^d$ into the balance equation $\mathbf{P} N = \mathbf{Q}$,

$$\mathbf{P}_e = [\mathbf{P} \quad \mathbf{P}_d]^T \quad (31)$$

$$\mathbf{Q}_e = [\mathbf{Q} \quad \mathbf{Q}_d]^T \quad (32)$$

The basic idea is to transform the problem with inequality constraints into a problem with only equality constraints that can be solved efficiently by equation (28). This is accomplished by the algorithm described below, and illustrated in **Fig. 18**. Note that the variable d represents the number of contact points included in the equality constraints.

- Step 0.* Initialization: case $d_0 > 0$ make $d = d_0$ and include the contact forces $\mathbf{P}_d \mathbf{N} = \mathbf{Q}_d \in \mathbf{R}^{d_0}$ into equations (31)(32). Case $d_0 = 0$, initialize $\mathbf{P}_e = \mathbf{P}$ and $\mathbf{Q}_e = \mathbf{Q}$.
- Step 1.* Calculate the partial solution \mathbf{N}_e considering only equality constraints from equation (28).
- Step 2.* Let the number of negative contact forces in the solution \mathbf{N}_e be d_n . Case $d_n > 0$ go to *Step 3*. Otherwise, this is the optimal solution. Calculate joint forces by equation (33). Finish.

$$\boldsymbol{\tau}_e = \mathbf{H}_q + \mathbf{J}^T \mathbf{N}_e \quad (33)$$

- Step 3.* Update $d = d + d_n$. Case $d \leq$ (free variables – balance equations), go to *Step 4*. Otherwise the problem can not be solved. Finish.
- Step 4.* Set the desired contact force at the contact points where resulted in negative forces to zero and include in the equality constraint $\mathbf{P}_d \mathbf{N} = \mathbf{Q}_d$. Return to *Step 1*.

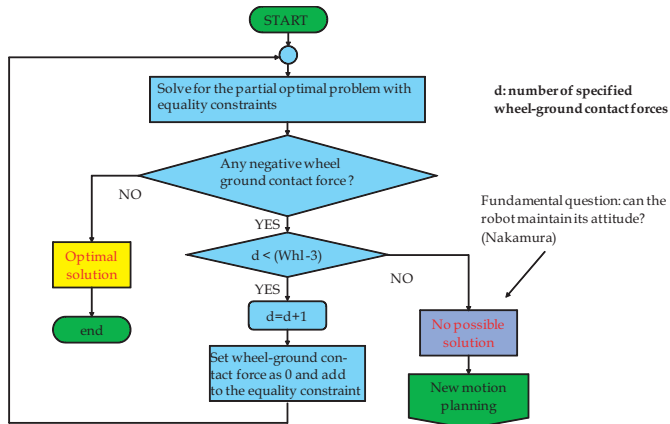


Fig. 18. Calculation flowchart

Although this algorithm is suited for real time applications, it does not search for all the combination of possible solutions. For this reason it might finish in *Step 3*, even a possible solution exists. However, for normal steering control, passing-over pipes and ditches, and

attitude control of KR-II, a possible solution was always found after a limited number of iterations.

4.4 Formulation of KR-II's Attitude Control

4.4.1 KR-II's variables

KR-II's motion freedoms can be grouped as: z-axes linear displacements $\mathbf{z} = [z_1 \ z_2 \ \dots \ z_6]^T \in \mathbf{R}^6$; θ -axes angular displacements $\boldsymbol{\theta} = [\theta_0 \ \theta_1 \ \dots \ \theta_6]^T \in \mathbf{R}^7$; wheel's (s-axes) angular displacements $\mathbf{s} = [s_0 \ s_1 \ \dots \ s_6]^T \in \mathbf{R}^7$; body's coordinate position $\mathbf{c} = [x_0 \ y_0 \ z_0]^T$ and attitude $\boldsymbol{\varphi} = [\phi_x \ \phi_y \ \phi_z]^T$ relative to the inertial coordinate. This accounts for 26 degrees of freedom.

In this work, balance and motion equations given by Equations (22)(23) were derived by Newton-Euler method, but other efficient virtual power methods (Thanjavur & Rajagopalan, 1997) could also be used. The inertial parameters for KR-II can be find in Fukushima & Hirose, 2000.

4.4.2 Simplifications

4.4.2.1 Wheel modeling

The wheel will be simplified to a simple model:

1. It is a thin circular plate with constant radius.
2. It contacts a horizontal plane even when moving on slopes.

However, the horizontal plane is set independently for each wheel so that this simplification is effective for motion over uneven terrains. Nonetheless, for stair climbing and step overcoming motions, a better contact point estimation algorithm should be used.

4.4.2.2 Other simplifications

1) External contact forces: the wheel's lateral and longitudinal forces are small because optimal trajectory is planned by the steering control, and also abrupt acceleration and deceleration are avoided. Moreover, moments between the tire and the ground are also negligible. For these reasons, the tire normal force F_{z_i} can be considered the only external force acting on the system. Hence the external contact force vector is given by

$$\mathbf{N} = [F_{z_0} \ F_{z_1} \ \dots \ F_{z_6}]^T \in \mathbf{R}^7 \quad (34)$$

2) Joint forces: z-axes and θ -axes motions can be independently planned because KR's z-axes orientations are controlled to be always vertical. In fact, θ -axes is position controlled and their desired angular displacements are planned by the steering control. On the other hand, although s-axes motion can be used for the attitude control, it would involve undesirable acceleration and deceleration in the system. For these reasons, z-axes forces will be set as the variables to be optimized.

$$\boldsymbol{\tau} = [f_{z_0} \ f_{z_1} \ \dots \ f_{z_6}]^T \in \mathbf{R}^7 \quad (35)$$

Note that f_{z_0} was included just for avoiding singularity in the calculation, but always result in $f_{z_0} = 0$.

3) Balance equations: from the above considerations, force balance in the z direction and moment balance around x and y directions are enough to model our system. Hence, the dimension of the balance equation $\mathbf{P} \mathbf{N} = \mathbf{Q}$ becomes $\mathbf{Q} \in \mathbf{R}^3$ and $\mathbf{P} \in \mathbf{R}^{3 \times 7}$.

4) Generalized accelerations: only a part of the 26 degrees of freedom of KR-II, $\mathbf{q}_s = [z^T \theta^T \phi_x \phi_y]^T$ and its time derivative $\dot{\mathbf{q}}_s = [\dot{z}^T \dot{\theta}^T \dot{\phi}_x \dot{\phi}_y]^T$ is used in the calculation. The acceleration variables are further simplified to

$$\ddot{\mathbf{q}}_a = [\ddot{x}_0 \quad \ddot{y}_0 \quad \ddot{z}_0 \quad \ddot{\phi}_x \quad \ddot{\phi}_y]^T \in \mathbf{R}^5, \quad (36)$$

and used as $\ddot{\mathbf{q}} \equiv \ddot{\mathbf{q}}_a$.

5) Other parameters: other dimensions are as follows: $\mathbf{H} \in \mathbf{R}^{7 \times 5}$; $\mathbf{C} \in \mathbf{R}^{7 \times 1}$; $\mathbf{G}_g \in \mathbf{R}^{7 \times 1}$; $\mathbf{J} \in \mathbf{R}^{7 \times 7}$; $\mathbf{P}_d \in \mathbf{R}^{d \times 7}$; $\mathbf{Q}_d \in \mathbf{R}^{k \times 1}$.

4.4.3 Attitude feedback law

The formulation described so far, solves for joint forces which balance the system in a given desired posture. This is fundamentally an inverse dynamics problem. A feedback control law shown below is added into equation (36).

$$\ddot{\phi}_X = \ddot{\phi}_{X_d} - K_{DX} \dot{\phi}_{X_m} + K_{PX} (\phi_{X_d} - \phi_{X_m}) \quad (37)$$

$$\ddot{\phi}_Y = \ddot{\phi}_{Y_d} - K_{DY} \dot{\phi}_{Y_m} + K_{PY} (\phi_{Y_d} - \phi_{Y_m}) \quad (38)$$

K_P, K_D are proportional and derivative gain and the indexes d,m stands for desired and measured values. This control law is equivalent to the Computed Torque Method (Markiewics, 1973) so that the closed-loop system stability can be analyzed in the same way.

4.5 Computer Simulation and Experimental Results

Computer simulation and experiment using the real robot KR-II, is here evaluated for an "obstacle passing over (without touching them)" where a box shape obstacle with width 300mm and height 150mm is considered. This motion was calculated considering a constant forward velocity of 100mm/s. The vertical motion of each segment is shown in Fig.19(a). Note that the calculated displacement includes a 10mm displacement for safety, resulting in a 160mm total vertical displacement.

4.5.1 Continuity of calculated forces

Discontinuities in the calculated forces occur when topological changes are caused by lifting-up or touching-down of the wheels. In this work these discontinuities are avoided by introducing desired contact forces using the equality constraints $P_d N = Q_d$ in Step 0. The desired forces when lifting-up is given as

$$F_{dn} = F_{UPn} \frac{(50 - Z_n)}{50}, \quad (39)$$

and when touching-down the ground is given as

$$F_{dn} = F_{DOWNn} \frac{(50 - Z_n)}{50}. \quad (40)$$

F_{UPn} is the optimal force calculated just before the wheel lift-up, i F_{DOWNn} is the optimal force calculated considering that the wheel has completely touch-down the ground, Z_n is the segment vertical displacement as shown in Fig.19(a). These equations are applied only in the interval $Z_n = 0 \sim 50$ mm. The constant 50 was derived considering KR-II's spring suspension stroke. For vertical displacements above 50, the desired contact force is set to zero. The simulation results shown in Fig.19(b)-(c) demonstrate the validity of the proposed method.

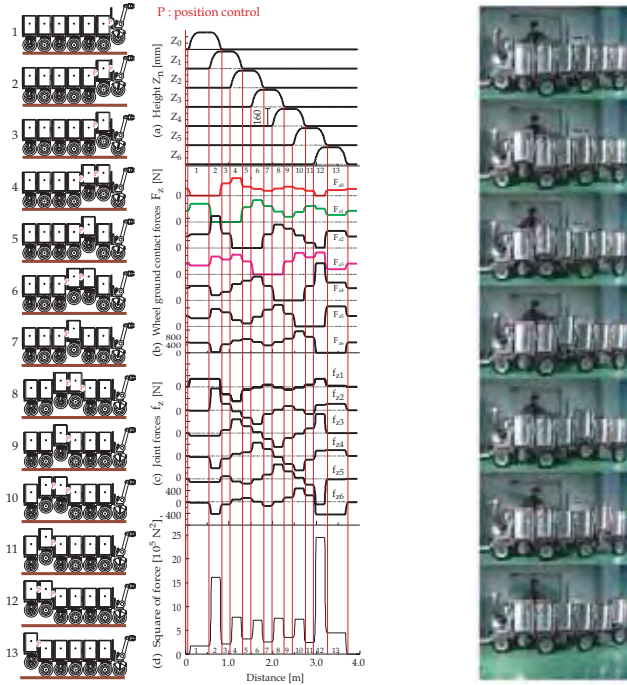


Fig. 19. Obstacle passing over simulation.

Fig. 20. Experiment overview



4.5.2 Experimental results

The experiment was held applying the feedforward command shown in Fig.19(c) and feedback command given by equations (37) and (38). The feedback gains were $K_{Px} = 65$, $K_{Dx} = 18$, $K_{Py} = 95$, $K_{Dy} = 16$, and all the computation was performed in real-time with a sampling-time of 20ms. The experiment was performed without forward motion, but actually lifting-up the segments to the specified height as shown in Fig.20. Fig.21(a) shows the performance of attitude control. Large attitude changes occur at times when more than one segment is lifted-up at the same time. Fig.21(b) is the plot of the sum of squares of z-axes joint forces measured during the experiment. It has a much higher magnitude than the simulation, but shows the same tendency compared to the plot in Fig.19(d). This experiment is an extreme case for the attitude control, when there are many segments being lifted-up from the ground at the same time. For normal manoeuvring on flat terrain or even on uneven terrain, most all wheels are in contact with the ground, so that the overall stability is much higher.

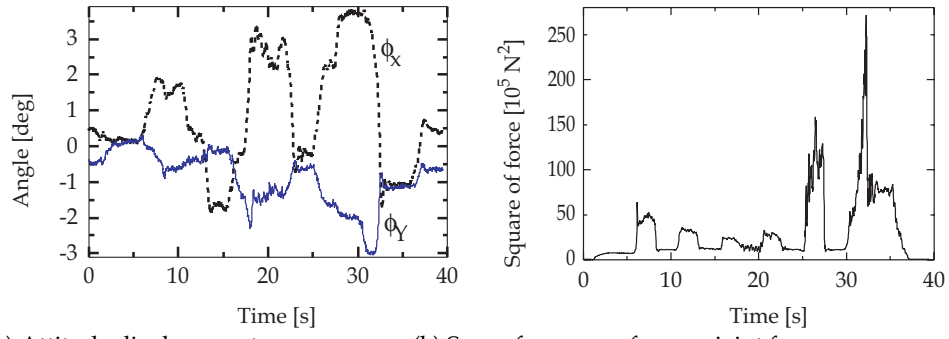


Fig. 22. KR-II moving around a shopping center street [1993]

5. Conclusion

The authors have designed and actually built a mechanical prototype of a class of articulated body mobile robots, 3.3m long, and mass of more than 400kg, called KR-II. Attitude control and steering control has been successfully implemented, and the robot can move stably in the outdoors, even on uneven terrain.

The presented steering control method is based on parameter representation for describing trajectories in an inertial reference frame, with travelled distance as a parameter. In doing so, the position of each element (in the case of the articulated body mobile robot KR-II, segment center positions) on the trajectory can be tracked by simple and effective numerical searching algorithms. For the real robot KR-II, the introduced method demonstrated good energy efficiency and trajectory tracking performance as well as real-time control feasibility. This method was successfully extended for use in the "W-Shaped Configuration", and it can be considered the best steering control scheme for articulated body mobile robots with long intersegment lengths, such as the KR-II.

The presented attitude control scheme is based in optimal force distribution using quadratic programming, which minimizes joint energy consumption. Similarities with force distribution for multifingered hands, multiple coordinated manipulators and legged walking robots were demonstrated. The attitude control scheme to maintain the vertical posture of the robot was introduced inside this force distribution problem.

The validity and effectiveness of proposed methods were verified by computer simulations and also experimentally using the actual mechanical model. Moreover, the introduced attitude control and steering control can be used not only for control of big "snake-like" robots, but even for walking machines at some extent.

Some negative points for developing such big robots, is the complexity in the mechanical design and also the high cost to build it, which makes the advance in this area of research a little bit slow, compared to other mobile robot systems. Nonetheless, sometime passed since the last prototype has been built (1990-2000), and we experienced many advances in actuators, computers, materials technology, so a much better design should be possible now. The authors hope the mechanical concept and practical results presented in this Chapter, could give enough insights for new developments in the area.

6. References

- Burdick, J. W.; Radford J. & Chirikjian, G. S. (1993). "Hyper-redundant robots: kinematics and experiments," *International Symposium on Robotics Research*, pp.1-16.
- Buss, M.; Hashimoto, H. & Moore, J. (1996). "Dextrous Hand Grasping Force Distribution," *IEEE Transactions on Robotics and Automation*, Vol.12, No.3, pp.406-418.
- Chen, Jeng-Shi; Cheng, Fan-Tien; Yang, Kai-Tarn; Kung, Fan-Chu & Sun, York-Yin (1998). "Solving the Optimal Force Distribution Problem in Multilegged Vehicles," *Proc. of the 1998 IEEE Intl. Conf. on Robotics and Automation*, pp.471-476, Belgium, May 1998.
- Cheng, F. T. & Orin, D. E. (1991). "Optimal Force Distribution in Multiple-Chain Robotic Systems," *IEEE Transactions on Systems, Man, and Cybernetics*, Vol. 21, No.1, pp. 13-24.
- Commissariat A l'Energie Atomique: "Rapport d'activite 1987," *Unité de Génie Robotique Avancé*, France, 1987.

- Fukushima, E. F. & Hirose, S. (1995), "How To Steer The Long Articulated Robot "KR-II"," *Proc. of the 7th Int. Conf. on Advanced Robotics (ICAR'95)*, Sant Feliu de Guixols, Spain, Sept. 20-22, 1995, pp. 729 - 735.
- Fukushima, E. F. & Hirose, S. (1996). "Efficient Steering Control Formulation for The Articulated Body Mobile Robot "KR-II"," *Autonomous Robots*, Vol. 3, No. 1, pp. 7-18.
- Fukushima, E. F. & Hirose, S. (2000), "Optimal Attitude Control for Articulated Body Mobile Robots," *CD-ROM Proc. of the International Symposium on Adaptive Motion of Animals and Machines (AMAM'00)*, Montreal, Canada, Aug. 08-12.
- Fukushima, E. F.; Hirose, S. & Hayashi, T. (1998). "Basic Manipulation Considerations For The Articulated Body Mobile Robot," *Proc. of the 1998 IEEE/RSJ Int. Conf. on Intelligent Robotics and Systems*, pp. 386-393.
- Goldfarb, D. & Idnami, A. (1983). "A numerically stable dual method for solving strictly convex quadratic programs", *Math. Programming*, Vol. 27, pp.1-33, 1983.
- Kerr, Jeffrey & Roth, Bernard (1986). "Analysis of Multifingered Hands," *The Intl. Journal of Robotics Research*, Vol.4, No.4, pp.3-17.
- Markefka, Duane W. & Orin, David E. (1998). "Quadratic Optimization of Force Distribution in Walking Machines," *Proc. of the 1998 IEEE Intl. Conf. on Robotics and Automation*, pp.477-483, Belgium, May 1998.
- Markiewics, B. R. (1973). "Analysis of the Computer Torque Drive Method and Comparison with Conventional Position Servo for a Computer-Controlled Manipulator," *Jet Propulsion Laboratory*, California Institute of Technology, TM 33-601, March 1973.
- Migads G. & Kyriakopoulos, J. (1997). "Design and Forward Kinematic Analysis of a Robotic Snake," *Proc. IEEE Intl. Conference on Robotics and Automation*, pp.3493-3497.
- Nahon, Meyer A. & Angeles, Jorge (1992). "Real-Time Force Optimization in Parallel Kinematic Chains under Inequality Constraints," *IEEE Trans. on Robotics and Automation*, Vol.8, No.4, pp.439-450, Aug.
- Nakamura, Y.; Nagai, K. & Yoshikawa, T. (1989). "Dynamics and Stability in Coordination of Multiple Robotic Mechanisms," *The Intl. Journal of Robotics Research*, Vol.8, No.2, pp.44-61.
- Nilsson, Martin (1997). "Snake Robot Free Climbing," *Proc. IEEE Intl. Conference on Robotics and Automation*, pp.3415-3420.
- Shan Y. & Koren Y. (1993). "Design and Motion Planning of a Mechanical Snake," *IEEE Transactions on System, Man and Cybernetics*, Vol.23, No.4, pp.1091-1100.
- Thanjavur K. & Rajagopalan R. (1997). "Ease of Dynamic Modelling of Wheeled Mobile Robots (WMRS) using Kane's Approach," *Proc. of IEEE Intl. Conference on Robotics and Automation*, pp.2926-2931.
- Tilbury, D.; Sordalen O. J. & Bushnell, L. (1995). "A Multisteering Trailer System: Conversion into Chained Form Using Dynamic Feedback," *IEEE Transactions on Robotics and Automation*, Vol.11, No.6, pp.807-818.
- Umetani, Y & Hirose S., (1974). "Biomechanical study pf serpentine locomotion", *Proc. Of 1st ROMANSY Symp.*, Udine, pp.171-184.
- Waldron, K. J.; Kumar, V. & Burkhardt, A. (1987). "An actively coordinated mobility system for a planetary rover," *Proc. 1987 ICAR*, pp.77-86
- Walker, Ian D.; Freeman Robert A. & Marcus, Steven I. (1988). "Dynamic Task Distribution for Multiple Cooperating Robot Manipulators," *Proc. IEEE Intl. Conf. on Robotics and Automation*, pp.1288-1290.

Modular Walking Robots

Ion Ion, Ion Simionescu, Adrian Curaj and Alexandru Marin
Politehnica University of Bucharest
Romania

1. Introduction

Since ancient times, Man has been tempted to imagine, conceive and accomplish machines, which can imitate patterns of the Nature. It was even born the belief that people building mechanical patterns, similar to those of other beings, had a better chance, to discover the secrets of life. The way animals walk, the way birds fly, have always been and it will probably remain the sources of inspiration and tasks of the scientific research.

The animals using their feet for walk can move freely, with substantive easiness in comparison with what the man-made robot can do. Animals' locomotion is superior to that of the wheeled or caterpillared robot, both energetically and operationally speaking, as well as from the point of view of its stability, irrespective of the terrain the movement happens on. As compared to the Nature's achievements, the Man, God's pride, thanks to his cleverness and skills, succeeded to grasp many secrets of his creator, but he is still far from the Latter's accomplishments. Never disheartened with failures Man has created instruments for permanent investigation and success has not failed to arrive.

No matter what the previous generations imagined or not, the present one is creating things, that provide solutions to many of his strivings and dreams, and this thank to the stored knowledge and the fresh opportunities of the technology which is in its full swing.

Studying the simplest but the most important movement types, such as the man's and the animals' movement, has been the scientists' most ancient preoccupation since the beginning of time. Mankind is so attached to the anthropomorphism, as it is almost impossible for it to conceive or imagine automatic systems, even equipped with artificial brain, which are not anthropomorphic.

In order to reach areas hard to get to, and where Man's life were jeopardized, the scientific research in time, and for different purposes, achieved mechanisms that thanks to their skills could cover several fields. Due to the special circumstances, regarding the vegetation and the terrain's state, and viewing the environment protection, the wheeled or the caterpillar machines, aiming at such applications, have a restrained mobility and thus, they considerably destroy the environment, the vegetation, bushes and the young trees, when passing through.

Walking robots protect the environment in a much better way, as their contact to the terrain is discrete, which considerably diminishes the area underwent to crushing; the robot's weight can be optimally distributed all over its leaning surface, by controlling the forces.

Altering the distance to the ground, the robot can pass over young trees or other vegetation, growing in the passage area.

Avoiding hurdles such as logs or tree trunks is a considerable advantage. Likewise, the movement on an unarranged terrain represents another advantage of the walking robot, as compared to the other types of vehicles.

Unlike the wheeled or caterpillar robot, the walking robot is a mechatronic system, its practical use requiring both the computer-assisted surveillance and the thorough checking by the movement systems. In this century, the locomotion using feet as a movement system was reckoned an inefficient movement means. Nevertheless, if it is take into consideration the infrastructure's costs to artificially create the roads for the wheeled robot or own roads for the caterpillar robot, arguments for these two robot types diminish in some of the cases.

Walking main feature is the very fact that the movement is not affected by the terrain's configuration. More and more applications requiring movement on a natural, unarranged terrain, made the feet-movement solution become more and more attractive.

Here there are the main features justifying the superiority of the walking robot as compared to the wheeled or caterpillared ones (Hiller M., Muller J., Roll U., Schneider M., Scroter D., Torlo M. & Ward D., 1999):

- the capability to move on unarranged terrains;
- the walking robot can step over certain hurdles by changing its height (terrain clearance);
- the possibility to change the configuration of the walking robot's shift system;
- the feet's contact to the terrain is discontinuous (it is accomplished only in the leaning phase), when a foot has the opportunity to select the contact point, while descending on the terrain, contingent of the latter's surface;
- the possibility to move on a soft terrain, which is sometimes more difficult for the wheeled or the caterpillar robot;
- the walking robot's active suspension accomplished by setting the proximity and force sensors in the outermost part of feet, enables the movement on uneven terrain under stable circumstances;
- the specific energy consumption is smaller with the movement on natural unarranged terrains as against other types of mobile robots;
- the better preservation of the terrain, that the robot moves on, especially in case it is made use of in specific farming or forestry activities.

Its apparent density grows higher than the normal values by the terrain settlement, namely its total porosity goes lower than the usual values. The artificial or anthrop sinking happens as a result of the heavy, insensible traffic, during the farming season, because of the transportation or for other reasons. The terrain settlement (compactness) is a process specific to the modern, intensive and strongly mechanized farming and the higher the mechanization level, the deeper the sinking.

The terrain compactness has many negative effects, whatever its nature. Thus, it diminishes the terrain's capability to keep water, it reduces the aeration and often considerably decreases the endurance to penetration and makes the terrain hard to plough. As a result of the terrain's decaying its productivity strongly drops and the crops sometimes diminish by 50 percents as compared to that on non-compacted terrains. Among the drawbacks of the walking robot, here they are some worth to remind:

- the movement checking is rather sophisticated thank to the large number of freedom degrees;
- they develop rather low speed;
- the energy consumption is higher than with the wheeled robot or that on caterpillars because of the many accelerations and decelerations of some elements in the mechanical system, during walking;
- they claim bigger manufacture, maintenance and the exploitation costs.

2. Structure of Walking Robot Displacement Systems

Some of the most significant components of the walking robots are the mechanisms of the displacement systems. The mechanisms of the displacement system can have three or more degrees of freedom, and are built so that the lower end of the last element, termed P , to follow any trajectory from the task space. Therefore, the point P must gets over an adequate trajectory with respect to the robot platform. This trajectory is corresponding to the gait type for the displacement. Some of these mechanisms have a simple structure and one or two degrees of freedom, so that the shape of the trajectory of the point P may be very little adjusted. These displacement systems may be commanded and controlled using the simple equipments. The utilization of the mechanisms with complicated structure, with many ways of adjustment, capable to ensure the displacements of the walking robot in the various conditions, involves existence of a very elaborate control equipment.

Generally, the mechanisms for the displacement systems may be divided into two categories:

- plane linkages, with the frame can rotates around a vertical axis fixed on the platform of the walking machine;
- spatial linkages.

The plane linkages have commonly two degree of freedoms and can be very simple, consisting of two links, or with a very complicated structure.

At all this, the lower end of the last link of the leg can get over any spatial trajectory in the work space.

In Fig. 1 is shown the Bessonov (Bessonov A.P. & Umnov N.V., 1973) leg mechanism, with nine elements and eleven pairs. This is a triple closed mechanism with two degrees of freedom.

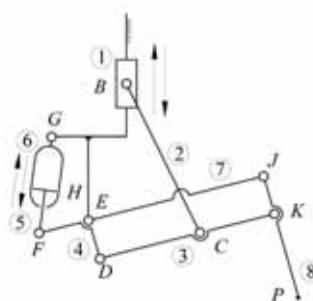


Fig. 1. Bessonov type leg mechanism

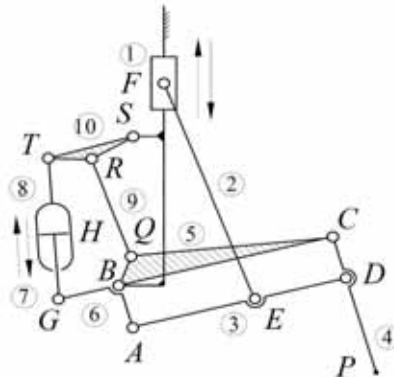


Fig. 2. ODEX-type leg mechanism

The ODEX-type leg mechanism (Song S.M. & Waldron K.J., 1989) is displayed in Fig. 2. This mechanism with four loops has eleven elements, 14 kinematics pairs and two degrees of freedom.

An orthogonal legged walking robot (Bares J) is shown in Fig. 3. The robot has at least two movement devices and each leg can exhibit an overlapping gait with respect to the other ones. Each leg is made of three links, serially connected through three driven pairs.

In Fig. 4 is shown a walking robot with six legs (Garrec P.). Each leg consists of a plane mechanism with one degree of freedom and constituted in such a way that the circular movement of a member driven by a motor is expressed by a horizontal rectilinear movement of the lower end of the last link. Each leg is connected to the platform by a revolute pair with vertical axis.

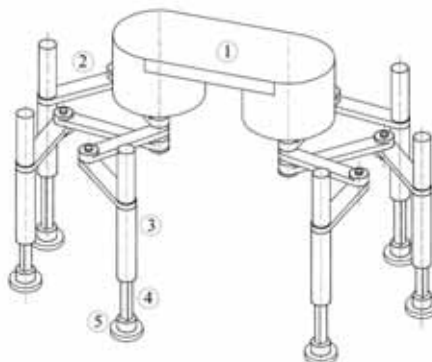


Fig. 3. A model of walking robot with six legs

The MERO experimental modular walking robot, built and tested at POLITEHNICA University of Bucharest, is shown in Fig. 5.

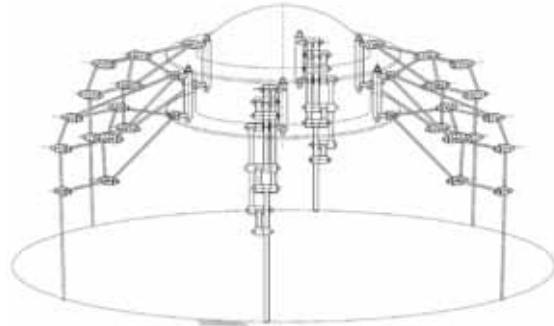


Fig. 4. Walking robot with six legs (Garrec P)



Fig. 5. MERO modular walking robot

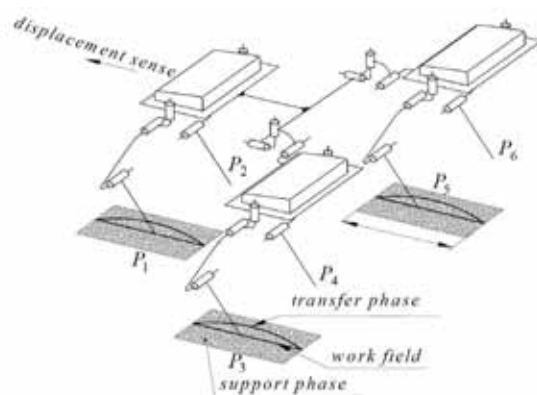


Fig. 6. Model of MERO walking modular robot

3. Kinematics Analysis of Displacement Systems

3.1. Mathematical model of gait for walking robots

The walking robot, unlike the wheels or caterpillars one, uses devices analogous to the man or animal legs. Unlike the wheel, the leg is not a system of continuous locomotion. Therefore, it has to be lifted away from the support phase, moved towards the advance direction of the walking robot and then laid down, following another cycle of another leg. As the walking robot has two or more legs, these moves have to be coordinated so that the move is ensured in conditions of the stability of the system. In order to allow a theoretical approach of the gait of the walking robot it is necessary to define a lot of terms. To achieve and manage a walking robot it is necessary to know all the walking possibilities, because the selection of the legs number and its structure depends on the selected type of the gait. The selection of the type of gait is a very complicated matter, especially in the real conditions of walking on the rough terrain. Therefore, it is necessary that the terrain surface to be selected before the type of gait is chose. According to the definitions given by McGhee (McGhee R.B. & Frank A.A., 1968), (McGhee R.B. & Orin D.E., 1976) and his collaborators, completed by Song and Waldron (Song S.M. & Waldron K.J., 1989), the gait can be periodic or non-periodic. According to these definitions it can state the following.

The transfer phase of a leg is the period of time when the foot is not in contact with the terrain; the period of time in which this phase occurs is marked by τ . The leg state of a leg in the transfer phase is 1.

The support phase of a leg is the period of time in which the foot is in contact with the terrain; the period of time when this phase occurs is called by ς . The leg state of a leg in the support phase is 0.

The gait is *periodic* if the similar states of the same leg, during successive strokes occur at the same time interval for all the legs; a different type of gait is the aperiodic gait; the period of time when a step of the periodic gait occurs is called *cycle time*.

The *duration of a cycle time* T is the duration of a complete cycle of locomotion of a leg, during a periodic gait and it results from the following equation: $T = \varsigma + \tau$.

3.2 Kinematics analysis of leg mechanisms

3.2.1 Positions of elements

The walking robots are able to move on a terrain with irregular surface. As a result, the leg mechanisms must have at least three degrees of freedom in the transfer phase [Ion I., Simionescu I. & Curaj A. 2003], (McGhee R.B., Frank A.A., 1968), (Song S.M. & Waldron K.J., 1989). An usually kinematics scheme for the leg mechanisms is displayed in Fig. 7.

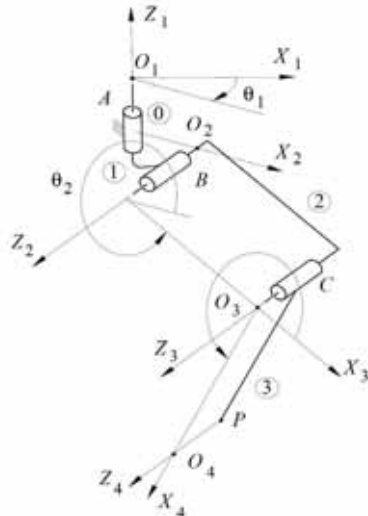


Fig. 7. Kinematics scheme of leg mechanism

This mechanism is build by three links, serially connected by three revolute pairs. All of the joints are driving ones. The lower end of the link (3) can be moved along an any spatial trajectory comprises in the operating field, with respect to the robot platform, with a pre-established displacement law.

The goal of the inverse kinematics analysis is to determine the variables of the driving pairs, i.e. the generalized coordinates, with respect to the position of the lower end of the link (3). The position of the point \$P\$, located to the lower end of the link (3), is defined with respect to the Denavit - Hartenberg axes system attached to this element [Denavit J., & Hartenberg R.S, 1955], (Uicker J.J.jr., Denavit J., Hartenberg R.S. 1965) by the coordinates \$x_{4P}\$, \$y_{4P}\$ and \$z_{4P}\$. The position of the point \$P\$ with respect to the Denavit - Hartenberg system \$O_1x_1y_1z_1\$ attached to the robot platform (0) may be calculated by equation:

$$\begin{vmatrix} 1 \\ x_{1P} \\ y_{1P} \\ z_{1P} \end{vmatrix} = \mathbf{A}_1 \mathbf{A}_2 \mathbf{A}_3 \begin{vmatrix} 1 \\ x_{4P} \\ y_{4P} \\ z_{4P} \end{vmatrix}. \quad (1)$$

The origin \$O_1\$ of the coordinate axes system attached to the robot platform is chosen in a convenient mode and specified by the distance \$s_1\$. The direction of the \$O_1x_1\$ axes is arbitrary and must be specified.

The leg mechanism shown in Fig. 7 has the following features:

- the axis of the pair \$A\$ is perpendicular to the axis of the pair \$B\$;
- the axis of the pair \$B\$ is parallel to the axis of the pair \$C\$.

Consequently, \$\alpha_1 = \pi/2\$, \$\alpha_2 = \alpha_3 = 0\$, \$s_2 = s_3 = 0\$, \$a_1 = 0\$.

The matrix equation (1) is equivalence to three scalar equations. In order to perform an inverse kinematics analysis of the leg mechanism, the system (1) is solved with respect to the unknowns θ_1 , θ_2 and θ_3 . This is a nonlinear system and must be used an adequate numerical method, for example the Newton – Raphson method (Simionescu I., Dranga M. & Moise V. 1995), (Hildebrand F.B. 1956). If the pair i is prismatic one, the angle θ_i is known exactly, and the distance s_i is unknown.

3.2.2 First time-derivatives of pair variables

Differentiating both sides of the equation (2) with respect to the time yields:

$$\begin{aligned} \begin{vmatrix} 0 \\ \dot{x}_{1P} \\ \dot{y}_{1P} \\ \dot{z}_{1P} \end{vmatrix} = & \left(\frac{\partial \mathbf{A}_1}{\partial \theta_1} \mathbf{A}_2 \mathbf{A}_3 \frac{d\theta_1}{dt} + \mathbf{A}_1 \frac{\partial \mathbf{A}_2}{\partial \theta_2} \mathbf{A}_3 \frac{d\theta_2}{dt} + \right. \\ & \left. + \mathbf{A}_1 \mathbf{A}_2 \frac{\partial \mathbf{A}_3}{\partial \theta_3} \frac{d\theta_3}{dt} \right) \begin{vmatrix} 1 \\ x_{4P} \\ y_{4P} \\ z_{4P} \end{vmatrix}. \end{aligned} \quad (2)$$

Noting that the problem is to be adapted to computer operation, a linear operator matrix \mathbf{Q}_θ is introduced to perform the indicated differentiation through the following definition

$$\frac{\partial \mathbf{A}_i}{\partial \theta_i} = \mathbf{Q}_\theta \mathbf{A}_i.$$

Under this definition, the \mathbf{Q}_θ is found to be (Uicker J.J.jr., Denavit J., Hartenberg R.S, 1965):

$$\mathbf{Q}_\theta = \begin{vmatrix} 0 & 0 & 0 & 0 \\ 0 & 0 & -1 & 0 \\ 0 & 1 & 0 & 0 \\ 0 & 0 & 0 & 0 \end{vmatrix}.$$

It provides a simplified method of taking the partial derivative, especially in computer operation. With these the equation (2) becomes

$$\begin{aligned} \begin{vmatrix} 0 \\ \dot{x}_{1P} \\ \dot{y}_{1P} \\ \dot{z}_{1P} \end{vmatrix} = & \left(\mathbf{Q}_\theta \mathbf{A}_1 \mathbf{A}_2 \mathbf{A}_3 \frac{d\theta_1}{dt} + \mathbf{A}_1 \mathbf{Q}_\theta \mathbf{A}_2 \mathbf{A}_3 \frac{d\theta_2}{dt} + \right. \\ & \left. + \mathbf{A}_1 \mathbf{A}_2 \mathbf{Q}_\theta \mathbf{A}_3 \frac{d\theta_3}{dt} \right) \begin{vmatrix} 1 \\ x_{4P} \\ y_{4P} \\ z_{4P} \end{vmatrix}. \end{aligned} \quad (3)$$

Equating the matrices from equation (3) element for element, would produce a system of three linear equations in three unknowns, namely: $\frac{d\theta_1}{dt}$, $\frac{d\theta_2}{dt}$ and $\frac{d\theta_3}{dt}$.

3.3 Second time-derivatives of pair variables

Rather than to take the time-derivative of $\frac{d\theta_i}{dt}$, $i = \overline{1, 3}$, from equations (3), it is convenient

to continue to approach established above in differentiating the matrix equation (3). To facilitate the differentiation of this equation, it is first necessary to find an expression for the time derivative of the matrix product

$$\mathbf{B}_i = \mathbf{A}_1 \dots \mathbf{A}_{i-1} \mathbf{Q}_\theta \mathbf{A}_i \dots \mathbf{A}_3,$$

that is

$$\begin{aligned} \frac{d\mathbf{B}_i}{dt} = & \frac{\partial \mathbf{A}_1}{\partial \theta_1} \dots \mathbf{A}_{i-1} \mathbf{Q}_\theta \mathbf{A}_i \dots \mathbf{A}_3 \frac{d\theta_i}{dt} + \dots + \mathbf{A}_1 \dots \frac{\partial \mathbf{A}_{i-1}}{\partial \theta_{i-1}} \\ & \mathbf{Q}_\theta \mathbf{A}_i \dots \mathbf{A}_3 \frac{d\theta_{i-1}}{dt} + \mathbf{A}_1 \dots \mathbf{A}_{i-1} \mathbf{Q}_\theta \frac{\partial \mathbf{A}_i}{\partial \theta_i} \dots \mathbf{A}_3 \frac{d\theta_i}{dt} + \\ & \dots + \mathbf{A}_1 \dots \mathbf{A}_{i-1} \mathbf{Q}_\theta \mathbf{A}_i \dots \frac{\partial \mathbf{A}_3}{\partial \theta_3} \frac{d\theta_3}{dt}. \end{aligned}$$

Again using the derivative operator to perform the differentiation, the time-derivative of the equation (3) is

$$\begin{aligned} \begin{vmatrix} 0 \\ \ddot{x}_{1P} \\ \ddot{y}_{1P} \\ \ddot{z}_{1P} \end{vmatrix} = & \left(\mathbf{Q}_\theta \mathbf{Q}_\theta \mathbf{A}_1 \mathbf{A}_2 \mathbf{A}_3 \left(\frac{d\theta_1}{dt} \right)^2 + 2 \mathbf{Q}_\theta \mathbf{A}_1 \mathbf{Q}_\theta \mathbf{A}_2 \mathbf{A}_3 \frac{d\theta_1}{dt} \frac{d\theta_2}{dt} + \right. \\ & + 2 \mathbf{Q}_\theta \mathbf{A}_1 \mathbf{A}_2 \mathbf{Q}_\theta \mathbf{A}_3 \frac{d\theta_1}{dt} \frac{d\theta_3}{dt} + 2 \mathbf{A}_1 \mathbf{Q}_\theta \mathbf{A}_2 \mathbf{Q}_\theta \mathbf{A}_3 \frac{d\theta_2}{dt} \frac{d\theta_3}{dt} + \\ & \left. + \mathbf{A}_1 \mathbf{Q}_\theta \mathbf{Q}_\theta \mathbf{A}_2 \mathbf{A}_3 \left(\frac{d\theta_2}{dt} \right)^2 + \mathbf{A}_1 \mathbf{A}_2 \mathbf{Q}_\theta \mathbf{Q}_\theta \mathbf{A}_3 \left(\frac{d\theta_3}{dt} \right)^2 + \mathbf{Q}_\theta \mathbf{A}_1 \mathbf{A}_2 \right. \\ & \left. \mathbf{A}_3 \frac{d^2\theta_1}{dt^2} + \mathbf{A}_1 \mathbf{Q}_\theta \mathbf{A}_2 \mathbf{A}_3 \frac{d^2\theta_2}{dt^2} + \mathbf{A}_1 \mathbf{A}_2 \mathbf{Q}_\theta \mathbf{A}_3 \frac{d^2\theta_3}{dt^2} \right) \begin{vmatrix} 1 \\ x_{4P} \\ y_{4P} \\ z_{4P} \end{vmatrix}. \end{aligned} \quad (4)$$

Equating the matrices from equation (4) element for element, would produce a system of three linear equations in three unknowns, namely $\frac{d^2\theta_1}{dt^2}$, $\frac{d^2\theta_2}{dt^2}$ and $\frac{d^2\theta_3}{dt^2}$. A new problem arises, however, when one of the pairs, for instance pair i , is prismatic. The \mathbf{A}_i transformation matrix for this pair is essentially the same before. However, the angle θ_i is known exactly, and the distance s_i is unknown. The linear operator matrix \mathbf{Q}_s is replaced by the operator \mathbf{Q}_s :

$$\frac{\partial \mathbf{A}_i}{\partial s_i} = \mathbf{Q}_s \mathbf{A}_i$$

Under this definition, the \mathbf{Q}_s matrix is found to be [30]:

$$\mathbf{Q}_s = \begin{vmatrix} 0 & 0 & 0 & 0 \\ 0 & 0 & 0 & 0 \\ 0 & 0 & 0 & 0 \\ 1 & 0 & 0 & 0 \end{vmatrix}.$$

Fig. 8 displayed the kinematics scheme of the mechanical system of a walking robot achieved in modular structure. Each module is made by a platform which is joined with two legs. The modules are joined together by the connecting kinematics chains. These chains have three degrees of freedom and are made from two elements that are pinned together by three revolute pairs. Each first and last element of the connecting kinematics chain is joined to a module platform. All the joints of the connecting chain are driving ones. As a result, each kinematic chain is a sequence of three R-type active kinematics groups, connected in series (Simionescu I. & Moise V., 1999). It is considered a coordinate axes system attached to the platform of the first module. The axes of the Denavit – Hartenberg trihedrons (Denavit J. & Hartenberg R.S., 1955) are denoted with two indexes. The subscript index denotes the

number of the kinematics pair in the chain, and the superscript index denotes the number of the leg.

The coordinate of the support point P^i of the leg (i) with respect to the platform coordinate axes system $O_0X_0Y_0Z_0$ are:

$$\begin{vmatrix} 1 \\ x_{0P}^i \\ y_{0P}^i \\ z_{0P}^i \end{vmatrix} = \mathbf{A}_0^i \mathbf{A}_1^i \mathbf{A}_2^i \mathbf{A}_3^i \begin{vmatrix} 1 \\ x_{4P}^i \\ y_{4P}^i \\ z_{4P}^i \end{vmatrix}, \quad i = 1, 2; \quad (5)$$

$$\begin{vmatrix} 1 \\ x_{0P}^i \\ y_{0P}^i \\ z_{0P}^i \end{vmatrix} = \mathbf{A}_0^i \mathbf{A}_1^7 \mathbf{A}_1^8 \mathbf{A}_1^9 \mathbf{A}_1^i \mathbf{A}_2^i \mathbf{A}_3^i \begin{vmatrix} 1 \\ x_{4P}^i \\ y_{4P}^i \\ z_{4P}^i \end{vmatrix}, \quad i = 3, 4; \quad (6)$$

$$\begin{vmatrix} 1 \\ x_{0P}^i \\ y_{0P}^i \\ z_{0P}^i \end{vmatrix} = \mathbf{A}_0^i \mathbf{A}_1^{10} \mathbf{A}_1^{11} \mathbf{A}_1^{12} \mathbf{A}_1^i \mathbf{A}_2^i \mathbf{A}_3^i \begin{vmatrix} 1 \\ x_{4P}^i \\ y_{4P}^i \\ z_{4P}^i \end{vmatrix}, \quad i = 5, 6. \quad (7)$$

In the direct kinematic analysis the variables of the all driving kinematic pairs are considered as known. The goal of the direct kinematics analysis is to simulate the displacement of the walking robot.

In the inverse kinematic analysis of the leg mechanism, the position x_{0P} , y_{0P} , z_{0P} , the velocity \dot{x}_{0P} , \dot{y}_{0P} , \dot{z}_{0P} and the acceleration \ddot{x}_{0P} , \ddot{y}_{0P} , \ddot{z}_{0P} of the point P with respect to the robot platform are considered as known. The unknowns of the problem are the variables of the driving pairs and their first and second time-derivative. The matrix equations (5), (6) and (7) are equivalent with three scalar equations and have six unknowns. As a result, three pair variables can be calculated by solving of the equations (5), (6) and (7) only. The remaining of three pair variables must be established so that the walking robot to adapt to the terrain in an optimum mode. The time-derivative of the variables of the driving pairs are calculated by solving the equation which arisen by differentiating of the equations (5), (6) and (7).1

$$\begin{aligned}
& \left\| \begin{array}{c} 1 \\ \dot{x}_{0P}^i \\ \dot{y}_{0P}^i \\ \dot{z}_{0P}^i \end{array} \right\| = \left(\mathbf{A}_0^i \mathbf{Q}_\theta \mathbf{A}_1^i \mathbf{A}_2^i \mathbf{A}_3^i \frac{d\theta_1}{dt} + \mathbf{A}_0^i \mathbf{A}_1^i \mathbf{Q}_\theta \mathbf{A}_2^i \mathbf{A}_3^i \frac{d\theta_2}{dt} * \right. \\
& \quad \left. + \mathbf{A}_0^i \mathbf{A}_1^i \mathbf{A}_2^i \mathbf{Q}_\theta \mathbf{A}_3^i \frac{d\theta_3}{dt} \right) \left\| \begin{array}{c} 1 \\ x_{4P}^i \\ y_{4P}^i \\ z_{4P}^i \end{array} \right\|, \quad i=1,2; \\
& \left\| \begin{array}{c} 1 \\ \dot{x}_{0P}^j \\ \dot{y}_{0P}^j \\ \dot{z}_{0P}^j \end{array} \right\| = \left(\mathbf{A}_0^j \mathbf{Q}_\theta \mathbf{A}_1^7 \mathbf{A}_2^8 \mathbf{A}_3^9 \mathbf{A}_1^i \mathbf{A}_2^i \mathbf{A}_3^i \frac{d\theta_1^7}{dt} + \mathbf{A}_0^j \mathbf{A}_1^7 \mathbf{Q}_\theta \mathbf{A}_2^8 \mathbf{A}_3^9 \mathbf{A}_1^i \mathbf{A}_2^i \mathbf{A}_3^i \frac{d\theta_2^8}{dt} \right. \\
& \quad \left. + \mathbf{A}_0^j \mathbf{A}_1^7 \mathbf{A}_2^8 \mathbf{Q}_\theta \mathbf{A}_3^9 \mathbf{A}_1^i \mathbf{A}_2^i \mathbf{A}_3^i \frac{d\theta_3^9}{dt} + \mathbf{A}_0^j \mathbf{A}_1^7 \mathbf{A}_2^8 \mathbf{A}_3^9 \mathbf{Q}_\theta \mathbf{A}_1^i \mathbf{A}_2^i \mathbf{A}_3^i \frac{d\theta_1^9}{dt} \right. \\
& \quad \left. + \mathbf{A}_0^j \mathbf{A}_1^7 \mathbf{A}_2^8 \mathbf{A}_3^9 \mathbf{A}_1^i \mathbf{Q}_\theta \mathbf{A}_2^i \mathbf{A}_3^i \frac{d\theta_2^9}{dt} + * \mathbf{A}_0^j \mathbf{A}_1^7 \mathbf{A}_2^8 \mathbf{A}_3^9 \mathbf{A}_1^i \mathbf{A}_2^i \mathbf{Q}_\theta \mathbf{A}_3^i \frac{d\theta_3^9}{dt} \right) \left\| \begin{array}{c} 1 \\ x_{4P}^j \\ y_{4P}^j \\ z_{4P}^j \end{array} \right\|, \\
& \quad i=3,4; \\
& \left\| \begin{array}{c} 1 \\ \dot{x}_{0P}^i \\ \dot{y}_{0P}^i \\ \dot{z}_{0P}^i \end{array} \right\| = \left(\mathbf{A}_0^i \mathbf{Q}_\theta \mathbf{A}_1^{10} \mathbf{A}_2^{11} \mathbf{A}_3^{12} \mathbf{A}_1^i \mathbf{A}_2^i \mathbf{A}_3^i \frac{d\theta_1^{10}}{dt} + \mathbf{A}_0^i \mathbf{A}_1^{10} \mathbf{Q}_\theta \mathbf{A}_2^{11} \mathbf{A}_3^{12} \mathbf{A}_1^i \mathbf{A}_2^i \mathbf{A}_3^i \frac{d\theta_2^{11}}{dt} + \right. \\
& \quad \left. + \mathbf{A}_0^i \mathbf{A}_1^{10} \mathbf{A}_2^{11} \mathbf{Q}_\theta \mathbf{A}_3^{12} \mathbf{A}_1^i \mathbf{A}_2^i \mathbf{A}_3^i \frac{d\theta_3^{12}}{dt} + \mathbf{A}_0^i \mathbf{A}_1^{10} \mathbf{A}_2^{11} \mathbf{A}_3^{12} \mathbf{Q}_\theta \mathbf{A}_1^i \mathbf{A}_2^i \mathbf{A}_3^i \frac{d\theta_1^{12}}{dt} + \right. \\
& \quad \left. + \mathbf{A}_0^i \mathbf{A}_1^{10} \mathbf{A}_2^{11} \mathbf{A}_3^{12} \mathbf{A}_1^i \mathbf{Q}_\theta \mathbf{A}_2^i \mathbf{A}_3^i \frac{d\theta_2^{12}}{dt} + * \mathbf{A}_0^i \mathbf{A}_1^{10} \mathbf{A}_2^{11} \mathbf{A}_3^{12} \mathbf{A}_1^i \mathbf{A}_2^i \mathbf{Q}_\theta \mathbf{A}_3^i \frac{d\theta_3^{12}}{dt} \right) \left\| \begin{array}{c} 1 \\ x_{4P}^i \\ y_{4P}^i \\ z_{4P}^i \end{array} \right\|, \\
& \quad i=5,6;
\end{aligned}$$

4. Force Distribution in Displacement Systems of Walking Robots

The system builds by the terrain on which the displacement is done and the walking robot which has three legs in the support phase is statically determinate.

When it leans upon four (or more) feet, it turns in a statically indeterminate system.

The problem of determination of reaction force components is made in simplifying assumption, namely the stiffness of the walking robot mechanical structure and terrain.

For establishing the stable positions of a walking robot it is necessary to determine the forces distribution in the shifting mechanisms. In the case of a uniform and rectilinear movement of the walking robot on a plane and horizontal surface, the reaction forces do not have the tangential components, because the applied forces are the gravitational forces only.

Determination of the real forces distribution in the shifting mechanisms of a walking locomotion system which moves in rugged land at low speed is necessary for the analysis of stability. The position of a walking system depends on the following factors:

- the configuration of walking mechanisms;
- the masses of component elements and their positions of gravity centers;
- the values of friction coefficients between terrain and feet;
- the shape of terrain surface.
- the stiffness of terrain;

The active surface of the foot is relatively small and it is considered that the reaction force is applied in the gravity center of this surface. The reaction force represents the resultant of the elementary forces, uniformly distributed on the foot sole surface. The gravity center of the foot active surface is called *theoretical contact point*.

To calculate the components of reaction forces, namely:

- normal component \bar{N} , perpendicular on the surface of terrain in the theoretical contact point;
- tangential component \bar{T} , or coulombian frictional force, comprised in the tangent plane at terrain surface in the theoretical contact point,

it is necessary to determine the stable positions of walking robots (Ion I., Simionescu I. & Curaj A., 2002), (Ion I. & Stefanescu D.M., 1999).

The magnitude of \bar{T} vector cannot be greater than the product of the magnitude of the normal component \bar{N} by the frictional coefficient μ between foot sole and terrain. If this magnitude is greater than the friction force, then the foot slips down along the support surface to the stable position, where the magnitudes of this component decrease under the above-mentioned limit.

Therefore, the problem of determining the stable position of a walking robot upon some terrain has not a unique solution. For every foot is available a field which covers all contact points in which the condition $T \leq \mu N$ is true. The equal sign corresponds to the field's boundary.

The complex behavior of the earth cannot be described than by an idealization of its properties. The surface of terrain which the robot walks on is defined in respect to a fixed

coordinates system $O\xi\eta\zeta$ annexed to the terrain, by the parametrical equations $\xi = \xi(u, v)$; $\eta = \eta(u, v)$; $\zeta = \zeta(u, v)$, implicit equation $F(\xi, \eta, \zeta) = 0$, or explicit equation $\zeta = f(\xi, \eta)$.

These real, continuous and uniform functions with continuous first partial and ordinary derivative, establish a biunivocal correspondence between the points of support surface and the ordered pairs (u, v) , where $\{u, v\} \in \mathbb{R}$. Not all partial first order derivatives are null, and not all Jacobians

$$\frac{D(\xi, \eta)}{D(u, v)}, \frac{D(\eta, \zeta)}{D(u, v)}, \frac{D(\zeta, \xi)}{D(u, v)}$$

are simultaneous null.

On the entire surface of the terrain, the equation expressions may be unique or may be multiple, having the limited domains of validity.

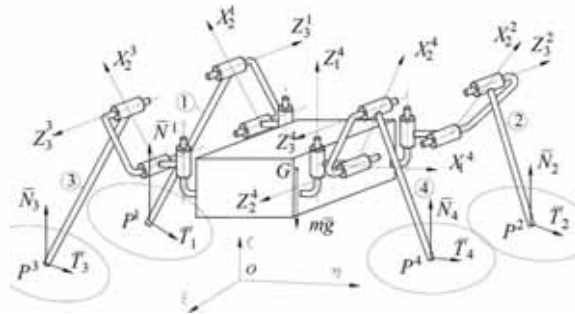


Fig. 8. The Hartenberg – Denavit coordinate systems and the reaction force components

The normal component \bar{N}_i of reaction force at the P_i contact point of the leg i with the terrain is positioned by the direction cosine:

$$\cos \alpha^i = \frac{A_i}{\sqrt{A_i^2 + B_i^2 + C_i^2}}; \quad \cos \beta^i = \frac{B_i}{\sqrt{A_i^2 + B_i^2 + C_i^2}};$$

$$\cos \gamma^i = \frac{C_i}{\sqrt{A_i^2 + B_i^2 + C_i^2}},$$

with respect to the fixed coordinate axes system, where:

$$A_i = \begin{vmatrix} \frac{\partial \eta^i}{\partial u_i} & \frac{\partial \zeta^i}{\partial u_i} \\ \frac{\partial \eta^i}{\partial v_i} & \frac{\partial \zeta^i}{\partial v_i} \end{vmatrix}; \quad B_i = \begin{vmatrix} \frac{\partial \zeta^i}{\partial u_i} & \frac{\partial \xi^i}{\partial u_i} \\ \frac{\partial \zeta^i}{\partial v_i} & \frac{\partial \xi^i}{\partial v_i} \end{vmatrix}; \quad C_i = \begin{vmatrix} \frac{\partial \xi^i}{\partial u_i} & \frac{\partial \eta^i}{\partial u_i} \\ \frac{\partial \xi^i}{\partial v_i} & \frac{\partial \eta^i}{\partial v_i} \end{vmatrix}.$$

The tangential component of reaction force, i.e. the friction force, is comprised in the tangent plane at the support surface. The equation of the tangent plane in the point P^i ($\xi_{P^i}, \eta_{P^i}, \zeta_{P^i}$) is

$$\begin{vmatrix} \xi^i - \xi_{Pi} & \eta^i - \eta_{Pi} & \zeta^i - \zeta_{Pi} \\ \frac{\partial \xi^i}{\partial u_i} & \frac{\partial \eta^i}{\partial u_i} & \frac{\partial \zeta^i}{\partial u_i} \\ \frac{\partial \xi^i}{\partial v_i} & \frac{\partial \eta^i}{\partial v_i} & \frac{\partial \zeta^i}{\partial v_i} \end{vmatrix} = 0,$$

or: $\xi^i A_i + \eta^i B_i + \zeta^i C_i - \xi_{Pi} A_i - \eta_{Pi} B_i - \zeta_{Pi} C_i = 0$.

The straight-line support of the friction force is included in the tangent plane:

$$\frac{\xi^i - \xi_{Pi}}{l_i} = \frac{\eta^i - \eta_{Pi}}{m_i} = \frac{\zeta^i - \zeta_{Pi}}{n_i},$$

therefore: $A_i l_i + B_i m_i + C_i n_i = 0$.

If the surface over which the robot walked is plane, it is possible that the robot may slip to the direction of the maximum slope.

Generally, the sliding result is a rotational motion superposed on a translational one. The instantaneous axis has an unknown position.

Let us consider

$$\frac{\xi - U}{\cos \alpha_r} = \frac{\eta - V}{\cos \beta_r} = \frac{\zeta}{\cos \gamma_r}$$

the equation of instantaneous axis under canonical form, with respect to the fixed coordinate axes system. The components of speed of the point P^i , on the fixed coordinate axes system with OZ axis identical with the instantaneous axis, are:

$$\bar{V}_X = -\omega Y i; \bar{V}_Y = \omega X j; \bar{V}_Z = \bar{V}_0,$$

The projections of the P^i point speed on the axes of fixed system $O\xi\eta\zeta$ are:

$$\begin{vmatrix} V_\xi \\ V_\eta \\ V_\zeta \end{vmatrix} = \mathbf{R} \begin{vmatrix} V_X \\ V_Y \\ V_Z \end{vmatrix},$$

where \mathbf{R} is the matrix of rotation in space.

The carrier straight line of P^i point speed, i.e. of the tangential component of reaction force, has the equations

$$\frac{\xi - \xi_{Pi}}{V_\xi} = \frac{\eta - \eta_{Pi}}{V_\eta} = \frac{\zeta}{V_\zeta},$$

and is contained in the tangent plane to the terrain surface in the point P^i :

$$V_\xi l + V_\eta m + V_\zeta n = 0.$$

To determine the stable position of the walking robot which leans upon n legs, on some shape terrain, it is necessary to solve a nonlinear system, which is formed by:

- the transformation matrix equation

$$\begin{vmatrix} 1 \\ X_{0Pi} \\ Y_{0Pi} \\ Z_{0Pi} \end{vmatrix} = \mathbf{A}\mathbf{A}_0^i\mathbf{A}_1^i\mathbf{A}_2^i\mathbf{A}_3^i \begin{vmatrix} 1 \\ X_{4Pi} \\ Y_{4Pi} \\ Z_{4Pi} \end{vmatrix},$$

where:

\mathbf{A} is the transformation matrix of coordinate of a point from the system $O_0X_0Y_0Z_0$ of the robot platform to the system $O\xi\eta\zeta$;

\mathbf{A}_i is the Denavit – Hartenberg transformation matrix of coordinates of a point from the system $O_{i+1}X_{i+1}Y_{i+1}Z_{i+1}$ of the element (i) to the system $O_iX_iY_iZ_i$ of the element ($i-1$) (Denavit J. & Hartenberg R.S., 1955), (Uicker J.J.jr., Denavit J., Hartenberg R.S., 1965):

- the balance equations

$$\sum_{i=1}^n \bar{R}_i + \bar{F} = 0; \quad \sum_{i=1}^n \bar{M}_{(R_i)} + \bar{M} = 0, \quad (8)$$

which expressed the equilibrium of the forces and moments system, which acted on the elements of walking robot.

The \bar{F} and \bar{M} are the wrench components of the forces and moments which represent the robot load, including the own weight.

The unknowns of the system are:

- the coordinates X_T, Y_T, Z_T and direction cosines $\cos \alpha_T, \cos \beta_T, \cos \gamma_T$ which define the platform position with respect to the terrain;
- the normal \bar{N}_i and the tangential $\bar{T}_i, i = \overline{1, n}$, components of the reaction forces;
- the direction numbers $l_i, m_i, n_i, i = \overline{1, n}$, of the tangential components;
- the position parameters $U, V, \cos \alpha, \cos \beta, \cos \gamma$ of the instantaneous axis;
- the magnitude of the V_0 / ω ratio, where V_0 is the translational instantaneous speed of the hardening structure (Okhotsimski D.E. & Golubev I., 1984). The system is compatible for $n = 3$ support points.

If the number of feet which are simultaneous in the support phase is larger than three the system is undetermined static and is necessary to take into consideration the deformations of the mechanical structure of the walking robot and terrain. In case of a quadrupedal walking robot, the hardening configuration is a six fold hyperstatic structure. To determinate the force distribution, one must use a specific method for indeterminate static systems.

The canonical equations in stress method are (Buzdugan Gh., 1980):

$$\begin{aligned} \delta_{11} x_1 + \delta_{12} x_2 + \dots + \delta_{16} x_6 &= -\delta_{10}; \\ \delta_{21} x_1 + \delta_{22} x_2 + \dots + \delta_{26} x_6 &= -\delta_{20}; \\ \dots \dots \end{aligned} \quad (9)$$

$$\delta_{61} x_1 + \delta_{62} x_2 + \dots + \delta_{66} x_6 = -\delta_{60};$$

where:

δ_{ij} is the displacement along the O_iX_i direction of stress owing to unit load which acts on the direction and in application point of the O_iX_j ;

δ_{i0} is the displacement along the X_i direction of stress owing to the external load when $O_iX_j = 0$, $i = \overline{1,6}$:

$$\begin{aligned}\delta_{i0} &= \sum_{p=1}^4 \int \frac{M_{y0} m_{yi}}{EI_{y1}} dx + \sum_{q=1}^4 \int \frac{M_{y0} m_{yi}}{EI_{y2}} dx, i = \overline{1,6}; \\ \delta_{ij} &= \sum_{p=1}^4 \int \frac{M_{xi} m_{xi}}{GI_{x1}} dx + \sum_{q=1}^4 \int \frac{M_{xi} m_{xi}}{GI_{x2}} dx + \\ &\quad + \sum_{q=1}^4 \int \frac{M_{xi} m_{xi}}{GI_{x3}} dx + \sum_{p=1}^4 \int \frac{M_{yi} m_{yi}}{GI_{y1}} dx + \\ &\quad + \sum_{q=1}^4 \int \frac{M_{yi} m_{yi}}{GI_{y2}} dx + \sum_{q=1}^4 \int \frac{M_{yi} m_{yi}}{GI_{y3}} dx + \\ &\quad + \sum_{p=1}^4 \int \frac{M_{zi} m_{zi}}{GI_{z1}} dx + \sum_{q=1}^4 \int \frac{M_{zi} m_{zi}}{GI_{z2}} dx + \\ &\quad + \sum_{q=1}^4 \int \frac{M_{zi} m_{zi}}{GI_{z3}} dx, \quad i = \overline{1,6}, j = \overline{1,6};\end{aligned}$$

GI_{xi} , $i = \overline{1,3}$, are the torsion stiffness of the legs elements lowers, middles and uppers respectively;

EI_{yi} and EI_{zi} , $i = \overline{1,3}$, are the bend stiffness of the legs elements lowers, middles and uppers respectively;

M are the bending moments in basic system which is loaded with basic charge;

m are the bending moments in the basic system loaded with the unit charge.

The definite integrals

$$I = \int_a^b M m dx$$

are calculated by the Simpson method:

$$I = \frac{b-a}{6} [(M_a + M_b)(m_a + m_b) + M_a m_a + M_b m_b].$$

To calculate the m_{xi} , m_{yi} , m_{zi} , M_{xi} , M_{yi} , M_{zi} , $i = \overline{1,6}$, seven systems are used (Fig. 8), namely:

- the system S_0 , where the single load is G , and $X_i = 0$, $i = \overline{1,6}$;

- the systems S_i , where the single load is $X_i = 1$, $i = \overline{1, 6}$.

The remaining unknowns, namely x_i , $i = \overline{7, 12}$, are calculated from the equations (9). The normal and tangential components of the reaction forces are calculated as function of the positions of tangent planes on the terrain surface at the support points.

The following hypotheses are considered as true:

- the stiffnesses of the legs are much less than the robot's platform stiffness;
- the four legs are identically.
- the cross sections of the leg's elements are constant.

In Fig. 9, a modular walking robot with six legs is shown. The hardening structure of this robot is a 12-fold hyperstatical structure.

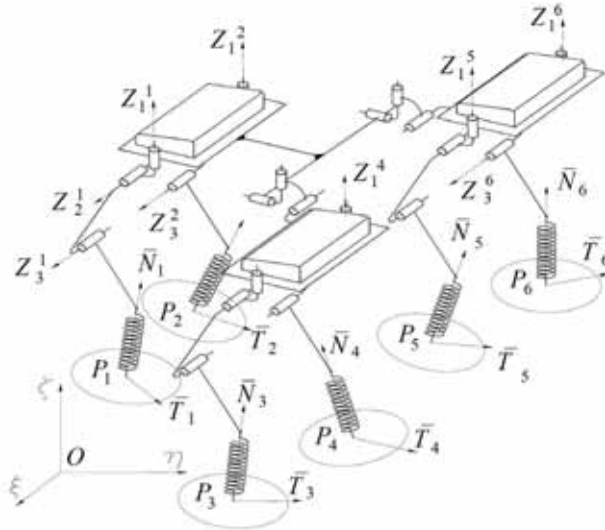


Fig. 9. The reaction force components in the support points of the modular walking robot

5. Movement of Walking Robots

Part of the characteristic parameters of the walking robot may change widely enough when using it as a transportation mean. For instance, the additional loads on board, change the positions of the gravity centers and the inertia moments of the module's platforms. Environmental factors such as the wind or other elements may bias the robot, and their influence is barely predictable. Such disturbances can cause considerable deviations in the real movement of the robot than expected.

Drawing up and using efficient methods of finding out the causes of such deviations, as well as of avoiding such causes, represent an appropriate way of enhancing the walking robot's proficiency and this at lower power costs.

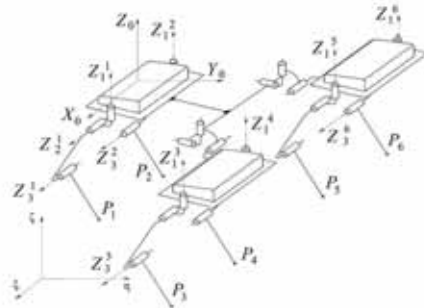


Fig. 10. Kinematics scheme of walking modular robot

Working out and complete enough mathematical pattern for studying the movement of a walking robot is interesting, both as regards the structure of its control system and verifying the simplifying principles and hypotheses, that the control program's algorithms rely on. The static stability issue is solved by calculating the positions of each foot against the axes system, attached to the platform, and whose origin is in the latter's gravity center (Waldron K.J. 1985).

The static stability of the gait is a problem which appears on the quadrupedal walking robot movement.

When a leg is in the transfer phase, the vertical projection of the gravity center of the hardening structure may be outside of the support polygon, i.e. support triangle. It is the case of the walking robot made by two modules. The gait 3×3 (Song S.M. & Waldron K.J., 1989), (Hirose S., 1991) of the six legged walking robot, made by three modules, is static stable (Fig. 10). S. Hirose defined the *stability margins* that are the limits distances between the vertical projection of the gravity center and the sides of the support triangle. To provide the static stability of the quadrupedal walking robots two methods are used:

- the waved gait,
- the swinging gait.

In the first case, before a leg is lifted up the terrain, all leg are moved so that the robot platform to be displaced in the opposite side to the leg that will be lifted. In this way, the vertical projection of the gravity center moved along a zigzag line.

In the second case, before a leg is lifted, this is extended and the diagonal-opposite leg is compressed.

So, the robot platform has a swinging movement, and the vertical projection of the gravity center also has a zigzag displacement. This gait can not be used if the robot load must be hold in horizontal position.

The length of the step does not influence the limits of the static stability of the walking robot because the mass of a leg is more less than mass of the platform.

A walking robot, which moves under dynamical stability condition can attain higher velocities and can make steps with a greater length and a greater height. But, the central platform of the robot cannot be maintained in the horizontal position because it tilted to the foot which is lifted off the terrain. The size of the maximum inclination angle depends to the forward speed of the walking robot.

The stability problem is very important at the moving of the quadrupedal walking robots. When a foot is lifted off the terrain and the other legs supporting the robot's platform are in contact with the terrain. If the vertical projection G' of the gravity center G of the legged robot is outside of the supporting polygon (triangle $P^1 P^2 P^3$, Fig. 11), and the cruising speed is greater than a certain limit, the movement of the robot happens under condition of the dynamical stability. When the leg (4) is lifted off the terrain, the walking robot rotates around of the straight line which passing through the support points P^2 and P^3 .

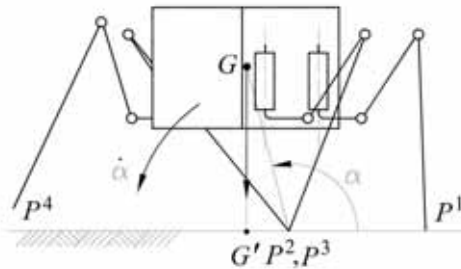


Fig. 11. The overturning movement of the walking robot

The magnitude of the forward speed did not influence the rotational motion of the robot around the straight line P^2P^3 . This rotational motion can be investigated with the Lagrange's equation (Appel P. 1908):

$$\frac{d}{dt} \left(\frac{\partial T}{\partial \dot{q}} \right) - \frac{\partial T}{\partial q} + \frac{\partial P}{\partial q} = Q \quad (10)$$

The kinetic and potential energies of the hardening configuration of the robot have the forms

$$T = (m AG^2 + I) \frac{\dot{\alpha}^2}{2}, \quad P = m g AG(1 - \sin \alpha), \quad (11)$$

and the generalized force is

$$Q = -m g AG \cos \alpha. \quad (12)$$

where m denotes the mass of the entire robot, I is the moment of inertia of the robot structure with respect to the axis passed by G and AG is the distance between the gravity center G and the rotational axis P^2P^3 ($\alpha > \pi/2$) (Fig. 11).

Substituting the (11) and (12) into (10), it results

$$\ddot{\alpha} = - \frac{2m g AG \cos \alpha}{I + m AG^2} \quad (13)$$

Because the moment of inertia of a body is proportional with its mass, the angular acceleration $\ddot{\alpha}$ does not dependent on the mass m .

The quadrupedal walking robot in question, which moved so that the step size is 0.2 m, with forward average speed equal to 3.63 m/s (13 km/h approximate) has the maximum inclination of the platform equal to 0.174533. This forward speed is very great for the usual applications of the walking robots. As a result, the movement of the legged robots is made under condition of the static stability. The conventional quadrupedal walking robots have

rather sluggish gaits for walking, but are unable to move smoothly and quickly like animal beings.

6. Optimization of Kinematic Dimension of Displacement Systems of Walking Robots

For the walking robot to get high shift performances on as many different terrain configurations as possible, and for increasing the robot's mobility and stability, under such circumstances, it is required a very careful survey on the trajectory's control, which involves both to determine the coordinates of the feet's leaning points, as related to the robot's body, and the calculation of the platform's location during the walking, as against a set system of coordinates in the field.

These performances are closely connected with the shift system's structure and the dimensions of the compound elements. For simplifying its mounting, it is accepted the existence of a point-shaped contact between the foot and the leaning area.

The shift system mechanism of any walking robot is built so that he could achieve a multitude of the toes' trajectories. These courses may change according to the ground surface, at every step. Choosing a certain trajectory depends on the topography of the surface that the robot is moving on. As one could already notice, during time, the shift mechanism is the most important part of the walking robot and it has one or several degrees of freedom, contingent of the kinematics chain that its structure relies on.

Considering the fact that the energy source is fixed on the robot's platform, the dimensions of the legs mechanism's elements are calculated using a multicritical optimization proceeding, which includes several restrictions. The objective function (Fox R. 1973), (Goldberg D. 1999), (Coley D. 1999) may express:

- the mechanical work needed for shifting the platform by one step ;
- the maximum driving force needed for the leg mechanism;
- the maximum power required for shifting, and so on.

These objective functions can be considered separately or simultaneously. The minimization of the mechanical work consumed for defeating of the friction forces can be considered in the legs mechanisms' synthesis also by a multicritical optimization.

The kinematics dimensions of the shift system mechanism elements are obtained as a result of several considerations and calculation taking into account the degree of freedom, the energy consumption, the efficiency, the kinematics performances, the potential distribution, the operation field and the movement regulating algorithm.

There are two possibilities in order to decrease the energy consumption of a walking robot. One of them is to optimize the shifting system of the robot. That could be performing by the kinetostatic synthesis of the leg mechanism with minimization of energy consumption during a stepping cycle.

A second possibility to decrease the energy consumption is the static balancing of the leg mechanism [Ebert-Uphoff I. & Gosellin C.M. 1998], (Ion I., Simionescu I. & Ungureanu M. 2001), (Simionescu I. & Ion I. 2001).

The energy consumption is especially depended on the moving law of the platform, which has the biggest mass.

The simplest constructional solution for the leg mechanisms of the walking robot uses the revolute pairs only. The linear hydraulic motor has only a prismatic pair (Fig. 12). This

mechanism consists of two plane kinematics chains. One of these kinematics chains is composed by the links (1), (2) and (3), and operated in the horizontal plane. The other kinematics chain operated in the vertical plane and is formed by the elements (4), (5), (6), (7), (8) and (9). The lengths of the elements (6) and (7), i.e. the distances IH and HP respectively, are calculated in terms of the size of the field in which the P point of the low end of the leg is displaced. The magnitudes of the driving forces F_{d2} between the piston (5) and the cylinder (4) and F_{d1} between the piston (8) and the cylinder (9) are calculated with the following relations:

$$\begin{aligned} F_{d1} = & \frac{Q_x(Y_H - Y_P) - Q_y(X_H - X_P)}{(X_H - X_L) \sin \varphi_2 - (Y_H - Y_L) \cos \varphi_2} + \\ & + \frac{(m_7 + m_8)g(X_H - X_L) - m_7g(X_{G7} - X_L)}{(X_H - X_L) \sin \varphi_2 - (Y_H - Y_L) \cos \varphi_2}; \end{aligned} \quad (14)$$

$$\begin{aligned} F_{d2} = & \frac{R_{69Y}(X_I - X_J) + R_{67Y}(X_I - X_H)}{(X_H - X_L) \sin \varphi_2 - (Y_H - Y_L) \cos \varphi_2} + \\ & + \frac{(m_5 + m_6)g(X_I - X_G) - m_6g(X_{G6} - X_G)}{(X_H - X_L) \sin \varphi_2 - (Y_H - Y_L) \cos \varphi_2} + \\ & + \frac{R_{69X}(Y_I - Y_J) - R_{67X}(Y_I - Y_H)}{(X_H - X_L) \sin \varphi_2 - (Y_H - Y_L) \cos \varphi_2}, \end{aligned} \quad (15)$$

where:

$$\begin{aligned} R_{69X} &= F_{d1} \cos \varphi_2; \\ R_{69Y} &= F_{d1} \sin \varphi_2 + m_9g; \\ R_{67X} &= -Q_X - F_{d1} \cos \varphi_2; \\ R_{67Y} &= (m_7 + m_8 + m_9)g - Q_Y - F_{d1} \sin \varphi_2; \\ \varphi_1 &= \arctan \frac{Y_G - Y_E}{X_G - X_E}; \\ \varphi_2 &= \arctan \frac{Y_L - Y_J}{X_L - X_J}. \end{aligned}$$

The m_i , X_{Gi} and Y_{Gi} represent the mass and the coordinates of gravity centre of element (i) respectively.

The mechanical work of the driving forces F_{d1} and F_{d2} , performed in the T time when the robot platform advances with a step by one single leg, has the form:

$$W = \int_0^T (F_{d1} \frac{dJL}{dt} + F_{d2} \frac{dEG}{dt}) dt, \quad (16)$$

where:

$$\frac{dEG}{dt} = \frac{1}{EG} \left[(X_G - X_E) \frac{dX_G}{dt} + (Y_G - Y_E) \frac{dY_G}{dt} \right];$$

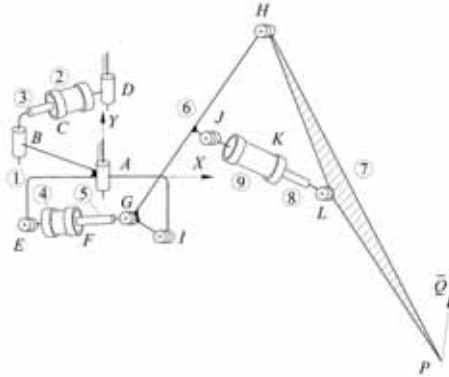


Fig. 12. Mechanism of leg

$$\frac{dJL}{dt} = \frac{1}{JL} \left[(X_L - X_J) \left(\frac{dX_L}{dt} - \frac{dX_J}{dt} \right) + (Y_L - Y_J) \left(\frac{dY_L}{dt} - \frac{dY_J}{dt} \right) \right];$$

$$EG = \sqrt{(X_G - X_E)^2 + (Y_G - Y_E)^2};$$

$$JL = \sqrt{(X_L - X_J)^2 + (Y_L - Y_J)^2};$$

$$X_G = X_I + GI \cos(\varphi_{IH} + \beta);$$

$$Y_G = Y_I + GI \sin(\varphi_{IH} + \beta);$$

$$X_L = X_P + PL \cos(\varphi_{PH} + \alpha);$$

$$Y_L = Y_P + PL \sin(\varphi_{PH} + \alpha);$$

$$\alpha = \arccos \frac{HP^2 + LP^2 - HL^2}{2HP \cdot LP};$$

$$\beta = \arccos \frac{HI^2 + GI^2 - GH^2}{2HI \cdot GI};$$

$$\varphi_{IH} = \arccos \frac{V_1 \sqrt{U_1^2 + V_1^2 - W_1^2} - U_1 W_1}{U_1^2 + V_1^2},$$

$$U_1 = 2HP(X_P - X_H), V_1 = 2HP(Y_P - Y_H),$$

$$W_1 = HP^2 + (X_P - X_I)^2 + (Y_P - Y_I)^2 - HI^2,$$

$$\varphi_{IH} = \arccos \frac{V_2 \sqrt{U_2^2 + V_2^2 - W_2^2} - U_2 W_2}{U_2^2 + V_2^2},$$

$$U_2 = 2HI(X_I - X_H), V_2 = 2HI(Y_I - Y_H),$$

$$W_2 = HI^2 + (X_P - X_I)^2 + (Y_P - Y_I)^2 - HP^2;$$

$$\begin{aligned}\frac{d\varphi_{IH}}{dt} &= \frac{HI}{E} \left(\frac{dY_P}{dt} \sin \varphi_{PH} + \frac{dX_P}{dt} \cos \varphi_{PH} \right); \\ \frac{d\varphi_{PH}}{dt} &= \frac{PI}{E} \left(\frac{dY_P}{dt} \sin \varphi_{IH} + \frac{dX_P}{dt} \cos \varphi_{IH} \right) \\ E &= HP \cdot HI \sin(\varphi_{IH} - \varphi_{PH}) \neq 0.\end{aligned}$$

The minimization of the mechanical work of the driving forces is done with constraints which are limiting the magnitudes of the transmission angles of the forces in the leg mechanism, namely:

$$R_1 = \Psi - \delta_{\min} \geq 0; R_2 = \delta_{\max} - \Psi \geq 0; \quad (17)$$

$$R_3 = \Theta - \delta_{\min} \geq 0; R_4 = \delta_{\max} - \Theta \geq 0; \quad (18)$$

and the magnitude of the Θ angle between the vectors \overline{HI} and \overline{HP} . This angle depends on the maximum height of the obstacle over which the walking robot can pass over, and on the maximum depth of the hollows which it may be stepped over:

$$R_5 = \Phi - \lambda_{\min} \geq 0; R_6 = \lambda_{\max} - \Phi \geq 0, \quad (19)$$

$$\text{where: } \Psi = \varphi_{IH} - \beta - \arctan \frac{Y_G - Y_E}{X_G - X_E};$$

$$\Theta = \varphi_{PH} + \arccos \frac{HL^2 + HP^2 - LP^2}{2HL \cdot HP} - \arctan \frac{Y_J - Y_L}{X_J - X_L};$$

$$\Phi = \varphi_{HP} - \varphi_{IH}.$$

The Ψ angle is measured between the vectors \overline{GI} and \overline{GE} . The dimensions $HI, HP, LP, HG, IJ, JH, \alpha$ and β of the elements and the coordinates X_E, Y_E, X_I, Y_I of the fixed points E and I are considered as the unknowns of the synthesis problem.

The necessary power for acting the leg mechanism is calculated by the relation

$$P = F_{d1} \frac{dEG}{dt} + F_{d2} \frac{dJL}{dt}. \quad (20)$$

The maximum power value is minimized in the presence of the constraints (17), (18) and (19).

7. Static Balancing of Displacement Systems of Walking Robots

The walking robots represent a special category of robots, characterized by having the power source embarked on the platform. This weight of this source is an important part of the total charge that the walking machine can be transported. That is the reason why the walking system must be designed so that the mechanical work necessary for displacement, or the highest power necessary to act it, should be minimal. The major energy consumption of a walking machine is divided into three different categories:

- the energy consumed for generating forces required to sustain the platform in gravitational field; in other word, this is the energy consumed to compensate the potential energy variation;

- the energy consumed by leg mechanism actuators, for the walking robot displacement in acceleration and deceleration phases;
- the energy lost by friction forces and moments in kinematics pairs.

The magnitude of reaction forces in kinematics pairs and the actuator forces depend on the load distribution on the legs. For slow speed, joint gravitational loads are significantly larger than inertial loads; by eliminating gravitational loads, the dynamic performances are improved.

Therefore, the power consumption to sustain the walking machine platform in the gravitational field can be reduced by using the balancing elastic systems and by optimum design of the leg mechanisms. The potential energy of the walking machine is constant or has a little variation, if the static balance is achieved. The balancing elastic system consist of by rigid and linear elastic elements.

7.1 Synthesis of Static Balancing Elastic Systems

The most usual constructions of the leg mechanisms have three degree of freedom. The proper leg mechanism is a plane one and has two degree of freedom (Fig. 13). This mechanism is articulated to the platform and it may be rotated around a vertical axis. To reduce the power consumption by robot driving system it is necessary to use two balancing elastic systems. One must be set between links (2) and (3), and the other - between links (3) and (4). Because the link (3) is not fixed, the second balancing elastic system can not be set. Therefore, the leg mechanism schematized in Fig. 13 can be balanced partially only (Streit, D.A. & Gilmore, B.J. , 1989).

It is well known and demonstrated that the weight force of an element which rotate around a horizontal fixed axis can be exactly balanced by the elastic force of a linear helical spring (Simionescu I. & Moise V. 1999). The spring is jointed between a point belonging to the element and a fixed one. The major disadvantage of this simple solution is that the spring has a zero undeformed length. In practice, the zero free length is very difficult to achieve or even impossible. The opposite assertions are theoretically conjectures only. A zero free length elastic device comprised a compression helical spring. In the construction of this device, some difficulties arise, because the compression spring, corresponding to the calculated feature, must be prevented from buckling. A very easy constructive solution, which the above mentioned disadvantage is removed, consists in assembly two parallel helical springs, as show in Fig. 13. The equilibrium of forces which act on the link (3) is expressed by following equation:

$$(m BC \cos\varphi_{3i} - m_{7F} X_F - m_{8I} X_I - m_2 X_{G2})g - F_{s7} BF \sin(\varphi_{3i} - \psi_{1i} + \alpha_1) - F_{s8} BI \sin(\varphi_{3i} - \psi_{2i} + \alpha_2) = 0, \quad i = \overline{1, 12}, \quad (21)$$

where:

m is the mass of distributed load on leg in the support phase, including the mass of the link (2) and the masses of linear helical springs (7) and (8), concentrated at the points H and J respectively;

m_{7F} and m_{8I} are the masses of springs (7) and (8), concentrated at the points F and I respectively;

$$\begin{aligned}
\Psi_{1i} &= \arctan \frac{Y_{F_i} - Y_H}{X_{F_i} - X_H}; \quad \Psi_{2i} = \arctan \frac{Y_{I_i} - Y_J}{X_{I_i} - X_J}; \\
X_{F_i} &= BF \cos(\varphi_i + \alpha_1); \quad Y_{F_i} = BF \sin(\varphi_i + \alpha_1); \\
X_{I_i} &= BI \cos(\varphi_i + \alpha_2); \quad Y_{I_i} = BI \sin(\varphi_i + \alpha_2); \\
F_{s7} &= F_{07} + k_7(HF_i - l_{07}); \quad F_{s8} = F_{08} + k_8(JI_i - l_{08}); \\
\alpha_1 &= \arctan \frac{y_{3F}}{x_{3F}}; \quad \alpha_2 = \arctan \frac{y_{3I}}{x_{3I}}; \\
HF_i &= \sqrt{(X_H - X_{F_i})^2 + (Y_H - Y_{F_i})^2}; \\
JI_i &= \sqrt{(X_J - X_{I_i})^2 + (Y_J - Y_{I_i})^2}.
\end{aligned}$$

The equations (21), which are written for twelve distinct values of the position angles φ_{3i} , are solved with respect to following unknowns: $x_{3F}, y_{3F}, x_{3I}, y_{3I}, X_H, Y_H, X_J, Y_J, F_{07}, F_{08}, l_{07}, l_{08}$. The undeformed lengths l_{07} and l_{08} of the springs given with acceptable values from constructional point of view.

The masses m, m_1, m_2, m_7, m_8 of elements and springs, and the position of the gravity center G_2 are assumed as knowns. In fact, the problem is solved in an iterative manner, because at the start of the design, the masses of springs are unknowns.

The angles φ_{3i} must be chosen so that, in the positions which correspond to the support phase, the loading of the leg is full, and in the positions which correspond to the transfer phase, the loading is null. The static balancing is achieved theoretically exactly in the positions defined by angles $\varphi_{33i}, i = \overline{1, 12}$. Between these positions, the unbalancing is very small and may be neglected.

If a total statically balancing is desired, a more complicated leg structure is necessary to be used. In the mechanism leg schematized in Fig. 14, the two active pairs are superposed in B . The second balancing elastic system is set between the elements (2) and (5).

The equilibrium equation of forces which act on the elements (3) and (5) respectively are:

$$\begin{aligned}
BC(R_{34Y} \cos\varphi_{3i} - R_{34X} \sin\varphi_{3i}) + (m_{7F} X_F + m_{8I} X_I + m_3 X_{G3})g + F_{s7} BF \sin(\varphi_{3i} - \varphi_{7i} + \alpha_1) + F_{s8} BI \sin(\varphi_{3i} - \varphi_{8i} + \alpha_2) &= 0; \\
BE(R_{56Y} \cos\varphi_{5i} - R_{56X} \sin\varphi_{5i}) + (m_{9N} X_N + m_{10L} X_L + m_5 X_{G5})g + F_{s9} BN \sin(\varphi_{5i} - \varphi_{9i} + \alpha_3) + F_{s10} BL \sin(\varphi_{5i} - \varphi_{10i} + \alpha_4) &= 0, \quad i = \overline{1, 12},
\end{aligned}$$

where: $\alpha_3 = \arctan \frac{y_{5N}}{x_{5N}}$; $\alpha_4 = \arctan \frac{y_{5L}}{x_{5L}}$;

$$F_{s9} = F_{09} + k_9(ML_i - l_{09}); \quad F_{s10} = F_{0,10} + k_{10}(QN_i - l_{0,10});$$

$$R_{34X} = \frac{U(X_D - X_E) - V(X_C - X_D)}{W};$$

$$R_{34Y} = \frac{V(Y_D - Y_C) - U(Y_E - Y_D)}{W};$$

$$U = g[m_4(X_{G4} - X_D) - m(X_P - X_D)];$$

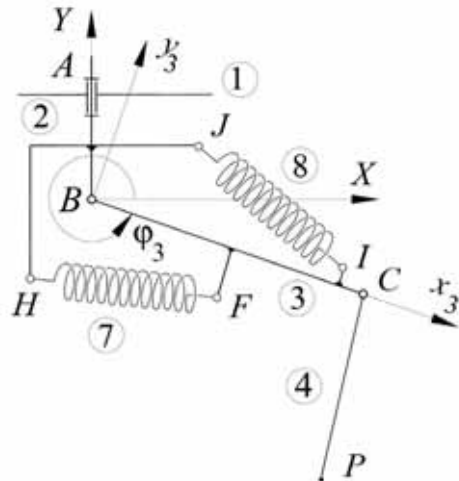


Fig. 13. Elastic system for the discrete partial static balancing of the leg mechanism

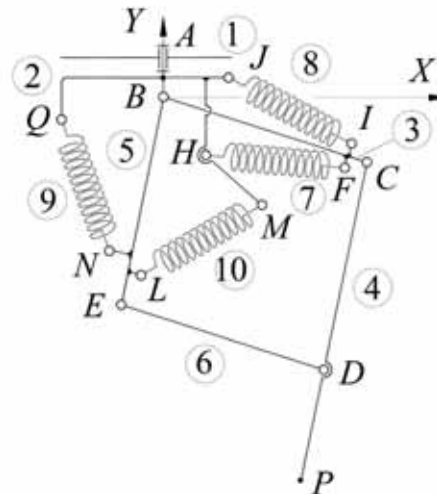


Fig. 14. Elastic system for the discrete total static balancing of the leg mechanism

$$V = g[m_6(X_{G6} - X_D) - (m_4 - m_6 - m)(X_E - X_D)];$$

$$W = Y_D(X_C - X_E) - Y_C(X_D - X_E) - Y_E(X_C - X_D);$$

$$R_{56X} = -R_{34X}; R_{56Y} = (m_4 + m_6 - m)g - R_{34Y}.$$

The magnitudes of the angles φ_{3i} and φ_{5i} are calculated as functions on the position of the point P . The variation fields of these, in support and transfer phase, must not be intersected. In the support phase, the point P of the leg is on the terrain. In the return phase, the leg is not on the terrain, and the distributed load on the leg is zero. The not intersecting condition can be easily realized for the variation fields of angle φ_3 . If the working positions of link (4)

are chosen in proximity of vertical line, the driving force or moment in the pair *C* is much less than the driving force from the pair *B*. This is workable by the adequately motions planning. In this manner, the diminishing of energy consumed for the walking machine displacement can be made by using the partial balancing of leg mechanism only.

The static balancing is exactly theoretic realized in twelve positions of the link (3), accordingly to the angle values φ_{3i} , $i = \overline{1,12}$, only. Due to continuity reasons, the unbalancing magnitude between these positions is negligible.

In order to realize the theoretic exactly static balancing of the leg mechanism, for all positions throughout in the work field, it is necessary to use the cam mechanisms. In Fig. 15 is shown a elastic system for continuous balancing, consist of a helical spring (7), jointed on the link (3) and the follower (8), which slides along the link (2). The cam which acted the follower, by the agency of role (9), is fixed on the link (3). The parametrical equations of directrices curves of the cam active surface are:

$$x_2 = Y_D \sin \varphi_3 \mp \frac{R \left(\frac{dY_D}{d\varphi_3} \cos \varphi_3 - Y_D \sin \varphi_3 \right)}{P};$$

$$y_2 = Y_D \cos \varphi_3 \pm \frac{R \left(\frac{dY_D}{d\varphi_3} \sin \varphi_3 + Y_D \cos \varphi_3 \right)}{P},$$

where *R* represents the role radius, and:

$$P = \sqrt{\left(\frac{dY_D}{d\varphi_3} \right)^2 + Y_D^2},$$

The ordinate *Y_D* of point *D* and its derivative $\frac{dY_D}{d\varphi_3}$ are calculated as solutions of following

differential equation which expressed the equilibrium condition of force system which are taken into consideration:

$$g(BC m + m_3 BG_3 + BF m_{7F}) \cos \varphi_3 + F_{s7} BF \sin(\varphi_3 - \psi) + Y_D R_{93} \sin \alpha = 0, \quad (22)$$

where the reaction force *R₉₃* between cam (3) and role (9) has the expression:

$$R_{93} = [F_{s7} \sin \psi + (m_8 + m_9 + m_{7F}) g] \cdot \frac{P}{Y_D},$$

and: $X_F = BF \cos \varphi_3$; $Y_F = BF \sin \varphi_3$;

$$X_H = 0; Y_H = Y_D - DH;$$

$$\alpha = \arctan \frac{\frac{dY_D}{d\varphi_3}}{Y_D}; \psi = \arctan \frac{Y_H - Y_F}{-X_F};$$

$$F_{s7} = F_{07} + k_7 (FH - l_{07});$$

$$FH = \sqrt{(X_F - X_H)^2 + (Y_F - Y_H)^2}$$

The mass m_7 of the helical spring (7) is assumed as concentrated in joints H and F , m_{7F} and m_{7H} respectively. The masses m , m_1 , m_2 , m_3 and m_4 of the bodies, dimensions BF , BC , DH and helical spring characteristics F_{07} , l_07 and, k_7 are considered known.

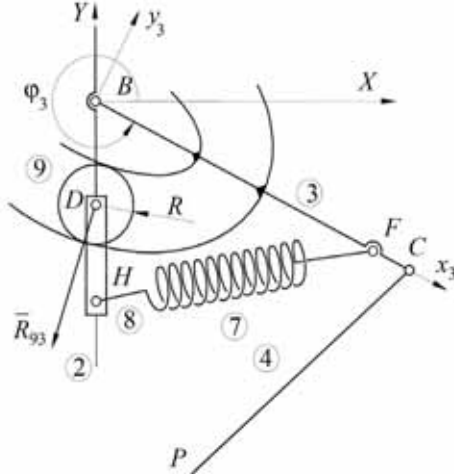


Fig.15. Elastic system for the continuous partial static balancing of the leg mechanism
VARIANT I

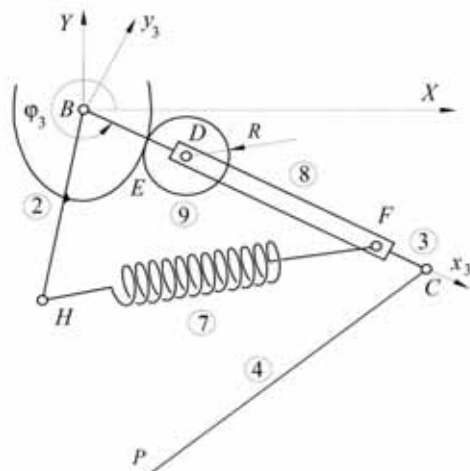


Fig.16. Elastic system for the continuous partial, static balancing of the leg mechanism
VARIANT II

The initial conditions, which are necessary to integrate the differential equation (22) are considered in a convenient mode, adequate to a known equilibrium position.

In Fig. 16 is schematized another elastic system for continuous balancing. The balancing helical spring (7) is jointed with an end to the follower (8) at the point F , and with the other

one to link (2), at point H . The cam is fixed to the link (2). The follower (8) slid along the link (3). The parametrical equations of directrice curves of the cam active surface are:

$$x_2 = X_D \mp \frac{R \left(\frac{dBD}{d\varphi_3} \sin \varphi_3 + X_D \right)}{Q},$$

$$y_2 = Y_D \pm \frac{R \left(\frac{dBD}{d\varphi_3} \cos \varphi_3 - Y_D \right)}{Q},$$

where: $X_D = BD \cos \varphi_3$, $Y_D = BD \sin \varphi_3$, and $Q = \sqrt{\left(\frac{dX_D}{d\varphi_3} \right)^2 + \left(\frac{dY_D}{d\varphi_3} \right)^2}$.

The distance BD and its derivative $\frac{dBD}{d\varphi_3}$ are calculated as solutions of following differential equation

$$\begin{aligned} F_{s7} \frac{Y_H (BD+DF) \cos \varphi_3}{FH} - R_{29} BD \cos(\varphi_3 - \alpha) - g(m_3 BG_3 + \\ + m_{4A} (BD+DF) + m_8 (BD+DG_8)) \cos \varphi_3 = 0, \end{aligned} \quad (23)$$

where:

$$\begin{aligned} R_{29} &= \frac{g(m_8 + m_9 + m_{7F}) - F_{s7} \cos(\varphi_3 - \psi)}{\cos(\varphi_3 - \alpha)}; \\ \alpha &= \arctan \frac{\frac{dBD}{d\varphi_3}}{BD}. \end{aligned}$$

8. Design of Foot Sole for Walking Robots

The feet of the walking robots must be build so that the robots are able to move with smooth and quick gait. If the fact soles were not shaped to fit with the terrain surface, then the foot would not be able to apply necessary driving forces and the resulting gait were not uniform. In a simplified form, the leg of a legged walking anthropomorphous robot is build of three parts (Fig. 17), namely thigh (1), shank (2) and foot (3). All of the joint axes are parallel with the support plane of the land. The legged robot foot soles have curved front and rear ends, corresponding to the toes tip and to the heel respectively. If the position of the axis of the pair A is defined with respect to the fixed coordinate axes system fastened on the support plane, the leg mechanism has a degree of freedom in the support phase and three degree of freedom in the transfer phase. Therefore, the angles φ_1 and φ_2 and the distance S , which define the positions of the leg elements, can not be calculated only in term of the coordinates X_A , Y_A . In other words, an unknown must.

be specified irrespective of the coordinates of the center of the pair A. In consequence, the foot (3) always may step on the land with the flat surface of the sole. The robot body may be moved with respect to the terrain without the changing of foot (3) position. This walking

possibility is not similarly with human walking and may be achieved only if the velocity and acceleration of the robot body is small. In general, the foot can be support on the land both with the flat surface and the curved front and rear ends. The plane surface of the sole and the cylindrical surface of the front end are tangent along of the generatrix R with respect to the mobile coordinate axes system is given by the coordinates x_{3R} and y_{3R} . The size of the flat surface of the foot, i.e. the position of the generatrix R , is determined from statically stability conditions in the rest state of the robot. The directrix curve of the cylindrical surface of the front end is defined by the parametrical equations

$$x_3 = x_3(\lambda), y_3 = y_3(\lambda)$$

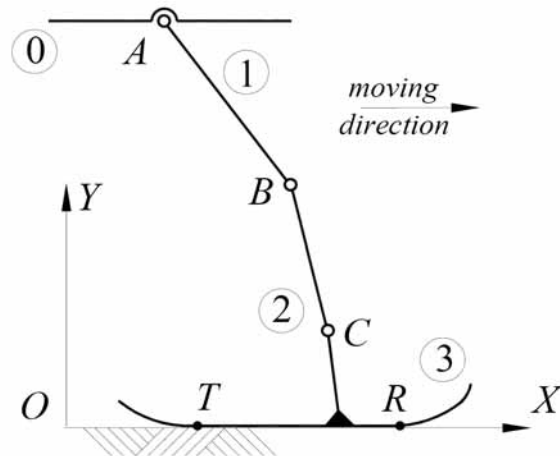


Fig. 17. Kinematics scheme of the an anthropomorphous leg

with respect to the mobile coordinate axes system attached to this element.

The generatrix in which the plane surface of the foot is tangent with the cylindrical surface of the front end is positioned by the parameter λ_0 :

$$x_{3R} = x_3(\lambda_0), y_{3R} = y_3(\lambda_0).$$

8.1. Kinematics Analysis of the Leg Mechanism

In the support phase, when the flat surface of the foot is in contact with the terrain (Fig. 18.a), the analysis equations are:

$$\begin{aligned} X_A + AB \cos \varphi_1 + BC \cos \varphi_2 - S &= 0; \\ Y_A + AB \sin \varphi_1 + BC \sin \varphi_2 - x_{3R} &= 0. \end{aligned} \quad (24)$$

The system is indeterminate because contains three unknowns, namely φ_1 , φ_2 and S . In order to solve it, the value of an unknown must be imposed, for example the angle φ_1 . It is considered as known the position of the pair axis A . In this hypothesis, the solutions of the system (24) are:

$$\varphi_2 = \arccos \frac{\sqrt{BC^2 - (x_{3R} - Y_A - AB \sin \varphi_1)^2}}{BC}$$

$$\text{or } \varphi_2 = \arcsin \frac{x_{3R} - Y_A - AB \sin \varphi_1}{BC};$$

$$S = \sqrt{BC^2 - (x_{3R} - Y_A - AB \sin \varphi_1)^2}.$$

The coordinates of the tangent point R have the expressions:

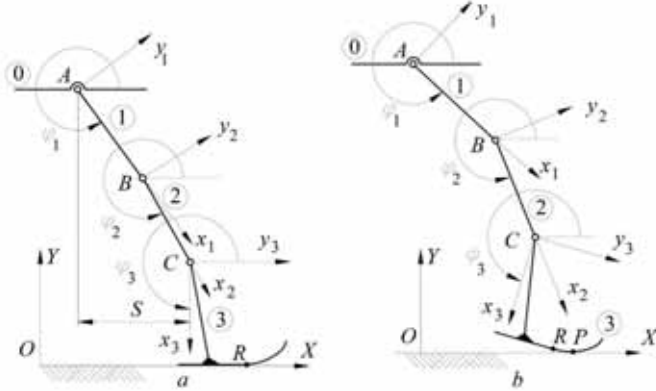


Fig. 18. The leg in the support phase

$$X_R = X_A + \sqrt{BC^2 - (x_{3R} - Y_A - AB \sin \varphi_1)^2} + y_{3R}$$

$$Y_R = 0.$$

In the end of the support phase, when the contact of the foot with the land is made along the generatrix which passes through the P point (Fig. 18.b), the analysis equations are:

$$Y_A + AB \sin \varphi_1 + BC \sin \varphi_2 + CP \sin(\varphi_3 + u) = Y_P;$$

$$X_A + AB \cos \varphi_1 + BC \cos \varphi_2 + CP \cos(\varphi_3 + u) = X_P;$$

$$\frac{\frac{dx_3}{d\lambda}}{\frac{dy_3}{d\lambda}} \Big|_{\lambda=\lambda_P} = -\tan \varphi_3,$$
(25)

where: $u = \arctan \frac{y_3(\lambda_P)}{x_3(\lambda_P)}$; $CP = \sqrt{x_3^2(\lambda_P) + y_3^2(\lambda_P)}$;

λ_P is the value of the λ parameter which corresponds to the generatrix which passes through the P point of the directrix curve;

$$X_P = X_R + \int_0^{\lambda_P} \sqrt{\left(\frac{dx_3}{d\lambda}\right)^2 + \left(\frac{dy_3}{d\lambda}\right)^2} d\lambda,$$

because it is assumed that the foot sole do not slipped on the land surface.

The equations (25) are solved with respect to the unknowns φ_2 , φ_3 and λ_P in term of the coordinates X_A , Y_A and the angle φ_1 .

By differentiation with respect to the time of the equations (25), result the velocity transmission functions:

$$\begin{aligned} \frac{dY_A}{dt} + AB \cos\varphi_1 \frac{d\varphi_1}{dt} + BC \cos\varphi_2 \frac{d\varphi_2}{dt} + CP \cos(\varphi_3 + u) \left(\frac{d\varphi_3}{dt} + \frac{du}{d\lambda} \frac{d\lambda}{dt} \right) + \frac{dCP}{d\lambda} \sin(\varphi_3 + u) \\ \frac{d\lambda}{dt} = 0; \\ AB \sin\varphi_1 \frac{d\varphi_1}{dt} + BC \sin\varphi_2 \frac{d\varphi_2}{dt} + CP \sin(\varphi_3 + u) \\ \left(\frac{d\varphi_3}{dt} + \frac{du}{d\lambda} \frac{d\lambda}{dt} \right) - \frac{dCP}{d\lambda} \cos(\varphi_3 + u) \frac{d\lambda}{dt} + \\ + \frac{dX_P}{d\lambda} \frac{d\lambda}{dt} - \frac{dX_A}{dt} = 0; \\ \frac{d^2y_3}{d\lambda^2} \frac{dx_3}{d\lambda} - \frac{d^2x_3}{d\lambda^2} \frac{dy_3}{d\lambda} \frac{d\lambda}{dt} - \frac{1}{\cos^2 \varphi_3} \frac{d\varphi_3}{dt} = 0, \\ \left(\frac{dy_3}{d\lambda} \right)^2 \end{aligned} \quad (26)$$

which are simultaneous solved with respect to the unknowns $\frac{d\varphi_2}{dt}$, $\frac{d\varphi_3}{dt}$ and $\frac{d\lambda}{dt}$,

$$\begin{aligned} \text{where: } \frac{du}{dt} &= \frac{\frac{dy_3}{d\lambda} x_3(\lambda) - \frac{dx_3}{d\lambda} y_3(\lambda)}{x_3^2(\lambda) + y_3^2(\lambda)} \frac{d\lambda}{dt}, \\ \frac{dCP}{dt} &= \frac{x_2(\lambda) \frac{dx_2}{d\lambda} + y_2(\lambda) \frac{dy_2}{d\lambda}}{CP} \frac{d\lambda}{dt}, \\ \frac{dX_P}{dt} &= \frac{d}{d\lambda} \left[\int_{\lambda_0}^{\lambda} \sqrt{\left(\frac{dx_3}{d\lambda} \right)^2 + \left(\frac{dy_3}{d\lambda} \right)^2} d\lambda \right] \frac{d\lambda}{dt}. \end{aligned}$$

Further on, by differentiation the equations (26) result the acceleration transmission functions:

$$\begin{aligned} \frac{d^2Y_A}{dt^2} + AB \left[\cos \varphi_1 \frac{d^2\varphi_1}{dt^2} - \sin \varphi_1 \left(\frac{d\varphi_1}{dt} \right)^2 \right] + BC \left[\cos \varphi_2 \frac{d^2\varphi_2}{dt^2} - \sin \varphi_2 \left(\frac{d\varphi_2}{dt} \right)^2 \right] + \\ + CP \cos(\varphi_3 + u) \left(\frac{d^2\varphi_3}{dt^2} + \frac{d^2u}{d\lambda^2} \left(\frac{d\lambda}{dt} \right)^2 + \frac{du}{d\lambda} \frac{d^2\lambda}{dt^2} \right) - CP \sin(\varphi_3 + u) \left(\frac{d\varphi_3}{dt} + \frac{du}{d\lambda} \frac{d\lambda}{dt} \right)^2 + \\ + \frac{d^2CP}{d\lambda^2} \sin(\varphi_3 + u) \left(\frac{d\lambda}{dt} \right)^2 + 2 \frac{dCP}{d\lambda} \cos(\varphi_3 + u) \end{aligned}$$

$$\begin{aligned}
& \left(\frac{d\varphi_3}{dt} + \frac{du}{d\lambda} \frac{d\lambda}{dt} \right) \frac{d\lambda}{dt} + \frac{dCP}{d\lambda} \sin(\varphi_3 + u) \frac{d^2\lambda}{dt^2} = 0; \\
& AB \left[\sin \varphi_1 \frac{d^2\varphi_1}{dt^2} + \cos \varphi_1 \left(\frac{d\varphi_1}{dt} \right)^2 \right] + BC \left[\sin \varphi_2 \frac{d^2\varphi_2}{dt^2} + \cos \varphi_2 \left(\frac{d\varphi_2}{dt} \right)^2 \right] + \\
& + CP \sin(\varphi_3 + u) \left(\frac{d^2\varphi_3}{dt^2} + \frac{d^2u}{d\lambda^2} \left(\frac{d\lambda}{dt} \right)^2 + \frac{du}{d\lambda} \frac{d^2\lambda}{dt^2} \right) + \\
& + CP \cos(\varphi_3 + u) \left(\frac{d\varphi_3}{dt} + \frac{du}{d\lambda} \frac{d\lambda}{dt} \right)^2 + \frac{d^2X_P}{d\lambda^2} \left(\frac{d\lambda}{dt} \right)^2 + \\
& + 2 \frac{dCP}{d\lambda} \sin(\varphi_3 + u) \left(\frac{d\varphi_3}{dt} + \frac{du}{d\lambda} \frac{d\lambda}{dt} \right) \frac{d\lambda}{dt} - \frac{d^2X_A}{dt^2} - \frac{d^2CP}{d\lambda^2} \cos(\varphi_3 + u) \left(\frac{d\lambda}{dt} \right)^2 - \frac{dCP}{d\lambda} \cos \\
& (\varphi_3 + u) \frac{d^2\lambda}{dt^2} = 0; \\
& \frac{\left(\frac{d^3y_3}{d\lambda^3} \frac{dx_3}{d\lambda} - \frac{d^3x_3}{d\lambda^3} \frac{dy_3}{d\lambda} \right) \frac{dx_3}{d\lambda} - 2A \frac{d^2x_3}{d\lambda^2}}{\left(\frac{dy_3}{d\lambda} \right)^3} \left(\frac{d\lambda}{dt} \right)^2 + \\
& \frac{A}{\left(\frac{dx_3}{d\lambda} \right)^2} \frac{d^2\lambda}{dt^2} - \frac{2 \sin \varphi_3}{\cos \varphi_3^3} \left(\frac{d\varphi_3}{dt} \right)^2 - \frac{1}{\cos^2 \varphi_3} \frac{d^2\varphi_3}{dt^2} = 0,
\end{aligned}$$

where $A = \frac{d^2y_3}{d\lambda^2} \frac{dx_3}{d\lambda} - \frac{d^2x_3}{d\lambda^2} \frac{dy_3}{d\lambda}$,

which are simultaneous solved with respect to the unknowns $\frac{d^2\varphi_2}{dt^2}$, $\frac{d^2\varphi_3}{dt^2}$ and $\frac{d^2\lambda}{dt^2}$

where:

$$\begin{aligned}
\frac{d^2u}{dt^2} = & \left[\frac{\frac{d^2y_3}{d\lambda^2} x_3(\lambda) - \frac{d^2x_3}{d\lambda^2} y_3(\lambda)}{x_3^2(\lambda) + y_3^2(\lambda)} - \right. \\
& \left. - 2 \frac{\frac{dx_3}{d\lambda} \frac{dy_3}{d\lambda} (x_3^2(\lambda) - y_3^2(\lambda)) - x_3(\lambda) y_3(\lambda) Q}{(x_3^2(\lambda) + y_3^2(\lambda))^2} \left(\frac{d\lambda}{dt} \right)^2 + \right. \\
& \left. + \frac{\frac{dy_3}{d\lambda} x_3(\lambda) - \frac{dx_3}{d\lambda} y_3(\lambda)}{x_3^2(\lambda) + y_3^2(\lambda)} \frac{d^2\lambda}{dt^2} \right];
\end{aligned}$$

$$Q = \left(\frac{dx_3}{d\lambda} \right)^2 - \left(\frac{dy_3}{d\lambda} \right)^2.$$

8.2. Forces Distribution in the Leg Mechanism

The goal of the forces analysis in the leg mechanism is the determination of the conditions of the static stability of the feet and of the whole robot. The leg mechanism is plane, and the reaction forces from the pairs are within the motion plane. The pressure on the contact surface or generatrix is assumed to be equally distributed. From the equilibrium equations of the forces which act on the leg mechanism elements (Fig. 19), the reaction forces from pairs A, B and C and the modulus and the origin of the normal reaction N are calculated. If the position of the origin of normal reaction force N results outside of the support surface, the foot overturns and walking robot lose its static stability. To avoid this phenomenon it is enforce that the origin of the normal reaction force to fill a certain position, definite by the distance d. In this case, a driving moment in the pair A, applied between the body (0) and the thigh (1) is added. This moment is the sixth unknown quantity of the forces distribution problem.

Taking into consideration the particularities of the contact between terrain and foot, the leg mechanism is analyzed in the following way:

- first: it is solved the equations (27), which define the equilibrium of the forces acting on the elements (1) and (2),
- second: it is solved the equations (28), which express the equilibrium of the forces acting on the foot (3).

The particularities consist in the fact that the foot (3) is supported or rolled without sliding on terrain.

As a result, the reaction force acting to the foot (3) has two components, namely \bar{N} along the normal on the support plane and \bar{T} holds in the support plane. The rolled without the front or rear end of the foot slide if $T < \mu N$ only, where μ is the frictional coefficient between foot and terrain.

The forces analysis is made in two situations.

1. The foot is supported with his flat surface on the terrain (Fig. 19.a).

The equations of the forces analysis which act on the links (1) and (2) are:

$$\begin{aligned} Q_X + F_{i1X} - R_{12X} + R_{01X} &= 0; \\ Q_Y + F_{i1Y} - m_1 g - R_{12Y} + R_{01Y} &= 0; \\ M_{01} + (F_{i1Y} - m_1 g)(X_{G1} - X_B) - F_{i1X}(Y_{G1} - Y_B) + R_{01X}(Y_A - Y_B) + R_{01Y}(X_B - X_A) + M_{i1} &= 0; \\ F_{i2X} + R_{12X} + R_{32X} &= 0; \\ F_{i2Y} - m_2 g + R_{12Y} + R_{32Y} &= 0; \\ (F_{i2Y} - m_2 g)(X_{G2} - X_B) - F_{i2X}(Y_{G2} - Y_B) + R_{32Y}(X_C - X_B) - R_{32X}(Y_C - Y_B) + M_{i2} &= 0, \end{aligned} \quad (27)$$

where $M_{01} = 0$.

$\bar{Q} = Q_x \bar{i} + Q_y \bar{j}$ is the direct acting load on the leg in the center of the pair A;

$$F_{ijX} = -m_j \frac{d^2 X_{Gj}}{dt^2}, \quad F_{ijY} = -m_j \frac{d^2 Y_{Gj}}{dt^2},$$

$$\begin{aligned}
M_{ij} &= -I_{Gj} \frac{d^2\varphi_j}{dt^2}; \quad j = \overline{1, 3}, \\
\frac{d^2X_{G1}}{dt^2} &= \frac{d^2X_A}{dt^2} - (x_{1G1} \sin \varphi_1 + y_{1G1} \cos \varphi_1) \frac{d^2\varphi_1}{dt^2} - \\
&\quad - (x_{1G1} \cos \varphi_1 - y_{1G1} \sin \varphi_1) \left(\frac{d\varphi_1}{dt} \right)^2; \\
\frac{d^2Y_{G1}}{dt^2} &= \frac{d^2Y_A}{dt^2} + (x_{1G1} \cos \varphi_1 - y_{1G1} \sin \varphi_1) \frac{d^2\varphi_1}{dt^2} - \\
&\quad - (x_{1G1} \sin \varphi_1 + y_{1G1} \cos \varphi_1) \left(\frac{d\varphi_1}{dt} \right)^2; \\
\frac{d^2X_{G2}}{dt^2} &= \frac{d^2X_A}{dt^2} - (x_{2G2} \sin \varphi_2 + y_{2G2} \cos \varphi_2) \frac{d^2\varphi_2}{dt^2} - \\
&\quad - (x_{2G2} \cos \varphi_2 - y_{2G2} \sin \varphi_2) \left(\frac{d\varphi_2}{dt} \right)^2 - \\
&\quad - AB(\sin \varphi_1 \frac{d^2\varphi_1}{dt^2} + \cos \varphi_1 \left(\frac{d\varphi_1}{dt} \right)^2); \\
\frac{d^2Y_{G2}}{dt^2} &= \frac{d^2Y_A}{dt^2} + (x_{2G2} \cos \varphi_2 - y_{2G2} \sin \varphi_2) \frac{d^2\varphi_2}{dt^2} - \\
&\quad - (x_{2G2} \sin \varphi_2 + y_{2G2} \cos \varphi_2) \left(\frac{d\varphi_2}{dt} \right)^2 - \\
&\quad + AB(\cos \varphi_1 \frac{d^2\varphi_1}{dt^2} - \sin \varphi_1 \left(\frac{d\varphi_1}{dt} \right)^2); \\
\frac{d^2X_{G3}}{dt^2} &= \frac{d^2X_A}{dt^2} - (x_{3G3} \sin \varphi_3 + y_{3G3} \cos \varphi_3) \frac{d^2\varphi_3}{dt^2} - \\
&\quad - (x_{3G3} \cos \varphi_3 - y_{3G3} \sin \varphi_3) \left(\frac{d\varphi_3}{dt} \right)^2 - AB(\sin \varphi_1 \frac{d^2\varphi_1}{dt^2} + \\
&\quad + \cos \varphi_1 \left(\frac{d\varphi_1}{dt} \right)^2) - BC(\sin \varphi_2 \frac{d^2\varphi_2}{dt^2} + \cos \varphi_2 \left(\frac{d\varphi_2}{dt} \right)^2); \\
\frac{d^2Y_{G3}}{dt^2} &= \frac{d^2Y_A}{dt^2} + (x_{3G3} \cos \varphi_3 - y_{3G3} \sin \varphi_3) \frac{d^2\varphi_3}{dt^2} - \\
&\quad - (x_{3G3} \sin \varphi_3 + y_{3G3} \cos \varphi_3) \left(\frac{d\varphi_3}{dt} \right)^2 + AB(\cos \varphi_1 \frac{d^2\varphi_1}{dt^2} - \\
&\quad - \sin \varphi_1 \left(\frac{d\varphi_1}{dt} \right)^2) + BC(\cos \varphi_2 \frac{d^2\varphi_2}{dt^2} - \sin \varphi_2 \left(\frac{d\varphi_2}{dt} \right)^2).
\end{aligned}$$

The equations (4) are simultaneous solved with respect to the unknowns R_{01X} , R_{01Y} , R_{12X} , R_{12Y} , R_{32X} and R_{32Y} .

The reaction force $\bar{R}_{ij} = R_{ijX}\bar{i} + R_{ijY}\bar{j}$ acts from the link (i) to the link (j).

Equations which expressing the equilibrium of the forces which act on the foot (3) are:

$$\begin{aligned} T - R_{32X} &= 0; \\ N - R_{32Y} - m_3 g &= 0; \\ N d + T Y_C - m_3 g (X_{G3} - X_C) &= 0, \end{aligned} \quad (28)$$

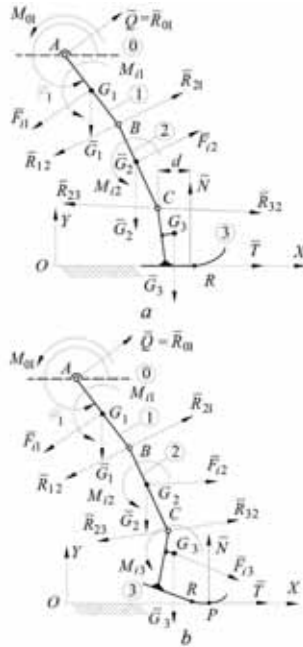


Fig. 19. Forces distribution in the leg mechanism

These equations are solved with respect to the unknowns N , T and d . If $T > \mu N$, the foot slipped on the terrain. In this case, the input moment $M_{01} \neq 0$ must be applied to the thigh (1). The magnitude of this moment is calculated by solving of the equations (27), where $R_{32X} < \mu N$. The sets of equations (27) and (28) are solved iteratively, until the difference between two successive iterations decreases under a certain limit.

2. The foot is supported with his front end on the terrain (Fig. 19.b)

The foot (3) may be in this position if a driving moment is applied in pair C , between links (2) and (3). The reaction forces from pair A and B are the solutions of the equations (29):

$$\begin{aligned} Q_X + F_{i1X} - R_{12X} + R_{01X} &= 0; \\ Q_Y + F_{i1Y} - m_1 g - R_{12Y} + R_{01Y} &= 0; \\ M_{01} + (F_{i1Y} - m_1 g)(X_{G1} - X_B) - F_{i1X}(Y_{G1} - Y_B) + R_{01X}(Y_A - Y_B) + R_{01Y}(X_B - X_A) + M_{i1} &= 0; \\ F_{i2X} + R_{12X} + R_{32X} &= 0; \\ F_{i2Y} - m_2 g + R_{12Y} + R_{32Y} &= 0; \\ (F_{i2Y} - m_2 g)(X_{G2} - X_B) - F_{i2X}(Y_{G2} - Y_B) + R_{32Y}(X_C - X_B) - R_{32X}(Y_C - Y_B) + M_{i2} - M_{23} &= 0, \end{aligned} \quad (29)$$

where $M_{01} = M_{23} = 0$.

The unknowns of these equations are R_{01X} , R_{01Y} , R_{12X} , R_{12Y} , R_{32X} and R_{32Y} .

Equilibrium of the forces which act on the foot (3) is expressed by equations (30):

$$T - R_{32X} + F_{i3X} = 0;$$

$$N - R_{32Y} - m_3 g + F_{i3Y} = 0; \quad (30)$$

$$M_{23} + M_{i3} + N(X_P - X_C) + T Y_C + (F_{i3Y} - m_3 g)(X_{G3} - X_C) - F_{i3X}(Y_{G3} - Y_C) = 0.$$

Solutions of these equations are N , T and M_{23} . If $T > \mu N$, the foot slipped on the terrain and the robot overturns.

8.3. Optimum Design of the Foot

The bottom surface of the foot of a walking robot may have various shapes. These surfaces differ by the size of the flat surface and the forms of the front and rear cylindrical surfaces. The most adequate form of the bottom surface of the foot, i.e. the expressions of the directrices of the front and rear cylindrical surfaces, is determined by optimization of some parameters. The objective function (Fox R. 1973), (Goldberg D. 1999), (Coley D. 1999), which is minimized in the optimization process may expressed:

- maximum angular velocity or $\frac{d^2\phi_3}{dt^2}$;
- the maximum driving forces or moments;
- etc.

The unknowns which respect to the objective function is minimized are:

- the lengths AB and BC of the links (1) and (2),
- the coordinate x_{3R} , y_{3R} of the point R ;
- the coefficients from the equations of the directrices curves of the surfaces of the front and rear ends.

The minimization of the objective function is performed in the presence of constrains which expressed:

- the directrix curves of the front and rear ends are tangent to the flat surface of the foot sole,
- the ordinate y_{3R} and y_{3T} of the points R and T respectively in which the directrix curves are tangent to the flat surfaces are limit by the minimum flat surface of the foot, to provide the static stability of the robot which rest.

9. Conclusions

The walking robots are used to unconventional displacement of the technological loads over the unarranged terrains. The modular constructions of the walking robots led to a more suppleness and very good adaptation to any terrain surface. The displacement is carried out at the very most circumstances and with a minimum expenditure of energy if the leg mechanisms are designed in accordance with the above prescriptions

10. References

- Appel P., (1908). *Tratait de Mécanique Rationnelle*, Gauthier-Villars, Paris
- Bares J. E., European Patent no A1 0399720.
- Bessonov A.P., Umnov N.V. (1973). *The Analysis of gaits in six legged Vehicles according to their static stability* Proc. Theory and Practice of Robots and Manipulators, Udine, Italy
- Buzdugan Gh., (1980) *Material Strength*, Ed. Didactică și Pedagogică, Bucarest, (in Romanian)
- Coley D. (1999). *An Introduction to Genetic Algorithms for Scientists and Engineers*, World Scientific
- Denavit J., Hartenberg R.S. (1955). *A kinematic notation for lower-pair mechanisms based on matrices*, Journal of Applied Mechanics, no.22
- Ebert-Uphoff I., Gosselin C.M. (1998). *Static Balancing of a Class of Spatial Parallel Platform Mechanisms*, Proceeding of the ASME Mechanisms Conference, Atlanta, USA
- Fox R. (1973). *Optimization Methods for Engineering Design*, Addison Wesley Publishing Comp,
- Garrec P., U. S. Patent no 5219410
- Goldberg D. (1999). *Genetic Algorithms in Search, Optimisation and Machine Learning*, Addison Wesley Publishing Comp.
- Hildebrand F.B. (1956). *Introduction in Numerical Analysis*, McGraw Hill Book Company
- Hiller M., Muller J., Roll U., Schneider M., Scroter D., Torlo M., Ward D. (1999). *Design and Realization of the Anthropomorphically Legged and Wheeled Duisburg Robot Alduro*, The Tenth World Congress on the Theory of Machines and Mechanisms, Oulu, Finland, June 20-24
- Hirose S. (1991). *Three Basic Types of Locomotion in Mobile Robots*, IEEE, pp. 12-17
- Ion I., Stefanescu D.M. (1999). *Force Distribution in the MERO Four-Legged Walking Robot*, ISMCR'99 - Topical Workshop on Virtual Reality and Advanced Human-Robot Systems, vol X, Tokyo, Japan, June 10-11
- Ion I., Simionescu I., Ungureanu M. (2001). *Discrete static balancing of the walking robots shifting systems mechanisms*, The Annual Symposium of the Institute of Solid Mechanisms - SISOM' 2001, Bucharest, May 24-25, , pp 202-207
- Ion I., Simionescu I., Curaj A. (2002). *MERO modular walking robot having applications in farming and forestry* The 5thInternational Conference on Climbing and Walking Robots, September 25-27, -Paris -France
- Ion I., Ungureanu M., Simionescu I. (2000). *Control System of MERO modular Walking Robot*, Proceedings of the International Conference on Manufacturing Systems, Bucharest, October 10-11, Romanian Academy Publishing House, pp 351-354 ISBN 973-27-0932-4.
- Ion I., Simionescu I., Curaj A. (2002). *Mobil Mechatronic System With Applications in Agriculture and Sylviculture*. The 2thIFAC International Conference on Mechatronic Systems, December 8-12, -Berkeley University - USA
- Ion I., Simionescu I., Curaj A. (2003). *The displacement of Quatrupedal Walking Robots*, Proceedings of the 11th World Congress in Mechanism and Machine Science, August 18-21, Tianjin - China.

- Ion I., Simionescu I., Curaj A., Ungureanu M (2004). *MERO modular Walking robot support of technological equipments* International Conference of Robots, Timisoara, Oct. 14 -17, Romania
- Kumar V., Waldron K.J. (1988). *Force Distribution in Closed Kinematics Chain*,: IEEE Journal of Robotic and Automation, Vol. 4, No. 6, pp. 657-664.
- Kumar V., Waldron K.J. (1988). *Force Distribution in Walking Vehicle*, Proc. 20th ASME Mechanism Conference, Orlando, Florida, Vol. DE-3, pp. 473-480.
- McGhee R.B., Frank A.A. (1968). *Stability Properties of Quadruped Creeping Gait*, Mathematical Biosciences, Vol. 3, No.2, pp. 331-351
- McGhee, R.B., Orin, D.E. (1976). *A Mathematical Programming Approach to Control of Joint Positions and Torques in Legged Locomotion Systems*,: Proc. 2nd CISM -IFTOMM Conference for the Theory and Practice of Robot Manipulators (ROMANSY), Warsaw, Poland, Sept. 14-17, pp. 225-231
- Nishikawa Masao et al. (1999). European Patent no. 0433091A2
- Okhotsimski D.E., Golubev I., (1984). *Mehanika i upravleniae dvijeniem avtomaticheskovo sgaiuscevo aparata*, Moscwa, "Nauka"
- Rossman T., Pfeiffer F(1999). *Control of tube Crawling Robot*, Automatisierungstechnik 47, Oldenbourg Verlag.
- Simionescu I., Moise V. (1999), *Mechanisms*, Technical Publishing House, Bucarest,. (in romanian)
- Simionescu I., Ion I., Ciupitu L. (1996). *Optimization of Walking Robots Movement Systems*, Proceedings of the VII International Congress on the Theory of Machines and Mechanisms, Liberec, Czech Republic, 3 - 5 September,
- Simionescu I., Moise V., Dranga M. (1995). *Numerical Methods in Engineering*, Technical Publishing House, Bucarest, 1995 (in romanian)
- Simionescu, I, Ion,I (2004) *Feet for two legged Walking Robots*, 35th International Symposium on Robotics , March 23-26, Paris – France.
- Simionescu I., Ion I. (2001). *Static Balancing of Walking Machines*, POLITEHNICA University of Bucharest, Sci. Bull., Series D, vol. 63 no. 1, pp.15 – 22.
- Song S.M., Waldron K.J. (1989). *Machines that Walk*, Massachusetts Institute of Technology Press, 1989.
- Song S.M., Lee J.K. (1988). *The Mechanical Efficiency and Kinematics Pantograph Type Manipulators*, Proceedings of the IEEE International Conference on Robotics and Automation, Philadelphia, Vol. I pp.414-420
- Streit, D.A., Gilmore, B.J. (1989). *Perfect Spring Equilibrators for Routable Bodies*, Journal of Mechanisms, Transmissions and Automation in Design, vol. 111, pp. 451 - 458.
- Uicker J.J.jr., Denavit J., Hartenberg R.S.(1965). *An Iterative Method for the Displacement Analysis of Spatial Mechanisms*, Trans. of the ASME, paper 63-WA-45.
- Waldron K.J. (1985). *Force and Motion Management in Legged Locomotion*, Proceedings of the 24th IEEE Conference on Decision and Control, Fort Lauderdale, pp.12-17
- Waldron K.J. (1996), *Modeling and Simulation of Human and Walking Robots Locomotion*, Advanced School, Udine, Italy,
- Nishikawa Masao et al, European Patent Application no. 0433091A2

Non-time Reference Gait Planning and Stability Control for Bipedal Walking

Xianxin Ke, Jinwu Qian and Zhenbang Gong

*School of Mechatronics & Automation, Shanghai University
China*

1. Introduction

In this increasingly aging society, the needs for robots to assist human activities in daily environments such as offices, homes, and hospitals are growing rapidly. In such environments originally designed for human beings, biped robots, which have almost the same mechanisms as a human, present many advantages than wheeled robots like obstacle avoidance capabilities for its possibility of discontinuous contact with the ground, which allows the robot to step over obstacles and climb stairs.

Biped walking robots have been in the research and development phase and biped robotics field has attracted a growing number of researchers during the last decades. Since the great success of the biped robot P2 developed by Honda in 1996(Kazuo, et al, 1998), more and more researchers focus their studies on biped robot, and have achieved many progresses. Honda has developed P3 and ASIMO afterwards. The latest version ASIMO can walk smoothly like a human being. As the most famous researcher on biped robots, Waseda University has developed many prototypes, their latest biped robot WABIAN can even make emotional gestures (Hashimoto, et al 1998). Although Sony is a new comer in biped robot researches, the excellent performances of Sony Dream Robot series biped robots have won good reputations, the latest robot SDR-4X can walk, dance, even stand up by itself after falling down. As a joint research platform in Japan, HRP-2 has realized co-operations with human such as lifting a desk in cooperation with people (Tanie, et al, 1999).

Although performances of those biped robots are exciting and impressive, progresses in theoretical analysis are far behind prototype developments, a stable biped walking remains a highly demanding task for its high degrees of complexity, coupling, highly nonlinear, and unstable. Generating a desired gait for dynamic locomotion of biped robots is one of the important research areas in the study of biped robots. The simplest method to generate a desired trajectory for a biped robot is called the inverted pendulum mode (Kajita, et al, 1995). It is based on the assumption that all the links of the biped robot but the hip link have a negligible mass, thus the hip link representing the sole mass of the biped robot, and that the biped robot contacts with the ground at a single invariant point on the sole in each cycle of the single-support phase. The trajectory obtained with the inverted pendulum mode, however, compromises locomotion stability due to the fact that the link masses, such as a foot, that are assumed to be negligible are not in fact negligible at all. An alternative method

called the gravity-compensated inverted pendulum method generates a leg trajectory with higher stability, while keeping the most of the simplicity of the inverted pendulum mode intact (J.H. Park, 1998). A more complicated method to generate a more stable trajectory is based on the Zero Moment Point (ZMP) equation, which describes the relationship between the joint motions and the forces applied at the ground (Yamaguchi, et al , 1996). The ZMP is simply the center of pressure at the feet or foot on the ground, and the moment applied by the ground about the point is zero, as its name indicates. Yamaguchi et al. (1996) and Li et al. (1992) used trunk swing motions and trunk yaw motions, respectively, to increase the locomotion stability for arbitrary robot locomotion. However, many previous researches have assumed a predetermined ZMP trajectory. Due to the difference between the actual environment and the ideal one, or a modeling error and the impact of foot-ground, biped robots are likely to be unstable by directly using the original planned gait. In order to maintain the stability of bipedal walking, the pre-planned gait needs to be adjusted. When the robot is passing through obstacles or climbing up stairs, the adjustment of the pre-planned gait may lead to the collision between the biped robot and the environment. Then the trajectory should be wholly re-planned, and the pre-planned gait becomes useless. This is the problem that conventional gait plan method encountered.

In the view of to separate the space and time, the gait of a bipedal walking can be decomposed into two parts: the geometric space path of the robot passing through, which reflect the relative movement between all moving parts of the robot; then the specific moments of the robot pass through the specific points of the geometric space path, which contain the velocities and accelerations information, and is connected to the reference of time. According to this view, we proposed a non-time reference gait planning method which can decouple the space restrictions on the path of the robot passing through and the walking stabilities. The gait planning is divided to two phases: at first, the geometric space path is determined with the consideration of the geometric constraints of the environment, using the forward trajectory of the trunk of the biped robot as the reference variable; Then the forward trajectory of the trunk is determined with the consideration of dynamic constraints including the ZMP constraint for walking stabilities. Since the geometric constraints of the environment and the ZMP constraint for walking stabilities are satisfied in different phases, the modification of the gait by the stability control will not change the geometric space path. This method simplifies the stability problem, and offline gait planning and online modification for stability can easily work together.

Gait optimization is a good way to improve the performance of bipedal walking. The optimization goal of walking stability is to make ZMP as near the center of support region as possible. This paper uses the outstanding ability of the genetic algorithm to gain a high stable gait.

Due to the difference between the actual environment and the ideal one, or a modeling error and the impact of foot-ground, online gait modification and stability control methods are needed for sure of the stable bipedal walking. When people feel about to fell down, they usually speed up the pace by instinct, and the stability is gradually restored. The changing of instantaneous velocity can restores the stability effectively. Combining the non-time reference gait planning method, a intelligent stability control strategy through modifying the instantaneous walking speed of the robot is proposed. When the robot falls forward or backward, this control strategy lets the robot accelerate or decelerate in the forward locomotion, then an additional restoring torque reversing the direction of falling will be

added on the robot. According to the principle of non-time reference gait planning, the non-time reference variable is the only one needs to be modified in the stability control. In this paper, a fuzzy logic system is employed for the on-line correction of the non-time reference trajectory. For testify the validity of this strategy, a humanoid robot climbing upstairs is presented using the virtual prototype of humanoid robot modeling method.

This paper presents the non-time reference gait planning and stability control method for a bipedal walking. Section 2 studied the non-time reference gait planning method and the gait optimization for higher walking stability using Genetic Algorithm (GA). Section 3 built up a virtual prototype model of a humanoid robot using CAD modeling, dynamic analysis and control engineering soft wares. Section 4 studied a stability control method based on non-time reference strategy, the simulation results of a humanoid robot climbing up stairs are presented, and the conclusions and future work follow lastly.

2. Non-time reference gait planning for bipedal walking

2.1 Spatial path planning

The model of the biped robot SHUR (shown in Fig.1) used in this paper consists of two 6-DOF legs and a trunk connecting them. Link the sizes and the masses of the links of the biped are given in Table 1.

name	mass (kg)	Ixx (kg.m ²)	Iyy (kg.m ²)	Izz (kg.m ²)	size (m)
foot	1.17	0.001248	0.0051309 4	0.0051309	Lf = 0.215 wf = 0.08 hf = 0.08
shin	2.79	0.0381378	0.0381378	0.0018755	Ls = 0.4
thigh	5.94	0.0686441	0.0686441	0.0089843	Lt = 0.36
trunk	40.2	3.13895	2.93628	0.526955	wb = 0.22 hb = 0.91

Table 1. Parameter of SHUR model

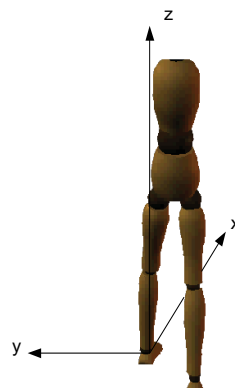


Fig. 1. Coordinate of a biped robot SHUR

When the trunk keeps upright and the bottoms of the feet keep horizontal in gait planning, the posture of the biped robot can be decided by the positions of hip and the ankle of the swinging leg (Huang, et al, 1999). The center of mass of the robot in x direction $x_{\text{hip}}(t)$ plays an important role in walking stability of forward movement in which the robot tends to fall down. And $x_{\text{hip}}(t)$ is a monotonic increase function similar to the time. So, $x_{\text{hip}}(t)$ can be taken as a reference variable instead of the reference variable, time, which is usually used. Firstly, the space trajectories of the movements of the hip and the ankle of the swing leg are programmed with considerations of environmental restrictions on the robot. Then the relative movements between parts of the biped robot are fixed. Finally, the trajectory of $x_{\text{hip}}(t)$ taken time as the reference variable is planned to control the position of ZMP to realize a stable walking.

The parameters of the bipedal walking in this chapter are set:

The step length of a single step is $S_s = 0.6m$,

The period of a single step is $T_s = 0.8s$,

The maximum height the swing leg passing through is $H_s = 0.2m$.

2.1.1 Spatial path planning for hip

Because of the symmetry and periodicity of the bipedal walking, only the gait of one single step needs to be planned. Without loss of generality, it is assumed a single-step starts with the left leg to be in support and the right leg begins to swing.

It is planned that the position of the hip is located at the middle of the gap between the left foot and right foot at the moment of the support leg switched.

In a single step period,

$$x_{\text{hip}}(t) \in \left[-\frac{S_s}{2}, \frac{S_s}{2} \right], \text{when } t \in [0, \frac{T_s}{2}] \quad (1)$$

Because of the symmetry and periodicity of the bipedal walking, $z_{\text{hip}} = f(x_{\text{hip}}) = z_{\text{hip}}(x_{\text{hip}})$ is a periodic function. The period is $\frac{T_s}{2} = T$.

When the robot is with single support and the support leg is vertical $x_{\text{hip}}(t) = 0$, the position of the hip reaches its highest point in whole cycle of bipedal walking:

$$z_{\text{hip}}(0) = \max[z_{\text{hip}}(x_{\text{hip}})] = l_{\text{shin}} + l_{\text{thigh}} \quad (2)$$

At the moment of the supporting foot switching, the position of the hip reaches its lowest point in a period for both legs having the geometry constraints. For sure of the satisfaction of the geometry constraints at the moment of supporting foot switched, it is planned that robot retains certain flection $\delta h = 0.1$.

$$\text{Then, } z_{\text{hip}}\left(-\frac{S_s}{2}\right) = z_{\text{hip}}\left(\frac{S_s}{2}\right) = \min[z_{\text{hip}}(x_{\text{hip}})] = \sqrt{(l_{\text{shin}} + l_{\text{thigh}})^2 - \left(\frac{S_s}{2}\right)^2} - \delta h \quad (3)$$

The fluctuation range of the position of the hip in z-direction is:

$$z_{\text{hipmag}} = \max[z_{\text{hip}}(x_{\text{hip}})] - \min[z_{\text{hip}}(x_{\text{hip}})] = l_{\text{shin}} + l_{\text{thigh}} - \sqrt{(l_{\text{shin}} + l_{\text{thigh}})^2 - (\frac{S_s}{2})^2} + \delta h \quad (4)$$

The mid value of the position of the hip is:

$$\text{mid}[z_{\text{hip}}(x_{\text{hip}})] = \min[z_{\text{hip}}(x_{\text{hip}})] + \frac{1}{2} z_{\text{hipmag}} \quad (5)$$

So, we adopt a cosine function:

$$z_{\text{hip}}(x_{\text{hip}}) = \frac{z_{\text{hipmag}}}{2} \times \cos(2\pi \frac{x_{\text{hip}}}{S_s}) + \text{mid}[z_{\text{hip}}(x_{\text{hip}})] \quad (6)$$

The velocity of the hip is:

$$\dot{z}_{\text{hip}} = \frac{\partial z_{\text{hip}}}{\partial t} = \frac{\partial}{\partial x_{\text{hip}}} z_{\text{hip}} \dot{x}_{\text{hip}} = -\frac{\pi z_{\text{hipmag}}}{2 S_s} \times \sin(2\pi \frac{x_{\text{hip}}}{S_s}) \dot{x}_{\text{hip}} \quad (7)$$

Thus:

$$\dot{z}_{\text{hip}}(-\frac{S_s}{2}) = 0, \quad \dot{z}_{\text{hip}}(\frac{S_s}{2}) = 0, \quad \dot{z}_{\text{hip}}(0) = 0 \quad (8)$$

Eq.8 means the trunk has no impact in z-direction at the moment of the supporting foot switches, which is useful to the smooth change of supporting foot. Substitute the specific parameters into the functions (Eq.6 and Eq.7), the space path and velocity of hip movement are as shown in Fig. 2.

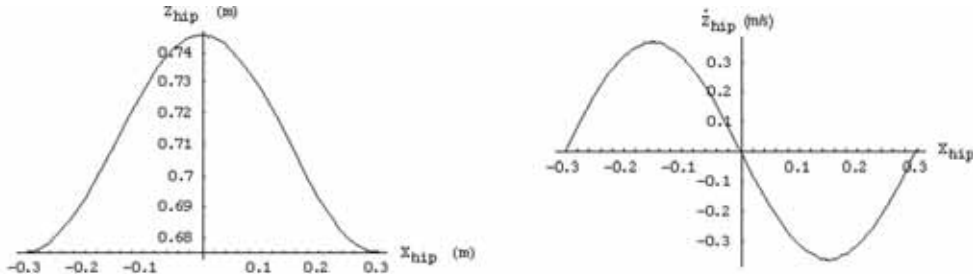


Fig. 2. Hip displacement (left) and velocity (right)

2.1.2 Spatial Path in x-direction (x_{ankle}) for the Ankle of the Swing Leg

In order to keep the process of take-off and step down smoothly, the soles of the feet are planned to be parallel to the ground during the walking process. We set x_{ankle} to be a function of x_{hip} :

$$x_{\text{ankle}} = f(x_{\text{hip}}) = x_{\text{ankle}}(x_{\text{hip}}) \quad (9)$$

At the moment of the robot shifting its supporting leg, $x_{\text{hip}}(t) = \pm S_s / 2$, the position of the ankle of the swing leg: $x_{\text{ankle}} = \pm S_s$.

When the robot stands with one foot vertically, $x_{\text{hip}}(t) = 0$, the ankle of the swing leg is just above the ankle of the supported foot, that is $x_{\text{ankle}} = 0$.

In order to prevent unwelcome impact during the take-off and step down process, there are constraints on velocity of the swing leg is:

$$\dot{x}_{\text{ankle}}\left(-\frac{S_s}{2}\right) = \dot{x}_{\text{ankle}}\left(\frac{S_s}{2}\right) = 0 \quad (10)$$

From above, we use a Sine Function (see Fig.3):

$$x_{\text{ankle}} = S_s \sin\left(\frac{x_{\text{hip}}}{S_s} \pi\right) \quad (11)$$

Its speed is:

$$\dot{x}_{\text{ankle}} = \frac{\partial}{\partial x_{\text{hip}}} x_{\text{ankle}} \dot{x}_{\text{hip}} = \pi \cos\left(\frac{x_{\text{hip}}}{S_s} \pi\right) \dot{x}_{\text{hip}} \quad (12)$$

Thus:

$$\dot{x}_{\text{ankle}}\left(-\frac{S_s}{2}\right) = \dot{x}_{\text{ankle}}\left(\frac{S_s}{2}\right) = 0 \quad (13)$$

So this path meets the requirements of no impact during supporting foot switching.

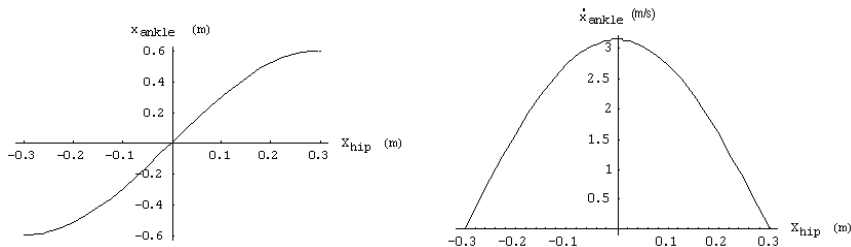


Fig. 3. Ankle displacement (left) and velocity (right) in x-axis of the Swing leg

2.1.3 Spatial Path in z-direction (z_{ankle}) for the Ankle of the Swing Leg

We plan z_{ankle} as a function of x_{hip} :

$$z_{\text{ankle}} = f(x_{\text{hip}}) = z_{\text{ankle}}(x_{\text{hip}}) \quad (15)$$

It follows the constraints as:

Constraints for no striking at the moment of take-off and step-down:

$$\dot{z}_{\text{ankle}}\left(-\frac{S_s}{2}\right) = \dot{z}_{\text{ankle}}\left(\frac{S_s}{2}\right) = 0 \quad (16)$$

The constraint of space path:

$$z_{\text{ankle}}\left(-\frac{S_s}{2}\right) = z_{\text{ankle}}\left(\frac{S_s}{2}\right) = 0, z_{\text{ankle}}(0) = H_s \quad (17)$$

According to the constraints above, we use a trigonometry function (see Fig.4):

$$z_{\text{ankle}} = \frac{H_s}{2} \cos\left(2\pi \frac{x_{\text{hip}}}{S_s}\right) + \frac{H_s}{2} \quad (18)$$

The speed of the Ankle is:

$$\dot{z}_{\text{ankle}} = \frac{\partial}{\partial x_{\text{hip}}} z_{\text{ankle}}(t) = \frac{-\pi}{S_s} \frac{H_s}{2} \sin\left(2\pi \frac{x_{\text{hip}}}{S_s}\right) \dot{x}_{\text{hip}}(t) \quad (19)$$

Thus

$$\dot{z}_{\text{ankle}}\left(-\frac{S_s}{2}\right) = 0, \quad \dot{z}_{\text{ankle}}\left(\frac{S_s}{2}\right) = 0, \quad \dot{z}_{\text{ankle}}(0) = 0 \quad (20)$$

That is, the swing leg will not strike with the ground during take-off and step-down process.

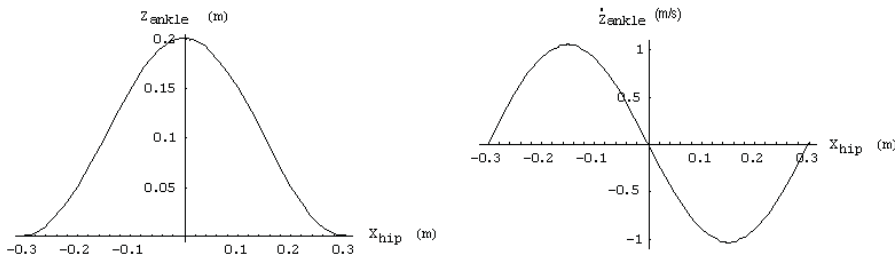


Fig. 4. Ankle displacement (left) and velocity (right) in z-axis of the Swing leg

Synthesize Eq.11 and Eq.18, we can get the spatial path of the ankle of the swing leg (Fig.5):

$$\begin{cases} x_{\text{ankle}} = S_s \sin\left(\frac{x_{\text{hip}}}{S_s}\pi\right) \\ z_{\text{ankle}} = \frac{H_s}{2} \cos\left(2\pi \frac{x_{\text{hip}}}{S_s}\right) + \frac{H_s}{2} \end{cases} \quad (21)$$

In which, $x_{\text{hip}}(t)$ is the referenced variable.

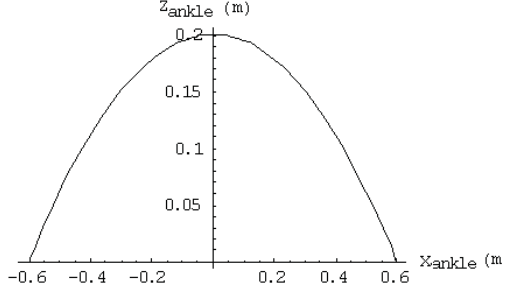


Fig. 5. Spatial path of the ankle of swing leg

2.2 Gait planning based on ZMP stability

Based on periodicity of bipedal walking and the symmetry of left leg and right leg, there are three equation restraints for x_{hip} :

Position constraints:

$$x_{\text{hip}}(0) = -\frac{S_s}{2}, x_{\text{hip}}(T_s) = \frac{S_s}{2} \quad (22)$$

Velocity constraint:

$$\dot{x}_{\text{hip}}(0) = \dot{x}_{\text{hip}}(T_s) \quad (23)$$

As well as two inequalities constraints:

In order to save energy as well as to have the unidirectional characteristic of the time, the speed of the robot's trunk should be greater than 0.

$$\dot{x}_{\text{hip}}(t) > 0 \quad (24)$$

For sure of bipedal walking is stable, x_{zmp} must be within the support region :

$$x_{\text{heel}} < x_{\text{zmp}} < x_{\text{toe}} \quad (25)$$

In order to meet these constraints at the same time, we use quintic polynomial to represent the trajectory of x_{hip} .

$$x_{\text{hip}} = a_0 + a_1 t + a_2 t^2 + a_3 t^3 + a_4 t^4 + a_5 t^5 \quad (26)$$

Then:

$$\begin{aligned} \dot{x}_{\text{hip}} &= a_1 + 2a_2 t + 3a_3 t^2 + 4a_4 t^3 + 5a_5 t^4 \\ \ddot{x}_{\text{hip}} &= 2a_2 + 6a_3 t + 12a_4 t^2 + 20a_5 t^3 \end{aligned} \quad (27)$$

Substituting three constraint equations into Eq.26 and Eq.27, we get three coefficients:

$$x_{\text{hip}}(0) = -\frac{S_s}{2} \Rightarrow a_0 = -\frac{S_s}{2} \quad (28)$$

$$\dot{x}_{\text{hip}}(T_s) = \dot{x}_{\text{hip}}(0) \Rightarrow a_2 = -\frac{3}{2}a_3 T_s - 2a_4 T_s^2 - \frac{5}{2}a_5 T_s^3 \quad (29)$$

$$x_{\text{hip}}(T_s) - x_{\text{hip}}(0) = S_s \Rightarrow a_1 = \frac{S_s}{T_s} + \frac{1}{2}a_3 T_s^2 + a_4 T_s^3 + \frac{3}{2}a_5 T_s^4 \quad (30)$$

Then we have:

$$x_{\text{hip}} = -\frac{S_s}{2} + \left(\frac{S_s}{T_s} + \frac{1}{2}a_3 T_s^2 + a_4 T_s^3 + \frac{3}{2}a_5 T_s^4\right)t + \left(-\frac{3}{2}a_3 T_s - 2a_4 T_s^2 - \frac{5}{2}a_5 T_s^3\right)t^2 + a_3 t^3 + a_4 t^4 + a_5 t^5 \quad (31)$$

$$\begin{aligned} \dot{x}_{\text{hip}} = & \left(\frac{S_s}{T_s} + \frac{1}{2}a_3 T_s^2 + a_4 T_s^3 + \frac{3}{2}a_5 T_s^4\right) + \left(-3a_3 T_s - 4a_4 T_s^2 - 5a_5 T_s^3\right)t \\ & + 3a_3 t^2 + 4a_4 t^3 + 5a_5 t^4 \end{aligned} \quad (32)$$

Up to now, the question of gait planning have been changed into solving the three coefficients of the quintic polynomial under the condition of speed inequality restraints (Eq.24, Eq.25), and maximizing the stability margin of ZMP.

2.3 Gait optimization based on walking stability using GA (Genetic Algorithm)

2.3.1 GA design

Genetic Algorithm (GA) has been known to be robust for search and optimization problems. GA has been used to solve difficult problems with objective functions that do not posses properties such as continuity, differentiability, etc. It manipulates a family of possible solutions that allows the exploration of several promising areas of the solution space at the same time. GA also makes handling the constraints easy by using a penalty function vector, which converts a constrained problem to an unconstrained one. In our work, the most important constraint is the stability, which is verified by the ZMP concept. This paper applies the GA to design the gait of humanoid robot to obtain maximum stability margin, so as to enhance the robot's walking ability.

For application of optimizing using GA, there are four steps:

- (1) Decide the variables which need to be optimized and all kinds of constraints;
- (2) Decide the coding and decoding method for feasible solution;
- (3) Definite a quantified evaluation method to individual adaptability;
- (4) Design GA program, determine the operating measure with gene, and set parameters used in GA.

The parameters are set:

Population scales $M=100$,
 Evolution generations $T=1000$,
 Overlapping probability $P_c=0.7$,
 And variation probability $P_m=0.03$

The variables to be optimized are: a_3 , a_4 and a_5

The speed constraint: $\dot{x}_{\text{hip}}(t) > 0, t \in [0, T_s]$ (33)

2.3.2 The determination of the optimized goal:

Set the projection point of the ankle of the supporting foot as the origin of the coordinate system (see Fig.1), the length from heel to the origin of the coordinate is $l_{heel} = 0.08m$, the length from the toe to the origin of coordinate is $l_{toe} = 0.135m$, the central position of the support foot is:

$$x_{footcenter} = \frac{l_{toe} - l_{heel}}{2} \quad (34)$$

In a bipedal walking cycle, the ZMP stability in x direction can be expressed as:

$$-l_{heel} < x_{zmp} < l_{toe} \quad (35)$$

The index of x_{zmp} offsetting the center of the support region is:

$$S_{index} = |x_{zmp} - x_{footcenter}| \quad (36)$$

The value of the index is smaller, the stable margin is bigger. Therefore the optimizing goal can be set as:

$$Object : Minimize [J(a_3, a_4, a_5)] \quad (37)$$

In which,

$$J(a_3, a_4, a_5) = Max[|x_{zmp}(t) - x_{footcenter}|, t \in [0, T_s]] \quad (38)$$

Taking the constraints in consideration, the optimizing goal is modified as:

$$Object : Minimize (J + g) \quad (39)$$

In which,

$$g = \begin{cases} 0 & \dot{x}_{hip} > 0 \\ l_{foot} & \dot{x}_{hip} \leq 0 \end{cases} \quad (40)$$

2.3.3 Optimized results

By using the toolbox of MATLAB-----Genetic Algorithm for Function Optimization of Christopher R .Houck, with the optimize process shown in Fig.6 and Fig.7, we get the optimized values of all variables:

$$\begin{aligned} a_3 &= 11.1184 \\ a_4 &= -13.9498 \\ a_5 &= 6.9642 \end{aligned} \quad (41)$$

The value of the optimize goal:

$$J(a_3, a_4, a_5) = 0.0555 \quad (42)$$

The minimum distance between X_{zmp} and the support region boundary is 0.052 m, so the stability margin is big enough. Substitute a_3 , a_4 and a_5 into X_{hip} , then the planned gait is obtained (refer to Fig.8):

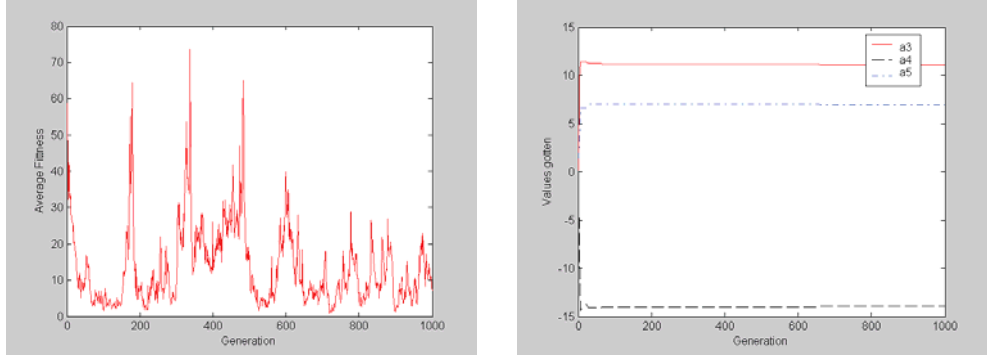


Fig. 6. Average adaptability (left) and the value of the variables (right)

Fig.9 shows that when the position of the center-of-gravity x_{cg} is outside the support region, the x_{zmp} of the planning gait optimized by using of Genetic Algorithm is still at the center of the support region. This optimized gait has greater stability margin, the capacity of anti-jamming improved during bipedal walking, and the physical feasible of the planned gait is guaranteed.

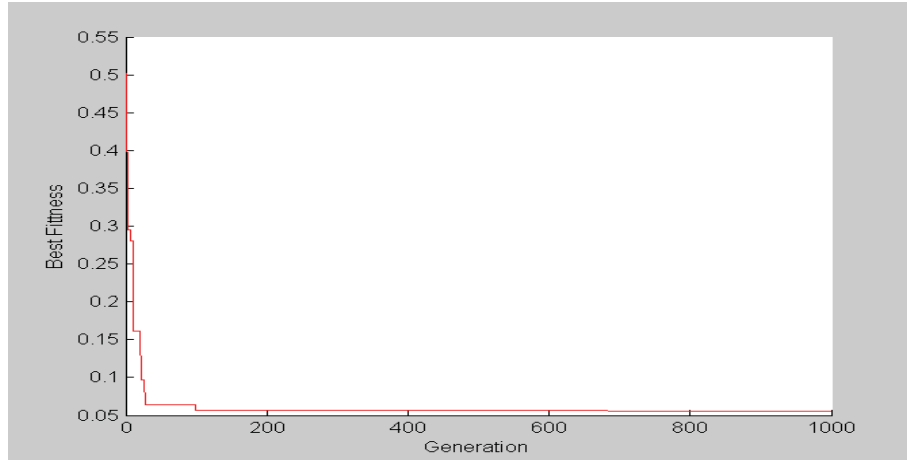


Fig. 7. Optimized adaptability

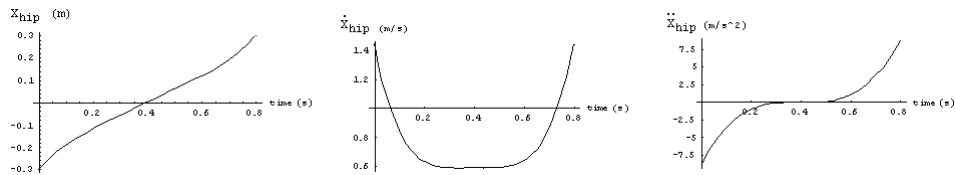


Fig. 8. Optimized Trajectories of X_{hip}

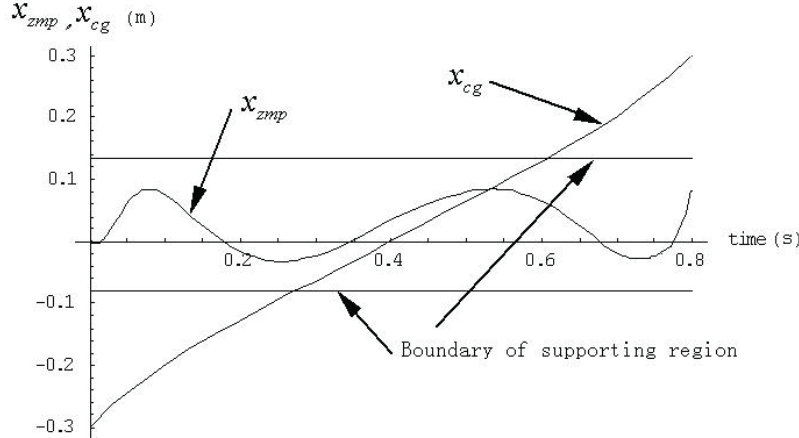


Fig. 9. Centre-of-Gravity and ZMP trajectories of the optimized gait

3. Virtual prototype model of humanoid robot

3.1 Mechanical model in ADAMS

For exactly building a virtual prototype of the humanoid robot SHUR, a various professional soft wares are used. The geometric model of the humanoid robot SHUR is built in professional three-dimensional CAD soft Pro/E, its dynamics simulation is in ADAMS soft ware, the design the robot control system is in MATLAB soft ware. Through ADAMS/Controls interface module, a real-time data channels between MATLAB and ADAMS is build, and an associated simulation is implemented.

The mechanical system model of the humanoid robot SHUR in ADAMS must include geometries, constraints, forces, torques and sensors. The procedure of building the model includes eight steps.

- (1) Building part models for all parts of the humanoid robot, then assembly part models together through applying geometric constraints as the robot being at the posture of standing.
- (2) Setup environment parameters of ADAMS;
- (3) Using the interface module of Mechanical/pro between Pro/e and ADAMS, the assembled model is imported into ADAMS;
- (4) Building pairs (joint) between each adjacent links, and applying locomotion constraint.
- (5) Building contact models between feet of the humanoid robot and the ground.
- (6) Setting locomotion constraints at particular joints.
- (7) Applying driving torques on joints relating to bipedal walking motion.
- (8) Building virtual sensors to receive state information of the system

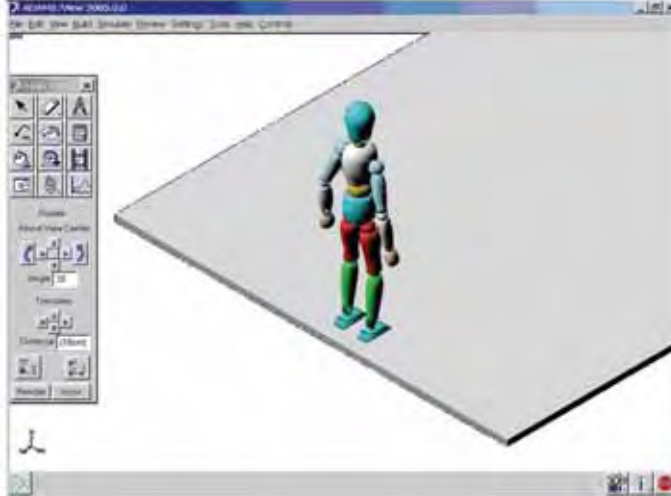


Fig. 10. Virtual prototype of humanoid robot SHUR

Fig.10 and Fig.11 show the virtual principle prototype of the humanoid robot SHUR, including 17 movable links, 16 ball hinge joints and the contact models between both feet and the ground.

= model_1	Model
+ abdomen	Part
+ chest	Part
+ ground	Part (ground)
+ head	Part
+ hip	Part
+ leftfoot	Part
+ leftforsarm	Part
+ lefthand	Part
+ leftshin	Part
+ leftshoulder	Part
+ leftthigh	Part
+ neck	Part
+ rightfoot	Part
+ rightforsarm	Part
+ righthand	Part
+ rightshin	Part
+ rightshoulder	Part
+ rightthigh	Part
JOINT_abdomen_hip	Spherical Joint
JOINT_chest_abdomen	Spherical Joint
JOINT_chest_leftshoulder	Spherical Joint
JOINT_chest_rightshoulder	Spherical Joint
JOINT_head_neck	Spherical Joint
JOINT_hip_leftthigh	Spherical Joint
JOINT_hip_rightthigh	Spherical Joint
JOINT_leftforsarm_lefthand	Spherical Joint
JOINT_leftshin_leftfoot	Spherical Joint
JOINT_leftshoulder_leftforsarm	Spherical Joint
JOINT_leftthigh_leftshin	Spherical Joint
JOINT_neck_chest	Spherical Joint
JOINT_rightforsarm_righthand	Spherical Joint
JOINT_rightshin_rightfoot	Spherical Joint
JOINT_rightshoulder_rightforsarm	Spherical Joint
JOINT_rightthigh_rightshin	Spherical Joint

Fig. 11. Basic components and main joints of SHUR

3.2 Virtual prototype system of humanoid robot SHUR

The input and output variables of the model in ADAMS are defined. The input variables are the required control variables, that is, the driving moment of the joints. The output variable is the measuring quantity of sensors, which are the state information of the system, mainly including: angular displacement, angular velocity, and angular acceleration of each joint and the state of whole robot, such as CoG, ZMP, and inclination state of the robot and so on. MATLAB soft ware is used to build a control system block diagram of the control system of humanoid robot SHUR (Fig.12). The ADAMS mechanical system must be included in block diagram, so as to complete a closed loop system including ADAMS and control system soft MATLAB.

The simulation of the whole system is processed by using suitable control laws. The 3D solid models, kinematics, dynamic model and animation simulation of the humanoid robot are supplied by ADAMS; the expected gait and the control algorithm are supplied by MATLAB, and the driving moment of each joint is the output of MATLAB. Through the interface provided by ADAMS/control module, MATLAB provides the control command of the driving moment of each joint to ADAMS; the latter will feedback the virtual sensor information of the system states into MATLAB, a real-time closed loop control system is completed. The result of the simulation may be displayed and saved through data, drawings and animations in ADAMS.

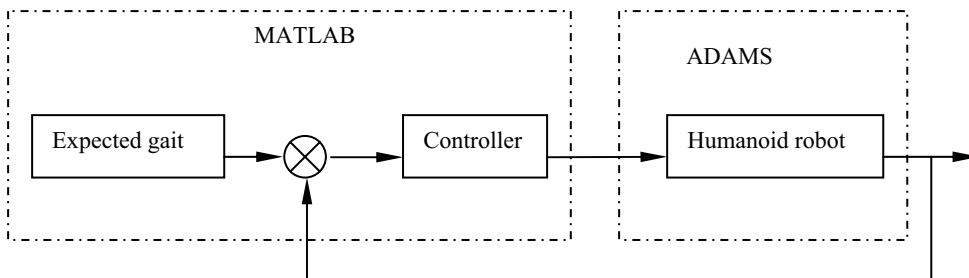


Fig. 12. Virtual prototype system of the humanoid robot SHUR

4. Non-time reference stability control method

4.1 Principle of stability control through modifying the walking speed

A biped robot may be viewed as a ballistic mechanism that intermittently interacts with its environment, the ground, through its feet. The supporting foot / ground "joint" is unilateral for there is no attractive forces, and underactuated since control inputs are absent. Formally, unilateral and underactuation are the inherent characteristics of biped walking, leading to the instability problem, especially un-expected falling down around the edge of the support foot. This stability problem can be measured by ZMP and or be measured by a more visual index of the degree of inclination of the robot. Almost every humanoid robot has installed the sensors like gyroscope to measure the degree of inclination of the robot. A virtual gyroscope is installed on the virtual prototype of the humanoid robot SHUR to measure the inclination angle of the posture of the upper body. This inclination angle is the object of the stability control in our research. At the same time, the inclination angle is also used as the feedback information of the close-loop stability control system.

To simplify the architecture of the controller, a 2-level control structure including coordination and control levels is introduced (see Fig.13).The coordination level is in charge of controlling the stability of bipedal walking. The main tasks of coordination level include gait planning; coordinate the movements of every part and giving command to the control level. The control levels receive the command from the coordination level and realize the trajectory tracking controls of every joint of the humanoid robot.

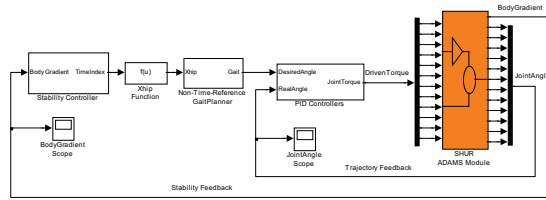


Fig. 13. Walking control system in MATLAB

The ZMP trajectory can be easily planned to be located in the valid support region at the phase of off-line gait planning. But in actual walk, there are the differences between the actual environment and the ideal one, or a modeling error , the impact of foot-ground, as well as external interference, which cause the real ZMP trajectory differ from the pre-designed one. If this difference is in open-loop state, the robot walks directly using the original planned gait, the stability may be broken down, the pre-planned gait can not be realized, so, it is necessary to correct the gait path on-line.

When people feel about to fell down, they usually quickens the pace to reduce the overturning moment and gradually restores to stable walk. The changing of instantaneous velocity can restores the stability effectively. Restoring the walk stability by changing instantaneous walk speed nearly has become a person's instinct of responding, which is gradually gained through the practices of bipedal walking. This paper uses the same method of human beings to achieve a stable walk. When the robot falls forward or backward, the strategy lets the robot accelerate or decelerate in the forward locomotion, then an additional restoring torque reversing the direction of falling will be added on the robot.

Does not lose the generality, taking robot falling forward around the edge of the toe of the support foot as an example, this paper uses an on-line correct method to accelerate the forward locomotion of the robot to restore the walking stability. When the robot is accelerated forward, there is an additional forward acceleration

$$\Delta\ddot{x}_{\text{hip}} > 0 \quad (43)$$

The robot receives a backward additional force

$$\Delta F_x = -m \Delta\ddot{x}_{\text{hip}} < 0 \quad (44)$$

The backward additional force will produce a restoring moment relating to the support foot, which is opposite to the direction of falling.

$$\Delta M_y = \Delta F_x h_{\text{cmb}} \quad (45)$$

In which, h_{cmb} is the height of the center of the mass of the trunk to the ground. The additional moment ΔM_y is helpful for ZMP to restore to the center of the support region.

For falling forward, this strategy of accelerating forward will also let the swing leg touch the ground sooner than original planning, so the robot will get a new support, the falling forward trend will be stopped.

When we off-line planned the robot space path, we had already considered the robot walking environmental factors like obstacles or the topographic factor like staircase specification, the ground gradient and so on. Therefore, the online gait modification had better not to change the robot space path which be planned off-line. Referring to the non-time gait planning principle, the non-time reference variable is the only one needs to be modified in the stability control. So the online modify algorithm can be realized easily based on offline gait planning, and the space path of the robot passing through remains unchanged.

Applying non-time gait planning algorithm, the whole gait-planning phase is divided into two phases, (1) planning the space walking path: Taking the forward locomotion of upper-body as the reference variable, considering the constraint of the environment, the walking path of a robot without collision with other objects is designed, thus the relating locomotion of the parts of the robot is obtained; (2) planning the trajectory of the non-time reference variable: according the constraint of ZMP stability, design the forward locomotion of upper-body. By changing the forward locomotion of upper-body. $x_{\text{hip}}(t)$, the dynamics characteristic can be changed to satisfy the walking stability condition while the space walking path maintains unchanged.

The trajectory of the upper body of the robot in forward direction is:

$$x_{\text{hip}} = a_0 + a_1 t + a_2 t^2 + a_3 t^3 + a_4 t^4 + a_5 t^5 \quad (46)$$

Applying non-time reference principle to the trajectory of the upper body in forward direction, we replace the variable (time t) in the quintic polynomial with a non-time parameter (time index $\text{time}_{\text{index}}$). The time index $\text{time}_{\text{index}}$ is a function of the time:

$\text{time}_{\text{index}} = f(t)$. In control and simulation, the time index $\text{time}_{\text{index}}$ is a discrete time series basically separated by the sample time interval (in virtual prototype, it is the time step length of simulation, SimTimeStep).

$$\text{time}_{\text{index}}^{n+1} = \text{time}_{\text{index}}^n + \text{SimTimeStep} + \Delta\text{time}_{\text{index}}^{n+1} \quad (47)$$

In which, $\Delta\text{time}_{\text{index}}$ is the time index correction decided according to the stability states of the robot.

For guarantee the robot will not stop or go back because of the gait correction, the time index should satisfy:

$$\text{time}_{\text{index}}^{n+1} > \text{time}_{\text{index}}^n \quad (48)$$

So the inequality must be satisfied:

$$\Delta\text{time}_{\text{index}} > -\text{SimTimeStep} \quad (49)$$

In certain scope, if $\Delta\text{time}_{\text{index}} > 0$, the forward walks speed is accelerated compare to the off-line planned one, otherwise decelerated. As shown in Fig.14, using a fuzzy controller to determinate the time index $\Delta\text{time}_{\text{index}}$ according to the upper body gradient which corresponding to the states of stability.

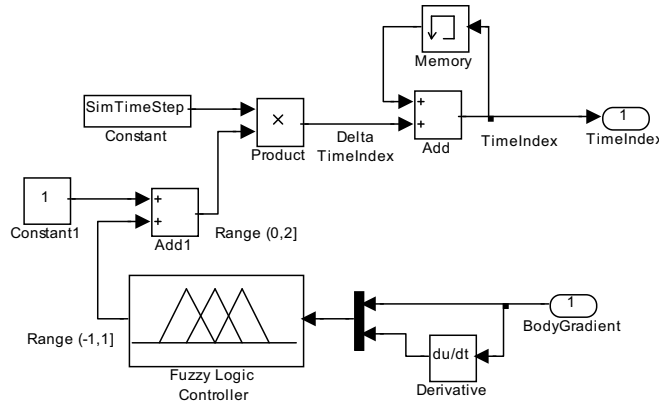


Fig. 14. Time index modification system using fuzzy controller

Regarding to general gait planning methods, the planned gaits in joint space are:

$$\theta_i = f(t) \quad i = 1, 2, \dots, n_{Joint} \quad (50)$$

If we replace the variable t in Eq.50 with the time index $time_{index}$, we can also correct the gaits online using the non-time reference stability control algorithm, according to the stability states of the bipedal walking. The relative motion paths of the joints remain unchanged after the gait correction, which means the robot space motion paths remain unchanged.

4.2 Design of Fuzzy Controller

Fuzzy control is a combination of fuzzy logic and control technology, and has advantages to control the systems which are indeterminate, highly nonlinearity and complex. So we adopt a fuzzy controller to achieve the nonlinearity mapping between the BodyGradient and the increment of the time index.

A fuzzy controller shown in Fig.16 is built by using the fuzzy controller tool box in MATLAB. The Inputs of the fuzzy controller are BodyGradient and GradientRate, and the output is Coefficient. Fig.17 shows the range of values and membership functions of these input and output variables.

The variable BodyGradient has three ranges: Forward, Okey and Backward. The variable GradientRate has three ranges: Negative, Neglectable and Positive. The variable Coefficient is classified into five ranges: Lower, Low, NoChange, Fast, and Faster.

There are many methods to derive fuzzy rules for the biped control(Pratt, et al,1998), either from intuitive knowledge of the biped control by human walking demonstration(G.O.A. Zapata, et al,1999), or information integration(Zhou,2000). Based on intuitive balancing knowledge, nine fuzzy rules are obtained as shown in Fig.17 (left), and the relationship between the inputs and the output of the fuzzy controller is shown in Fig.17 (right)

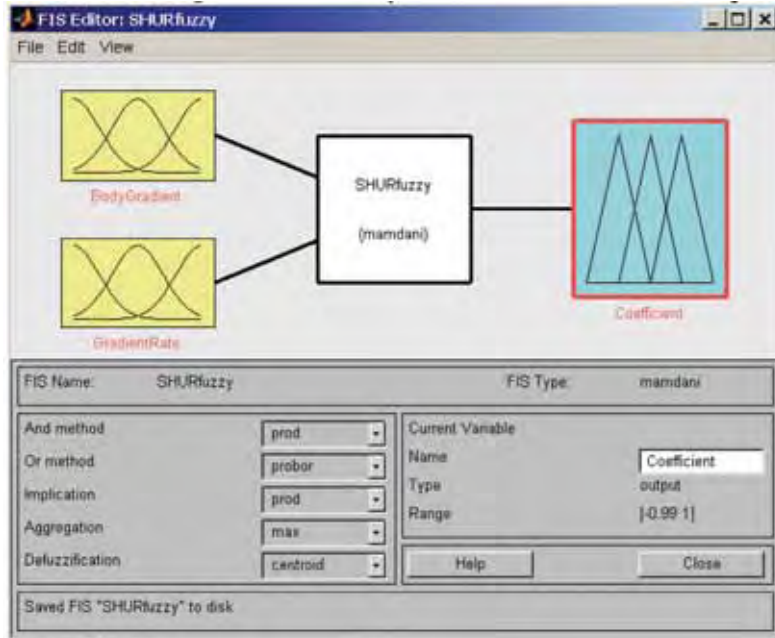


Fig. 15. Structure of the fuzzy system

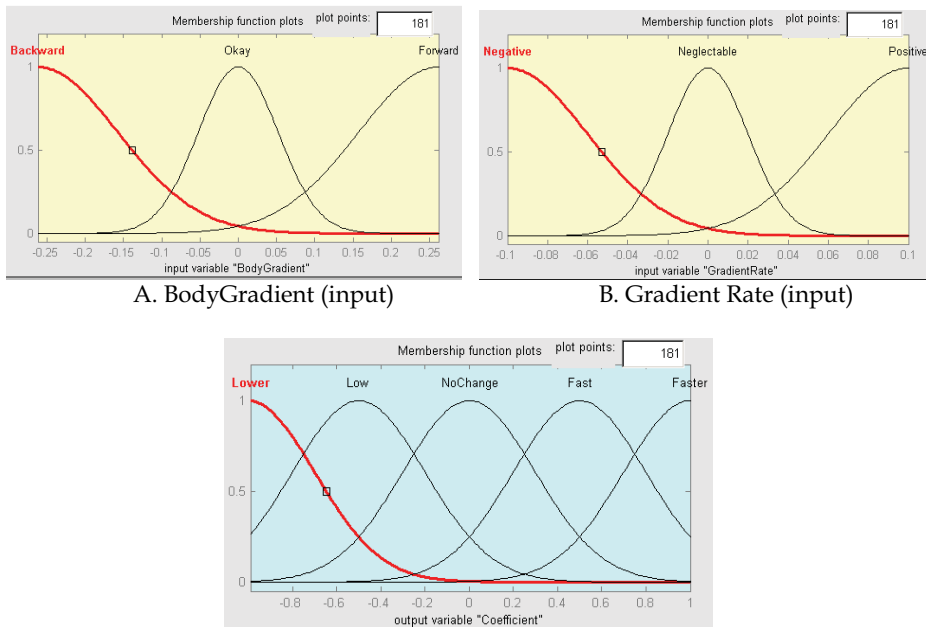


Fig. 16. Membership functions of the input and output variables of the fuzzy controller

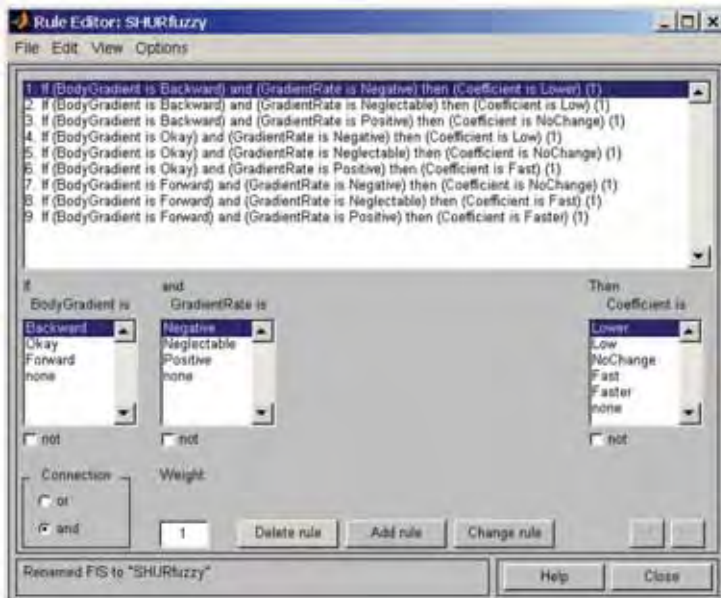


Fig. 17. Nine fuzzy rules of the fuzzy controller

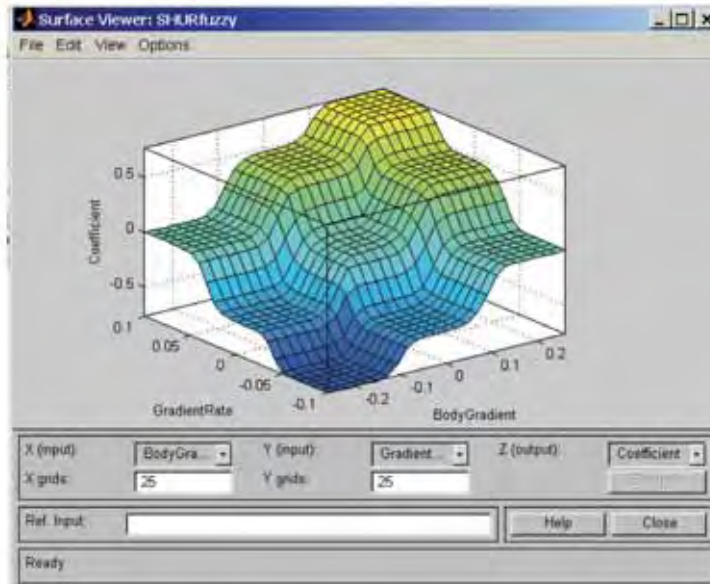


Fig. 17. Fuzzy rules (left) and the relationship between the input and output of the controller (right)

4.3 Simulations of climbing upstairs

The simulation of climbing up stairs is realized by the virtual prototype of humanoid robot SHUR, using the non-time reference dynamic stability control strategies. The simulation parameters include, the height of the stair is 0.15m, and the depth of the stair is 0.2m, the period of a single step is 0.8s. The beginning and the ending phases of the gait have a single step period. Fig.18 shows the virtual prototype of the humanoid robot SHUR and the virtual environment including stairs. Fig.19 shows motion sequences t of climbing upstairs.

5. Conclusions and discussions

A non-time reference gait planning method is proposed. The usual reference variable, time, is substituted by a non-time variable in gait, so the whole gait-planning phase can be divided into two phases, (1) planning the space walking path: Taking the forward locomotion of upper-body as reference variable, considering the constraint of the environment, the walking path of a robot without collision with other objects is designed, thus the relative locomotion of the parts of the robot is obtained; (2) planning the trajectory of the non-time reference variable: according to the constraint of ZMP stability, design the forward locomotion of upper-body. The gait-planning problem is changed to the optimization problem. Using the excellent optimization and searching property of Genetic Algorithm, the gait with good stability is obtained. This non-time reference gait planning methods has advantages in passing obstacles, climbing upstairs or downstairs and other similar situation in which the walking path is specified. In the progress of stability control, the non-time reference variable is the only one need to be modified, so the online modify algorithm can be realized easily based on offline gait planning.

Combining the non-time reference gait planning method, the intelligent stability control strategy through modifying the instantaneous walking speed of the robot is proposed. When the robot falls forward or backward, the strategy lets the robot accelerate or decelerate in the forward locomotion, then an additional restoring torque reversing the direction of falling will be added on the robot. For falling forward, this strategy will also let the swing leg touch the ground sooner than original planning, so the robot will get a new support, the falling forward trend will be stopped. According to the principle of non-time reference gait planning, the non-time reference variable is the only one needs to be modified in the stability control. The incline state of the upper-body, which reflects the stability state of the robot directly, is used as the input signal of a fuzzy controller; the correction of the non-time reference trajectory is used as the output of the fuzzy controller. Then the walking speed is changed, so the gait of the robot is modified online to realize stable dynamic walking without changing the off-line planned walking space path. For testify the validity of this strategy, the humanoid robot climbing upstairs is realized using the virtual prototype of humanoid robot.

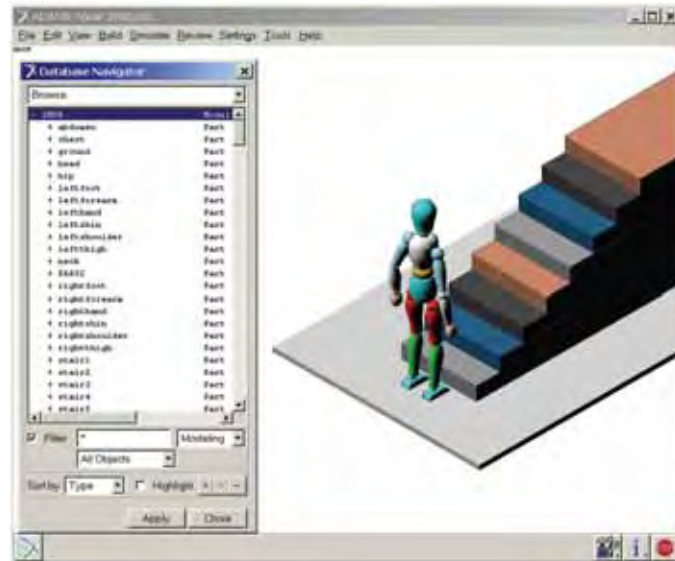


Fig. 18. Virtual prototype of a humanoid robot with virtual environment including stairs



Fig. 19. Motion sequences of a humanoid robot climbing stairs

6. References

- C. Zhou .Neuro-fuzzy gait synthesis with reinforcement learning for a biped walking robot, *Soft Comput.* 4 (2000) 238–250.
- G.O.A. ;Zapata&R.K.H. Galvao, T. Yoneyama, Extraction fuzzy control rules from experimental human operator data, *IEEE Trans. Systems Man Cybernet. B* 29 (1999) 398–406.
- Hirai Kazuo; Hirose Masato & Haikawa Yuji(1998). The development of honda humanoid robot [A]. *Proceedings of 1998 IEEE International Conference on Robotics & Automation*. Belgium. May 1998:1321-1326
- J.H. Park& K.D. Kim(1998). Biped robot walking using gravity-compensated inverted pendulum mode and computed torque control, *Proc. IEEE Internat. Conf. on Robotics and Automation*, Leuven, Belgium, 1998. vol.4, pp. 3528-3533
- J. Pratt & G. Pratt. Intuitive control of a planar bipedal walking robot, in: *Proc. of IEEE Conf. on Robotics and Automation*, 1998, pp. 2014–2021.
- J. Yamaguchi; N. Kinoshita; A. Takanish, et al(1996). Development of a dynamic biped walking system for humanoid development of a biped walking robot adapting to the humans' living Goor, *Proc. IEEE Internat. Conf. on Robotics and Automation*, Minneapolis, MN, 1996, pp. 232–239.
- K.Taniguchi (1999). MITI Humanoid Robotics Project. *The 2nd International symposium on humanoid robot*, 1999.Tokyo: 71-76
- Q. Li; A. Takanish & I. Kato(1992).Learning control of compensative trunk motion for biped walking robot based on ZMP stability criterion, *Proc. IEEE=RSJ Internat. Workshop on Intelligent Robotics and Systems*, Raleigh, NC, 1992, pp. 597–603.
- Q.Huang; H.Arai & K.Taniguchi(1999). A High Stability Smooth Walking Pattern for Biped Robot. *IEEE International Conference on Robotics and Automation*, 1999,pp:65-71
- S.Hashimoto, et al (1998).“ Humanoid Robots in Waseda University -Hadaly-2 and WABIAN” *IARP First International Workshop on Humanoid and Human Friendly Robotics* , October Japan , 1998 , pp. I-2: 1-10
- S. Kajita& K. Tani(1995)., Experimental study of biped dynamic walking in the linear inverted pendulum mode, *Proc. IEEE Internat. Conf. on Robotics and Automation*, Nagoya, Japan, 1995, pp. 2885–2891.

Design Methodology for Biped Robots: Applications in Robotics and Prosthetics

Máximo Roa, Diego Garzón and Ricardo Ramírez

*National University of Colombia
Colombia*

1. Introduction

Bipedal walk as an activity requires an excellent sensorial and movement integration to coordinate the motions of different joints, getting as a result an efficient navigation system for a changing environment. Main applications of the study of biped walking are in the field of medical technology, to diagnose gait pathologies, to take surgical decisions, to adequate prosthesis and orthosis design to supply natural deficiencies in people and for planning rehabilitation strategies for specific pathologies. The same principles can also be applied to develop biped machines; in daily situations, a biped robot would be the best configuration to interact with humans and to get through an environment difficult for navigation. If the biped robot is designed with human proportions, the robot could manage his way through spaces designed for humans, like stairs and elevators, and hopefully the interaction with the robot would be similar to interaction with a human being.

The National University of Colombia has been working on the design and control of biped robots, supported by two research groups, Biomechanics and Mobile Robots. The joint effort of the groups has produced three biped robots with successful walks, based on a single idea: if an appropriate design methodology exists, the resulting hardware must have appropriate dynamical characteristics, making easier the control of the walking movements. The design process successfully merges two lines of research in bipedal walk, passive an active walks, by using gait patterns obtained thanks to the simulation of a knee passive walker to create the trajectory followed by the control of an active biped robot. Our actual line of research in biped robots is to use biped robots reproducing the human gait pattern as engineering tools to test the behavior of below-knee prostheses, thus producing a biped robot with heterogeneous legs that allows the evaluation of how the prosthetics influence the normal gait of the robot while it is walking as a human.

2. Design Methodology

Biped robot design should be based on a design methodology that produces an appropriate mechanical structure to get the desired walk. We use a design methodology that groups passive and active walk relying on dynamic models for bipedal gait (Roa et al., 2004). The methodology is an iterative process, as shown in Fig. 1. The knowledge of biped robot

dynamics allow us to develop simple and efficient control systems, based on the system dynamics and not on assumptions of a simplified model, such as the inverted pendulum, which provides valid results in simulation, but validation is difficult because of the challenge represented by the measure of position, speed or acceleration of the centre of mass in a real robotic mechanism.

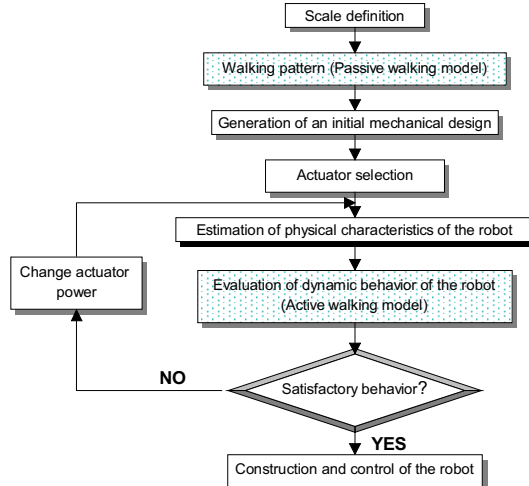


Fig. 1. Design methodology for biped robot design

The dynamical model for an actuated walk is the base in the design methodology used here; it is presented in Section 3. Geometrical and kinematical data are used to solve the model. Geometric variables of the robot (mass, inertia moment, length, and position of the centre of mass for each link) can be defined with different criteria, e.g. if the biped robot is intended to be a model of human gait, it is useful to scale anthropometrical proportions with an suitable scale factor. These data can be easily acquired using a CAD solid modeler software for a preliminary design. Kinematical data constitute the gait pattern for the robot. This pattern can be acquired from two approximations: extracted from a gait analysis of normal people in a gait laboratory, or generated through the simulation of passive walking models. The last approach has probed useful to obtain gait patterns at different speeds. The methodology outlined here assures that the controlled system is mechanically appropriate to get the desired walking patterns.

3. Dynamical Models for Biped Walkers

The main step in the development of a biped robot is the study and modeling of bipedal walk. The dynamical study can be accomplished from two points of view: passive and active walk. In passive walk the main factor is the gravitational influence on artificial mechanisms, getting a device to walk down a slope without actuators or control. In active walk there are different actuators which introduce energy to the mechanism so it can walk as desired. The models, passive and active, begin with a symmetry assumption: the geometric variables for the two legs are identical. Besides, the two legs are composed of rigid links connected by pin

joints, so each joint has just one degree of freedom. Although real walk is a three dimensional process, the models (and robots) will consider a planar walk, describing the movements in the sagittal plane (progression plane) of motion.

3.1 Passive Walk

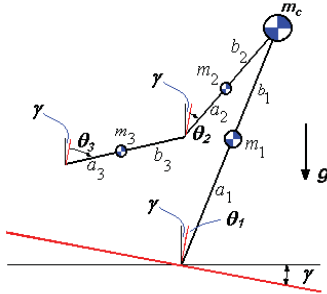


Fig. 2. Kneed-passive walker

McGeer (McGeer, 1990) presented the passive walk concept based on the hypotheses of understanding human gait as the influence of a neuromotor control mechanism acting on a device moved only by the gravity influence (Mochon & McMahon, 1980). McGeer first studied the passive walk through simple models, developed subsequently by different researchers (Goswami et al., 1996; Garcia et al., 1998). The model used in this work is the passive dynamic walker with knees (Fig. 2), original of McGeer (McGeer, 1990; Yamakita & Asano, 2001). The model has three links: stance leg (1), thigh (2) and shank (3), and four punctual masses (each link has a concentrated mass, and there is one additional mass at the hip, m_c). The robot has punctual feet with zero mass. Each link is described with the distal (a) and proximal (b) lengths to the concentrated mass in the link. The angles θ describe the angular position of the links with respect to the vertical line, and γ is the slope angle.

Fig. 3 shows the diagram of a gait cycle. The cycle begins with both feet on the ground. The swing leg (thigh and shank) moves freely (under gravity action) until the knee-strike, when the thigh and shank are aligned and become one single link, preventing a hyperextension in the knee. This is the beginning of the two-links phase, when the robot behaves as a compass gait walker. The gait cycle ends when the swinging leg hits the ground (heel-strike); at this point, the swing and the stance leg interchange their roles, and a new gait cycle begins.

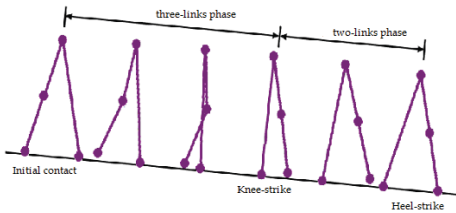


Fig. 3. Gait cycle in kneed-passive walk

Dynamic equations for the knee-passive walker have the general matricial form

$$D(\theta)\ddot{\theta} + H(\theta, \dot{\theta})\dot{\theta} + G(\theta) = 0 \quad (1)$$

with $D(\theta)$ the matrix of inertial terms, $H(\theta, \dot{\theta})$ the matrix with coriolis and centripetal terms and $G(\theta)$ the vector of gravitational effects. There are two transition events: the knee strike and the heel strike. Knee strike can be included in the above differential equation by using an artificial restriction λ_r (Yamakita & Asano, 2001)

$$D(\theta)\ddot{\theta} + H(\theta, \dot{\theta})\dot{\theta} + G(\theta) = -J_r^T \lambda_r \quad (2)$$

With

$$\begin{aligned} \lambda_r &= -\chi_r^{-1} J_r D(\theta)^{-1} (H(\theta, \dot{\theta})\dot{\theta} + G(\theta)) \\ \chi_r &= J_r D(\theta)^{-1} J_r^T, \quad J_r = [0 \quad -1 \quad 1] \end{aligned} \quad (3)$$

Thus, the same dynamic model can be used for the three links phase (before the knee strike) and the two links phase (after the knee strike). The transition equations for the heel strike are obtained from the conservation of angular momentum:

$$\begin{pmatrix} m_c l_1^2 + m_1 a_1^2 + m_1 l_1 (l_1 - b_1 \cos 2\alpha) & m_1 b_1 (b_1 - l_1 \cos 2\alpha) \\ -m_1 b_1 l_1 \cos 2\alpha & m_1 b_1^2 \end{pmatrix} \begin{pmatrix} \dot{\theta}_1^+ \\ \dot{\theta}_3^+ \end{pmatrix} = \begin{pmatrix} (m_c l_1^2 + 2m_1 a_1 l_1) \cos 2\alpha - m_1 a_1 b_1 & -m_1 a_1 b_1 \\ -m_1 a_1 b_1 & 0 \end{pmatrix} \begin{pmatrix} \dot{\theta}_1^- \\ \dot{\theta}_3^- \end{pmatrix} \quad (4)$$

and this event happens when $\dot{\theta}_1^- + \dot{\theta}_3^- = 0$.

To simplify the numerical simulation, we normalize the dynamic and transition equations using the following adimensional parameters

Mass ratios:

$$\mu = \frac{m_c}{m_1}, \quad \mu_1 = \frac{m_2}{m_1}, \quad \mu_2 = \frac{m_3}{m_1} \quad (5)$$

Length ratios:

$$\beta = \frac{b_1}{a_1}, \quad \beta_1 = \frac{a_2}{a_1}, \quad \beta_2 = \frac{b_2}{a_1}, \quad \beta_3 = \frac{b_3}{a_1} \quad (6)$$

However, not all of these numbers are independent; because of the symmetry of the walker there are some restrictions:

$$m_1 = m_2 + m_3, \quad l_1 = l_2 + l_3, \quad b_1 = \frac{m_2 b_2 + m_3 (l_2 + b_3)}{m_2 + m_3} \quad (7)$$

Normalized equations for the dynamical model are

$$m_1 a_1^2 \left[D_n(\theta) \ddot{\theta} + H_n(\theta, \dot{\theta}) \dot{\theta} + \frac{1}{a_1} G_n(\theta) \right] = -J_r^T \lambda_r \quad (8)$$

With

$$D_n(\theta) = \begin{pmatrix} 1 + (\mu + \mu_1 + \mu_2)(1 + \beta)^2 & -(1 + \beta)[\mu_1 \beta_2 + \mu_2(\beta_1 + \beta_2) \cos(\theta_1 - \theta_2)] & -\mu_2 \beta_3(\beta + 1) \cos(\theta_1 - \theta_3) \\ -(1 + \beta)[\mu_1 \beta_2 + \mu_2(\beta_1 + \beta_2) \cos(\theta_1 - \theta_2)] & \mu_1 \beta_2^2 + \mu_2(1 + \beta)^2 & \mu_2 \beta_3(\beta_1 + \beta_2) \cos(\theta_2 - \theta_3) \\ -\mu_2 \beta_3(\beta + 1) \cos(\theta_1 - \theta_3) & \mu_2 \beta_3(\beta_1 + \beta_2) \cos(\theta_2 - \theta_3) & \mu_2 \beta_3^2 \end{pmatrix} \quad (9)$$

$$H_n(\theta, \dot{\theta}) = \begin{pmatrix} 0 & -(1 + \beta)(\beta_2 + \mu_2 \beta_1) \sin(\theta_1 - \theta_2) \dot{\theta}_2 & -\mu_2 \beta_3(\beta + 1) \sin(\theta_1 - \theta_3) \dot{\theta}_3 \\ -(1 + \beta)\beta_2 + \mu_2 \beta_1 \sin(\theta_1 - \theta_2) \dot{\theta}_1 & 0 & \mu_2 \beta_3(\beta_1 + \beta_2) \sin(\theta_2 - \theta_3) \dot{\theta}_3 \\ \mu_2 \beta_3(\beta + 1) \sin(\theta_1 - \theta_3) \dot{\theta}_1 & -\mu_2 \beta_3(\beta_1 + \beta_2) \sin(\theta_2 - \theta_3) \dot{\theta}_2 & 0 \end{pmatrix} \quad (10)$$

$$G_n(\theta) = \begin{pmatrix} -[1 + (\mu + \mu_1 + \mu_2)(1 + \beta)]g \sin(\theta_1 + \gamma) \\ [\mu_1 \beta_2 + \mu_2(\beta_1 + \beta_2)]g \sin(\theta_2 + \gamma) \\ \mu_2 \beta_3 g \sin(\theta_3 + \gamma) \end{pmatrix} \quad (11)$$

And the normalized heel-strike condition is

$$Q_n^+(\alpha) \dot{\theta}^+ = Q_n^-(\theta) \dot{\theta}^- \text{, for } \dot{\theta}^\pm = \begin{bmatrix} \dot{\theta}_1^\pm \\ \dot{\theta}_3^\pm \end{bmatrix} \quad (12)$$

with

$$Q_n^+(\alpha) = m_1 a_1^2 \begin{pmatrix} \mu(1 + \beta)^2 + 1 + (1 + \beta)^2 - \beta(1 + \beta) \cos 2\alpha & \beta^2 - \beta(1 + \beta) \cos 2\alpha \\ -\beta(1 + \beta) \cos 2\alpha & \beta^2 \end{pmatrix} \quad (13)$$

$$Q_n^+(\alpha) = m_1 a_1^2 \begin{pmatrix} (\mu(1 + \beta)^2 + 2(1 + \beta)) \cos 2\alpha - \beta & -\beta \\ -\beta & 0 \end{pmatrix} \quad (14)$$

The model is fully described by the set of differential nonlinear equations (8), along with the normalized heel-strike transition equations (12). The previous model is solved in Matlab using a 4th order Runge Kutta routine with numerical error of 10⁻⁶. In order to get a stable motion, the joint variables (displacement and velocity) must follow a cyclic trajectory. Such trajectory can be found with appropriate initial conditions at the beginning of one step. The characteristics of the gait (velocity, time period, step length) depend on the geometry and inertial properties of the robot and the slope of the plane. We arbitrarily choose ranges for the adimensional numbers and solve repeatedly the equations to find the stable limit cycle for each particular walker. Results for each particular model include the angle and velocity progression for each link vs. time (Fig. 4) and the phase planes for each of the links (Fig. 5); the example uses the same numerical values as in (Yamakita & Asano, 2001). Stability is verified through the jacobian eigenvalues, as described in (Garcia, 1999).

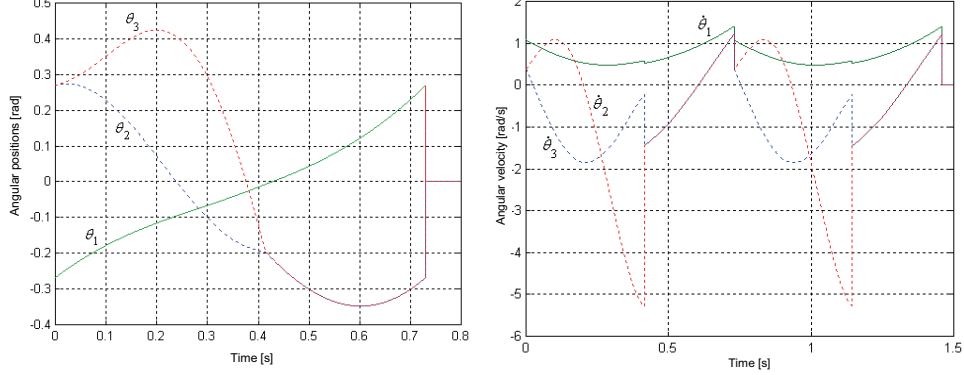


Fig. 4. Angles and angular velocity vs. time

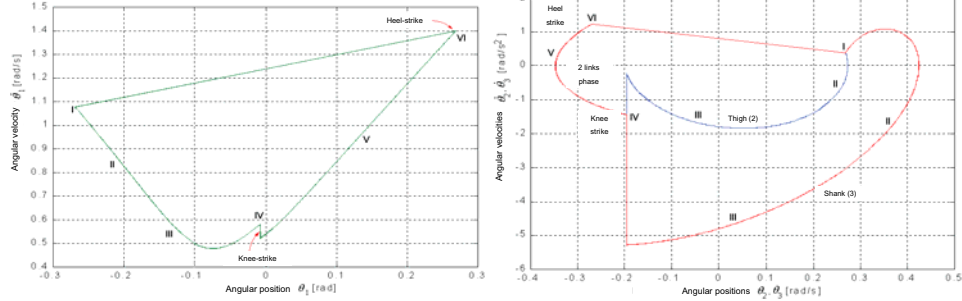


Fig. 5. Phase planes for the three links. Left: stance leg, Right: thigh and shank

The extensive simulation of the dynamical model establishes some interesting limits to get a periodic limit cycle (Roa et al., 2006). The conditions on the mass distribution (obtained with numerical simulations) to get stable limit cycles are

$$m_c > m_2 + m_3 , \mu > 1 , m_2 \geq m_3 , \mu_1 \geq \mu_2 \quad (15)$$

And the conditions on the length ratios are

$$a_2 \geq b_2 , \beta_1 \geq \beta_2 , a_3 \geq b_3 \quad (16)$$

Table 1 shows the anthropometric data for mass and length in the human body (Winter, 1990). Note that the whole leg accounts for 16% of the total body mass. The human body naturally fulfills the conditions (15) and (16) provided by the numerical simulation of the passive walker, when considering the HAT mass as a concentrated mass in the hip.

Link	Link mass/Total mass of the body	Center of mass/ Link length	
		Proximal	Distal
Thigh	0.100	0.433	0.567
Shank and foot	0.061	0.606	0.394
Shank	0.0465	0.433	0.567
Complete leg	0.161	0.447	0.553
HAT (Head, Arms and Trunk)	0.678	-	-

Table 1. Mass and length for different links in the human body

Table 2 shows the relations existing between the gait parameters for two models with similar mass and length proportions in the compass gait (Goswami et al., 1996b). For instance, the walking features are identical between two models with the same mass proportion μ . Moreover, the features for a walker with length proportion $\beta=b_1'/a_1'$ can be compared with the features for other walker with the same ratio following the relations in Table 2, based on the scalar $k_a=a_1/a_1'$. As an interesting result, the same relations hold for the kneeled walker. If two kneeled passive robots have the same proportions (i.e. the same adimensional mass numbers) the robots have exactly the same walking behavior. Modifications in the length of link 1 keeping the same proportion with a reference model affect all the gait parameters by a scale factor, except for the angle progression vs. time. This fact gives an interesting insight into one of the supporting hypotheses in human gait analysis: that every person, no matter his height, and in consequence, his limb length (considering a normal biotype), describes the same angle trajectory for each link in his gait cycle.

Model with lengths a_1' and b_1'	Model with lengths a_1 and b_1
θ	θ
$\dot{\theta}$	$\frac{1}{\sqrt{k_a}}\dot{\theta}$
L	$k_a L$
T	$\sqrt{k_a} T$
v	$\sqrt{k_a} v$

Table 2. Mass and length for different links in the human body

Thus, the analysis and numerical simulation of the passive walk model produces gait patterns for different slope angles in the movement of the robot (used to get different walking speeds in the real robots), which may be applied in different types of robots when considering the similarity criteria described in Table 2.

3.2 Actuated Walks

In dynamic walk, we consider robots moved under the effect of an actuator (servomotor, pneumatic muscle, elastic actuator, etc). The basic model used in the design process for biped robots is a five segments model, shown in Fig. 6; this model has been used previously

in other works (Lum et al., 1999). The robot has two feet, two thighs, a HAT (Head, Arms & Trunk) and punctual foot. The model of the robot has a planar walk (in the sagittal plane). Physical parameters of the model include the link mass (m), inertia moment (I), length (l), distance between the center of mass and distal point of the link (a) and the segment angle with respect to the vertical (ϕ) (with positive direction as defined in Fig.6).

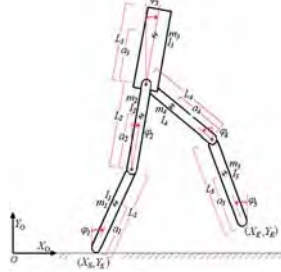


Fig. 6. Five segments model for biped walk, external torques

The gait equations, obtained with lagrangian dynamics, can be expressed in the form

$$D(\phi)\ddot{\phi} + H(\phi, \dot{\phi}) + G(\phi) = T \quad (17)$$

with $D(\phi)$ a 5×5 matrix containing the inertial terms, $H(\phi, \dot{\phi})$ a 5×1 vector with the effects of the coriolis and centripetal forces, $G(\phi)$ is a 5×1 vector containing the gravitational effects and T is the vector for moments (generalized external torques) over each segment. The components of each matrix are

Matrix of inertial terms $D(\phi)$

$$\begin{aligned}
 D_{11} &= I_1 + m_1 a_1^2 + (m_2 + m_3 + m_4 + m_5) l_1^2 \\
 D_{12} &= [m_2 l_1 a_2 + (m_3 + m_4 + m_5) l_1 l_2] \cos(\phi_1 - \phi_2) \\
 D_{13} &= m_3 l_1 a_3 \cos(\phi_1 - \phi_3) \\
 D_{14} &= [m_4 l_1 (l_4 - a_4) + m_5 l_1 l_4] \cos(\phi_1 + \phi_4) \\
 D_{15} &= m_5 l_1 (l_5 - a_5) \cos(\phi_1 + \phi_5) \\
 D_{21} &= D_{12} \\
 D_{22} &= I_2 + m_2 a_2^2 + (m_3 + m_4 + m_5) l_2^2 \\
 D_{23} &= m_3 l_2 a_3 \cos(\phi_2 - \phi_3) \\
 D_{24} &= [m_4 l_2 (l_4 - a_4) + m_5 l_2 l_4] \cos(\phi_2 + \phi_4) \\
 D_{25} &= m_5 l_2 (l_5 - a_5) \cos(\phi_2 + \phi_5) \\
 D_{31} &= D_{13} \\
 D_{32} &= D_{23} \\
 D_{33} &= I_3 + m_3 a_3^2 \\
 D_{34} &= D_{35} = 0 \\
 D_{41} &= D_{14}
 \end{aligned} \quad (18)$$

$$\begin{aligned}
D_{42} &= D_{24} \\
D_{43} &= D_{34} = 0 \\
D_{44} &= I_4 + m_4(l_4 - a_4)^2 + m_5l_4^2 \\
D_{45} &= m_5l_4(l_5 - a_5)\cos(\varphi_4 - \varphi_5) \\
D_{51} &= D_{15} \\
D_{52} &= D_{25} \\
D_{53} &= D_{35} = 0 \\
D_{54} &= D_{45} \\
D_{55} &= I_5 + m_5(l_5 - a_5)^2
\end{aligned}$$

Vector of coriolis and centripetal forces $H(\varphi, \dot{\varphi})$:

$$\begin{aligned}
H_1 &= [m_2l_1a_2 + (m_3 + m_4 + m_5)l_1l_2]\sin(\varphi_1 - \varphi_2)\dot{\varphi}_2^2 + m_3l_1a_3\sin(\varphi_1 - \varphi_3)\dot{\varphi}_3^2 \\
&\quad - [m_4l_1(l_4 - a_4) + m_5l_1l_4]\sin(\varphi_1 + \varphi_4)\dot{\varphi}_4^2 - [m_5l_1(l_5 - a_5)]\sin(\varphi_1 + \varphi_5)\dot{\varphi}_5^2 \\
H_2 &= -[m_2l_1a_2 + (m_3 + m_4 + m_5)l_1l_2]\sin(\varphi_1 - \varphi_2)\dot{\varphi}_1^2 + m_3l_2a_3\sin(\varphi_2 - \varphi_3)\dot{\varphi}_3^2 \\
&\quad - [m_4l_2(l_4 - a_4) + m_5l_2l_4]\sin(\varphi_2 + \varphi_4)\dot{\varphi}_4^2 - [m_5l_2(l_5 - a_5)]\sin(\varphi_2 + \varphi_5)\dot{\varphi}_5^2 \\
H_3 &= -[m_3l_1a_3]\sin(\varphi_1 - \varphi_3)\dot{\varphi}_1^2 - [m_3l_2a_3]\sin(\varphi_2 - \varphi_3)\dot{\varphi}_2^2 \\
H_4 &= -[m_4l_1(l_4 - a_4) + m_5l_1l_4]\sin(\varphi_1 + \varphi_4)\dot{\varphi}_1^2 - [m_4l_2(l_4 - a_4) + m_5l_2l_4]\sin(\varphi_2 + \varphi_4)\dot{\varphi}_2^2 \\
&\quad + [m_5l_4(l_5 - a_5)]\sin(\varphi_4 - \varphi_5)\dot{\varphi}_5^2 \\
H_5 &= -[m_5l_1(l_5 - a_5)]\sin(\varphi_1 + \varphi_5)\dot{\varphi}_1^2 - [m_5l_2(l_5 - a_5)]\sin(\varphi_2 + \varphi_5)\dot{\varphi}_2^2 \\
&\quad - [m_5l_4(l_5 - a_5)]\sin(\varphi_4 - \varphi_5)\dot{\varphi}_4^2
\end{aligned} \tag{19}$$

Vector of gravitational effects $G(\varphi)$

$$\begin{aligned}
G_1 &= -[m_1a_1 + (m_2 + m_3 + m_4 + m_5)l_1]g\sin\varphi_1 \\
G_2 &= -[m_2a_2 + (m_3 + m_4 + m_5)l_2]g\sin\varphi_2 \\
G_3 &= -[m_3a_3]g\sin\varphi_3 \\
G_4 &= [m_4(l_4 - a_4) + m_5l_4]g\sin\varphi_4 \\
G_5 &= [m_5(l_5 - a_5)]g\sin\varphi_5
\end{aligned} \tag{20}$$

This model contains the effect of external torques; however, torques exerted on the segments of the biped walker (human or robot) are internal moments caused by muscular forces or joint actuators; it is necessary to do an angle and torque transformation to get the internal torques in each joint. Fig. 7 illustrates the definitions for the model with internal torques. Let the vector of internal torques be

$$\tau = [\tau_1 \ \tau_2 \ \tau_3 \ \tau_4]^T \tag{21}$$

with τ_1 the torque in the knee of the stance leg, τ_2 the torque in the hip of the stance leg, τ_3 the torque in the hip of the swing leg and τ_4 the torque in the knee of the swing leg. Note that four of the five degrees of freedom ($\varphi_1, \varphi_2, \varphi_3, \varphi_4, \varphi_5$) may be directly controlled by the torques applied in the four joints. The angle φ_1 in the contact point with the floor (a hypothetical joint 0) may be indirectly controlled using the gravitational effects and the

movement of the links in the robot. The existence of this underactuated DOF, that can not be directly controlled, is one of the most important features in bipedal walk.

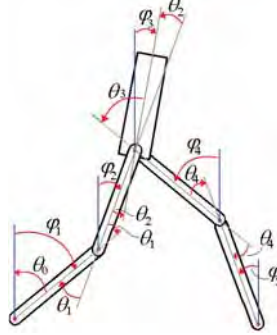


Fig. 7. Five segments model for biped walk, considering internal torques

The variables for the dynamical model with internal torques are

$$\theta = \begin{bmatrix} \theta_0 \\ \theta_1 \\ \theta_2 \\ \theta_3 \\ \theta_4 \end{bmatrix} = \begin{bmatrix} -\varphi_1 \\ \varphi_1 - \varphi_2 \\ -\varphi_2 + \varphi_3 \\ \varphi_3 + \varphi_4 \\ \varphi_4 - \varphi_5 \end{bmatrix} \quad \tau = \begin{bmatrix} \tau_0 \\ \tau_1 \\ \tau_2 \\ \tau_3 \\ \tau_4 \end{bmatrix} = \begin{bmatrix} -T_1 - T_2 - T_3 + T_4 + T_5 \\ T_2 + T_3 - T_4 - T_5 \\ -T_3 + T_4 + T_5 \\ T_4 + T_5 \\ -T_5 \end{bmatrix} \quad (22)$$

The gait equations for this model have the general form

$$d(\theta)\ddot{\theta} + h(\theta, \dot{\theta}) + g(\theta) = \tau \quad (23)$$

The components for the matrices in the previous equation are obtained directly from the dynamical model with external torques.

Matrix of inertial terms $d(\theta)$

$$d(\theta) = [d_{i1} \ d_{i2} \ d_{i3} \ d_{i4} \ d_{i5}], i=1,2,\dots,5$$

with

$$\begin{aligned} d_{i1} &= -A_{i1} - A_{i2} - A_{i3} + A_{i4} + A_{i5} \\ d_{i2} &= -A_{i2} - A_{i3} + A_{i4} + A_{i5} \\ d_{i3} &= A_{i3} - A_{i4} - A_{i5} \\ d_{i4} &= A_{i4} + A_{i5} \\ d_{i5} &= -A_{i5}, \end{aligned} \quad \text{and} \quad (24)$$

$$\begin{aligned} A_{1j} &= -D_{1j} - D_{2j} - D_{3j} + D_{4j} + D_{5j} \\ A_{2j} &= D_{2j} + D_{3j} - D_{4j} - D_{5j} \\ A_{3j} &= -D_{3j} + D_{4j} + D_{5j} \\ A_{4j} &= D_{4j} + D_{5j} \\ A_{5j} &= -D_{5j} \end{aligned}$$

$j=1,2,\dots,5$

Vector of coriolis and centripetal forces $H(\varphi, \dot{\varphi})$:

$$h(\theta, \dot{\theta}) = \begin{bmatrix} h_1 \\ h_2 \\ h_3 \\ h_4 \\ h_5 \end{bmatrix} = \begin{bmatrix} -H_1 - H_2 - H_3 + H_4 + H_5 \\ H_2 + H_3 - H_4 - H_5 \\ -H_3 + H_4 + H_5 \\ H_4 + H_5 \\ -H_5 \end{bmatrix} \quad (25)$$

Vector of gravitational effects $G(\varphi)$

$$g(\theta, \dot{\theta}) = \begin{bmatrix} g_1 \\ g_2 \\ g_3 \\ g_4 \\ g_5 \end{bmatrix} = \begin{bmatrix} -G_1 - G_2 - G_3 + G_4 + G_5 \\ G_2 + G_3 - G_4 - G_5 \\ -G_3 + G_4 + G_5 \\ G_4 + G_5 \\ -G_5 \end{bmatrix} \quad (26)$$

The initial data to solve the model are 1) geometrical data (basic dimensions of the robot) and 2) kinematical data (angular positions, velocities and accelerations in each joint). The kinematical data can be either data from a passive walk model (as the kneeled passive walker) or data from a human gait analysis. Our human gait patterns were obtained in the gait laboratory at CIREC (Colombian Research Institute for Human Rehabilitation); Fig. 8 shows a gait analysis, and Fig. 9 illustrates the type of data obtained in the lab, in this case, the angular positions for each one of the joints.

The dynamical model can be simulated to get torque charts for each of the actuators composing the robot; these charts are guidelines for the appropriate actuator selection in the design process. A more complex dynamical model (for instance, a robot with seven links) may be obtained following the same guidelines previously described. Movement in the frontal plane (if required for a non-planar robot) can be modeled with the behavior of a simple inverted pendulum coupled to the movement in the sagittal plane.



Fig. 8. A gait analysis at the laboratory.

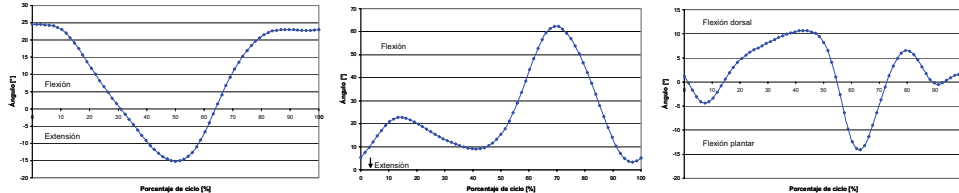


Fig. 9. Angular positions for the hip (left), knee (center) and ankle (right), as obtained from a gait analysis

4. Applications

4.1 Biped Robots

Using the proposed methodology, we have currently developed three biped robots. Our first prototype of a biped walking robot, called UNROCA-I (Fig. 10), was conceived as the simplest actuated robot that could achieve a two dimensional walk. The dynamical model for the robot has five links: a HAT and two links for each leg (the minimum required to get a walking movement in the sagittal plane, i.e. to change the supporting surface of the robot in the walking progression); it has punctual feet. The robot has two actuators in each leg (two servomotors in the knees and two at the hip). The feet are not necessary if we conceive the robot as a machine with continuous movement to keep the balance, although they are required if it is necessary to keep a static position. The robot attains a two dimensional walk thanks to a mechanical restriction, a walking guide. The robot moves with a guiding car that slides on a horizontal supporting bar. The walking guide prevents the hip oscillation in the frontal plane and the hip rotation in the transversal plane. The design preserves symmetry with respect to the sagittal plane; all of the mechanical and electrical components were mounted respecting this symmetry.



Fig. 10. Biped walking robot UNROCA-I

The robot has a trajectory following control; the position for each joint at every instant is fixed in advance (from a gait pattern), and the control system verifies this positioning. Servos have an internal feedback PD control to assure their position with a low overshoot and a fast response. Although we got a successful walking device, this prototype showed

several design and performance problems: the guide design forced us to use a counterweight to begin the walking movement, the straight line walking provides severe restrictions on the workspace, and there are differences between the predefined trajectories and the actual movements of the robot. These disadvantages forced us to completely redesign the prototype.



Fig. 11. Biped walking robot UNROCA-II

The second prototype, UNROCA-II, was conceived as a design evolution of the predecessor, thus it should solve the main problems detected in the previous one; Fig. 11 shows the prototype. Once again, we use a planar gait, but now describing a circle around a central support, getting more freedom in the robot movements; other walkers have previously used this kind of support (Pratt, 2000; Chevallereau et al., 2003). The robot uses anthropometrical proportions; it has 6 DOF, two ankles, two knees and two joints at the hips. We used normal human gait as well as passive walking gait patterns to produce the trajectory for each of the joints, so we could change the velocity of progression for the movement by changing the walking pattern; the dynamic model for the robot is the seven links model.

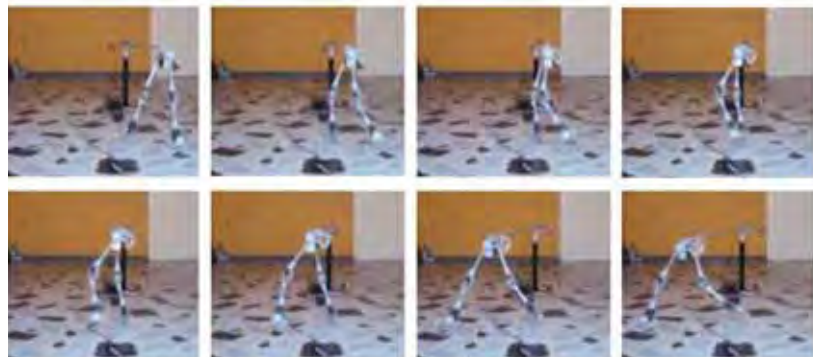


Fig. 12. Walking sequence for the robot UNROCA-II

We use a PD control to assure the prescribed gait: the position for each joint at every instant is given by the gait pattern, and the control system enforces this position. The internal potentiometers in the servos were used to get the reference signal for the closed loop position control. The control was implemented with microcontrollers, one for each couple of servos (for example, one micro controls the hip movements), plus a central controller to

synchronize the joint controllers. This robot corrected most of the errors of the first robot: it does not require external help to walk, and the closed loop control makes it more robust in front of perturbations. The ankle joint has two servos, making it easier to control them. The planar walk is approximated via a circular walk, eliminating the space limitations of the previous robot. The control system of the robot reacts well in the presence of small perturbations; the robot can start his walk with open (split) legs, seated or on its knees. Besides, with small obstacles in the walk path, the robot recovers its normal gait pattern once it has overcome the obstacles.



Fig. 13. Biped walking robot UNROCA-III

The third prototype of biped robot is shown in Fig. 13. This platform has picked up the previous experiences, resulting in a four DOF platform (two joints in the knees and hips), plus two passively actuated ankles. This robot does not require any external help to walk; it achieves stability thanks to an oscillating mass in top of the hip, so it actually attains a 3D walk. The oscillating mass couples and controls the gait in the sagittal and frontal planes. We used big feet to keep static stability while not moving, but they are not used to get stability in the walking process, as shown in Fig. 13; stability is assured through the appropriate movement of the counterweight in the hip according to a valid ZMP (Zero Moment Point) trajectory.



Fig. 14. Walking sequence for the robot UNROCA-III, side and front view

The three robots have achieved a satisfactory performance. From a simple point of view, the robots achieve their objective: they perform walking movements that allow them to move on two legs. The performance measurement was qualitative, as it is difficult to define parameters to measure the efficiency of movements in this kind of robots. The first robot

uses the horizontal restriction guide as an additional support. The second robot has a more satisfactory walk, although its walking style in circles implies an additional slipping effect due to the radius of the circular trajectory. The third prototype walks without any external help and without the previous problems. All of the prototypes have anthropometrical proportions and use passive walking gait patterns as well as physiological gait patterns (obtained in the gait lab at CIREC) to provide the trajectory for each one of the joints.

The fundamental achievement of these prototypes is the use of a simple control system that allows them to get a stable walk, and makes them able to overcome small perturbations. This achievement was possible thanks to the previous dynamical study, using an appropriate scaling to implement the human gait pattern and using a design methodology that takes into account the physical and dynamical features of the implemented system. Robots become an example of control systems adapting to the system dynamics, thus optimizing the power requirements on the actuators, the sensors and electronics used on the robot. The implemented gaits do not use a complex sensorial system, but the robots can extend its capabilities to become more robust to environment changes (for instance, to walk stairs).

4.2 Prosthesis Evaluation

The group of Biomechanics at the National University of Colombia has developed a number of prostheses for the lower limb, such as dynamic feet, devices for alignment of total knee prostheses, and A/K & B/K (Above and below knee) prostheses; Fig. 15 shows, for instance, a damper device for lower limb prosthetics in patients with transtibial amputations (Ramirez et al., 2005). The evaluation of such devices usually implies a qualitative test using a gait laboratory to acquire data from the gait of an amputee patient; subjective criteria such as pain relief and comfort in the walk are considered as part of the evaluation. We are actually working towards the use of biped robots to avoid subjective performance evaluation of the prostheses; providing a testbed for new designs before they are tested in real patients. Other groups are developing projects along this line for A/K prostheses, in the so-called Biped Robot with Heterogeneous Legs (BRHL) (Xu et al., 2006).



Fig. 15. Damper device for lower limb prosthetics

The evaluated prosthesis replaces one of the legs of the biped robot, and the other leg is properly balanced to keep the balance of the robot. As the robot reproduces the physiological human gait pattern, the behavior of the prostheses is evaluated, thus providing reliable data on its dynamical characteristics and its influence on the global gait behavior, and avoiding the inherent subjectivity of prostheses evaluation in real patients.

8. References

- Chevallereau, C.; Abba, G.; Aoustin, Y.; Plestan, F.; Westervelt, E.R.; Canudas-De-Wit, C. & Grizzle, J.W. (2003). RABBIT: a Testbed for Advanced Control Theory. *IEEE Control Systems Magazine*, Vol. 23, No. 5, pp 57-79, 0272-1708.
- Garcia, M.; Chatterjee, A.; Ruina, A. & Coleman, M. (1998). The simplest walking model: stability, complexity and scaling. *ASME J. Biomechanical Engineering*. Vol.120, No.2, pp 281-288, 0148-0731.
- Goswami, A.; Benoit T. & Bernard E. (1996). *Compass - Like Biped Robot. Part I: Stability and Bifurcation of Passive Gaits*, Research Report, INRIA (Institut National de Recherche en Informatique et en Automatique), 0249-6399.
- Goswami, A.; Espiau, B. & Keramane A. (1996). Limit Cycles and their Stability in a Passive Bipedal Gait. *Proc. Int. Conf. Robotics and Automation - ICRA 1996*, pp. 246-251, 0-7803-2988-0.
- Lum, H.K.; Zribi, M. & Soh, Y.C. (1999). Planning and control of a biped robot. *Int. J. Eng. Science*, Vol.37, pp 1319-1349, 0020-7225.
- McGeer T. (1990). Passive dynamic walking. *Int. J. of Robotic Research*, Vol. 9, No.2, pp 62-82, 0278-3649.
- Mochon, S. & McMahon T. (1980). Ballistic walking: an improved model. *Mathematical Biosciences*, Vol.52, pp 241-260, 0025-5564.
- Pratt, J. (2000). Exploiting Inherent Robustness and Natural Dynamics in the Control of Bipedal Walking Robots. Ph.D. Thesis, MIT, USA.
- Ramirez, A.M.; Garzon, D.A.; Roa, M.A. & Cortes, C.J. (2005). Test on Patient of Damper Device for Lower Limb Prosthetic. *Gait & Posture*. Vol.22, No.S1, pp S48, 0966-6362.
- Roa, M.; Cortés, C. & Ramírez R. (2004). Design methodology for biped robots with an application. *Proc. CARS & FOF 2004*, pp 438-446.
- Roa, M.A.; Villegas, C.A. & Ramírez, R.E. (2006). Extensive modeling of a 3 DOF passive dynamic walker. In: *Climbing and Walking Robots*, M.O. Tokhi, G.S. Virk & M.A. Hossain, pp. 349-356, Springer, 3-540-26413-2, Berlin.
- Winter, D.A. (1979). *Biomechanics and Motor Control of Human Movement*, Wiley Interscience, 1990, 0471509086.
- Xu, X.; Xie, H.; Wang, B. & Tan, J. (2006). Gait Perception and Coordinated Control of a Novel Biped Robot with Heterogeneous Legs. *Proc. Int. Conf. Intelligent Robots and Systems - IEEE/RSJ IROS 2006*, pp. 356-361, 1-4244-0259-X.
- Yamakita, M. & Asano, F. (2001). Extended passive velocity field control with variable velocity fields for a kneeled biped. *Advanced Robotics*, Vol. 115, No.2, pp 139-168, 0169-1864.

Amphibious NDT Robots

Tariq P. Sattar, Hernando E. Leon-Rodriguez and Jianzhong Shang
*London South Bank University
 United Kingdom*

1. Introduction

Oil, petrochemical, and food processing industries worldwide store their raw materials and product in tens of thousands of storage tanks. The tanks are mostly constructed using welded steel plates and therefore subject to corrosion and weld cracking. Testing the structural integrity of these storage tanks with non-destructive testing (NDT) techniques is an expensive and time consuming activity. The walls of a large tank can usually be tested manually (for corrosion thinning and weld defects using ultrasonic techniques) from outside the tank. Access to most areas of a wall is obtained by constructing scaffolding or abseiling down from the top. However, erecting scaffolding is expensive and the inspection is tedious and slow. These costs can be reduced and the inspection speeded up by using climbing robots that deploy ultrasonic probes with scanning arms. However, there are some areas of the wall that cannot be accessed from the outside, for example at the base where the walls are protected by striker plates to run off rain water, or behind wind girders around the tank that are used to strengthen the tank, or obviously in tanks that are partially or fully buried in the ground. Similarly, storage tanks on ships cannot be inspected from the outside because they are surrounded by ballast tanks. To inspect the walls in these cases, the inspection has to be performed from inside the tank.

Additionally, a primary source of trouble in tanks is the floor which can corrode quickly in localised areas due to ground chemistry and suffer damage to welds through soil movement. The floors can be inspected reliably only by entering the tank.

Entry into tanks can be performed only when the tank has been emptied and thoroughly cleaned when it contains hazardous materials. The operation is hugely expensive requiring transportation of product to other tanks or locations, outages that last many months with subsequent loss of revenue, and cleaning costs incurred by repeated cleaning of the tank till all product is removed.

Very large cost savings can be made by performing internal and in-service inspection of the walls and floors of storage tanks by using robots that can be inserted into a tank through manholes. The robots will have to operate in the product contained in the tank (e.g. crude oil, refined petroleum products, chemicals, liquors, etc.) and the robot should be capable of gaining access to target areas that are to be inspected (tank wall areas, floor areas, and welds on the walls or floor).

To further reduce the cost of inspection, the robots should be versatile so that the same robot can perform many types of inspection once inserted into a tank. Also, the robots should be able to work in different types and sizes of tank. A versatile robot will be required to be compact so that it can be inserted through the smallest manhole and operate in small spaces. It should be able to swim through the product to provide access to a given inspection target, climb on the walls of the tank when these are to be inspected, and it should be able to descend onto the floor and move around on it with controlled motion trajectories. It should be able to operate in air on the floor when a tank is emptied of most of its product leaving only an inch or two of product on the floor. This latter scenario is useful because a tank product can be drawn off relatively easily but cleaning the tank till all product is removed is extremely difficult. Therefore the ability to operate on the floor of a tank with a few inches of liquid submerging the NDT sensors and acting as a couplant between the UT probe and the floor plates will still save the costs of cleaning and obviate the need for supplying a couplant. Finally, the robot should be intrinsically safe when operating in flammable and explosive environments.

This chapter describes some robot designs that aim to accomplish these requirements. Two wall-climbing, floor moving and swimming robots are described that operate while submerged in liquids stored in oil and petrochemical storage tanks. It outlines, in section 2, the industrial requirements for deploying a range of non-destructive testing (NDT) probes and techniques on the floors and walls of storage tanks while operating in liquids or in air, in explosive environments, and in cluttered and constrained spaces.

The design of two robots that have been developed to satisfy these requirements is explained in detail in sections 2.4 and 3. NDT results obtained with the robotic systems are presented.

Some other robots that have been developed to inspect tank floors are "Maverick" produced by Solex Robotics in USA, "Tank Ray" produced by Raytheon in the USA and "OTIS" produced by In Tank Services, (Berger et al 1990; Schempf 1994; King et al 1992; Solex Robotics).

2. Design of Floor and Wall Climbing Robot, RobTank, to Inspect the Internal Walls and Floors of Oil and Petrochemical Storage Tanks

This section describes a robot that is designed to enter a wide variety of storage tanks when in service and inspect the floor and internal walls of the tank while submerged in the product liquid.

2.1 Robotic NDT in Oil and Petrochemical Storage Tanks

Leakages from the floor of oil and chemical storage tanks lead to pollution and soil contamination. It is therefore essential to periodically inspect the floor to decide when to take a tank out of operation and repair it. Current inspection practices require tanks to be emptied and cleaned before an inspection can commence (Rusing 1994; Raad 1994). The total time to empty, clean and inspect a storage tank can be between 1 to 9 months on the larger crude oil tanks. Despite safety procedures, the cleaning operators are exposed to hazardous chemicals and other hazardous conditions for long periods of time. Tanks can remain out of service for quite long periods with direct economic and operational implications. Huge savings in cost and inspection times could be obtained by performing in-service inspection

of tank floors and walls with robotic devices. Given the large variety and types of storage tanks, to achieve this inspection it is necessary to develop mobile robots capable of:

- Entering tanks through manhole openings that can be as small as 300 mm diameter.
- Traveling on uneven tank surfaces and through sediment layers on the floor.
- Deploying a payload of Non Destructive Testing (NDT) sensors for the inspection of top and bottom corrosion on the tank floor.
- Changing surfaces from the floor to the wall to inspect lower parts of the tank that may be inaccessible from outside.
- Operating in explosive and hazardous liquids such as crude oil, petroleum products, ammonia, etc.
- Navigating in the tank to locate the position of defects and avoiding obstacles.

The design of robotics to perform inspection of storage tanks depends on whether the products in a tank are clean or dirty:

(a) Clean storage tanks containing blended oil products or chemicals.

The size of this type of tank varies from about 2 to 20 meters in diameter and usually has a fixed roof. Spot readings are taken on the floor, patch and annular plates in a 'domino' pattern with ultrasonic thickness measurements (USTM). Any suspect areas and other critical items such as drain sumps are then scanned manually. The inspection authority or utility operator can vary the amount of NDT carried out based on the initial results. This method does have the drawback that isolated areas of under floor corrosion could remain undetected.

On the larger diameter tanks, magnetic flux leakage (MFL) is used for the initial inspection. A portable trolley with an array of sensors is pushed manually over the floor to detect 40% thickness loss. Detected plate thinning is marked with paint by an operator for further evaluation. Floor plate closer than 75 mm to the tank wall is inspected with a hand held unit. Suspect areas are further examined using either vacuum box or magnetic particle inspection methods.

(b) Crude and fuel oil storage tanks

Crude oil tanks that have not been opened for cleaning for five or more years usually have large deposits of sludge (wax and sand) that can be up to 5 meters deep. These tanks have floating roofs, either double skin or pontoon type, with many manhole openings (for agitator entry). The diameter of these tanks is between 20 and 100 meters and construction material is carbon steel. They have annular floor plates with a minimum thickness of 12.5mm. Central floor plate thickness may vary between 6 to 12mm. The preparation periods for entry and internal inspection are lengthy with 6-9 months required for removal of the oil, gas, and sludge banks. Another 3-6 months are required for the process of washing the tank clean of all oil and venting it before men can enter the tank. The cleaned tank is inspected visually, then with Magnetic Flux Leakage (MFL) or Low Frequency Eddy-Current techniques to find problem areas, and finally UT is used to validate the findings. Dependent on technique, annular floor plate thickness up to 35mm can be achieved with discrimination between topside and under floor corrosion. Examination of floor plate welds is a time consuming and difficult task due to residue of product and poor lighting condition. Fuel oil storage tanks may be fitted with heating coils (usually 50mm diameter steam pipes), which hamper floor inspection. Many of these large diameter tanks have steel girders welded around the tank perimeter between half and two-thirds its height to strengthen the

tank. Unless adequate drainage is provided, they become water traps and subsequent corrosion sites.

2.2 Intrinsic Safety of a Robot in Explosive Environments

For a robot to operate safely in a flammable and explosive environment, its design is constrained by the overriding need to make it intrinsically safe. To meet BASEEFA requirements for Certification of the robot as intrinsically safe, all electronics, drive motors, and shaft encoders on board the robot must be housed in a single enclosure that is sealed and purged with inert gases so that oxygen is removed from the enclosure.

A system to sense the pressure in the enclosure and cut-off power supply to the robot at the operator's end, when pressure falls below a threshold value, must be incorporated.

There is an explosion risk in the "Vapor" zone when inserting a robot into a tank. One solution is to use a purged funnel through which the robot is passed into the liquid.

The robot must be constructed with materials that prevent build up of electrical static and should avoid sharp corners where a discharge could occur.

2.3 Buoyancy in Water and in Crude Oil

The buoyancy of swimming and wall-climbing robots operating in liquids depends on the density of a particular liquid. A versatile robot that can operate in many liquids ranging from water to crude oil therefore needs to actively control its buoyancy.

The oil industry uses API gravity as a measure of crude density. This is an inverse measure, the higher the API number, the lower the density. The API gravity is given by equation 1:

$$\text{API gravity} = \frac{141.5}{\text{specific gravity at } 60^\circ\text{F}} - 131.5 \quad (1)$$

Where, specific gravity is the ratio of density of oil to density of water. Light crude oil has a API gravity of more than 40. At API = 40, density of water is 998 kg m^{-3} , the density of light crude is 823.42 kg m^{-3} . Heavy crude oil, typically API gravity of 20 or less, has a density of 932.13 kg m^{-3} (For comparison, the density of olive oil is 920 kg m^{-3}).

A robot designed to be neutrally buoyant in water (with either mass or volume control), will experience a negative buoyancy force in oil. For example, if the robot weight in air is 998 kg and its volume is 1 m^3 , it will be neutrally buoyant in water but will experience a negative force of 66 kg in heavy crude with API gravity of 20. The same robot in light crude API gravity of 40, will experience a negative buoyancy force of 175 kg.

It is helpful to make a wall-climbing robot neutrally buoyant so that gravity forces are unimportant. When swimming, the robot buoyancy can be altered around its neutral buoyancy to ascend and descend the robot or varied rapidly to regulate its depth at a given set-point. It needs to be negatively buoyant when inspecting the floor so that it can apply sufficient pressure for good traction and contact of ultrasonic NDT sensors in the form of wheel probes.

In conclusion, sufficient range of mass or volume change should be designed into the buoyancy tanks to enable the same robot to operate in all types of liquid with neutral buoyancy when climbing walls and with negative buoyancy when on the floor.

2.4 Tank Floor and Wall Inspection with Entry into the Tank by RobTank

"Rob Tank Inspec" is a European project that has developed a robot called RobTank for in-service inspection of storage tanks filled with hazardous liquids. The robotic system is intended for largely clean tanks with a sediment layer on the floor that is not more than 50 mm thick. The applied inspection methods allow the evaluation of tank floor and wall condition in order to prevent leakage situations or prioritize maintenance works.

The mobile robot and its payload of NDT sensors and instrumentation are designed to test the following target areas:

- Under base corrosion: The fitting of shielding plates (to run off rain water) prevents access from the outside to under-wall corrosion areas. Current practice is to fit shielding plates to all tanks that are refurbished. The inspection robot deployed internally can provide access to this area of the annular plate.
- Sump drains: Another area of corrosion. The area requires scan inspection rather than spot inspection.
- Wind girders: Another area of corrosion. Can be inspected manually from the inside on floating roofs when roof falls below girder level. However, fixed roof tanks require inspection by a robot that may be operates both in liquid as well as air depending on whether the inspection is being performed in-service or on a tank that has been emptied for cleaning.
- Under heavier deposits of sludge: Experience has shown that likely areas of corrosion in crude oil tanks are to be found in areas where there is a heavy deposit of sludge.
- Under heating coils (steam coils): The area under heating coils in crude oil tanks is a particular area of corrosion.

Two wall-climbing and floor moving RobTank prototypes were constructed with the following three modules.

2.4.1 Module 1: Surface Changing Mobile Robot

The first version of the RobTank mobile robot (figures 1 and 2) can enter oil and chemical storage tanks through minimum 300 mm diameter manhole openings in the roof. The dimensions of the mobile robot are 200x200x500 mm. The robot is expected to operate in a pH range that is towards the alkaline side 5 to 12, in liquid temperatures from 0 to 70°C and pressure up to 3 bar. Its weight is about 20 kg with NDT sensors and it is designed to operate on rough floor surfaces through sludge deposits up to 50 mm deep and on tank walls. The maximum travel speed is up to 150 mm/sec. The flaw detector is able to measure internal and external corrosion with a thickness resolution of 1 mm on plate thickness ranges from 6 to 25 mm.

The problem was to design a small vehicle that meets the constraint that it should be able to enter a tank through manhole openings of minimum 300 mm diameter while being able to deliver the required NDT payload, transfer between floor and tank walls and climb on a tank wall.

The vehicle design incorporates a sealed, purged and pressurized central box which houses the servo motors, controller cards, NDT instrumentation (24 channel TD Scan Flaw Detector) and navigation sensors.

Two independently controlled servomotors provide the drive for the wheels of the vehicle. The motors are housed in the sealed and purged central box with motor shafts emerging from the box. These shafts are sealed with nitrile pressure seals rated to IP69. A single

propeller mounted on top of the vehicle provides the thrust force for adhesion to the wall. The thrust force is also useful when scanning with NDT sensors on the tank floor to get sufficient wheel traction and contact force. The on-board servo systems are programmed from outside the tank via a serial communications link. Trajectory control of the vehicle is by teleoperation via a Windows based software interface.

To obtain a very compact and lightweight design, special DC motors and ClickServo motor control boards are daisy chained to provide multi-axis control which reduces the umbilical size to two twisted pairs for serial full duplex communications to a remote station at a distance of 100 meters.

Two shaft encoders on the vehicle's drive motors provide feedback for control of the motors. The decoder counters can be interrogated via an RS 485 serial communications cable on the Operator's PC. Software running here can compute the speed and the position of the vehicle relative to a starting position and output it to any other module when required.

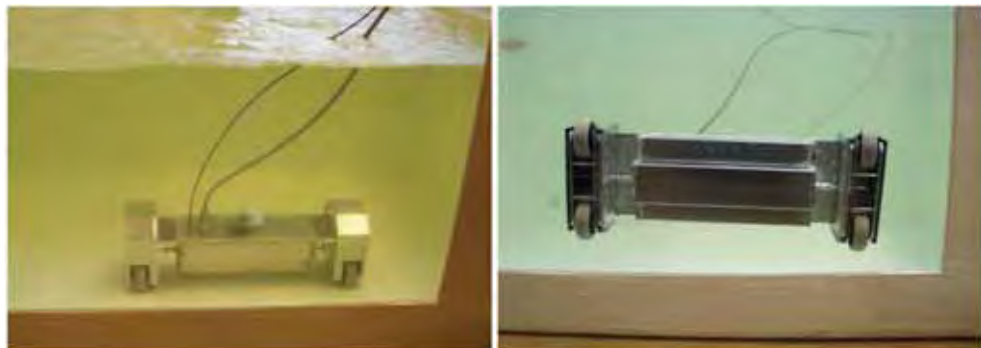


Fig. 1. Left: Robtank immersed in a water tank while inspecting the tank floor; Right: Robot climbing on a glass wall after transition from floor to wall



Fig. 2. Left: Solid drawing of RobTank; Right: Vehicle climbing on curved wall (3 metre diameter)

Test trials of the first vehicle and specifications of the NDT flaw detector, navigation and UT sensor circuits, motors to rotate bulk wave probes, and an infra red vision system indicated

that it would be necessary to redesign the first prototype so that these components could fit inside the sealed and purged enclosure on the vehicle.

Development of Vehicle Prototype 2

A second prototype vehicle has been developed (figures 3 - 6) that now has an additional mechanism. This comprises of an extendible arm and set of wheels to enable easier and more reliable surface changing capability. Two vehicle propellers provide sufficient thrust forces for adhesion to a wall with the shape of each propeller and associated flow duct engineered to increase the thrust.

An array of ultrasonic wheel probes and two bulk-wave ROBULK probes look for corrosion thinning on the floor and walls up to half a meter ahead and under inaccessible floor areas. Sensor probes (4 immersion probes, 4 wheel probes and two rotating probes) are mounted on the vehicle chassis (see figures 4-5). The signal cables from these probes enter a water tight and pressurized chamber on the vehicle. Routing of these cables in a densely packed chamber is a problem. The rotating probe position is measured and controlled with shaft encoder feedback. Encoder signals are brought into the central chamber servo drive signals taken out to the two ROBULK probe motors.

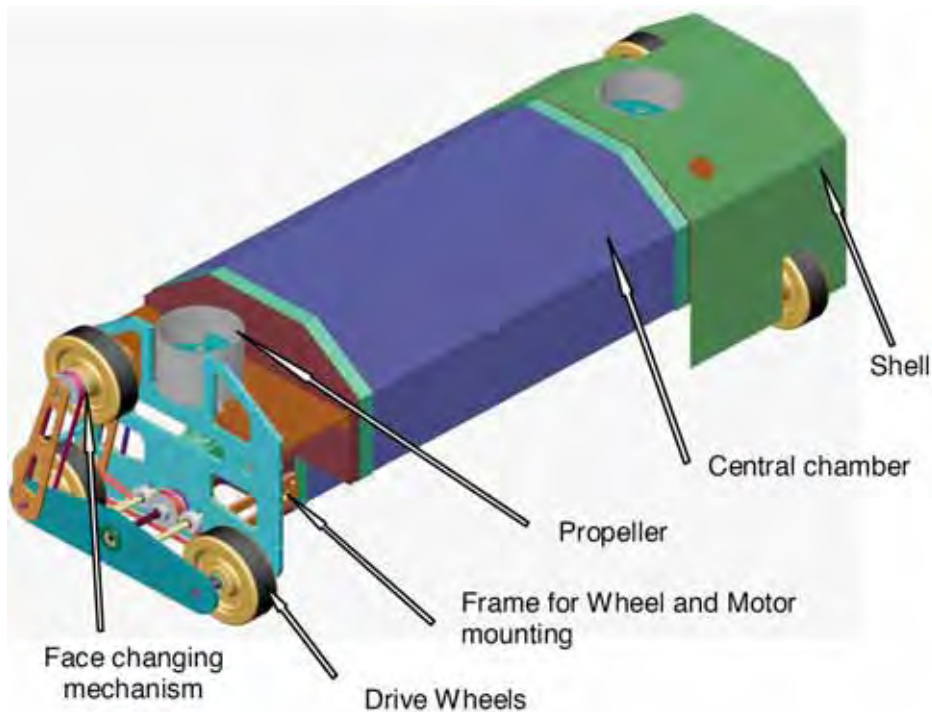


Fig. 3. RobTank: Prototype 2 vehicle with a surface changing mechanism and two thrusters. The Central chamber houses all motors, encoders, servo drives and NDT instrumentation

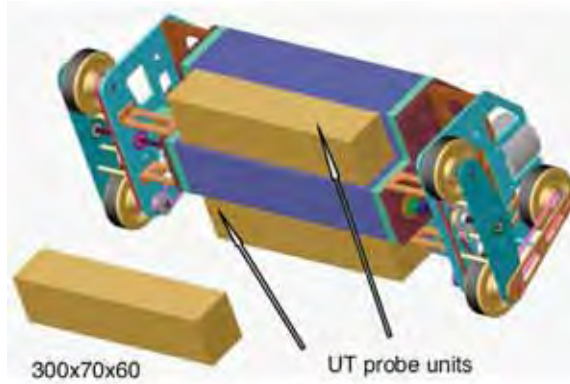


Fig. 4. Underside mounting position for the array of ultrasonic (UT) probes



Fig. 5. Left: RobTank with full payload of 4 ultrasonic wheel probes, 4 compression probes and 2 rotating probes; Right: RobTank on the floor of a water storage tank, Sines oil refinery



Fig. 6. Left: RobTank before entry through manhole in the roof of a ATG storage tank, Sines oil refinery, Portugal; Right: Ultrasonic NDT tests in oil sludge

2.4.2 Module 2: NDT Probes and Instrumentation

The NDT sensor payload suitable for measuring internal and external corrosion with a thickness resolution of 1mm comprises of two probe arrays, each 30cm long with 15 to 20mm pitch, mounted to the front and rear of the inspection robot.

The minimum detectable area is a 6mm diameter flat-bottomed hole at a range of 3 mm. A surface coverage of 3m² per minute and surface speed of 10 m per minute is realizable with this arrangement. The inspection system is able to measure plate thickness between 6-25mm with minimum thickness of 3mm.

One set of 0° (in the front of the vehicle, top of picture in figure 5) high efficiency twin wheel probes have been developed to cope with large crude oil tank inspection difficulties and environment conditions (penetration of debris and sludge on the tank floor).

They are designed to European Standard EN10160 (July 1999) for the UT examination of steel planar plates. Tests on single and twin crystal probes scanning the surfaces of crude oil tank environments simulated in a laboratory showed a good ability to cope with a range of conditions. This resulted in the development of a wheel probe system consisting of a high efficiency ultrasonic inspection twin wheel probe that obtains good data with a fluid gap or direct contact, ability to monitor wall thickness despite changes in probe orientation, size of probe, frequency of element and coverage, and the influence of sludge, sand and other tank constituents.

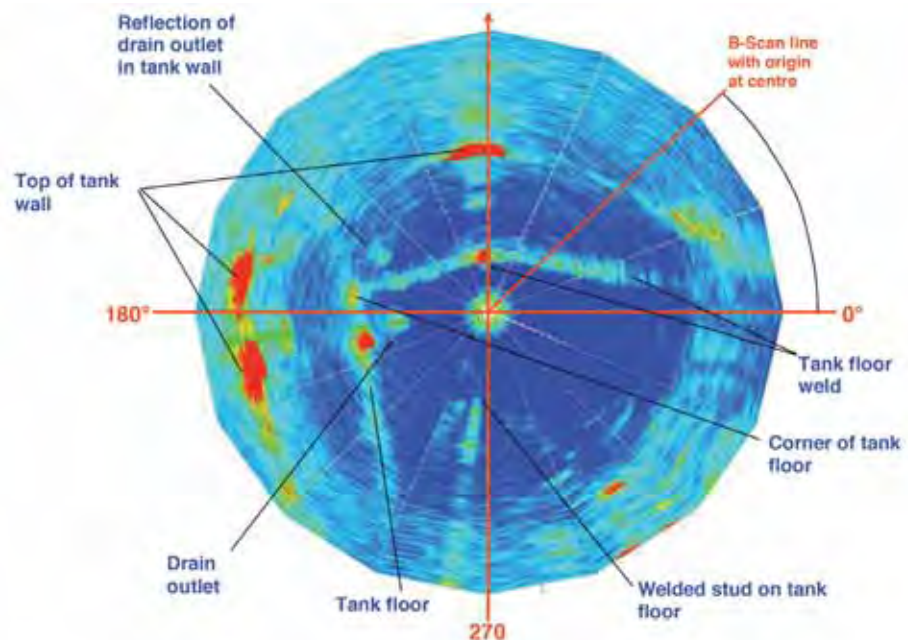


Fig. 7. Linear B Scan transformed to a Rotary B Scan to clarify tank features

Two long range ultrasonic probes that can look ahead through the floor are mounted on the sides of the inspection robot to detect hidden corrosion in areas that can only be reached with angled probes and not with 0° probes. These probes were developed after research

established that they will provide 100% coverage of large plate areas to give identification of potentially corroded areas in the plate with a look forward distance of 50 cm.

Tests show that the range of the ROBULK ultrasonic probe is approximately 1m in water, proper calibration is essential, the probe is tolerant of small coupling gaps and will work through thin sand layers albeit with reduced range. The probe can be motorized and encoded to produce a radar type B scan plot to detect the edges of tanks, welds, etc and can therefore be used for navigation. The sound wave dives under unattached obstacles and can therefore inspect under striker plates.

Figure 7 shows the wealth of information that can be obtained with a rotating bulk wave probe operated in a small water tank fitted with a drain outlet, welded stud and a weld in the floor. All these features are visible in figure 7 as is the weld between the tank floor and two walls with the corner visible. The waves travel up the walls of the tank and the top of the walls is also visible in the figure.

A commercially available TD-Scan 24 channel flaw detector with dimensions of 170x60x104 mm is contained in the purged box on-board the robot. The TD-Scan instrument integrates a pulser/receiver, A/D converter, encoder inputs (the requirement is for one bi-directional input to describe forward/backward travel), and 2 unidirectional encoders to control the ROBULK probes). Software for data acquisition, display and analysis in all standard NDT formats is provided. The TD Pocket uses TTL signals from one of the robots incremental encoders to position stamp the NDT data.

2.4.3 Module 3: Navigation Sensors and Electronic Circuits

An Ultrasonic emitter Tower was mounted on top of the vehicle to simultaneously emit four ultra-sound signals to receivers mounted on the external wall of a tank. Each emitter is the hexamite "HE123 Underwater Ultrasonic Sensor". A stack of three small electronics cards (overall dimensions of 100x100x60 mm) fire the ultrasonic emitters and process signals from the receivers. Four receivers on each face of the robot look out for reflections from obstacles in the tank. The system was unable to locate the robot in a large tank due to signals from reverberations of the walls caused by winds swamping the reflected ultrasonic signals and was eventually abandoned.

An on-board Infrared camera and associated electronics is fixed to the front of the vehicle (overall size is 70x70x185 mm) with a coaxial cable relaying images to an external monitor. The final product will aim to meet all safety regulations for working in explosive atmospheres specified in API 653, API 575, Directive 94/9/EC (regulations CEN EN 1127-1:1997, CEN EN 50014:1997 and CENELEC EN 50284:1999) and Directive 1999/92/EC.

2.4.4 Laboratory and Field Trials

The fully assembled RobTank system was tested initially in laboratory water tanks and in two firefighting water tanks in a Petrogal refinery in Portugal. The fire fighting training tanks were used to assess the ability of the robot system to work on aged tank surfaces quite similar to the oil storage tanks in the refinery. The tanks were emptied, cleaned and a complete assessment and comparison of different inspection techniques carried out. The performance of the Rob Tank robot was compared with these results.

Two major difficulties occurred at the laboratory trials stage, the solution of which resulted in significant delays to execution of the project plan. One difficulty related to the surface

changing ability of the vehicle. The addition of the NDT sensor payload changed the balance of the vehicle in addition to increasing its mass. The transition of the vehicle from the floor to a wall became erratic. As a result, a new mechanism was added to the front of the vehicle that comprised of a controlled buoyancy module (shown in figure 5 on top of the vehicle). This is activated before climbing a wall, thereby reducing the turning torques required to change surfaces. The second, more serious, difficulty was due to EMC problems caused by the PWM servo amplifiers used to control the propellers and wheel drive motors. The close proximity of parallel runs of NDT signal cables, PWM amplifiers and shaft encoder signals resulted in the swamping of low amplitude signals from the NDT sensors. A great deal of time was spent isolating the problems with redesign of probe cables, probe holders, screening, separation of flaw detector and amplifier grounds, and return of ground paths back from the vehicle through its umbilical to a ground on the operators end of things.

Finally, RobTank was field tested in the Sines Oil refinery in Portugal. The vehicle performed as required in a badly corroded and buckled storage tank used for training in fire fighting. It was able to move reliably on the floor of the tank with a "light touch" with the two propellers turned off, and with more traction with the propellers rotating at full speed. Transfer from the floor onto very distorted tank walls was accomplished every time and the vehicle could easily climb to the level of liquid in the tank.

Entry through a manhole on the roof of an AGT tank was easily performed by one operator without using any lifting equipment. The vehicle inspected the floor and walls of this tank without any major problems.

The robot, at this stage in its development, has not sought certification for operation in explosive environments. Therefore it has not been tested in oil. However, the vehicle has been operated in a shallow bath filled with oil to test the NDT probes. These have given data comparable to the laboratory tests.

3. Design of Amphibious Swimming and Floor Moving Robot to Inspect Welds and Corrosion in FPSO Tanks

The RobTank design objectives have been extended further by developing an amphibious and mobile robotic inspection system to test welds located inside a floating production storage offloading tank (FPSO tank). FPSO tanks [Shimamura 2002] are storage tanks on ships that store oil off-loaded from off-shore platforms.

Currently these welds are inspected manually by first emptying and cleaning the tank. This is a time consuming and expensive operation that requires operators to enter a hazardous environment.

Significant cost reductions can be made if the inspection is performed with a robot that enters the tank when it is either nearly empty with two or three centimetres of oil remaining on the tank floor or preferably when it is of full of oil. In the first case the robot would operate in air and an explosive environment but would eliminate the need to swim the robot through a very complicated maze of partitioning walls and rows of strengthening plates that occur every 700-900 mm. In the second case the robot would swim to a strengthening plate and operate under oil thereby eliminating the need to empty the tank.

The FPSO inspection task and suitable Non-destructive Testing methods are reported in (Sattar et al 2005; Sattar et al 2002). Figure 8 shows two FPSO tanks (lighter or yellow area)

in the cross-section of a ship hull. The strengthening plates are visible on the floor of each tank.

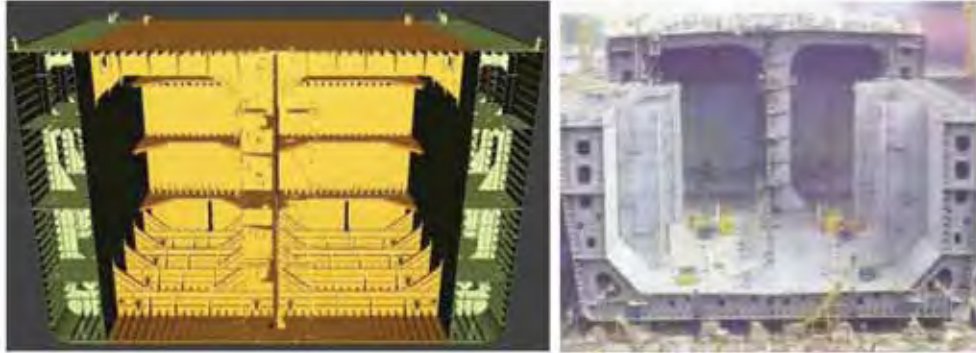


Fig. 8. Cross-section of the hull of a ship with two FPSO tanks, showing rows of strengthening plates welded between the floor and side walls

For structural safety the welds are tested regularly. The main inspection task is to test the welds on plates used to strengthen the walls and floor of the tank. Currently the welds are inspected manually after emptying the tank of product and thoroughly cleaning it. There is a large cost associated with the cleaning and inspection tasks. A pair of tanks are emptied, cleaned and inspected in 3-4 weeks with costs between £25-30K. A pair of FPSO tanks and ballast tanks inspected in the first five years costs £60-70k. This cost rises to £150-200k to inspect 3 pairs of cargo tanks and 3-4 pairs of ballast tanks after ten years. These costs can be reduced substantially by sending a robot into the tank without first emptying it thereby saving the cost of cleaning and emptying.

Weld cracks are caused by fatigue and are of two types. Low-Cycle fatigue is driven by panel deflection when filling and emptying tanks causes cracks at the toe of a bracket, generally in the secondary material. High-Cycle fatigue is driven by wave pressure on the side and bottom shell of the tanks. It causes cracks at cut-outs where shell longitudinal strengthening plates connect to cut outs in the frames.

The floor plate of the tank, usually 18-25mm thick, is tested for corrosion caused by coating breakdown. Pits can develop at the rate of 2-3 mm/year and even faster at the rate of 5mm/year if more corrosive crude is present.

3.1. The Inspection Environment

Obtaining access to welds on strengthening plates on the walls and the floors of the tank is not easy. The environment is cluttered with rows of strengthening plates that are 600-900 mm apart. The robot has to operate between two adjacent longitudinal strengthening plates separated by a distance of 600-900 mm with the transverse frames separated by a distance of 4.5m. The robot therefore has to be quite small, mass approximately 20kg, so that it can be inserted easily by one or at most two operators through a manhole of minimum diameter 600mm.

Access to welds can be obtained by swimming over the plates from one section of the tank to another and then landing on a wall or floor between the plates.

3.2 Access to Floor Welds with a Swimming and Floor Moving Robot

FPSO Tanks in the North Sea are cleaned first with pressurized crude oil to agitate wax and sludge, and then cleaned with hot sea water. The water is removed prior to inspection by human operators, normally only a few centimeters are left on the bottom. The water in the tank tends to be fairly clean, though when disturbed can mix with the oil residues. Therefore, the inspection could be done by leaving the tank full of water and then gaining access to welds by swimming to a test site.

Brazilian off-shore FPSO's are not cleaned with hot water because they are operated in higher temperatures. Therefore, they are cleaned with pressurized oil only thus eliminating the cost of establishing a process that cleans the water before returning it to the sea. Here, a swimming robot would have to operate in crude oil and would therefore have to meet intrinsic safety requirements for operation in explosive environments. With zero visibility in crude oil, the problems of getting around the tank by swimming are considered to be insurmountable. However, emptying and cleaning the tank to the last few inches of oil on the floor and inspecting the welds with a robot still gives savings in costs and prevents human operators having to perform the NDT manually. Provided the cleaning systems are working, there is very little residue on the floor, though there is always a waxy film. In places there will be a 2-3mm of wax, like shoe polish on the bottom of the tank but not on the side walls.

3.3 NDT Techniques for FPSO Inspection

Work in tanks is always potentially hazardous and thus a system which can minimize the need for personnel entry is obviously beneficial. The development of a remote tool will only improve structural integrity, and thus potentially reduce leakage, if it can deliver a higher level of inspection than is currently achieved.

The deck and bottom plating is normally 20-25mm thick. Bottom stiffeners are typically T-shaped with the web 650 x15mm, and the flange 250x25mm. Side shell stiffeners are generally bulb bars, 200-400wide and 12-15mm thick. Apart from butt joints joining plates together, all connections are fillet weld 6-10mm throat thickness depending on the section. Welding size is variable and depends on the design. Coating is provided by a paint layer 300-500 microns thick. The NDT is required to identify through thickness cracks that are 5-10mm long (these are currently generally found by visual inspection). If smaller cracks can be detected that would be bonus. It is also important to identify coating defects or pitting on the bottom plates.

The project has developed an NDT Sensor Payload that is suitable for robotic deployment and that obtains better NDT data in a hazardous environment than possible with manual inspection. Towards this end, array probes have been developed to use the following NDT techniques: Eddy current technique, ultrasonic creep waves, and the ACFM (Alternating Current Field Measurement) technique.

The Eddy Current Array technique is used to inspect the tank floor for corrosion pitting in the presence of sludge and wax. The robot carries a set of array probes and its motion results in a surface scan. A feasibility study with a conventional eddy current system shows that the conventional eddy current may work to pick up corrosion type of defect, if all the parameters are optimized. Therefore a system has been developed that consists of a conventional eddy current probe array.

ACFM (Alternating Current Field Measurement) techniques: ACFM is an electromagnetic inspection technique that provides one pass inspection. It has a high tolerance to lift off and requires no electrical contact so that it can be used to detect through coatings. It provides crack detection and sizing and is suitable for weld inspection. To cover the weld cap, toes and HAZ of a welded joint, it is necessary to either use a simple single sensor probe and scan several times or use a multisensor array probe and cover the required area in a single pass. An underwater ACFM array probe has been developed that can be deployed on the robotic vehicle. The probe detects and sizes surface breaking cracks at or in close proximity to the welds to be inspected. The probe design weighs approximately 1.2kg in air. The maximum dimensions are 87mm wide x 117mm long x 117mm high. The materials have been chosen to be mainly stainless steel for structural parts and PEEK for parts that will not be subject to great loads.

Modifications still need to be made to make existing instrumentation intrinsically safe.

3.4 Design of Amphibious Mobile Robot

The design of the robot is shown in figures 9 and 10. This design is a further development of RobTank that has been developed for in-service inspection of oil and chemical storage tanks. Further development of this design has added a variable buoyancy tank that can quickly and accurately control buoyancy around the neutral buoyancy of the robot.

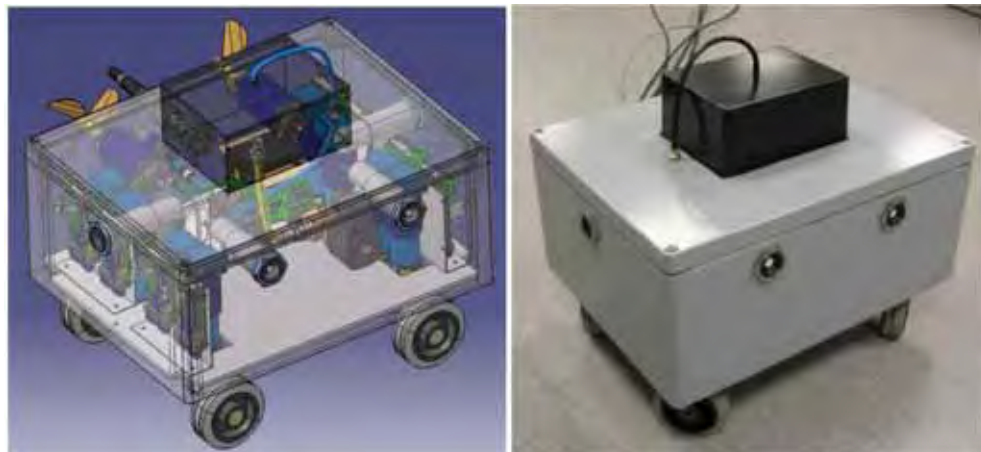


Fig. 9. Amphibious mobile robot showing the variable buoyancy tank on top of the sealed chamber housing the servo drive systems

The robot is designed to operate in air as well as submerged in water (at this stage) though eventually it will be made intrinsically safe to operate in crude oil (API 20 to 40). It consists of a buoyancy tank on top that adjusts its buoyancy around neutral by controlling its mass. A depth sensor provides the feedback to regulate the depth at which the robot is required to maintain its position (Shang et al 2006).

All control systems are embedded on-board the robot in a gas pressurized central chamber sealed to prevent the ingress of water through any leaks at the rotating shafts emerging from the central chamber and through NDT sensor probe cables. The reason for placing most

hardware systems onboard the robot is to reduce the size of the umbilical cord so that cable management becomes easier.

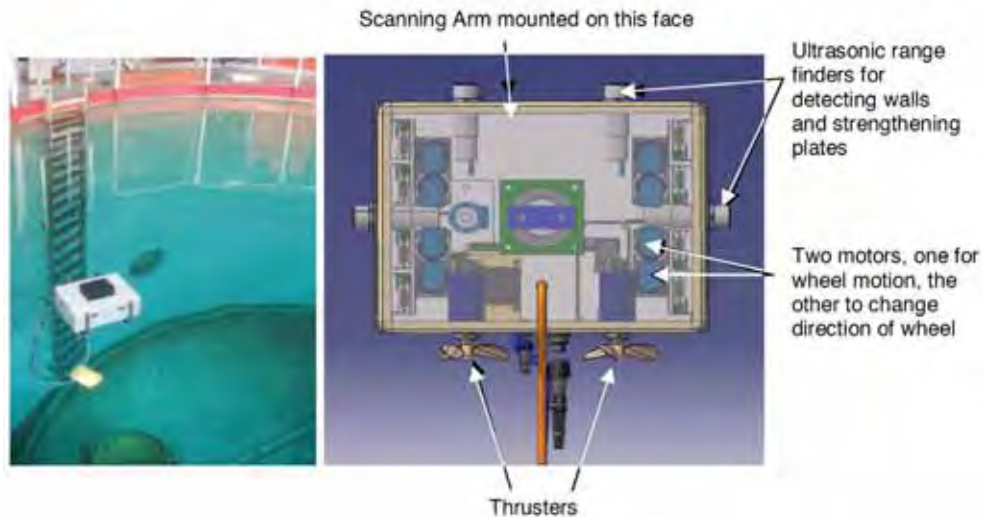


Fig.10. Left: Swimming trials in 7meter deep tank; Right: Plan view of the robot showing location of ultrasonic range sensors and the six drive motors and two thruster motors

The outer dimensions of the robot are (mm): 410L x 300W x 300H. Its mass in air is 12 kg and it can carry a payload of 8kg.

On-board embedded servo controllers with encoder feedback control the speed and position of the robot. High level control is from an operators console via RS 485 twin pair communications with on-board controllers.

Both depth and horizontal motion is controlled simultaneously to swim the robot to a test site on a wall or above a floor area that is to be tested.

After insertion of the robot through a manhole in the top deck, positive or negative buoyancy control is used to swim the robot vertically to a specified depth and to maintain that depth with neutral buoyancy. Two independent, speed controlled thrusters move the robot in a horizontal plane in the forward and reverse direction or rotate it to face in any direction.

A system of four ultrasonic sensors operating at 10 KHz and a rotating ultrasonic sensor at 5 MHz profile the surrounding strengthening plates and tank walls. These sensors are used to align the robot and to guide it autonomously along welds between the floor and strengthening plates and the toe ends of the plates. The Cartesian scanner shown in figure 11 carrying an ACFM probe scans the welds after the robot has been positioned correctly.

Robot trajectory in a constrained space for precise weld following around plates and side walls requires motion that is straight-line along welds, 90° rotation to present the scanner arm correctly when going from a plate to a side-wall and back onto the next plate. Special mechanisms have been designed to rotate all four wheels through turning angles between $\pm 180^\circ$ and to independently control the speeds of all four wheels.

3.5 Scanning Arm

The robot is required to follow weld lines, stopping to deploy NDT probes with a scanning arm.

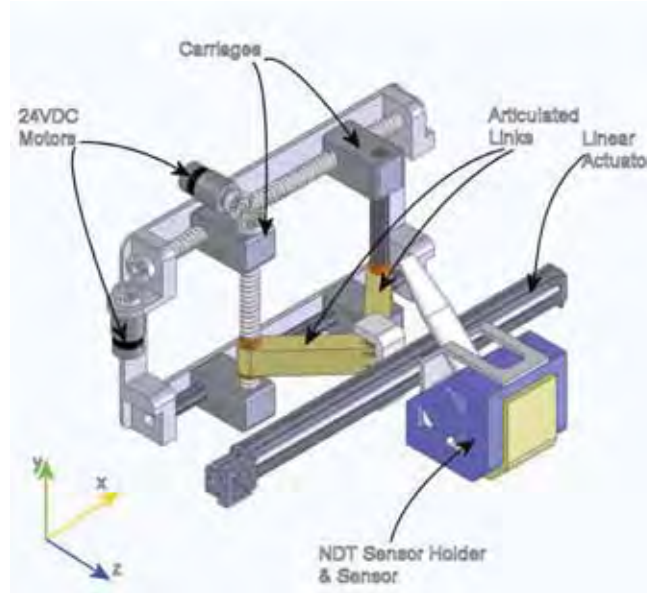


Fig. 11. Mechanical Scanner Design

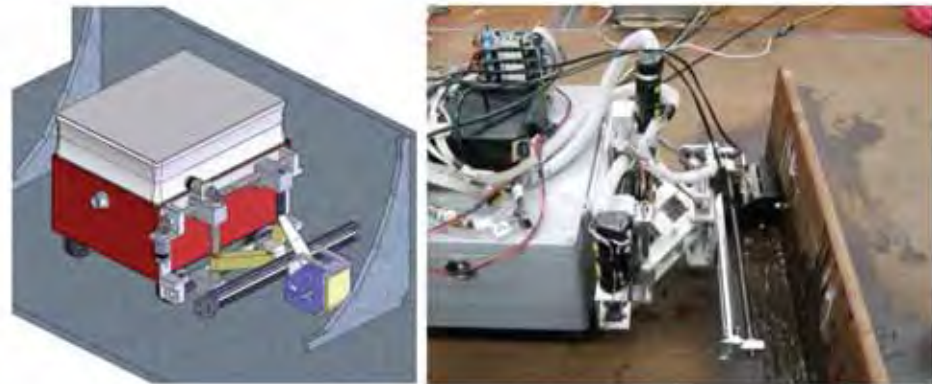


Fig. 12. Scanner mounted on front face of robot, shown deploying an ACFM NDT probe while located between two stiffener plates in a FPSO tank

Figure 12 shows the robot with a scanning arm fitted to one of the faces. The robot is shown between two strengthening plates (stiffeners) and the side wall of a tank. The NDT sensor shown is an ACFM probe.

The arm consists of two sets of 12mm diameter threaded shaft mechanisms, paired with guide shafts and their respective motor modules.

A horizontal threaded shaft and its dedicated motor module are mounted onto a back plate, which connects the scanner to the robotic platform. By setting the motor accordingly, the threaded shaft mechanism is able to provide the carriages with linear actuation along the X axis.

The mechanical scanning arm designed to be used for carrying and deploying each NDT sensor at the desired location, is depicted in figure 11.

The carriage itself comprises of a vertical shaft and a linear guide shaft jointed with articulated links to a linear guide actuator, which in turn is connected to the sensor holder that carries the sensor of each respective NDT method. The actuation provided by the motor module which is mounted onto the back plate, allows the carriage to move the threaded shaft and the guide shaft mechanism in opposite directions, thus moving inwards or outwards allowing actuation for the NDT sensor holder along the Z axis.

Motion along the Y Axis is achieved by the actuation of the vertical threaded shaft.

Finally, the linear actuator which is placed between the articulated links and the sensor holder drives the sensors along the X axis.

The scanning arm's modular configuration allows the sensor holder and thus the sensors to move along three degrees of freedom, so they can be placed safely and accurately into position in order to carry out the inspection of the welding. The retractable feature of the scanner arm contributes to the compact build of the overall system so it can be inserted easily into the inspection area and maintains its manoeuvrability by keeping the centre of mass close to the robot. When expanded, the sensor's tip can reach up to 350mm in front of the robotic platform and with a linear guide actuator of 400mm in operational length, the sensor can inspect hardly accessible corners of the tank's structure. The bearing load that the arm can hold may reach up to 4Kg , depending on the NDT method used at that time, which at this expanded position, will result to a required torque of 8Nm that the 24VDC motors are able to safely sustain.

The linear displacement of each module is measured by the encoders which are embedded into the 24V DC motor arrangements. Due to the harsh environment under which the system is subjected to operate, delicate in construction components like the motor controller, motor drives and various custom electronics are shielded in to an IP69 enclosure inside the robotic platform's casing. The linear guide actuator is composed of a one-piece outer rail surrounding an inner block, a ball screw drive through the block's centre, and two linear motion guide raceways per each side of the block, that overall provide for a rigid actuator function and positional accuracy in the order of tenths of a millimetre.

In order to avoid potential undesired contact with an object, the robot's scanner must be able to map the space axially in front and on the side of the scanner. For the completion of this objective, 4 distance-measuring sensors are to be integrated on the sensor holder. The readings from these sensors as the scanner holder extends and retracts, will assist the robot's overall behaviour while inspecting.

3.6 Following Motion Trajectories

The robot is required to follow strengthening plate welds by keeping the scanning arm parallel to a plate and rotating itself through ninety degrees after it has reached the tank wall. The space between two strengthening plate is very constrained so that large turning circles are not possible. The required trajectory is shown in figure 13.

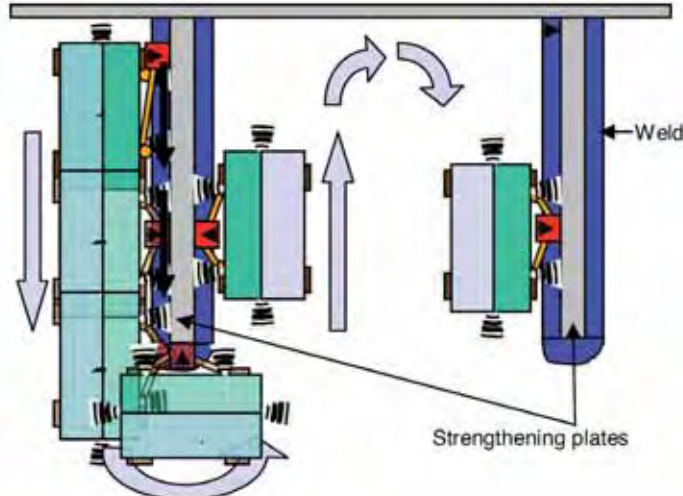


Fig. 13. Robot trajectory between two adjacent strengthening plates

This trajectory is possible provided the four wheels can be turned through any angle between zero and ninety. A special mechanism actuated by two motors has been developed to permit this turning. Four mechanisms are required, one for each wheel.

Two ultrasonic range finders are mounted on the front face of the robot. The scanning arm is mounted on this face.

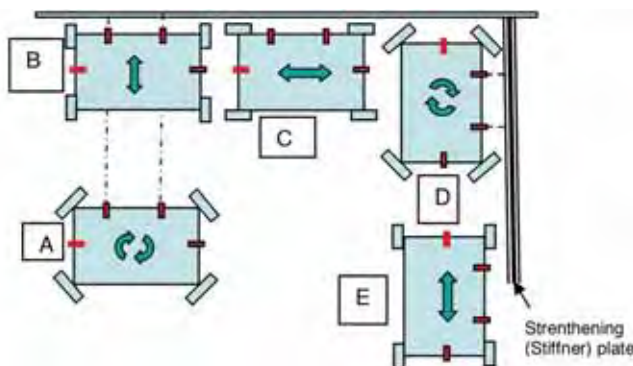


Fig. 14. Sensor guided straight-line and rotational motion of robot to follow back-wall and plate welds

The trajectory that shows the principle of operation in figure 14 starts in position A. The robot can be rotated at the same position coordinates by turning all wheels to be at a pre-computed angle. The distance measured by each sensor is equalized by rotating anti-clockwise. The wheels are turned to face the wall as in position B and the robot moved towards the tank wall till it is at a required distance. The robot then moves along the wall towards the strengthening (stiffener) plate, maintaining the required distance, position C.

When the side range sensor detects the strengthening plate, the robot is rotated to face the plate, as shown in position D. The robot then aligns itself to be parallel and at a desired distance from the plate. The wheels are turned as in position E and the robot moves along the plate, inspecting the weld with the scanning arm.

3.7 Tests of Robot Motion when Operating in Air

The vehicle platform shown in figure 15 has been developed to test the motion of the robot when following a trajectory along stiffener welds.



Fig. 15. Left: Platform to test robot motion and trajectory following capability. Right: Fully assembled robot performing NDT on a mock-up with Creep waves

The mechanisms to rotate the robot at the same spot to find a stiffener or wall and then adjust the robot position to be normal to the wall have worked as expected.

A limitation is the range of the ultrasonic sensors which work reliably up to 1.5 metres when the orientation angle of the robot is less than fifteen degrees.

The robot is able to autonomously follow the weld along the stiffener plates and the side walls of the FPSO tank while maintaining the correct distance from the wall and stiffener plates.

3.8 Profiling Surrounding Plates with a Ultrasonic Radar

Experiments have been conducted to develop ultrasonic pulse echo radar that will enable the robot to detect the presence and distance of stiffener plates in a dark medium such as crude oil. This radar will be in addition to the four ultrasonic range finders mounted on the front and sides of the robot. The ultrasonic probe/mirror arrangement shown in figure 16 was rotated by $\pm 60^\circ$ starting from the corner of two plates at right angles to each other. A C-scan image displays the detected plates and the corner where the two plates join. A grid of points was created where the probe was positioned.

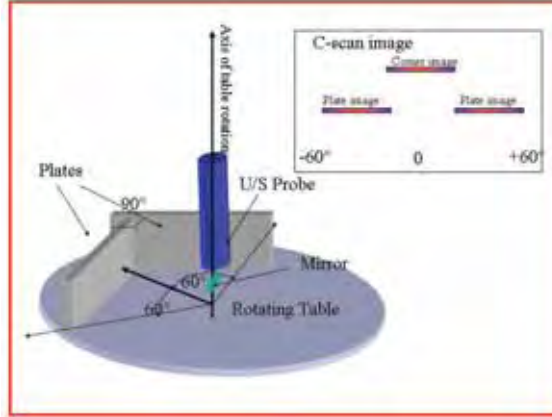


Fig. 16. Ultrasonic radar probe setup to detect plates

An algorithm has been developed to compute plate distances from c-scan data. The distance of each plate from the 0,0 co-ordinate was $x = 127.28$ mm and $y = 127.28$ mm.

Measurements were made by first looking at the corner and then rotating the table by $\pm 60^\circ$ to measure the wall distances.

The measured values for co-ordinate position 0,0 were $x = 126.25$ and $y = 130.46$, giving measurement errors of 1.03 and -2.18 mm respectively. Measurements were repeated with the probe at other grid points. The measurement errors were within ± 4 mm, giving sufficient resolution to enable accurate profiling of the surrounding plates and other objects.

Further work is being done to select a suitable probe frequency to give optimum results in oil and to develop the real-time computational algorithm to profile the objects and plates surrounding the robot

3.9 Results and Discussion

Figure 17 shows the A-scan results from the ultrasonic creep probe measurements with the defects at the beginning and end of the weld. In this experiment, an ultrasonic creep wave probe has been used to measure weld on a stiffener plate.

The experimental setup is shown in figure 18. The creep wave probe consisting of dual crystal with an angle 24° at 4MHz was used. The choice of the frequency is related to the range of the inspection.

Creep waves appear when the longitudinal wave is propagating at an angle greater than 75° but less than 90° . The optimum angle for a strong creep wave signal had to be determined within this range. In this application, the optimum value was found at a refracted angle of 80° . It has enough cover range to make it possible to inspect both fillet welds in the stiffener plate to the T-joint from the other side.

Figure 17 also shows that the background noise is relatively high compared to the received signal.



Fig. 17. A-scan results from ultrasonic creep. (Position 1) defect at the beginning of the weld and (Position 2) defect at the end of the weld

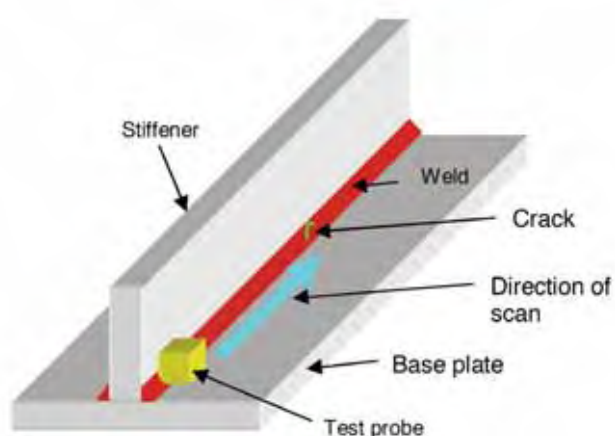


Fig. 18. Experimental setup for data collection using ACFM and ultrasonic creep wave probes

Due to this reason, determination of the defect size is difficult. The scan was then repeated using the ACFM probe.

In the case of the ACFM sensor, a 50 kHz corrosion probe was used. The coils used to generate Eddy-current field in the test surface are placed either side of the test area. Their position will determine the direction of current flow, which must be across the cracks if the perturbations in the field are to be at a maximum.

Sensor coils used in conventional eddy-current testing can be absolute (a simple single coil) or differential (a coil split into oppositely wound halves). In this experiment, the probe has a diameter of 50mm and provides B_x and B_z responses from defect depth. B_x and B_z corresponds to the field in the horizontal and vertical directions (Note: B_x is perpendicular to the current and parallel to the surface of the test sample, and the B_z is perpendicular to the surface of the test sample. For deployment on fatigue cracked weld toes for example where a crack is parallel to the weld, the x -direction will be parallel to the crack edge)

Finally, since the sensitivity of the technique is also dependent on the area sensed by the coil, the smaller the area, the higher the sensitivity, the pairs of coils were arranged in arrays, that gave coverage of the whole weld surface.

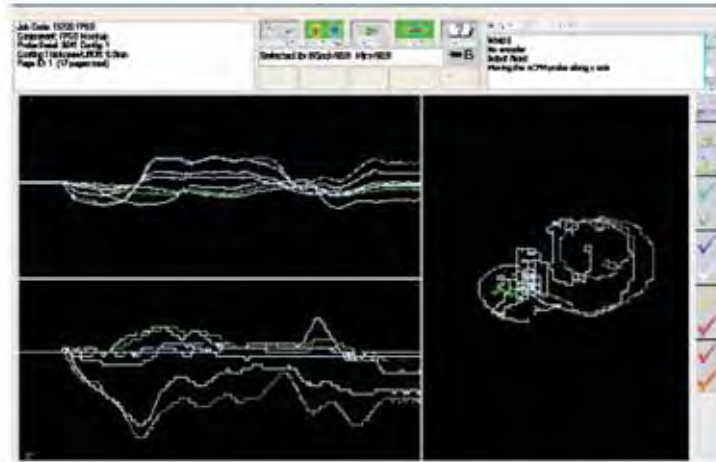


Fig. 19. ACFM results: Scanning arm moves the probe – robot is parked

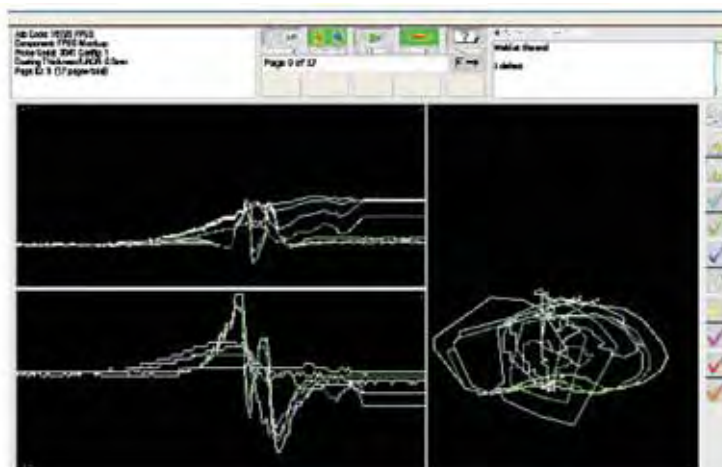


Fig. 20. ACFM results: Robot moves along the weld- arm is parked

Examples of the ACFM waveforms are shown in figures 19 and 20.

These figures illustrate the Bx and Bz data of defects at the beginning and end of weld. Both ACFM and ultrasonic data are well correlated, indicating the position of the defects.

Figure 19 shows results obtained by testing the weld with the robot parked and the scanning arm moving the ACFM probe along the weld.

Figure 20 shows the test performed by keeping the arm stationary while moving the robot along the weld.

Both methods were able to detect the defect indicating that provided the robot is able to keep a constant distance from the stiffener plates it may be enough to drag the probe over the weld.

4. Conclusion

Three prototype robots have been developed to gain entry into a large range of oil, petrochemical and process storage tanks. The robots are lightweight and compact so that they can be transported by one or two operators and easily inserted through the smallest manholes.

The robots are amphibious, being able to operate in air and while submerged in liquids. They have been tested in water but the design incorporates the features to enable rapid progression to operation in oil and other flammable and explosive liquids.

Between them, the robots can inspect:

- (a) The walls of storage tanks that may not be accessible from the outside due to rain plates and in partially or fully buried tanks. Wall inspection can be performed only when the tank is full of product.
- (b) The floors of storage tanks for corrosion and pitting by scanning the floor plates with ultrasonic compression probes, creep waves, and long range ultrasonic mapping of the floor area. This inspection can be performed in air or while submerged in liquids.
- (c) Welds by automatically following the weld seams along stiffener plates and wall plates while testing the weld using ACFM techniques with a scanning motion being performed by an arm. Raster motion trajectories can be easily achieved. This inspection can be performed in air or in liquids.
- (d) Tanks with constrained spaces and cluttered environments by swimming over obstacles to reach inspection target areas.

The robots are prototypes that have demonstrated the feasibility of climbing, swimming and working on the floors of storage tanks in air and in water while performing NDT with a number of techniques. The designs have addressed the requirements for performing NDT in explosive environments but still have some way to go before they can be certified for operation in these tanks. Future work will aim to develop fully integrated systems that include the drive systems for the scanning arm in the sealed central chamber of the FPSO robot so that the intrinsic safety requirement of a single purged enclosure is achieved. The problem of a navigation system able to give sufficient information about the whereabouts of the robot in an opaque medium and closed steel tank is still not fully solved though local detection of the immediate surroundings and odometers give some knowledge. Nevertheless the robots can be operated in clean liquids where vision systems and operator line of sight is sufficient for teleoperation of the robots to a target area where the on-board sensors can take over and guide the robot through a pre-planned trajectory and inspection sequence.

5. Acknowledgements

This work was funded by the European Community through the CRAFT project FPSO INSPECT (COOP-2004-508599) [1] with the following partnership: NDT Consultant (UK), TSC Inspection Systems (UK), Isotest Engineering (Italy), Tecnitest Ingenieros (Spain), Spree Engineering Ltd (UK), Miltech Hellas S.A. (Greece), ZENON (Greece), Kingston Computer Consultancy (UK), BP (UK), Petrobras (Brazil) and London South Bank University (UK).

The Project is coordinated and managed by TWI (UK). The Nueva Granada Military University of Colombia, sponsors the Ph.D studies of H.E. Leon Rodriguez.

The ACFM NDT results are the work of TWI Ltd, Cambridge (UK) and the results from experiments on ultrasonic radar are the work of Isotest Engineering, Italy.
The work on RobTank Inspec was funded by the European Community through the FP6 programme (Competitive and sustainable growth). Project coordinator was ISQ Ltd (Portugal). Partners: Tecnatom (Spain), Phoenix Inspection Systems (UK), OIS (UK), London South Bank University (UK), Petrogal (Portugal).

6. References

- Berger A., Knape B., Thompson B. (1990) Development of a Remote Tank Inspection (RTI) Robotic System, Proceedings of 1990 American Nuclear Society Winter Meeting, Washington D.C., November 1990
- European CRAFT project FPSO-INSPECT, Non-Intrusive In-Service Inspection Robot for Condition Monitoring of Welds Inside Floating Production Storage and Off-loading (FPSO) Vessels, EU 6th Framework Programme, Co-operative Research Project, COOP-CT-2004-508599, December 2004.
- King R.D., Raebiger, R.F., Friess R.A. (1992) Consolidated-Edison-Company-Of-New-York, Inc - Petroleum Fuel-Oil Tank Inspection Program, Proceedings of the American Power Conference, Chicago, Illinois, Vol 54, Pt 1 and 2 Moving Ahead While Protecting the Environment, pg. 983-988
- Raad J.A. (1994) Techniques for Storage Tank Inspection, Materials Evaluation, July 1994, pg 806-7
- Rusing, J.E. (1994) The NDT Perspective on Above Ground Storage Tanks, Materials Evaluation, July 1994, pg 801-804
- (a) Sattar T.P., Leon-Rodriguez H., Shang J., (2005) Automated NDT Of Floating Production Storage Oil Tanks With A Swimming And Climbing Robot, in Proceedings of the 8th International Conference on Climbing and Walking Robots and the Support Technologies for Mobile Machines (CLAWAR 2005), Editors Tokhi, Virk and Hossain, ISBN-10 3-540-26413-2, Springer, ISBN-13 978-3-540-26413-2, pp. 935-942
- (b) Sattar T.P., Zhao Z., Feng J., Bridge B., Mondal S., Chen S., (2002) Internal In-service Inspection of the floor and walls of Oil, Petroleum and Chemical Storage Tanks with a Mobile Robot, Proceedings Of 5th International Conference on Climbing and Walking Robots and the Support Technologies for Mobile Machines, Edited by Philipe Bidaud and Faiz Ben Amar, ISBN 1 86058 380 6, 2002, pp 947-954, Professional Engineering Publishing Ltd. UK
- Schempf H. (1994). Neptune-Above-Ground Storage Inspection Robot System, Proceeding of IEEE International Conference on Robotics and Automation, San Diego, Vols 1-4, Part 2, pg. 1403-1408
- Shang, J., Sattar, T.P., Leon Rodriguez , H.E, (2006) PDA Depth Control of a FPSO Swimming Robot, Proceedings of the 9th International Conference on Climbing and Walking Robots and the Support Technologies for Mobile Machines (CLAWAR 2006)
- Shimamura Y. (2002) FPSO/FSO: State of the art, J. Mat. Sci. Technol. 2002, pp 60-70.

Test Methods and Knowledge Representation for Urban Search and Rescue Robots

Craig Schlenoff, Elena Messina, Alan Lytle, Brian Weiss and Ann Virts

National Institute of Standards and Technology (NIST)

USA

1. Introduction

Urban Search and Rescue (USAR) is defined as “the strategy, tactics, and operations for locating, providing medical treatment, and extrication of entrapped victims.” (Federal Emergency Management Agency 2000) USAR teams exist at national, state, and local levels. At the national level, the Federal Emergency Management Agency (FEMA), which is part of the Department of Homeland Security, has Task Forces that respond to major disasters. There are many challenges in diverse disciplines entailed in applying robots for USAR. Examples include range and penetration limitations for wireless radio signals that send commands to the robots from the operator control station, the ability of the platforms to withstand moisture, dust, and other contaminants, and the resolution of onboard navigation cameras.

NIST is working with FEMA Task Force members to define performance requirements and standard test methods as well as to assess the deployment potential of robots applied to the USAR domain. The development process being employed during this effort is driven by user-defined requirements, which were initially articulated by FEMA responders during an initial set of workshops hosted by NIST. Responders also identified different deployment categories for robots within USAR missions. These deployment categories describe types of capabilities or features the robots should have, along with tradeoffs. Thirteen different categories were defined, which may not necessarily map to thirteen different robot types (i.e., a particular robot may serve within more than one category).

Supporting efforts are detailing robot capabilities and deployment environments in unambiguous computer-readable formats. An ontology is being used as the neutral representation format for the robot characteristics. A complementary effort is attempting to quantify and characterize the environment into which the robots will be deployed. Taxonomies of buildings (pre and post-collapse) are being developed, as well as methods of deriving mathematical representations of the surfaces which the robots must cross. This chapter discusses all of these efforts in depth, as they are key enablers in the quest to match robot capabilities to the deployment environments.

Source: Climbing & Walking Robots, Towards New Applications, Book edited by Houxiang Zhang,
ISBN 978-3-902613-16-5, pp.546, October 2007, Itech Education and Publishing, Vienna, Austria

Several requirements for robots applied to USAR involve mobility capabilities. Aerial, ground, and aquatic robots can all play a part in USAR operations and have unique mobility challenges and requirements. It is clear, however, that the usefulness of robots in USAR is highly dependent on their mobility capabilities as they must be able to negotiate highly unstructured environments. This chapter will highlight aspects of mobility that are relevant to robots that can walk or climb. The chapter is structured as follows. Section 2 describes the initial requirements-gathering phase for this project and details the requirements that were produced. This is followed by a discussion in Section 3 of the test method development and standardization approach, including descriptions of some of the more fully-developed test methods. Section 4 discusses the tools and techniques that have been created to capture performance data as robots are tested. Response robot exercises are described in Section 5. Section 6 covers the knowledge representation efforts, including the robot specifications and ontology and the structural collapse taxonomy. Conclusions are presented in Section 7.

2. Defining the Performance Requirements for USAR Robots

Although the potential for utilizing robots to assist rescuers in USAR operations was recognized prior to this project's inception, a methodical capture of responders' views of how they would use robots and what the detailed performance requirements were for robots had not occurred previously. Beginning in Fall 2004, NIST worked closely with DHS Science and Technology and FEMA to initiate a series of workshops that defined the initial set of performance requirements for robots applied to USAR. The first three workshops deliberately did not include robot technologists and vendors, so as to not initially bias the input from the end users with knowledge of existing technologies or approaches. Once a substantial body of requirements was gathered from responders, in subsequent workshops, robot technology providers (researchers, vendors, other government programs) were encouraged to participate.

The requirements definition process during the initial set of workshops was comprised of identifying and describing individual requirements, defining how a robot's performance with respect to a given requirement is to be measured, and, where possible, specifying the objective (desired) and threshold (minimum or maximum) performance values. The resulting list of requirements totaled over 100. These were grouped into several broad major categories. One major category, 'System', was further decomposed into sub-categories. These categories as well as the other major categories are shown in Table 1. A draft report detailing the process, the initial set of requirements, and the robot deployment categories is found at the NIST web site (Messina et.al. 2005).

Human-System Interaction	Pertaining to the human interaction and operator(s) control of the robot
Logistics	Related to the overall deployment procedures and constraints in place for disaster response
Operating Environment	Surroundings and conditions in which the operator and robot will have to operate
Safety	Pertaining to the safety of humans and potentially property in the vicinity of the robots
System:	Overall physical unit comprising the robot. This consists of the sub-components below:
- Chassis	The main body of the robot, upon which additional components and capabilities may be added. This is the minimum set of capabilities (base platform).
- Communications	Pertaining to the support for transmission of information to and from the robot, including commands for motion or control of payload, sensors, or other components, as well as underlying support for transmission of sensor and other data streams back to operator
- Mobility	The ability of the robot to negotiate and move around the environment
- Payload	Any additional hardware that the robot carries and may either deploy or utilize in the course of the mission
- Power	Energy source(s) for the chassis and all other components on board the robot
- Sensing	Hardware and supporting software which sense the environment

Table 1. Major requirements categories

Responders defined the requirements, the metrics for each, and for most of them provided objective and threshold values. The performance objectives and thresholds are dependent on the specific mission in some cases. For instance, the resolution of the onboard cameras depends on the range at which objects must be observed and on the types of objects. An aerial robot may need to provide responders information about whether a roadway ahead is blocked or clear. Another robot, aerial or ground-based, may be required to help the structural specialist assess the size of cracks in the structure.

As noted, there is no typical USAR scenario. FEMA teams (and other organizations) may respond to hurricanes, explosions, or earthquakes. The buildings may be wood frame, concrete, brick, or other construction. They may have to search subterranean, wet, confined spaces and tunnels or they may have to climb up the sides of buildings whose facades have

fallen away. During the initial three requirements definition workshops, potential robot deployment categories (which could correspond to different disaster types or aspects of a response) were enumerated. Twelve categories were defined, which detailed the capabilities that the robot should have, along with the deployment method, and tradeoffs. Ground, aerial, and aquatic robot deployments are represented. The deployment categories are listed in Table 2. In some cases, the requirements therefore need to be defined according to mission or deployment type.

Robot Category	Employment Role(s)
Ground: Peek Robots	Provide rapid audio-visual situational awareness; provide rapid HAZMAT detection; data logging for subsequent team work
Ground: Collapsed Structure–Stair/Floor climbing, map, spray, breach Robots	Stairway & upper floor situational awareness; mitigation activities; stay behind monitoring
Ground: Non-collapsed Structure--Wide area Survey Robot	Long range, human access stairway & upper floor situational awareness; contaminated area survey; site assessment; victim identification; mitigation activities; stay behind monitoring
Ground: Wall Climbing Deliver Robots	Deliver Payloads to upper floors; provide expanded situational awareness when aerial platforms are unavailable or untenable
Ground: Confined Space, Temporary Shore Robots	Adaptive, temporary shoring; provide stay behind monitoring; victim triage & support
Ground: Confined Space Shape Shifters	Search; provide stay behind monitoring
Ground: Confined Space Retrieval Robots	Retrieve objects from confined spaces; provide stay behind monitoring
Aerial: Survey/Loiter Robots	Provide overhead perspective & sit. awareness; provide HAZMAT plume detection; provide communications repeater coverage
Aerial: Rooftop Payload Drop Robots	Payload delivery to rooftops; provide overhead perspective; provide communications repeater coverage
Aerial: Ledge Access Robot	Object retrieval from upper floors; crowd control with a loudspeaker object attached, provide situational awareness
Aquatic: Variable Depth Sub Robot	Structural inspection; leak localization/mitigation; object (body) recovery
Aquatic: Bottom Crawler Robot	Water traverse; rapid current station keeping; object recovery

Table 2. Robot Deployment Categories

Correlations were performed of the first set of requirements versus the deployment types. Responders were asked to note which requirements applied to which deployments. The data were analyzed to uncover which requirements affected the greatest number of missions, hence would be the most commonly-needed. An initial set of requirements was thus selected for conversion to test methods. After responders had opportunities to experiment with a wide variety of different robot platforms within various scenarios and deployments, they selected three of the twelve deployment categories as being highest priority. This selection reflected both their opinion that these were missions in which robots could provide the best utility and for which the robots seemed most technologically mature:

- Ground: Peek robots. Small, throwable robots that are able to be deployed into very confined spaces and send video or potentially sensor data back to the operators.
- Aerial, Survey/Loiter Robots. These robots could “look over the hill” to assess the situation and determine at least which roads are passable. USAR Teams don’t necessarily expect aerial robots to assess structural integrity or even detect victims. They would like to be able to monitor atmospheric conditions from these platforms as well.
- Ground: Non-collapsed Structure--Wide area Survey Robots. These robots could support a downrange reconnaissance mission. They don’t necessarily have to enter confined spaces or traverse rubble piles, but they do need to be able to climb stairs or at least curbs and modest irregular terrain. They would typically move quickly down range (at least 1 km) to assess the situation and deploy multiple sensors (chemical, biological, radiological, nuclear, and explosive) with telemetry.

3. Measuring Robots Performance Against the Requirements

Among the key products of this program are standard test methods and metrics for the various performance requirements and characteristics defined by the responders. The test methods should be objective and clearly defined, and ideally, they will also be reproducible by robot developers and manufacturers to provide tangible goals for system capabilities. This will enable robot and component developers to exercise their systems in their own locations in order to attain the required performance.

The resulting standard test methods and usage guides for USAR robots will be generated within the ASTM International Homeland Security Committee through the E54.08 Subcommittee on Operational Equipment.

Draft test methods are evaluated several times by the responders and the robot developers to ensure that both communities find them representative and fair. Test methods measure performance against a specific requirement or set of requirements. The complementary usage guides help interpret the test method results for a given type of mission or deployment.

In this section, we will discuss the test methods to assess visual acuity, field of view, and maneuverability over uneven terrain, pitch/roll surfaces, ramps, stairs, and confined spaces.

To illustrate the effect of different deployment categories on the performance requirements, we will start by discussing the visual acuity and field of view test method. This test method

assesses performance to address the responders' requirements listed in Table 3. The specifics of the test set up were designed to address specifically the three types of robot deployments selected as highest priority, noted above.



Fig. 1. Tumbling E's

The test method utilizes the Tumbling E optotype (character) in eye charts that are to be viewed by the operator at the control station remotely located from the robot, which is positioned at specified distances from two eye charts (near and far). Far Vision Visual Acuity is important for both unmanned air vehicles (UAVs) and ground vehicles for wide area survey. Zoom is required for ground vehicles for wide area survey. Near Vision Visual Acuity is important for ground vehicles for wide area survey in examining objects at close range and also for small robots that operate in constrained spaces. Figure 1 shows a sample line of tumbling E's. The operator is to indicate which side of the letter E is open (top, left, right, bottom) for each letter in a row. The smallest row that is correctly read in its entirety is the one that is noted on the form. The test is conducted in both ambient light and dark conditions (both of which are measured and noted). If the robot is traversing dark areas (which is likely in USAR missions), onboard illumination is necessary. However, if the illumination is not adjustable, close by objects will be "washed out" by the strong lighting. This case will become evident if the robot illumination enables reading the far-field chart, but precludes viewing the near-field one.

Type	Sub-Type	Requirement
Chassis	Illumination	Adjustable
Sensing	Video	Real time remote video system (Near)
Sensing	Video	Real time remote video system (Far)
Sensing	Video	Field of View
Sensing	Video	Pan
Sensing	Video	Tilt

Table 3. Requirements addressed by Visual Acuity Test Method

Common terrain artifacts are used in multiple test methods and are specifically aimed at representing a world that's not flat. They are meant to provide reproducible and repeatable mobility or orientation challenges. Step Field Pallets (Figure 2) provide repeatable surface topologies with different levels of "aggressiveness." Half-cubic stepfields (referred to as

“orange”) provide orientation complexity in static tests, such as Directed Perception. Full-cubic step fields (“red”) provide repeatable surface topologies for dynamic tests, such as for locomotion. The sizes of the steps and width of the pallets are scaleable according to the robot sizes. Small size robots can use pallets that are made of 5 cm by 5 cm posts. Mid-sized robots can use pallets made of 10 cm by 10 cm posts. Large-sized robots use pallets made of clusters of four 10 cm by 10 cm posts. The topologies of the posts can be biased in three main ways: flat, hill, and diagonal configurations. Ž



Fig. 2. Step Fields Provide Reproducible Terrain Challenges

Pitch/Roll Ramps provide non-flat flooring for orientation complexity. As implied by the name, the orientation of the ramp can be along the direction of robot travel or perpendicular to it. Different types of ramps are concatenated as well. The angles of the ramps can be 5°, 10°, or 15°.

In terms of how the performance is measured in these test methods, there is a wide variance in the abilities and levels of experience of the operators. Therefore each test method’s data capture form includes a selection of the operator’s self-declared experience level (novice, intermediate, or expert). When the “official” data is collected for a robot (once the test method is a standard), the robot manufacturer will supply the operator(s) that will conduct the test. We expect to strive for statistically significant numbers of trials, so that the data is averaged over numerous repetitions. Ideally, the performance data will include the level of expertise and can thus be further analyzed for disparities by this particular demographic.

Basic robot speeds and maneuverability on different terrains are measured in a series of tests. To measure basic locomotion abilities and sustained speeds, the robots are to traverse a prescribed course. The terrain types may be paved, unpaved (including vegetated), or a variant of abstracted, but repeatable, rubble-like terrain. The course may be a zig-zag pattern or a figure 8 pattern. For a zig-zag course, the test proctor notes the time it takes the robot to reach the end in one direction, and then proceed back to the origin. For a figure 8 course, the robot may be required to complete a given number of laps. A variant of these mobility tests is one that measures the ability of a robot to traverse confined spaces. In this test, step field pallets are inverted and placed over another set of pallets (see Fig. 3). This test measures the ability of robots to maneuver in very small spaces.

Special cases of mobility are tested using ramps and stairs. A pattern of way points is

marked on a ramp (at a variable angle), which the robot is to follow on an inclined plane. Ability to do so and time to complete is noted for each angle, which is gradually increased until the robot may no longer accomplish this safely. For robots that are able to climb walls or move while inverted, the test can be extended to accommodate these configurations. For the mobility on stairs, the ability of the robot to ascend and descend several flights of stairs



Fig. 3. Example Mobility Tests. Left: Confined Space Cubes; Right: Inclined Plane with waypoint pattern

of different steepness is measured. Whether the stairs have enclosing walls or just railings, as well as whether they have risers or are open, are among the variables.

Other test methods, not described in this chapter, measure the robot packaging volume and weight, the situational awareness afforded by the operator control station and sensors, aerial station-keeping, the ability to access different spatial zones with visual and mission-specific sensors, the ability to grasp and move objects at different locations, and wireless communications range.

The next section describes the infrastructure that is in place to capture data during the implementation of the test methods.

4. Data Collection – Audio/Visual

When a robot attempts a test method, performance data is captured through both quantitative measurements and Audio/Visual (A/V) data collection. The data collected in the former varies based upon the specific test method, while the latter is somewhat constant. A quad video and single audio collection system is managed throughout each test method to capture a clear representation of both the operator's and robot's actions during these performance evaluations. This A/V data collection system is composed of the control and display hub (shown in Figure 4) and supported by in-situ cameras and an operator station-based microphone. A PC-output splash screen showing the pertinent run information initiates the A/V collection and displays the robot name, operator's skill level, test method, etc. While a robot operates within a test method, video is captured of the robot from multiple perspectives (includes a combination of ground-based and ceiling mounted

cameras), the operator's hand interactions with the robot's control system, the robot's visual user interface, and the PC display output of the robot tracking system (maze test method, only). A microphone in the operator room captures all the sounds the operator is exposed to throughout their performance which might include audible user interface feedback or operator comments.

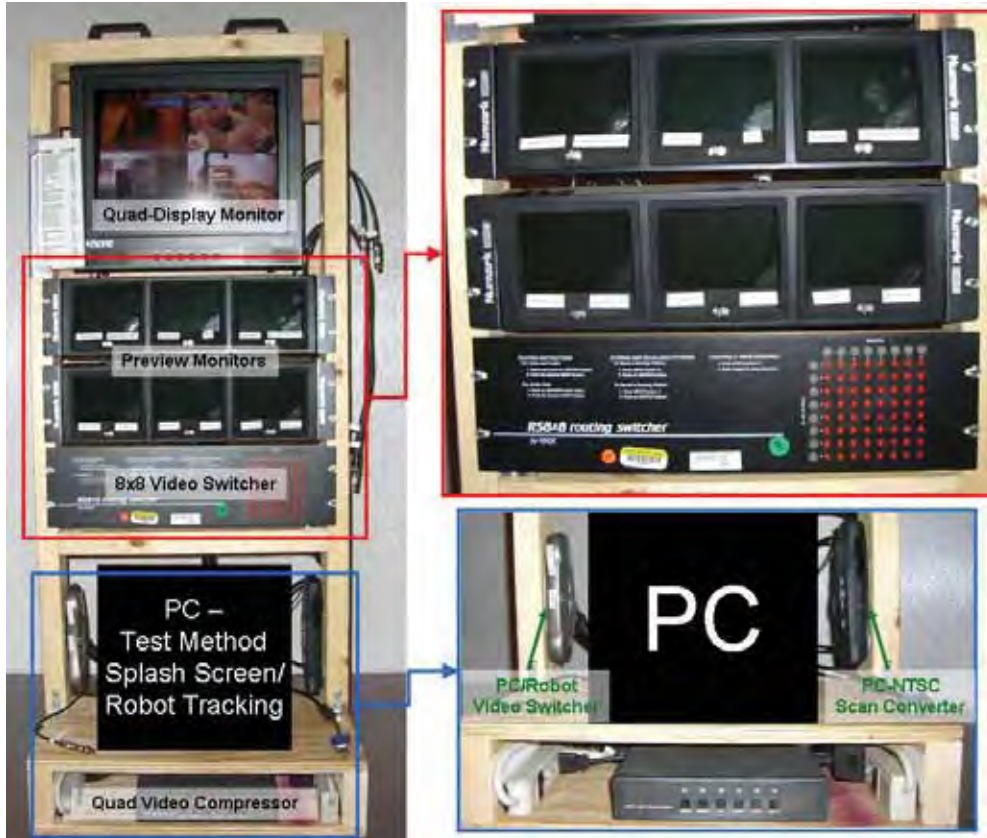


Fig. 4. Quad Audio/Video Control and Display Hub

The video and audio feeds are sent into the control and display hub. While the audio output is sent directly to the digital recording device, the video signals go through preview monitors and switchers before the final four video outputs are fed into the quad compressor and split out to a large display monitor and the digital recording device. Typically, the A/V manager has more than four video sources per test method, but only has the discretion to pick the two opportune robot video sources (displayed in the upper-right and upper-left quadrants) while the other two video sources default to the operator's control station (lower-left quadrant) and robot visual user interface (lower-right quadrant).

5. Response Robot Exercises

The robot manufacturers and researchers and eventual end-users need to reach common understandings of the envisioned deployment scenarios, environmental conditions, and specific operational capabilities that are both desirable and possible for robots applied to USAR missions. Toward that end, NIST organizes events that bring emergency responders together with a broad variety of robots and the engineers that developed them to work within actual responder training facilities. These informal response robot evaluation exercises provide collaborative opportunities to experiment and practice, while refining stated requirements and performance objectives for robots intended for search and rescue tasks. In each instance, search scenarios are devised using facilities available at the training facility. NIST-built simulated victims are placed within the scenarios. These may exhibit several signs of life, including human form (typically partial), heat, sound, and movement. Robot providers are encouraged to work closely with responders to determine the best way to deploy robots into these scenarios. Operation of the robots by the responders by the end of the exercise is a key goal. This enables responders to familiarize themselves with the capabilities of the robots and to provide direct feedback to the robot manufacturers and researchers about strengths and weaknesses of robots applied to this domain. Three exercises have been held to date at FEMA USAR Task Force training facilities and are briefly described in this section.

In August of 2005, the first response robot exercise for this project was held in the desert training facility for Nevada Task Force 1. Fifteen ground (including throw-able, wall-climbing, confined space, complex terrain reconnaissance, and other sub-categories), 3 aerial, 2 aquatic, and 2 amphibious robots participated. FEMA Task Force members from the local team, as well as from several other areas of the country devised search scenarios and operated robots through them. At this time, there was one nascent test method - visual acuity - that was piloted.

The second exercise was hosted by Texas Task Force 1 at Disaster City in April 2006. (Jacoff and Messina 2006) More than 30 robots participated in 10 scenarios at this 21 hectare facility. The robot demographics spanned 16 models of ground vehicles, 2 models of wall climbers, 7 models of aerial vehicles including a helicopter, and 2 underwater vehicles. The scenarios included aerial survey of a rail accident using a variety of small and micro aerial vehicles (primarily fixed wing). Fig. 7 shows some of the scenarios. At this point, there were several emerging test methods available to be evaluated. A standards task group meeting was held after the exercise to gather input and test method critiques from the responders and vendors. At a separate meeting, the responders selected the three focus robot categories discussed above and provided an assessment of the robot maturity levels and relative strengths and weaknesses.

Maryland Task Force 1 hosted an exercise in August 2006. This event placed heavy emphasis on evaluation of the eleven draft test methods. This exercise included 24 models of ground robots, 2 models of wall climbers, and 2 models of aerial robots, which had to run through all relevant test methods before proceeding to the scenarios. In addition to the search and rescue training scenarios, there was an *ad hoc* experiment integrating portable radiation sensors with robots.

Collaborating with NIST researchers who are working on radiation sensor standards, sensor vendors participated, providing sensors that were integrated with robots and deployed in a test method (directed perception) and in a scenario. Standards working group meetings for the communications, human-system interaction, and sensor teams were held, to capture lessons learned during the piloting of the test methods.

After conducting four such exercises, several salient observations emerged. There are many useful roles that robots can play in helping responders in USAR missions. In particular, the three high priority deployment types selected by responders can fulfill useful functions. There are some additional technological and engineering improvements still generally needed. For instance, robots must be able to withstand very harsh conditions, including submersion in water. Some of the robots developed for military applications are ready to confront these challenges, but most others are not.

One current limitation present in most robots that have participated in the exercises pertains to the wireless communications between the robot and the operator control unit (OCU). Commands are sent from the OCU to the robot and telemetry or sensor data is sent back. There are issues with limitations in the range for line of sight communications as well as for non-line of sight. Responders would like to be able to send a robot a kilometer downrange or into a collapsed concrete structure and still be able to communicate with it. Adding autonomy to the robots, so that they may continue their mission even when out of range, or at least return to the last location where they had radio contact would greatly increase their robustness. Interference between robot radios and other communications equipment also is a common problem.

Better and more sensors are desired. Responders would like better navigation aids, such as Global Positioning System (GPS) and the ability to show the robot coordinates and direction of view. They would like to have onboard mapping of environments when navigating through smoke. The cameras currently used for navigation could be better-placed to afford a higher perspective to improve path planning and obstacle avoidance. Assistance in gauging depth is needed.

The mobility of ground robots, in general, needs improvement. There are very few platforms that can even attempt to traverse rubble piles, such as those commonly found at FEMA USAR training facilities. Tracks on robots (which are commonly used) can easily come off or catch loose debris and become disabled. Stairs can foil some robots, especially if they are dusty or otherwise slippery. A robot locomotion design based on walking, if complemented with semi-autonomous gaits, could adapt to a wide variety of terrains and conditions. Search dogs regularly participate at the response robot exercises, and their ability to traverse rubble piles and other challenging terrain is unsurpassed. Wall-climbing robots have been favorably received. Responders like the ability to peer over the tops of buildings or use the ceiling, which may be intact, to survey a collapsed area. Figure 5 shows examples of wall-climbers in action. The wall-climbers need to improve their robustness and be able to deal with changes in the wall or ceiling surfaces. Discontinuities or protuberances can cause them to lose contact with the wall and fall.



Fig. 5. Examples of wall-climbing robots

6. Knowledge Representation Efforts

As mentioned earlier, knowledge representation is a key enabler in the quest to match robot capabilities to the deployment environments. With the large number of disparate robots that are currently available, responders need an easy way to quickly determine which robot is most appropriate for their current mission. This section describes three efforts which are currently underway to represent robot capabilities and structural collapse types with the goal of providing various tools to assist responders in choosing the best robot for their mission. They are the Robot Pocket Guide, the Robot Capability Ontology, and the Structural Collapse Taxonomy.

6.1. The Robot Pocket Guide

Over the past year, NIST has been developing a robot pocket guide to provide responders with easy access to high-level specifications of robots. The guide is designed to fit in a responder's pocket and currently contains information about 28 robots that have participated in the aforementioned exercises. Robots are classified as either ground, wall-climbed, aquatic, or aerial. Sample pages of the pocket guide are shown in Figure 6. The NanoMag¹ is classified as a wall climbing robot (as shown by the tab on the right). Information that is included about the NanoMag on the left page along with a picture of the robot and its operator control unit include its width, length, height, weight, turning diameter, maximum speed, etc. On the right page, there is information about how the robot performed in the test methods described earlier. Because the test methods have not yet been

¹ Certain commercial software and tools are identified in this paper in order to explain our research. Such identification does not imply recommendation or endorsement by the National Institute of Standards and Technology, nor does it imply that the tools identified are necessarily the best available for the purpose.

finalized, all that is shown is how the information will be represented. Similar information is included about the other 27 robots. As more robots participate in the upcoming exercises, information about them will be added to the pocket guide.

NanoMag
Inuktun
www.inuktun.com/
1-877-468-5886

Manufacturer's Specs:

- Width: 17" (43.1cm)
- Length: 12" (30.4 cm)
- Height: 3.5" (8.8 cm)
- Weight: 5 lbs (2.26kg)
- Turning Dia: TBD
- Max Speed: 0.5 ft/min (0-1.5 m/min)
- Power Source: TBD
- Endurance: TBD
- Tether: 100ft (30m)
- Control: teleoperated
- Sensors: TBD
- Payload: TBD
- Manipulator: n/a

Cache packaging, weight, setup, tools
Packages: Ropacks _____ Pelicans _____ Hardiggs _____
Weights: Shipping _____ Deployed _____ Setup Time: X min. Tools: standard

Directed Perception (boxes with holes):
Level 1: Face, Eye (x of 3), Haz. (x of 3), Chem. (x of 3), Therm. (x of 3) Time:
Top: Eye (x of 6), Haz. (x of 6), Chem. (x of 6), Therm. (x of 6) Time:
Level 2: Face, Eye (x of 3), Haz. (x of 3), Chem. (x of 3), Therm. (x of 3) Time:
Top: Eye (x of 6), Haz. (x of 6), Chem. (x of 6), Therm. (x of 6) Time:
Level 3: Face, Eye (x of 3), Haz. (x of 3), Chem. (x of 3), Therm. (x of 3) Time:
Top: Eye (x of 6), Haz. (x of 6), Chem. (x of 6), Therm. (x of 6) Time:
Level 4: Face, Eye (x of 3), Haz. (x of 3), Chem. (x of 3), Therm. (x of 3) Time:
Top: Eye (x of 6), Haz. (x of 6), Chem. (x of 6), Therm. (x of 6) Time:

Incline Plane:
Max Operating Angle: Grnd. (20, 30, 40, 50, 60, 70, 80), Wall (90), Inverted: (100, 135, 180)

Radio Communications:
LOS: (x m, time, near field acuity), ELOs: (x m, time, near field acuity)

Visual Acuity:
Ambient (lx/lumens): near field (xx), far field (xx), zoom (xx).
Dark (lx/lumens): near field (xx), far field (xx), zoom (xx) – var. illumination: (yes/no)

Wall Climber

Radio Tx: (tether only)
Radio Rx: (tether only)

86

87

Fig. 6. The NanoMag page in the robot pocket guide

6.2. The Robot Capability Ontology

6.2.1. Overview

The goal of this Robot Capabilities Ontology effort is to develop and begin to populate a neutral knowledge representation (data structure) capturing relevant information about robots and their capabilities. This ontology will help to assist in the development, testing, and certification of effective technologies for sensing, mobility, navigation, planning, integration and operator interaction within search and rescue robot systems. It is envisioned that a first responder would query this knowledge representation using a graphical front end to find robots that meet the criteria (e.g., size, weight, heat resistance, etc.) they need to perform a desired mission in a disaster site. This knowledge representation must be flexible

enough to adapt as the robot requirements evolve. As such, we have chosen to use an ontological approach for representing these requirements.

6.2.2. Sample Scenario

Passenger rail cars were hit by industrial hazmat tanker cars of unknown substance and both trains partially derailed, as shown in Figure 7. After initial analysis, it was determined that ground robots should circumnavigate all trains over the tracks, various debris, and rubble. The robots should map the perimeter along with the location and positions of each car, including under the elevated car. Robots should search the Sleeper Car ramping up from the ground, and search each curtained alcove on both sides looking for simulated victims. For the Crew Car on its side, robots should be inserted to explore the interior to locate any victims or read the placards on hazardous canisters that may be in the mailroom. Access to the mailroom is too small for a responder in Level A suit.



Fig. 7. Train Wreckage Scenarios

The first responders need to decide which robots to use out of their available cache of robots. They go to their laptop and enter their requirements for the robots. They use pull-down boxes and text entry boxes to state that they need a robot that can traverse rubble 15 cm (6 inches) in diameter, has sensor capabilities that can develop a 3-D map of the environment, can withstand various hazmat conditions, and can fit into alcoves as small as 1 meter (3 feet) in width and height. They must also have sensors that can identify victims by heat signatures. Lastly, they must have vision capabilities that read signs with 2.5 cm (1 inch) lettering from a distance of 3.2 meters (7 feet) away. Based on their requirements, two robots are returned that are acceptable. However, one of the robots also has heat resistance up to 90 degrees celsius (200 degrees Fahrenheit), which is not important for this scenario but is very important for another disaster site nearby which partnering first responders are addressing. The first responder decides to use the robot without the heat resistance and requests that specific robot through the user interface.

6.2.3. Related Work

To the best of the authors' knowledge, only a handful of projects exist that have addressed the challenge of developing a knowledge representation for Urban Search and Rescue (USAR). One such effort is being performed at the University of Electro-Communications in

Tokyo, Japan (Chatterjee and Matsuno 2005). This work intends to identify the necessity and scope of developing ontology standards for describing the rescue robot features and for describing the disaster scenarios in the context of search and rescue effort coordination. It is intended to support the decision process of assigning any particular robot platform to any specific disaster site and to prioritize allocation of available robot-aided rescue teams to specific disaster areas among many demanding sites. At the time that this paper was written, a list of requirements existed for the information that should be contained in the ontology, but no effort had been performed to model them within a formal data structure.

SPAWAR (Space and Naval Warfare Systems Command) has developed the Mobile Robot Knowledge Base (MRKB) (Joint Robotics Program 2005), which provides the robotics community with a web-accessible, centralized resource for sharing information, experience, and technology to more efficiently and effectively meet the needs of the robot system user. The resource includes searchable information on robot components, subsystems, mission payloads, platforms, and Department of Defense (DOD) robotics programs. In addition, the MRKB website provides a forum for technology and information transfer within the DOD robotics community and an interface for the Robotic Systems Pool (RSP). The RSP manages a collection of small teleoperated and semi-autonomous robotic platforms, available for loan to DOD and other qualified entities. The objective is to put robots in the hands of users and use the test data and fielding experience to improve robot systems. Minimal information about the robots is contained on this website itself (it primarily includes a picture, overall characterization, and cost). Each robot site also contains a link to the robot manufacturer's page where more detailed information can be found out.

There have been efforts at the Center for Robot Assisted Search and Rescue (CRASAR) in the development of taxonomies for robot failures (Carlson et.al. 2004) and issues pertaining to social interactions between robots and humans (Burke et.al. 2004). A failure is defined as the inability of the robot or the equipment used with the robot to function normally. Both complete breakdowns and noticeable degradations in performance are included. The effort developed a taxonomy to gain insight into how and why mobile robots fail. *Failures* are categorized based on the source of failure and are divided into *physical* and *human* categories, following dependability computing practices. *Physical failures* are subdivided into classes based on common systems found in all robot platforms, these being *effector*, *sensor*, *control system*, *power*, and *communications*. *Effectors* are defined as any components that perform actuation and any connections related to those components. This category includes for example, *motors*, *grippers*, *treads*, and *wheels*. The control system category includes the on-board computer, manufacturer provided software, and any remote operator control units (OCU). *Human failures* (also called human error) are subdivided into *design* and *interaction* subclasses. Mistakes are caused by fallacies in conscious processing, such as misunderstanding the situation and doing the wrong thing. Slips are caused by fallacies in unconscious processing, where the operator attempted to do the right thing but was unsuccessful. Each failure, regardless of physical or human, has two attributes, repairability and impact. The severity of the failure is evaluated based on its impact on the robot's assigned task or mission. A terminal robot failure is one that terminates the robot's current mission, and a non-terminal failure is one that introduces some noticeable degradation of the robot's capability to perform its mission. The repairability of the failure is described as either field-repairable or non-field-repairable. A failure is considered field-repairable if it can be repaired under favorable environmental conditions with the equipment that

commonly accompanies the robot into the field. This work focuses solely on robot failure, while the work that is described in the remainder of this section also takes a classification approach but focuses on robot capabilities in a more general sense.

6.2.4. Ontology Overview

Using the requirements discussed earlier in this chapter [Section 2] as the underlying basis, a knowledge representation was developed to capture the requirements. The goal was to develop a knowledge representation that would allow for:

- Less ambiguity in term usage and understanding
- Explicit representation of all knowledge, without hidden assumptions
- Conformance to commonly-used standards
- Availability of the knowledge source to other arenas outside of urban search and rescue
- Availability of a wide variety of tools (reasoning engines, consistency checkers, etc.)

To address this, we used an ontological approach to represent these requirements. In this context, an ontology can be thought of as a knowledge representation approach that represents key concepts, their properties, their relationships, and their rules and constraints. Whereas taxonomies usually provide only a set of vocabulary and a single type of relationship between terms (usually a parent/child type of relationship), an ontology provides a much richer set of relationship and also allows for constraints and rules to govern those relationships. In general, ontologies make all pertinent knowledge about a domain explicit and are represented in a computer-interpretable fashion that allows software to reason over that knowledge to infer additional information.

The benefits of having a robot ontology are numerous. In addition to providing the data structures to represent the robot requirements, the robot ontology can allow for:

- The selection of equipment and agents for rescue operations
- Assistance in the exchange of information across USAR teams
- The ability to find the available resources that address a need
- The identification of gaps in functionality that can drive research efforts

The following sections describe the infrastructure that was used to develop the robot ontology as well as the current status of its development.

6.2.5. Infrastructure

The Robot Ontology has been developed to ensure compliance with existing formal and *de facto* standards as well as ensuring compatibility with existing tools and software infrastructures. More specifically, the Robot Ontology leverages the Protégé ontology development tool and the OWL/OWL-S specification, as described below.

Before an ontology can be built, a decision must be made as to which tool (or set of tools) should be used to enter, capture, and visualize the ontology. For this work, we decided to use Protégé (Schlenoff et.al. 2004). Protégé is an open source ontology editor developed at

Stanford University. It supports class and property definitions and relationships, property restrictions, instance generation, and queries. Protégé accommodates plug-ins, which are actively being developed for areas such as visualization and reasoning.

Protégé provides a suite of tools to construct domain models and knowledge-based applications with ontologies. At its core, Protégé implements a rich set of knowledge-modeling structures and actions that support the creation, visualization, and manipulation of ontologies in various representation formats. It supports class and property definitions and relationships, property restrictions, instance generation, and queries. Protégé can be customized to provide domain-friendly support for creating knowledge models and entering data. Further, Protégé can be extended by way of a plug-in architecture and a Java-based Application Programming Interface (API) for building knowledge-based tools and applications. Protégé was chosen due to its strong user community, its ability to support the OWL language, its ease of use (as determined by previous experience), and its ability to be extended with plug-ins such as visualization tool.

We decided to use the OWL-S upper ontology (The OWL Services Coalition 2003) as the underlying representation for the Robot Ontology in order, among other reasons, to leverage the large and ever-growing community and to ensure compatibility with the XML (eXtensible Markup Language) format. OWL-S is a service ontology, which supplies a core set of markup language constructs for describing the properties and capabilities of services in an unambiguous, computer-interpretable format. OWL-S, which is being developed by the Semantic Web Services arm of the Defense Advanced Research Projects Agency (DARPA) Agent Markup Language (DAML) program, is based on OWL (Harmelen and McGuiness 2004). OWL is an extension to XML and RDF (Resource Description Framework) schema that defines terms commonly used in creating a model of an object or process. OWL is a World Wide Consortium (W3C) recommendation, which is analogous to an international standard in other standards bodies.

OWL-S is structured to provide three types of knowledge about a service, each characterized by the question it answers and shown in Figure 8:

- What does the service require of the user(s), or other agents, and provide for them? The answer to this question is given in the ``profile.'' Thus, the class *SERVICE* presents a *SERVICEPROFILE*
- How does it work? The answer to this question is given in the ``model.'' Thus, the class *SERVICE* is describedBy a *SERVICEMODEL*
- How is it used? The answer to this question is given in the ``grounding.'' Thus, the class *SERVICE* supports a *SERVICEGROUNDING*.

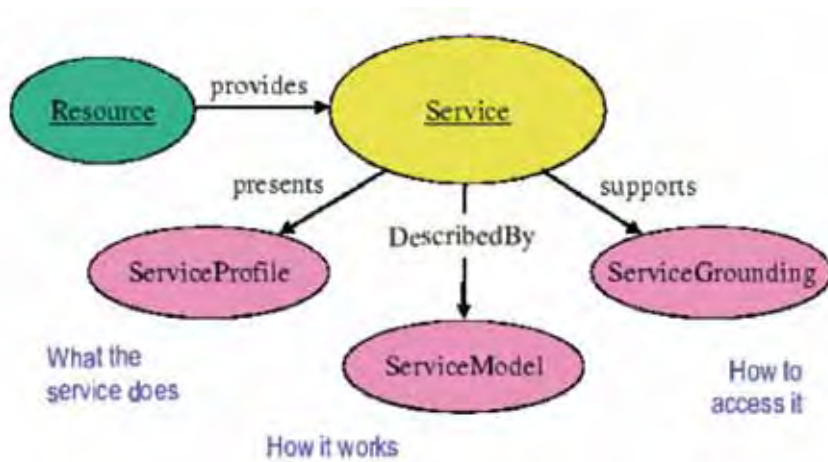


Fig. 8. OWL-S Ontology Structure

6.2.6. Ontology Structure

To capture the requirements described earlier in the paper, an initial structure for the Robot Ontology has been developed. A screenshot of the ontology in Protégé is shown in Figure 9. The column on the left shows the classes that are represented in the ontology (e.g., *Capability*, *Robot*, *User Interface*). The box on the right shows the attributes that are associated with the highlighted class (*Robot*). Robots have attributes such as *hasCommunicationCapability*, *hasHumanFactorsCapabilities*, *hasLocomotionCapabilities*, etc. Each one of these attributes may point to a class (shown in parenthesis next to the attribute name) which contains more specific information about the value of that attribute.

The main concept in the ontology is *Robot*, where a robot can roughly be defined as a mechanism with locomotion and sensing capability which a human user may interact with from a remote location. A Robot can be thought of as having three primary categories of information, namely:

- Structural Characteristics – describes the physical and structural aspects of a robot
- Functional Capabilities – describes the behavioral features of the robot
- Operational Considerations – describes the interactions of the robot with the human and the interoperability with other robots

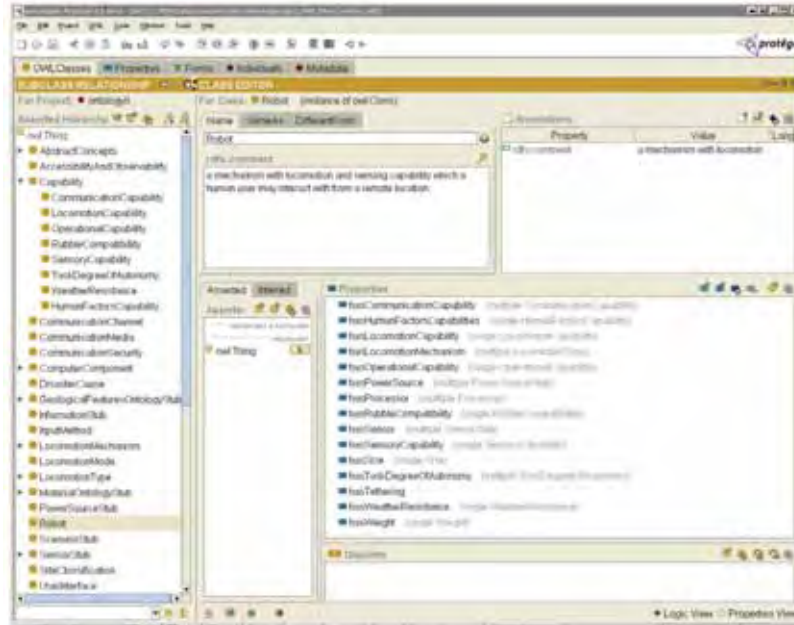


Fig. 9. The Robot Capabilities Ontology

In the Robot Ontology, structural characteristics are primarily captured in the definition of the robot itself. These characteristics include (but are not limited to):

- Size -(e.g., minimum and maximum length, width, and height (depending on robot configuration))
- Weight
- Tethering (i.e., yes or no)
- Power Source
- Locomotion Mechanism (e.g., wheeled, walking, crawling, jumping, flying, etc.)
- Sensors (e.g., camera, FLIR, LADAR, SONAR, GPS, Audio, Temperature Sensor, etc.)
- Processors

Many of the above are direct attributes of the Robot class. The Robot class and its attributes are shown in Figure 9. Another important thing to notice in Figure 9 are the classes that end in the word "stub". These are meant to be placeholders to integrate in more established (and hopefully standardized) representations. Examples of these "stubs" include GeologicalFeatureOntologyStub, InformationStub, MaterialOntologyStub, PowerSourceStub, ScenarioStub, and SensorStub.

Examples of knowledge captured in the functional capabilities category include (but are not limited to):

- Locomotion Capabilities (e.g., max. speed, max. step climbing, max. slope climbing, etc.)
- Sensory Capabilities (e.g., min. visibility level, map building capability, self-localization, system health, etc.)
- Operational Capabilities (e.g., working time, setup time, max. force available to push, mean time before failure (MTBF), mean time between maintenance (MTBM), required tools for maintenance, run time indicator, sustainment (spares and supplies), etc.)
- Weather Resistance (e.g., max. operating temp, max. submergibility level, etc.)
- Degree of Autonomy (e.g., joint level dependency, drive level dependency, navigation level dependency, etc.)
- Rubble Compatibility (e.g., ability to historically operate well in certain terrains)
- Communications (e.g., communication media, communication channel frequency, content standards, information content, communication locking, communication encryption)

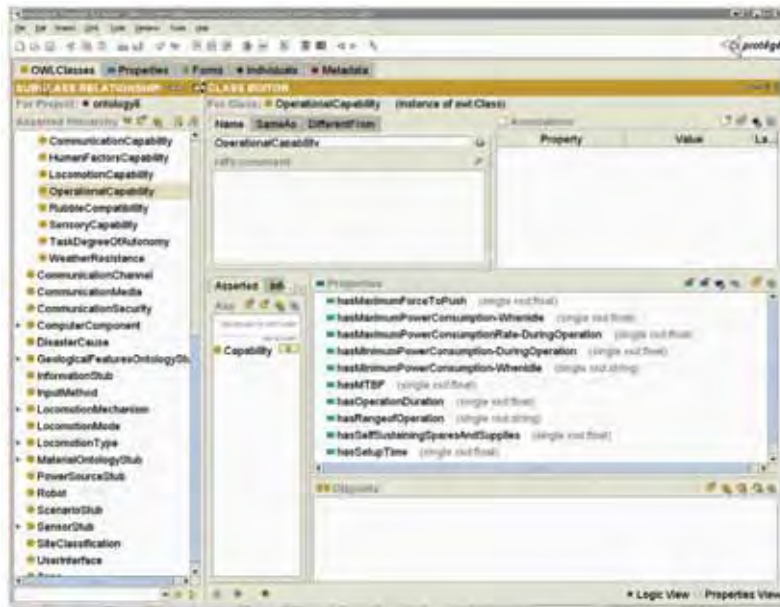


Fig. 10. Operational Capability Attributes

Figure 10 shows an example of the operational capabilities that may be associated with a robot. Note in this figure that some attributes have “primitive” attributes as their type (e.g., float, string, Boolean). This implies that, instead of pointing to another class of object to capture the data associated with that attribute, the data is captured directly in that primitive type.

Examples of knowledge captured in the operational considerations category include (but are not limited to):

- Human Factors (operator ratio, initial training, proficiency education, acceptable usability, auto-notification, display type, packaging)
- Intra-Group Interaction (i.e., interaction with other similar robots)
- Inter-Group Interaction (i.e., interaction with other 3rd party robots or computers)

Figure 11 shows an example of the human factors attributes that may be associated with a robot.

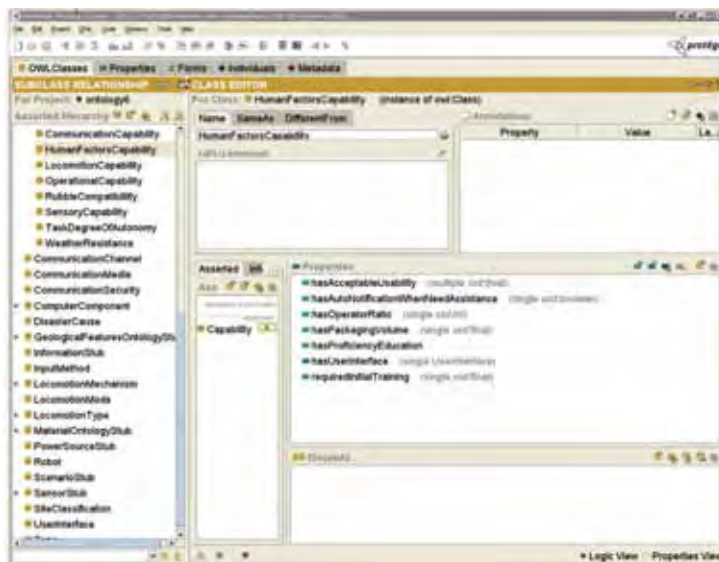


Fig. 11. Human Factors Attributes

6.2.7. Future Work

This section describes our progress in developing a robot ontology for USAR. To date, the Robot Ontology contains 230 classes, 245 attributes (properties), and 180 instances. As the project progresses, it is expected that the ontology will grow considerably. Although strong progress has been made, there is still quite a lot of work to be accomplished. Future work will focus on (in no particular order):

- Continue to specialize the robot ontology structure to provide greater level of detail in the areas that have already been addressed
- Explore other standards efforts and existing ontologies that can be leveraged, such as ontologies for sensors, power sources, materials, and environment.
- Continue to incorporate the requirements from the requirements workshops into the robot ontology structure
- Develop a user interface to help the end user query the ontology. A simple user interface is shown in Figure 12.



Fig. 12. Sample User Interface to Ontology

6.3. Structural Collapse Taxonomy

6.3.1. Overview

When a disaster occurs, previously benign terrain may become difficult or impossible to traverse. Buildings collapse, roads and bridges are destroyed, and previously smooth, obstacle free terrain may contain large obstacles and discontinuities. In order to perform search and rescue operations, responders must know what form of mobility they must use to traverse affected areas. For operational scenarios, the terrain must be assessed in order to employ assets that possess the correct mobility techniques to get to desired locations. In a research and development scenario, a description and classification of potential operating environments is necessary to effectively guide system development. This is particularly true for the development of performance-based standards for Urban Search And Rescue (USAR) robots.

An essential element in defining performance metrics is to be able to clearly understand and describe the operating environment of the system under test. For USAR robotics, both qualitative and quantitative measures of the environments in which platforms are tested and deployed are of great interest. For examples of qualitative measures of an environment, consider trail rating systems for ski slopes or the Beaufort Wind Force Scale for estimating wind speed from sea state. A quantitative metric in the USAR context could be a specific measure of the traversability of the terrain surface derived using techniques such as height, slope, and roughness estimation from plane fitting, fractal dimension analysis or wavelet energy statistics. Traversability is a well-studied discipline, particularly in the context of unmanned ground vehicle path planning. The challenge is to standardize a universally-

accepted measure for system evaluation. An interesting qualitative approach would be to develop a method to score USAR environments similar to the Yosemite Decimal System (YDS) for evaluating climbing routes. Although subjective, the YDS has evolved into an effective method for quantifying route difficulty, albeit for only one mobility platform – humans. From this discussion one can imagine a specific robot platform with an UDS (USAR Decimal System) number of x for an environment with terrain characterization of y . A different platform may – and likely will – have a different UDS number for the same environment. The two measures taken together would provide comparable and verifiable information about the mobility of the robot platform.

To address the performance metric need, NIST is conducting research in characterizing terrain traversability for USAR robots (Molino et.al. 2006). The desired result is a set of algorithms that are capable of analyzing a terrain surface and predicting which robots would be able to successfully navigate the terrain. To support this research effort, NIST has gathered high-resolution point clouds of several training disaster scenarios and made those available for all interested researchers. In addition to characterization algorithms, there is also a desire to develop representative models of these training scenarios for use in simulation environment discussed in Section 5. The difficulty is to provide models of sufficient fidelity that the collapsed terrain is correctly simulated for mobility physics and maintains important features such as void spaces and terrain roughness, without overwhelming the current generation of game engines. A related effort involves developing a framework for integrating building classification, disaster type, and collapse type to provide general descriptions of probable operating environments.

6.3.2. Structural Collapse Taxonomy

In the context of emergence response and disaster estimation, buildings are normally classified by model building type and occupancy class. For building types, primary factors include the building materials used for constructing the structural frame, the lateral-force-resisting system, and the height of the structure. A simplified classification system is shown in Table 4.

Type of Construction ¹	Wood, Masonry ² , Steel, Concrete ³
Type of Structure	Shear Wall ⁴ or Moment Frame
Height	Low-rise (≤ 6 stories) ⁵ , Mid-rise (6-10 stories), High (>10)
Notes:	
(1) Refers to materials making up structural frame;	
(2) Masonry is typically further divided into reinforced or unreinforced	
(3) Concrete is typically further divided into cast-in-place or pre-cast	
(4) Masonry is only shear wall;	
(5) Masonry is usually never > 6 stories and wood is usually never > 4 stories. Therefore masonry and wood default to low-rise	

Table 4. Simplified Building Type Schema

The American Society of Civil Engineers (ASCE) and the Structural Engineering Institute (SEI) issued a standard for the seismic evaluation of existing buildings (ASCE SEI 2003). ASCE/SEI 31-03 publication defines 15 base building types with subcategories resulting in 24 separate building descriptions. The building types are organized by the building material and the lateral-force-resisting system. Building height is not a factor. A complete listing of the 24 types is provided in Table 5.

W1	Wood Light
W1A	Multi-Story, Multi-Unit Residential Wood Frames
W2	Wood Frames, Commercial and Industrial
S1	Steel Moment Frames with Stiff Diaphragms
S1A	Steel Moment Frames with Flexible Diaphragms
S2	Steel Braced Frames with Stiff Diaphragms
S2A	Steel Braced Frames with Flexible Diaphragms
S3	Steel Light Frames
S4	Steel Frames with Concrete Shear Walls
S5	Steel Frames with Infill Masonry Shear Walls and Stiff Diaphragms
S5A	Steel Frames with Infill Masonry Shear Walls and Flexible Diaphragms
C1	Concrete Moment Frames
C2	Concrete Shear Wall Buildings with Stiff Diaphragms
C2A	Concrete Shear Wall Buildings with Flexible Diaphragms
C3	Concrete Frames with Infill Masonry Shear Walls and Stiff Diaphragms
C3A	Concrete Frames with Infill Masonry Shear Walls and Flexible Diaphragms
PC1	Precast/Tilt-up Concrete Shear Wall Buildings with Flexible Diaphragms
PC1A	Precast/Tilt-up Concrete Shear Wall Buildings with Stiff Diaphragms
PC2	Precast Concrete Frames with Shear Walls
PC2A	Precast Concrete Frames without Shear Walls
RM1	Reinforced Masonry Bearing Wall Buildings with Flexible Diaphragms
RM2	Reinforced Masonry Bearing Wall Buildings with Stiff Diaphragms
URM	Unreinforced Masonry Bearing Wall Buildings
URMA	Unreinforced Masonry Bearing Wall Buildings with Stiff Diaphragms

Table 5. Common Building Types (from ASCE / SEI 31-03)

A more detailed building classification system is used in the FEMA Hazards U.S. Multi-Hazard (HAZUS-MH) system (FEMA 2007; Schneider et.al. 2006). This system is a standard methodology and associated software program for estimating potential losses from earthquakes, floods, and hurricane winds. HAZUS-MH not only includes model building types based upon structural systems (material and design) but also occupancy class and

height. There are 28 different occupancy classes (e.g., hospital, school, apartment building, etc.) and 36 different model building types. The model building types are an extension of those shown in Table 4, factoring in low-, mid-, and high-rise classifications. In HAZUS-MH, estimates of potential damage are modeled from building type, while occupancy class is solely used for estimating loss (Kircher et.al. 2006). For USAR robotic system design and deployment, occupancy class is an important consideration to understand potential human occupancy, potential obstacles and void spaces due to interior elements, and the potential for other hazards (e.g., toxic or explosive atmospheres).

Another building classification system of note is from the FEMA 154 Rapid Visual Screening of Buildings for Potential Seismic Hazards manual. This manual adopted the model building types used the FEMA 310 Prestandard for Seismic Evaluation, which was the precursor to ASCE/SEI 31-03. As a result, FEMA 154 uses just the base 15 model building types used in ASCE/SEI 31-03. FEMA 154 is the second edition of a document first published by the Advanced Technology Council in 1988 of the same name and known in the response community as ACT-21. In ACT-21, there were 12 base building types as shown in Table 6. This is important because the FEMA USAR community adopted the ACT-21 designations and those designations are described responder training materials (FEMA 2006). Responders will be familiar with the ACT-21 designations, but may not be aware of the expanded classifications developed in ASCE/SEI 31-03 and HAZUS-MH.

W1	Wood Buildings (All Types)
S1	Steel Moment Resisting Frames
S2	Braced Steel Frames
S3	Light Metal Buildings
S4	Steel Frames with Concrete Shear Walls
C1	Concrete Moment Frames
C2	Concrete Shear Wall Buildings
C3/S5	Concrete/Steel Frames with Infill Unreinforced Masonry
TU/PC1	Precast/Tilt-up Concrete Shear Wall Buildings
PC2	Precast Concrete Frames
RM	Reinforced Masonry
URM	Unreinforced Masonry

Table 6. Common Building Types (from ATC-21)

In addition to building type and occupancy class, other parameters which should be taken into consideration are the type of structural loading causing the collapse and the type of collapse itself. Basic structural loading categories include earthquakes, windstorms, explosions, fire, flood, failure of construction bracing, urban decay, overload, and vehicle impact (e.g. cars, trains, planes, etc.). Overall types of collapses include partial, total, and progressive collapse. Often, specific building types collapse in familiar ways for various structural loads, yielding several categories of collapse patterns. An example would be the pancake, v-shape, lean-to, and cantilever earthquake collapse patterns. Structural loading categories and basic collapse patterns are discussed in .

6.3.3. USAR Terrain Characterization Data Collection

To support the development of mobility performance metrics, characterization algorithms, and simulation environments, NIST research engineers teamed with a 3D imaging service provider to produce high resolution laser scan data of three of the operational scenarios at the TX-TF1 Disaster City training facility at College Station, TX. These scenarios included the rubble pile (#2), the wood pile (#3), and the train wreck. 3D image data were collected using two commercially-available terrestrial laser scanners over the course of three days. Each scenario was scanned from multiple locations and each scan location was registered using targets. These targets were independently measured with a total station to provide survey control. Figures 13 (A & B) and 14 (A & B) show elements of the 3D imaging process



Fig. 13. (A) Setting up a scan of the rubble pile. Scan locations must be carefully chosen to obtain sufficient scene data to capture the existing conditions and enable tie in to prior scans using pre-positioned targets. (B) Since the laser scanner is a line-of-sight device, obtaining sufficient information for a disordered scene such as the rubble pile requires numerous scan locations throughout the environment.

A laser scanner is a 3D imaging device that uses a laser to measure the distance to an object. The laser beam is scanned both horizontally and vertically over time to image the operator-designated field of view. The distance, azimuth, and elevation information collected from each measurement in the scan is used to create high-resolution point clouds containing hundreds of thousands of points. Individual scans are then merged through a process called registration to create geometrically accurate point clouds of the scenes.



Fig. 14. (A).The wood pile was imaged using three 'overhead' scans and several ground-level scans. This view was taken from a scissors-lift. (B) Imaging the train wreck.

Figures 15 (A & B) and 16 (A & B) depict screen captures of the scenes from a point cloud viewing package. Within the point cloud software, camera viewpoints can be changed to examine the 3D data from multiple viewing angles and measurements such as point-to-point distance can be readily determined.

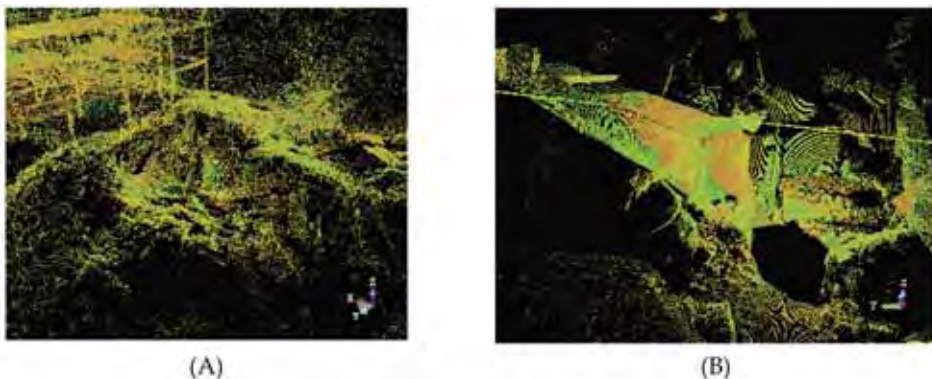


Fig. 15. (A) Registered perspective view of rubble pile.(B) Single scan from the rubble pile. The long 'tube' structure is made of two jersey barriers which form a tunnel through the pile. The scanner was placed at the entrance to the tunnel. The point cloud viewpoint was rotated in the 3D viewing software to show the tunnel.

There are many potential uses for these data. First, NIST will investigate means of representing the types of environments and specifically the complexities within the environment (especially for rubble) to see if there are predictable and consistent ways of representing rubble or other difficult terrain quantitatively. Second, NIST, along with partner organizations, is investigating how to represent the point clouds and/or derivative terrain models within simulation environments such as USARSim. Importing point, polygonal, or surface models of realistic training scenarios into simulation systems can

make the training scenarios themselves accessible to a wider set of developers. As an example, several robots are being modeled within USARSim with vehicle physics and scene interaction capability. Responders, researchers, developers, and other interested personnel will be able to navigate the scenarios at Disaster City – to some degree of fidelity – without having to physically travel to the location. Intelligent behaviors for semi-autonomous robots can also be virtually tested within the Disaster City models. The three images shown in Figure 17 depict this progression.

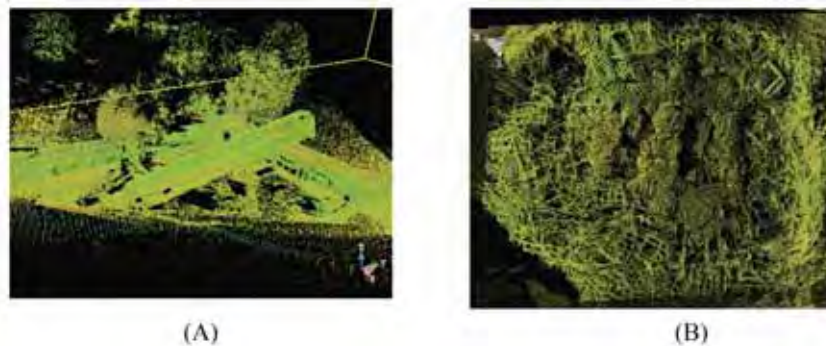


Fig. 16. (A) A bird's-eye-view of the full 3D point cloud of the train wreck. (B) A plan view of the wood pile.



Fig. 17. A) Robot approaching a tunnel passage under rubble pile. B) Laser scanner captures high-resolution geometry data of all surfaces. C) Resulting “point cloud” of range data provides extremely accurate (ground-truth) model of actual rubble to support rubble classification and high-fidelity simulation environments for robot development and training.

Finally, this type of sensed data can provide a preview of the kinds of data that may become available through sensors mounted on robots. Whereas the sensors used to capture this data are large, heavy and can require up to an hour to capture a scan; smaller, lighter 3D imaging sensors that generate data at sufficient rates to support real-time robot operations are starting to enter the market. These devices will not provide as high a resolution nor cover as large an area, but they will be able to give responders a much clearer understanding of the configuration of interior spaces searched by robots rather than 2D

images alone. As automated or semi-automated algorithms to create maps of areas explored by robots become more capable, sensors that provide rich range information will be crucial.

The 3D image data collected during the responder event has been made available to researchers worldwide to foster development USAR robot development.

7. Conclusion

In this paper, we described an effort in which NIST is working with FEMA Task Force members to define performance requirements and standard test methods as well as to assess the deployment potential of robots applied to the USAR domain. This process has resulted in draft test method specifications based upon a well-defined set of robot requirements, which are currently making their way through the standardization process. This chapter also describes a set of knowledge representation efforts that are underway to make it easier for responders to easily determine the best robot for the environment in which they are confronted. These knowledge representation efforts range from fairly informal – a paper-based robot pocket guides which give high-level specification of robot characteristics to more formal – an ontology-based representations which allow users to search for the most appropriate robot based on a more comprehensive set of the robots characteristics. A complementary effort is attempting to quantify and characterize the environment into which the robots will be deployed. Taxonomies of buildings (pre and post-collapse) are being developed, as well as methods of deriving mathematical representations of the surfaces which the robots must cross.

Though much progress has been made, there is still much work to be done. The existing test methods still need to be further refined (with continual input from the responders) and continue through the standards development process. Additional test methods will be developed to address some of the additional requirements as the current ones continue to mature.

From the knowledge representation perspective, the pocket handbook is by far the most mature and has been given to the responders that have been involved in the previous evaluations. It will continue to evolve as feedback comes back from the responders and as more robots participate in future exercises. The structural collapse taxonomy and the robot capabilities ontology are earlier in the development process, and are still in the process of being populated with relevant information. Recent efforts in the robot capabilities ontology effort are focusing on developing/enhancing a front-end user interface (UI) to the ontology that would allow a responder to interact with the system using terminology that is familiar to them. A search engine will be developed that links the UI to the ontology to allow the responder to quickly find the best robot that meets his/her requirements.

8. References

- ASCE SEI (2003). 31-03 *Seismic Evaluation of Existing Buildings*, Reston, VA.
Burke, J., Murphy, R., Rogers, E., Lumelsky, V. & Scholtz, J. (2004). Final Report for the DARPA/NSF Interdisciplinary Study on Human-Robot Interaction. *IEEE*

- Transactions on Systems, Man, and Cybernetics - Part C: Applications and Reviews* Vol. 34, No. 2,
- Carlson, J., Murphy, R. & Nelson, A. (2004). Follow-Up Analysis of Mobile Robot Failures.
- Chatterjee, R. & Matsuno, F. (2005). Robot Description Ontology and Disaster Scene Description Ontology: Analysis of Necessity and Scope in Rescue Infrastructure Context.
- Federal Emergency Management Agency (2000). *Urban Search and Rescue Response System In Federal Disaster Operations: Operations Manual.*, 9356.1-PR,
- FEMA (2006). *National USAR Response System Structural Collapse Technician Training Manual.*,
- FEMA (2007). *HAZUS-MH*,
- Harmelen, F. & McGuiness, D. (2004). OWL Web Ontology Language Overview.
- Jacoff, A. & Messina, E. (2006). DHS/NIST Response Robot Evaluation Exercises.
Gaithersburg, MD.
- Joint Robotics Program (2005). Mobile Robots Knowledge Base.
- Kircher, C.A., Whitman, R.V. & Holmes, W.T. (2006). HAZUS Earthquake Loss Estimation Methods. *Natural Hazards Review* Vol. 7, No. 45,
- Messina, E., Jacoff, A., Scholtz, J., Schlenoff, C., Huang, H., Lytle, A. & Blitch, J. (2005). Statement Of Requirements For Urban Search and Rescue Robot Performance Standards.
- Molino, V., Madhavan, R., Messina, E., Downs, T., Jacoff, A. & Balakirsky, S. (2006). Traversability Metrics for Urban Search and Rescue Robots on Rough Terrains. Proceedings of the 2006 Performance Metrics for Intelligent Systems (PerMIS) Conference.
- Schlenoff, C., Washington, R. & Barbera, T. (2004). Experiences in Developing an Intelligent Ground Vehicle (IGV) Ontology in Protege. Bethesda, MD.
- Schneider, P.J., Schauer, B.A. & Pe, M. (2006). HAZUS – Its Development and Its Future. *Natural Hazards Review* Vol. 7, No. 40,
- The OWL Services Coalition (2003). *OWL-S 1.0 Release*,
<http://www.daml.org/services/owl-s/1.0/owl-s.pdf>,

Simplified Modelling of Legs Dynamics on Quadruped Robots' Force Control Approach

José L. Silvino¹, Peterson Resende¹,

Luiz S. Martins-Filho² and Tarcísio A. Pizzoli³

¹*Univ. Federal de Minas Gerais*, ²*Univ. Federal de Ouro Preto*, ³*Univ. Federal de Viçosa Brazil*

1. Introduction

The development of the service and intervention robotics has stimulated remarkable projects of mobile robots well adapted to different kinds of environment, including structured and non-structured terrains. On this context, several control system architectures have been proposed looking for the improvement of the robot autonomy, and of the tasks planning capabilities, as well reactive characteristics to deal with unexpected events (Medeiros et al., 1996; Martins-Filho & Prajoux, 2000). The proposed solutions to the locomotion on hazardous and strongly irregular soils include adapted wheels robots, rovers, robots equipped with caterpillar systems, and walking robots. Some of this robot designs are inspired on successful locomotion systems of mammals and insects.

The legged robots have obtained promising results when dealing with terrains presenting high degrees of difficulty. This is quite curious to notice that ideas concerning this robotic locomotion system have been present since the first idealistic dreams of the robotics history, and nowadays this approach has gained the interest and attention of numerous researchers and laboratories.

Let's mention some of the relevant works involving legged robots: Hirose et al. (1989) proposes an architecture for control and supervision of walking; Klein and Kittivatcharapong (1990) study optimal distribution of the feet-soil contact forces; Vukobratovic et al. (1990) work on the robot dynamics modelling and control; Pack and Kang (1995) discuss the strategies of walk control concerning the gaits; Perrin et al. (1997) propose a detailed platform and legs mechanisms modelling for the dynamics simulation; Tanie (2001) discusses the new perspectives and trends for the walking machines; Schneider and Schmucker (2001) work on force control of the complete robot mechanical system.

1.1 The Context of this Study

A walking robot can be described as a multibody chained dynamical system, consisting of a platform (the robot body) and a number of leg mechanisms that are similar to manipulator robotic arms. Considering the locomotion control of robots with significant masses, the main approaches are based on force control, this means that the leg active joints actuators produce torques and/or forces resulting on contact forces in the feet-soil contacts. For instance, this

principle of locomotion control can be seen in (Hirose et al., 1989; Martins-Filho & Prajoux, 2000; Schneider & Schmucker 2001). As a consequence, the system produces angular and linear accelerations on the chained mechanism components, and the robot moves to execute the required locomotion task.

Evidently, on this control approach, for the control of the walking robot position and velocity, the system should have the robot dynamics model to allow the efforts determination that must be produced by the joint actuators (Cunha et al., 1999). The dynamics model provides the relation between the robot state variables (acceleration, velocity, position) and the active joint torques/forces, taking into account the robot design, geometry, masses and inertias and other physical characteristics.

The main purpose of this work is the careful analysis of the effects of an eventual simplification on the dynamical equations of a small quadruped robot. The simplification effects are verified through the comparison between results of numerical simulations of the complete dynamical model, and of the simplified model, where the $C(q, dq/dt)$ and $G(q)$ are negligible.

The Fig. 1 shows the general aspects of the design of the considered quadruped robot. As can be seen, this robot is composed by a square platform, called the robot body, supported by four identical leg mechanisms. The mechanical design of each 3-joints leg is depicted on the Fig. 2.

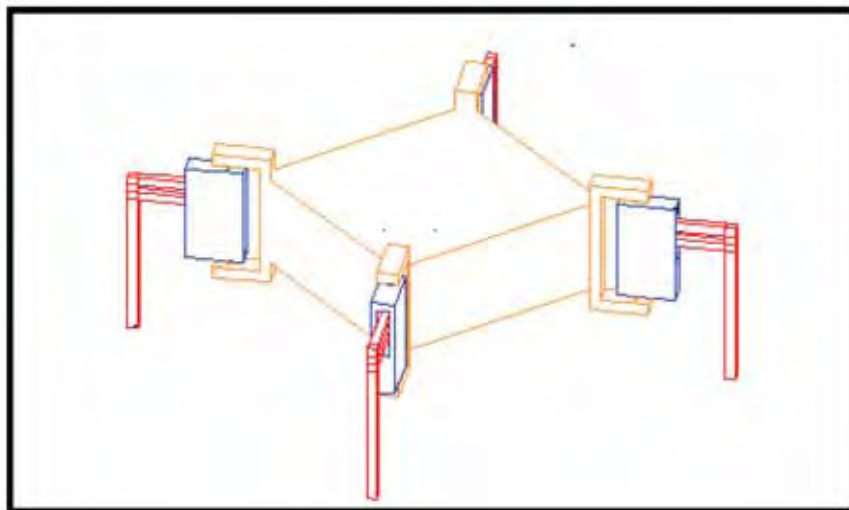


Fig. 1. The design of the studied quadruped robot

The Sect. 2 presents the dynamical model of the leg mechanisms, discusses the computation of important matrices appearing in this model, and analyses the workspace of the proposed leg design. The analysis of details of the dynamical model, that can be simplified considering the physical characteristics of the studied walking robot, is shown in Sect. 3. The following section (Sect. 4) describes the numerical simulations, and presents the obtained results and its analysis. The Sect. 5 closes the chapter with the work conclusions and comments about the future works on this research subject.

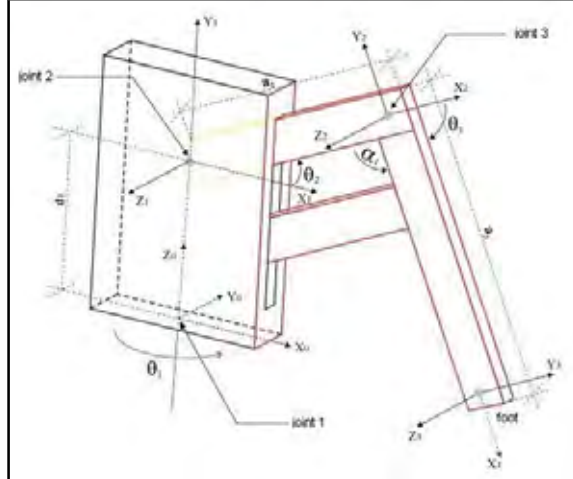


Fig. 2. The proposed prototype design of the leg mechanism

2. Dynamical Modelling of the Leg Mechanism

The leg mechanism model is based on the actuators dynamics, composed by servomotors and reductions gears, as well the friction effects on this active joints (Coulomb and viscous friction). Moreover, all the robot's links are taken as been completely rigid, a usual model assumption.

Let $q_i = \theta_i$ the i -th rotational joint angle, the complete state configuration of each leg is defined by a vector of generalized coordinates as follows:

$$q = [\theta_1 \quad \theta_2 \quad \theta_3]^T \quad (1)$$

Considering the kinematics energy, E_c , and the potential energy, E_p , the conservative Lagrangian for the system is given by:

$$L(q, \dot{q}) = E_c - E_p \quad (2)$$

And the equations of motion of this dynamical system are described as follows:

$$\frac{d}{dt} \left(\frac{\partial L}{\partial \dot{q}_i} \right) - \frac{\partial L}{\partial q_i} = Q_i \quad (3)$$

where $L(q, dq/dt) = E_c - E_p$, and Q_i is the vector of generalized force corresponding to the generalized coordinate q_i . The kinematics energy of each leg mechanism is obtained by the summation of the leg links energies, K_{ci} .

Considering the linear velocity of each link's centre-of-mass, the vector $d\mathbf{p}_i/dt$, and the angular velocity $\boldsymbol{\omega}$, the resulting equation is:

$$\begin{aligned}\dot{\mathbf{p}}_i &= J_{L1}^{(i)} \cdot \dot{\mathbf{q}}_1 + J_{L2}^{(i)} \cdot \dot{\mathbf{q}}_2 + J_{L3}^{(i)} \cdot \dot{\mathbf{q}}_3 \\ \dot{\boldsymbol{\omega}}_i &= J_{A1}^{(i)} \cdot \dot{\mathbf{q}}_1 + J_{A2}^{(i)} \cdot \dot{\mathbf{q}}_2 + J_{A3}^{(i)} \cdot \dot{\mathbf{q}}_3\end{aligned}\quad (4)$$

$J_{L1}^{(i)}, J_{L2}^{(i)}, J_{L3}^{(i)}$ are the i -th row vectors of the matrix J (dimension 3x3) for the linear velocities of the links 1, 2 and 3, and $J_{A1}^{(i)}, J_{A2}^{(i)}, J_{A3}^{(i)}$ are the i -th row vectors of the matrix J for the angular velocities of the links 1, 2 and 3. The kinematics energy of each link results of the translational and rotational terms:

$$K_i = \frac{1}{2} \dot{\mathbf{p}}_i^T \cdot m_i \cdot \dot{\mathbf{p}}_i + \frac{1}{2} \boldsymbol{\omega}_i^T \cdot I_i \cdot \boldsymbol{\omega}_i \quad (5)$$

where m_i and I_i are the mass and the inertia tensor expressed in the base coordinates system, respectively. Applying the results of Eq. (4) in the Eq. (5), the expression for the total kinetics energy of each three degrees-of-freedom leg.

$$K = \frac{1}{2} \sum_{i=1}^3 (\dot{\mathbf{q}}^T \cdot J_L^{(i)T} \cdot m_i \cdot J_L^{(i)} \cdot \dot{\mathbf{q}} + \dot{\mathbf{q}}^T \cdot J_A^{(i)T} \cdot I_i \cdot J_A^{(i)} \cdot \dot{\mathbf{q}}) \quad (5)$$

The term $H(\mathbf{q})$ can be defined as a symmetric square matrix based on the each link's tensor of inertia. Consequently, is possible to obtain:

$$H(\mathbf{q}) = \sum_{i=1}^3 (J_L^{(i)T} \cdot m_i \cdot J_L^{(i)} + J_A^{(i)T} \cdot I_i \cdot J_A^{(i)}) \quad (6)$$

The matrix $H(\mathbf{q})$ represents the mass characteristics of the leg mechanism. This matrix is called matrix of inertia tensor. The matrix elements $H_{ii}(\mathbf{q})$ are related to the effective inertias, and the $H_{ij}(\mathbf{q})$, with $i \neq j$, are related to the coupling inertia. Using these properties, the Eq. (5) can be re-written in a compact form:

$$K = \frac{1}{2} \dot{\mathbf{q}}^T H(\mathbf{q}) \cdot \dot{\mathbf{q}} \quad (7)$$

The potential energy E_p , considering a leg mechanism composed by rigid links, is function exclusively of the gravity. The vector \mathbf{g} represents the gravitational acceleration. The overall potential energy of each leg is given by:

$$E_p = \sum_{i=1}^3 m_i \cdot \mathbf{g}^T \cdot \mathbf{r}_i \quad (8)$$

where r_i is the position of the centre-of-mass of each link, described in the base coordinates system.

The Lagrangian formulation provides the motion equations of the robotic leg mechanism system, using the kinematics and potential energies, the forces and torques actuating on the leg (excluding the gravitational and inertial forces, i.e. the generalized forces). This formulation results in the following equation:

$$\frac{d}{dt} \left(\frac{\partial L}{\partial \dot{q}_i} \right) - \frac{\partial L}{\partial q_i} = \frac{d}{dt} \left(\frac{\partial E_c}{\partial \dot{q}_i} - \frac{\partial E_p}{\partial \dot{q}_i} \right) - \left(\frac{\partial E_c}{\partial q_i} - \frac{\partial E_p}{\partial q_i} \right) = Q_i \quad (9)$$

Considering that the derivative of E_c is obtained as follows:

$$\frac{d}{dt} \left(\frac{\partial E_c}{\partial \dot{q}_i} \right) = \frac{d}{dt} \left(\sum_{j=1}^3 H_{ij} \cdot \dot{q}_j \right) = \sum_{j=1}^3 H_{ij} \cdot \ddot{q}_j + \sum_{j=1}^3 \frac{dH_{ij}}{dt} \cdot \dot{q}_j \quad (10)$$

the time derivative of H_{ij} is given by:

$$\frac{dH_{ij}}{dt} = \sum_{j=1}^3 \frac{\partial H_{ij}}{\partial q_k} \cdot \frac{dq_k}{dt} = \sum_{j=1}^3 \frac{\partial H_{ij}}{\partial q_k} \cdot \dot{q}_k \quad (11)$$

$$\frac{d}{dt} \left(\frac{\partial E_p}{\partial \dot{q}_i} \right) = 0 \quad (12)$$

$$\frac{\partial E_c}{\partial q_i} = \frac{\partial}{\partial q_i} \left(\frac{1}{2} \sum_{j=1}^3 \sum_{k=1}^3 H_{jk} \cdot \dot{q}_j \cdot \dot{q}_k \right) = -\frac{1}{2} \sum_{j=1}^3 \sum_{k=1}^3 \frac{\partial H_{jk}}{\partial q_i} \cdot \dot{q}_j \cdot \dot{q}_k \quad (13)$$

$$\frac{\partial E_p}{\partial q_i} = \sum_{j=1}^3 m_j \cdot g^T \cdot \frac{\partial r_j}{\partial q_i} \quad (14)$$

For the Eq. (14), the partial derivative of r_{ij} with respect to q_i is equal to the j -th component of the i -th column of the Jacobian matrix J_l (linear velocities). The equation becomes:

$$\frac{dH_{ij}}{dt} = \sum_{j=1}^3 \frac{\partial H_{ij}}{\partial q_k} \cdot \frac{dq_k}{dt} = \sum_{j=1}^3 \frac{\partial H_{ij}}{\partial q_k} \cdot \dot{q}_k \quad (15)$$

This term is called gravitational term, and it is represented by G_i :

$$G_i = \sum_{j=1}^3 (m_j \cdot g^T \cdot J_{Li}^{(i)}) \quad (16)$$

Considering the original equation of the Lagrangian formulation (Eq. (9)), and taking into account the last developments, the resulting equation is given by:

$$\sum_{j=1}^3 H_{ij} \cdot \ddot{q}_j + \sum_{j=1}^3 \sum_{k=1}^3 h_{ijk} \cdot \dot{q}_j \cdot \dot{q}_k + G_i = Q_i \quad (17)$$

where $h_{ijk} = \partial H_{ij} / \partial q_k$

The Eq. (17) can be rewritten under a compact form as follows:

$$D(q) \cdot \ddot{q} + C(q, \dot{q}) \cdot \dot{q} + G(q) = u + J(q)^T \cdot F_e \quad (18)$$

$D(q)$ is a matrix 3×3 that represents the inertial torques, including the torques resulting of link interactions; $C(q, dq/dt)$ is a matrix 3×3 that represents the centrifugal and Coriolis forces; U is a vector 3×1 of control torques (to be defined by the robot control function), $J(q)$ is the Jacobian matrix, also with dimension 3×3 , and F is the vector 3×1 of generalized forces/torques produced by the environment of the work space (this vector is expressed in the base coordinate system) (Asada, 1986; Cunha et al. 1999).

2.1 Computation of the Matrices $D(q)$, $C(q, dq/dt)$ and $G(q)$

The locomotion system of the considered quadruped robot controls independently each one of the leg mechanisms and their active joints. As a consequence, the overall robot control can be divided into the leg subsystems and integrated by the resulting efforts on the hips, finally closing the chained system. Based on this principle, the modelling of robot dynamics will consider the leg mechanisms initially independently. For the derivation of this leg model, it's necessary to obtain the matrices $D(q)$, $C(q, dq/dt)$, and $G(q)$. These matrices expressions are determined by the equations of the direct kinematics for the proposed robot design. Adopting the Denavit-Hartenberg convention for manipulator robots (Spong & Vidyasagar, 1989), the direct kinematics provides the vector x of the leg-end position, $x = [x_p \ y_p \ z_p]^T$. The expression of this vector is:

$$x = \begin{bmatrix} x_p \\ y_p \\ z_p \end{bmatrix} = \begin{bmatrix} a_3 c_I c_2 c_3 - a_3 c_I s_2 s_3 + a_2 c_I c_2 \\ a_3 s_I c_2 c_3 - a_3 s_I s_2 s_3 + a_2 s_I c_2 \\ a_3 s_2 c_3 + a_3 c_2 s_3 + a_2 s_2 + d_I \end{bmatrix} \quad (19)$$

where a compact notation was adopted to simplify the equation: $c_i = \cos(\theta_i)$, $s_i = \sin(\theta_i)$, $c_{ij} = \cos(\theta_i + \theta_j)$, $s_{ij} = \sin(\theta_i + \theta_j)$. The Jacobian matrix $J(q)$ is determined as follows:

$$J = \begin{bmatrix} -a_2 s_I c_2 - a_3 s_I c_{23} & -a_2 c_I s_I - a_3 c_I s_{23} & -a_3 c_I s_{23} \\ a_2 c_I c_2 + a_3 c_I c_{23} & -a_2 s_I s_2 - a_3 s_I s_{23} & -a_3 s_I s_{23} \\ 0 & a_2 c_2 + a_3 c_{23} & a_3 s_2 c_{23} \end{bmatrix} \quad (20)$$

The linear and angular velocities of the leg links, with respect to their centres-of-mass, are given by:

$$\begin{aligned} p_1 &= \begin{bmatrix} 0 & 0 & 0 \\ 0 & 0 & 0 \\ 0 & 0 & 0 \end{bmatrix} \cdot q \\ p_2 &= \begin{bmatrix} -r_2 s_I c_2 & -r_2 c_I s_I & 0 \\ r_I c_I c_2 & -r_2 s_I s_2 & 0 \\ 0 & r_2 c_2 & 0 \end{bmatrix} \cdot q \\ p_3 &= \begin{bmatrix} -a_2 s_I c_2 - r_3 s_I c_{23} & -a_2 c_I s_I - r_3 c_I s_{23} & -r_3 c_I s_{23} \\ a_2 c_I c_2 + r_3 c_I c_{23} & -a_2 s_I s_2 - r_3 s_I s_{23} & -r_3 s_I s_{23} \\ 0 & a_2 c_2 + r_3 c_{23} & r_3 s_2 c_{23} \end{bmatrix} \cdot q \end{aligned} \quad (21)$$

$$\begin{aligned} w_1 &= [I \ 0 \ 0] \cdot \dot{q} \\ w_2 &= [I \ I \ 0] \cdot \dot{q} \\ w_3 &= [I \ I \ I] \cdot \dot{q} \end{aligned} \quad (22)$$

The matrix $D(q)$ can be now determined. Its expression is given by:

$$D(q) = (m_1 \cdot p_1^T \cdot p_1 + I_1 \cdot w_1^T \cdot w_1) + (m_2 \cdot p_2^T \cdot p_2 + I_2 \cdot w_2^T \cdot w_2) + (m_3 \cdot p_3^T \cdot p_3 + I_3 \cdot w_3^T \cdot w_3) \quad (23)$$

where m_1 , m_2 and m_3 are mass value of the links, and I_1 , I_2 and I_3 are the moments of inertia with respect to the centre-of-mass of each leg link.

The matrix $C(q, dq/dt)$ is composed by the elements h_{ijk} that are multiplied by the vector dq/dt . The elements h_{ijk} are determined using the matrix $D(q)$ thought the relation $h_{ijk} = (\partial D_{ij}/\partial \eta_k)$. Consequently, is possible to obtain:

$$C(q, \dot{q}) = \begin{bmatrix} \sum_{k=1}^3 h_{11k} \cdot q_k & \sum_{k=1}^3 h_{12k} \cdot \dot{q}_k & \sum_{k=1}^3 h_{13k} \cdot \ddot{q}_k \\ \sum_{k=1}^3 h_{21k} \cdot q_k & \sum_{k=1}^3 h_{22k} \cdot \dot{q}_k & \sum_{k=1}^3 h_{23k} \cdot \ddot{q}_k \\ \sum_{k=1}^3 h_{31k} \cdot q_k & \sum_{k=1}^3 h_{32k} \cdot \dot{q}_k & \sum_{k=1}^3 h_{33k} \cdot \ddot{q}_k \end{bmatrix} \quad (24)$$

The matrix $G(q)$ is given by the expression of the gravitational contributions $G_i = m_j g T J_{L_i}^{(i)}$.

Taking the equations of the system dynamics, the robot system states can be obtained directly by the expression of the joints acceleration d^2q/dt^2 . This expression is given by:

$$\ddot{q} = D(q)^{-1} \cdot [-C(q, \dot{q}) \cdot \dot{q}] + D(q)^{-1} \cdot [-G(q) + u + J(q)^T \cdot F_e] \quad (25)$$

On this expression, the matrix $D(q)$ is invertible. It's a consequence of the leg mechanism design, specially chosen to avoid the singularities and allowing the leg to produce the required efforts. The state vector $q = [q_1 \ q_2 \ q_3]^T$, denoting the joint variables, determines uniquely the foot position. This vector is obtained by integrating the Eq. (25).

2.2 The Workspace of the Leg Mechanisms

The workspace for a given legs configuration of the robot consists of all possible translations and rotations for the robot components (robot body and leg links). The physical constraints of each joint, as well the free space restrictions, are also considered for the workspace determination. We search the intersection of the so-called kinematic and static workspace to have the resultant workspace.

This approach is usually applied in geometry optimisation of the mechanism design, determination of the number of joints and selection of the active joints. It's also applied in the determination of forces and torques on the active joints, and computation of force distribution among supporting legs (Klein & Kittivatcharapong, 1990; Zhang et al., 1996a; Zhang et al., 1996b).

There are two methods that can be used to analyse the leg kinematic workspace: the forward analysis, and the inverse analysis. Forward analysis determines the workspace using a function of space configuration $w=f(q)$, with $q=[q_1 \ q_2 \ q_3]^T$, considering the physical limits for q . Inverse analysis determines the workspace through the inverse function, i.e. mapping the function $q=g(w)$ for a given mechanism position and orientation, and verifying if the configuration relative to q is located inside the allowed space.

The kinematic workspace in this work is investigated by the inverse kinematics equations. Four constraints must be taken into account in the kinematic workspace analysis of the leg mechanism: the joints coordinates, the leg velocity limit, the leg acceleration limit, and the geometric interference of the leg.

Considering the performance of the present available actuators, and the development of geometric studies concerning the robot platform, we can say that the main constraints to the velocity and acceleration limits of the leg movements are the physical joints limits and its

geometric interference (Zhang et al., 1996a). Therefore, the problem constraints can be expressed by:

$$\theta_{\min} \leq \theta_{ij} \leq \theta_{\max} \quad (26)$$

where θ_{ij} is the j -th joint of the i -th leg. Rewriting this equation using a vector of kinematics' constraints, we have:

$$q_{\min} \leq q_j \leq q_{\max} \quad (27)$$

where $q_{\min} = [\theta_{1\min} \ \theta_{2\min} \ \theta_{3\min}]^T$ and $q_{\max} = [\theta_{1\max} \ \theta_{2\max} \ \theta_{3\max}]^T$.

The variation of θ_{ij} angles for a specific i -th leg is function of the robot body position and orientation. The i -th foot position can be obtained by inverse analysis. Considering the feet positions, the position and the orientation of the robot body, we can compute $q = [q_1 \ q_2 \ q_3]^T$. The difference vectors, $\Delta q_{\max} = q_{\max} - q_i$ and $\Delta q_{\min} = q_{\min} - q_i$, are used to determine when a boundary point is attained, i.e. if Δq_{\max} or Δq_{\min} is a null vector the leg configuration is on a workspace frontier. Scanning all the joint angles ranges, the total workspace of the leg mechanism is determined (Zhang et al. 1996a).

On the other hand, the study of the robot static workspace considers three types of constraints: the limits of force and torque on active joints, the maximum and minimum reaction forces on the soil-feet interface, and static friction coefficient of the feet-soil contact.

The expression of these constraints, considering the j -th joint of the i -th robot leg, is given by:

$$\begin{aligned} F_{\min} &\leq F_{ij} \leq F_{\max} \\ T_{\min} &\leq T_{ij} \leq T_{\max} \\ f_{\min} &\leq f_{iz} \leq f_{\max} \\ \mu_t &= f_{xy} / f_z = (f_x^2 + f_y^2)^{1/2} / f_z \leq \mu \end{aligned} \quad (28)$$

where F_{ij} is the joint force, T_{ij} is the joint torque, f_{iz} is the reaction force on the soil-foot interface, and μ is the static friction coefficient. The ratio μ_t between the tangent and normal components of the reaction force on the soil-foot contact must respect the friction constraint, i.e. $\mu_t \leq \mu$ (Klein & Kittivatcharapong, 1990; Martins-Filho & Prajoux, 2000; Zhang et al., 1996b). For the analysis of the constraints listed above, we consider the static constraint vector defined by:

$$\begin{aligned} c_{\max} &= [F_{\max}^T \ T_{\max}^T \ f_{\max}^T \ \mu] \\ c_{\min} &= [F_{\min}^T \ T_{\min}^T \ f_{\min}^T \ \mu] \end{aligned} \quad (29)$$

Considering the feet positions, the position and the orientation of the robot body, we can compute $c = [F_{ij}^T \ T_{ij}^T \ f_{ij}^T \ \mu_t]^T$. The difference vectors, $\Delta c_{max} = c_{max} - c_i$ and $\Delta c_{min} = c_{min} - c_i$, are used to determine when a boundary point is attained, i.e. if Δc_{max} or Δc_{min} is a null vector the leg configuration is on a workspace frontier. Scanning all the c vector range, the total static workspace of the leg mechanism is determined (Zhang et al. 1996b).

Graphical representations of the kinematic and static workspaces, considering the adopted quadruped robot and leg mechanisms design, are shown in the Fig. 3 and Fig. 4, respectively.

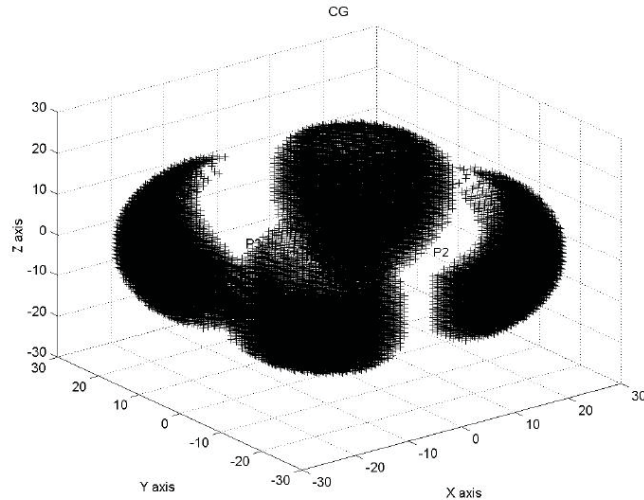


Fig. 3. The kinematic workspace of the studied quadruped robot

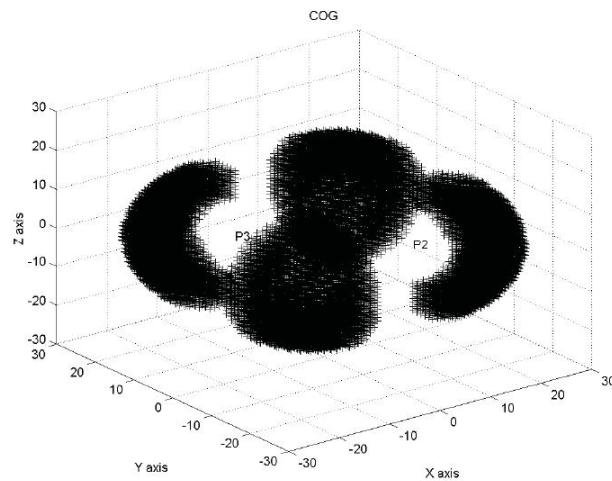


Fig. 4. The static workspace of the studied quadruped robot

3. Analysis of Matrices $C(q, dq/dt)$ and $G(q)$

The position control problem of a system represented by the Lagrangian formulation can be solved through the application of a PD (proportional plus derivative) control approach. The PD control law is defined to determine the control torque to be produced on the active joints (Bucklaew et al., 1999). The expression of this proposed control is given by:

$$u = K_p \cdot \tilde{q} + K_d \cdot \dot{\tilde{q}} \quad (30)$$

where K_p and K_d are positive define matrices with constant gain values, and $\tilde{q} = (q_d - q)$ is the position error.

Applying this control law on the expression of d^2q/dt^2 , the vector dq/dt can be determined, and the vector q , the leg joints state, is available by integrating the differential equation. In this equation, the matrices $C(q, dq/dt)$ and $G(q)$ appear explicitly. These matrices must be computed at each new value of q and dq/dt , and these quantities change continuously with the time. For a system with tree degrees-of-freedom or more, as the case of the robot considered in this work, the computation requires a considerable number of arithmetic operations and amount of time of controller processing. This system is supposed to be working on real-time, and this computation charge and time can represent a difficulty or trouble.

The elements of the matrix $C(q, dq/dt)$ are computed using the matrix $D(q)$. And this matrix $D(q)$ is a function of the links' masses, of the linear and angular velocities of these links, and it is also a function of the links' moments of inertia (taken on their own centres-of-mass). It is computed at each variation step of q . If the masses of the robot's links are small comparing to the body mass, that's the case of the quadruped robot considered in this work, the respective moments of inertia are also small. Analysing the velocities, the linear and the angular, we see that if the robot is moving relatively slow (that's the case of when the robot is performing a safe and stable gait), these velocities values are low. The contribution of another term, the Coriolis force, is dependent of the link velocity, consequently the relative significance of the matrix $C(q, dq/dt)$ is low. The same conclusion can be taken of the analysis of the matrix $G(q)$, the gravitational contribution, that's a direct function of the links' masses.

4. Numerical Simulations and Results

The proposed model simplification was tested through numerical simulations. The motion of the robotic leg mechanism was simulated using two dynamical modelling, the complete one and the simplified one. For these simulations, a closed loop control scheme was defined applying the PD strategy to define the active joints torques to be produced by the servomotors. The control of the leg motion aims to track desired trajectories of the joint angles vector. The analysis of the results is based on the comparative performance of the two different models and on the verification of the tracking errors.

The simulation scenarios are defined in terms of leg manoeuvres involving the three active joints of the mechanism, taking into account the leg workspace limits. The values of the mechanism's physical parameters are defined based on a realistic future realization of a leg

prototype. These parameters and the respective values considered on the numerical simulations are shown in the Tab. 1.

extension of lifting and landing (m)	0.10 ± 0.010
displacements (m)	longitudinal: 0.08 ± 0.008 vertical: 0.06 ± 0.006 lateral: 0.05 ± 0.005
loads (kg)	vertical: 4.5 ± 0.45 horizontal: 1.0 ± 0.1 lateral: 0.5 ± 0.05
geometrics dimensions (m)	first link: 0.12 ± 0.012 second link: 0.08 ± 0.008 link thickness: 0.02 ± 0.002
number of joints	3
weight (kg)	2.0 ± 0.2

Table 1. The considered values of the leg mechanism's parameters

The first manoeuvre concerns the first joint, commanding the corresponding servo from an initial configuration $q_{init} = [\theta_1 \ \theta_2 \ \theta_3]^T = [0^\circ \ 0^\circ \ 90^\circ]^T$ to a final configuration $q_{fin} = [\theta_1 \ \theta_2 \ \theta_3]^T = [45^\circ \ 0^\circ \ 90^\circ]^T$, and returning to the initial configuration. The results for the numerical simulation of the complete model and the simplified model can be seen in Figs. 5 and 6, respectively.

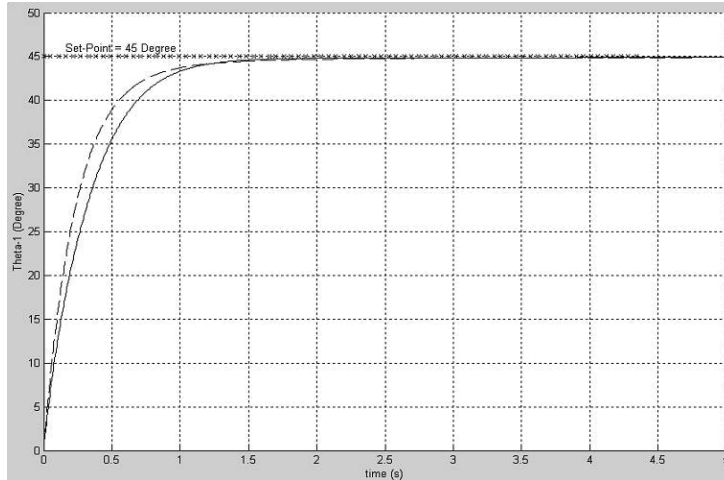


Fig. 5. Results of numerical simulation of the first step of the first manoeuvre (complete model “—” and simplified model “---”)

In the second manoeuvre, the leg mechanism was commanded using the second joint. The servo departs from an initial configuration $q_{init} = [\theta_1 \ \theta_2 \ \theta_3]^T = [90^\circ \ 0^\circ \ 50^\circ]^T$ and it is commanded to a final configuration $q_{fin} = [\theta_1 \ \theta_2 \ \theta_3]^T = [90^\circ \ 30^\circ \ 50^\circ]^T$, and returning to the

initial configuration. The results for the numerical simulation of the complete model and the simplified model can be seen in Figs. 7 and 8, respectively.

In the third and last manoeuvre, the leg mechanism was commanded using the third joint. The servo departs from an initial configuration $q_{init} = [\theta_1 \ \theta_2 \ \theta_3]^T = [90^\circ \ 0^\circ \ 90^\circ]^T$ and it is commanded to a final configuration $q_{fin} = [\theta_1 \ \theta_2 \ \theta_3]^T = [90^\circ \ 30^\circ \ 45^\circ]^T$, and returning to the initial configuration. The results for the numerical simulation of the complete model and the simplified model can be seen in Figs. 9 and 10, respectively.

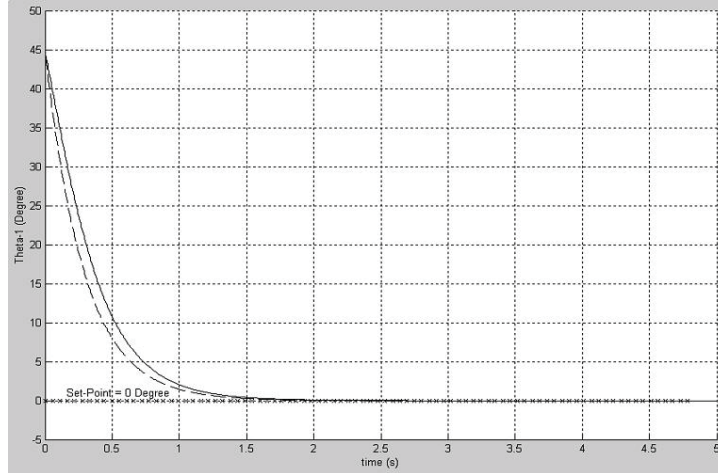


Fig. 6. Results of numerical simulation of the second step of the first manoeuvre (complete model “—” and simplified model “- - -”)

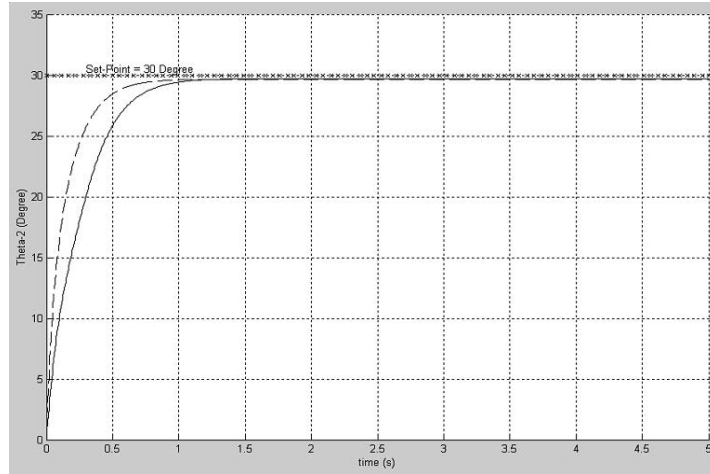


Fig. 7. Results of numerical simulation of the first step of the second manoeuvre (complete model “—” and simplified model “- - -”)

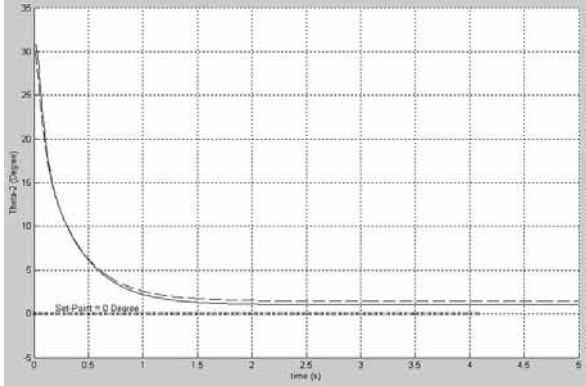


Fig. 8. Results of numerical simulation of the second step of the second manoeuvre (complete model “—” and simplified model “---”)

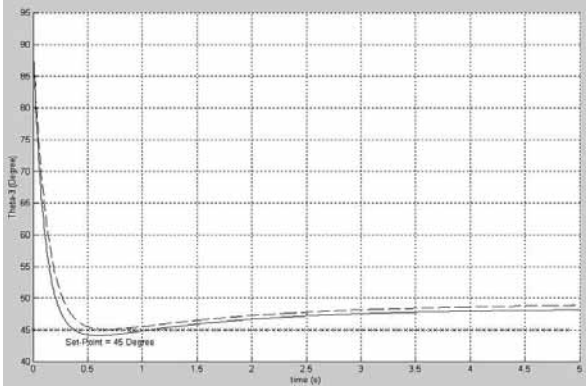


Fig. 9. Results of numerical simulation of the first step of the third manoeuvre (complete model “—” and simplified model “---”)

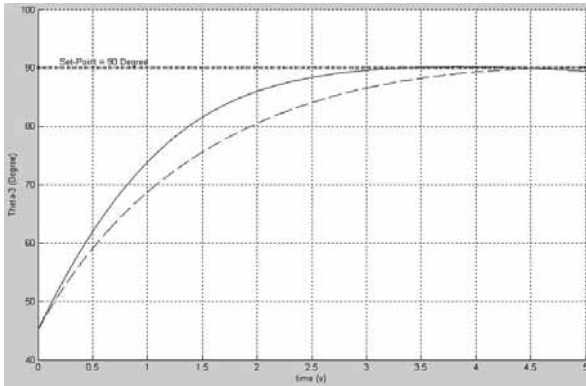


Fig. 10. Results of numerical simulation of the second step of the third manoeuvre (complete model “—” and simplified model “---”)

Considering the obtained results of numerical simulations (see Figs. 5, 6, 7, 8, 9 and 10), we can verify that the dynamical responses are approximately similar for the two models of the robot dynamics, with and without the matrices $C(q, dq/dt)$ and $G(q)$. The difference between the two models are limited to around 2 degrees on the steady state behaviour of the amplitude, and a delay around 10 degrees on the transitory phase.

As an immediate consequence, the number of calculation operations for the determination of the value of robot's joints state, using the system accelerations, is significantly reduced. In terms of computation time, the estimation of gain is around 9% of reduction.

5. Conclusion

In this work, a dynamical model simplification was implemented and analysed considering a small quadruped mobile robot, equipped with pantographic leg mechanisms. This specific leg design and characteristics were considered, as well the context of realistic possible physical realization (dimensions, masses, inertias) of a laboratory prototype. A simplification was proposed aiming the reduction of computational efforts for the evaluation of the matrices $C(q, dq/dt)$ and $G(q)$, corresponding respectively to the centrifugal and Coriolis forces, and to the gravitational dynamical contributions.

The resulting advantages of the presented proposition were verified when comparing the numerical simulations of the leg mechanism motions taking the complete and simplified models. The obtained results of dynamical performance for both cases are very similar, i.e. the difference is around 1 degree on steady state, and a delay bellow 2 degrees on the transitory phase. On the other hand, the computation time reduction using the simplified model is quite expressive (around 9%). These two facts confirm the validity of using the proposed simplified model, it can be useful on experimental applications of locomotion control approaches based on the dynamical model of the walking robot. For instance, this time reduction can be advantageous for pre-computed torque and feedforward control approaches. Considering the critical requirements of the real-time control of a complex system as a legged mobile robot.

The future works include the construction of the leg mechanism and robot prototypes, the application of the simplifications proposed here on this experimental legged robot, and the analysis of this system performance using diverse force control approaches.

6. References

- Asada, H. and J. J. E. Slotine (1986). *Robot Analysis and Control*. Ed. Wiley-Interscience Publications, New York, USA.
- Baroni, P., G. Guida, S. Mussi and A. Venturi (1995). A distributed architecture for control of autonomous mobile robots. *Proceedings of IEEE International Conference on Robotics and Automation*. Nagoia, Japan.
- Bucklaew, T. P. and C.-S. Liu (1999). A new nonlinear gain structure for PD-type controllers in robotic applications. *Journal of Robotic Systems*, Vol. 16, No. 11, pp. 627-649.
- Craig, J. J. (1986). *Introduction to Robotics Mechanics and Control*. Ed. Addison Wesley Publishing Company, Stanford University, USA.

- Cunha, A.C., C. C. Bier, D. Martins and F. Passold (1999). Metodologia seqüencial para simulação numérica de técnicas de controle para robôs manipuladores (*in português*). *Proceedings of Iberian Latin-American Congress on Computational Methods in Engineering*. EPUSP, São Paulo, Brazil.
- Fu, K. S.; R. C. Gonzalez and C. S. G. Lee (1987). *Robotics: control, sensing, vision and intelligence*. Ed. McGraw-Hill Book Company, New York, USA.
- Hirose, S., K. Yoneda, R. Furuya and T. Takagi (1989). Dynamic and static fusion control of quadruped walking vehicle. *Proceedings of IEEE International Conference on Intelligent Robots and Systems*. Tsukuda, Japan.
- Klein, C.A. and S. Kittivatcharapong (1990). Optimal force distribution for the legs of a walking machine with friction cone constraints. *IEEE Transactions on Robotics and Automation*. Vol. 6, No. 1, pp. 73-85.
- Martins-Filho, L. S. and R. Prajoux (2000). Locomotion control of a four-legged embedding real-time reasoning in the force distribution. *Robotics and Autonomous Systems*, Vol. 32, No. 4, pp. 219-235.
- Medeiros, A.D., R. Chatila and S. Fleury (1996). Specification and validation of a control architecture for autonomous mobile robots. *Proceedings of IEEE International Conference on Intelligent Robots and Systems*. Osaka, Japan.
- Schneider, A. and U. Schmucker (2001). Forced legged platform KATHARINA for service operations, *Proceedings of the International Conference on Climbing and Walking Robots*, Karlsruhe, Germany.
- Spong, M. W. and M. Vidyasagar (1989). *Robot Dynamics and Control*. Ed. John Wiley and Sons, New York, USA.
- Tanie, K. (2001). New trends of walking robotics research and its application possibilities, *Proceedings of the International Conference on Climbing and Walking Robots*, Karlsruhe, Germany.
- Zhang, D.J. Sanger and D. Howard (1996), Workspaces of a walking machine and their graphical representation. Part I : Kinematic Workspaces, *Robotica*. Vol. 14, No. 1, pp. 71-79.
- Zhang, S.J., D.J. Sanger and D. Howard (1996), Workspaces of a walking machine and their graphical representation. Part II : Static Workspaces, *Robotica*. Vol. 14, No. 2, pp. 219-226.

The Bio-Inspired SCORPION Robot: Design, Control & Lessons Learned

Spenneberg Dirk and Kirchner Frank

*DFKI- German Research Center for Artificial Intelligence, Robotics Lab
University of Bremen, Faculty of Mathematics and Computer Science
Germany*

1. Introduction

This chapter will review the SCORPION robot project (Kirchner et al., 2002). The goal of the SCORPION robot project was the development of a very robust eight-legged robot, which is capable to traverse very steep and unstructured terrain without high-level planning or using complex exteroceptive sensors, e.g., a laserscanner.

The SCORPION robot is now a field-tested system which was successfully deployed in various kinds of outdoor terrain (e.g. rocky, sandy).

Currently, the SCORPION robot design is in discussion to be used in future extraterrestrial exploration missions into steep craters on the Moon or Mars (Spenneberg et al., 2004).

In the following sections we will describe the steps we undertook to achieve this goal.

In Section 2, we will describe the different mechatronical design steps and discuss briefly the problems faced and the solutions developed.

Then we will discuss in section 3 the different possibilities for a control approach of a legged outdoor robot and describe the developed hybrid bio-inspired approach (Spenneberg, 2005a), which combines posture control with CPG (Central Pattern Generator)-based control and reflex control.

Subsequently, we will discuss the achieved performance. Concluding, we will discuss the lessons learned and future steps to utilize the full potential of walking and climbing robots (section 4).

2. Mechatronical Development

For the development of the SCORPION robots, real scorpions have been used as an archetype. Scorpions belong to the class of spiders and have eight legs.

The SCORPION project started in 1999.

Since then, one integration study and four systems have been built in an iterative design approach to achieve the final robustness of SCORPION IV.

Integration Study (1999)

Source: Climbing & Walking Robots, Towards New Applications, Book edited by Houxiang Zhang,
ISBN 978-3-902613-16-5, pp.546, October 2007, Itech Education and Publishing, Vienna, Austria

The first full system which was built was the integration study in autumn of 1999 (see Fig. 3). This system was used to test the interaction between electronics and the first software concepts together with a first version of 3DOF (degrees of freedom)-legs.

The legs consisted of a thoracic joint for pro- and retraction, a basalar joint for elevation/depression of the leg, and the distal joint integrated into the basalar segment driving the distal segment via a bevel gear (see Fig. 1).

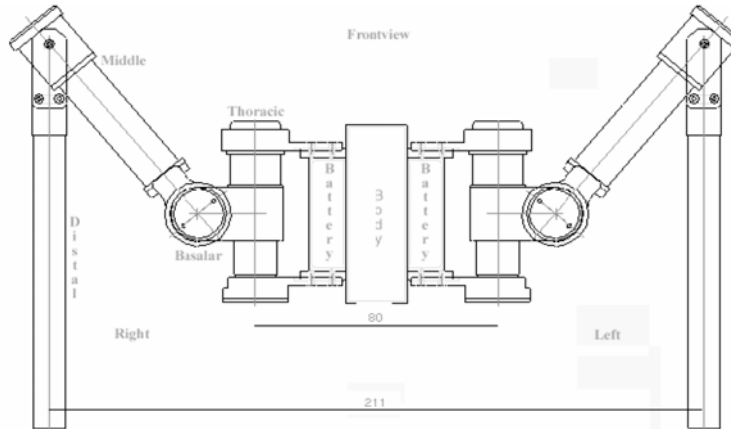


Fig. 1. The mechanical design of the SCORPION legs. This front view of the robot shows left and right side legs with the body (SCORPION II) in the center. Each leg consists of 5 parts: 1) thoracic joint, 2) basalar joint, 3) distal joint, which is integrated into the middle segment driving the distal segment via a bevel gear.

This reduction of down to three DOFs is supported by studies on real scorpions (Bowerman, 1975), which describe that mainly only three joints are used for ground locomotion. (Ayers, 2002) and (Cruse et al., 1999) are supporting the idea that for an adequate model of invertebrate walking three joints per leg are sufficient. The existing additional joints are mainly used by the animals for other functions, e.g., ingestion or prey hunting.

The legs of the integration study have been developed using mainly light composite materials, e.g., POM and small 10mm motors with plastic gears. The developed control hardware consisted of custom-made microcontroller boards featuring C164 and C167 boards.

The integration study has been used for aerial walking tests on a supporting stand.

It has been extremely useful to test the low-level software drivers and first locomotion control concepts very early in the project. Furthermore, it allowed testing the concepts of using nine microcontrollers in a network. Eight C164, one controlling one leg, were used and one C167 for the central control and to interface the robot to an external operator. These microcontrollers were connected via a CAN-Bus.

Figure 2. depicts this hardware architecture which was used till SCORPION III.

This configuration allowed high flexibility for simple testing of different concepts thus ensuring fast software development.

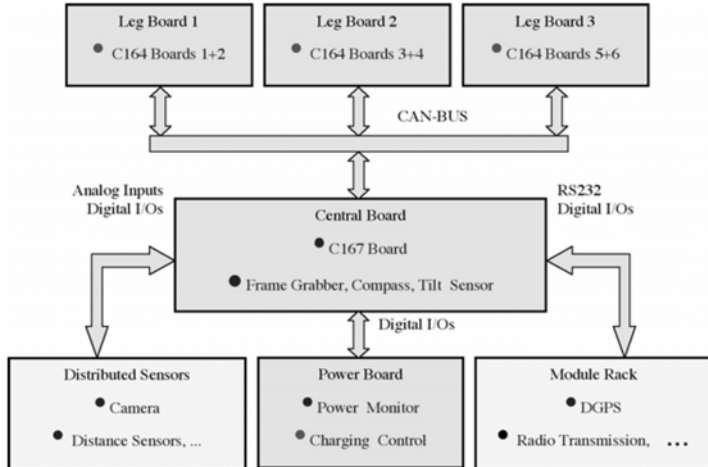


Fig. 2. Hardware architecture of the Integration Study and SCORPION I-III

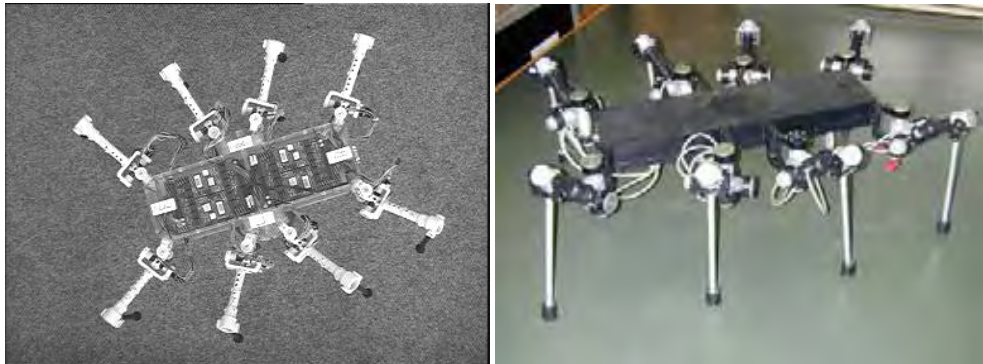


Fig. 3. (a) SCORPION Integration Study

(b) SCORPION I

SCORPION I (2000)

In the meantime, a new leg and corpus design was developed which resulted in the first robot prototype "SCORPION I", weighting 9.5 kg. It used 18mm motors of the company Faulhaber with approx. max. 2Nm torque each.

The design of the legs was fully shielded with special gaskets to allow outdoor deployments.

For the mantle material of the legs aluminium was introduced. Because of the shielded design the system was able to work underwater, too. Fig. 3. (b) shows the robot.

The new motor-gear combinations produced enough force to carry the body, but the bevel gear in the distal segment were worn out after a dozen operation hours, because the production accuracy of the bevel gear modules had been too low (this was addressed in SCORPION II).

Thus, as a simple solution, we fixed the distal joint in a position where it was perpendicular to the ground in an M-shape position (like in Fig. 1) and used only the upper two joints for

further experiments. In this configuration, with using only two motors per leg, the robot was able to walk up to 10cm/s and inclination up to 10°. It was furthermore able to overcome obstacles up to 5cm.

The sealing of the system worked very well, but if you are in the early development of a robot, we recommend not sealing a system, because of the disadvantages regarding maintenance time.

A further result of the experiments was that the basalar joints were working in most experiments at their limits. Due to the body, the contact points of the contra-lateral legs were too far away from each other. This resulted in a lever applying high forces to the basalar joint for just keeping the body above the ground. To reduce this, the next system needed to be more slender.

SCORPION II (2000)

In the winter of 2000 SCORPION II (see Fig. 4) addressing the above described problems was completed.

A mayor challenge in the design of the leg modules was the constraint to build an outdoor-capable walking machine with shielded actuators while at the same time achieving a good ratio between the leg weight and its lift capacity. In the design of SCORPION II we have achieved a ratio of 1:8 incorporating shielding from the environment. This was possible by using high ratio planetary gears in combination with a new powerful DC-motor resulting in 3.5 Nm max torque. The increased ratio was necessary as we intended to be able to climb obstacles, which would exceed the robot's own height. Thus, in certain situations single legs would have to be able to pull/push at least 3/4 of the robot's weight.

Another aspect in leg design is the speed of the leg to react fast enough to disturbances from the environment. So simply increasing the gear ratio does help to gain the torques desired but it also decreases the reactive speed of the module.

To fulfill all of these goals, we increased the produced torque and speed of the actuators by using the new 22mm motors from Maxon Motors and kept the gear ratio we used in SCORPION I.

Another optimization, which was conducted to increase the outdoor robustness, was to pass the cable harness mainly through the inner leg (via new inner cable ducts) instead of keeping it outside of the leg. This significantly reduced the risk of getting entangled with the leg.

In addition, we developed a slender aluminium-body aimed at maximum stability and easy maintenance.

In its side-pockets, this system contained NiCD-batteries with 28.8 V and 1.8Ah enabling an operation of 30 minutes with full speed of 20cm/s. It was able to climb up inclinations of 15° and to overcome obstacles up to 20cm.

The system was equipped with an ultrasound-sensor in the front and a camera-system as well at the front as on an optional sting which was connected to the back of the robot. To control the robot it was equipped with a bidirectional DECT-radio-link. In addition to the basic motion control featuring CPG, posture, and reflex control (see section 3), the software of this system included first higher level behaviours, e.g. autonomous obstacle avoidance and a balancing behaviour based on integrated inclinometers.



Fig. 4. SCORPION II in the SWRI rockchannel



Fig. 5. SCORPION II as a six-legged system

This system was matured to a degree that realistic outdoor tests were conducted, e.g. on the Small Robotic Vehicle Test Bed of the Southwest Research Institutes (SWRI) in San Antonio (TX, USA). These tests gave valuable input for the next design steps. In principle, such outdoor tests carried out together with impartial observers and on an unknown test site are extremely helpful during such projects. They help to identify very quickly the real performance of systems which normally are tested only under lab conditions.

On the basis of the eight-legged design, for comparison tests a shorter six-legged version was built. In Fig. 5. this version with an additional pack of batteries is shown. The major result of this comparison is that due to the reduced weight the six-legged version is faster on flat terrain, but because of the loss of static stability in comparison to the eight-legged robot, the six-legged one is slower in steep terrain. There, its walking patterns have to be reduced to low-frequency patterns, where at any point of time only one leg is in the air in order to keep the necessary stability.

SCORPION II was already a robust system, but some of the outdoor tests showed that the rigid body was a source of problems, e.g. for steep stair-climbing. Furthermore, the system lacked a good sensor for ground contact detection, which led to a suboptimal stance motion in uneven terrain. At that moment it was only possible to monitor the temporal behavior of the current of the basalar joint to estimate whether the ground was hit, which is very unreliable without a model of the robot in its environment.

In addition to this, the system had no compliance yet, which resulted in undamped external forces which were sometimes higher than the specified maximum forces for the gears, thus reducing the lifetime of the legs.

SCORPION III (2001)

Therefore a different design was developed to address these issues, which resulted in SCORPION III finished in autumn 2001.

As opposed to the other SCORPION robots, this system did not have one single rigid body but consisted of three body segments linked by rubber buffers. This design enabled the system to adapt automatically to its environment, which on the one hand is an advantage regarding shock reduction and ground adaptivity, but on the other hand a problem for the control, since the body deformation has to be taken into account.



Fig. 6. The flexible SCORPION III



Fig. 7. SCORPION IV

Therefore, for such a construction we advise to implement sensors to measure the deformation.

Another change was to remove the bevel gear design to actuate the distal segment. SCORPION III used three identical motor tubes for each joint (see Fig. 6.) which reduced production- and maintenance-costs.

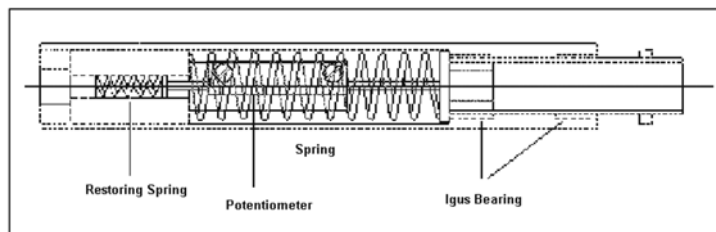


Fig. 8. New compliant distal segment

In addition, compliance was integrated into the distal segment of a leg (see Fig.). The distal segment was manufactured as spring damped chamber with a built-in potentiometer. This approach enabled us to measure, contact, and load on individual legs, while the spring mechanisms acted as a damping component to reduce in combination with the flexible body the impact of high forces on the leg.

During the SCORPION project we were not able to thoroughly enhance and test this design, because the new, longer planned, and light-weight MPC555+FPGA controller board, which was optimized for our computational needs and replaced the network of five boards with nine microcontrollers (see Figure 2.) became available by spring of 2002.

Due to its length of approx. 40cm, it did not fit the design of the SCORPION III.

Therefore, we stopped working on SCORPION III, which is a very interesting system and if it would be equipped with sensors to measure the deformation and appropriate models for feeding this information into the control loop, it would be a very robust and adaptive system.

SCORPION IV (2002)

Most of the enhancements from SCORPION III entered the design of SCORPION IV.

For SCORPION IV (see Fig. 7.), the body concept of SCORPION II was slightly modified to be equipped with 3.0Ah, 28.8V NiMh batteries in the side pockets and with the new hardware board (see Fig. 9.) which was introduced in spring of 2002.



Fig. 9. SCORPION control board featuring an MPC555 and a Xilinx Virtex E FPGA

This six-layered board combines all features of the former control boards and provides additional options. In comparison to the former control network, it saves 1.5kg and 60% of the volume. Its speciality is the usage of a reprogrammable FPGA to read in all signals from up to 32 joints: motor current, position, as well as the values from the pressure sensors. These values are used in a PID-controller (control frequency of 2 KHz) programmed into the FPGA to produce PWM-signals for the control of up to 32 motors.

The main features are:

- 40Mhz 32Bit MPC555 Power PC Microcontroller with MIOS & CapCom-Units,
- 64 TPU-Channels, 2 CAN-Interfaces, 3 serial ports
- Up to 81 A/D-channels
- Virtex E XCV400E (432 Pins) FPGA with approx. 570.000 gates connected directly to the memory bus of the MPC555 – data exchange via an Dual-Port RAM which is programmed into the FPGA
- 8 MB Flash EEPROM, 4 MB SRAM memory on-board
- 32 DC-motordrivers (right side of the picture) with up to 5A max.
- 32 on-board current sensors
- 1.8V, 3.3V, 5V und 15V power supply
- 12-36V operating voltage, power consumption <6W
- Direct programming of the FPGA form the MPC555 via SelectMAP Mode (time < 1s)

This board allowed reducing the width and length of the SCORPION II design.

To increase the stability of the system and to reduce weight, the body of SCORPION IV got a rib-design. This also increased the ability to dissipate heat.

In principle, the design shown in Fig. 7. is the design of the SCORPION robot till today.

In the following years, minor modifications to improve the performance were carried out.

We integrated a two-spring-system into the legs for increased sensor response of the ground sensor and better shock-reduction. Furthermore, in all systems we used motor encoders for the joint position measurement, which meant that calibration was needed. In 2003 we exchanged these with high-precision potentiometers, which are working very reliable.

Summing up we can say, that the iterative development approach was a full success. The SCORPION IV system is still in use and part of research projects, where we are using this robot for crater exploration experiments in the context of space applications. A copy of this system is also installed at the NASA Ames research centre.

The performance results gained with this system are described in section 4, following our discussion of the control approach.

3. Development of the Control Approach

There are already a lot of different approaches for controlling locomotion in multipods. These approaches can be divided into three different groups.

The first group contains all those approaches which are using as accurately as possible physical models for the exact control of kinematical chains like the model-based approaches for industrial manipulators (model-based approach).

The second group comprises all approaches which are using in their core bio-inspired control mechanisms (bio-inspired approach).

The third group enfolds adaptive approaches which are using learning algorithms to develop locomotion control mechanisms (adaptive approach).

Examples for the adaptive approach are

- (Kirchner 1998) using a hierarchical Q-learning for evolving a goal-directed walking behaviour on the six-legged robot "Sir Arthur".
- (Maes 1990) describing an early locomotion learning experiment on the walking robot "Genghis" based on positive and negative feedback and elementary locomotion building blocks.
- (Ispeert 2005) describing the use of evolutionary algorithms to develop locomotion mechanisms for a salamander robot on the basis of oscillator models.

The work on adaptive approaches is interesting, but, in principle, here the walking robots are only used as a case study for more general learning algorithms. The work on using learning algorithms for walking robots does not provide us with a general architecture for programming walking robots. Thus, in the following, we will focus deeper on the bio-inspired and model-based approaches and compare them.

Examples for the model-based approach are

- (Loeffler 2003) describing a control approach with three different layers. On the highest layer, the trajectories for the limbs of the two-legged robot Johnnie are computed. This is based on three basic walking patterns: standing, walking, jogging. These patterns are divided into their different phases (e.g. swing-, stance-phase). For all of the walking patterns, optimized trajectories are computed offline and can be accessed from an online-table. Because of deviations, an additional reduced dynamic-model was implemented (second level) on an external Pentium III (800 Mhz) which is fed with the data from the orientation sensor and used to

compute adaptations of the joint trajectories. On the lowest level, a PID-controller is implemented which controls the joint.

- (Go 2005) is a recent example of using a kinematical model for the control of a six-legged robot. Because of the needed constraints to find a closed solution for the inverse kinematical problem, this algorithm cannot be used in uneven terrain. It assumes for example that the body coordinate system is kept parallel to the ground all the time, which is impossible on uneven terrain. In addition, slippage at the foot tips is not foreseen in the model.

What is described in (Go 2005) is a general problem of the model-based methods. They normally lack the information required from the environment in order to model exactly the behaviour of the system in its corresponding surroundings and, furthermore, they are computational expensive. Without well-defined constraints like used in (Go 2005), a closed solution cannot be found, resulting in applying very time-consuming iterative methods which are unusable for real-time control.

If we look at systems like the SCORPION robot, the use of a model-based approach seems also extremely prudent because these multipods are statically stable in almost every situation. This means that at every time step the system can be frozen in its motion while at the same time keeping its current position and orientation. Taking a two-legged or four-legged system this is more often than not the case, so that one has to take the dynamics into account.

But for a six- or eight-legged system more elegant and simpler solutions can be found which lead us into the field of bio-inspired concepts.

Even the most primitive biological systems solve problems that reach far beyond the capabilities of today's technical systems (Kirchner, 2002). The biomimetic approach to robotics is the attempt to apply solutions created by evolution to technical systems. This approach is not restricted to mechanical engineering but includes and puts emphasis on the behaviour of autonomous systems, i.e., the algorithms that map from sensory stimuli to motor acts. Well-known approaches can be found in (Cruse et al., 1999, Beer et al., 1997, Spenneberg , 2005a, Gassmann et al., 2001).

These approaches are using aspects of decentralized control and neglect the need of complex internal models; instead they are primarily reactive approaches.

In the following, the development of our bio-inspired PCR-approach for the SCORPION robots is described.

It is based on major identified low-level locomotion concepts found in biological systems which are Central Pattern Generators and reflexes and posture primitives.

CPG-Control

A Central Pattern Generator (CPG) is the major biological motoric mechanism to control and to produce rhythmic motion. They are characterized by the ability to produce rhythmic motion patterns via oscillation of neuronal activity without the need of sensory feedback (Wilson, 1961).

However, many CPGs get sensory feedback, e.g., about the load and the position on the corresponding driven joint.

Thus CPGs are mostly used for closed loop control of the rhythmic motion of actuators.

To modulate the behaviour of the motion, their rhythmic patterns can be changed in frequency, phase, and amplitude.

This functionality based on biological neurons and executing muscles cannot be transferred directly on a walking robot because it possesses motor-driven joints instead of muscles.

From the robotics point of view it is reasonable to develop a more abstract CPG model which captures only the basic principles of the functionality of CPG motor control.

The CCCPG-approach (Ayers 2002) is a possible step in that direction, but its mechanisms are tightly connected to the research on the organisation of the neuronal circuits of lobsters and the Nitinol-actuators used in the underwater lobster robot for which the CCCPG-approach was developed.

Instead, we pursued the goal to formulate a more general CPG-model which has no direct biological archetype.

Important features of CPG control is the ability to describe and hence produce motion with rhythmic signals, which can be modulated in their phase, frequency, and amplitude, to change the resulting motion in its timing of execution, its duration, and its strength/speed.

In our model, the closed loop control (via sensory load and position feedback) can be implemented by a PID-controller.

If we use a modifiable rhythmic trajectory to provide set values for a standard PID-controller, which receives the position signal from the corresponding joint, we have a closed loop control of the rhythmic motion in different load states comparable to the behaviour of a real CPG.

Recapitulating, this means that our abstract CPG-model consists of a controller-module and a unit to produce rhythmic trajectories in the joint angle space.

In a first attempt to describe the rhythmic trajectories we used splined sinusoids (Spenneberg & Kirchner 2001, Spenneberg & Kirchner 2000).

This worked very well for first walking experiments, but if more complex pattern, consisting of a multitude of splined sinusoids a more general and flexible method to produce a rhythmic function is preferable.

Therefore we chose to describe a CPG-Pattern P as a function of part-wise fitted together third-order polynomials of the form:

$$y(t) = \sum_{a=0}^n k_a \cdot t^a \quad (1)$$

A part X is described by the coefficients of the polynom $k_a(X)$, its length $l(X) \in \mathbb{N}_0$ on the x-axis, the phase offset $\Theta(X) \in [0,1]$, its scalability $S(X) \in [0,1]$, and an optional subpart-list, if the part is constructed by subparts.

A complete rhythmic pattern is then described by a list of parts with the end of the list pointing to the start of the list.

To describe a part, Bezier-polynomials are used which are described by the following equation:

$$P0 \cdot t^3 + P1 \cdot 3 \cdot t^2 \cdot (1-t) + P2 \cdot 3 \cdot t \cdot (1-t)^2 + P3 \cdot (1-t)^3 = P \quad (2)$$

$P0$ and $P3$ are supporting points and $P1$ and $P2$ are control points of the curve.

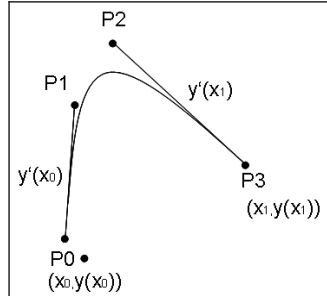


Fig. 10. A Bezier Curve

This coherence is illustrated in Fig. .

Bezier curves are smooth (optimal for DC-motor-control) and the controllable gradients at their end-points allowing a smooth transition from one part to the next which make them favourable for motor control.

If, like here, the Bezier curves are used only to describe a trajectory in the 2-dimensional joint angle space in dependence of the time t , these curves are functions which reduce the computation of the polynomial coefficients:

$$\begin{aligned} k_0 &= y_o \\ k_1 &= y'(x_0) \\ k_2 &= \frac{(2y'(x_0) + y'(x_1)) \cdot x_1^2 + 3(y_0 - y_1) \cdot x_1}{-x_1^3} \\ k_3 &= \frac{2y_1 - (y'(x_0) + y'(x_1)) \cdot x_1 - 2y_0}{-x_1^3} \end{aligned} \quad (3)$$

In this solution, P1 and P2 are only used to compute the gradients $y'(x_0)$ and $y'(x_1)$.

A position-algorithm computes in every time-step t for the current Part X_a of the whole pattern P (consisting of n parts and with a offset Θ) a simple equation (see Spenneberg, 2005a for details) to get the actual position (joint angle) in the rhythmic trajectory.

For a smooth transition between parts, we defined typical constraints namely that the connection points between the parts have the same value and that the first derivative of them is identical.

To get an even more compact way of describing trajectories, we distinguish only two types of supporting points, (Type 0)-points where $y'(x)=0$ (extreme points) and all other points (Type 1).

The gradient of the Type 1 points is given by the gradient of the line through its direct neighbour points.

The length $l(X_a)$ of a part X_a is equivalent to the difference $x_1(a) - x_0(a)$.

An example of a resulting pattern is shown in Fig. . The following parameters have been used(x,y,type): $\Theta = 0$; $X_0 = (0,0,1)$; $X_1 = (5,40,0)$; $X_2 = (10,0,1)$; $X_3 = (30,-20,0)$; $X_4 = (50,0,1)$.

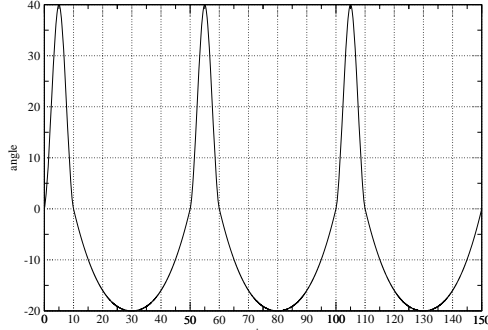


Fig. 11. Example Lateral Leading Pattern (Basalar Joint) using the Bezier Spline approach

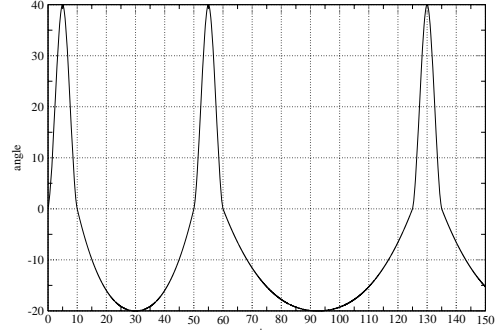


Fig. 12. Example of Period scaling

To modulate such a pattern in their phase, their frequency, and their amplitude, functions can be found easily. In principle, this is done by scaling the coefficients of the polynom or by applying an offset to the polynom. More details can be found in (Spenneberg, 2005a).

As we have seen from examples in biology (Bowerman, 1975), in some cases not the whole pattern has to be scaled, e.g., observations on invertebrates have shown that they change their swing-period only slightly when the step-period is prolonged.

To map this property, we introduced the scalability $S \in [0,1]$ for each part, which indicates if this part X is scaled, when the whole Pattern P is scaled.

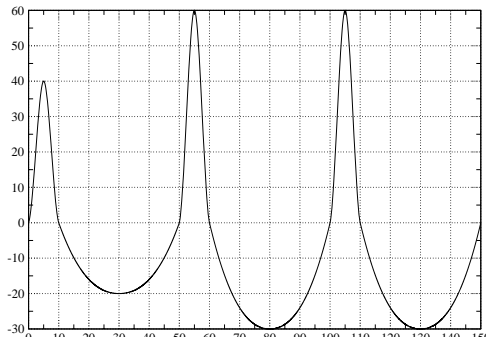


Fig. 13. Example of amplitude scaling

Figure 12 shows an example where the period of the whole pattern was newly scaled at $t = 50 t$, but the first parts were configured as non-scalable $S(X_0) = S(X_1) = 0$. Figure 13 shows an example where the amplitude of the pattern is scaled. An example for defining patterns with offsets to let the robot walk forward is presented in Figure 14.

Recapitulating this CPG-model allows the production of rhythmic and smooth motion patterns on the basis of Bezier-splines, which can be described very compactly by their

supporting points and their types. These patterns can be modulated easily in their phase, amplitude, and frequency. In addition, parts which have not to scale can be selected.

In addition, this approach allows also the combination of CPG-patterns or a smooth fading between different simultaneously active patterns. Therefore, patterns have an activation and the activation of the hitherto pattern is decreasing over a certain period and the activity of the new pattern is increasing (Spenneberg & Kirchner, 2001).

As long as more than one pattern is active in parallel, the current position is computed as an average of the current position in both patterns weighted with their activity. The same idea can be used when more than one pattern is active. This allows, for example, transition between lateral walking and forward walking as well as the overlay of a lateral walking pattern with a forward walking pattern, which results in a diagonal walking pattern (see also the combination of patterns in Fig.).

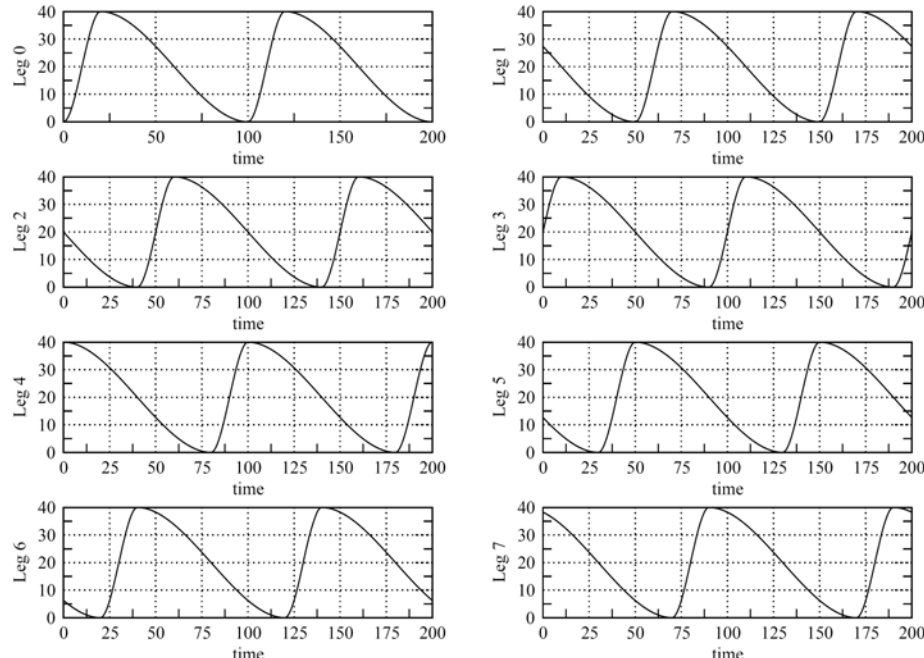


Fig. 14. SCORPION forward/backward walking pattern (Left: Thoracic joint; Right: Basalar joint) using the Offset from (Bowerman, 1975) using the CPG-model

More examples for using this CPG-model can be found in (Spenneberg et al., 2004 and Spenneberg et al., 2005a).

The Posture and the Reflex Model:

To control the posture of a joint, we integrated the ability to apply an offset to the y-Axis (joint angle) of the rhythmic patterns (see Fig.). If there is no rhythmic activity, we can also use the posture control for direct control of each joint, e.g., for manipulating objects.

Biological Reflexes are neuronal mechanisms which transform sensory input into motoric action - often with using one or more interneurons. The motoric action depends mostly on the strength of the stimulus and the interneuron circuit.

In contrast to the common assumption that reflexes are fixed reactions, it is possible that interneurons can be reprogrammed and thus change the motoric action (Reichert 1993).

In addition, the occurrence of reflexes is often sent to higher neuronal centres.

Therefore, a simple reflex model has an input-, activation-, and a response-function (see Fig.).

Furthermore, the reflex can be controlled via control signals from higher levels, e.g. the threshold can be changed to weaken the reactivity of the reflex in certain states. In the lateral walking, for example, a stumbling correction reflex (Forssberg, 1979) which is reasonable and found in forward walking would not work appropriately or produce an adverse behaviour. Therefore this reflex should be inhibited during lateral walking by applying proper control signals.

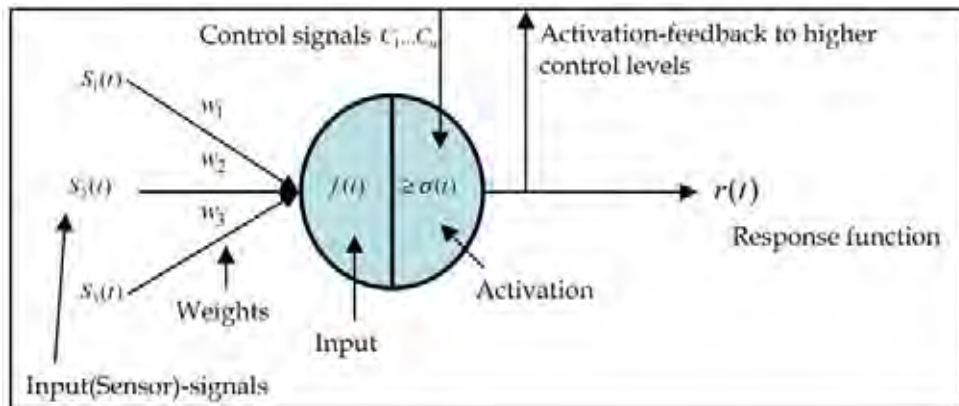


Fig. 15. Reflex model

The control signals C_i are given from the outside (see Fig.).

The response function $r(t)$ is activated when $a(f(t))$ is positive, and is responsible for the reaction of the controlled motor-joint(s).

An example of the reflex is the well-known tumbling correction reflex implemented in the SCORPION and ARAMIES (Spenneberg, 2006) robot. This reflex and corresponding data can be found in (Spenneberg & Kirchner, 2001).

It is only active in the first two thirds of the swing phase of a leg. If the leg hits an obstacle, a response is triggered which lifts the legs higher up to overcome the disturbance.

In the stance phase this response is not triggered when the leg is disturbed. The input for the input function is the current drawn by the shoulder motor which drives the leg forward (thoracic joint of the SCORPION). Because of the low load on the leg in the swing phase, the threshold is chosen low (via the control signals), thus disturbances (blocking the motor) will activate the reflex. In the stance phase the threshold is set high, thus resulting in no activation of the reflex. The response function, the real joint angle, and current data during a reflex activation in forward walking are shown in Fig..

Integration of the Models into a General Framework

All components, rhythmic motion control (using the CPG-model), posture control, and reflex control are integrated into the motoric level of a joint as depicted in Fig..

In the PCR (Posture-CPG-Reflex) approach, each joint has its own motoric level which is modulated and coordinated by the behavioural level (see Fig.).

The input values for the motoric layer are:

1. the activations for each CPG-pattern ACT_i and the corresponding amplitudes A_i (of pattern i), the execution period P_{Leg} (identical for the whole leg), and the phase Ph_{leg} (identical for the whole leg) for the rhythmic production part
2. the offsets O_j and its corresponding weights W_j for the posture control part
3. the control-signals C_r for the reflex part.

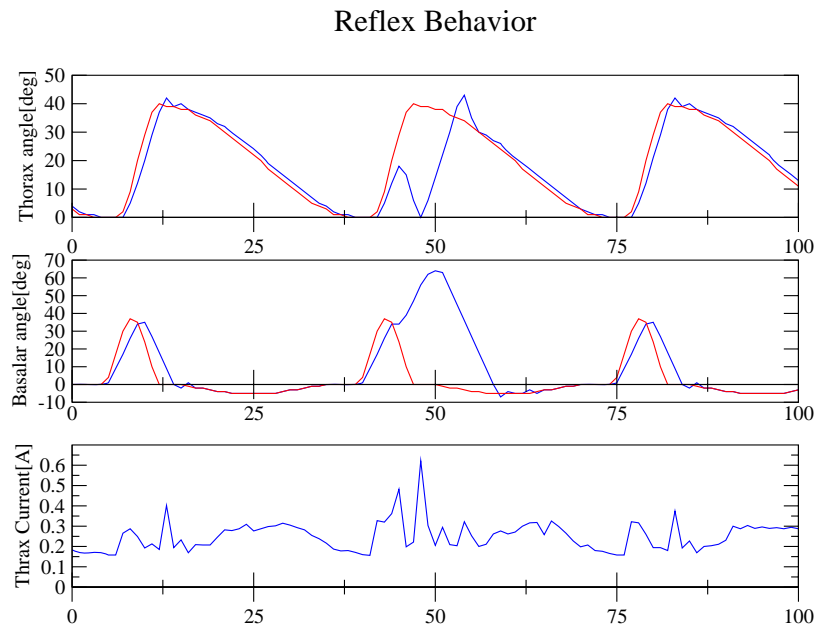


Fig. 16. Data of the stumbling correction reflex (red: set values form the CPG, blue: real values): As soon as the current of the thoracic joint exceeds the threshold of 0.45A the reflex gets triggered and overwrites the signals from the CPG. The reflex function moves the leg back and up and then as fast as possible forward. After 12 time-steps the activity of the reflex declines and the CPG takes over control.

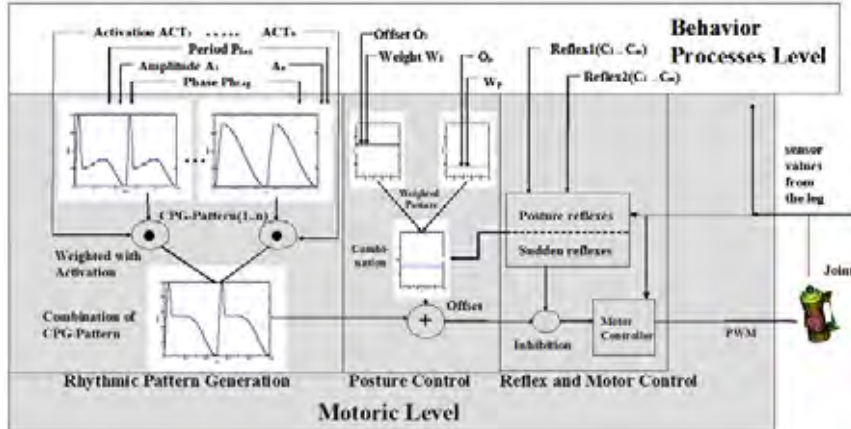


Fig. 17. Motoric layer controlling one joint

On these input values, several behaviour processes can take influence at the same time. The result is computed by a merge-process which uses a weighted sum principle (for further details see (Spenneberg, 2005b).

In the rhythmic pattern generation part, all active CPG-patterns are weighted with their activation resulting in one final pattern which is the weighted sum of all active patterns, e.g. if a forward walking pattern and a diagonal walking pattern is active simultaneously and with the same strength the result will be a diagonal walking pattern.

This final pattern can then be offset regarding the angle by the Posture Control.

Again, in the Posture Control we can have simultaneous and weighted influences which form one final offset for each joint. After the offset is applied, this pattern is fed to the motor controller which moves the joint according to the given trajectory, if no inhibitions from reflexes take place.

Therefore, the motor controller gets the current and position values from the joint.

The reflexes also get these values. We implemented two types of reflexes. Type-1: Reflexes which control the posture and are almost all the time active (low threshold). They take influence on the offset via their response function to control, for example, pitch and roll of the system or to keep the distal joint perpendicular to the ground when the SCORPION robot walks forward. Type-2: Reflexes, like the above described "Stumbling Correction Reflex", which inhibits the values from the rhythmic and posture control and writes its own values to the motor controller.

To coordinate the joints via their motoric layer, the behavioural layer is responsible (see Figure 19.).

For the rhythmic locomotion coordination motor programmes are introduced.

An example of a motor programme, Forward Walking, is presented in Fig..

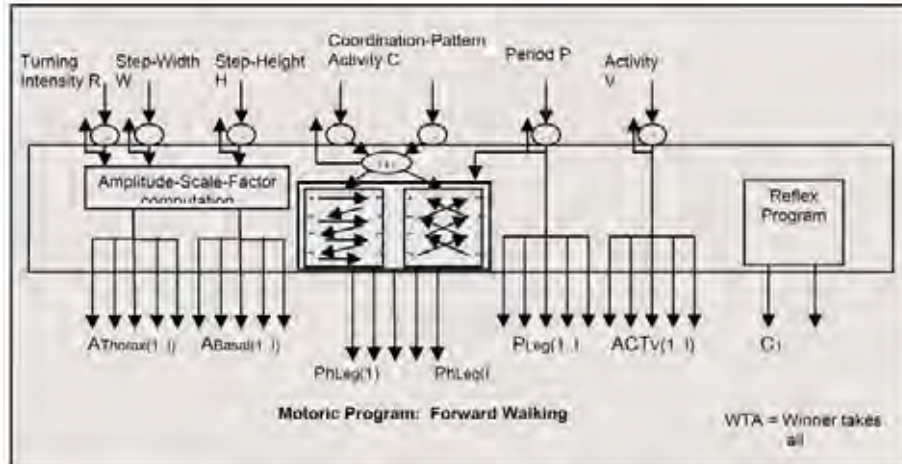


Fig. 18. Example of a motoric programme

A motor programme serves as an interface between the motoric layer of each joint and the higher levels of control and is responsible for the control of a complex movement.

For example, the interface of the forward walking motor programme provides the higher level with an abstraction which makes the control of forward motion of a legged system almost as simple as the control of a wheeled system. The controllable input parameters are: The turning-intensity R (which corresponds to a turning radius clock-/ or counter-clockwise), the step-width, the step height, the Activity C_i for the different coordination patterns (e.g. wave pattern, tetrapod-pattern, Bowerman-coordination pattern (see Bowerman, 1975)), the execution period P (determining the step frequency), and the activity of the motor programme. To control the turning radius as well as step width and step height, new amplitudes for the CPGs are calculated and sent to the corresponding patterns at the motoric level, the coordination pattern is realized by sending the corresponding fixed phase offsets to the CPGs of the different legs. The activities as well as the period are passed without further processing to the corresponding CPGs on the motoric layer.

The motor programmes are modulated by behaviour systems (BS) (again more than one BS can take influence on the input values of a motor programme) implementing more complex functions, e.g., an obstacle avoidance, which is based on a distance sensor.

For the posture control we have a comparable interface, the posture programmes. They are sensory motor loops modulating the posture control of each joint, e.g. to control a certain height of the overall robot (Body Height Control) or a certain tilt (Tilt Control).

An overview of this architecture is presented in Figure 19.

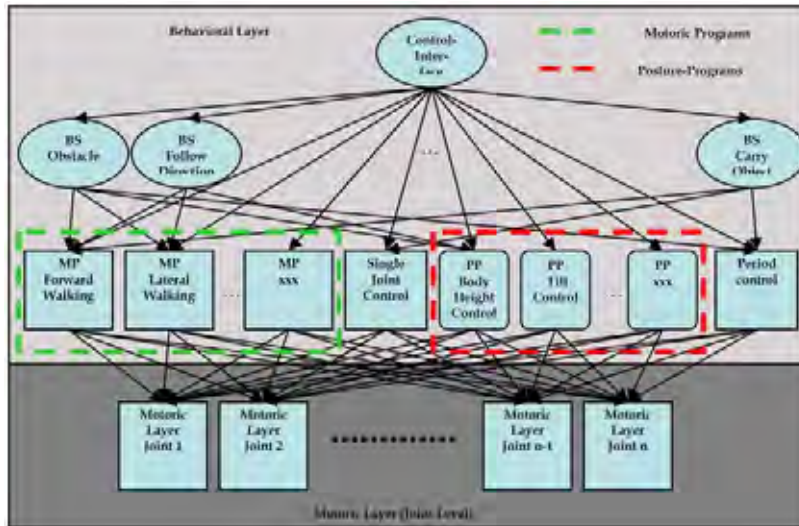


Fig. 19. Overview of the software hierarchy (Black arrows are showing simultaneous influences taken onto the input values), on the top layer a external control interface is shown, instead of this interface a planer can be used in the future.

One advantage of this modular approach is that via the abstraction of the motoric layer and the motor and posture programmes a legged robot can be controlled as easily as a wheeled or tracked system and thus a lot of the methods already developed on wheeled platforms can be reused.

In addition, the approach provides very flexible and potent interfaces on each level. For the implementation of this control approach on our hardware platform (featuring the MPC555) we developed a special microkernel which supports this kind of behaviour-based architecture. Here, the communication between the processes by using the merging based on a weighted sum principle is among other merging functions already supported on the microkernel level. For further details see (Spenneberg 2005b).

Results

During the last years we did several tests with the SCORPION robot. In addition we successfully tested the approach on four-legged systems, i.e. the robots AIMEE (Albrecht et al., 2004) and ARAMIES (Spenneberg et al., 2006).

The SCORPION IV can now move with up to 30cm/s which is half a body-length per second. This speed-enhancement is partly based on the integration of compliance into the distal joints, which allowed together with optimized CPG-patterns running at 1.2Hz to accelerate the movement in stance-direction already in the late swing phase.

The SCORPION IV is able to move through various terrains (rock fields (with boulders up to 28cm diameter), asphalt, sand, gravel, grass). This was tested at several outdoor locations. The system can overcome by means of reflexes singular obstacles (perpendicular to the ground) of up to 30cm height (8 cm more than its ground clearance). Non singular obstacles like rubble piles can be overcome, if the variance in this rubble pile does not exceed this maximum possible height change.

The system is able to safely walk up an inclination of 35° while overcoming smaller obstacles of 10cm height. For steeper slopes a special coordination pattern can be used which moves one leg after the other forward before all legs stance together. This allows depending on the ground to move up slopes of 45° on the cost of speed. For these experiments the standard rubber feet of the SCORPION have been used, still better climbing abilities are likely to be achieved, if special designed feet would be developed.

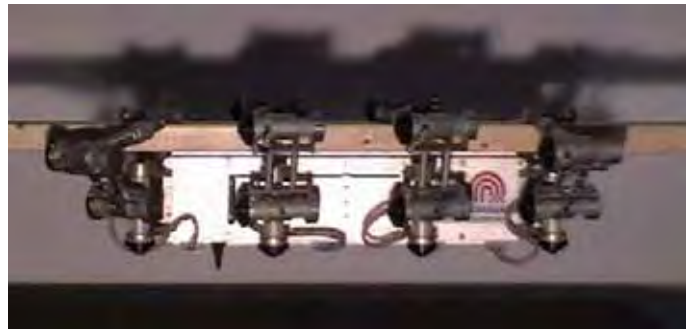


Fig. 20. SCORPION Robot using the PCR approach to climb along a beam

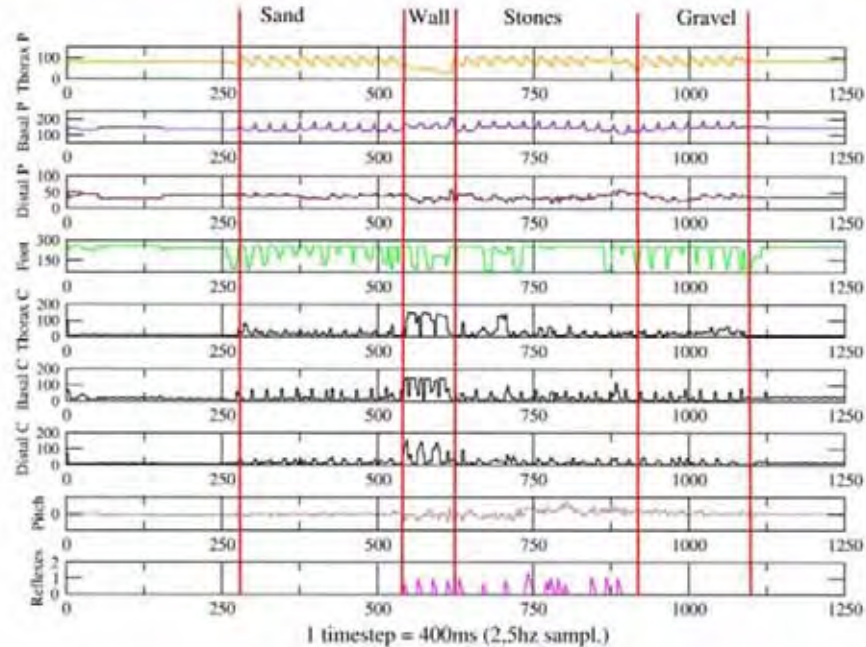


Fig. 21. Data from the left foremost leg in a run through a test-bed consisting of a sand part, a stone wall, a rock-field, and a gravel field. Line 1-3: real joint angle values, line 4 footpressure sensor data, line 5-7: current values, line 8: pitch value of the body, line 9: value for reflex occurrences.

These results have been obtained from tests in the locomotion lab of the University of Bremen as well as at the South West Research Institute in San Antonio in Texas.

Furthermore, we have proven that the control approach could not only be used for locomotion but for other movements, like climbing along a beam (see Fig.) or manipulating objects, too. This is primarily done by combining the standard CPGs with a totally different basic posture. To climb along a beam, for example, is achieved by activating the forward walking pattern for the foremost and hindmost legs and by using a posture where the robot sticks to the beam.

Based on these results, we can argue that the PCR-approach is a very flexible and efficient tool for programming new locomotion behaviours and that SCORPION IV is a very robust walking robot.

Because of the clear distinction between rhythmic control, posture control, and reflex control necessary adaptation to an existing programme can be done with low effort, which make this approach suitable for bottom up programming. The introduction of motoric programmes supports also this modularization for high reusability.

On the other hand we also experienced that the PCR-approach is sub-optimal for the production of energy-optimized trajectories. Here, model-based approaches could provide better solutions. But they would need very accurate modelling of the environment to achieve this theoretically possible better performance. Therefore, better sensors and high computational power would be needed, which are not available yet and would make such systems tremendously expensive.

Another approach for the modelling of the environment might be to use the proprioceptive data of the walking robots for terrain classification to enhance the information gained by exteroceptive sensors. To test this, a self-growing neural network approach - growing cell structures - was used to distinguish between different substrates. An example of the used proprioceptive data is shown in Fig.. The classifier was able to distinguish three groups: a) gravel/sand, b) the wall, and c) the rock-field(stones) from each other by using this data as input values. More details can be found in (Spenneberg & Kirchner (2005c).

4. Conclusions

The PCR-approach showed that it is possible to define models for the low-level biological motoric concepts and combine them, so that they can be used with a behaviour-based control approach in a flexible way. The control of the posture, while the system is walking, gives additional flexibility in comparison to the CCPG approach (Ayers 2002) or the Walknet approach (Cruse 1999).

In addition, the combination of different walking patterns, e.g., for an omni-directional movement, produces a rich motion repertoire on the basis of a small set of elementary locomotion patterns which are defined with few parameters.

But, recapitulating, none of the existing bio-inspired approaches including the PCR-approach yet is able to use the full motion potentials which walking robots have.

Especially in very complex environments, e.g. steep slopes or the earlier mentioned random stepping fields, these reactive approaches show their limits. On the other hand, these are the environments, where the, in principle, higher mobility of ambulating systems in comparison to wheeled or tracked systems, would pay off.

One way for the future will be the combination of the bio-inspired approaches with approaches to model the environment plus the robot and to plan steps before their execution. But, as we have already discussed such an approach would need to work firstly on a correct model and secondly would have to be based on very accurate motion execution. The problem of 3D-world-modelling and kinematical modelling in real time has yet to be solved before this path becomes an option.

Perhaps, regarding this issue it is reasonable to get inspired again by the research on biological systems.

They seem to use such complex world models only seldom, especially if we study invertebrates. One explanation why these systems can nonetheless operate in such difficult environments, is that their extremely high number of acquired sensory information and the high number of corresponding sensomotoric feedback loops plays a crucial role in the motion adaptation.

For example, the legs of insects are covered with thousands of partly specialized sensors. Thus, these systems are much more embedded into the world than our robots. Biological systems in comparison to the robots are fully situated in the world and hence can still cope in the mentioned environments without complex internal world-models. We believe that they can use this sensory information to locally model and classify their environment very accurately, the experiment described above for the terrain classification is a first hint in this direction.

Due to this hypothesis, we see one of the major challenges for robotics to close this sensorial gap by advancing the mechatronical design and the integration of a multitude of sensors into the material of our robotic systems, e.g. developing a leg which is made by "intelligent aluminium" which already contains hundreds of pressure sensors. This provides us with a second challenge: To find suitable algorithms and concepts to process these signals in parallel. In addition, the design of these walking robots can be improved by developing a self-adapting "intelligent morphology" which requires still less control to produce terrain-suited locomotion patterns. Here especially the ongoing work on passive walkers and elastic actuation looks very promising with view to the future.

5. References

- Albrecht M.; Backhaus T.; Planthaber S.; Stoeppeler H.; Spenneberg D.; & Kirchner F. (2005) Aimee: A four-legged robot for robocup rescue. In *Proceedings of CLAWAR 2005*. Springer, 2005.
- Ayers, J. (2002). A conservative biomimetic control architecture for autonomous underwater robots. In Ayers, Davis, and Rudolph, editors, *Neurotechnology for Biomimetic Robots*, pages 241--260. MIT Press, 2002.
- Beer, R.D; Quinn R.D. ; Chiel, H.J ; & Ritzmann, R.E. (1997). Biologically-inspired approaches to robotics. In *Communications of the ACM*, 40(3):30–38, 1997.
- Bowerman, R.F. (1975). The control of walking in the SCORPION - I. leg movements during normal walking. In *Journal of Comparative Physiology*, 100:1 183–196, 1975.
- Cruse, H; Dean, J; Kindermann D.; Schmitz J., & Schumm, M. (1999). Walknet - a decentralized architecture for the control of walking behaviour-based on insect studies. In G.Palm, editor, *Hybrid Information Processing in Adaptive Autonomous Vehicles*. Springer, 1999.

- Gaßmann, B.; Scholl, K. U.; & Berns, K (2001). Behaviour control of Lauron III for walking in unstructured terrain. In *Proceedings of CLAWAR 2001*, pages 651--658, 2001.
- Go, Y.; Yin, X.; & Bowling A. (2005) Navigability of multi-legged robots. In *IEEE/ASMETransactions on Mechatronics*, 2005.
- Ijspeert A.J.; Crespi A. ; & Cabelguen J.M. (2005) Simulation and robotics studies of salamander locomotion. Applying neurobiological principles to the control of locomotion in robots. In *Neuroinformatics*, 3 (3):0 171--196, 2005.
- Kirchner, F. (1998) Q-learning for complex behaviours on a six-legged walking machine. In *Journal of Robotics and Autonomous Systems*, 25, 256--263, 1998.
- Kirchner, F. ; Spenneberg, D. & Linnemann. R. (2002) A biologically inspired approach towards robust real world locomotion in an 8-legged robot. In J.Ayers, J.Davis, and A.Rudolph, editors, *Neurotechnology for Biomimetic Robots*. MIT-Press, Cambridge, MA, USA, 2002.
- Löffler, K; Gienger K.; & Pfeiffer F. (2003) Sensor and control design of a dynamically stable biped robot. In *Proc. of the International Conference on Robotics and Automation 2003*, pages 484--490, 2003.
- Maes P.; & Brooks R.A. (1990). Learning to coordinate behaviours. In *National Conference on Artificial Intelligence*, pages 796--802, 1990.
- Reichert, H. (1993) *Introduction to Neurobiology* (book). Thieme, 1993.
- Spenneberg, D.; & Kirchner, F. (2000) Omnidirectional walking in an eight legged robot. In *Proceedings of the 2nd Int. Symposium on Robotics and Automation (ISRA2000)*, Monterrey, N.L., Mexico, 2000.
- Spenneberg, D.; & Kirchner, F. (2001) An approach towards autonomous outdoor walking robots. In *Proceedings of the 10th Int. Conf. on Advanced Robotics (ICAR 2001)*, Budapest, Ungarn, 2001.
- Spenneberg D.; Kirchner F. & de Gea, J.(2004). Ambulating robots for exploration in rough terrain on future extraterrestrial missions. In *Proceedings of the 8th ESA Workshop on Advanced Space Technologies for Robotics and Automation (ASTRA 2004)*. European Space Agency, November 2004
- Spenneberg D. (2005a). A hybrid locomotion control approach. In *Proceedings of the CLAWAR 2005 Conference*, September 2005.
- Spenneberg, D. ; Albrecht, M.; Backhaus, T. (2005b) M.o.n.s.t.e.r.: A new behaviour-based microkernel for mobile robots. In *Proceedings of the ECMR 2005*, September 2005.
- Spenneberg, D. ; & Kirchner, F. (2005c) Learning spatial categories on the basis of proprioceptive data. In *Proceedings of the 3rd International Symposium on Adaptive Motion in Animals and Machines*, September 2005
- Wilson, D.M (1961) The central nervous control of flight in a locust. In *Journal of Experimatal Biology*, 38: 471--490, 1961.

A Climbing Robot for Cleaning Glass Surface with Motion Planning and Visual Sensing

Dong Sun, Jian Zhu and Shiu Kit Tso

*Department of Manufacturing Engineering and Engineering Management
City University of Hong Kong
Hong Kong*

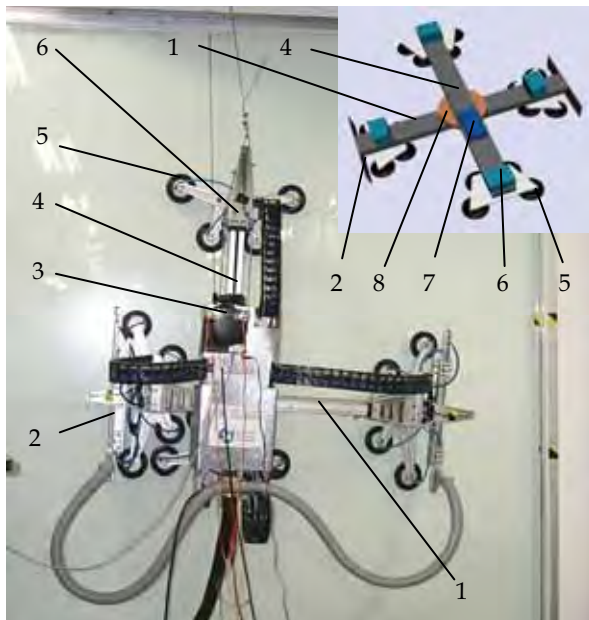
1. Introduction

There exists increasing demand for the development of various service robots to relieve human beings from hazardous jobs, such as cleaning glass-surface of skyscrapers, fire rescue, and inspection of high pipes and walls (Balaguer et al., 2000; La Rosa et al., 2002; Zhu et al., 2002). Fig. 1 shows our recently developed climbing robotic system aimed to clean glasses of high-rise buildings, using suction cups for adhering to the glass and a translation mechanism for moving. This robot can reach a maximum speed of 3 m/min and has the ability to cross cracks and obstacles less than 35mm in height and 80mm in width. Utilizing a flexible waist, the robot can easily adjust its orientation.

Motion planning of the service robot plays an important role to enable the robot to arrive in the target position and avoid or cross obstacles in the trajectory path. There are considerable approaches in the literature to address the motion planning problem of car-like or walking robots, such as Lamiriaux and Laumond (2001), Boissonnat etc. (2000), Hasegawa etc. (2000), Chen et al. (1999), Hert and Lumelsky (1999), Egerstedt and Hu (2002), Mosemann and Wahl (2001), to name a few. All these algorithms are not suitable to our cleaning robot applications. This is because 1) the movement mechanism of the climbing robot uses translational suction cups, which is different from the other robots; and 2) the climbing robot works in a special environment, i.e., the glass wall, which is divided into many rectangle sections by horizontal and vertical window frames, and the robot must be able to cross the window frames to clean all sections. Because of these characteristics, there exists a demand for a unique motion planning scheme for the climbing robot application.

Another key issue to the success of the climbing robot application lies in an effective sensing capability. To do the cleaning work on the glass surface, the cleaning robot must know when to begin or stop the cleaning job, how to control the orientation (or moving direction), and how to cross the window frame. Therefore, it is necessary to measure the robot orientation, the distance between the robot and the window frame, and the distance between the robot and the dirty spot to be cleaned. Some recent works on the sensing system of cleaning robots have been reported in the literature (Malis et al., 1999; Ma et al., 1999). Simoncelli et al. (2000) utilized the ultrasonic sonar for automatic localization. Kurazume and Hirose (2000) proposed the so-called "cooperative positioning system" to

repeat a searching process until the target position was reached. However, in a climbing robot on the glass surface, many traditional methodologies with laser and ultrasonic sensors etc. cannot be applicable to measure the distance between the robot and the window frame. This is because that the height of the window frame is usually low and the light beam sent by the sensor is difficult to reach the frame unless the beam is exactly parallel to the glass surface. Due to inevitable installation errors, the sensors are usually hard to ensure that the light beam is parallel to the glass surface exactly. Cameras are often used for the robot's localization, visual servoing, and vision guidance. Malis et al. (2000) used two cameras for 2-D and 2-1/2-D visual servoing and proposed a multi-camera visual servoing method. However, the use of a number of cameras may not be suitable to the climbing robot because 1), it is difficult to establish a big zone of intersection of points of view when using several cameras, and 2), using a number of cameras increases the load weight and thus affects the safety of the climbing robot. Based on eigenspace analysis, a single camera was used to locate the robot by orienting the camera in multiple directions from one position (Maeda et al., 1997). The drawback of this eigenspace method is that the measuring performance may vary as environment changes. In addition, the depth information is lost and the distance between the camera and the target object cannot be measured by traditional single camera.



- | | |
|-----------------------------|---------------------------|
| 1. Horizontal (X-) Cylinder | 2. Brush |
| 3. Visual Sensor | 4. Vertical (Y-) Cylinder |
| 5. Suction Cup | 6. Z-Cylinder |
| 7. Slave CPU | 8. Rotation Cylinder |

Fig. 1. Main structure of the climbing robot

This chapter presents our approaches to solving the above two challenging problems, motion planning and visual sensing, for a climbing glass-cleaning robot. Some works have been reported in Zhu etc. (2003) and Sun etc. (2004). The reminder of the chapter is organized as follows. In section 2, structure of the climbing robot is introduced. In section 3, motion planning of the robot on a multi-frame glass wall is presented. In section 4, a visual sensing system that is composed of an omnidirectional CCD camera and two laser diodes, is shown to enable the robot to measure its orientation and the distance between the robot and the window frame. Experiments are performed in section 5 to demonstrate the effectiveness of the proposed approach. Finally, conclusions of this work are given in section 6.

2. Structure of the Cleaning Robot

The cleaning robotic system consists of a mobile climbing robot, a supporting vehicle, a compressor, and a computer. The climbing robot sticks on the glass surface to perform the cleaning job. The supporting vehicle supplies electrical power and cleaning liquid. The compressor acts as the air source. Through communication between the computer and the robot, the human operator can examine and control the operation of the robot.

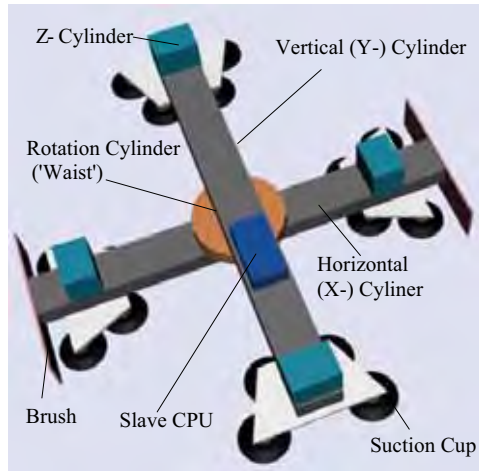


Fig. 2. Main structure of the climbing robot

The developed climbing robot has a length of 1220 mm, a width of 1340 mm, a height of 370 mm, and a weight of 30 Kg. The body of the robot is mainly composed of two rodless cylinders perpendicular to each other, as shown in Fig. 1. The stroke of the horizontal (X-) cylinder is 400mm, and that of the vertical (Y-) cylinder is 500mm. Actuating these two cylinders alternately, the robot moves in the X or Y direction. As shown in Fig. 2, four short Z-cylinders are installed at the two ends of each rodless cylinder. By stretching out or drawing back the piston beams of these four cylinders, the robot can move in the Z direction. At the intersection of two rodless cylinders, a rotational cylinder named the robot's waist is installed, by which the robot can rotate around the Z-pivot. Two specially designed brushes, each composed of a squeegee and a sucking system, are fixed at the two

ends of the horizontal cylinder. The squeegee cleans dirty spots on the glass surface using cleaning liquid provided by the supporting vehicle. The sucking system collects and returns the sewage to the supporting vehicle for recycling.

The robot employs suction pads for adhesion. Four suction pads, each with a diameter of 100mm, are installed on each foot of the robot. The total sixteen pads provide a suction force enough to withstand 15 Kg payload. The robot uses a translational mechanism for the movement. With the operating mode of sticking-moving-sticking, the robot can complete a series of motions including moving, rotation, and crossing obstacles. The rotation of the robot is controlled by adjusting rotation angles of the rotational cylinder. The robot can rotate 1.6 degrees per step around Z-pivot until reaching the desired posture.

The control system of the robot is based on a master and a slave computer. The master computer is located on the ground and manipulated by the human operator directly. The slave computer is embedded in the body of the robot. Using the feedback signal of sensors installed on the robot, the slave computer controls the movement and the posture of the robot to achieve automatic navigation on the glass surface. The master computer obtains the information and identifies the status of the robot by the visual sensing system together with the communication between the master and the slave computers with a RS422 link. In case of emergency, the human operator can directly control the robot according to the actual situation.

The movement of the robot is achieved by alternately sucking and releasing the suction cups installed on the horizontal and vertical rodless cylinders. The slave computer sends ON or OFF signals to connect or disconnect the vacuum generator with air source, resulting in sucking or releasing the corresponding suction cups. Vacuum meters measure the relative vacuum of the suction cups and check the safety of the robot. If the vacuum degree of the suction cups is less than -40 kPa, an alarm signal is sent to the master computer.

Fig. 3 illustrates the developed cleaning robot climbing on the commercial building of City Plaza in Hong Kong.



Fig. 3. The climbing robot on site trial outside a commercial building (provided by BBC)

3. Motion Planning

For simplicity, the robot moves horizontally and vertically to clean the whole glass surface in the motion planning. As an example, Fig. 4 illustrates a trajectory path of the robot within a rectangular glass section. The starting point is located in the up-right side of the glass section. The robot moves toward the left side horizontally while cleaning the glass surface. When arriving at the boundary of the glass section, the robot moves down a distance l and then moves back to the right side horizontally. Note that the distance l is equal to the length l_b of the brush cleaning path, and l_b is determined by considering the size of the brush and the dimension of the glass section. Repeating the above procedures, the whole glass section can be cleaned. The ending position is located in the down side of the glass section. During cleaning the sewage may drop down and makes the downside glass surface dirty. Therefore, the cleaning work should be performed from the upside to the downside.

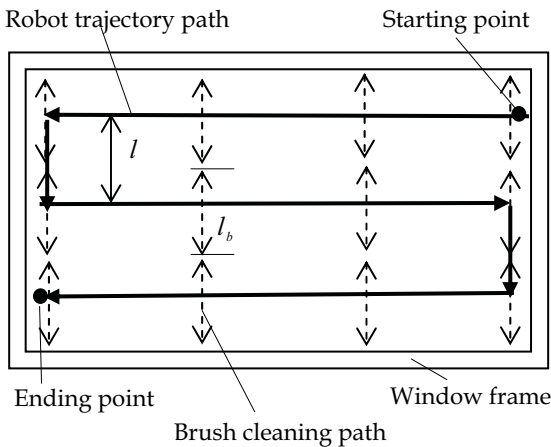


Fig. 4. Robot motion path on the glass

3.1 Orientation Adjustment of the Robot

When the climbing robot moves along the desired trajectory, the robot orientation is affected by various disturbances, especially by the gravitational force of the robot itself. To ensure a successful trajectory following, the robot must be able to adjust its orientation automatically. The orientation of the robot is measured by the visual sensor installed on the robot, relative to the window frame. Two laser diodes send two laser lights to the window frame so that an image of the frame can be acquired. The orientation of the robot relative to the window frame can be calculated by analyzing and comparing the image coordinates of two laser points. The technical details of this measurement are given in the next section.

Based on the orientation measured by the visual sensor, the controller actuates the rotational cylinder to adjust the orientation of the robot. The orientation is adjusted by the sticking-releasing-sticking mode, as shown in Fig. 5. Firstly, the suction cups installed on the vertical cylinder are released (see Fig. 5 (1)). Secondly, the rotational cylinder is actuated to rotate the vertical cylinder (see Fig. 5 (2)). Then, the suction cups on the vertical cylinder are sucked, and meanwhile, the suction cups on the horizontal cylinder are released (see Fig. 5

(3)). Finally, the rotational cylinder is actuated again to rotate the horizontal cylinder (see Fig. 5 (4)).

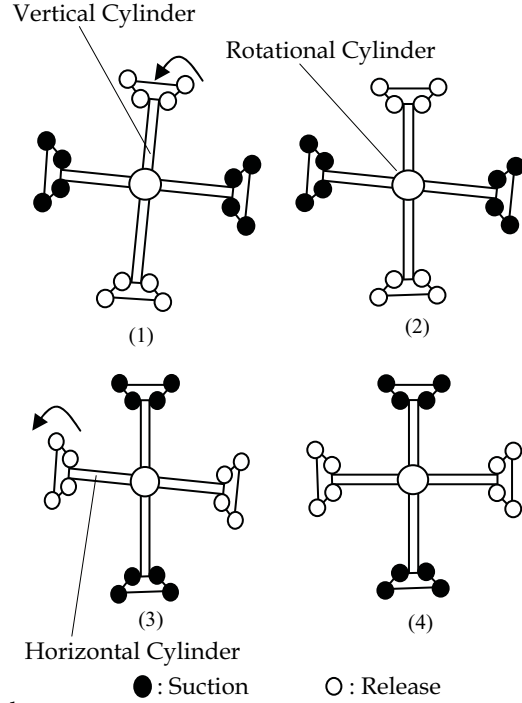


Fig. 5. Rotation of the robot

3.2 Crossing the Window Frame

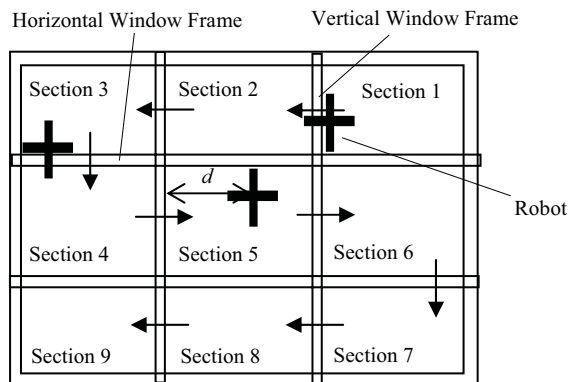


Fig. 6. Path planning of the climbing robot in a multi-frame glass wall

The window frames separate the whole glass wall into several sections, as shown in Fig. 6. After cleaning one section, the robot must be able to cross the vertical or horizontal window frame to enter another section. The two major steps for the robot to cross the window frame are:

1) Measuring the distance between the robot and the window frame

The distance between the robot and the window frame, denoted by d as seen in Fig. 6, is an important factor to evaluate the position of the robot in each section. When this distance is close to zero, the robot prepares to cross the window frame. The visual sensor is employed to measure the distance between the robot and the window frame. According to the theory of triangulation, one laser diode is needed to measure the distance. The distance is measured by analysis and calculation of the pixel coordinate of the laser point, based on the position and posture of the CCD camera relative to the laser diode, which will be shown in the next section.

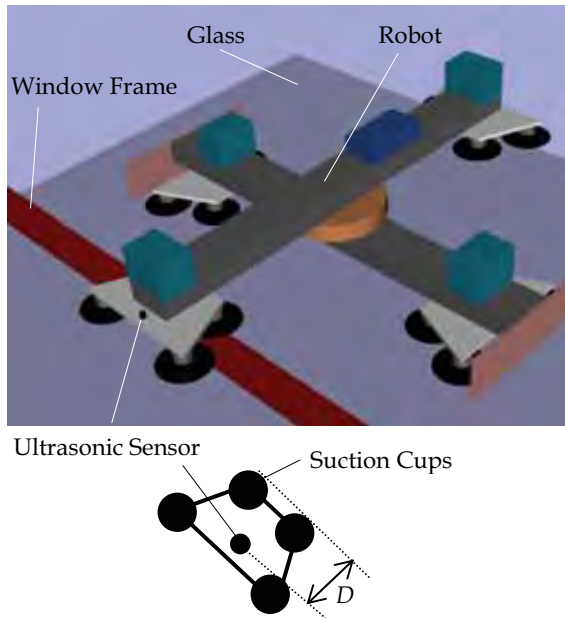


Fig. 7. Ultrasonic sensors installed on the robot

2) Crossing the window frame

After measuring the distance between the robot and the window frame, the robot plans its motion to cross the frame. Four ultrasonic sensors are installed to help the robot to detect whether the suction cups have crossed the window frame, as shown in Fig. 7, where D ($=300\text{mm}$) denotes the distance between the ultrasonic sensor and the boundary of suction cups. When the ultrasonic sensor is crossing the window frame, the ultrasonic sensor measures the height of its position relative to the surface of the window frame. After the ultrasonic sensor crosses the window frame, the height measured by the ultrasonic sensor is the one relative to the glass surface. Since the height measurements in the two cases are

different, the robot knows whether the ultrasonic sensor has crossed the window frame. When the ultrasonic sensor lies in the window frame, the robot also knows when the suction cups will follow the ultrasonic sensor to cross the window frame after moving a distance D .

4. Visual Sensing

The visual sensing hardware system consists of an oriented CCD camera with the model number Sony EVI-D30 (J), two laser diodes, and a capture card. Two laser diodes, fixed on the camera as "eyes" of the sensing system, send two laser lights to find the window frame and generate two laser marks. The distances between the reference points and the window frame, and the orientation of the robot relative to the window frame, can be determined by analyzing image pixel coordinates u and v of two laser points in the image plane.

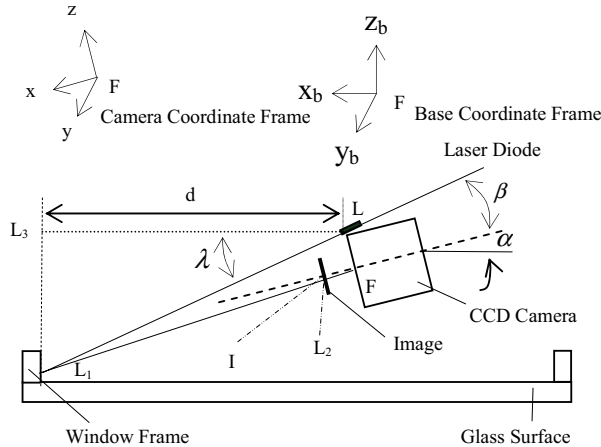


Fig. 8. Measurement of the robot position

4.1 Position Measurement

The theory of triangulation will be utilized in the measurement. Fig. 8 (left view) illustrates how the robot position is measured by the visual sensing system. The launching point of the laser diode is represented by L . Point L_1 is the laser mark on the window frame. Point L_2 is the corresponding point of L_1 in the image plane, where I denotes the center of the image. Treating the focal point of the camera as the origin, denoted by F , a base coordinate frame represented by $F-x_b y_b z_b$ is established, where x_b coordinate axis is parallel to the glass surface and perpendicular to the window frame, y_b coordinate axis is parallel to both the window frame and the glass surface(x_b-y_b plane), and z_b coordinate axis is perpendicular to the glass surface(x_b-y_b plane), as shown in Fig. 8. Using F as the same origin, another coordinate frame named camera coordinate frame, represented by $F-xyz$, is also established, where x axis is parallel to line $I-F$ that is the main light pivot of the camera, y axis is the same as y_b axis of the base coordinate frame, and z axis is perpendicular to the $x-y$ plane. Denote $[x_0, y_0, z_0]^T$, $[x_1, y_1, z_1]^T$ and $[x_2, y_2, z_2]^T$ as coordinates of the points L , L_1 and L_2 , respectively. Denote u

and v as coordinates in pixel in the image plane, and u_0 and v_0 as the pixel coordinates of the central point L .

Since the focal point F is located in the line L_1-L_2 , the line L_1-L_2 can be represented by

$$\frac{x}{x_2} = \frac{y}{y_2} = \frac{z}{z_2} \quad (1)$$

Define β as the tilt angle of the laser diode relative to the camera (around y axis, anti-clockwise), γ as the pan angle (around z axis, anti-clockwise). Then, the line $L-L_1$ can be represented by

$$\frac{x-x_0}{1} = \frac{y-y_0}{\tan \gamma} = \frac{z-z_0}{-\tan \beta} \quad (2)$$

From (1) and (2), we can derive coordinates of point L_1 in pixel coordinate u , i.e.,

$$[x_1, y_1, z_1]^T = K_u + [x_0, y_0, z_0]^T \quad (3)$$

$$\text{where } K_u = \begin{bmatrix} -x_0 d_x (u - u_0) - y_0 f \\ d_x (u - u_0) + f \tan \gamma \\ -x_0 d_x (u - u_0) \tan \gamma - y_0 f \tan \gamma \\ d_x (u - u_0) + f \tan \gamma \\ x_0 d_x (u - u_0) \tan \beta + y_0 f \tan \beta \\ d_x (u - u_0) + f \tan \beta \end{bmatrix}, \text{ in which } d_x \text{ and } d_y \text{ are distances between two}$$

adjacent pixels in two directions of the image plane, and f denotes the focal distance.
The distance between L and L_1 , represented by $|LL_1|$, is

$$|LL_1| = \sqrt{(x_1 - x_0)^2 + (y_1 - y_0)^2 + (z_1 - z_0)^2} \quad (4)$$

Define α as the tilt angle of the camera in the base coordinate frame. The angle between the line $L-L_1$ and the line $L-L_3$ (parallel to x_b axis) is

$$\lambda = \arccos\left(\frac{\cos \alpha - \sin \alpha \tan \beta}{\sqrt{1 + \tan^2 \beta + \tan^2 \gamma}}\right) \quad (5)$$

Then, the distance between point L and the window frame is

$$d = |LL_1| \cos \lambda \quad (6)$$

Substituting (3), (4) and (5) into (6) yields d in pixel coordinate u , i.e.,

$$d = \frac{a_1 u + a_2}{u + a_3} \cos(\alpha + \beta) \quad (7)$$

where $a_1 = \frac{-x_0}{\cos \beta}$, $a_2 = \frac{x_0 u_0 d_x - y_0 f}{\cos \beta d_x}$, and $a_3 = \frac{-u_0 d_x + f \tan \gamma}{d_x}$.

In a similar manner, the distance d can be derived as the function of the pixel coordinate v .

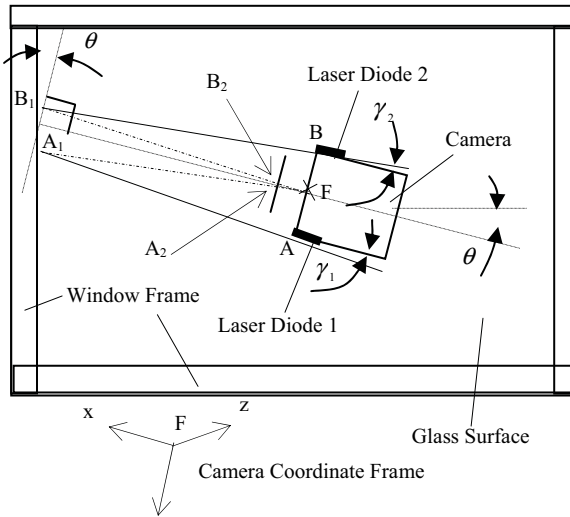


Fig. 9. Measurement of the robot orientation

4.2 Orientation Measurement

Fig. 9 (front view) illustrates a measurement of the robot orientation using the visual sensing system, where two laser diodes are needed. Points A and B are launching points of laser diodes 1 and 2, respectively. Points A_1 and B_1 are the corresponding laser marks in the window frame. γ_1 and γ_2 are the pan angles of laser diodes 1 and 2 relative to the camera. Denote the positions of the left point A and the right point B in the camera coordinate frame by $[x_L, y_L, z_L]^T$ and $[x_R, y_R, z_R]^T$, respectively. In the x - y plane, the line A - A_1 is represented by

$$\frac{y - y_L}{\sin \gamma_1} = \frac{x - x_L}{\cos \gamma_1} \quad (8)$$

Note that the pixel coordinates of the laser point A_2 in the image plane are u_L and v_L . In the x - y plane, the coordinates of A_2 are $(f, d_x(u_0 - u_L))$. Then, the line F - A_1 is represented by

$$\frac{y}{d_x(u_0 - u_L)} = \frac{x}{f} \quad (9)$$

Combining (8) and (9), the coordinates of point A_1 are derived by

$$x_{A1} = \frac{f(y_L - x_L \tan \gamma_1)}{d_x(u_0 - u_L) - f \tan \gamma_1} \quad (10)$$

$$y_{A1} = \frac{d_x(u_0 - u_L)(y_L - x_L \tan \gamma_1)}{d_x(u_0 - u_L) - f \tan \gamma_1} \quad (11)$$

In a similar manner, the coordinates of point B_1 , denoted by x_{B1} and y_{B1} , can be derived. Finally, the pan angle of the robot relative to the window frame is given by

$$\theta = \arctan\left(\frac{x_{B1} - x_{A1}}{y_{B1} - y_{A1}}\right) \quad (12)$$

As seen in Fig. 9, θ denotes the orientation of the robot on the glass, based on which the robot can rotate its waist to reach a desired posture.



Fig. 10. Motion test at the City University of Hong Kong

5. Experiments

The robot was tested in cleaning a glass wall of the academic building at the City University of Hong Kong, as shown in Fig. 10. The robot operation includes: 1) adjusting the orientation by rotating the waist, 2) cleaning the glass wall with brash, and 3) crossing the

window frame from one glass section to another section. The successful demonstrations show that the climbing robot can clean the glass wall automatically and effectively.

When the robot cleans the glass wall, detection of the orientation is important for the robot to move along the desired trajectory, and measurement of the distance between the robot and the window frame is also important to infer the robot to cross the window frame. A series of experiments were performed to evaluate the effectiveness of the visual sensing system in measuring the robot's orientation and the distance between the robot and the window frame.

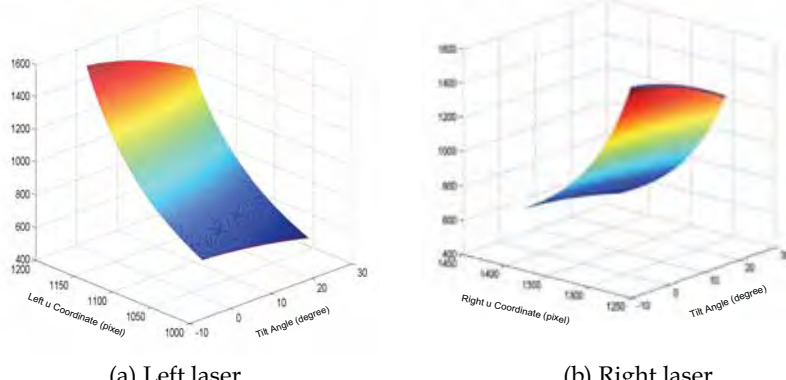


Fig. 11. Distance between the robot and the window frame -- u coordinate of the left/right laser point and tilt angle of the camera

5.1 Measurement of the Robot Position

Firstly, the visual sensing system was calibrated by acquiring images and analyzing u or v coordinates of the laser points when the robot was at different calibration positions on the glass surface. With the least square fitting, the distance between the robot and the window frame could be developed from the calibration as a function of u coordinate of the left laser point u_L (pixel) and the tilt angle of the camera α (degree). The detailed procedures of calibration are listed in the following:

1. Move the robot to an arbitrary position and measure the distance between the robot to the window frame (i.e., the distance d is 100 mm), and then use the camera to acquire the title angle α and the pixel coordinates u_R (and u_L).
2. Move the robot to the other positions and obtain a series of calibration data;
3. Obtain coefficients a_1, a_2, a_3 and β , with the least square fitting method, from equation (7).

Through the above calibration procedures, we obtained $a_1 = 16.67$, $a_2 = -185839.97$, and $a_3 = -1286.21$. Then, the distance is derived from Simoncelli et al. (2000) as

$$d = \frac{16.67 u_L - 185839.97}{u_L - 1286.21} \cos(\alpha + 9.2^\circ) \text{ (mm)} \quad (13)$$

In a similar manner, the distance d could be developed as the function of u coordinate of the right laser point, i.e.

$$d = \frac{33.09 u_R + 96310.74}{u_R - 1197.37} \cos(\alpha + 8.9^\circ) \text{ (mm)} \quad (14)$$

The distance functions in v coordinate of the two laser points were also developed. After comparison, we found that the distance measurement with u coordinate was more accurate than with v coordinate in this experiment. Figs. 11 (a) and(b) illustrate the relationships described in equations (13) and (14), respectively.

In the following experiments, equation (13) was used to measure the position of the robot on the glass surface. Experimental results of the relationship between the measurement error and the distance measured is shown in Fig. 12, where the squared points denote the measurement errors with different distances, and the solid line denotes a trend of the measurement errors as the distance increases. When the camera pans 90 degrees anti-clockwise, the distance between the robot and the left window frame can be measured. When the camera pans 90 degrees clockwise, the distance between the robot and the right window frame can be measured. To solve the error accumulative problem of the measured distance, the visual sensor needs to be reset after several measurements. Note that the camera distortion may affect the measurement of d . It is seen from Fig. 12 that the measurement error is small (i.e., < 10 mm) when the distance is not large (i.e., < 1000 mm). In case of large distance, the camera distortion correction should be considered.

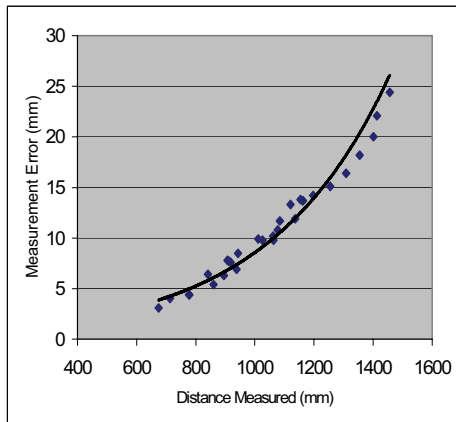


Fig. 12. Trend of the distance measurement errors

5.2 Measurement of the Robot Orientation

The visual sensing system was further calibrated to find the relationship between the robot's orientation and the u coordinates of the left and the right laser points in the image. With the least square fitting, the following relationship can be derived from the calibration:

$$\theta = \arctg\left(\frac{-691.2 u_L - 798.34 u_R + 1841988.56}{u_L u_R - 1234.92 u_L - 1282.83 u_R + 1584334.83}\right) \quad (15)$$

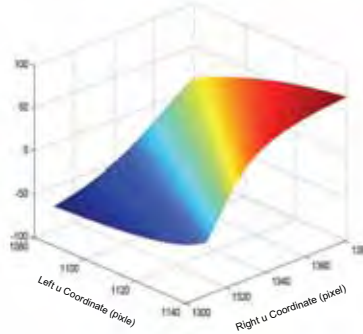


Fig. 13. Measurement of the robot orientation based on u coordinates of the left and right laser points

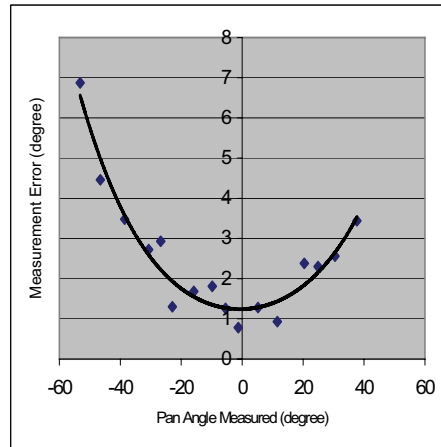


Fig. 14. Trend of orientation-measure errors

Fig. 13 illustrates the relationship between the pan angle θ and the coordinates u_L and u_R . The relationship between the pan angle and the measurement errors is shown in Fig. 14, where the squared points denote the measurement errors with different orientations, and the solid line denotes a trend of the orientation measurement errors as the pan angle changes. Note that the pan angle error may contribute to the overall measurement error. However, in certain applications, the effect of the pan angle error to the distance measurement is not serious. In our experiment, we found when the robot climbed over 2 m horizontally on the glass surface, the pan angle of the robot is less than 6 degrees.

The orientation of the robot may be affected by the gravitational force, especially when the robot climbs horizontally. When the robot climbed over 2 m horizontally on the glass

surface, the pan angle of the robot was found to be less than 6 degrees in the experiment. When the pan angle was measured to be positive, the robot rotated its waist clockwise to reach the desired horizontal or vertical orientation. When the pan angle was measured to be negative, the robot rotated anti-clockwise until reaching its desired posture.

5.3 Measurement of the Location of the Dirty Spot

The pattern recognition technique was used to find out the dirty spot to be cleaned and then to obtain the image of the laser mark. Equation (14) was used to measure the distance between the robot and the dirty spot. Based on the measured distance and the pan angle of the camera, the location of the dirty spot can be known. The experimental results of locating dirty spots are shown in Table 1.

	ψ (degree)	Tilt Angle (degree)	Right Coordinate u (pixel)	D (mm)	Measure error (x, y) (mm)
1	37	11	1364	798.2	(2.6, 3.7)
2	65	17	1400	633.3	(3.2, 1.6)
3	52	22	1410	577.0	(2.5, 2.1)
4	53	11.6	1370	768.6	(3.5, 2.6)
5	54	5	1325	1066.1	(7.1, 3.4)
6	75	2.4	1311	1205.6	(10.3, 2.0)
7	67	9	1348	890.3	(6.1, 2.0)
8	65	5	1327	1050.1	(7.7, 2.6)
9	78	10.4	1358	830.0	(5.9, 1.4)

Table 1. Experimental results of locating the position of the dirty spot

6. Conclusions

This chapter presents an application of a climbing robot for the glass cleaning service. The robot is constructed by two rodless cylinders and a rotation cylinder. The robot can adjust its orientation to maintain in the desired trajectory path. After finishing the cleaning work in one section of the glass wall, the robot can cross the window frame to enter another section. A visual sensing system, which is composed of an omnidirectional CCD camera and two laser diodes, is applied to measure the robot's position and orientation on the glass wall. Experiments demonstrate that with the assistance of the proposed motion planning and visual sensing technologies, the climbing robot can perform cleaning work on the glass wall effectively. Future work will be toward developing more efficient motion control system and reducing size/weight of the climbing robot.

7. Acknowledgement

This work was supported in part by a grant from Research Grants Council of the Hong Kong Special Administrative Region, China [Reference No. City 11119706], and a grant from the City University of Hong Kong (Project no. 7002127).

8. References

- Balaguer, C.; Gimenez, A.; Pastor, J. M. V.; Padron, M. & Abderrahim, M. (2000). Climbing autonomous robot for inspection applications in 3D complex environments. *Robotica*, Vol. 18, No. 3, pp. 287-297.
- Boissonnat, J. D.; Devillers, O. & Lazard, S. (2000). Motion planning of legged robots. *SIAM Journal on Computing*, Vol. 30, No. 1, pp. 218-246.
- Chen, C. H.; Kumar V. and Luo, Y. C. (1999). Motion planning of walking robots in environments with uncertainty. *Journal of Robotic Systems*, Vo. 16, No. 10, pp. 527-545.
- Egerstedt M. and Hu, X. (2002). A hybrid control approach to action coordination for mobile robots. *Automatica*, Vol. 38, No 1, pp. 125-130.
- Hasegawa, Y.; Arakawa T. & Fukuda, T. (2000). Trajectory generation for biped locomotion robot. *Mechatronics*, Vol. 10, No. 1-2, pp. 67-89.
- Hert S. & Lumelsky, V. (1999). Motion planning in R^3 for multiple tethered robots. *IEEE transactions on robotics and automation*, Vol. 15, No. 4, pp. 623-639.
- Kurazume, R. and Hirose, S. (2000). Development of a cleaning robot system with cooperative positioning system. *Autonomous Robots*, Vol. 9, No. 3, pp. 237-246.
- Lamiraux, F. & Laumond, J. P. (2001). Smooth motion planning for car-like vehicles. *IEEE Transactions on Robotics and Automation*, Vol. 17, No. 4, pp. 498-501.
- La Rosa, G.; Messina, M.; Muscato, G. & Sinatra, R. (2002). A low-cost lightweight climbing robot for the inspection of vertical surfaces. *Mechatronics*, Vol. 12, No. 1, pp. 71-96.
- Ma, Y.; Kosecka, J. and Sastry, S. S. (1999). Vision guided navigation for a nonholonomic mobile robot. *IEEE Trans. Robot. Automat.*, Vol. 15, No. 3, pp. 521-536.
- Maeda, S.; Kuno, Y. & Shirai, Y. (1997). Mobile robot localization based on eigenspace analysis. *Systems and Computers in Japan*, Vol. 28, No. 12, pp. 11-21.
- Malis, E.; Chaumette, F. and Boudet, S. (2000). Multi-cameras visual servoing. *Proc. IEEE Conf. Robot. Automat.*, pp. 3183-3188, San Francisco, CA, USA, April 2000.
- Malis, E.; Chaumette, F. & Boudet, S. (1999). 2-1/2-D visual servoing. *IEEE Trans. Robot. Automat.*, Vol. 15, No. 2, pp. 238-250.
- Mosemann H. and Wahl, F. M. (2001). Automatic decomposition of planned assembly sequences into skill primitives. *IEEE Transactions on Robotics and Automation*, Vol. 17, No. 5, pp. 709-718.
- Simoncelli, M.; Zunino, G.; Christensen, HI and Lange, K. (2000). Autonomous pool cleaning: Self localization and autonomous navigation for cleaning. *Autonomous Robots*, Vol. 9, No. 3, pp. 261-270.
- Sun, D., Zhu, J., Lam, C. and Tso, S. K. (2004). A visual sensing application to a climbing cleaning robot on the glass surface. *Mechatronics* , Vol. 14, pp. 1089-1104.
- Zhu, J.; Sun D. and Tso, S. K. (2002). Development of a tracked climbing robot. *Journal of Intelligent and Robotic Systems*, Vol. 35, No. 4, pp. 427-444.
- Zhu, J.; Sun D. and Tso, S. K. (2003). Application of a service climbing robot with motion planning and visual sensing . *Journal of Robotic Systems*, Vol. 20, No. 4., pp. 189-199.

Ball-shaped Robots

Tomi Ylikorpi and Jussi Suomela
*Helsinki University of Technology
Finland*

1. Introduction

A sphere is "the set of all points in three-dimensional space lying the same distance (the radius) from a given point (the centre)" (Encyclopedia Britannica Online). In terms of robotics, a spherical structure can freely rotate in any direction and all positions are stable. The shape of a sphere provides complete symmetry and a soft, safe, and friendly look without any sharp corners or protrusions, which is advantageous when a robotic device is dealing with people.

The principle of mobility for a ball-shaped robot is usually based on the movement of the robot's centre of gravity (cog) inside the spherical shell. The further the cog is from the centre of the ball, the greater the driving torque. Naturally, the ball diameter defines the maximum distance and the total mass limits the unbalanced mass being moved inside the ball. Often the available torque is quite modest compared to the total weight of the robot. An alternative method to create torque is based on the inertia of a rotating mass; inside the ball a rotating mass is accelerated and generates a counter-torque that drives the ball in the opposite direction. As the torque is a result of acceleration, the speed limit of the rotating mass sets a time limit for the applied torque. Hence this method can be used only for short periods and it also requires a means to decelerate the rotating mass back to rest. Inertia can, however, be used for orienting the ball when selecting the desired rolling direction.

A large diameter for the robot helps to generate greater driving torque and, at the same time, resistive torque from environmental objects such as stones or doorsteps remains lower. Hence large size is a benefit, while the overall mass then tends to increase. Technological developments with robotic balls aim to maximise the driving torque while minimising the mass, providing steering capability, modifying sphere surface texture to achieve the desired terrain interaction, and generating autonomous functions through sensors and added intelligence. The greatest technical challenges are the robot's limited off-road capability and the challenge of controllability. Step-climbing capability is defined by the radius of the ball and the ratio of the masses of the cover and the unbalanced mass. Typically, the static step-climbing capability is less than $0.25 \times R$. The possibility of rotation in all directions makes the control of the ball challenging. Ball oscillation during movement is difficult to handle and the control system requires powerful actuators to compensate the oscillations.

While the propulsion system is located inside the ball it can be hermetically sealed to provide the best possible shield for the interior parts. The spherical shape maximises the internal volume with respect to surface area and provides optimal strength against internal

overpressure or under-pressure, which is an important feature for underwater and space applications. Ball-shaped autonomously moving vehicles have a long history, and recent studies have described a variety of applications in different environments, including marine, indoors, outdoors, zero-gravity and planetary exploration.

1.1 Illustration Credits

All the patent drawings have been adopted from the website of the United States Patent and Trademark Office; Patent Full-Text and Full-Page Image Databases (<http://www.uspto.gov/patft/>) accessed during the period May 21st 2007 – May 25th 2007 (USPTO, 2007).

2. Mechanical Construction

This chapter presents some technical structures for spherical robots that have adopted different mechanical constructions. The study is limited here to robots moving over terrain with an internal power and traction system. Floating and flying robots, as well as wheeled robots with spherical or semi-spherical wheels, are omitted. Wind-propelled balls and human-carrying marine vessels are included as curiosities. The robots can be classified according to the following properties:

Power source

- internal spring or rubber band
- internal electrical/combustion motor
- internal human muscle power
- external wind thrust

Control and degrees of freedom (dof.)

- forward rolling only
- fixed manually pre-set off-balance (curved path)
- cyclic, mechanically disturbed balance (oscillating path)
- shell texture-activated randomly changing direction
- reactive change of rolling direction
- reactive activation of steering function
- controlled in one direction
- controlled in two dofs.

Steering method

- tilting of rolling axis
- internal movable rolling axis
- inertia steering
- several mobile masses

Control method

- mechanical reaction
- electrical reaction

- radio control
- computer control

Internal traction method

- uniaxial
- biaxial
- single-wheel
- bicycle
- tricycle or four-wheel
- wheel-track
- multiple mobile masses
- deformation of shell

Engineers are often advised not to reinvent the wheel. However, a quick search of the U.S. Patent office database immediately reveals more than 50 patents related to the autonomous mobility of a ball-shaped object. These patents date from 1889 to 2005 and all comprise a mobile counterweight that is used to generate ball motion. The examples presented in this chapter show several of the properties presented in the list above.

2.1 Early 1-dof Spring-driven Models

The 'Toy' by J.L. Tate, patented in the U.S. in 1893 (U.S. Patent 508,558), presents a spherical vehicle that carries an internal 1-dof. counter-mass driven by an elastic spring. Fig. 1 (left) shows a counter-mass (C) carried by a central axis (B), an elastic spring (E), and a drum (D) that winds the spring when the ball is first manually rotated. Upon the release of the ball the spring would unwind from the drum and make the ball rotate in a forward direction. There is no other steering except bouncing off external obstacles, which, however, is often enough to allow the ball to continue its motion successfully. This basic principle was later presented in several other patents in which the internal mechanical arrangement or construction of the spring was modified. The most complex designs utilise clock-springs and are accompanied by gearboxes.

In 1906, B. Shorthouse patented a design that offered the possibility of manually adjusting the position of the internal counterweight in order to make the ball roll along a desired curved trajectory instead of a straight path (U.S. Patent 819,609). Fig. 1 (right) shows how the counter-mass and its support (g) can be placed at an angle to the rolling axis (f), which then remains in a tilted position relative to the horizontal.

Ever since then, patents have presented mechanisms to produce more or less irregular rolling paths for self-propelled balls. The toy shown in Fig. 2 dates back to 1909 and shows how the counter-mass (16) is made to move in a circular path inside the sphere by means of a gear (18). The internal motion of the counter-mass makes the rolling axle change its attitude continuously and the ball proceeds along a wobbly 'zig-zag' path, as described by the inventor (U.S. Patent 933,623).

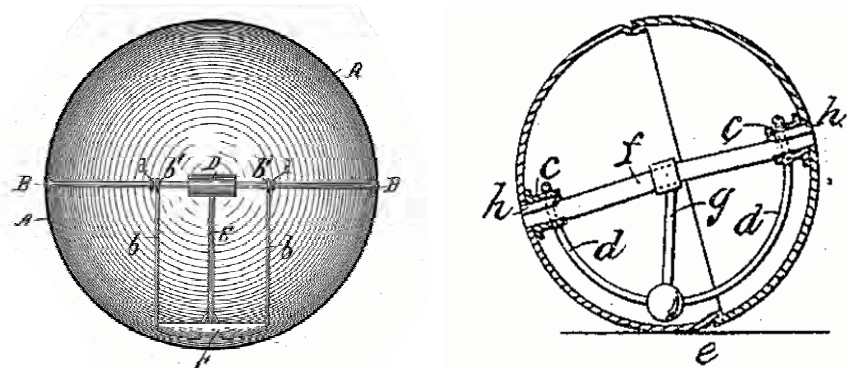


Fig. 1. (left) Toy by J.L. Tate (U.S. Patent 508,558); (right) Self-Propelling Device by B. Shorthouse (U.S. Patent 819,609)

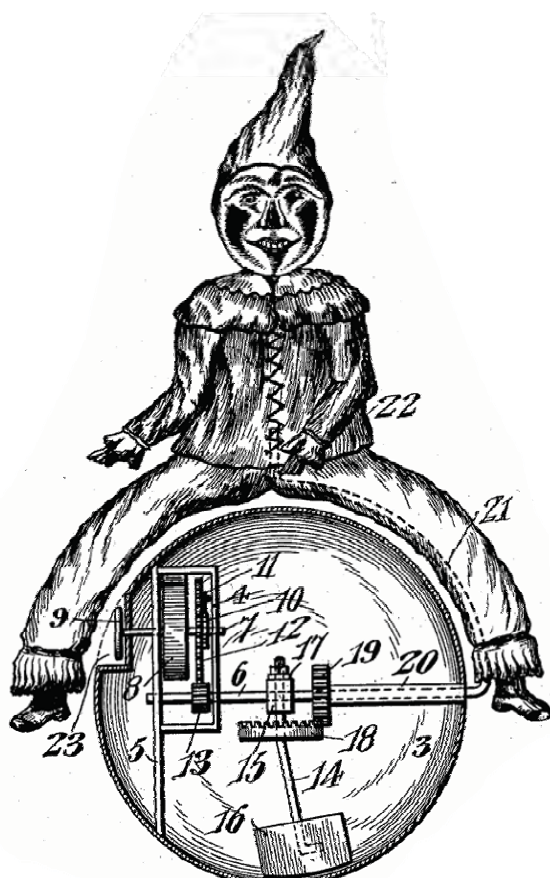


Fig. 2. Mechanical Toy by E.E. Cecil (U.S. Patent 933,623)

2.2 Man-carrying Models

Spherical vehicles to carry people were first developed for marine applications, such as that of W. Henry in 1889 (Fig. 3, left). This vehicle, floating in the water with its passenger, was balanced by the mass of the ballast and the weight of the passenger. The vehicle would move in a manner very similar to the toys described above, with a balanced mass inside and with its outer surface rolling. Steering would be achieved by tilting the axis of rotation by moving the passenger mass inside the vehicle, while the driving force comes from a hand-operated crank. (U.S. Patent 396,486) In 1941, J.E. Reilley patented a ball-shaped car (Fig. 3, right) (U.S. Patent 2,267,254).

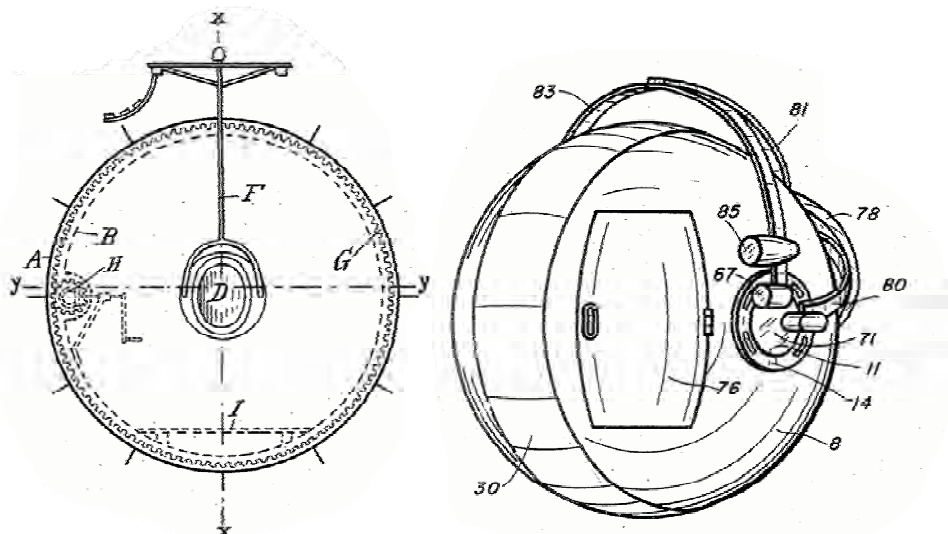


Fig. 3. (left) Marine vessel by W. Henry (U.S. Patent 396,486); (right) A spherical vehicle by J.E. Reilley (U.S. Patent 2,267,254)

In some cases, a person would enter a ball and operate it directly without any additional means, like a hamster inside a treadmill, as in Fig. 4 (left), dated 1958. (U.S. Patent 2,838,022) In 1969 S. E. Cloud patented a spherical structure that could accommodate a human being or even vehicles inside it (Fig. 4. right). The main objective was in inflatable/deflatable structure that could be easily stored and transported. He did not pay attention to the mobility of such a device. (U.S. Patent 3,428,015) In 1980 C. Maplethorpe and K. E. Kary patented a manned vehicle equipped with a seat and a pedal mechanism for use on land or water shown in Fig. 5 (left). (U.S. Patent 4,386,787) L. R. Clark Jr. and H. P. Greene Jr. patented yet another idea for a human-carrying spherical vehicle that could be steered by relocating the centre of gravity in a very similar manner to hang-gliders (Fig. 5 right). (U.S. Patent 4,501,569) In 1988 J. S. Sefton patented an open-mesh spherical structure for a man-carrying vehicle (Fig. 6 left). (U.S. Patent 4,729,446) Fig. 6 (right) presents a complex drive mechanism also intended for the transport of human beings. The design, patented by A. Ray in 1971, incorporates tracks composed of several wheels. Coordinated motion of the tracks and the wheels inside the spherical shell allow the ball's rolling direction to be controlled.

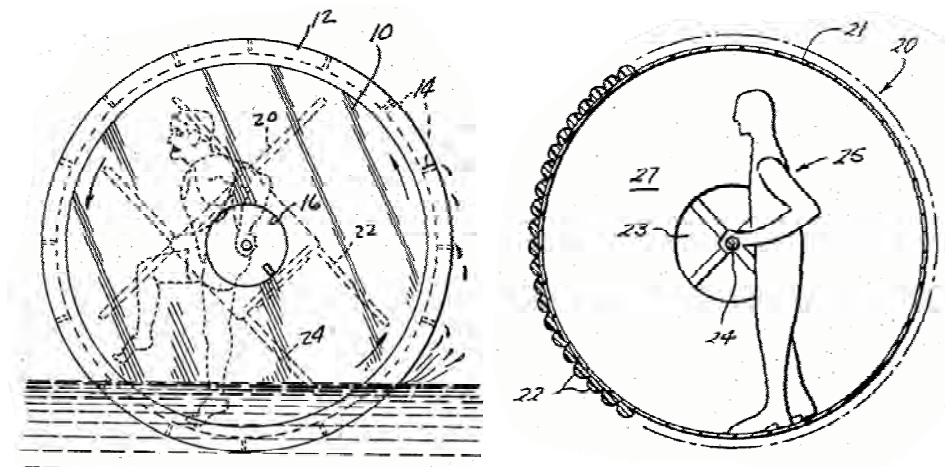


Fig. 4. (left) Spherical water craft by W. E. Wilson (U.S. Patent 2,838,022); (right) Spherical vehicle by S. E. Cloud (U.S. Patent 3,428,015)

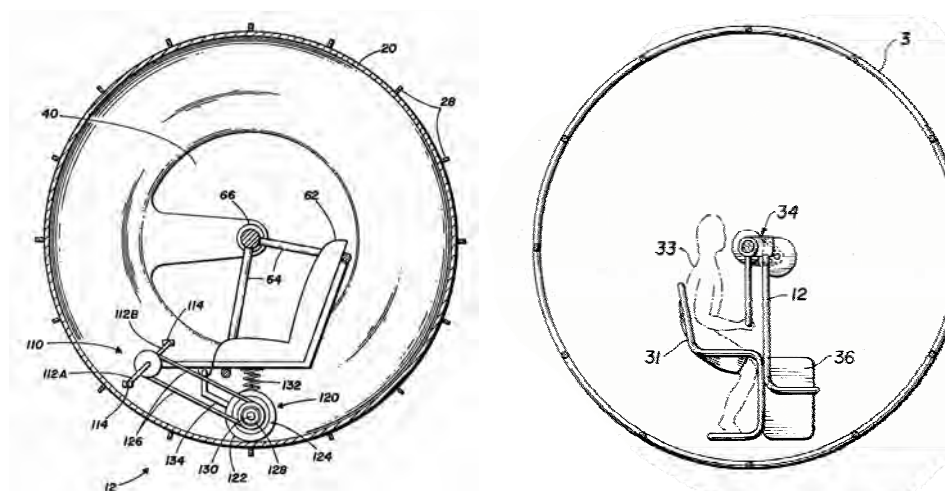


Fig. 5. (left) Spherical vehicle by C. Maplethorpe and K. E. Kary (U.S. Patent 4,386,787); (right) Yet another spherical vehicle by L. R. Clark Jr. and H. P. Greene Jr. (U.S. Patent 4,501,569)

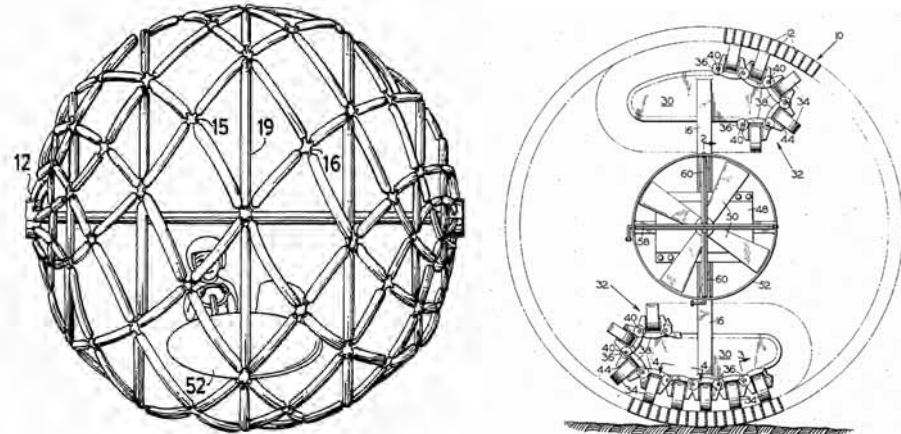


Fig. 6. (left) Mobile sphere by J. S. Sefton (U.S. Patent 4,729,446); (right) Spherical vehicle by A. Ray (U.S. Patent 3,746,117)

2.3 Electrical 1 and 2-dof. Models

A mechanical spring as a power source was displaced by a battery and an electric motor in two almost parallel patents; one by E. A. Glos (U.S. Patent 2,939,246, filed 1958) and another by J.M. Easterling (U.S. Patent 2,949,696, filed 1957). The design by Glos also included a gravity-operated switch that activated and de-activated the motor in desired positions. Easterling notes that upon contact with objects the motor is capable of driving the counter mass over the upper dead centre, which makes the ball autonomously reverse for a half-revolution. At the same time, as Easterling notes, the ball may also change its rolling direction. This property makes the ball move almost endlessly; this was referred to in several later patents and also modern-day toys such as the 'Squiggleball', 'Weaselball', and 'Robomaid', as well as the 'Thistle' concept of Helsinki University of Technology (to be presented later). Fig. 8 presents a 'Squiggleball' opened to show the battery compartment and electric motor and gears enclosed inside a plastic housing. The design is not very different from that of Easterling. One specific property of the 'Squiggleball' is a thick rubber band (not shown in the figure) that is placed along the rolling circumference on the outer surface. The thick band adds friction to the floor, but also makes the rolling axis tilt slightly to one side or the other. This makes the ball run along slightly curved paths and upon collision and autonomous reversing it always changes the rolling direction. Thus it can also get out of dead ends. Consequently, electric motors were introduced with several different mechanical solutions that were already at least partly familiar from earlier spring-driven inventions. Further development introduced shock and attitude sensing with mercury switches that would control the motor operation and rolling direction, as well as adding light and sound effects.

An active second freedom for a motorised ball was introduced by McKeehan in 1974 (U.S. Patent 3,798,835), as shown in Fig. 9 (left). This ball's structure is also different from the previous designs. Instead of the rolling axis extending across the complete ball, there is a support post that carries the rotating mass in the centre. Thus the rolling axis is perpendicular to the post, and the post itself rotates along with the shell so that its ends – or

poles - are on the rolling circumference. Since the post is rotating in the middle of the ball the counter-mass must be divided into two halves, one on each side of the post. McKeahan's design shows two pendulums driven by a single motor. These provide one degree of freedom that also utilises an inertial switch to change the rolling direction in the event of a collision. Another dof. is provided by another motor that spins the post - and the rolling axis - around the longitudinal axis of the post. Should the post be in a vertical position while spinning, then the rolling axis would adopt a new rolling direction. Should the post be in a horizontal position spinning would cause the ball to roll sideways in the direction the actual rolling axis is pointing in. Any other position of the post and combined motion of the post and pendulum rolling would produce quite a complex motion. The post-driving motors can also be activated with an inertial switch in the event of a collision.

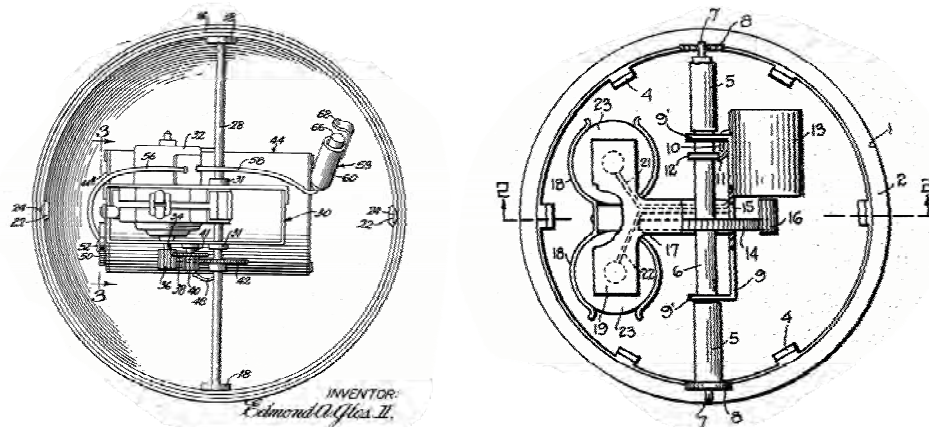


Fig. 7. (left) Toy ball by E. A. Glos (U.S. Patent 2,939,246); (right) Toy by J. M. Easterling in 1957 (U.S. Patent 2,949,696)



Fig. 8. 'Squiggleball' opened to show the interior parts (Image: TKK)

The spherical vehicle control system of L. R. Clark Jr. et al. in 1985 (U.S. Patent 4,501,569) resembles a motorised version of B. Shorthouse's Self-Propelling Device of 1906. In addition to two degrees of freedom, Clark's design also provides full controllability of both by means of two servo motors. One motor (No. 8 in Fig. 9 right) drives the ball forward and the other (15) moves the pendulum and adjusts the position of rolling axis. Continuous control is realised with radio control equipment

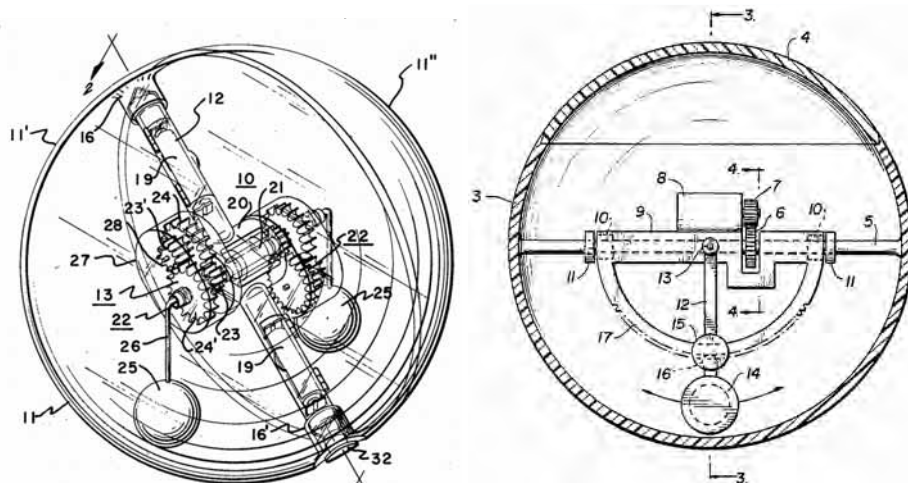


Fig. 9. (left) Motor driven ball toy by McKeehan (U.S. Patent 3,798,835); (right) Steerable ball toy by L. R. Clark Jr. et al. (U.S. Patent 4,501,569)

2.4 Hamster-wheel Models

The counterweight was usually constructed with a lever rotating around the ball's axis of rotation. Mobility was provided by generating torque directly to the lever. The amount of torque needed from the power system was directly proportional to the mass of the counterweight and length of the lever arm. During the development of the 'Thistle' at TKK it was soon realised that this approach sets high requirements for the motor torque and in fact the actual driving torque for the ball may be much less than the torque applied by the motor. In 1918, A. D. McFaul patented a spring-driven hamster-ball design (a derivative of a hamster treadmill), where the counterweight was moved by friction between the ball's inner surface and traction wheels mounted on the counterweight (Fig. 10). In this construction, the length of the lever arm no longer affects the required power-system torque (but the diameter of the friction wheels does), and similar mobility can be achieved with less internal torque. This is of great benefit in low-torque spring-driven toys and balls with a large diameter.

In McFaul's design a single axis with two traction wheels was supported from the ball rolling axis. C. E. Merrill et al. placed a three-wheeled vehicle freely inside the ball in 1973 (U.S. Patent 3,722,134). Subsequently several patents placed a three- or four-wheeled vehicle inside the ball. Some vehicles are completely free inside, while others have some additional support from structures inside the ball; see Fig. 12. Advanced radio-controlled cars with full steerability placed inside also provide full steerability for the ball.

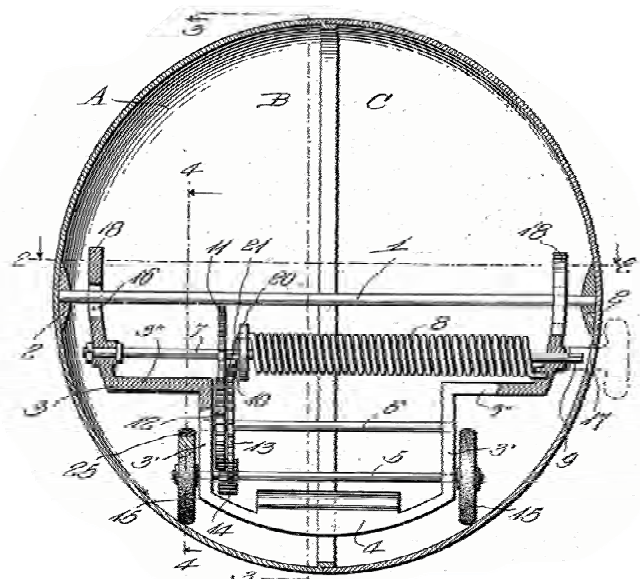
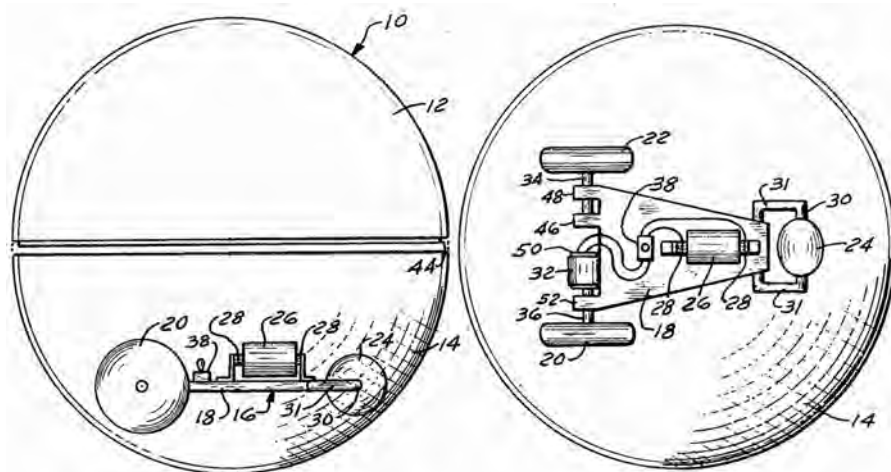


Fig. 10. Early hamster-ball by A.D. McFaul (U.S. Patent 1,263,262)



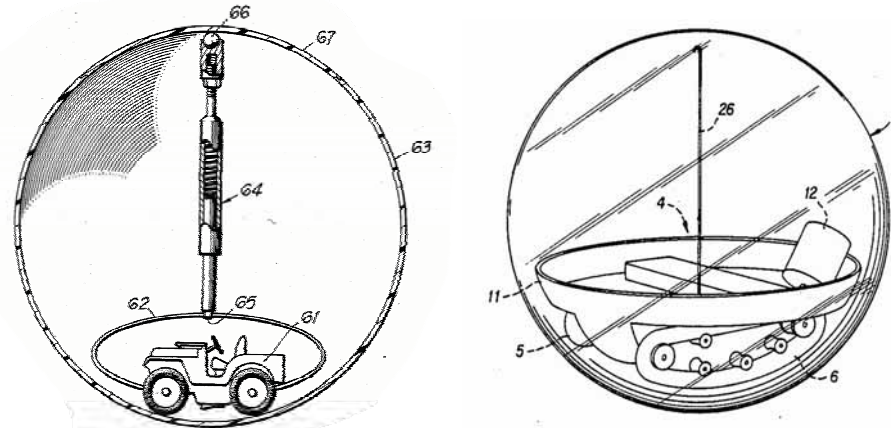
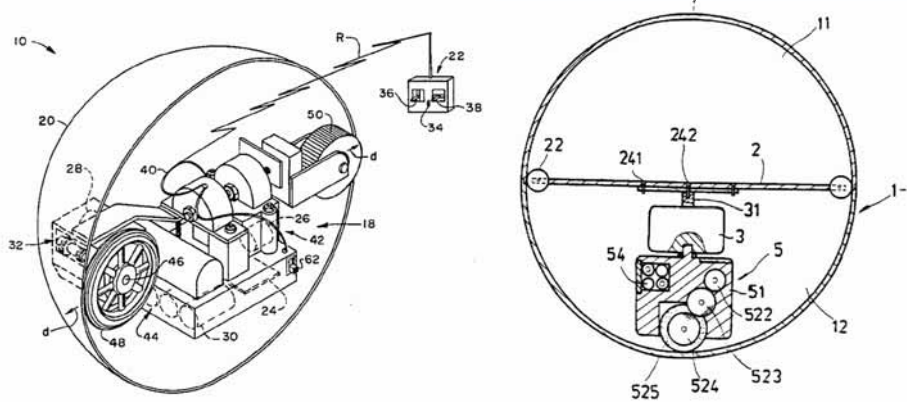


Fig. 12. (left) Mechanised toy ball by D. E. Robinson (U.S. Patent 4,601,675); (right) Radio controllable spherical toy by H.V. Sonesson (U.S. Patent 4,927,401)

2.5 Steerable Models

The above-mentioned radio controlled vehicles inside the ball provided full steerability. Apart from four-wheeler, radio-controlled single-/two-wheelers have also been presented, as shown in Fig. 13. This approach was also briefly adopted in the course of the development of the 'Rollo' robot at Helsinki University of Technology (to be presented later). Ku's design is a single wheel without a support post that would extend over the complete ball diameter. Instead, the wheel (525) gets support from a horizontal plane (2), which is supported on the inner surface of the ball with rollers (22). A servo motor (3) is used to freely control the wheel rolling direction. The driving and controllability of this kind of vehicle is very simple and straightforward, as has also been learned at TKK in the Rollo project.



In addition to the ‘Vehicle inside the sphere’ composition, steerability has also been introduced in older two-axis mechanisms, as already presented by Clark Jr., who patented a design with a controlled pendulum in 1985. A similar approach was also adopted by M. Kobayashi in 1985 (U.S. Patent 4,726,800) and by Michaud et al. in 2001 (U.S. Patent 6,227,933). Michaud also equipped the central rolling axis with an instrument platform for an on-board computer and electronics.

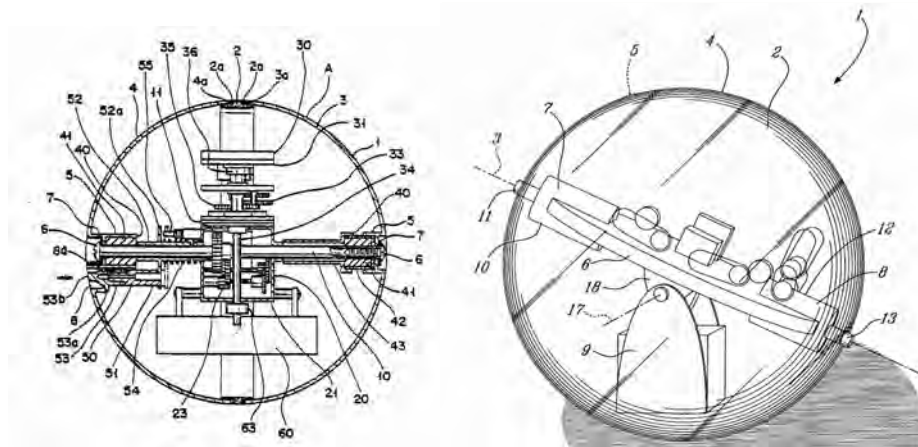


Fig. 14. (left) Radio-controllable toy vehicle Robot ball by M. Kobayashi (U.S. Patent 4,726,800); (right) Robot ball by F. Michaud et al. (U.S. Patent 6,227,933)

2.7 Rollo Robot

The Automation Technology Laboratory of Helsinki University of Technology developed ball-shaped robots to act as home assistants as early as in 1995. Rollo can act as a real mobile telephone, event reminder, and safety guard. The first-generation mechanics were similar to those of Martin, while the second generation was a radio-controlled four-wheeler slightly resembling that of Merril et al. To operate properly, both designs required a strong, accurate, and expensive cover. The early stages of the development of Rollo are described in Halme et al. (1996a), Halme et al. (1996b), and Wang & Halme (1996). The third-generation design is quite different from any of those presented before. It does carry a rolling axis extending through the ball, like most of the older designs. However, the rolling axis is not fixed to the ball surface, but it can rotate along the circumference on a rim gear; see Fig. 15. The rolling direction is selected by turning the rolling axis along the rim gear, which must then lie in the horizontal position. However, during rolling, the rim gear also rotates around the axis and there are only two positions where the robot can select the rolling direction (i.e. when the rim gear lies horizontally). In these two cases a similar motor rotation yields to opposite directions of rotation along the rim gear. The robot always has to advance a full number of half-revolutions, after which it needs to determine which direction along the rim gear is the correct one. The revolutions of the rim gear are counted by means of an inductive sensor. Continuous steering of the robot is also possible in theory, but in practice it would be a very demanding task.



Fig. 15. 2nd, 1st, and 3rd generations of the Rollo (Image: TKK)

The large instrument board along the rolling axis carries an on-board computer and advanced communication and interactivity tools, such as a camera, microphone, and a video link. Communication with the control station is achieved using a radio modem. The robot is equipped with a Phytec MiniModul-167 micro-controller board using a Siemens SAB C167 CR-LM micro-controller. The robot has sensors for temperature, pan, tilt, and heading of the inner mechanics and pulse encoders for motor rotation measurement. The local server transmits controls to the robot using commands that are kinematics-invariant (i.e., they use the work environment variables only). The commands include heading, speed, and running time/distance. Coded graphical signs mounted on the ceiling are utilised by means of the on-board camera to determine the absolute location of the robot when necessary. The system has an automatic localisation command, which causes the robot to stop, wait for some time to smooth out oscillations, turn the camera to the vertical position, find the visible beacons and automatically calculate the position, which is then returned to the control station.

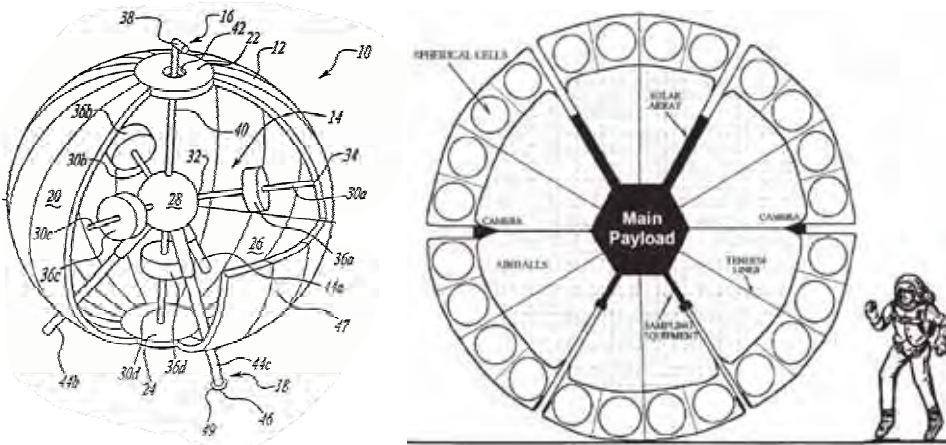
The robot can be programmed as an autonomous device or it can be teleoperated via the internet. The user interface contains a virtual model of the remote environment where the video input and virtual models are overlaid to produce the augmented reality for robot guidance. Augmented reality provides an efficient medium for communication between a remote user and a local system. The user can navigate in the virtual model and subsequently use it as an operator interface.

As one application, an educational system has been developed for virtual laboratory exercises which university students can do over the internet. The overall experimentation system includes versatile possibilities to set up interactive laboratory exercises, from an elementary level to more advanced levels. Topics include mechatronics, robot kinematics and dynamics, localisation and navigation, augmented VR techniques, communication systems, and internet-based control of devices.

A second application, the Home Helper system, provides a mobile multimedia platform for communications between people at home and assistants working outside. The system is connected to various networked devices at home. The devices provide potential for remote security surveillance, teleoperation of the devices, and interactive assistance to people living at home.

2.7 Other Methods of Mobility

The most recent inventions have introduced novel solutions to alter the position of the ball's centre of gravity. One example is the Spherical Mobile Robot by R. Mukherjee, patented in 2001, which uses several separate weights that are moved with the aid of linear feed systems (U.S. Patent 6,289,263); see Fig. 14 (left). Abas Kangi has presented a spherical rover for the exploration of the planet Mars (Kangi, 2004). The shell of this rover consists of several small cells that can be inflated and deflated upon command. The deflation of certain cells around the support area in the lower part of the sphere causes instability and makes the ball rotate in a controlled manner. The rover would be used to search for water on the surface of Mars.



The motorised motion of such a ball equipped with a steerable pendulum was also studied earlier. However, the motorised concept was abandoned when it was realised that the mass increase did not justify the achievable driving torque and that relatively small rocks could easily trap the ball. (Hajos et al., 2005)

There are several organisations exploring Mars Tumbleweed concepts, including the NASA Jet Propulsion Laboratory (JPL), NASA Langley Research Center (LaRC), Texas Technical University (TTU), and the Swiss Federal Institute of Technology. The parties have adopted different approaches towards the construction of the ball shape and structure in order to maximise wind thrust force and cross-terrain mobility. (Antol et al., 2003)



Fig. 15. Tumbleweed concept under testing (Antol et al., 2003)

3.2 The Thistle

The Thistle is a large low-mass wind-propelled ball inspired by the Russian Thistle plant. A 1.3-metre ball represents a model of a larger 6-metre version that was proposed for operation on the surface of Mars for autonomous surface exploration. In order not to be fully dependent on occasional wind energy, the Thistle was equipped with a 2-dof. drive system that provided full steerability and motorised locomotion. (Ylikorpi et al., 2004)

This study, funded by the European Space Agency under the ARIADNA programme, focused on new innovations derived from nature to develop a novel system to provide a robust and efficient locomotion system to be used for exploring other planets. The Automation Technology Laboratory of Helsinki University of Technology explored the cross-terrain capabilities of both wind-driven rovers and unbalance-driven rovers and performed a comparison between those. As a consequence it is possible to identify different

operational scenarios. One scenario would be a large and light purely wind-driven ball, like the Tumbleweed. Another scenario would be a large but slightly heavier ball equipped with a limited capability to move with the aid of a motor. The cross-terrain capability of this rover with wind propulsion would be slightly more limited than that of the Tumbleweed, but the motor would allow the ball to get around the largest obstacles and could be used to orient the ball for scientific purposes. A third alternative would be completely motor-driven, much smaller but also much heavier than the other two. It would be able to carry a large amount of heavy instrumentation and the ball shape would protect it against the danger of tipping over. The problem of available energy would be the same as with conventional rovers. (Ylikorpi et al., 2006)

3.3 Mobility of Unbalanced Mass-driven Balls and Wind-driven Balls

As the ball hits an obstacle, it adopts a new point of contact. If we wish to surmount the obstacle the torque needed must be calculated according to this new point of contact between the ball and the object. As the contact point moves from the ground to the obstacle, the torque caused by the vertical ballast force or horizontal wind-load changes too.

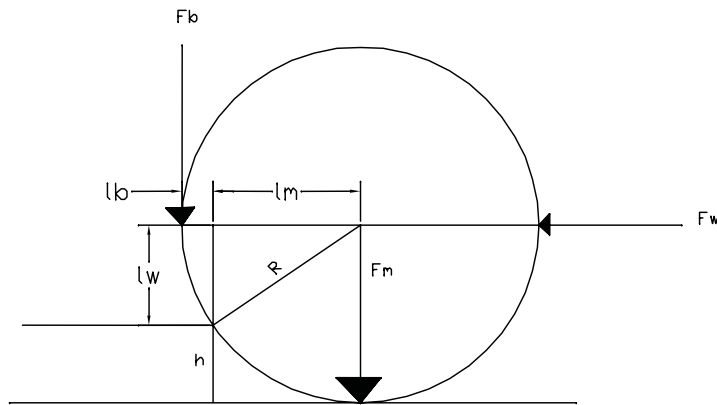


Fig. 16. Loads acting on a sphere surmounting an obstacle

Consider Fig. 16. The ball shell, with a radius R , has a weight F_m . F_b is the weight of the driving unbalanced mass and l_b is the distance between the mass and the contact point with the obstacle. L_m is the distance from the contact point to the ball shell centre of gravity. L_w is the vertical distance from the obstacle to the centre of the ball, and F_w is the thrust force from the wind. The figure assumes that the driving unbalanced mass is located at the outer surface of the ball shell. In practice this is not true; the mass will be located inside the ball, at a distance that is smaller than the ball radius R . The difference is taken into account in the calculations.

If the rolling ball meets an obstacle of height h , the mass load of the shell F_m generates a resistive torque T_m with a moment arm L_m .

$$T_m = F_m \cdot l_m \quad (1)$$

by geometry :

$$T_m = m \cdot g \cdot \sqrt{2 \cdot R \cdot h - h^2} \quad (2)$$

where :

g = gravity, m = ball mass

If wind load F_w is used for locomotion, the resulting torque T_w with a wind-load arm of moment l_w must overcome the resisting torque. We make an assumption that the wind load centre goes through the centre of the sphere.

$$T_w = F_w \cdot l_w \quad (3)$$

by geometry :

$$T_w = F_w \cdot (R - h) \quad (4)$$

The wind force F_w needed to surmount an obstacle can be calculated by setting $T_w = T_m$, from which follows:

$$F_w = m \cdot g \cdot \sqrt{\frac{2 \cdot R \cdot h - h^2}{(R - h)^2}} \quad (5)$$

Drag means a force on an object subjected to a fluid flow. Granger (1995) presents two formulae to define friction drag and pressure drag. From these the pressure drag is dominant for a blunt and smooth object, while friction drag increases as the surface gets rougher. In the case of the ball pressure drag can be used;

$$D_p = C_{Dp} \left(\frac{1}{2} \delta U^2 A_p \right) \quad (6)$$

where :

D_p = drag force

C_{Dp} = drag coefficient

δ = fluid density

U = flow velocity

A_p = cross – sectional area

The drag coefficient depends greatly on the geometry, surface properties, wind velocity, and air density. Heimendahl et al. (2004) and Hajos et al. (2005) present some experimental results for the C_D of different ball-shaped structures. It is reasonable to assume that a smooth ball on Mars would have a drag coefficient of 0.4, while with some added structural complexity it can be increased to 0.8. Making $C_D > 1$ would require the accurate design and

testing of a structure consisting of plate-like structures. The air density is 0.02 kg/m^3 for Mars and 1.29 kg/m^3 for the air on Earth.

The formulae presented now make it possible to calculate the force generated on the ball by the prevailing wind, or the other way around; the wind velocity needed to surmount a defined obstacle. The results will be presented and compared to unbalanced drive later in this chapter.

Study Fig. 16 again; if using unbalanced ballast mass for locomotion, the sphere mass must be divided into two portions: an evenly distributed structural mass acting through the shell centre and resulting in resistive torque, and the ballast mass causing F_b and having a moment of arm l_b . The figure shows the ballast mass to be located exactly on the outer surface, i.e. $l_b + l_m = R$. In reality this would not be the case. The length of moment arm l_b depends on the mechanical structure and ball size. For small spheres the ratio $(l_b + l_m)/R$ could be roughly 0.5, while the ratio approaches 1 as the sphere diameter increases. For a 6-m ball $(l_b + l_m)/R$ could have an estimated value of $2 \text{ m}/3 \text{ m}$ or 0.66. In the following calculations the value 0.66 is used for $(l_b + l_m)/R$. Now the resulting driving torque T_b can be calculated;

$$T_b = F_b * (0.66 * R - l_m) \quad (7)$$

Fig. 17 collects the calculation results for a given obstacle size with total ball mass, wind velocity, and driving unbalanced ballast mass as variables. It shows how a 6-m and 80-kg Thistle could be driven over 40-cm obstacles by a 30-m/s Martian wind. The same weight and size ball with an internal 60-kg motorised ballast mass would also surmount the same obstacle using the motor for propulsion. Hence in this scenario both methods of mobility could be used. However, the wind propulsion would be effective only during the strongest Martian storms. The mass reserved for the 6-m spherical shell remains 20 kg.

Reducing the total mass accommodates more modest wind speeds but also requires a lighter shell structure. Mass reserved for the shell structure is quite low and so inflatable structures are very interesting.

Similar comparison can be done with differing obstacle sizes. Mobility requirement can be set different for different locomotion methods. In order to utilise Martian wind more effectively total system mass can be reduced. As a consequence the ball would surmount the obstacles with less wind, or surmount even larger obstacles when driven by the wind. Motor drive would then have smaller unbalanced mass and motor-driven mobility would be reduced. The motor would be then used merely to get around the obstacles instead of getting over them.

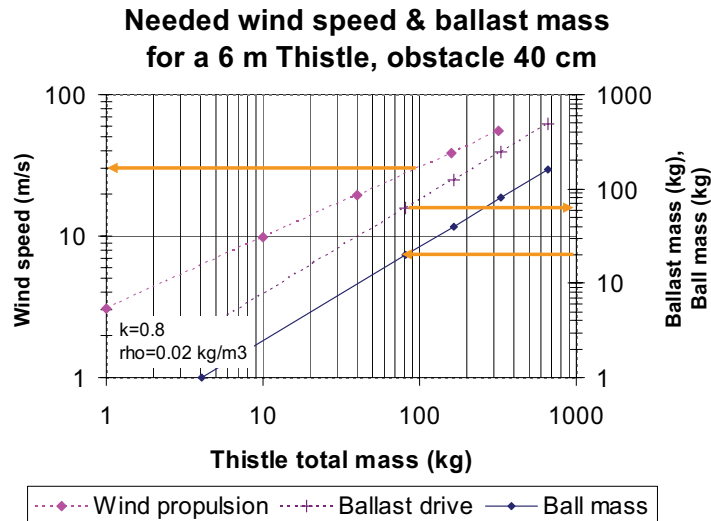


Fig. 17. Comparison of wind and ballast propulsion for the 6-m Thistle (Ylikorpi, 2005)

4. Thistle Prototype

Fig. 18 presents a small-scale prototype of the Thistle ball built at the TKK Automation Technology laboratory. Without internal driving mechanisms and assuming a low drag coefficient as a consequence of the open structure of the ball, a terrestrial 5-m/s wind is supposed to propel the roughly 4-kg and 1.3-m prototype shell over obstacles 10 cm high. When actively driven by a motorised 5-kg ballast mass, the prototype rolls over 4-cm obstacles. Driving tests with the Thistle show that locomotion is quite clumsy and somewhat chaotic. Its structural flexibility and sectional circumference make the ball advance in short bursts. If a tilt angle is introduced by means of the steering system, the Thistle follows a spiral-like path while rolling in which the radius of curvature decreases towards the end of the motion. The torque margin of the drive system allows the ballast mass to be rotated a complete revolution around the axis of rotation. This means that when the Thistle stops at an obstacle, the ballast mass finally travels over the upper dead centre and, in consequence, the Thistle autonomously backs off by half revolutions. Because of its instability the Thistle also simultaneously turns slightly. This behaviour enables the Thistle to circumvent obstacles autonomously and without any active steering. The Thistle was also tested on a snow bed during Finnish winter conditions. The soft structure of the snow effectively damped out the structural vibrations of the Thistle, while driving and steering were clearly easier and overall behaviour was more predictable. Fig. 18 (left) presents the driving and steering mechanism of the Thistle. The battery and two motors are mounted on a pivoted lever that hangs from bearings on the central rolling axis. The drive motor rotates the lever via a tooth belt and a large sprocket wheel. The tilting motor adjusts the angle of the lever with the aid of a lead screw. The motors are controlled with a radio control system and motor controllers familiar from toy cars. (Ylikorpi et al., 2004)



Fig. 18. (left) Thistle mechanism; (right), 1.3-m Thistle rolling on snow bed (TKK)

5. Other Recent and Related Development

In addition to the robots presented, there are several other similar devices, mostly intended for demonstration or simply for toys. The 1.5-metre-diameter scale models of the Tumbleweed Rover (Matthews, 2003) and Windball (Heimendahl et al., 2004) are intended for Mars exploration. Both of them are purely wind-driven, the only mobility-related actuation being re-shaping the structure by inflation/deflation (Tumbleweed) or with the aid of shape memory alloys (Windball). On Mars, 6-metre versions of these models would be used to carry out scientific tasks such as surface mapping and atmospheric measurements. The 15-cm Roball (Michaud & Caron, 2001) performed an important role in a study of interaction between the robot and small babies. It is anticipated that the 15-cm Cyclops (Chemel et al., 1999) and 50-cm Rotundus will be used to inspect and guard industrial plants (Knight, 2005). The Sphericle is used as an educational tool for learning the dynamics and control of a ball-shaped robot (Bicchi et al., 1997).

6. Control of Ball-shaped Robots

This chapter has shown a large variety of mechanical constructions of ball-shaped robots. As the operating principles of different models are different, so the kinematic and dynamic equations describing ball behaviour are different. Thus control algorithms for different robots become different. The possibility of rotation in all directions makes the control of the ball challenging. In addition, a hard-surfaced unbalanced ball on a smooth floor behaves like a pendulum; any change in motor torque or disturbance from its surroundings easily generates oscillation that attenuates very slowly. Oscillation around the rolling axis is controlled in TKK's Rollo by means of a closed-loop system that controls the drive motor torque. The control loop is equipped with attitude sensors and gyroscopes that measure the forward and backward motion of the payload mass. Controlling the sideways oscillation is a

more difficult task, since we do not possess any actuators in this direction. So far, no active instrumentation has been included for this, but, in future, passive dampers or an active closed-loop controlled movable counter-weight or pendulum may be considered. The kinematics and control of the early versions of Rollo are discussed in Halme et al. (1996a). Apart from the development of Rollo at TKK, Bicchi et al. (1997) also describe the kinematics, dynamics, and motion planning of the single-wheel ball robot Sphericle. Laplante (2004) discusses the kinematics and dynamics of ball robots in great detail and develops a control scheme to steer a pendulum-driven Roball along curved paths. Regarding the same ball robot, Michaud & Caron (2001) write more about higher-level behaviours and interaction with people.

7. Conclusion

Throughout history, ball-shaped toys have been quite popular and they still exist. Developments in computer technology, wireless data transfer, and digital cameras have given them many advanced operational capabilities. Autonomous ball-shaped robots are being introduced back into modern homes, this time not only as toys, but also as serving and guarding robots. Future work in this field will concentrate on analysing and developing the dynamics and control of the ball, as well as on applications and interaction with the environment and people.

The utilisation of large wind-propelled balls for Mars exploration has been widely studied in many separate institutions. The main advantages are large size, low mass, and autonomous mobility, accompanied by the disadvantage of limited steerability. Only the future will tell if the current expensive Mars exploration missions will be followed by low-cost autonomous missions utilising the Windball, Tumbleweed, or Thistle carrying instruments in the search for life on Mars or other extraterrestrial bodies.

8. References

- Antol, J.; Calhoun, P.; Flick, J.; Hajos, G.; Kolacinski, R.; Minton, D.; Owens, R. & Parker, J. (2003). *Low Cost Mars Surface Exploration: The Mars Tumbleweed*, NASA/TM-2003-212411, National Aeronautics and Space Administration, Langley Research Center, Hampton, Virginia 23681-2199, August 2003
- Bicchi, A.; Balluchi, A.; Prattichizzo, D. & Gorelli, A. (1997). *Introducing the Sphericle: an Experimental Testbed for Research and Teaching in Nonholonomy*, Centro E. Piaggio, Universita di Pisa, Pisa (Italy), Facolta di Ingegneria, Universita di Siena, Siena (Italy)
- Chemel, B.; Mutschler, E. & Schempf, H. (1999). Cyclops: Miniature Robotic Reconnaissance System, *IEEE Int. Conf. on Robotics and Automation (ICRA '99)*, Vol. 3, May, 1999, pp. 2298-2302
- Granger, R. A. (1995). *Fluid Mechanics*, Dover Edition, Dover Publications Inc. New York, 1995
- Hajos, G.; Jones, J.; Behar, A. & Dodd, M. (2005). An Overview of Wind-Driven Rovers for Planetary Exploration, *Proceedings of 43rd AIAA Aerospace Sciences Meeting and Exhibit*, Reno, Nevada, Jan. 10-13, 2005

- Halme, A. ; Schönberg T. & Wang Y. (1996a). Motion Control of a Spherical Mobile Robot, *Proceedings of 4. International Workshop on Advanced Motion Control*, Tsu, Japan, 1996
- Halme, A. ; Suomela J., Schönberg T. & Wang Y. (1996b). A Spherical Mobile Micro-Robot for Scientific Applications, *Proceedings of ASTRA 96*, ESTEC, Noordwijk, The Netherlands, Nov. 1996
- Heimendahl, M.; Estier, T.; Lamon, P. & Siegwart, R. (2004). *Windball*, Swiss Federal Institute of Technology Lausanne, Autonomous Systems Laboratory, 2004
- Kangi, A. (2004). Wormsphere Rover Pattern for Discovering Underground Water on Mars' Surface, *Journal of the British Interplanetary Society (JBIS)*, Vol. 57, September/October 2004, pp. 298-300
- Knight, W. (2005). Spherical robot provides rolling security cover, *New Scientist Special report*, 28 January 2005. [Online, accessed 29 May 2007]
URL: <http://www.newscientisttech.com/channel/tech/dn6932-spherical-robot-provides-rolling-security-cover.html>
- Laplante, J-F. (2004). *ÉTUDE DE LA DYNAMIQUE D'UN ROBOT SPHÉRIQUE ET DE SON EFFET SUR L'ATTENTION ET LA MOBILITÉ DE JEUNES ENFANTS*, Mémoire de maîtrise ès sciences appliquées, Spécialité : génie mécanique, Sherbrooke, Québec, Canada
- Matthews, J. (2003). *Development of the Tumbleweed Rover*, NASA Jet Propulsion Laboratory, Robotic Vehicles Group, Pasadena, California, May 2003
- Michaud, F. & Caron, S. (2001). *Roball, the Rolling Robot*, LABORIUS - Research Laboratory on Mobile Robotics and Intelligent Systems, Universite de Sherbrooke, Sherbrooke, Quebec, Canada
- USPTO (2007). *United States Patent and Trademark Office; Patent Full-Text and Full-Page Image Databases*. [Online, accessed 21 May 2007 – 25 May 2007]
URL : <http://www.uspto.gov/patft/>
- Wang , Y. & Halme, A. (1996). *Spherical Rolling Robot*, Research Reports, Series A, Nr. 15, Feb. 1996, Automation Technology Laboratory, Helsinki University of Technology
- Ylikorpi, T.; Halme, A. ; Jakubik, P.; Suomela, J. & Vainio, M. (2004). Biologically inspired solutions for robotic surface mobility, *Proceedings of 8th ESA Workshop on Advanced Space Technologies for Robotics and Automation*, ESTEC, Noordwijk, The Netherlands, Nov. 2-4, 2004
- Ylikorpi, T. (2005). *A Biologically inspired rolling robot for planetary surface exploration*, Licentiate Thesis, Helsinki University of Technology, Automation technology laboratory, Espoo, Finland
- Ylikorpi, T.; Halme, A. & Suomela, J. (2006). Comparison Between Wind-Propelled Thistle and Motor-Driven Un-Balanced Thistle, *Proceedings of 44th AIAA Aerospace Sciences Meeting and Exhibit*, Reno, Nevada, Jan. 9-12, 2006

Complex and Flexible Robot Motions by Strand-Muscle Actuators

Masakazu Suzuki
Tokai University
Japan

1. Introduction

Robots are now requested to perform more and more complex tasks such as rescue activities in quite practical environments such as rough terrains. It is necessary for robots to have versatile joints that can flexibly adapt to such task environments and realize complex motions. It is desired to develop small and low cost actuators which can flexibly adapt to task environment. Flexibility in robot joints is especially necessary in the environment where the robots work around humans. The conventional joint mechanism makes the robots structurally complex, then heavy and large, and expensive. In addition it is difficult for them to control joint stiffness in order to handle soft objects or contact human body. Stiffness control by software servomechanism based on the reaction force from the object measured after contact has been actively investigated. But the time lag of servomechanism often results in undesirable response. On the other hand mechanical stiffness control causes no time lag because the stiffness is determined before the contact with work objects. Vertebrates' joints easily realize joint angle control and stiffness control simultaneously by their antagonistic muscles. A wide variety of artificial muscles are being actively investigated (ex. Proc. 2nd Conf. on Artificial Muscles, 2004). McKibben artificial muscle is the most well-known pneumatic actuator and there are many applications including energy efficient low power joint (Linde, 1999). Another type of vertebrate-joint-like actuator developed by the author's group is Strand-Muscle Actuator, StMA (Suzuki et al., 1997). The actuator can adapt to various tasks and environmental changes. The StMAs, having nonlinear elastic characteristics, realize joint angle/stiffness control, even for multi-DOF joints, by antagonistic actuator installation on the joint. In addition the actuator is expected to realize multi-DOF complex and flexible motions with simple mechanism. The joint angle/stiffness control by StMAs has been investigated, and legged walking robots as well as a multi-DOF human-shoulderlike joint, 5 fingered hands have already been developed. This chapter is to introduce the development and application of the StMAs.

The StMA-based joints are suitable for complex and flexible motions in spite of their simple mechanism, and extendable joint mechanism will be possible with them. An StMAbased joint with redundant muscles realizes failure tolerant angle/stiffness control. The effectiveness has already been verified by legged walking robots, 5 fingered hands, and 3-

DOF joints. The former sections of the chapter describe the characteristics and control scheme of the StMAs. The latter sections are on some applications: One is the realization of springy walk (quick and energy-efficient rhythmical walk) by a 6-legged StMA-based robot (Suzuki & Ichikawa, 2004). Actuator drive pattern optimization with utilizing the actuators' elastic characteristics results in fast and dexterous actions. Another is on online optimal muscle coordination of multi-DOF joints (Suzuki & Mayahara, 2007). For smooth and dexterous motions real-time cooperative muscle tension control is necessary. A method for optimal redundant muscle coordination is proposed, and it is then successfully applied to an StMA-based 3-DOF joint.

2. Strand-Muscle Actuator

In this section the Strand-Muscle Actuator is introduced, where its mechanism and basic characteristics are presented.

2.1 Mechanical composition and drive principle

A Strand-Muscle Actuator (StMA) has a very simple mechanism (Fig.1). It is composed of a motor and a strand muscle that consists of two (or more) muscle fibers. Giving a torsion to the *strand-muscle* by the motor, the muscle contracts. The motor side end is referred to as the actuator's *driving-end*, and the other side is the *effected-end*. The StMA is a kind of artificial muscle that has nonlinear elastic characteristics like mammal's muscles. Various joints are

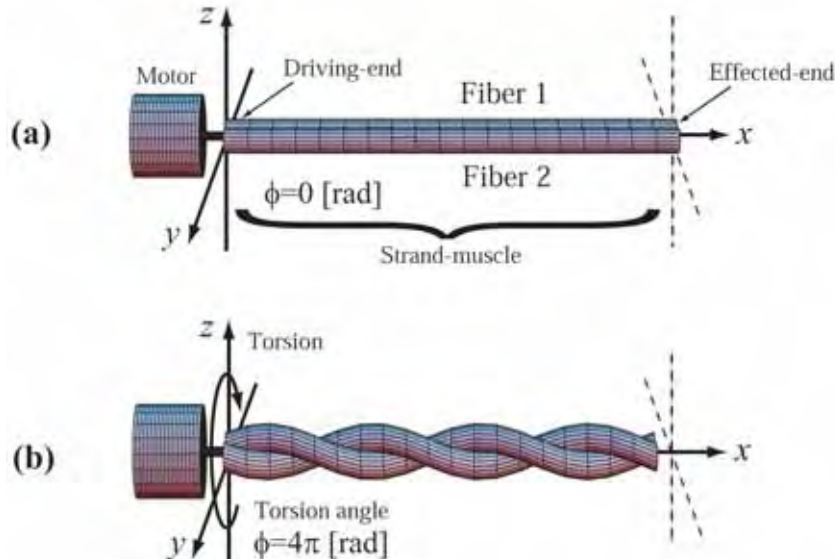


Fig. 1. A Strand-Muscle Actuator with two muscle fibers: (a) natural state and (b) contraction by torsion

realized by antagonistic installation of several StMAs (Fig.2, Fig.9 and Fig.10). In spite of their small size, light weight, and simple mechanism, the StMAs easily realize joint angle/stiffness control. In addition the actuator is expected to realize multi-DOF complex and flexible motions.

Motor and muscle fiber Both DC motors and stepping motors may be used depending upon the actuator use. Since a strand-muscle functions as a speed reducer, very small gearless DC motors can be used. And geared DC motors with a small gear ratio are also used to achieve adequate torque and speed with small motors. Stepping motors are convenient for small-step muscle torsion. Therefore the actuator's basic characteristics in subsection 2.2 have been

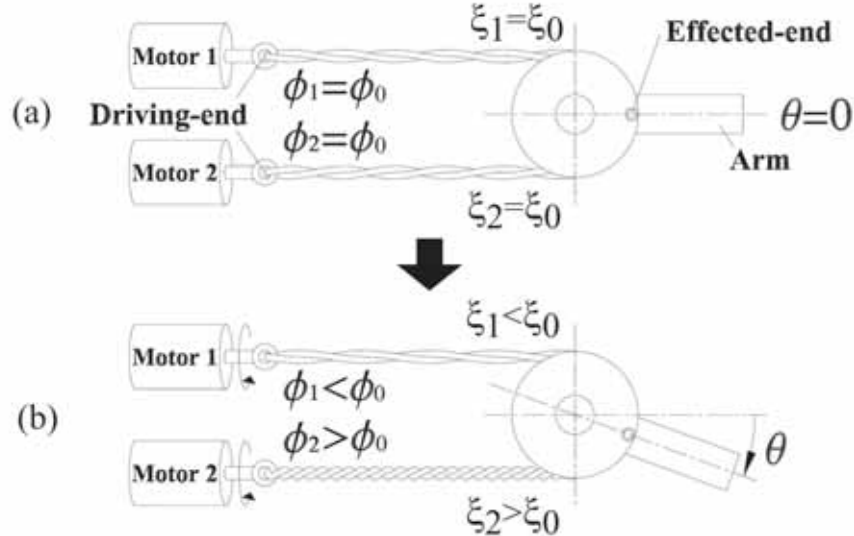


Fig. 2. A pulley-type 1-DOF joint actuated by antagonistic two Strand-Muscle-Actuators

investigated by driving StMAs with stepping motors. Practically, however, all the StMAs for robot joints are presently driven by DC motors in order to make the most use of the StMA's advantages: small, light, simple mechanism.

A muscle fiber of strand-muscle is an elastic thread with circular section. The ideal muscle fiber has elasticity only in the fiber axis direction without diameter change by elongation, no fiber surface friction, no bending stiffness. Actually, however, such ideal characteristics cannot be realized. Various materials such as cotton, wool, nylon, glass fiber, carbon fiber, aramid fiber, silicon rubber and so on have been investigated. At present some kinds of fishing lines such as Flyline (polyester fiber coated with polyvinyl chloride), are used as suitable muscle fiber material.

Contraction by torsion Consider a strand-muscle that consists of two ideal muscle fibers of natural length L and radius r (Fig.3). In the StMA's natural state, the muscle is twistless torsion angle $\phi = 0$, it is not slack, but no tension is exerted ($T = 0$).

Twisting the fiber strand by angle $\phi > 0$ by the motor the muscle contracts. When the effected-end is free, the muscle length ℓ is determined only by ϕ , and is obtained by a simple geometrical analysis. The locus of the circular section's center of each fiber forms a helix:

$$y = r \cos \frac{\phi}{\ell} x, z = r \sin \frac{\phi}{\ell} x \quad (0 \leq x \leq \ell)$$

From the fact that the length of the locus is L , the muscle length is obtained as

$$\ell = \sqrt{L^2 - r^2 \phi^2} \quad (1)$$

From (1) the muscle contraction ξ is then given as

$$\xi = L - \ell = L - \sqrt{L^2 - r^2 \phi^2} \quad (2)$$

When the muscle most densely coils, it contracts to $\ell = 4nr$ where n is the number of coil turns. Then, theoretically, the muscle length is $\ell = L / \sqrt{1 + \pi^2 / 4} \approx 0.537L$, which means the maximum muscle contraction is about 46% of the natural length. Actually, however, the full contraction is difficult to achieve because of uneven twist and large torsion moment. The maximum contraction in practical use is about 30%.

Contraction under tension If the effected-end is not free, the muscle generates tension, say T . This tension is utilized as source of power of the StMA, i.e., StMAs transform rotational torque into linear tensile force. The contraction ξ is then the sum of contraction by torsion $\xi_\phi > 0$ and extension by tension $\xi_T < 0$, i.e., $\xi = \xi_\phi + \xi_T$. In this situation fiber surface friction and diameter decrease cannot be ignored. The extension by tension has a complicated relation to ϕ , T and fiber material. The relation should thus be experimentally determined.

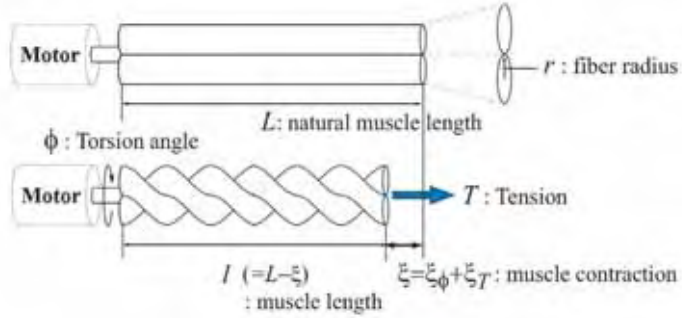


Fig. 3. A Strand-Muscle Actuator in twisted and tense state

2.2 Basic Characteristics

Mechanical characteristics For practical use the relation among the muscle contraction ξ , and the torsion angle ϕ and exerted tension T for a pair of specific muscle fibers should be known and available. Such a relation, $\xi(\phi, T)$, is referred to as the actuator's basic mechanical characteristics or *basic characteristics* in short. The formula $\xi(\phi, T)$ is obtained by motion experiments, and utilized as the control knowledge for StMA control. Note that the characteristics are dependent also on natural length L , fiber radius r and material, though they are not explicitly expressed for simplicity.

The basic characteristics are obtained by measuring ξ under a constant tension T with a device as shown in Fig.4. Increasing and decreasing torsion angles were repeatedly given for 100 times ($n = 1, 2 \dots 100$) by a stepping motor with sufficient torque. Some typical results for nylon fiber, cotton fiber and Flyline are shown in Fig.5 I, II and III, respectively.

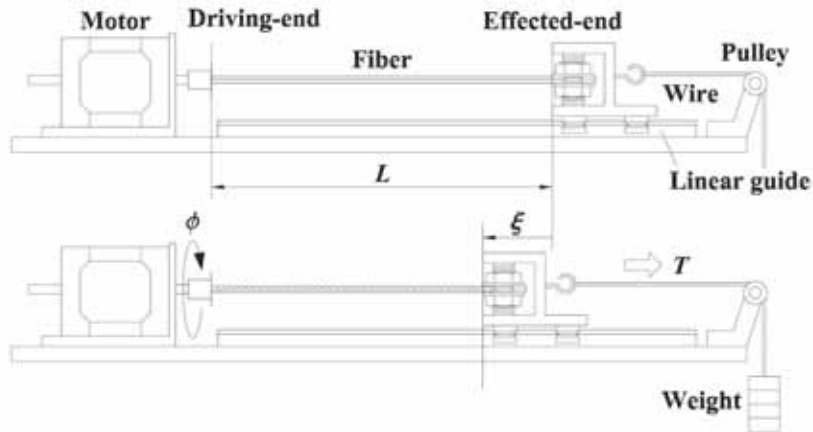


Fig. 4. Experimental device for basic characteristics

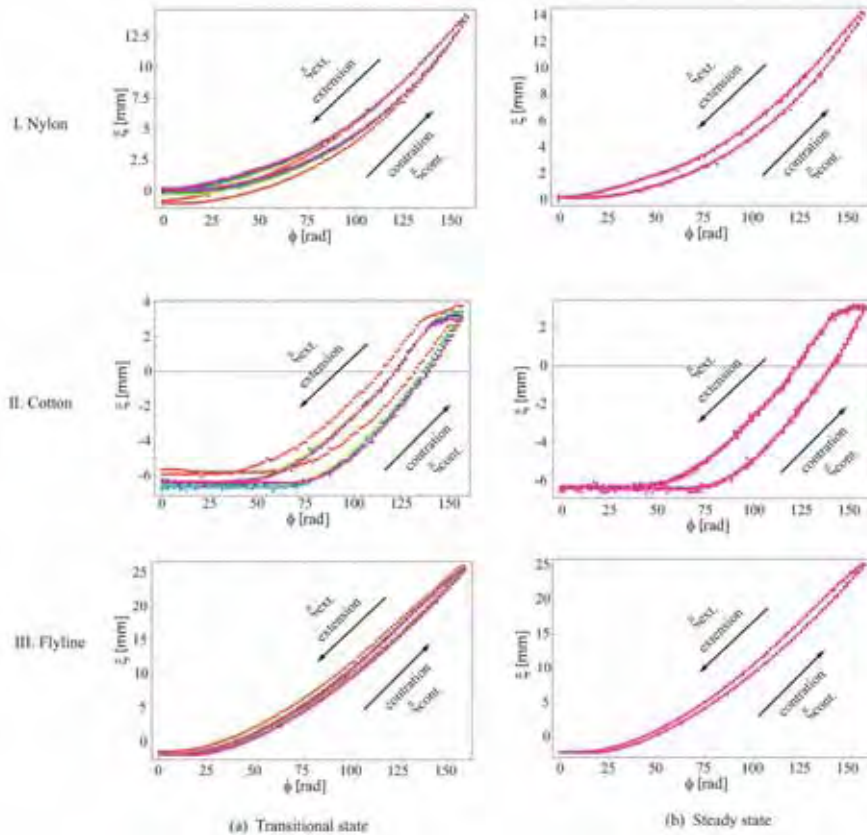


Fig. 5. Basic characteristics of I. nylon, II. cotton, and III. Flyline in (a) transitional state and (b) steady state

The $\phi - \xi$ curves in transitional state ($n = 1, 20, 40, 60, 80, 100$) gradually change as motions are repeated (Fig.5(a)). Hence some break-in operations are necessary before practical use until the characteristics converge to steady states. Even in the steady state ($n = 90 \sim 100$), however, they have some hysteresis (Fig.5(b)). Among various materials Flyline has the best characteristics, *i.e.*, least number of necessary break-in operations, highest repeatability and smallest hysteresis error ($|\xi_{ext}(\phi, T) - \xi_{cont}(\phi, T)|$) which can be negligible for control use.

Based on the result stated above, Flyline has been adopted as the main muscle fiber material, and investigated in detail. The hysteresis error in operation range (usually, $0.05L \leq \xi \leq 0.25L$) is very small, therefore the contraction/extension average $\frac{1}{2}(\xi_{ext}(\phi, T) - \xi_{cont}(\phi, T))$ was used as the practical basic characteristics for control.

Experimental formula of basic characteristics in the form of characteristics in the form of

$$\xi(\phi, T) = \sum_{0 \leq i+j \leq 3} a_{i,j} T^i \phi^j \quad (3)$$

is considered, whose coefficients $a_{i,j}$ were then determined by least mean square approximation. As seen in Fig.6 the measured contraction coincides with the curves by experimental formula very well, and they can be used for practical control with sufficient accuracy. Note the initial contraction $\xi(0, T) < 0$ is caused by the preload tension T . The

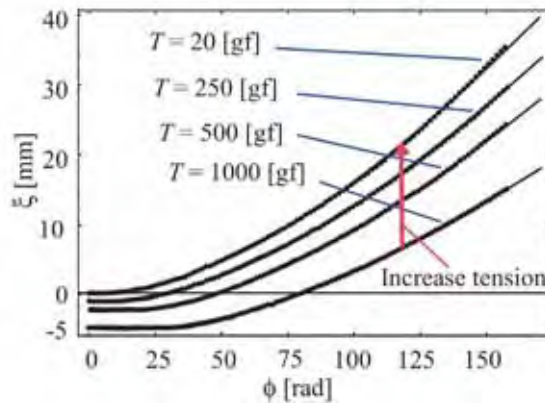


Fig. 6. Experimental formulae of basic characteristics (solid line) and measured muscle contraction (dots) for Flyline

diagram says that twisting the muscle moves the effected-end under constant tension, while it increases the tension when the effected-end is fixed. The 3D expression of the formula (3) is shown in Fig.7.

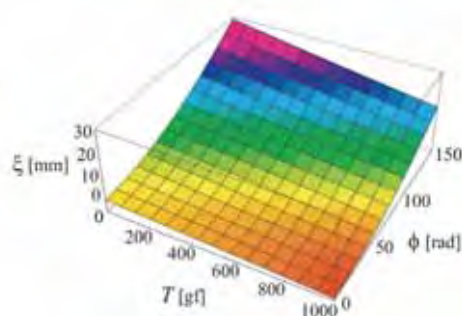


Fig. 7. 3D expression of basic mechanical characteristics $\xi(\phi, T)$ for Flyline

Muscle stiffness The strand-muscles have nonlinear elastic characteristics. Consider muscle stiffness S_M defined as

$$S_M = \frac{\partial T}{\partial \xi} \quad (4)$$

The muscle stiffness $S_M(\phi, T)$ is obtained from (3) by calculating $\left(\frac{\partial \xi(\phi, T)}{\partial T} \right)^{-1}$, which

is shown in Fig.8. It should be noted that the muscle is less stiff as the torsion angle increases if the tension is constant.

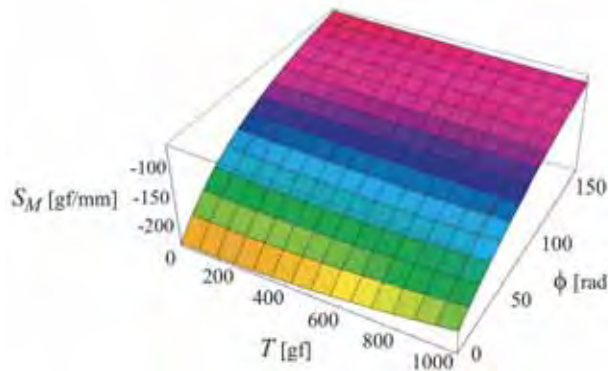


Fig. 8. 3D expression of muscle stiffness $S_M(\phi, T)$

Control characteristics For a complex and flexible robot motion by parallelly installed many elastic muscles, simple open-loop on/off muscle control with only the motion performance evaluated seems preferable to precise feedback control of every muscle length $\ell(t)$, or precise realization of torsion angle $\phi(t)$ by feedback control. That is the case especially in complex motions by a multi-DOF joint with highly parallel installation of StMAs. And then the relation between muscle contraction ξ and motor drive time t is much more convenient to use.

The actuator's basic control characteristics $\xi(t, T)$ is a formula expressing the contraction ξ of a muscle of natural length L under a constant muscle tension T generated by driving the motor for $t[\text{sec}]$ with impressed voltage V_c . Note that L and V_c are usually fixed and omitted to show for simplicity. In the following sections the basic control characteristics $\xi(t, T)$ are used instead of $\xi(\phi, T)$.

3. Angle/Stiffness Control of StMA-based Joints

The control scheme for 1-DOF StMA-based joint and some experimental results are presented.

3.1 StMA-based joint

1-DOF joint rotation is realized by antagonistically installed two actuators (Fig.2, Fig.9). Use of a pulley as in Fig.2 makes the joint rotation angle θ linear to muscle contraction ξ , the analysis and control are then easy. But the flexibility of mechanical composition will be lost.

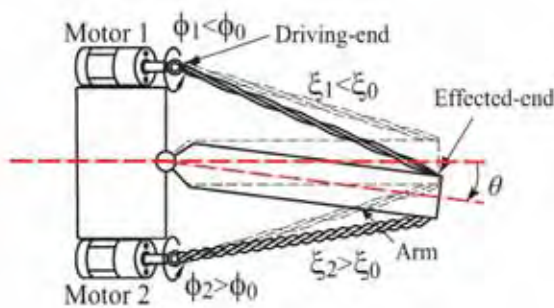


Fig. 9. A direct-connect-type StMA-based 1-DOF joint

Another type of actuator installation with its driving-end and effected-end directly connected as in Fig. 9. is suitable for constructing multi-DOF joints. A multi-DOF joint with high failure tolerance is realized by equipping several redundant actuators in parallel as in Fig. 10. Control of such multi-DOF joints is discussed in section 5.

With the antagonistic muscles the joint stiffness control is easy as well as joint angle control. In spite of simple structure the muscle itself functions as a speed reducer and a stiffness regulating mechanism. Hence downsizing and weight saving are easily achieved. The speed reduction ratio (gear ratio), ϕ/θ , depends mainly upon the muscle lengths, the muscle assignment and the pulley radius in case of a pulley-type joint. In addition the muscle tensions, or joint stiffness, also affect the ratio.

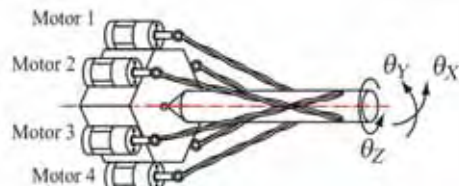


Fig. 10. An StMA-based 3-DOF joint with 6 StMAs

It is possible to select/increase muscles according to the actual use because the muscles are easy to equip and replace. This leads to another good feature: the joint characteristics can be easily improved, variable structure, or moreover, extendable joint mechanism might be possible.

3.2 Control of StMA-based Joints

StMA-based joints realize flexible and complex motions. On the other hand the mathematical model of the actuator is difficult to establish because of various non-linear factors to consider such as fiber bending moment, fiber surface friction and so on. When redundant actuators are installed on a multi-DOF joint and motions to realize become complex, the modeling is more difficult. It is necessary to utilize some additional learning technique, though StMAs are basically controlled based on the control equation derived from geometrical analysis with preliminary experiments.

Joint angle control Consider a joint in Fig.2 with two StMAs of the same material/radius /length muscles driven with the same motor voltage. In this case joint angle remains $\theta = 0$ when $\xi_1 = \xi_2$, i.e., $\phi_1 = \phi_2$ even if the muscles are twisted and tense (Fig.2(a)). When $\phi_1 \neq \phi_2$ contractions ξ_1, ξ_2 are different, and then the joint rotates (Fig.2(b)). The angle θ is determined by the linear geometric relation

$$\theta = \frac{\xi_1}{R} - \bar{\theta} = -\frac{\xi_2}{R} + \bar{\theta} \quad (5)$$

where R is the pulley radius, $\pm \bar{\theta}$ are the upper/lower bound of the operation ranges realized when muscle 1 or 2 is in natural state. Practically however, the geometric equation (5) needs to be compensated according to the experimental control result in order to improve control accuracy. The compensated equation is given in the form of

$$\theta = \frac{c_1 \xi(t, T)}{R} + c_2 \bar{\theta} + c_3, \text{ where } |c_1|, |c_2| \approx 1, |c_3| \ll 1.$$

In case of a direct-connect-type joint as shown in Fig.9 the angle θ is determined, in general, by a non-linear geometric relation

$$\theta = f(\xi_1) - \bar{\theta} = -f(\xi_2) + \bar{\theta} \quad (6)$$

where f is determined by the layout of actuator mounting, i.e., position of driving/effected-ends of the muscles.

Both for linear and non-linear types, an StMA-based-joint angle control is achieved by realizing necessary muscle contractions ξ_1 and ξ_2 based on the basic control characteristics $\varepsilon(t, T)$. Fig.11 shows the relation between the drive time t and (imaginary) joint angles

θ_1, θ_2 when the muscles are separately set so that joint angles are $\theta_1 = -\bar{\theta}, \theta_2 = \bar{\theta}$ without muscle twist under a constant tension T . When actuator 1 is driven from an initial state

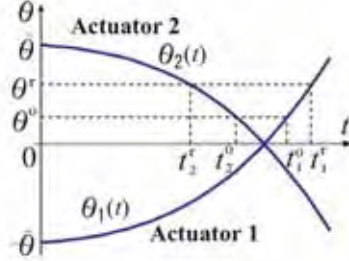


Fig. 11. Actuator state curves for joint angle control under constant tension

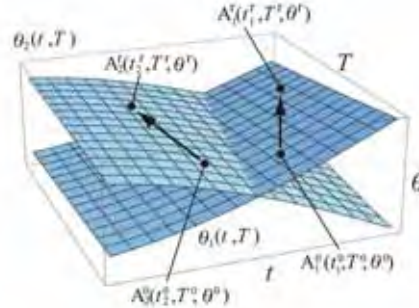


Fig. 12. Actuator state surfaces for joint angle/stiffness control

with keeping the tension T , the joint angle θ_1 changes along the curve $\theta_1(t) = \xi_1(t, T) / R - \bar{\theta}$. Such is the case also for the curve $\theta_2(t) = -\xi_2(t, T) / R + \bar{\theta}$. Actually, only states with $\theta = \theta_1(t_1) = \theta_2(t_2)$ are possible since the muscles are antagonistically connected to the common arm. Suppose that $\theta = \theta^0$ in the initial state. In order to realize joint angle θ^r the actuators are then driven for $t_1^r - t_1^0$ and $t_2^r - t_2^0$, respectively, where t_m^0, t_m^r are obtained as $t_m^0 = \theta_m^{-1}(\theta^0), t_m^r = \theta_m^{-1}(\theta^r), m = 1, 2$. ($t_m < 0$ means drive in reverse direction for $|t_m|$)

Extending the curved lines in Fig.11 in terms of T , the actuator state surfaces in Fig.12 is obtained. At the points A_1^0, A_2^0 the muscles realize joint angle θ^0 under the tension T^0 . In order to realize a desired state $\theta = \theta^r, T = T^r$ represented at A_1^r and A_2^r , the necessary drive times t_1 and t_2 are obtained from the target joint angle and muscle tension by the joint control equation

$$t_m = \theta_m^{-1}(\theta^r, T^r) - \theta_m^{-1}(\theta^0, T^0), m = 1, 2 \quad (7)$$

The control result for $\bar{\theta} = 40$ [deg], $R = 16.5$ [mm] is shown in Fig.13 (left). The joint angle control with accuracy less than 2 [deg] is possible for a wide range of muscle tension.

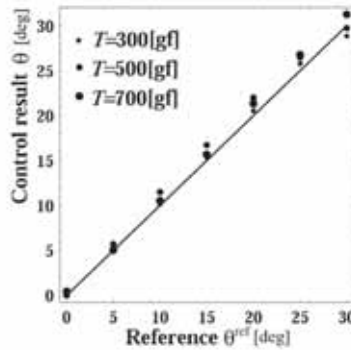


Fig. 13. Experimental result of joint angle control

Joint stiffness control The joint stiffness S_J is defined as

$$S_J = \frac{\partial M}{\partial \theta}$$

where M is the moment given to the joint which has a specified angle θ under a constant tension T . The result of stiffness control experiment is given in Fig.14 to show the wide controllable joint stiffness range.

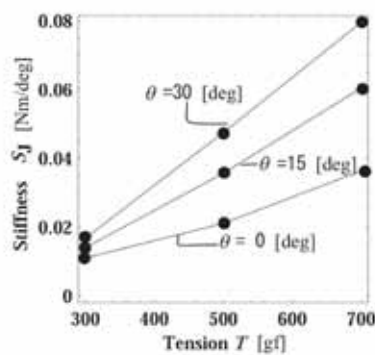


Fig. 14. Experimental result of joint stiffness control

The result says that the joint stiffness can be controlled through muscle tension control without joint angle change. As mentioned in subsection 2.2 the muscle is less stiff for larger torsion angle ϕ . Therefore an StMA for flexible, *i.e.*, soft joints needs longer muscle with larger initial torsion. The resultant joint angle/stiffness control had enough accuracy, and it was verified to be effective for hexapod walking.

4. Energy Efficient Walking of Legged Robots

In order for robots to perform dexterous behaviors in practical environments, quick actions such as fast walk and rapid turn with small energy cost are desired. The purpose of the work introduced in this section is thus realization of springy walk, *i.e.*, quick and energy-efficient rhythmical walk by StMA-based legged robots.

In the following a 6-legged StMA-based walking robot, SMAR-III, is introduced and the experimental result of walking is presented. A method for springy walk by actuator drive pattern optimization is presented and the prospect of fast and energy efficient walk is given.

4.1 StMA-based Walking Robot

Several StMA-based hexapod walking robots have already been made. SMAR-II (Fig.15, left) has 12 active joints, all antagonistically driven by StMAs. The StMA's elastic property contributes to the walking ability in rough terrain. Small roughness is overcome without sensing. Another StMA-based robot, SRAMI (Fig.15, right), is a miniature size hexapod that swings each leg with a 2-DOF joint. SRAMI carries two 006P-9V batteries on the back and walk with the battery power. They walk but slow, and do not necessarily make the most of the StMA advantages.

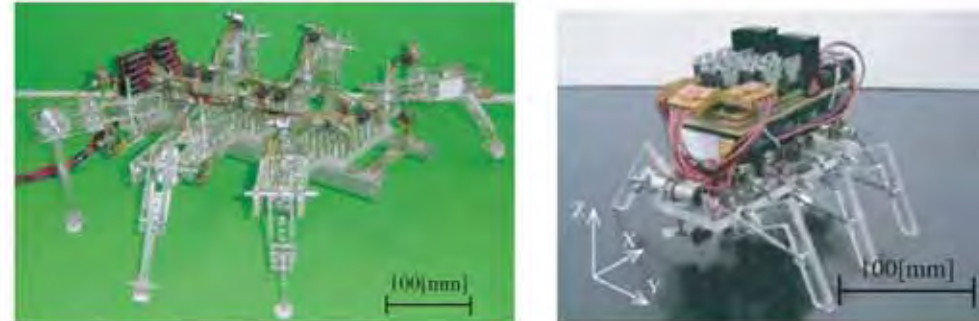


Fig. 15. StMA-based hexapod walking robots: SMAR-II (left) and SRAMI (right)

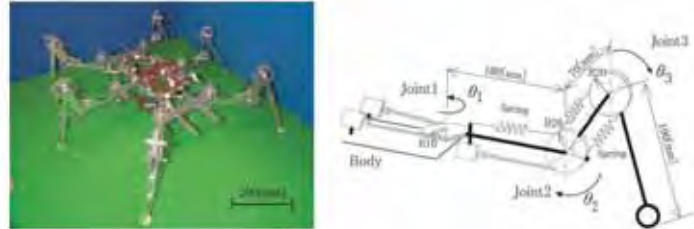


Fig. 16. StMA-based hexapod walking robot SMAR-III: Overview (left) and leg mechanism (right)

The SMAR-III (Fig.16) has 18 joints, 12 of which are driven by 18 StMAs. Each leg has three joints. Joint 1 and 2 are active 1-DOF joints, which are driven by antagonistic and semi-antagonistic StMAs, respectively. Joint 3 is a passive 1- DOF joint which contributes springy



Fig. 17. Tripod gait walking of SMAR-III

walk. Each StMA consists of a DC motor with reduction gear ratio 1/33 and PE-Line (polyester-twine fishing line) of $\phi = 0.5[\text{mm}]$ as muscle fibers. The size is 445 L×571W×195H[mm] in its basic posture, and the weight is 1.47 [kg] (without power supply, computer and cables). Every actuator is driven by a simple on/off control.

Walking is realized according to a predefined on/off actuator drive pattern based on the control equation. Straight tripod walk on a flat terrain has been realized and the captured motion is shown in Fig.17. The walking velocity is about 75 [mm/sec] that is much faster than 15 [mm/sec] by SMAR-II.

4.2 Energy efficient Springy Walk

It is true that the walking by SMAR-III is much faster than conventional, but it is still not so efficient. The simulated motion of θ_1 of the leg 1 (left foreleg) during walking is shown in Fig.18 (left). Without actuator drive pattern optimization in terms of energy efficiency and walking speed there remains an undesirable vibration after each stride (dotted ovals), i.e.,

time consuming body swinging without forward move. It makes walking velocity lower and wastes elastic energy.

Efficient and rhythmical walking is realized by utilizing the actuators' elasticity property and the inertia force by the motion. In other words, the energy efficient walking with a low-duty- ratio intermittent drive is realized by storing the elastic energy obtained from inertia force of each leg by leg-swinging during swing phase and inertia force of the body during support phase. The criterion function for optimal actuator drive is, for example, defines as

$$J(\boldsymbol{a}) = \frac{1}{d_w(t_w)} \left(\alpha \int_0^{t_w} \|\mathbf{V}(t)\|^2 dt + \beta t_w \right) \quad (8)$$

where \boldsymbol{a} is the parameter vector that specifies actuator drive pattern such as walking cycle and on/off switching timing for each actuator, $\mathbf{V}(t)$ is motor drive voltage vector, t_w is the walking time, $d_w(t_w)$ is the walking distance for t_w . The criterion is to minimize the energy consumption per unit walking distance (by the 1st term) and to maximize walking velocity (by the 2nd term).

The result of optimizing the drive pattern for joint 1 (Fig.18 right) says that the walking speed can be nearly doubled with less energy consumption. It was shown that springy walk based on the actuator drive pattern optimization technique will be possible. The optimization of the joint 1 motion realizes, as it were, rhythmical swinging walk and besides

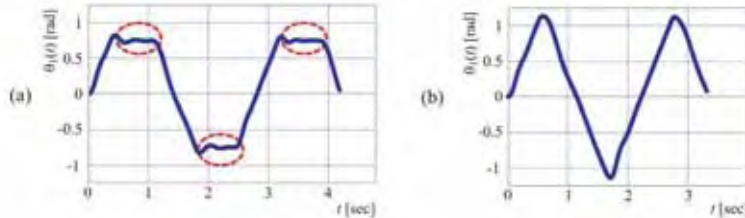


Fig. 18. Motion of joint 1 in (a) nonoptimal and (b) optimal actuator drive pattern

rhythymical hopping walk will be realized by optimizing the joint 2 motion.

5. Muscle Coordination of Multi-DOF Joints

General-purpose robotic manipulators with controllable joint stiffness like human arm joints are now desired. A human arm dexterously realizes complex motions by use of multi-DOF joints with redundant muscles. Although muscle coordination is essential for smooth motions and is an old problem, it is still an open problem (Latash & Turvey, 1996), and actively investigated in various fields (Yang et al., 2001, Tahara et al., 2005).

In this section the mechanism and control scheme for an StMA-based multi-DOF joint with redundant muscles are presented. An StMA-based robot arm is introduced first. Next a

muscle coordination method for StMA-based multi-DOF joint with redundant actuators is presented.

5.1 Strand-Muscle-Actuator-based Robot Arm

The StMA-based Robot Arm (StMA-RArm) is a robotic manipulator modeled on a human arm (Fig.19 left). It is composed of StMA-based Robot Shoulder (StMA-RS)(inside the dotted lines in Fig.20), a 1-DOF elbow (Joint 3), a 1-DOF wrist (Joint 4) and a simple 4-fingered hand. The mechanical composition is shown in Fig.20. The posture where the arm hangs down as in Fig.20 is referred to as the basic posture. It has 12 actuators at the StMARS, 2 at elbow, 4 at wrist-hand part, total 18 StMAs. DC geared motors of power rating 0.7[W] and 0.4[W], and Flyline of $\phi 1.0[\text{mm}]$ and PE line of $\phi 0.5[\text{mm}]$ for muscle fiber are used. For weight saving the fingers are controlled with 3 StMAs and auxiliary leaf springs. The size is 215W×194T×465H[mm], the weight is approximately 1.7[kg] (without controller circuits, computer, power supply).

Muscle vector A *muscle vector* is the vector from an effected-end to its corresponding driving-end (Fig.19 right). The muscle length is given by the norm of the muscle vector. For n -th actuator of Joint m to realize a desired posture θ the muscle vector $\ell_{mn}(\theta)$ is calculated from the coordinates of driving-end $P_{Emn}(\theta)$ and effected-end $P_{Dmn}(\theta)$ as

$$\ell_{mn}(\theta) = P_{Dmn}(\theta) - P_{Emn}(\theta), \quad m = 1, 2, 3, 4, \quad n = 1, 2, \dots, N_m \quad (9)$$

where N_m is the number of actuators for Joint m . $P_{Emn}(\theta)$ and $P_{Dmn}(\theta)$ are obtained from each effected/driving-ends P_{Emn}^0 , P_{Dmn}^0 in the basic posture by use of the

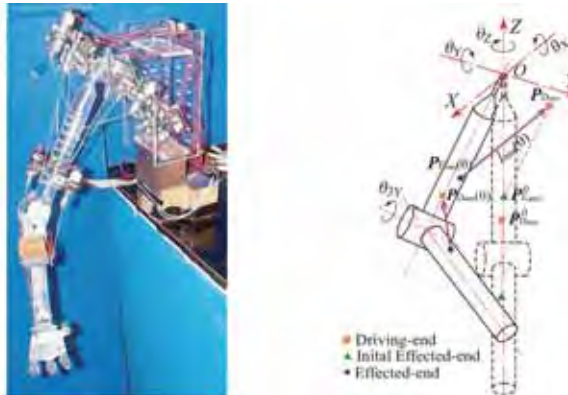


Fig. 19. StMA-RArm: Overview (left) and kinematic model of shoulder-elbow part (right)

rotational transformation matrix $\Sigma_m^H(\theta)$ as

$$\mathbf{P}_{Dmn}(\boldsymbol{\theta}) = \sum_m^H(\boldsymbol{\theta}) \mathbf{P}_{Dmn}^0, \mathbf{P}_{Emn}(\boldsymbol{\theta}) = \sum_m^H(\boldsymbol{\theta}) \mathbf{P}_{Emn}^0 \quad (10)$$

The necessary muscle contraction ξ_{mn} from the natural length L_{mn} is then

$$\xi_{mn}(\boldsymbol{\theta}) = L_{mn} - \|\boldsymbol{\ell}_{mn}(\boldsymbol{\theta})\|, \quad (11)$$

which is realized according to the StMA control method in section 3.

3-DOF Shoulder Parallel installation of StMAs easily realizes versatile multi-DOF joints. The StMA-RS is a human-shoulder-like high failure-tolerant 3-DOF joint with redundant muscles. It consists of Joint 1 (3-DOF) using a ball joint and Joint 2 (1-DOF). The motion ranges are $-20 \leq \theta_{1x}, \theta_{1y} \leq 50[\text{deg}]$, $-60 \leq \theta_{1z} \leq 60[\text{deg}]$ for Joint 1, and $0 \leq \theta_{2x} \leq 30[\text{deg}]$ for Joint 2. With cooperation of the two joints it achieves a large arm motion area. Both joints have redundant actuators, *i.e.*, 7 actuators ($A_{11} \sim A_{17}$) for Joint 1, and 5 actuators ($A_{21} \sim A_{25}$) for Joint 2. That contributes to the large capacity of joint stiffness control and failure tolerance. That is, wide range of joint stiffness can be realized for a wide variety of joint angle, and the motion of the joint can be easily recovered to some extent for some muscle breakage.

5.2 Control of 3-DOF Shoulder

Joint 1 and Joint 2 have a common center of rotation, therefore they can be regarded as a single 3-DOF joint with joint angle represented by $[\theta_x, \theta_y, \theta_z]$.

Muscle tension to resist external force Consider a 3-DOF joint driven by N StMAs. Let T_n be the tension generated by actuator n , and $\mathbf{T} = \{T_n\} \in \mathbf{R}^N$ be the tension vector composed of each actuator tension. An StMA generates tension in one direction only, and hence $T_n \geq 0$ always holds. The positive direction of \mathbf{T} is the same as

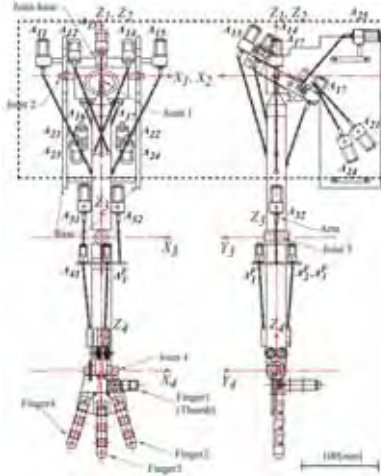


Fig. 20. Mechanism of StMA-RArm

that of the corresponding muscle vector. The moment $\mathbf{M} \in \mathbf{R}^3$ around the origin in posture $\boldsymbol{\theta}$ by the tension \mathbf{T} is then given as

$$\mathbf{M} = \mathbf{H}(\boldsymbol{\theta})\mathbf{T} \quad (12)$$

where $\mathbf{H}(\boldsymbol{\theta}) \in \mathbf{R}^{3 \times N}$ is given as

$$\mathbf{H}(\boldsymbol{\theta}) = [\mathbf{h}_1(\boldsymbol{\theta}) \ \mathbf{h}_2(\boldsymbol{\theta}) \ \cdots \ \mathbf{h}_N(\boldsymbol{\theta})] \quad (13)$$

$$\mathbf{h}_n(\boldsymbol{\theta}) = P_{En}(\boldsymbol{\theta}) \times \mathbf{u}_n(\boldsymbol{\theta}), n = 1, 2, \dots, N \quad (14)$$

$$\mathbf{u}_n(\boldsymbol{\theta}) = \frac{\ell_n(\boldsymbol{\theta})}{\|\ell_n(\boldsymbol{\theta})\|} \in \mathbf{R}^3, n = 1, 2, \dots, N \quad (15)$$

Conversely the tension needed to keep the posture $\boldsymbol{\theta}$ under an external moment \mathbf{M} is given as the general solution of (12) as

$$\mathbf{T} = \mathbf{H}^\#(\boldsymbol{\theta})\mathbf{M} + (\mathbf{I}_N - \mathbf{H}^\#(\boldsymbol{\theta})\mathbf{H}(\boldsymbol{\theta}))\boldsymbol{\beta} \quad (16)$$

where $\mathbf{H}^\#(\boldsymbol{\theta}) \in \mathbf{R}^{N \times 3}$ is the pseudo-inverse of $\mathbf{H}(\boldsymbol{\theta})$, $\mathbf{I}_N \in \mathbf{R}^{N \times N}$ is identity matrix and $\boldsymbol{\beta} \in \mathbf{R}^N$ is an arbitrary vector. Note that the 2nd term of the right side of (16) does not affect joint torque. The joint stiffness can be controlled by adjusting the tension \mathbf{T} , within $T_n \geq 0$, by use of $\boldsymbol{\beta}$

Angle control experiments The experimental Joint 1 angle control result of X-axis and Y -axis rotation for $0 \leq \theta_X, \theta_Y \leq 50$ [deg] with $\mathbf{M} = 0$ and $\boldsymbol{\beta} = (100 \ 100 \ \dots \ 100)^T$ are shown in Fig.21. Experiments show good angle control result for both θ_X and θ_Y for angles less than 40[deg].

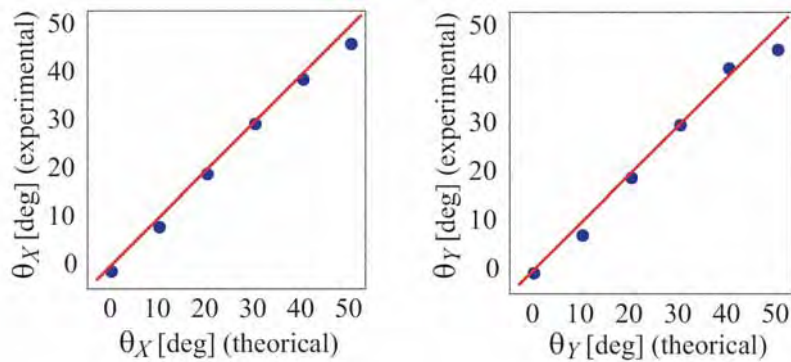


Fig. 21. Result of Joint1 angle control for X-axis rotation (left) and Y -axis rotation (right)

6. Optimal Redundant Muscle Coordination

The StMA-RArm realizes versatile flexible motions with StMA-RS. On the other hand the muscle tension combination to realize a specific task is not unique because of the redundant muscles. In order to realize complex tasks in practical environment, online optimal muscle tension combination adapting to varying situation is necessary because offline target tension setting is impossible.

In this section the method given in section 5 is applied to the online optimal muscle coordination for StMA-RS. As an optimization technique Particle Swarm Optimization (PSO) (Kennedy & Eberhart, 2001) is used with modification so that it keeps the suboptimal solution set in the steady state to adapt to time-variant objective function. The method realizes not only desired joint angle but keeping adequate joint stiffness and actuator load averaging all at the same time by optimal combination of muscle tension. In the following a method of online redundant muscle coordination by use of Vibrant Particle Swarm Optimization is presented, and some numerical experiments are given.

6.1 Optimal Cooperative Control of Redundant Muscles

The muscle tension combination to keep a certain posture is not unique because of the arbitrary vector β in (16). Therefore the tension combination for the robot arm with redundant muscles should be optimized for an adequate performance criterion. The optimal tension here means, for example, the state that keeps adequate joint stiffness without exerting excessive tension on partial muscles. For practical use the time trajectory of $\beta(t)$ must be optimized for desirable muscle cooperation for all t with keeping specified joint angle $\theta(t)$, and torque $M(t)$. In other words, an optimization problem for a time variant object function must be solved. Consider the following problem to obtain the optimal tension combination by optimizing the arbitrary vector β .

$$\begin{aligned} P_T(t) : \min_{\beta(t)} J(\beta(t)) = & c_1 f_v(T(\beta(t))) + \frac{c_2}{N} \|T(\beta(t)) - T^r(t)\| \\ \text{subj. to } & T(\beta(t)) \geq 0 \end{aligned}$$

where $T(\beta(t))$ is obtained from (9),(10),(13)~(16). f_v is standard deviation. $T^r(t)$ is a target muscle tension distribution, $c_1, c_2 > 0$ are weighting coefficients. The first term in the criterion function aims at minimization of tension variation, the second term seeks realization of desirable tension distribution corresponding to given tasks. c_1 should be larger to prevent tension concentration, and c_2 should be larger when the realization of target tension is more important. The latter is the case, when different kinds of muscles are used for a joint and each muscle has different maximum allowable tension, for example.

6.2 Vibrant PSO For Time-variant Optimization

Consider a time-variant optimization problem $P(t)$ formulated as

$$\mathbf{P}(t) : \min_{\mathbf{x}(t)} f(t, \mathbf{x}(t)) \quad (17)$$

$$\text{subj. to } \mathbf{x}(t) \in \mathbf{G} \quad (18)$$

where $\mathbf{x}(t) = \{\mathbf{x}_n(t)\} \in R^N$ and (18) is upper/lower bounds constraints.

Consider to use the Particle Swarm Optimization (PSO) to solve $P(t)$. PSO is a form of swarm intelligence, and is vigorously investigated as a powerful multi-agent type optimization technique (Kennedy & Eberhart, 2001). PSO is modeled by particles in multi-dimensional space that have a position and a velocity. Based on their memory of their own best position and knowledge of the swarm's best position the particles (*i.e.*, the agents) adjust their own velocity and move through the search space to search the optimum.

In the canonical PSO many agents $\{\mathbf{x}_i\}$ (particles) are scattered in the search domain. Each agent searches the optimum using the following three kinds of information: (a) speed of the agent represented in discrete form by $\Delta\mathbf{x}_i$, (b) *personal best*: the best performance point realized by the agent, so-called pbest, represented by \mathbf{x}_i^{pb} , and (c) *global best*: the best performance point realized by all the agents, so-called gbest, represented by \mathbf{x}^{gb} . Movement of each agent (search point) is then given by

$$\mathbf{x}_i^{k+1} = \mathbf{x}_i^k + \Delta\mathbf{x}_i^k \quad (19)$$

$$\Delta\mathbf{x}_i^k = v_1 + v_2 + v_3 = w\Delta\mathbf{x}_i^{k-1} + c_p r_p (\mathbf{x}_i^{pb} - \mathbf{x}_i^k) + c_g r_g (\mathbf{x}^{gb} - \mathbf{x}_i^k) \quad (20)$$

where \mathbf{x}_i^k represents $\mathbf{x}_i(k\Delta t)$ for $i = 1, 2, \dots, n_p$; $k = 0, 1, 2, \dots$, and $w, c_p, c_g > 0$ are weighting coefficients, $0 < r_p r_g < 1$ are random numbers. v_1, v_2, v_3 in (20) correspond to (a), (b), (c), respectively.

It is expected that the steady-state swarm of PSO holds the time-variant optimum $\mathbf{x}^*(t)$. The canonical PSO is, however, inapplicable to time-variant optimization as it is. Therefore the canonical PSO is modified by introducing 1) inter-agent distance control, and 2) agent variety maintenance. The modified PSO is referred to as Vibrant PSO (Vi-PSO) (Suzuki & Mayahara, 2007).

Inter-agent distance control By adding a vector v_4 to (20) to prevent convergence to \mathbf{x}^{gb} , the PSO is made vibrant:

$$\Delta\mathbf{x}_i^k = v_1 + v_2 + v_3 + v_4 \quad (21)$$

$$v_4 = \frac{c_d}{(c_e \|\mathbf{x}^{gb} - \mathbf{x}_i^k\| + 1)^\alpha} \cdot \frac{\mathbf{x}^{gb} - \mathbf{x}_i^k}{\|\mathbf{x}^{gb} - \mathbf{x}_i^k\|} \quad (22)$$

where $c_d, c_e > 0, \alpha > 1$. If $\mathbf{x}^{gb} - \mathbf{x}_i^k \approx 0$, an adequate unit vector generated by randomization is used instead. And in the Vi-PSO the search domain is normalized because the size of the domain affects the optimization through the use of the distance between an agent and \mathbf{x}^{gb} in (22).

Agent variety maintenance As optimization progresses the distribution of agents becomes uneven, which often hinders optimum tracking. Hence some agents are probabilistically erased and new agents are produced at each time step. This selection/production reduces the uneven distribution, and increases the variety of agents. The Vi-PSO keeps suboptimal agents in steady state by adapting to the time varying object function by continuously searching near the current optimum.

6.3 Muscle Tension Optimization for StMA-RS

Problem setting The Vi-PSO is applied to problem $\mathbf{P}_T(t)$ in subsection 6.1, which is a muscle tension optimization for the StMA-RS control to adequately determine β for all t in control period.

Consider here to determine the muscle tension trajectory $\mathbf{T}(t) = \{T_i(t)\} \in \mathbf{R}^7$ in the case of controlling the joint angle θ_y continuously from -15° to 15° in $0 \leq t \leq 10$ with moment around y -axis, $M_y = 100$, exerted (Fig.22).

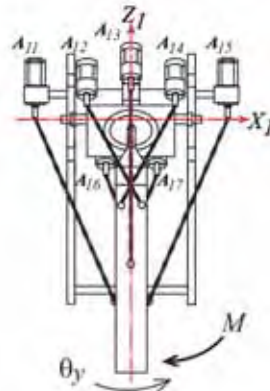


Fig. 22. StMA-based shoulder control problem: y -axis rotation under external moment

That is, the problem $\mathbf{P}_T(t)$ with the following specification in (16) is considered.

$$\boldsymbol{\theta}(t) = \begin{bmatrix} \theta_x \\ \theta_y \\ \theta_z \end{bmatrix} = \begin{bmatrix} 0 \\ 3t - 15 \\ 0 \end{bmatrix}, \quad \mathbf{M}(t) = \begin{bmatrix} 0 \\ 100 \\ 0 \end{bmatrix} \quad (23)$$

To prevent unrealistic elongation force (repulsive force between driving-end and effectedend), that is, to keep $T_i \geq 0$, a penalty function was added to the object function. The parameters used are $c_1 = 1, c_2 = 1, \mathbf{T}^r = (100, 100, \dots, 100)^T \in \mathbf{R}^7$ in object function, $w = 0.9, c_p = 0.1, c_g = 0.01, c_d = 0.25, c_e = 20, \alpha = 4$ in Vi-PSO. And the positions of driving/effected-ends of the StMA-RS in the basic posture are

$$\begin{aligned} A_{11} : \quad P_{D11}^0 &= (-65, 0, -30), & P_{E11}^0 &= (-12.5, 0, -180) \\ A_{12} : \quad P_{D12}^0 &= (-40, 55, 5), & P_{E12}^0 &= (8.8, -8.8, -80) \\ A_{13} : \quad P_{D13}^0 &= (0, 60, 30), & P_{E13}^0 &= (0, 12.5, -145) \\ A_{14} : \quad P_{D14}^0 &= (40, 55, 5), & P_{E14}^0 &= (-8.8, -8.8, -80) \\ A_{15} : \quad P_{D15}^0 &= (65, 0, -30), & P_{E15}^0 &= (12.5, 0, -180) \\ A_{16} : \quad P_{D16}^0 &= (-35, -35, -64), & P_{E16}^0 &= (8.8, 8.8, -140) \\ A_{17} : \quad P_{D17}^0 &= (35, -35, -64), & P_{E17}^0 &= (-8.8, 8.8, -140) \end{aligned}$$

Optimization result Optimization results are shown in Fig.23 and 24. The time charts of $\beta(t)$ and $\mathbf{T}(t)$ are shown in Fig.23. Note that $\mathbf{T}(t)$ was calculated using (16) with $\beta(t)$, and

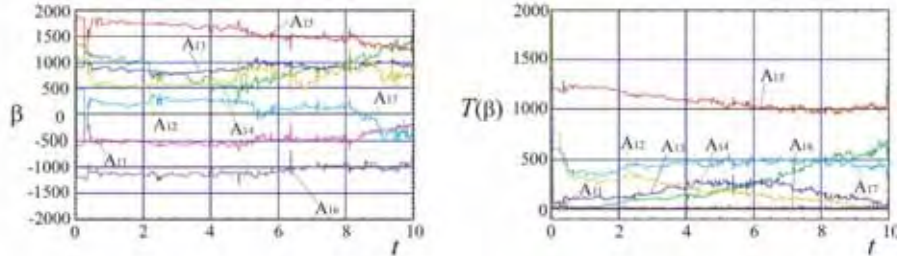


Fig. 23. Transition of muscle tension optimizing vector β and resultant muscle tension

hence the resultant $\mathbf{T}(t)$ always realizes the target joint angle $\theta(t)$ and moment $\mathbf{M}(t)$.

Muscle tensions waved bitterly at the initial stage of the optimization, but as optimization progresses, the movement settled down. The tension was concentrated to A_{15} which can generate y -axis moment efficiently. Most tensions were larger than the target tension

$T_i^r = 100$ because the target was much smaller than the necessary ones to resist $\mathbf{M}(t)$.

Therefore the second term in the objective function in this case worked to minimize muscle tensions.

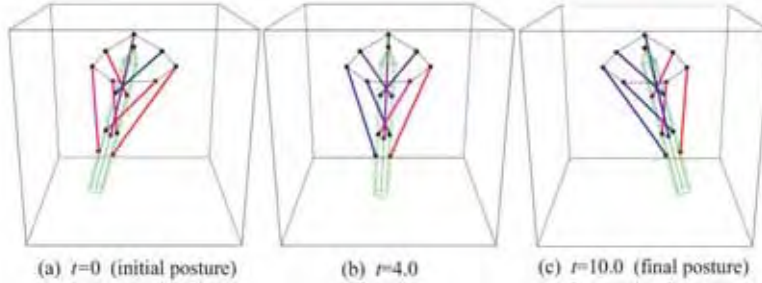


Fig. 24. Transition of posture and muscle tension

Fig.24 visually shows the posture and muscle tension transition. A muscle is colored red when its tension is large, blue when small. Except the initial state (a), where optimization does not progress yet, right side muscles have mainly large (red) tensions to resist the external moment. On the other hand left side ones have small (blue) ones, especially in later state, because no large tension is necessary for the requested motion.

Smoothing for practical use In Vi-PSO the optimal solution moves jumping from one point to another, therefore optimal β and corresponding muscle tension show non-smooth transition as in Fig.23, and so inadequate to use for control as it is. For practical use it is necessary to smooth the tension transition, for example by filtering the transition. Fig.25 shows the smoothed β and corresponding muscle tension.

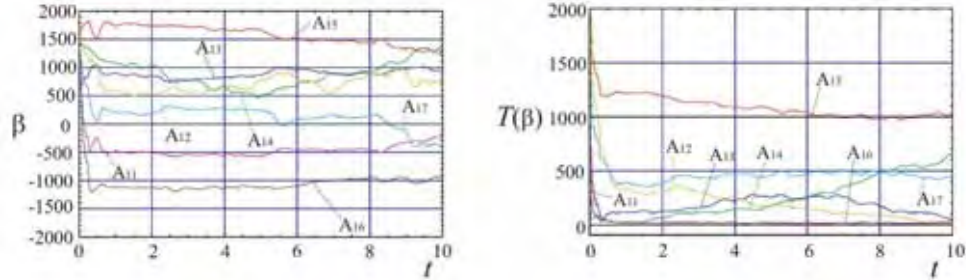


Fig. 25. Transition of smoothed β and corresponding muscle tension ($c_1 = 1, c_2 = 1$)

It should be noted that the smoothed tension $T(t)$ strictly realizes the target joint angle $\theta(t)$ for $M(t)$, although the smoothed β is not strictly optimal for the criterion.

Modifications depending on circumstances In order to adapt to task environment the object function is modified depending upon the circumstances.

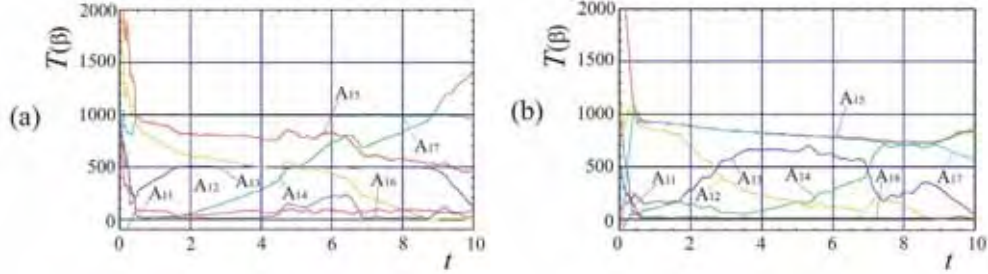


Fig. 26. Transition of muscle tension for modified criterions

Fig.26(a) shows the optimization result for $\mathbf{P}_T(t)$ with altered object function parameters $c_1 = 0.1, c_2 = 1$ and $\mathbf{T}^r = (100, 500, 500, 500, 100, 1000, 1000)^T$. Comparing to the result in Fig.25 a smaller weight c_1 to evaluate muscle tension distribution minimization was used. As a result large tensions were permitted for strong muscles like A_{14} and A_{17} , the tension for weak A_{15} was restrained, and some muscles exert near targeted tensions. Fig.26(b) shows the optimization result for a min-max criterion: $J(\beta(t)) = \max_n \{T_n(\beta(t))\}$, which shows a smooth transition of the maximum muscle tension. The maximum tension was minimized as intended, i.e., much smaller than the counterparts in Figs.25 and 26(a), which will contribute to lessen the possibility of muscle failure. The result says that adequate muscle coordination control according to situation change was successfully realized.

The real-time muscle coordination control of redundant muscles by use of Vibrant PSO was presented and shown to be effective for 3-DOF StMA-based joint motion control with considering optimal muscle tension distribution. With the target muscle tension $\mathbf{T}(t)$ obtained by solving $\mathbf{P}_T(t)$ and the necessary contraction of each muscle obtained from joint angle $\theta(t)$ by use of (9) and (11), an StMA-based robot is controlled based on the basic characteristics.

7. Discussions

Towards biped walking humanoid Development of humanoid robots is increasingly active. A biped walking mechanism using StMAs is now under development. The muscle coordination in multi-DOF joints and its online optimal control presented in sections 5 and 6 are applicable not only to shoulder control, but also to any multi-DOF joints such as wrists, hip joints, ankles and neck, or even to eyes and tongue movement.

The StMAs are small, light and simple. They are suitable for application to robotic hands, in which many actuators must be installed in the palm or in the forearm. The StMAbased hand in Fig.27 has 20 StMAs installed at the forearm, and the tension is transferred to wrist and fingers through tendon sheaths. 12 actuators are used as finger flexor muscles with leaf springs used as the corresponding extensor muscles. Leaf springs are also useful as the base

for force sensor with strain gauges. The hand in fact can measure the weight of grasping objects with a strain-gauge-based force sensor at the wrist.

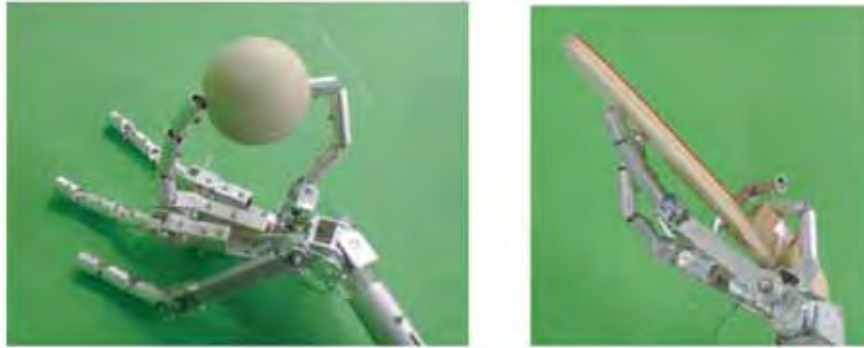


Fig. 27. StMA-based 5-fingered hand pinching a ping-pong ball and gripping a ping-pong racket

For practical utilization more investigation on the strand muscle itself, especially muscle fiber, and motor might be necessary. A strand muscle should be composed not by using handy materials, but by elaborately designed muscle fibers. More compact motors such as ultrasonic motors, or some innovative motors will drastically extend the StMA's applicability.

For autonomous realization of complex tasks A humanoid robot has so many joints. From the practical point of view, it seems almost impossible to precisely plan/specify all the joint motions in a top-down manner. An action planning/control strategy generated in a bottom-up manner with some hierarchical structure is inevitable. It is especially the case for StMA-based robots, each of whose joints is driven by two or more actuators.

The authors are researching an evolutionary behavior learning methodology with a hierarchical structure: Intelligent Composite Motion Control, ICMC (Suzuki, 2000), and applying it to robot behavior realization (Suzuki et al., 2001). The ICMC aims for realizing intelligent robots that can realize complex behaviors adaptively just by giving them the motion control for fundamental element motions. Starting from fundamental motions, complex behaviours are gradually realized by successive learning. In order to realize truly intelligent robots that flexibly and dexterously accomplish complex tasks like the human in the future, the behaviour realization must not be just an ad hoc execution but should be an acquisition with large capabilities. The ICMC gives a systematic behavior acquisition method by building up a capacious action intelligence network called the knowledge array network, which adaptively grows step-by-step in an evolutionary manner (Suzuki, 2005). The future work on the StMAs therefore includes the application of the methods presented in this chapter to practical tasks based on the ICMC.

8. References

- Kennedy, J.; Eberhart, R. C. (2001). *Swarm Intelligence*, Morgan Kaufmann
- Latash, M. L.; Turvey, M. T. (1996), Dexterity And Its Development, Lawrence Erlbaum Associates Publishers
- Linde, R. Q. van der (1999), Design, analysis, and control of a low power joint for walking robots, by phasic activation of McKibben muscles, *IEEE T. Robotics and Automation*, Vol. 15, No. 4, pp.599-604
- Suzuki, M.; Akiba, H.; Ishizaka, A. (1997), Strand-muscle robotic joint actuators (in Japanese), *Proc. 15th RSJ Annual Conf.*, pp.1057-1058
- Suzuki, M. (2000), A method of robot behavior evolution based on Intelligent Composite Motion Control, *Journal of Robotics and Mechatronics*, Vol.12, No.3, pp.202-208
- Suzuki, M.; Scholl, K.-U.; Dillmann, R. (2001), Complex and dexterous soccer behaviours based on the Intelligent Composite Motion Control, *Proc. 4th Int. Conference on Climbing and Walking Robots*, Karlsruhe, pp.443-450
- Suzuki, M.; Ichikawa, A. (2004), Toward springy robot walk using Strand-muscle actuators, *Proc. 7th Int. Conf. Climbing&Walking Robots*, pp.467-474, Madrid
- Suzuki, M. (2005), Evolutionary acquisition of complex behaviors through Intelligent Composite Motion Control, *Proc. 6th IEEE Int. Symp. Computat. Intelligence in Robotics and Automation*, Espoo
- Suzuki, M.; Mayahaya, T. (2007), Optimal Muscle Coordination of A Robot Joint using Vibrant Particle Swarm Optimization, *Proc. 13th IASTED Int. Conf. Robotics and Applications*, Wuerzburg, to appear
- Tahara, K. et al. (2005), Sensory-motor control of a muscle redundant arm for reaching movements – convergence analysis and gravity compensation, *Pros. 2005 IEEE/RSJ Int. Conf. on Intelligent Robots and Systems (IROS 2005)*, pp.517-522
- Yang, N. F. et al. (2001), A function description for the human upper limb pointing movements performance, *Proc. 23rd Annual Int. Conf. IEEE Engineer. in Medicine and Biology Society*, Vol.2, pp.1236-1239
- Proc. 2nd Conf. on Artificial Muscles (2004), Ikeda, Japan

Dynamic Walk of Humanoids: Momentum Compensation Based on the Optimal Pelvic Rotation

Hiroshi Takemura¹, Akihiro Matsuyama², Jun Ueda²,
Yoshio Matsumoto², Hiroshi Mizoguchi¹ and Tsukasa Ogasawara²

¹*Tokyo University of Science, ²Nara Institute of Science and Technology
Japan*

1. Introduction

Biped walking for humanoid robot has almost been achieved through ZMP theory (Takanishi, et al., 1985) (Goswami, 1999) (Kajita, et al., 2002). The research on humanoids has begun to focus on achieving tasks using the arms during walking (Harada, et al., 2003). In order to achieve a stable biped walking, the momentum around the perpendicular axis generated by the swing leg must be counterbalanced. In a normal human walk, the upper body compensates this momentum, i.e., by rotating the thorax (or shoulders) and swinging the arms in an antiphase of the swing leg (van Emmerik & Wagenaar, 1996) (Lamoth, et al., 2002) (LaFiandra, et al., 2003). For humanoid control, some researches have been presented for momentum compensation using the motion of the entire body including the arms (Yamaguchi, et al., 1993) (Kagami, et al., 2000) (Yamane & Nakamura, 2003) (Kajita, et al., 2003). However, momentum compensation by the upper body is undesirable for a humanoid that uses its arms to achieve a task since this type of compensation limits the degree of freedom (DOF) for the task. In addition, the fluctuation of the upper body has a bad effect not only on the task accomplishment, but also on visual processing since most vision systems are attached to the head part. As a result, it is desirable to preserve as many degrees of freedom of the upper body as possible, and to suppress the fluctuation of the body at the same time. The walking action including momentum compensation should be completed only by the lower body, which leads to a simplification of motion planning. Improving the performance of humanoids through observations of humans walk seems natural. Recently, however, in the field of exercise and sports science, a clarification of efficient motion in the human has begun, and this clarification has been accompanied by improvements in the measuring equipments used for this endeavor. Many common features can be observed in the motion of contact sport athletes, i.e., they move so as not to twist their trunks as much as possible. The particular pelvic rotation walk called a trunk-twistless walk has been empirically investigated from the observation of contact sport athletes (Ueda, et al., 2004). The walking action including the momentum compensation is completed only by the lower body. The upper-body DOF can be used for accomplishing a task. It is said that

this trunk-twistless walk tend to have an advantage in the energy efficiency in humanoids and human athletes. Furthermore, a relative phase of the swing leg and the pelvic rotation tends to be in an anti-phase when compared with the normal walk of humans. However, there seems to be no analysis result to explain these tendencies.

This chapter presents a method of momentum compensation around the perpendicular axis of the stance foot during dynamic walk of humanoid robots. The characteristics of the trunk-twistless walk are described the result of quantitatively investigation from the observation of contact sport athletes and are analyzed by using the mathematical model. The relative phase of the swing leg and the pelvic rotation appears to be in an antiphase when compared with the normal walk of humans. This leads to the possibility of momentum compensation by pelvic rotation, and this characteristic of the pelvic rotation is implemented to a humanoid conducted. A method of determining the optimal rotation of the humanoid's waist is proposed based on a minimization of the momentum around the perpendicular axis. In this chapter, we confirm that the torque around the perpendicular axis is reduced in the humanoid trunk-twistless walk when compared to a standard humanoid walk without the twisting of the trunk or swinging of the arms.

2. Human Walking Measurement

2.1 Methods and Subjects

Three healthy male subjects who are accustomed to the trunk-twistless walk served as subjects. All subjects are contact sport athletes of rugby football, karate, and kendo (the Japanese art of fencing) respectively. All subjects have been coaches. Their mean age, body height, and body weight were 42.6 ± 7.0 years (Mean \pm S.D.), 171.33 ± 1.52 cm, and 79.3 ± 6.02 kg. Subjects were given several minutes to get used to treadmill walking. The treadmill velocity was set to 1.5 km/h, 3.0 km/h and 4.0 km/h. The normal walk and the trunk-twistless walk were measured for 30 seconds.

A motion capture system with twelve cameras (Vicon Motion Systems Ltd.) was used to measure three dimensional kinematics data (sampling frequency 120Hz) from the reflective markers shown in Figure 1 (a). Two 3-axis accelerometers were attached on both iliac crests to measure the antero-posterior and medio-lateral accelerations of the pelvis. The twisting angle of the trunk was measured using the four markers shown in Figure 1 (b). The thoracic and pelvic rotation around the perpendicular axis, θ_{thorax} and θ_{pelvis} in Figure 2 are measured by the markers on both clavicles and both iliac crests respectively. Both angles are set to 0 when the subject is exactly facing the forward direction. The yaw-axis torque exertion from the stance foot to the floor is defined as τ_{LF} and τ_{RF} for each foot¹. When τ_{LF} increases to positive and exceeds the maximum static friction, the body begins to rotate clockwise due to the slip that occurs at the stance foot.

2.2 Comparison of Trunk Twisting and Pelvic Rotation

For the measurement result, it can be observed that the step width of the athlete's walk is wider than the normal walk, and the posture of the stance feet is in external rotation. In

¹ The foot rotation around the perpendicular axis is the main focus of this chapter. Whenever context permits, we use torque/moment to the torque around the perpendicular/yaw axis.

addition, the amplitude of pelvic rotation is small, and the relative phase between the swing leg and the pelvis is different compared to the normal walk.

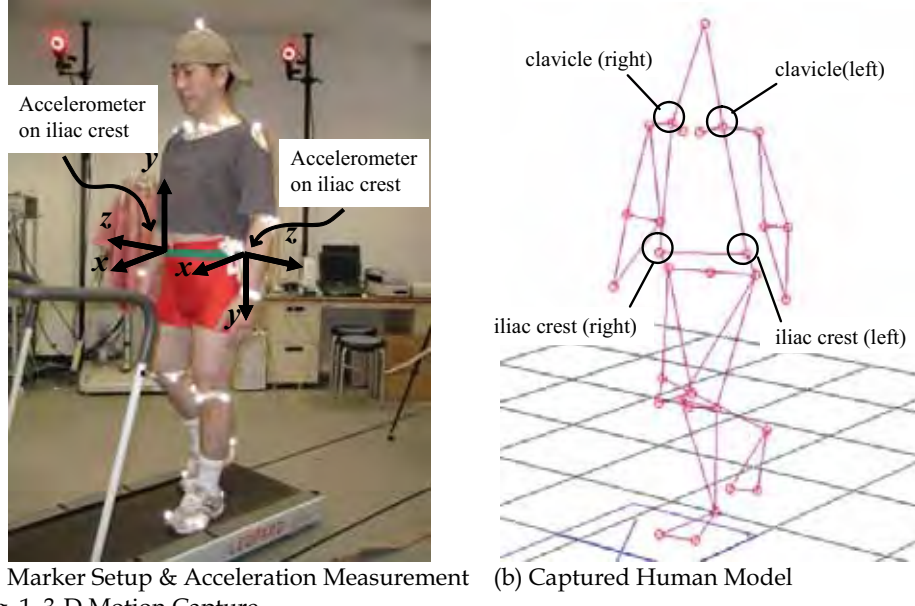


Fig. 1. 3-D Motion Capture

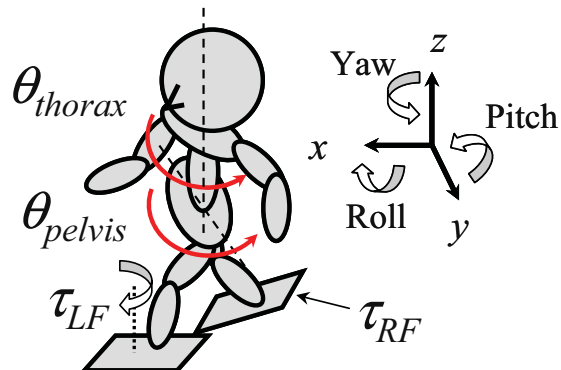


Fig. 2. Pelvis-thorax Rotating Angle and Yaw Moment of Stance Foot

The twisting angle of trunk θ_{twist} is obtained by subtracting θ_{pelvis} from θ_{thorax} :

$$\theta_{twist} = \theta_{pelvis} - \theta_{thorax} \quad (1)$$

Figure 3 shows the typical thorax, pelvis, and twisting angles at 4.0 km/h. The bottom graph shows the stance phase, Left heel Contact (LC) and Right heel Contact (RC). In the trunk-twistless walk, the relative phase between the pelvic and thoracic rotation is smaller, resulting in a smaller twisting angle of trunk than in the normal walk. In comparison to the stance phase, the relative phase between the leg and the thorax is almost the same for both types of walking, but the difference can be found in the pelvic rotation.

The counterclockwise rotation of the pelvis is observed for the normal walk when the right leg is in the air, whereas in the trunk-twistless walk, the clockwise rotation is observed in the same period. As a result, the relative phase of the swing leg and the pelvic rotation can be said to be in an antiphase for the trunk-twistless walk compared to the normal walk.

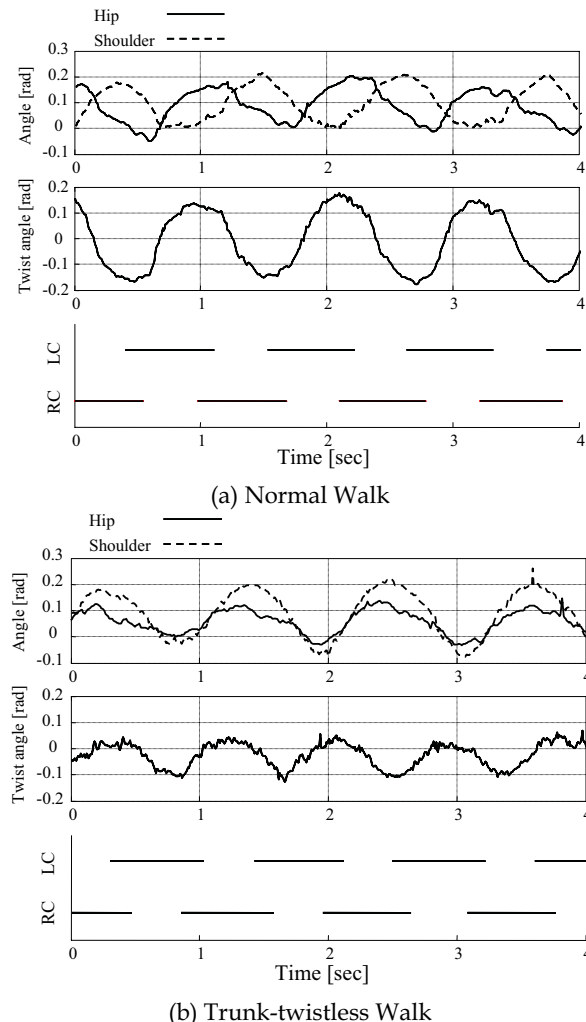


Fig. 3. Twisting Angle of Trunk

2.4 Characteristics of Momentum Compensation of the Trunk-twistless Walk

The trunk-twistless walk was quantitatively investigated from the observation of contact sport athletes (Ueda et al., 2004). The typical characteristics in comparison with the normal walk are:

- (1) Externally rotated posture of the stance feet,
- (2) Wide stance width,
- (3) Small relative phase between the pelvic and thoracic rotation (Small trunk twisting),
- (4) Curved COP trajectory (Torque transmission at the stance foot),
- (5) Antiphase of the swing leg and the pelvic rotation.

In a normal human walk, the momentum is compensated by the upper body, i.e., by rotating the thorax (or shoulder) and swinging the arms in antiphase of the swing leg. This motion leads to canceling the torque at the stance foot and avoiding the rotational slip. However, in contact sports, the upper-body posture should be maintained to the front as much as possible in preparation for contacting against the environments. A similar phenomenon can be observed when the contact increases the intensity of the upper-body exercise. It is assumed that the contact sport athletes perform the trunk-twistless motion for the upper-body exercise. A decreased pelvic and thoracic rotation, similar to the above case, has been observed with a load carriage (carrying a heavy backpack) (LaFiandra, et al., 2003). Without twisting the trunk or swinging the arms, the momentum should be compensated by other methods. The results of the investigation suggest that the momentum is simultaneously compensated passively by the friction at the stance foot and actively by the antiphase pelvic rotation.

In Figure 2, τ_{LF} increases when the right leg is accelerated and swing forward in the initial part of left leg stance phase. In the normal walk where the leg and the pelvis are in-phase, the momentum due to the increase of θ_{pelvis} also increases τ_{LF} . In this case, the sum of the momentum should be compensated by trunk twisting and arm swinging. On the other hand, in the trunk-twistless walk where the leg and the pelvis are in an antiphase, the decrease of θ_{pelvis} cancels τ_{LF} . Also, the momentum of inertia of the pelvis is not large when compared to the momentum of inertia of the legs; in other words, the total momentum is not compensated only by this active pelvic rotation. However, the twisting action of the trunk seems unnecessary when combined with passive compensation. In this chapter, we focus on this antiphase pelvic rotation, and apply this antiphase rotation to dynamic walking by humanoids.

3. Analysis of Trunk-twistless Walk for Momentum Compensation

3.1 Lower Body Analysis Model

In Section 2, the antiphase pelvic rotation was observed in the trunk-twistless walk of contact sport athletes, and the characteristics of the trunk-twistless walk were described. Then, the effect of the trunk-twistless walk on momentum compensation at the stance foot and energy efficiency is investigated by using a mathematical model. In order to analyze of the trunk-twistless walk, a lower body analysis model is proposed. We especially focus on hip joints of human and pelvic rotation. An upper body rotation is not considered, because the upper body rotation (above the chest) can be cancelled by a chest joint and an analysis

object is trunk-twistless walk. Figure 4 shows a four joints link model which has only two joints as each hip joint. To simplify the analysis, the 2D model as viewed from top of the 3D model is also proposed (Figure 4 (b)). In the Figure 4, J_{pelvis} and J_{leg} are the moment of inertia of pelvis and leg. θ_{st} and θ_{sw} are the pelvic rotation angle of support leg and swing leg respectively. ρ and ϕ are the pitch angle of support and swing legs. τ_{st} and τ_{sw} are the torque of support leg and swing leg pelvic joint. f_{st} and f_{sw} are the load force of support and swing leg. A condition of constraint ($\theta_{st} = -\theta_{sw}$) is added for keeping the direction of foots. p_{st} and p_{sw} are the position of the support leg and swing leg. p_{st} and p_{sw} are given by

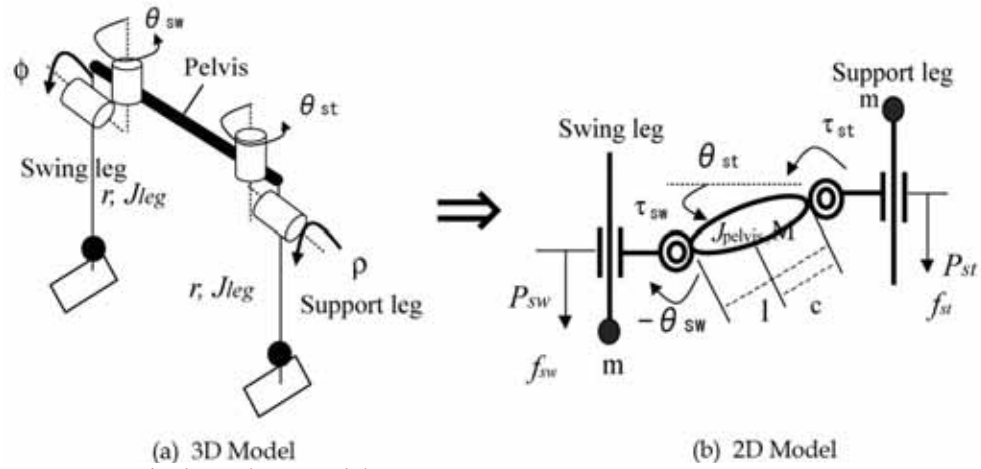


Fig. 4. Lower body analysis model

$$p_{st} = r \sin \rho, \quad p_{sw} = r \sin \phi \quad (2)$$

An equation of motion of the proposed model is derived from the Lagrange's equation as follow:

$$L = \frac{1}{2} J_{pelvis} \dot{\theta}_{st}^2 + \frac{1}{2} J_{leg} \dot{\theta}_{sw}^2 + \frac{1}{2} M \mathbf{V}_G^2 + \frac{1}{2} m(l \dot{\theta}_{st} + \dot{p}_{st} + \dot{p}_{sw})^2 + \frac{1}{2} m \dot{p}_{st}^2 \quad (3)$$

where V_G is the velocity of center of gravity. The forces and the torques are given by

$$\begin{bmatrix} J_{pelvis} + Mc^2 + ml^2 & 0 & ml - Mc \sin \theta_{st} & ml \\ 0 & J_{leg} & 0 & 0 \\ ml & 0 & m & m \\ ml - Mc \sin \theta_{st} & 0 & M + 2m & m \end{bmatrix} \begin{bmatrix} \ddot{\theta}_{st} \\ \ddot{\theta}_{sw} \\ p_{st} \\ p_{sw} \end{bmatrix} + \begin{bmatrix} 0 \\ 0 \\ 0 \\ -Mc \dot{\theta}_{st}^2 \cos \theta_{st} \end{bmatrix} = \begin{bmatrix} \tau_{st} \\ \tau_{sw} \\ f_{st} \\ f_{sw} \end{bmatrix} \quad (4)$$

where M and m are the mass of body and leg respectively. c is the length from joint to waist position. Therefore, the momentum around the perpendicular axis of the support foot τ_{sf} is given by

$$\tau_{sf} = \tau_{st} + f_{st}l \cos \theta_{st} \quad (5)$$

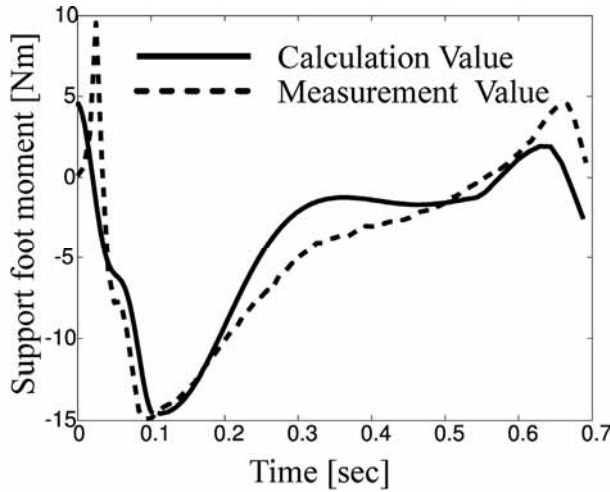


Fig. 5. Momentums around the perpendicular axis of the support foot

3.2 Verification of the proposed model

In order to evaluate the proposed model, a verification experiment is confirmed comparing the momentums around the perpendicular axis of the support foot, which measured by a force plate and calculated by using the proposed model. Three healthy male subjects served as subjects. The normal walk was measured for ten steps. The motion capture system with twelve cameras was used to measure three dimension kinematics data (sampling frequency

120Hz) for calculating the momentum around the perpendicular axis by using the proposed model. The floor reactive force and moment was also measured concurrently by using the force plate (Kistler Co Ltd.). The momentums around the perpendicular axis of the support foot at one step are shown in Figure 2. The both moment peaks of each subject are around 0.1 second. The sharp of the lines is almost same. The mean square error is less than 5%. The calculated results are qualitatively and quantitatively in agreement with the experimental results. Then, the proposed model can be used for analyzing the trunk-twistless walk.

3.3 Effect on Momentum Compensation and Energy Efficiency

The moment at the support foot and energy consumption are calculated by the proposed model when the pelvic rotation only changed. In order to analysis of the trunk-twistless walk, the pseudo-trunk-twistless walk is generated by using the measured 3D motion capture data as following steps. First, the motion captures system was used to measure three dimensional kinematics data. All subjects were given several minutes to set used. The treadmill velocity was set to 1.5 km/h, 3.0 km/h and 4.0 km/h. The normal walk was measured for 30 seconds. Second, the pelvic rotation trajectory θ_{st} and the pitch angle of the support leg ρ are calculated from the measured 3D motion capture data. Last, to generate the pseudo-trunk-twistless walk, the ρ is fixed, and the θ_{st} is forcibly changed to produce the phase difference between the pelvic rotation and the swing leg (from 0 to 360 [deg]). Note that all patterns have the same trajectory, velocity, posture, and landing positions for the foot in the air by using the redundancy of the waist and leg part. As a result, the walking velocity, step length, and step width are the same. The only difference is the pelvic rotation. Figure 6 shows typical examples of the walking posture of the normal walk and the pseudo-trunk-twistless walk (anti-phase). From Figure 6, the anti-phase pelvic rotation can be observed in the pseudo-trunk twistless walk, and the posture of the support feet is in external rotation. In addition, the relative phase between the swing leg and the pelvis is different compared to the normal walk. Then, the generated pseudo-trunk-twistless walk is applied to the proposed model to calculate the momentums around the perpendicular axis of the support foot and energy consumption. The energy consumption $E(t)$ is given by

$$E(t) = \int_0^t U dt \quad (6)$$

where U is the kinetic energy. The each parameter is defined in table 1 from the anatomical insight.

Parametar	Description	Value
M	Weight of waist	10.32[kg]
m	Weight of leg	10.08 [kg]
L	Length of waist	0.5[m]
c	Center of waist	0.25[m]
r	Length of leg	0.68[m]
J_{pelvis}	Moment of inertia of waist	0.98[kgm ²]
J_{leg}	Moment of inertia of leg	0.23[kgm ²]

Table 1. Parameter value of the model

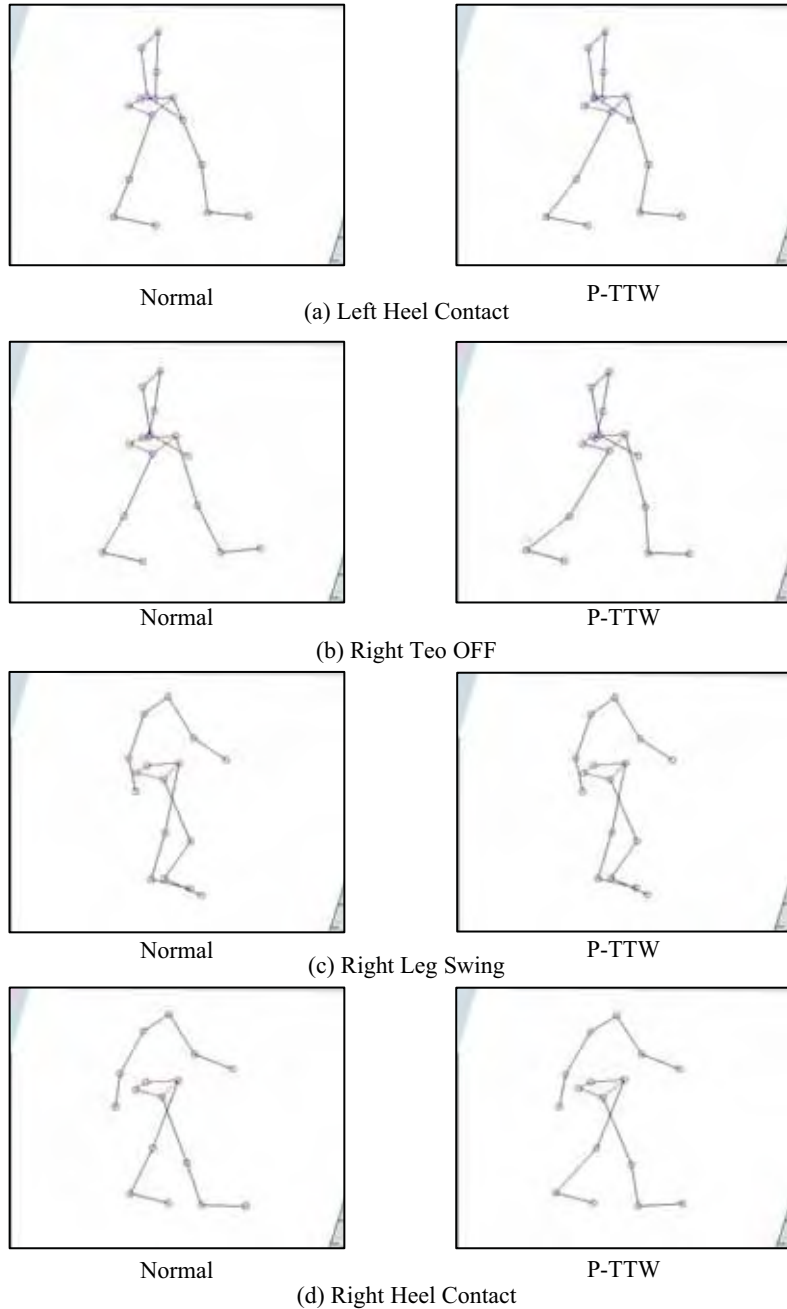


Fig. 6. Generated Pseudo-Trunk-Twistless Walking (P-TTW) Motion

Results of one subject are shown in Figure 7 and Figure 8. Figure 7 shows the energy consumption when the phase difference of the pelvic rotation is only changed. Figure 8 shows the momentums around the perpendicular axis when the walking velocity is 4.0 km/h. Table 2 shows the phase differences of normal walk, minimum energy consumption and minimum moment perk, and also shows averages of reduction rate of energy consumption and moment perk when comparing of the normal walking. The phase difference of normal walking is in an angle around 33.7 [deg]. However, the phase difference of minimum energy consumption and minimum moment perk is in an angle around π . The momentum perk around the perpendicular axis is reduced 33.6 [%] and the energy consumption is also reduced 45.6 [%] when compared to the normal walking. The antiphase pelvic rotation was observed in the trunk-twistless walk. The phase difference of around π is the antiphase pelvic rotation. The trunk-twistless walk can be reduced the moment perk and energy consumption. These results are suggested that the possibility of improving efficiency of momentum compensation and energy consumption to change the phase difference between the pelvic rotation and the swing leg at the normal walking pattern. This result strongly supports the previous investigation (Ueda et al., 2004).

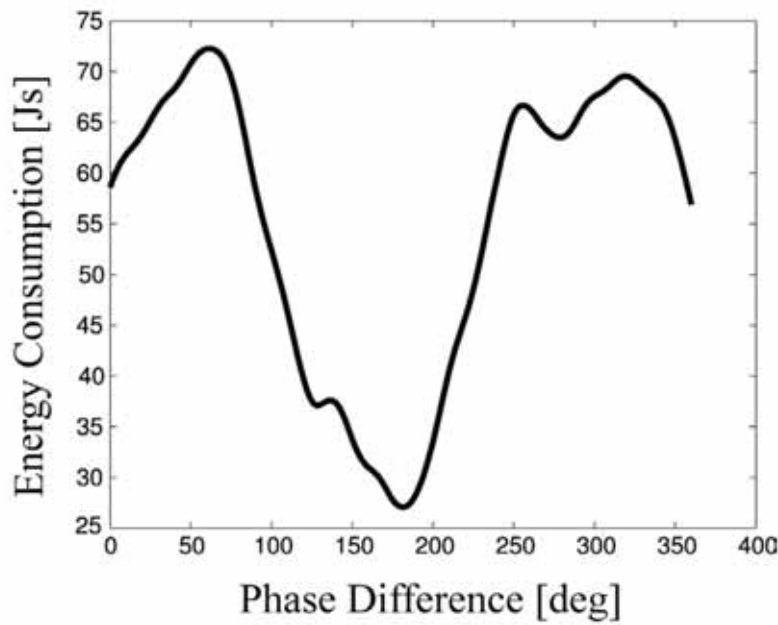


Fig. 7. Energy Consumption and Phase Difference (3.0km/h)

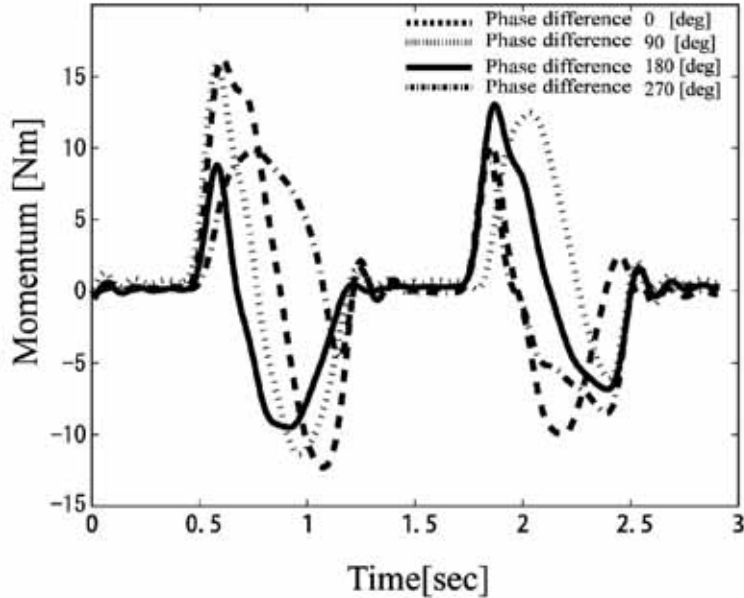


Fig. 8. Momentums in Each Phase Difference (4.0 km/h)

Walking velocity [km/h]	1.5	3.0	4.0	Average
Phase difference of normal walking (Ave.)[deg]	31	34	36	33.7
Phase difference of minimum moment perk (Ave.) [deg]	210	210	150	190
Phase difference of minimum energy consumption (Ave.) [deg]	197	180	217	198
Reduction rate (moment perk) (Ave.) [%]	32.3	32.3	36.3	33.6
Reduction rate (energy consumption) (Ave.) [%]	49.6	32.3	55.0	45.6

Table 2. Phase Differences and Reduction Rate of Energy Consumption and Moment Per

4. Moment Compensation for Humanoids using Waist Rotation

4.1 Humanoid Robot: HRP-2

Figure 9 shows the overview and the actuator configuration of the humanoid HRP-2 (Inoue, 2000) used in this chapter. Its height is 154cm and weight is 58kg, which are close the height and weight of a human. HRP-2 has 30 DOF in total. One characteristic of the HRP-2 is a joint around the perpendicular axis between the chest and the waist (called "chest joint"). Along with the hip joints, the chest part and the waist part rotate independently around the perpendicular axis as shown in Figure 9 (a). The pelvic rotation can be implemented to HRP-

2 by correlating the robot's waist to a human's pelvis and its chest to a human's thorax. A simulation software, Open HRP (Hirukawa, et al., 2001), is also available.

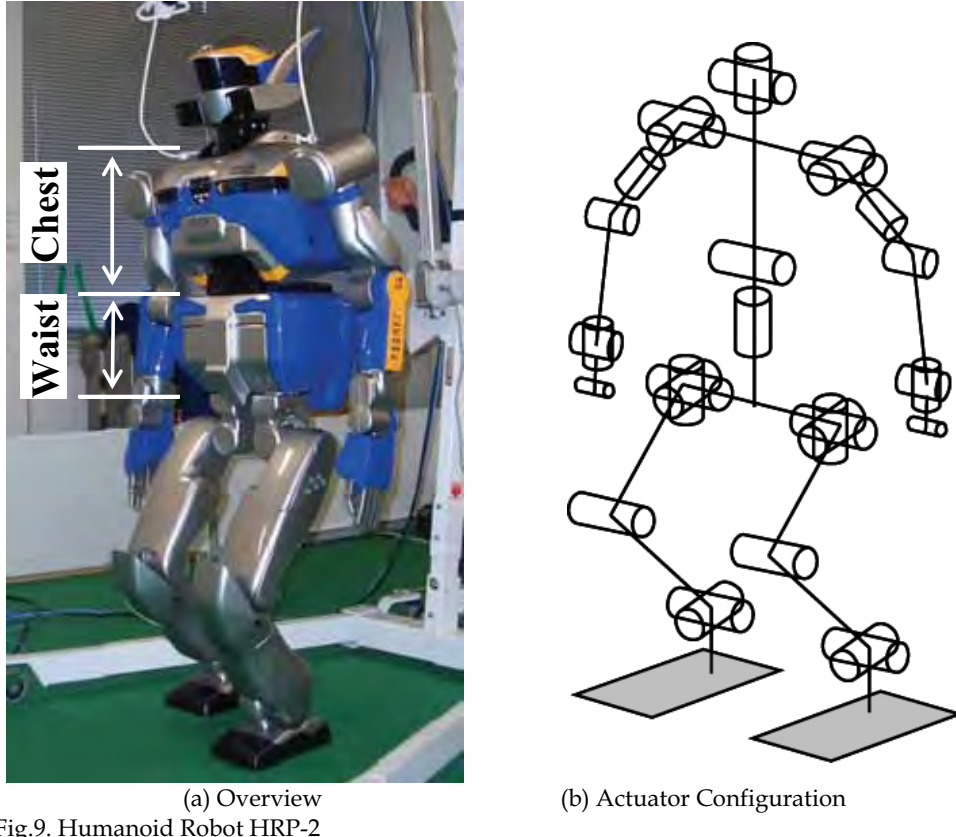


Fig.9. Humanoid Robot HRP-2

4.2 From Athlete Measurements to Humanoids

In Section 2, the antiphase pelvic rotation was observed in the trunk-twistless walk of contact sport athletes. The advantages of the application to humanoids are as follows: One goal of the research on humanoids is to achieve a task where the humanoid carries a load or interacts with environments (Harada, et al., 2003) using its upper body. The use of the upper body for walking itself, however, is undesirable for this purpose. The walking action including momentum compensation should be completed only by the lower body in order to preserve the freedom of the upper body.

In general, humanoids have larger feet for static stability; hence the maximum friction torque of the sole is larger than the human's. The rotational slip was not generated without considering the momentum in a low-speed walking pattern; however, this slip becomes a problem when the walking velocity is increased. In this case, the trunk-twistless walk preserves the upper body's DOF by waist rotation. As a secondary effect, the trunk-twistless

walk provides the humanoids with an easy visual processing using a vision system attached to the head part.

4.3 Evaluation of Humanoid Walk

The walking pattern with swinging arms and twisting trunk, which is common to the majority of people, cannot be regarded as a humanoid's standard walk. In this chapter, we apply the antiphase pelvic rotation of athletes to humanoids. First, the standard walk of a humanoid is defined to make clear the effects on momentum compensation without using the upper body. Note that we use "standard" for a humanoid walk to distinguish this walk from the "normal" walk of humans. In the standard walk of a humanoid, the upper body (above the chest) is not twisted and is planned to facing the forward direction. The swinging of arms is not performed; therefore, the walking action is completed only by the lower body. The waist rotation is set in-phase of the swing leg for the humanoid's standard walk, the same as in a human's normal walk. In contrast, the antiphase rotation of the waist is performed for the proposed walk of the humanoid, and is calculated by Equation (9) presented in the following section. The step width is set equal to the shoulder's width for all patterns by applying the result of the step width, which allows us to use a standard pattern generator (Kajita, et al., 2002). Note that all patterns have the same trajectory, velocity, posture, and landing positions for the foot in the air by using the redundancy of the waist and leg part. As a result, the walking velocity, step length, and step width are the same. The only difference is the pelvic rotation.

4.4 Generation of Optimal Pelvic Rotation

In section 3, the pseudo-trunk-twistless walk is generated by forcibly producing the phase difference. In this section, the optimal pelvic rotation is determined by using the proposed mathematical model based on a minimization of the momentum around the perpendicular axis as following equation:

$$J = \int_0^T \tau_{sf}^2 dt \rightarrow \min \quad (7)$$

where τ_{sf} is the momentum around the perpendicular axis of support foot. A perturbed trajectory $\theta_{st}(t) + \delta\theta_{st}(t)$ is considered. A functional of the perturbed trajectory is given by

$$\begin{aligned} \tilde{J} &= \int_0^T f(\theta_{st} + \delta\theta_{st}, \dot{\theta}_{st} + \delta\dot{\theta}_{st}, \ddot{\theta}_{st} + \delta\ddot{\theta}_{st}, t) dt \\ &= \int_0^T f(\theta_{st}, \dot{\theta}_{st}, \ddot{\theta}_{st}, t) dt + \int_0^T \left(\frac{\partial f_{st}}{\partial \theta_{st}} \delta\theta_{st} + \frac{\partial f_{st}}{\partial \dot{\theta}_{st}} \delta\dot{\theta}_{st} + \frac{\partial f_{st}}{\partial \ddot{\theta}_{st}} \delta\ddot{\theta}_{st} \right) dt \\ &\quad + o(\delta\theta_{st}^2, \delta\dot{\theta}_{st}^2, \delta\ddot{\theta}_{st}^2) \\ &= J + \delta J \end{aligned} \quad (8)$$

A necessary condition is Equation (9) calculated based on Euler-Poisson equation.
(9pt)

$$\frac{\partial f_{st}}{\partial \theta_{st}} - \frac{d}{dt} \left(\frac{\partial f_{st}}{\partial \dot{\theta}_{st}} \right) + \frac{d^2}{d^2 t} \left(\frac{\partial f_{st}}{\partial \ddot{\theta}_{st}} \right) = 0 \quad (9)$$

The optimal pelvic rotation is generated based on the motion capture data and Equation (9). We confirmed that the peak momentum around the perpendicular axis is reduced by 42% on an average in the optimal pelvic rotation walk when compared to the normal walk measured by the motion capture system.

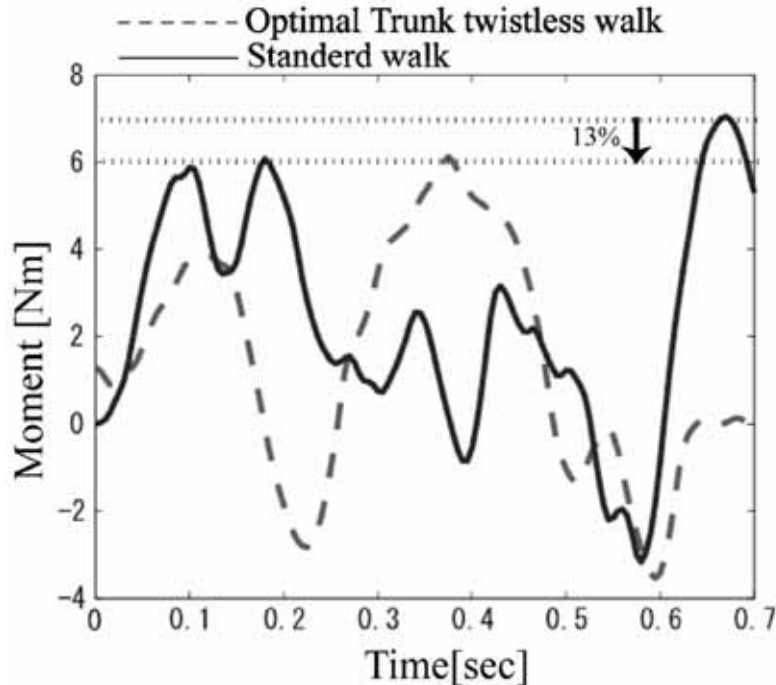


Fig. 10. Perpendicular Axis Momentum

5. Dynamic Walking of Humanoid

The effect of the waist rotation for reducing the support foot torque is confirmed. The antiphase waist rotation is realized in the proposed walk. We apply the optimal pelvic rotation to humanoid robot HRP-2 (Figure 5). The standard walk of a humanoid is defined that a single supporting time is 0.7[s], a double supporting time is 0.1[s], a step width is 0.25[m], the phase difference is in-phase, and without arm swing. The momentums around the perpendicular axis are shown in Figure 10. The peak momentum around the perpendicular axis of the proposed walk decrease in 13% is observed, and the amount of integration of the momentum is also reduced by 18% when compared to the standard walk. The validity of the proposed walk can be observed not only in the peak torque but also in the average torque.

6. Conclusion

In this chapter, the trunk-twistless walk of contact sport athletes was described from a motion measurement and the trunk-twistless walk was analyzed by using the mathematical model. The proposed optimal relative phase of the swing leg and the pelvic rotation was applied to the walk of humanoid HRP-2. The walking action including the momentum compensation was completed only by the lower body, so that the upper body DOF can be used for accomplishing a task. Using the proposed walk, the stance foot torque and the energy consumption were both reduced.

The future work includes an evaluation of the energy efficiency of the trunk-twistless walk, both in humanoids and human. An optimization program for an efficient walking pattern should be investigated. The authors wish to thank Kenji Shirae and Atsutoshi Ikeda of Nara Institute of Science and Technology for the data processing required for this research.

7. References

- Takanishi, A.; Ishida, M.; Yamazaki, Y. & Kato, I. (1985). The realization of dynamic walking by biped walking robot WL-10RD, *Proceedings of International Conference on Advanced Robotics*, pp. 459-466, Tokyo, Japan, September, 1985.
- Goswami, A. (1999). Postural Stability of Biped Robots and the Foot Rotation Indicator (FRI) Point, *International Journal of Robotics Research*, Vol.18, No.6, pp. 523-533.
- Kajita, S.; et al. (2002). A Realtime Pattern Generator for Biped Walking, *Proceedings of 2002 International Conference on Robotics and Automation*, Washington DC, May, 2002, pp. 31-37.
- Harada,K. ;Kajita, S.; Kaneko, K. & Hirukawa,H. (2003). ZMP Analysis for Arm/Leg Coordination, *Proceedings of 2003 IEEE/RSJ International Conference on Intelligent Robots and Systems*, Las Vegas, Nevada, October, 2003, pp.75- 81.
- van Emmerik,R. E. A.; Wagenaar,R. C. (1996). Effects of walking velocity on relative phase dynamics in the trunk in human walking, *Journal of Biomechanics*, Vol. 29, No. 9, pp. 1175-1184, 1996.
- Lamoth, C.J.C.; Beek, P.J. & Meijer, O.G. (2002). Pelvis-thorax coordination in the transverse plane during gait, *Gait & Posture*, Vol. 16, No. 2, pp. 101-114, 2002.
- LaFiandra, M; Wagenaar, R.C.; Holt, K.G. & J.P. Obusek. (2003). How do load carriage and walking speed influence trunk coordination and stride parameters?, *Journal of Biomechanics*, Vol. 36, No. 1, pp. 87-95, 2003.
- Yamaguchi, J.; Takanishi, A. & Kato, I. (1993). Development of a biped walking robot compensating for three-axis moment by trunk motion, *Proceedings of 1993 International Workshop on Intelligent Robotics and Systems*, Yokohama, Japan, pp. 561-566.
- Kagami, S.; Kanehiro, F.; Tamiya, Y.; Inaba, M. & Inoue, H. (2000). AutoBalancer: An Online Dynamic Balance Compensation Scheme for Humanoid Robots, *Proceedings of 4th International Workshop on Algorithmic Foundation on Robotics*, pp. 329-340, 2000.
- Yamane K. & Nakamura, Y. (2003). Dynamics Filter-Concept and Implementation of Online Motion Generator for Human Figures, *IEEE Transactions on Robotics and Automation*, Vol.19, No.3, pp.421-432, 2003.

- Kajita, S.; Kanehiro, F.; Kaneko, K.; Fujiwara, K.; Harada, K.; Yokoi, K. & Hirukawa, H. (2003). Resolved Momentum Control: Humanoid Motion Planning based on the Linear and Angular Momentum, *Proceedings of 2003 IEEE/RSJ International Conference on Intelligent Robots and Systems*, pp. 1644-1650.
- Ueda, J.; Shirae, k.; Matsumoto, Y.; Oda, S. & Ogasawara, T. (2004). Momentum Compensation for the Fast Dynamic Walk of Humanoids based on the Pelvic Rotation of Contact Sport Athletes, *Proceedings of IEEE/RSJ International Conference on Humanoid Robots*.
- Inoue, H., et al., (2000). HRP, Humanoid Robotics Project of MITI, *Proceedings of IEEE/RAS International Conference on Humanoid Robots*.
- Hirukawa, H.; Kanehiro, F. & Kajita, S. (2001). OpenHRP, Open Architecture Humanoid Robotics Platform, *Proceedings of 2001 International Symposium on Robotics Research*.

Attitude Control of a Six-legged Robot in Consideration of Actuator Dynamics by Optimal Servo Control System

H. Uchida* and K. Nonami†

*Kisarazu National College of Technology, †Chiba University
Japan

1. Introduction

There are more than 100 million land mines buried throughout the world, and, at present, the removal of these mines is primarily being done by hand. Our research group has suggested a mine detection method using six-legged robots, such as COMET-I, II, and III, to establish the land mine detection and removal technology. Mine detection by six-legged robots such as COMET-II and III have two manipulators at the front of the body designed for mine detection. Since most mine detection is performed on irregular terrain, it is necessary for a six-legged robot to maintain a stable posture in the mine detection using two manipulators. The authors have examined attitude control methods for achieving stable land mine detection by six-legged robot. With respect to the attitude control, we have examined the control method to control the height of the body and the pitching and the rolling angles according to the force reference signal in the perpendicular direction at the supporting leg. As an attitude control method, we have applied the extended sky hook suspension control (ESHSC) (Uchida & Nonami, 2001), the optimal servo control system (Uchida & Nonami, 2002), and the sliding mode control (Uchida & Nonami, 2003). These methods targeted COMET-II, each leg link of which is driven by a direct current motor. However, at present, the research is conducted using COMET-III, in an attempt to develop it for practical use. Leg links of the COMET-III are driven by hydraulic actuators. When the above-mentioned attitude control methods are applied to COMET-III, it is difficult to realize stable attitude control because of the delay of the hydraulic actuators. Therefore, it is desirable to establish an attitude control method considering the delay of the actuator. In the present study, as a model considering the delay of the hydraulic actuator, we construct a mathematical model in which inputs are the driving torque of the thigh links in the supporting legs and the outputs are the height of the body, the pitching angle, and the rolling angle. The optimal servo control system in modern control theory is designed for this model. The validity of the proposed control method is verified by simulations performed using a 3D model of the COMET-III, in which the delay of the hydraulic actuator is modeled.

2. Mine Detecting Six-legged Robot (COMET-III) and CAD Model

Figure 1 shows the COMET-III mine detecting six-legged robot, which was developed at Chiba University. Figure 2 shows a 3D CAD model of COMET-III generated using mechanical analysis software. One leg of the robot has three degrees of freedom, and each joint is driven by a hydraulic actuator. The ankle of the leg has two degrees of freedom so that the sole of the entire bottom surface of the foot touches the ground. The parameters of COMET-III are shown in Table 1. The mass of the robot is approximately 1,200 [kgf]. The width of the body is 2,500 [mm], and the length of the body is 3,500 [mm]. The height of the body is 850 [mm]. An attitude sensor is attached to the body of COMET-III to detect the pitching and rolling angles. In addition, a six-axis force sensor is attached to each leg. In the present study, we verify the validity of the proposed attitude control method using a 3D model.



Fig. 1. COMET-III mine detecting six-legged robot

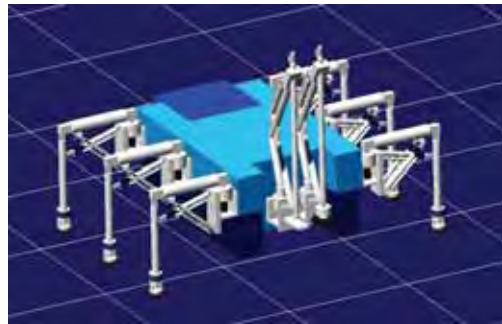


Fig. 2. 3D CAD model of COMET-III

Weight	1,200 [kgf]
Width of the body	2,500 [mm]
Length of the body	3,500 [mm]
Height of the body	850 [mm]

Table 1. Parameters of COMET-III

3. Walking Pattern

In the present study, it is desirable that there be little risk of the robot falling down, so that the attitude control method is examined. Therefore, static walking, which has high stability, is adopted. The effectiveness of the proposed method is verified by the walking pattern of five supporting legs. The leg numbers of a six-legged robot are shown in Figure 3. Figure 4 shows the walking pattern by five supporting legs. The period of the swing phase is 3 [s], and one period of the gait is 18 [s]. In Figure 4, the white area indicates a swing phase, and the black area indicates a supporting phase. Therefore, the order of the swing motion of the legs is II→III→IV→I→IV→V.

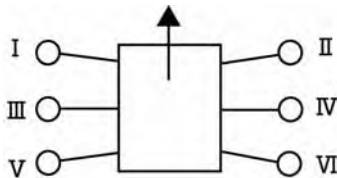


Fig. 3. Leg numbers

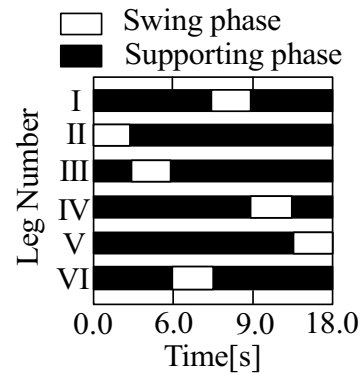


Fig. 4. Walking pattern

4. Attitude Control Method

This chapter examines the attitude control method that must be applied in the case of walking and mine detection work on irregular terrain such as a minefield. On even terrain, each angle of the joint is controlled to follow desired values, which are obtained by inverse-kinematics. However, on irregular terrain, it is difficult for only position control to keep the walking and attitude stable. Therefore, it is necessary for the attitude control to recover the body inclines by adding a force to the supporting legs. This attitude control is realized by controlling the force in the perpendicular direction of each supporting leg. Moreover, it is necessary to consider the delay of the hydraulic actuator because the hydraulic actuator is used for COMET-III.

In the present study, as a model considering the delay of the hydraulic actuator, we make a mathematical model in which the inputs are the driving torque of the thigh link in the

supporting legs and the outputs are the height of the body, the pitching angle, and the rolling angle. In this process, we must seek the force acting the supporting legs, so that the force is obtained by an approximation formula using the angle and the angular velocity of the thigh link and the virtual spring and dumping coefficient. The delay of the hydraulic actuator is considered because this model calculates the force and the attitude in the perpendicular direction of the supporting leg from the state value of the thigh link. The optimal servo control system in modern control theory is designed for this model.

4.1 Mathematical Model of the Thigh Link

The leg links of the six-legged robot used in this research have three degrees of freedom, namely, the shoulder (θ_{1i}), the thigh (θ_{2i}), and the shank (θ_{3i}) ($i = 1, \dots, 6$). Equation (1) shows the transfer function of the thigh link, which is very important in the case of the attitude control of COMET-III. The delay model of the hydraulic actuator is approximated by a 1st-order Pade approximation.

$$G(s) = \frac{\alpha\omega_n^2}{s^2 + 2\zeta\omega_n + \omega_n^2} \bullet \frac{1 - \frac{1}{2}sT}{1 + \frac{1}{2}sT} \quad (1)$$

Figure 5 shows the step reference response of the PD feedback control system for the system shown as Eq. (1). A delay of approximately 0.2 [s] occurs.

The description of the state space in Eq. (1) is as follows:

$$\dot{x}_i = \begin{bmatrix} 0 & 1 & 0 \\ 0 & 0 & 1 \\ 0 & a_1 & a_2 \end{bmatrix} x_i + \begin{bmatrix} 0 \\ 0 \\ 1 \end{bmatrix} u_i(t) \quad (2-a)$$

$$\theta_{2i} = [c_1 \ c_2 \ 0] \begin{bmatrix} x_{i1} \\ x_{i2} \\ x_{i3} \end{bmatrix}, \quad (i = 1, \dots, 6) \quad (2-b)$$

where

x_i : state variable vector u_i : input vector

θ_{2i} : angle of each thigh i : foot number

a_1, a_2, c_1, c_2 : coefficients obtained by Eq. (1).

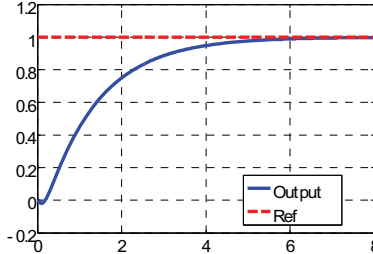


Fig. 5. Step response of the thigh driven by the hydraulic cylinder

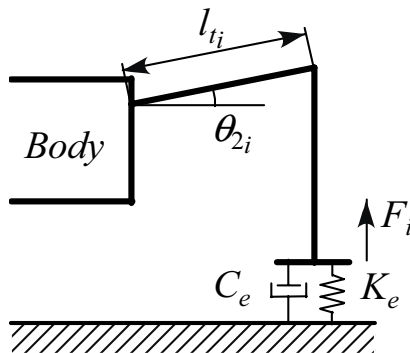


Fig. 6. Relationship between the angle of thigh and the force in the perpendicular direction of the supporting leg.

4.2 Mathematical Model from the Input of the Thigh Link to the Attitude of the Body

Figure 6 shows the relationship between the angle of the thigh and the force in the perpendicular direction of the supporting leg. In Fig. 6, l_{ti} is the length of the thigh, and C_e and K_e are the damping and the spring coefficient of the ground, respectively. The following assumptions are used in Fig. 6.

- ① The shank always becomes vertical to the ground ($\theta_{3i} = 0$).
- ② The change of θ_{2i} is small.

According to the above assumptions, the force F_i in the perpendicular direction of the supporting leg is given by the following equation:

$$F_i = l_{ti}K_e\theta_{2i} + l_{ti}C_e\dot{\theta}_{2i} \quad (3)$$

Substituting Eq. (2) for Eq. (3), F_i is given by the following equation:

$$F_i = l_{ti}K_e c_{1i} x_{21i} + l_{ti}(K_e c_{2i} + C_e c_{1i})x_{22i} + l_{ti}C_e c_{2i} x_{23i} \quad (4)$$

Moreover, the height, and the pitching and rolling angles of the body are controlled by controlling the force in the perpendicular direction of the supporting leg. The motion equations of the force and the moment equilibrium in the perpendicular direction and the pitching and rolling axes in the case of support by six legs are given by Eq. (5). Figure 7 shows the coordinates of each foot.

$$\left\{ \begin{array}{l} M\ddot{z} = F_1 + F_2 + F_3 + F_4 + F_5 + F_6 - Mg \\ I_p \ddot{\theta}_p = y_1 F_1 + y_2 F_2 + y_3 F_3 + y_4 F_4 + y_5 F_5 + y_6 F_6 \\ I_r \ddot{\theta}_r = x_1 F_1 + x_2 F_2 + x_3 F_3 + x_4 F_4 + x_5 F_5 + x_6 F_6 \end{array} \right\} \quad (5)$$

where

M : mass of the body g : acceleration of gravity

I_p : inertia around the pitching axis I_r : inertia around the rolling axis

Substituting Eq. (4) for Eq. (5), and by defining the 24th-order state value as $x = [x_{11}, x_{21}, x_{31}, x_{12}, \dots, x_{36}, \theta_p, \theta_r, z, \dot{\theta}_p, \dot{\theta}_r, \dot{z}]^T$, which consists of the state values of each thigh link, the pitching and rolling angles, the height of the body and its velocity, the following state equation is obtained:

$$\begin{bmatrix} \dot{x}_1 \\ \dot{x}_2 \\ \dot{x}_3 \\ \dot{x}_4 \\ \dot{x}_5 \\ \dot{x}_6 \\ \dot{x}_7 \\ \dot{x}_8 \end{bmatrix} = \begin{bmatrix} A_{11} & 0_{3 \times 3} \\ 0_{3 \times 3} & A_{22} & 0_{3 \times 3} \\ 0_{3 \times 3} & 0_{3 \times 3} & A_{33} & 0_{3 \times 3} \\ 0_{3 \times 3} & 0_{3 \times 3} & 0_{3 \times 3} & A_{44} & 0_{3 \times 3} & 0_{3 \times 3} & 0_{3 \times 3} & 0_{3 \times 3} \\ 0_{3 \times 3} & 0_{3 \times 3} & 0_{3 \times 3} & 0_{3 \times 3} & A_{55} & 0_{3 \times 3} & 0_{3 \times 3} & 0_{3 \times 3} \\ 0_{3 \times 3} & A_{66} & 0_{3 \times 3} & 0_{3 \times 3} \\ 0_{3 \times 3} & A_{78} & 0_{3 \times 3} \\ A_{81} & A_{82} & A_{83} & A_{84} & A_{85} & A_{86} & 0_{3 \times 3} & 0_{3 \times 3} \end{bmatrix} \begin{bmatrix} x_1 \\ x_2 \\ x_3 \\ x_4 \\ x_5 \\ x_6 \\ x_7 \\ x_8 \end{bmatrix} +$$

$$\begin{bmatrix} B_1 & 0_{3x1} & 0_{3x1} & 0_{3x1} & 0_{3x1} & 0_{3x1} \\ 0_{3x1} & B_2 & 0_{3x1} & 0_{3x1} & 0_{3x1} & 0_{3x1} \\ 0_{3x1} & 0_{3x1} & B_3 & 0_{3x1} & 0_{3x1} & 0_{3x1} \\ 0_{3x1} & 0_{3x1} & 0_{3x1} & B_4 & 0_{3x1} & 0_{3x1} \\ 0_{3x1} & 0_{3x1} & 0_{3x1} & 0_{3x1} & B_5 & 0_{3x1} \\ 0_{3x1} & 0_{3x1} & 0_{3x1} & 0_{3x1} & 0_{3x1} & B_6 \\ 0_{3x1} & 0_{3x1} & 0_{3x1} & 0_{3x1} & 0_{3x1} & 0_{3x1} \\ 0_{3x1} & 0_{3x1} & 0_{3x1} & 0_{3x1} & 0_{3x1} & 0_{3x1} \end{bmatrix} u + \begin{bmatrix} 0_{3x1} \\ d_8 \end{bmatrix} = g \quad (6)$$

where,

$$x_i = \begin{bmatrix} x_{1i} \\ x_{2i} \\ x_{3i} \end{bmatrix} \quad (i = 1 \sim 6), \quad x_7 = \begin{bmatrix} z \\ \dot{\theta}_p \\ \theta_r \end{bmatrix}, \quad x_8 = \begin{bmatrix} \dot{z} \\ \dot{\theta}_p \\ \dot{\theta}_r \end{bmatrix},$$

$$A_{ii} = \begin{bmatrix} 0 & 1 & 0 \\ 0 & 0 & 1 \\ 0 & a_1 & a_2 \end{bmatrix} \quad (i = 1, \dots, 6), \quad A_{78} = \begin{bmatrix} 1 & 0 & 0 \\ 0 & 1 & 0 \\ 0 & 0 & 1 \end{bmatrix}$$

$$A_{8i} = \begin{bmatrix} \frac{K_e l c_1}{M} & \frac{K_e l c_2 + C_e l c_1}{M} & \frac{C_e l c_1}{M} \\ \frac{K_e l c_1}{I_p} y_i & \frac{K_e l c_2 + C_e l c_1}{I_p} y_i & \frac{C_e l c_1}{I_p} y_i \\ \frac{K_e l c_1}{I_r} x_i & \frac{K_e l c_2 + C_e l c_1}{I_r} x_i & \frac{C_e l c_1}{I_r} x_i \end{bmatrix} \quad (i = 1, \dots, 6),$$

$$B_i = \begin{bmatrix} 0 \\ 0 \\ 1 \end{bmatrix} \quad (i = 1, \dots, 6), \quad u = \begin{bmatrix} u_1 \\ u_2 \\ u_3 \\ u_4 \\ u_5 \\ u_6 \end{bmatrix}, \quad d_8 = \begin{bmatrix} 1 \\ 0 \\ 0 \end{bmatrix}$$

Equation (6) is rewritten as follows:

$$\dot{x} = Ax + Bu + fg \quad (7)$$

Here, each row shows the following:

- 1st ··· 3rd : 1st ··· 3rd column is Eq. (2) and shows the dynamics of Leg I.
- 4th ··· 6th : 4th ··· 6th column is Eq. (2) and shows the dynamics of Leg II.
- 7th ··· 9th : 7th ··· 9th column is Eq. (2) and shows the dynamics of Leg III.
- 10th ··· 12th : 10th ··· 12th column is Eq. (2) and shows the dynamics of Leg IV.
- 13th ··· 15th : 13th ··· 15th column is Eq. (2) and shows the dynamics of Leg V.
- 16th ··· 18th : 16th ··· 18th column is Eq. (2) and shows the dynamics of Leg IV.
- 19th ··· 21st : shows the relationship among the angular velocity $\dot{\theta}_p$, $\dot{\theta}_r$, and \dot{z} .
- 22nd ··· 24th : shows the equation of motion in Eq. (5).

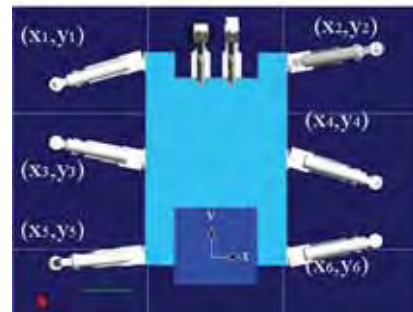


Fig. 7. Coordinates of each leg

4.3 Optimal Servo System

The servo system that the system shown by Eq. (7) follows to the desired value is designed.

$$\begin{cases} \dot{z} = r - cx \\ \dot{x} = Ax + Bu + fg \end{cases} \quad (8)$$

where, \dot{z} is the error vector between the desired vector and the output vector. Equation (8) is given in matrix form as follows:

$$\begin{bmatrix} \dot{z} \\ \dot{x} \end{bmatrix} = \begin{bmatrix} 0 & -c \\ 0 & A \end{bmatrix} \begin{bmatrix} z \\ x \end{bmatrix} + \begin{bmatrix} 0 \\ B \end{bmatrix} u + \begin{bmatrix} 0 \\ d \end{bmatrix} g + \begin{bmatrix} I \\ 0 \end{bmatrix} r \quad (9)$$

Equation (9) is described in equation form as follows:

$$\dot{x}_g = A_g x_g + B_g u + d_g g + f_g r \quad (10)$$

The feedback (FB) control input u_b to the actuator driving the thigh link is obtained in order to minimize the following cost function:

$$J = \int [x_g(t)^T Q x_g(t) + u(t)^T R u(t)] dt \quad (11)$$

where $Q(n \times n)$ and $R(m \times m)$ are the weighting matrixes given by the design specifications, and $Q \geq 0, R > 0$. The control input to minimize Eq. (11) is as follows:

$$u_b^o = -R^{-1} B_g^T P x \quad (12)$$

where $P(n \times n)$ is the solution of the following Riccati equation:

$$P A_g + A_g^T P - P B_g R^{-1} B_g^T P + Q = 0 \quad (13)$$

Figure 8 shows a block diagram of the optimal servo control system.

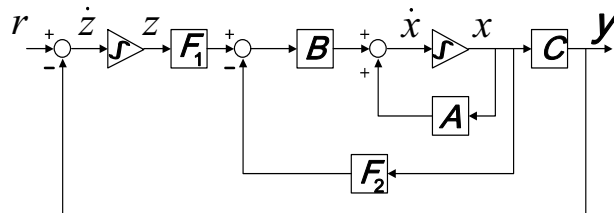


Fig. 8. Block diagram of optimal servo control system

4.4 Making a Controlled System for an Uncontrolled System

We examined the controllability for the system as Eq. (10), which is constructed using Eq. (2). However, it has become an uncontrollable system. The 3rd-order delay system is then approximated to the delay system of the 2nd-order model, which is given by following equation:

$$G(s) = \frac{\omega_n^2}{s^2 + 2\zeta\omega_n s + \omega_n^2} \quad (14)$$

In order to obtain the same results for the 3rd-order model as were obtained for the 2nd-order model, both the values of the magnitude and the phase in the Bode diagram coincide with the angular velocity of the walking speed. We searched the values ω_n and ζ to satisfy the above condition and obtained the results of $\omega_n = 9$ [rad/s] and $\zeta = 0.9$. Figure 9 shows a comparison of the bode plot for the 2nd-order system and the 3rd-order system. In Fig. 9, the solid line shows the 2nd-order model, and the dashed line shows the 3rd-order model. The solid line drawn around 0.6 [rad/s] at the angular velocity in the figure shows the angular velocity of the walking in this research. The difference between the systems is significant in the high-frequency range. However, in this study, in the bandwidth of the walking speed, the magnitude and the phase coincide. Therefore, we consider this approximation to be appropriate, and so the attitude control method is designed to replace Eq. (2) with Eq. (14), and the effectiveness is verified. The system described by Eq. (7) becomes the 19th-order model.

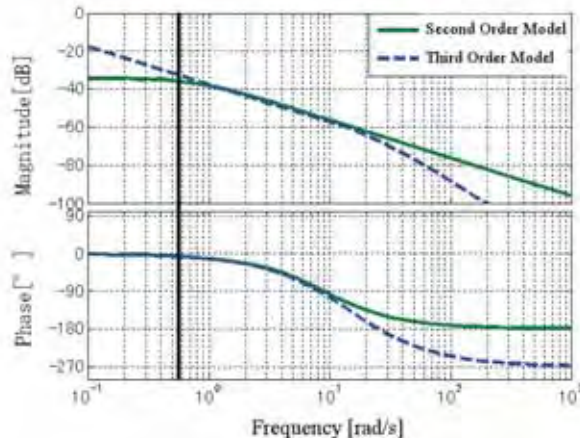


Fig. 9. Comparison of bode plots for the 2nd-order system and the 3rd-order system

5. 3D Simulation

In this section, in order to verify the validity of the attitude control method considering the delay of the hydraulic actuator, we examine the walking characteristics on even terrain and on irregular terrain using the 3D model of the COMET-III six-legged robot. We then discuss the performance of the attitude control method considering the delay by the simulation results. The shoulder and shank parts of the leg links are controlled by the PD control, which is a very popular control method to follow the desired value θ_{1ir} and θ_{3ir} ($ir = 1, 2, \dots, 6$) obtained by solving inverse-kinematics. In addition, in the case of walking with five supporting legs, the attitude control is applied for the five supporting legs, except for one swinging leg. The swinging leg is controlled by the PD control.

5.1 Walking on Even Terrain

Figure 10 shows the 3D simulation results of the proposed attitude control method on even terrain. Figures 10(a), 10(b), and 10(c) show the time response of the pitching angle, the rolling angle, and the height of the body, respectively. The variation of the attitude is very small, and the attitude control works to recover the variation. The six-legged robot can realize a stable walk.

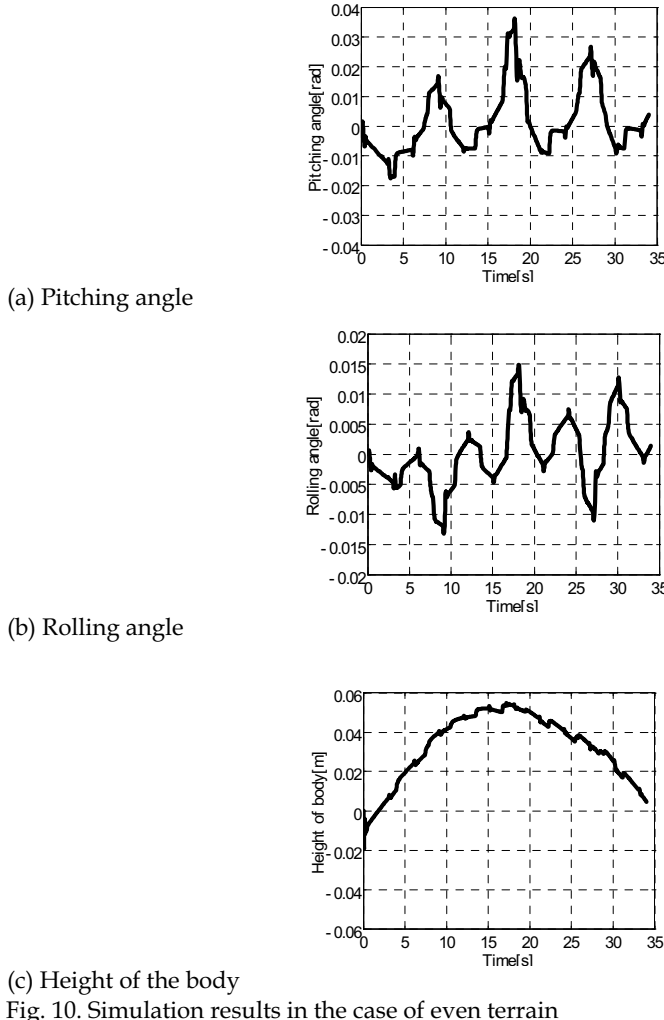


Fig. 10. Simulation results in the case of even terrain

5.2 Walking on Irregular Terrain

Figure 11 shows the simulation case for irregular terrain, in which the six-legged robot walks over a 10 [cm] high step. The six-legged robot starts to climb the step at 3 [s] and leaves the step at 54 [s]. Figure 12 shows the 3D simulation results for irregular terrain.

Figures 12(a), 12(b), and 12(c) show the time response of the pitching angle, the rolling angle, and the height of the body, respectively. The vibrations occur in the pitching and rolling angles. In addition, approximately 40 [s] is required to settle down at the height of the body of approximately 0 [m]. However, the influence of the step is slight and the six-legged robot can realize a stable walk. Moreover, Fig. 13 shows the animation results of the 3D simulation on irregular terrain. Figures 13(a), 13(b), and 13(c) show animations at the times of 3.45 [s], 70.8 [s], and 136.25 [s], respectively. In Fig. 13(c), two manipulator attached to the front part of the body are pushed into the ground. However, this causes no particular problem, because it does not influence the walking operation. Based on the above-mentioned results, the attitude control method that considers the dynamics of the actuator proposed in the present study is effective.

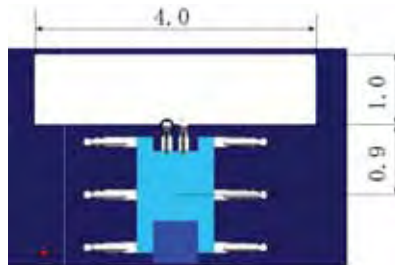
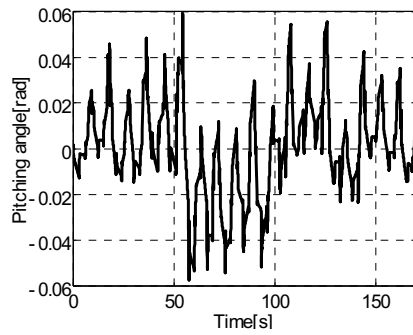
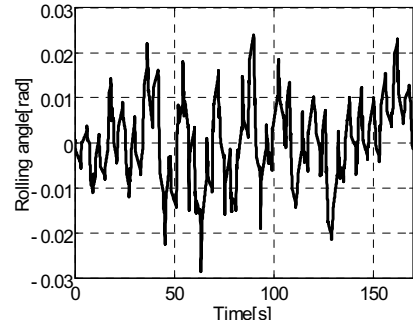


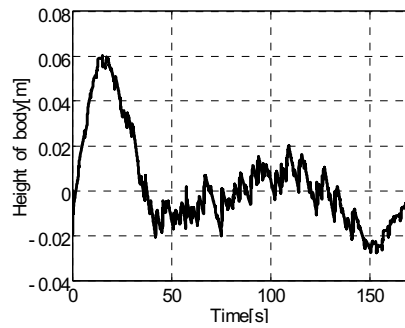
Fig. 11. Case of walking on uneven terrain



(a) Pitching angle



(b) Rolling angle

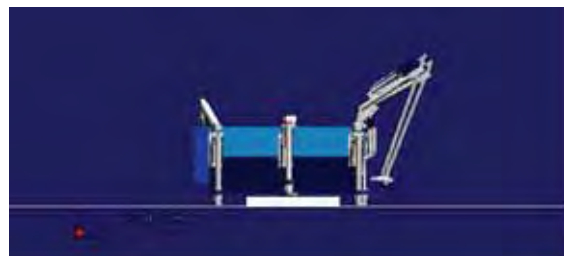


(c) Height of the body

Fig. 12. Simulation results in the case of irregular terrain



(a) Simulation time: 3.45 [s]



(b) Simulation time: 70.8 [s]



(c) Simulation time: 136.25 [s]

Fig. 13. Animations of walking on uneven terrain

6. Conclusion

In the present study, we examined the attitude control method considering the delay of the hydraulic actuator whereby the mine detection six-legged robot can realize stable walking on irregular terrain without to make an orbit of the foot for irregular terrain. The following results were obtained.

- (1) As an attitude control method considering the delay of the actuator of the thigh links, we derive a mathematical model in which the inputs are the driving torque of the thigh links in the supporting legs and the outputs are the height of the body, the pitching angle, and the rolling angle.
- (2) The 3rd-order delay system is approximated as a 2nd-order delay system, and an optimal servo control system is applied as the attitude control method.
- (3) The validity of the proposed attitude control method is discussed based on 3D simulations of walking on even terrain and irregular terrain.

The effectiveness of the proposed control method will be examined experimentally in the future. Moreover, the method by which to improve the transition response with the time delay system will be examined.

7. References

- Uchida, H. & Nonami, K. (2001), Quasi force control of mine detection six-legged robot COMET-I using attitude sensor, *Proceeding of 4th International Conference on Climbing and Walking Robots*, pp 979-988, ISBN 1 86058 365 2, Karlsruhe, Germany, September, 2001, Professional Engineering Publishing, London.
- Uchida, H. & Nonami, K. (2002), Attitude Control of Six-Legged Robot Using Optimal Control Theory, *Proceeding of 6th International Conference on Motion and Vibration Control*, pp 391-396, Saitama, Japan, August, 2002, The Dynamics, Measurement and Control Division of Japan Society of Mechanical Engineers, Tokyo.
- Uchida, H. & Nonami, K. (2003), Attitude control of six-legged robot using sliding mode control, *Proceeding of 6th International Conference on Climbing and Walking Robots*, pp 103-110, ISBN 1 86058 409 8, Catania, Italy, September, 2003, Professional Engineering Publishing, London.

A 4WD Omnidirectional Mobile Platform and its Application to Wheelchairs

Masayoshi Wada

*Dept. of Human-Robotics, Saitama Institute of Technology
Japan*

1. Introduction

The aging of society in general and the declining birth rate have become serious social issues world wide, especially in Japan and some European countries. It is reported in Japan that the number of people over 65 years old would reach 30,000,000 in 2012 and increase to over 30% of total population by 2025 (estimated and reported in 2006 by the National Institute of Population and Security Research, Japan). Wheelchairs are currently provided mainly for handicapped persons however, such rapid growth in the elderly population suggests that the numbers of electric wheelchair users will soon increase dramatically.

Currently, reconstruction of facilities to make them barrier-free environments is a common method. Such reconstruction of existing facilities is limited mainly to large cities because large amounts of money can be invested in facilities used by large numbers of people. However, it would be economically inefficient and therefore quite difficult to reconstruct facilities in small towns occupying small populations. Moreover, the aging problem is more serious in such small towns in local regions because of the concurrent decline in the number of young in rural areas where the towns are dispersed and not centralized. Thus, economic and time limitations make the reconstruction of existing facilities to accommodate wheelchair users unfeasible.

One solution to this problem would be to improve wheelchair mobility to adapt to existing environments. Electric wheelchairs, personal mobiles, and scooters are currently commercially available not only for handicapped persons but also for the elderly. However, those mobile systems do not have enough functionalities and capabilities for moving around existing environments including steps, rough terrain, slopes, gaps, floor irregularities as well as insufficient traction powers and maneuverabilities in crowded areas. By the insufficient capabilities of the mobile system, independency of users is inhibited. For example, wheelchair users in Japan must call station staff for help for both getting on and off train cars, because large gaps and height differences exist between station platforms and train cars. To alleviate these difficulties, station staff place a metal or aluminum ramp between the platform and the train. This elaborate process may make an easy outing difficult and cause mental stress.

Source: Climbing & Walking Robots, Towards New Applications, Book edited by Houxiang Zhang,
ISBN 978-3-902613-16-5, pp.546, October 2007, Itech Education and Publishing, Vienna, Austria

Addition to this, electric wheelchairs are difficult to maneuver especially for elderly people who have little experience using a joystick to operate a driven wheel system. Current wheelchairs need a complex series of movements resembling parallel automobile parking when he or she wants to move sideways. The difficulties in moving reduce their activities of daily living in their homes and offices.

From this viewpoint, the most important requirements for wheelchairs are maneuverability in crowded areas indoors and high mobility in rough terrain outdoors. Current wheelchair designs meet one or the other of these requirements but not both. To ensure both maneuverability and mobility, we propose an omnidirectional mobile system with a 4WD mechanism.

In this chapter, we discuss the development of the omnidirectional mechanism and control for the 4WD. After analyzing basic 4WD kinematics and statics, basic studies are presented using a small robotic vehicle to demonstrate the advantages on the 4WD over conventional drive systems, such as rear drive (RD) or front drive (FD). Based on the experimental data, a real-scale wheelchair prototype was designed and built. To demonstrate the feasibility of the proposed system, including omnidirectional mobility and high mobility, the result of prototype test drives are presented.

2. Existing Wheelchair Drive Mechanisms

2.1 Differential Drives

The differential drives used by most conventional wheelchairs, both hand-propelled and electrically driven, have two independent drive wheels on the left and right sides, enabling the chair to move back and forth with or without rotation and to turn in place. Casters on the front or back or both ends keep the chair level (Fig.1) [Alcare], [Meiko]. This drive maneuver in complex environments because it rotates about the chair's center in a small radius.

The differential drive's drawback is that it cannot move sideways. Getting a wheelchair to move sideways involves a complex series of movements resembling parallel automobile parking. The small-diameter casters most commonly used also limit the wheelchair's ability to negotiate steps.

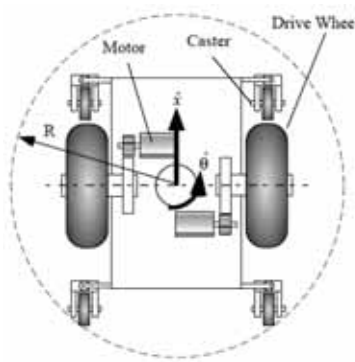


Fig. 1. Differential drive wheelchair with four casters front and back

2.2 Differential 4WD Drives

The 4WD drive was invented in 1989 [Farnam, 1989] (Fig. 2(a)) and was recently applied to a product [Kanto] to enhancing differential drive traction and step negotiation (Fig. 2(b)). The 4WD drive has a pair of omniwheels on the front and a pair of normal wheels on the back. The omniwheel and normal wheel on the same side of the chair are connected by a transmission and driven by a common motor to ensure the same speed in the direction of movement, so all four wheels of the 4WD provide traction. Motors on the left and right drive normal/omniwheel pairs via synchronous-drive transmissions to allow differential driving by the 4WD.

The 4WD controlled in differential drive mode has the center of rotation at the mid-point of the normal back wheels, meaning that spinning in a turn requires more space than for the original differential drive (dotted curve, Fig. 3), limiting indoor maneuverability.

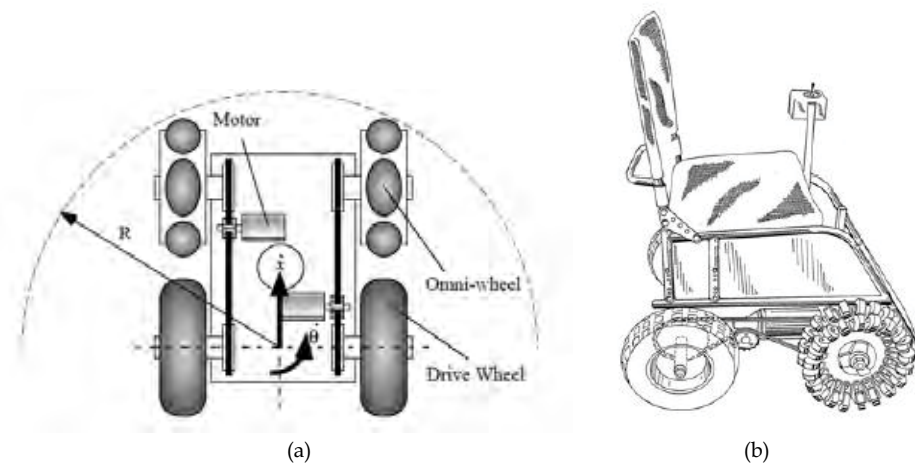


Fig. 2. 4WDdrive (a) and a wheelchair with 4WD [Farnam, 1989](b)

2.3 Omnidirectional Drive

Omnidirectional drives used on electric wheelchairs [Fujian], [Wada, 1999] were developed to enhance standard wheelchair maneuverability by enabling them to move sideways without changing chair orientation. Examples include the Universal and Mechanum wheels. In Fig. 3, an omnidirectional vehicle with Mechanum wheels uses rollers on the large wheel's rim inclining the direction of passive rolling 45 degrees from the main wheel shaft and enabling the wheel to slide in the direction of rolling. The standard four-Mechanum-wheel configuration assumes a car-like layout.

The inclination of rollers on the Mechanum wheel causes the contact point relative to the main wheel to vary, resulting in energy loss due to conflicts among the four motors. Because four-point contact is essential, a suspension mechanism is needed to ensure 3-degree-of-freedom (3DOF) movement.

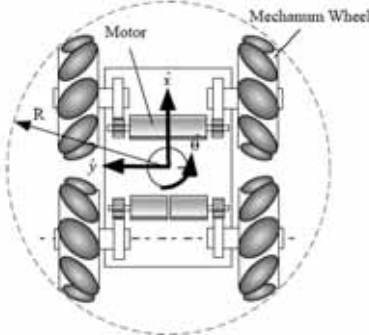


Fig. 3. Four-wheel omnidirectional wheelchair

2.4 Summary

Maneuverability and mobility are essential to barrier-free environments. As discussed above, existing wheelchair designs fulfill one requirement or the other but not both. Omnidirectional wheelchairs are highly maneuverable indoors but dynamically unwieldy outdoors, while 4WD wheelchairs, although highly mobile outdoors, require a 4WD mechanism that prevents them from changing their orientation independently. The maneuverability of the original 4WD must thus be improved to move in complex environments.

To meet these requirements in a single wheelchair design, we propose a new omnidirectional 4WD in the sections below. Although invented in 1989, the kinematics and statics of the original 4WD configuration has not been discussed in depth. In basic studies enabling 4WD to be applied to an omnidirectional mobile base, we analyze 4WD statics and kinematics before discussing the wheelchair's omnidirectional mechanism and control algorithm.

3. Static Analysis for Wheel-and-step

Figure 4 shows a vehicle with a 4WD configuration in which the motor torque is distributed and transmitted to both front and rear wheels. In this configuration, the front and the rear wheels are actively driven in the same speed.

Before bumping a step edge, both the front and the rear wheel provide respective traction forces, F_f and F_r , in the horizontal direction to propel the vehicle forward. However, right after a wheel touches a step edge, the traction force distributed to the front wheel, F_f , changes its direction and applies the moment to flip up the center of the front wheel that has contacted the step edge. The applied force from the rear wheel, F_r , is still directed horizontally after the bump. Figure 5 shows statics of the front wheel in a 4WD system contacting a step edge. In this case, the condition to surmount the step is derived as,

$$F_f + F_r \cos \theta \geq W_f \sin \theta \quad (1)$$

When the vehicle weight and motor torque are equally distributed to the front and rear wheel, namely $W_f=W_r$, $F_f=F_r=F/2$. Equation (1) would be,

$$F \geq W \frac{2 \sin \theta}{1 + \cos \theta} \quad (2)$$

Equation (2) gives the required minimum motor power for overcoming the specific step height. Next, we have to consider the limitation of the traction forces which are restricted by the friction coefficient between the wheel and the ground or step edge.

Let μ be the friction coefficient at the contact point on the wheel. The traction force at each wheel is restricted as,

$$\begin{aligned} F_f &\leq \mu W_e \\ F_r &\leq \mu W_r \end{aligned} \quad (3)$$

where W_e is a force component directing along the line O-B in the figure which is represented as,

$$W_e = W_f \cos \theta + F_r \sin \theta \quad (4)$$

From Eq. (3) and Eq. (4) we get,

$$W_f \sin \theta \leq \mu^2 W_r \sin \theta + \mu(W_f + W_r) \cos \theta \quad (5)$$

Again we suppose that the vehicle weight is equally distributed and motor torque is transmitted in the same ratio to the front and the rear wheels, the slip condition for 4WD is given by following relationships from Eq. (5).

$$\mu \leq \frac{1 - \cos \theta}{\sin \theta} \quad (\text{if } \sin \theta \neq 0) \quad (6)$$

Theoretical load curves derived by Eq. (2) and Eq. (6) are shown together with the experimental results in Section 6.

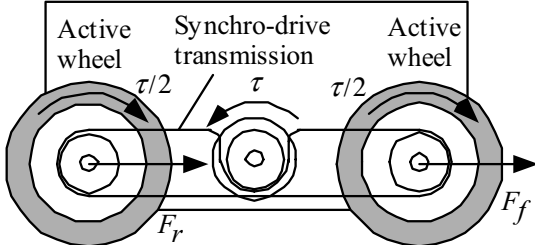


Fig. 4. 4WD drive transmission

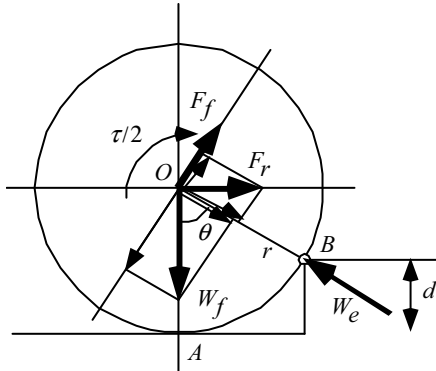


Fig. 5. Statics of the 4WD front wheel contacting a step edge

4. Kinematics of 4WD Drive Mechanism

In this chapter, we analyze the motions of the front omniwheels driven by synchro-drive transmissions for deriving the kinematic condition for non-slip drive.

Figure 6 is a schematic top view of a 4WD mechanism. When the two rear wheels are driven by independent motors to travel in velocities v_R and v_L on the ground with no slips, the wheels allow the vehicle to rotate about the point on the ground indicated O_r (Instantaneous Center of Rotation, ICR) in Fig. 6. It is well known that the vehicle's forward velocity and rotation are represented by the wheel velocities as follows,

$$\begin{aligned}\dot{x}_v &= \frac{v_R + v_L}{2} \\ \dot{\phi}_v &= \frac{v_R - v_L}{W}\end{aligned}\tag{7}$$

where W is a tread of the mobile base (displacement of the two parallel wheels). Now considering a velocity vector on a specific point p on the 4WD mechanism which location is (x_p, y_p) as shown in the figure. The components of vector v_p along the X- and Y-directions of the vehicle coordinate system, indicated as v_{px} and v_{py} , are represented as,

$$\begin{aligned} v_{px} &= \dot{x}_v - \ell \dot{\phi}_v \sin \theta_p \\ v_{py} &= \ell \dot{\phi}_v \cos \theta_p \end{aligned} \quad (8)$$

Note that $\ell \sin \theta_p = y_p$ and $\ell \cos \theta_p = x_p$, and the following relations are derived.

$$\begin{aligned} v_{px} &= \left(\frac{1}{2} - \frac{y_p}{W} \right) v_R + \left(\frac{1}{2} + \frac{y_p}{W} \right) v_L \\ v_{py} &= \frac{x_p}{W} (v_R - v_L) \end{aligned} \quad (9)$$

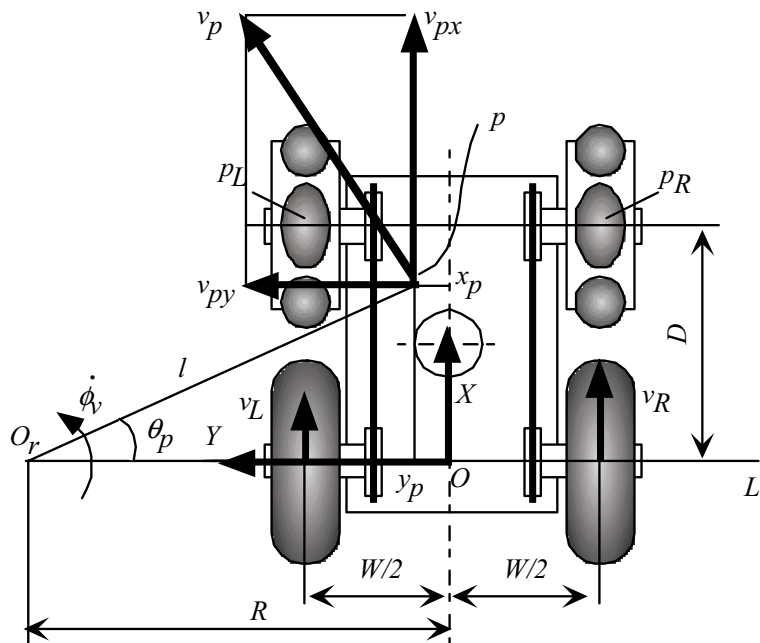


Fig. 6. 4WD kinematics

The location of the contact point of the front left omniwheel is defined as $(x_p, y_p) = (D, W/2)$ on the vehicle coordinate system. From Eq. (9), the velocity components at left omniwheel are represented as,

$$\begin{aligned} v_{px} &= v_L \\ v_{py} &= \frac{D}{W} (v_R - v_L) \end{aligned} \quad (10)$$

Thus only when $y_p = W/2$, velocity component in the X-direction of the left omniwheel becomes completely identical to the rear wheel velocity and is independent from the right wheel motion. The velocity component in the Y-direction is generated as a passive motion by free rollers on the omniwheel. The velocity components of right side omniwheel can be derived in the same manner as,

$$\begin{aligned} v_{px} &= v_R \\ v_{py} &= \frac{D}{W} (v_R - v_L) \end{aligned} \quad (11)$$

From these analyses, it is clear that omniwheels can follow the rear wheel motion with no slip or conflict as long as the contact point of the omniwheel is located completely on the line which is passing through the contact point of the rear wheel with directing the wheel rolling direction. Thus, omni and normal wheel pairs on the same side of the 4WD mechanism can be driven by a synchro-drive transmission with a common motor.

5. Powered-Caster Control System

5.1 Powered-caster Control for Twin Caster Configuration

The powered-caster drive systems were developed by the authors group [Wada, 1996], [Wada, 2000]. The drive system enables holonomic and omnidirectional motions with the use of normal wheels rather than a class of omniwheels.

Two types of caster configurations are available for the powered-caster drive system including the single-caster type (a normal wheel with a steering shaft supporting the wheel with a caster offset) and the twin-caster type (two parallel normal wheels supported by a steering shaft with a caster offset). To apply the powered-caster control, the configuration of a wheel mechanism has to have a caster offset between drive wheel(s) and a steering axis.

Figure 7 illustrates an omnidirectional vehicle design for AGV (Automated Guided Vehicle) with a drive unit which forms a twin caster configuration [Wada, 2000]. Two drive wheels and a steering mechanism are mounted on the drive unit where each wheel or a steering is driven by a respective motor. The displacement between the midpoint of the two wheels and the center of the steering shaft, called caster offset, s , and the displacement between two wheels, called vehicle tread, W , are respectively indicated in Fig. 7. Thus, the wheels and the steering shaft form a twin-caster configuration. Coordination of these three motors allows the vehicle body to move in an arbitrary direction with arbitrary magnitude of velocity from any configuration of the drive unit.

Relationships between wheel velocities and the motion of the drive unit, which is defined as the velocity and the rotation at the center of the steering axis are derived as (see [Wada, 2000] for details),

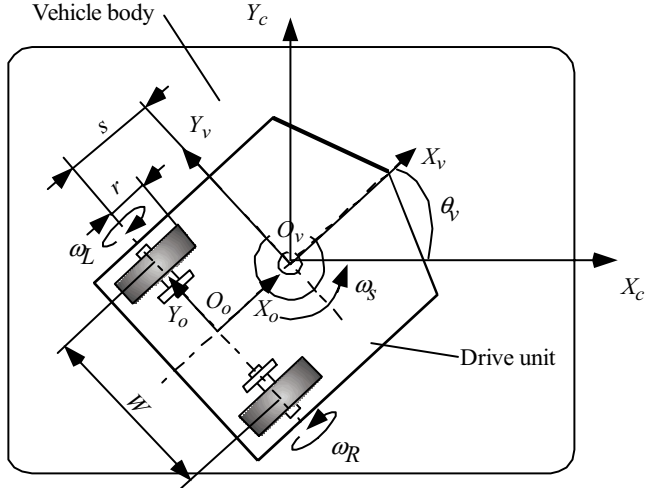


Fig. 7. Omnidirectional AGV with a twin-caster drive

$$\begin{pmatrix} \dot{x}_v \\ \dot{y}_v \\ \dot{\theta}_v \end{pmatrix} = \begin{pmatrix} r/2 & r/2 \\ rs/W & -rs/W \\ r/W & -r/W \end{pmatrix} \begin{pmatrix} \omega_R \\ \omega_L \\ \omega_S \end{pmatrix} \quad (12)$$

where r is the wheel radius. Note here that the rotation of the drive unit, $\dot{\theta}_v$, in Eq. (12) is not independent from the translation velocity, \dot{x}_v and \dot{y}_v , the third motor is required to compensate for the rotation of the drive unit and direct the vehicle body to the desired direction. In the wheelchair applications, desired motion is given along the vehicle body coordinate system since a joystick is fixed and moves together with the chair. Considering these effects, Eq. (12) can be resultantly united with the rotation of the vehicle body as shown below.

$$\begin{pmatrix} \dot{x}_c \\ \dot{y}_c \\ \dot{\theta}_c \end{pmatrix} = \begin{pmatrix} J_{11} & J_{12} & 0 \\ J_{21} & J_{22} & 0 \\ r/W & -r/W & 1 \end{pmatrix} \begin{pmatrix} \omega_R \\ \omega_L \\ \omega_S \end{pmatrix} \quad (13)$$

where,

$$\begin{aligned}
 J_{11} &= \frac{r \cos \theta_v}{2} - \frac{rs \sin \theta_v}{W} \\
 J_{12} &= \frac{r \cos \theta_v}{2} + \frac{rs \sin \theta_v}{W} \\
 J_{21} &= \frac{r \sin \theta_v}{2} + \frac{rs \cos \theta_v}{W} \\
 J_{22} &= \frac{r \sin \theta_v}{2} - \frac{rs \cos \theta_v}{W}
 \end{aligned} \tag{14}$$

Note that θ_v is rotation of the vehicle body relative to the drive unit, namely rotation created by the third motor. A 3x3 matrix in the right side of the Eq. (13), called a Jacobian, is a function of the orientation of the drive unit relative to the vehicle body, θ_v . All elements in the Jacobian can always be calculated, and determinant of the Jacobian may not be zero for any θ_v . Therefore there is no singular point on the mechanism and an inverse Jacobian always exists. 3D motion commands, \dot{x}_c , \dot{y}_c and $\dot{\theta}_c$, are translated into three motor references by the inverse of Eq. (13), i.e. inverse kinematics. The three motors are controlled to provide the reference angular velocities by independent speed controllers for omnidirectional movements. Thus, holonomic 3DOF motion can be realized by the proposed mechanism.

This class of omnidirectional mobility, so called "holonomic mobility", is very effective to realize the high maneuverability of a wheelchair by an easy and simple operation.

5.2 Powered-caster Control for 4WD Mechanism

Now we refer back to control of the 4WD mechanism. As mentioned in Section 2.2, for applying 4WD to a wheelchair design, there must be an offset between the rear wheels and the center of the chair to allow enough room on the front side for mounting the omniwheels. When the wheelchair is controlled in a differential drive manner, the offset distance makes the maneuverability of the wheelchair worse, as mentioned previously. However, that offset allows us to apply the powered-caster control for the 4WD mechanism with a third motor. Therefore, by adding the third motor to the original 4WD mechanism for rotating a chair, coordinated control of three motors enables the wheelchair to realize independent 3DOF omnidirectional motion.

For wheelchair applications, a 4WD drive unit can be held level since omniwheels are installed in the front end of the drive unit. Therefore, no caster is required to support a chair base or the drive unit. Figure 8 illustrates a schematic of an omnidirectional mobile base with a 4WD mechanism.

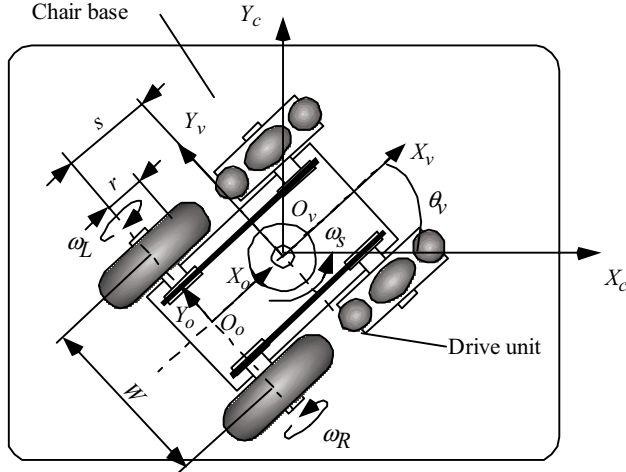


Fig. 8. Omnidirectional mobile base with 4WD

6. Basic Experiments Using a Small Robot

Figure 9 shows an overview of a small vehicle designed for experiments for fundamental studies. The vehicle is equipped with four wheels, where the front two wheels are omniwheels and rear two are normal rubber tires. A servo motor is installed on each side of the vehicle to drive the right or left wheel(s) independently. The servo motor for driving wheels is located at the midpoint between the front and rear wheels, as shown in the figure. Each motor torque is distributed to the front and rear wheel shafts by pulley-belt synchro-drive transmission(s). The dimension of the prototype is approx. 450 mm in width and 350 mm in length. The vehicle body is made of aluminum on which four wheels and two motors are mounted. All four wheels are 100 mm in diameter. The wheelbase is 200 mm and the tread is 430 mm. The capacity of the motors is 100 W.



Fig. 9. Omnidirectional mobile platform with 4WD for experiments

6.1 Step Climb Capability

To test the step climb capability for the 4WD system, a series of experiments was performed using the small vehicle. The following three configurations were tested,

1) 4WD configuration with 4 normal wheels

The front omniwheels shown in Fig. 9 are changed to normal wheels to avoid the wheel mechanically seizing the step edge. This configuration allows both front and rear wheels to make pure touching contacts with floor and the step.

2) Rear drive configuration

The transmission belts for the front wheels are removed from the 4WD configuration with four normal wheels. Therefore, only rear wheels provide traction forces. This configuration is tested to clarify the advantage of the 4WD system over the conventional drive system.

3) 4WD configuration with two omniwheels in front and two normal wheel in the rear. The surface of the omniwheel is not continuously smooth. Mechanical gaps between the free rollers are found on the surface that can make mechanical seizing contact between a step edge and the wheel. This contact is different from pure point contact by which traction force is not independent from the friction coefficient. Through the mechanical seizing contact, motors can provide larger torque which allows the vehicle to surmount the higher step than the 4WD configuration with four normal wheels. This configuration is for finding the difference between the contact condition between front wheels and a step edge.

On each test, the vehicle runs towards the step at a very slow speed to avoid the dynamic effects. A step made of wood plates which can be re-configured from 2.5 mm to 50 mm in height. The velocities of the right and left wheel motors are controlled by respective motor controllers with PD feedback loops to which the identical velocity command is given by analog voltage provided from a potentiometer operated by a human.

In the experiments, motor torques on the right and left are measured throughout each trial run. Figure 10 shows one of the test results which includes detected motor torques. When a wheel successfully climbs to the top of a step, a peak appears in the torque profile. When both the front and the rear wheels climb the step, two peaks can be measured. By reading the torque at the top of the peak from the torque profile, the required torques for the step climbing for front wheel and rear wheel can be derived after noise reduction, as shown in the figure.

The dashed line in the lower part of Fig. 11 shows the required torques vs. step height that are theoretically calculated by Eq. (2) for the 4WD configuration that wheel diameter, $D=100$ mm, vehicle weight, $M=7$ kg, and friction coefficient $\mu=0.7$. To clarify the advantage of the 4WD system over the conventional rear drive system (RD), required torque for the RD configuration is also plotted by a dashed line at the top of the figure. The emphasized thick parts in the continuous curves indicate that slip conditions are satisfied in the areas for RD and 4WD. Equation (6) gives the slip condition for the 4WD mechanism.

The experimental results are also shown in the same figure by triangles, circles and squares which indicate that the small vehicle successfully surmounted a step, h in height with motor peak torque τ . The maximum motor torque that can be provided by a 100 W motor,

0.95 Nm, is also illustrated by a dashed line in the figure. It is clear that the limitation of the step height is restricted by slip conditions but not by the insufficient motor power.

In the experiments, the RD vehicle could surmount a step 10 mm in height (triangles show experimental data) while theoretical results suggests approx. 8 mm is the limitation for satisfying the slip condition. On the other side, the 4WD vehicle with four normal wheels could surmount a step 35 mm in height (circles), which is more than three times the RD, while 32.5 mm is the limit in step height suggested by the theoretical slip condition, Eq. (6). A series of the required torques for each step height shows good agreement with the theoretical results. As the step height increases, the required motor torque for RD increases dramatically compared with the one for 4WD. For instance, for the RD vehicle to overcome a step 300 mm in height, the motor must provide approx. $\tau=1$ Nm which exceeds the current maximum motor torque with the friction coefficient $\tau =2.3$ which is not achieved by a normal tire.

The 4WD vehicle equipped with omniwheels in front overcame a 50mm step (squares) which is same dimension as its radius. Even in this case, the required motor torque calculated by Eq. (2) agreed with the experimental results while limitation given by the slip condition was broken by the mechanical seizing contacts between the wheels and the step edge.

These experiments verified that the analysis well estimated the required torque and the limitation of the maximum step heights for the vehicle with flat surface tires. This value can be regarded as a guaranteed step height which should be considered the maximum step climb capability in a design process.

Thus, the fundamental static models of wheel-and-step for 4WD are derived which provide a useful model for designing the 4WD large-scale vehicle. Moreover, the improved mobility and the step climb up capability of the 4WD system are clarified through theory and experiments.

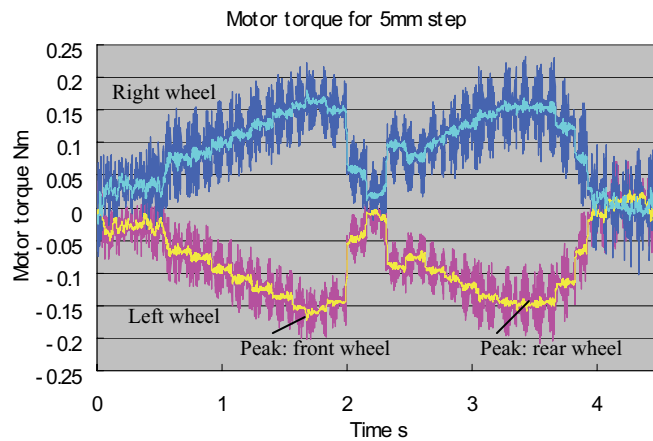


Fig. 10. Motor torques measured by experiment: Noisy plots (pink and blue) at negative and positive area are detected motor torques for left and right motors. Light plots (yellow and light blue) around the center of noisy signals are motor torques with noise reduced for measuring peaks for climbing the step

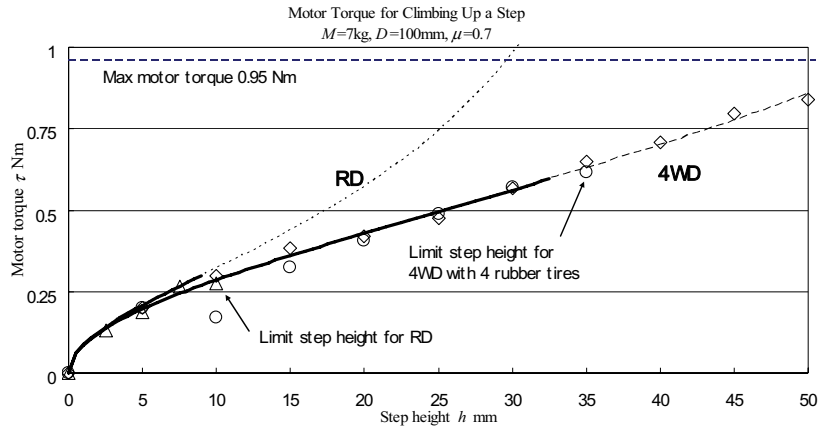


Fig. 11. Required motor torque vs. surmountable step height:

Lines 1) lower: 4WD, 2) upper: RD, dashed lines denote theoretical motor torque while thick lines represent surmountable parts that meet slip conditions. Triangles are experimental results of the RD configuration, circles represent a 4WD which has four normal rubber tires, and squares represent a 4WD having omniwheels in front and normal wheels in the rear

6.2 Omnidirectional Mobility

To verify the omnidirectional control of a 4WD mechanism, the proposed algorithm is installed on the control system for the vehicle prototype. Each of the three motors is controlled by the velocity controller.

The operator can control the vehicle through a 3D joystick which provides individual 3D motion command to the vehicle controller. Two motors for the wheel drive are coordinated to translate the center of the vehicle body to the desired direction. The rotation and orientation of the 4WD base can be calculated by the dead-reckoning algorithm by using shaft encoders installed on those motors. Based on the result of the dead-reckoning, the angular velocity of the vehicle body is controlled by the third motor to compensate for the rotation of the 4WD mechanism and to direct the body in the desired direction. To achieve this control, the reference motor velocity commands are given by the inverse of Eq. (13).

The velocity-based control system is useful for the wheelchair application because the power is provided intermittently to the motors. When the wheelchair user does not touch a joystick for a pre-specified time, power to the motors is cut off to preserve the battery charge. If the motors are controlled by the position controller, large torques may sometimes be provided to the motor when wheels are passively rotated and large position errors are accumulated during the no-power period. To avoid this kind of dangerous situation, motors used to power wheelchairs should be driven by velocity controllers.

Figure 12 shows a set of screen shots of the video in which the vehicle motion in the experiment was recorded. The steering shaft is located on the center of the 4WD mechanism. Initially, the vehicle is located in the center of the picture frame (a). Then it starts to move to

the right side of the frame (b)-(e), where the center of the vehicle moving in right direction with the orientation of the vehicle body (octagon plate) are constant. After stopping at the right side, it moves back toward the left (f)-(k). The vehicle body changes its orientation from right to left around the center in frames (h), (i) and (j), which is called a "flipping" motion by powered-caster control. After reaching the left side of the frame (k), the vehicle returns to the initial position. From a set of snapshots, it is shown that typical holonomic motion was successfully presented by the prototype vehicle with a 4WD mechanism.

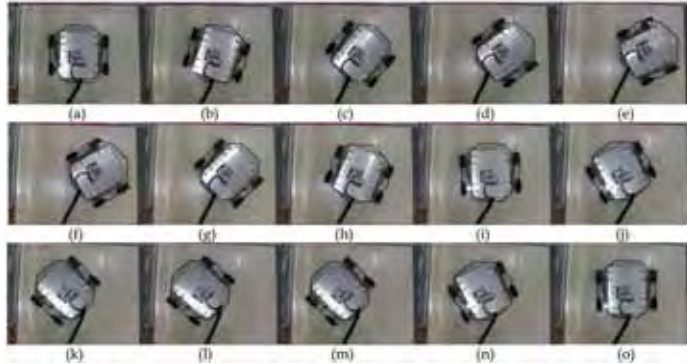


Fig. 12 Snapshots of the mobile robot in the experiment: The robot moved from center of the picture frame to the right side then went to the left and back to original position.

During the motion, robot body (the octagon shaped transparent acryl plate) keeps constant orientation

7. Design of a Wheelchair Prototype

In the prototype design, the static model discussed in Section 3 was used for the fundamental design calculation. The wheelbase and tread of the 4WD mechanism are 400 mm and 535 mm, respectively. Those dimensions are determined to satisfy the limitation for a wheelchair that is 600 mm in width and 700 mm in length, as shown below. The required step height which can be surmounted by the wheelchair is approx. 100 mm. The maximum running speed for a continuous drive is 6 km/h which is same as conventional wheelchairs in Japan.

** Wheelchair Specifications**

Dimension	
Width	600 mm
Length	700 mm
Height	450 mm
Weight	
Total	180 kg (human + wheelchair)
Wheelchair	80 kg (including batteries)
Speed	6 km/h
Surmountable step height	100 mm

To satisfy these specifications for the 4WD mobile system, the load curves derived by Eq. (2) and Eq. (6) are used for the design process shown in Fig. 13. For determining the wheel diameter of the 4WD, several combinations of wheel diameters and gear ratios were calculated and compared as wheelchair specifications by load curves. First, to maintain the rated driving velocity, 6 km/h, gear ratio between motor shaft and the wheel shaft are determined by the wheel diameter, since the rated rotation of the nominated motors are both 3000 rpm. Then load curves can be plotted by substituting a determined parameter, weight, gear ratio and friction coefficient, into Eqs. (2) and (6) for each case. In the figure, the maximum torque from a 300 W motor is plotted by dashed line. For the 100 mm step, a 200 W motor may be too small and a 400 W motor is over the specification. From Fig. 13 again, it is obvious that the $D=250$ mm case does not meet the requirement for sufficient motor torque and friction condition to overcome the 100 mm step. In the case of $D=350$ mm or over, the step climb capability is increased, however, the dimension of the mobile platform would need to be larger, especially in the longitudinal direction. Therefore $D=300$ mm is acceptable from an overall standpoint in terms of dimension, speed, motor power and step climb capability.

By the analysis, it is expected that the prototype wheelchair can step over a 100 mm step when the friction coefficient is kept to $\mu=0.7$ or over.

Based on the design process described above, a prototype wheelchair was designed and built.

Figure 14(a) shows an overview of the wheelchair prototype. The vehicle is equipped with four wheels, where the two front wheels are omniwheels and the two rear are normal rubber tires. Figure 14(b) shows right side of the drive mechanism in which a front omniwheel and rear normal tire are shown. Both wheel shaft rotations are synchronized by belt pulley transmissions which are not shown but illustrated in the figure. The configuration of the omniwheel used in the front wheels is also shown in the figure which enables continuous changes of the contact point between passive rollers. The wheel has inner and outer rollers which are arranged to keep the contact points on the center of the wheel width, thus resulting in small gaps and continuous contact changes between the rollers.

A 300 W servo motor is installed and connected to the drive shaft via a gear unit which translates the direction of the motor rotation at a right angle for driving the wheel shafts via the synchro-drive transmission (the gear units are seen in bottom view in Fig. 15).

In the design process, the wheelchair weight was estimated to be less than 80 kg including batteries however, actual prototype weights approx. 100 kg. Therefore, maximum total weight, 180 kg, gives a limitation of 80 kg for the wheelchair user.

A tablet PC is used for the controller of the wheelchair, in which calculations of the kinematics, inverse kinematics, motor feedback control and dead-reckoning, are executed together with the I/O and wireless communication process. The proposed omnidirectional control algorithm is also programmed on the control system of the prototype.

8. Experiments

8.1 Omnidirectional Motion

Figure 16 shows a series of snapshots of the experiment in which the prototype wheelchair presented the omnidirectional motion. In this experiment, the wheelchair was programmed

to track the reference trajectories automatically without joystick operation. The wheelchair moved in a lateral direction while maintaining the chair orientation, causing the drive unit orientation to vary. The location of center of the chair was controlled by two wheel motors located on the reference straight line facing the lateral direction at all times. Figure 17 also shows another omnidirectional motion to translate in backward. At the initial configuration, the drive unit orientation had almost agreed with the chair, it moved backward, changed the direction of motion and directed the moving direction. This series of motion is called “caster flip” which is unique for proposed omnidirectional control systems.

8.2 Step climb capability

As shown in the experiments of omnidirectional motions, the 4WD drive unit directs the moving direction spontaneously after the small travel. Therefore, step climb capability is limited by the large wheel diameter and not by the small diameter of the free rollers.

Figure 18 shows an experiment where the prototype attempted to climb a 90 mm step with no load on the chair. In the experiment, the front wheels successfully climbed the step, but the rear wheels failed and both front and rear wheels slipped. In Section 3, a design calculation was discussed under the assumption that the total weight of the wheelchair was equally distributed to the front and rear wheels. When the rear wheels bump the step edge, this assumption can not be satisfied because of the upward inclination of the chair.

In the next experiment, the extra 40 kg weight was mounted on the front side of the chair, as shown in Fig. 19, to reduce the change of the load distribution ratio between front and rear. In this case, the prototype could surmount the 90 mm step, even though the total weight increased 40 kg from the first experiment. From these experiments, it is clear that the prototype wheelchair has enough power and capability to climb a 90 mm step, but needs to improve the load distribution of the wheelchair between the front and the rear wheels.

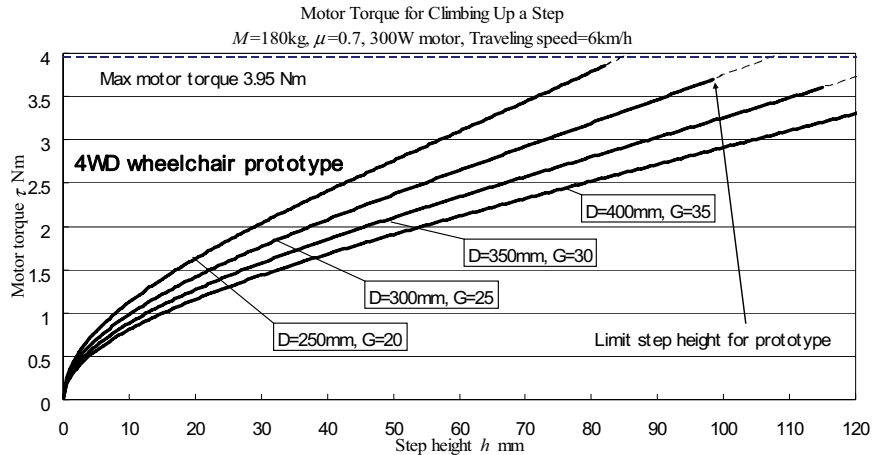


Fig. 13. Surmountable step height vs. required motor torques and friction condition satisfied area for 4WD wheelchair prototype design for wheel diameters $D=250, 300, 350$ and 400 mm

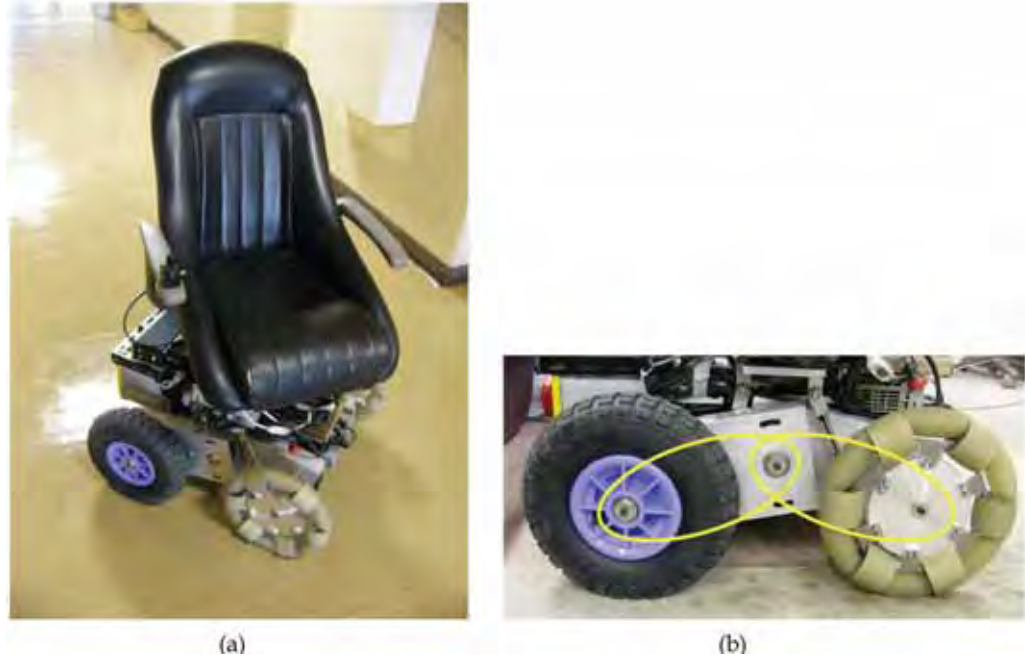


Fig. 14. 4WD omnidirectional wheelchair prototype, overview (a) and synchronized 4WD transmission (b)

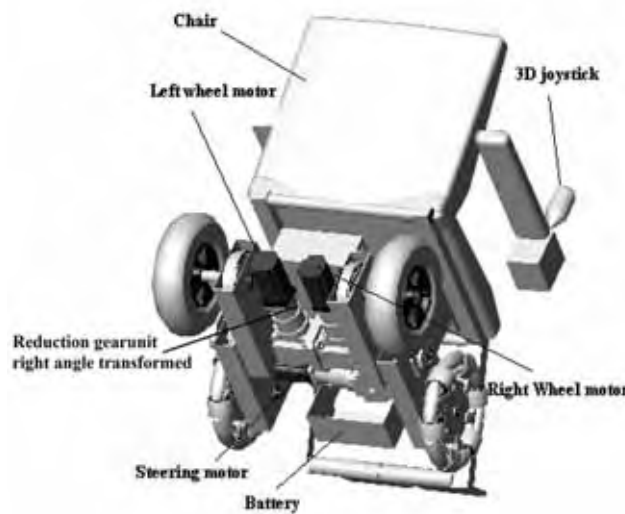


Fig. 15. Prototype bottom view by 3D CAD

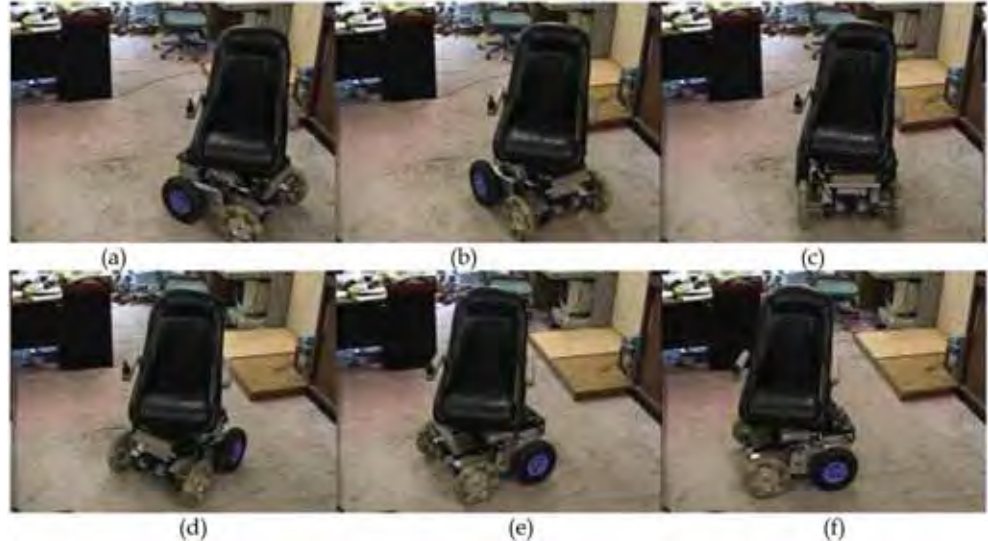


Fig. 16. Lateral motion of the wheelchair prototype; it moves in sideways while maintaining the chair orientation from the right side to the left of the picture frames

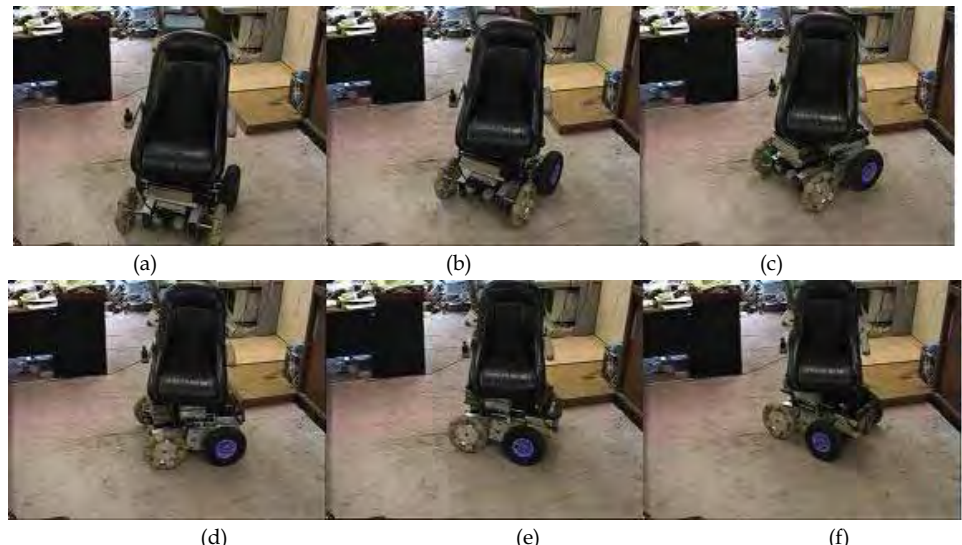


Fig. 17. The prototype moving in backward; it moves in backward while maintaining the chair orientation



Fig. 18. Snapshots of the wheelchair in experiment: Climbing up a 90 mm step. Rear wheels failed to step up and all wheels slipped



Fig. 19. Snapshots of the wheelchair in experiment: Climbing up a 90 mm step with carrying 40 kg weight on the chair

9. Conclusion

Conventional electric wheelchairs can not meet requirements for both maneuverability and high mobility in rough terrain in a single design. Enhancing their mobility could facilitate the use of wheelchairs and other electric mobile machines and promote barrier-free environments without re-constructing existing facilities.

To improve wheelchair step-climbing and maneuverability, we introduced a 4WD with a pair of normal wheels in back and a pair of omniwheels in front. A normal wheel and an omniwheel are connected by a transmission and driven by a common motor to make them rotate in unison. To apply the 4WD to a wheelchair platform, we conducted basic analyses on the ability to climb steps.

After analyzing the original 4WD statics and kinematics and determining theoretical mechanical conditions for non-slip omniwheel driving, we derived the required motor torque and slip conditions for step-climbing.

We discussed powered-caster control for the 4WD where control was applied to coordinate velocity provided by two rear wheels. Powered-caster control enables the center of the vehicle to move arbitrarily with an arbitrary configuration of the 4WD. Orientation of the vehicle is controlled separately from movement by the third motor on the 4WD.

Theoretical results and omnidirectional control were verified in experiments using a small vehicle configured selectively for RD, FD, and 4WD. In experiments, step-climbing and

required motor torque were measured for a variety of step heights. The results agreed quite well with theoretical results. In experiments, a 4WD transmission enabled the vehicle to climb a step three times higher than a vehicle with an RD transmission without changing motor specifications or wheel diameter. The derived wheel-and-step model is useful for designing and estimating the mobility of wheeled robots.

For omnidirectional control of the 4WD, velocity-based coordinated control of three motors on the robot was verified through experiments in which omnidirectional movement was successfully achieved.

To verify the availability of the proposed omnidirectional 4WD system for wheelchair applications, a prototype was designed and built. The prototype wheelchair presented holonomic and omnidirectional motions for advanced maneuvering and easy operation using a 3D joystick. It also showed a basic step climb capability which can go over a 90 mm step. Improvement in the load distribution would be the next subject of this project, together with the development of a stability control mechanism which keeps static stability of a chair by an active tilting system.

10. Acknowledgements

This project was supported by the Industrial Technology Research Grant Program in 2006 from the New Energy and Industrial Technology Development Organization (NEDO), Japan.

11. References

- Alcare Corporation, "Jazzy1113".
- Jefferey Farnam (1989). "Four-wheel Drive Wheel-chair with Compound Wheels," *US patent 4,823,900*.
- Fujian Fortune Jet Mechanical & Electrical Technology Co., Ltd. , All-direction Power-driven Chair "FJ-UEC-500" and "FJ-UEC-600"
- Kanto Automobile Corporation, "Patrafour".
- T.Inoh, S.Hirose and F.Matsuno(2005), "Mobility on the irregular terrain for rescue robots," *Proceedings of the RSJ/JSME/SICE 2005 Robotics Symposia*, pp. 39-44, 2005. (in Japanese)
- Meiko Corporation, "M-Smart".
- M.Wada and H. H. Asada(1999),"Design and Control of a Variable Footprint Mechanism for Holonomic and Omnidirectional Vehicles and its Application to Wheelchairs," *IEEE Transactions on Robotics and Automation*, Vol.15, No.6, pp978-989, Dec.1999.
- M.Wada (2005)," Studies on 4WD Mobile Robots Climbing Up a Step," *Proceedings of the 2006 IEEE International Conference on Robotics and Biomimetics (ROBIO2006)* pp.1529-1534, Kunming, China, Dec 2006.
- M.Wada and S.Mori(1996)," Holonomic and Omnidirectional Vehicle with Conventional Tires," *Proceedings of the 1996 IEEE International Conference on Robotics and Automation (ICRA96)*, pp3671-3676.

- M.Wada, A.Takagi and S.Mori(2000), "Caster Drive Mechanisms for Holonomic and Omnidirectional Mobile Platforms with no Over Constraint," *Proceedings of the 2000 IEEE International Conference on Robotics and Automation (ICRA2000)*, pp1531 -1538.
- M.Wada(2005)," Omnidirectional Control of a Four-wheel Drive Mobile Base for Wheelchairs," *Proceedings of the 2005 IEEE International Workshop on Advanced Robotics and its Social Impacts (ARSO05)*.
- M.Wada (2005), "An Omnidirectional 4WD Mobile Platform for Wheelchair Applications," *Proceedings of the 2005 IEEE/ASME International Conference on Advanced Intelligent Mechatronics*, pp. 576-581.

Evolution of Biped Locomotion Using Linear Genetic Programming

Krister Wolff and Mattias Wahde

*Department of Applied Mechanics, Chalmers University of Technology
Sweden*

1. Introduction

Gait generation for bipedal robots is a very complex problem. The basic cycle of a bipedal gait, called a stride, consists of two main phases, namely the single-support phase and the double-support phase, which take place in sequence. During the single-support phase, one foot is in contact with the ground and the other foot is in swing motion, being transferred from back to front position. In the double-support phase, both feet simultaneously touch the ground, and the weight of the robot is shifted from one foot to the other. During the completion of a stride, the stability of the robot changes dynamically, and there is always a risk of tipping over. Thus it is crucial to actively maintain the stability and walking balance of the robot at all times.

In the conventional engineering approach, there are two main methods for bipedal gait synthesis: Off-line trajectory generation, and on-line motion planning (Wahde and Pettersson, 2002; Katic and Vukobratovic, 2003). Both these methods rely on the calculation of reference trajectories, such as e.g. trajectories of joint angles, for the robot to follow. An off-line controller assumes that there exists an adequate dynamic model of the robot and its environment, which can be used to derive a body motion that adheres to a stability criterion, such as e.g. the zero-moment point (ZMP) criterion (Li et al., 1992; Huang et al., 2001; Huang and Nakamura, 2005; Hirai et al., 1998; Yamaguchi et al., 1999; Takanishi et al., 1985) that requires the ZMP to stay within an allowable region, namely the convex hull of the support region defined by the feet. An on-line motion controller, on the other hand, uses limited knowledge of the kinematics and dynamics of the robot and its environment (Furusho and Sano, 1990; Fujimoto et al., 1998; Kajita and Tani, 1996; Park and Cho, 2000; Zheng and Shen, 1990). Instead, simplified models are used to describe the relationship between input and output. This method also relies much on real-time feedback information.

Control policies based on classical control theory, like the ones outlined above, have been successfully implemented on bipedal robots in a number of cases, see e.g. the references mentioned in the previous paragraph. When the robot is operating in a well-known, structured environment, the abovementioned control methods normally work well. However, the success of these methods relies on the calculation of reference trajectories for the robot to follow. When the robot is moving in a realistic, dynamically changing environment such reference trajectories can rarely be specified, since the events that might occur can never be predicted completely. Furthermore, a control policy based on

conventional control theory will lead to lack of flexibility in an unpredictable environment (Taga, 1994). A shift towards biologically inspired control methods is therefore taking place in the field of robotics research (Katic and Vukobratovic, 2003). Such methods do not, in general, require any reference trajectories (Beer et al., 1997; Bekey, 1996; Quinn and Espenschied, 1993).

A common approach in biologically inspired control of walking robots is to use artificial neural networks (ANNs). A review of such methods can be found in (Katic and Vukobratovic, 2003). It is also common to employ the paradigm of artificial evolution (evolutionary algorithms, EAs) to optimize controllers that may consist of, for example, recurrent neural networks (RNNs) (Reil and Massey, 2001), finite state machines (FSMs) (Pettersson et al., 2001), or any other control structure of sufficient degree of flexibility (Boeing et al., 2004). The controller may also consist of a structure coded by hand (Wolff and Nordin, 2001). A related approach is to use genetic programming (GP), which is a special case of EAs, to generate control *structures* (or programs), for locomotion control of robots, see (Wolff and Nordin, 2003; Ziegler et al., 2002).

In some cases, the evolutionary optimization (or generation) of program structures may be applied to a certain component of the overall controller as, for example, in (Ok et al., 2001), where a feedback network was generated using GP. However, to the authors' knowledge, there exist only a few examples, such as (Wolff and Nordin, 2003; Ziegler et al., 2002), which go beyond parametric optimization and generate also the complete structure of a controller for bipedal walking. As an additional example, in (Wolff et al., 2006), both the structure and the parameters of a central pattern generator (CPG) network were evolved, using a genetic algorithm (GA) as the optimization method.

In the work described in this chapter, linear genetic programming (LGP) was used to generate gait control programs from first principles for simulated bipedal robots. Two slightly different approaches will be presented. In the first approach, the control system of the robot consisted of evolved programs generated from a completely random starting point, whereas, in the second approach, the joint torques were forced to vary sinusoidally, even though the (slow) variation of the parameters of the sinusoidal torques was evolved from a random starting point, using LGP. It should be noted that no explicit model of the bipedal system was provided to the controllers in either case, and neither were the evolved controllers given any *a priori* knowledge on how to walk (except, perhaps, for the forced sinusoidal variation in the second approach).

2. Evolutionary Robotics

Many problems in robotics, e.g. the generation of bipedal gaits, can be formulated as optimization problems. Traditional optimization techniques generally require the existence of a mathematical, fixed objective function, i.e. a function $f = f(x_1, x_2, \dots, x_n)$, where x_1, x_2, \dots, x_n are the variables of the problem. In robotics applications, such as gait generation, the value of the objective function can normally only be obtained by actually letting the robot execute its behavior (for example, walking), and then studying the results. In such applications, even though the value of the objective function can always be obtained, it cannot be computed without an (often lengthy) evaluation of a (physical or simulated) robot. Thus, analytical expressions for, say, the derivative of the objective function cannot be

obtained. Furthermore, in robotics, the control system (robotic brain) being optimized does not always have a fixed structure. For example, in cases where the robotic control system consists of an ANN, the number of nodes (neurons) in the network may vary during optimization, meaning that the *number* of variables in the objective function varies as well. Thus, for problems of this kind, other optimization methods than the traditional ones are more appropriate. As the name implies, in evolutionary robotics, the optimization is carried out by means of EAs. In addition to coping with structures of variable size and implicit objective functions of the kind described above, EAs can also handle non-differentiable objective functions containing variables of any kind, e.g. real-valued, integer-valued, Boolean etc.

2.1 Evolutionary Algorithms

EAs are methods for search and optimization inspired by Darwinian evolution. An EA maintains a set (population) of candidate solutions to the problem at hand. The members of the set are referred to as individuals. Before the evaluation of an individual, a decoding step is often carried out, during which the genetic material of the individual is used for generating the structure that is to be evaluated. In a standard GA, as well as in certain implementations of GP (such as LGP), the genetic material is in the form of a linear chromosome consisting of a sequence of numbers referred to as genes.

After decoding, each individual is evaluated and assigned a fitness value¹ based on its performance. Once the individuals have been evaluated, new individuals are generated by means of genetic operators such as selection, crossover, and mutation. The genetic operators are normally stochastic. For example, selection is normally, and rather obviously, implemented such that individuals with high fitness values have a higher probability of being selected (for reproduction) than individuals with low fitness value. Crossover combines the genetic material of two individuals. Mutations are random modifications of genes that provide the algorithm with new material to work with.

2.2 Linear Genetic Programming

LGP is a specific type of EA and, as such, it consists of the same basic components: A population of candidate solutions, the genetic operators, certain selection methods, and a fitness function. The main characteristic of LGP, however, concerns the representation of individuals. An individual in LGP is referred to as a program, and it consists of a linear list of instructions that are executed by a so-called virtual register machine (VRM) during the evaluation of the individual (Huelsbergen, 1996). Common LGP implementations use two-register and three-register instructions. The three-register instructions work on two source registers and assign the result to a third register, $r_i := r_j + r_k$. In two-register instructions, the operator either requires only one operand, e.g. $r_i := \sin r_j$, or the destination register acts as a second operand, e.g. $r_i := r_j + r_i$ (Brameier, 2003). The registers can hold floating point values, and all program input and output is communicated through the registers.

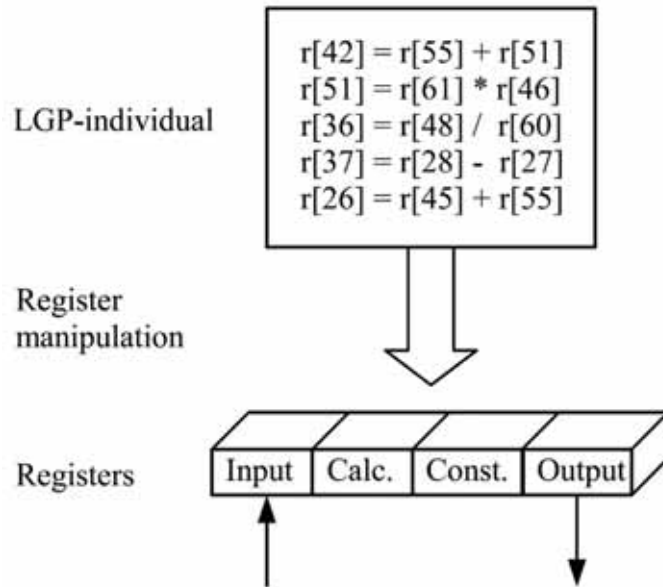


Fig. 1. Schematic description of the evaluation of an individual in LGP. The input is supplied to the input registers. The constant registers are supplied with values at initialization. During execution by the VRM, the LGP individual manipulates the contents of the calculation registers, by running through the sequence of instructions, starting with the topmost instruction. When the program execution has been completed (i.e. when the evaluation reaches the end of the program), the result is supplied to the output registers

Note that the LGP structure facilitates the use of multiple program outputs. By contrast, functional expressions like GP trees calculate one output only. Apart from registers assigned as either input or output registers, a program in LGP consists of registers holding constant values, which do not change during the program execution, as well as registers used as temporary calculation registers. Of course, additional constants can be built during execution, for example by adding or multiplying the contents of two constant registers and placing the results in one of the calculation registers. The values of the input registers are usually protected from being overwritten during the execution of the program. A conceptual description of LGP is given in Fig. 1.

In addition to the registers, an LGP instruction consists of an operator. Operations commonly used in LGP are arithmetic operations, exponential functions, trigonometric functions, Boolean operations, and conditional branches (Brameier, 2003). Conditional branching in LGP is usually defined in the following way: If the condition in the IF statement evaluates to *true*, the next instruction is executed. If, on the other hand, the condition in the IF statement evaluates to *false* the next instruction is skipped, and program execution jumps to the subsequent instruction instead (i.e. the first instruction after the one that was skipped). The evolutionary search process of LGP begins with a randomly

generated initial population, and is driven by the genetic operators selection, crossover and mutation. Selection favors individuals with high fitness values.

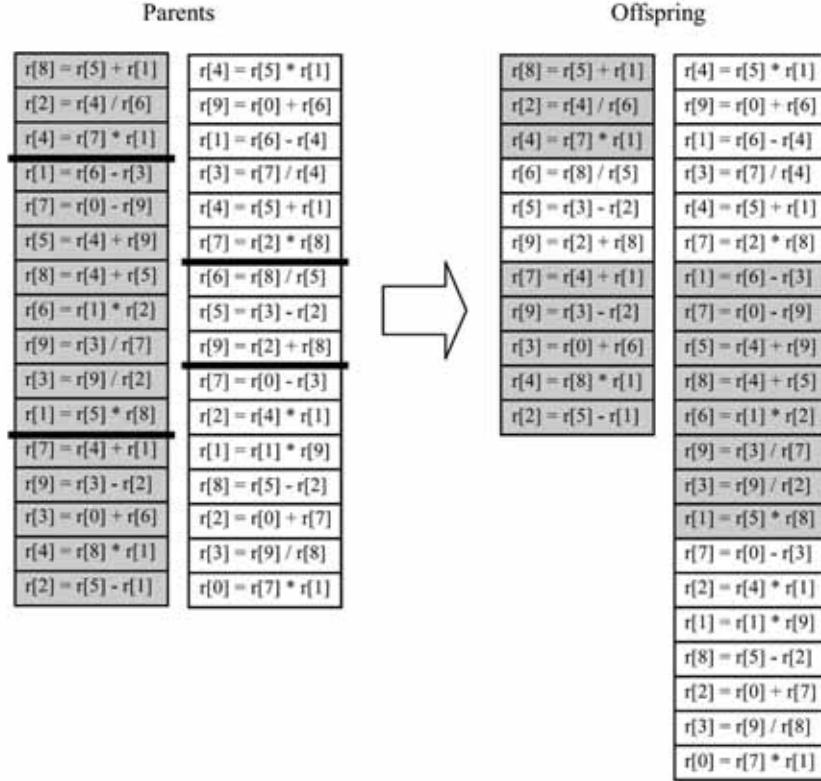


Fig. 2. Two-point crossover in LGP. Two crossover points are randomly chosen in each parent's genome. The instructions between the crossover points are swapped, and the resulting individuals constitute the offspring

Any of the fitness-proportionate selection schemes commonly associated with EAs, or tournament selection, may be applied with LGP. Crossover works by swapping linear genome segments of parent individuals as shown in Fig. 2. The mutation operator simply replaces a randomly chosen instruction by another, randomly generated, instruction.

Finally, as in any application involving an EA to search for a sufficiently good solution in a complex problem domain, finding a proper fitness measure that guides the evolution in the desired direction is crucial. This issue will be further discussed in Subsects. 3.1.4 and 3.2.4.

2.3 Evolution in Physical Robots Versus Simulations

In the work described in this chapter, evolution of robot controllers has been studied using realistic, physical simulators. Furthermore, in previous work, as well as in the work of other

researchers, evolution of gait programs in real, physical robots has been investigated as well (Wolff and Nordin, 2001; Wolff et al., 2007; Ziegler et al., 2002). As clearly shown by those examples, evolution in real, physical hardware is indeed achievable. In general, however, evolution in hardware is much more challenging than evolution in simulators, for several reasons: First, evolution in real robots can be very demanding for the hardware (i.e. the robots), thus requiring frequent replacement of parts such as servo motors. Obviously, this problem does not occur in simulations.

Second, the process of evolution in a simulator can relatively easily be parallelized, given that appropriate computational resources are available. A straightforward approach for parallelization is to divide the population into a number of subpopulations, or demes, where each deme is assigned to a separate processor. In such applications, individuals are allowed to migrate (with low probability) from one deme to another during evolution. A corresponding parallelization in the case of evolution in real, physical robots would be more difficult and costly: It would require multiple instances of the robot, as well as duplicate experimental environments. However, there are some examples of an ER methodology, where the entire evolutionary process takes place on a *population* of physical robots (Ficici et al., 1999; Watson et al., 1999).

Third, evaluation of individuals in simulators can often be carried out several times faster than real-time, which is not the case for evaluation of individuals in real robots: Evolution in physical robots is very time-consuming, something that normally restricts the number of evaluated generations considerably (Wolff and Nordin, 2001; Wolff et al., 2007).

While evolution in simulators is more convenient from the researcher's viewpoint than evolution in physical robots, the simulation approach presents other problems. The main issue concerns whether the controllers obtained from the simulation can be transferred to a real, physical robot. This problem is referred to as the reality gap (Jakobi et al., 1995). Although there are some serious difficulties associated with the process of transferring evolved programs to a real, physical robot, for the type of study presented here there is no realistic alternative to simulations: Evolution of bipedal gait controllers, in the way described in this chapter, could hardly be achieved directly in a real, physical robot, due to the large number of evaluations required in order to obtain useful results. Furthermore, regardless of the difficulties involved in transferring simulations results to physical robots, a simulation study may provide valuable qualitative insight concerning, for example, the choice of suitable sensory modalities, before the (often costly) construction of a physical robot is initiated.

3. LGP for Bipedal Gait Generation

While LGP can, in principle, be applied to almost any optimization problem, some adjustments and special considerations are of course needed in complex applications such as gait generation. In the work described here, two different implementations of LGP were used, namely (1) an implementation in the C language using the Open Dynamics Engine¹ (ODE) physics simulator, and (2) an implementation using the EvoDyn physics simulator (Pettersson, 2003). In the following subsections these two implementations will be described in detail.

¹ <http://ode.org/>

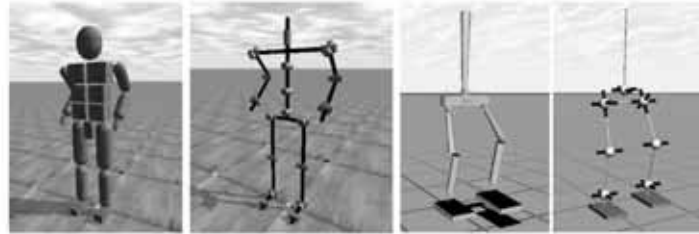


Fig. 3. The leftmost panel shows the bipedal model used in the ODE simulations, and the second panel from the left shows its kinematics structure with 26 DOFs. The two right panels show the 14-DOF robot model used in the EvoDyn simulations

3.1 ODE Implementation

3.1.1 Physics Simulator

In the first implementation the ODE simulator was used. This simulator is available both for the Windows and Linux platforms. In ODE, the equations of motion are derived from a Lagrange multiplier velocity-based model, and a first order integrator is employed. The bipedal model used in connection with ODE has 26 degrees of freedom (DOFs) and is shown in the two leftmost panels of Fig. 3.

3.1.2 Controller Model

In the ODE implementation, a motor is associated with each joint. The physics engine is implemented in such a way that the motors can be controlled by simply setting a desired speed and a maximum torque that the motor will use to achieve that speed. However, in this implementation the speed and maximum torque values of each joint motor were preset. Thus, the evolving controller just has to set the rotational direction, (+) or (-), for each joint of the robot.

The control loop as a whole is executed in the following way: (the numbers below correspond to the numbers shown in Fig. 4) (1) At time step t the robot's sensors receive perceptual input S , which is fed into the sensor registers. Simultaneously, the robot's current joint angles are recorded in both the input and output (I/O) registers, and in the calculation registers (the constant registers were supplied with values at the LGP initialization). (2) The VRM then executes the program specified by the LGP-individual, manipulating the contents of the calculation registers. During this stage, the I/O, sensor, and constant registers are read-only. (3) When program execution has been completed (i.e. when the last instruction of the program has been executed), motor signal generation (MSG) is initiated: A modified signum function, defined as

$$\varepsilon(x) = \begin{cases} -1 & \text{if } x < k \\ +1 & \text{if } x > k \\ 0 & \text{otherwise} \end{cases} \quad (1)$$

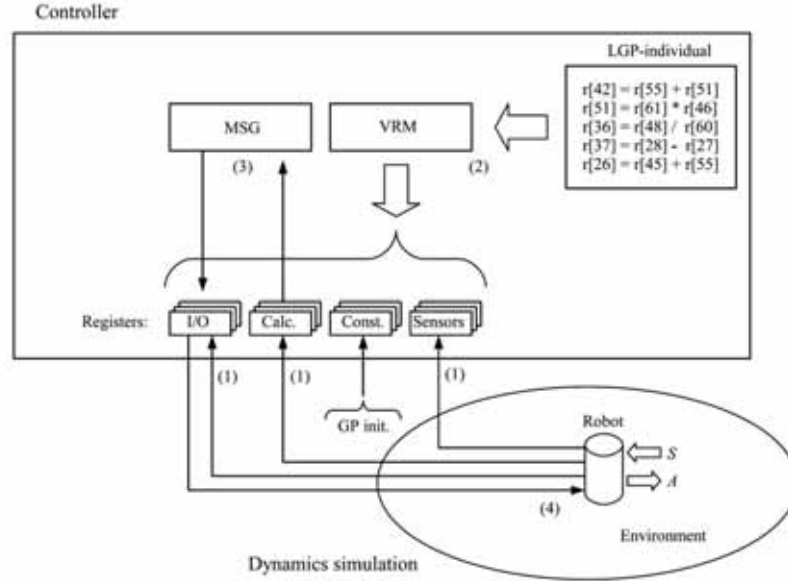


Fig. 4. Schematic depiction of the flow of information through the robot control system, which consists of the following main parts: The LGP-individual, which specifies the control program, the VRM, which interprets and executes the LGP individual, the MSG module, which generates the actual motor signals, and the registers, which constitute the interface between the control system and the robot

is then applied to the contents of the calculation registers, and the result is placed in the I/O registers. The value of the parameter κ was empirically determined to 0.12, and this value was used throughout the simulations. (4) These motor signals are then sent to the robot for execution in time step $t + K$. Thus, motor signals are only updated every K^{th} time step, in order to avoid very rapid (and therefore unrealistic) oscillations of the joints.

3.1.3 Simulation Setup

The ODE implementation was used in 60 independent simulation runs, in which the effects of varying specific parameter settings were examined, as illustrated in Table 3. In these simulations the robot was controlled by a program specified by an LGP-individual, as described in the previous subsection. Current joint angles were used as input to the controller, together with measurements, obtained directly from the physics simulation, of linear and angular accelerations of certain body parts of the robot.

The registers used by the VRM were implemented in the following way: Registers $r_1 - r_{26}$ were used as input and output registers, i.e. they were fed with the robot's current joint angle positions in the input stage of the control loop, and then fed with motor signals in the

Instruction type	General notation	Input range
Arithmetic operations	$r_i := r_j + r_k$ $r_i := r_j - r_k$ $r_i := r_j \times r_k$ $r_i := r_j / r_k$	$r_i, r_j, r_k \in \mathbf{R}$
Trigonometric functions	$r_i := \sin r_j$	$r_i, r_j \in \mathbf{R}$
Conditional branches	$\text{if}(r_j > r_k)$ $\text{if}(r_j \leq r_k)$	$r_j, r_k \in \mathbf{R}$

Table 1. Instruction set used in the simulations

output stage. There was one register of this type associated with each DOF of the robot. The registers $r_{27} - r_{52}$ were assigned as internal calculation registers of the VRM, i.e. they could be used to store intermediate results of the computations. At the beginning of the LGP run, registers $r_{53} - r_{55}$ were supplied with constant values, and finally, registers $r_{56} - r_{67}$ were associated with sensor input. The sensor signals used were the linear acceleration rates of the robot's feet in three dimensions, and the linear and angular acceleration rates of the robot's head, also in all three dimensions. A first-order, moving average filter with a window size of ten time steps was used with the sensor signals. In this implementation an instruction was encoded as a set of integers, e.g. {55, 51, 3, 42}. The first and second elements of an instruction refer to the registers to be used as arguments, the third element corresponds to the operator, and the last element determines where to put the result of the operation. The complete instruction set is shown in Table 1. The arithmetic operators used here were encoded in the chromosome as *add* = 1, *sub* = 2, *mul* = 3, *div* = 4, and *sine* = 5. Conditional branching operators were encoded in the third element as 6 = *if*($r[j] > r[k]$), and 7 = *if*($r[j] \leq r[k]$). When decoded, the instruction given above as an example is interpreted as $r[42] = r[55] \times r[51]$. Furthermore, in order to avoid division by zero, a slightly modified division operator was defined such that, if the denominator was exactly equal to zero, the operator returned a large, but finite, constant value, here set to 10^8 .

In the simulations, all individuals started from the same upright pose, oriented with their sagittal plane parallel to the x-axis. All the individuals were evaluated for a time period of 36 seconds, long enough for the robot to have the possibility of completing several gait cycles.

There were several ways in which the evaluation process of an individual could be terminated: First of all, there was, as already mentioned, a maximum allowed evaluation time for every individual. Second, if an individual caused the robot to fall over before its maximum evaluation time was reached, the evaluation was automatically terminated. Third, excessive energy consumption, as described below, could also cause the termination of an individual. Last, in order to speed up the evolutionary process, another conditional termination criterion was introduced, defined according to the following expression:

$$\frac{F(i) + i_c}{t_i} < \frac{F_c + i_c}{i_c} \quad (2)$$

Parameter	Value	Description
κ	0.12	MSG threshold value
K	8	MSG update interval
τ_{\max}	10 Nm	Maximum torque
C_1	0.001	LGP constant
C_2	0.01	LGP constant
C_3	0.1	LGP constant
F_c	20.0	Termination constant
i_c	1000	Termination constant
dt	0.009 s	Time step length
T	36 s	Evaluation time

Table 2. Parameters used in the ODE-based simulations

where $F(i)$ equals the fitness contribution at time step t_i , F_c and i_c are constants, set to 20.0 and 1000 respectively. The interpretation of the above inequality is that the fitness contribution in each time step should grow at least linearly with time. The right hand side of the inequality is a constant, specifying the minimal growth rate accepted. If the expression evaluates to *true* at some point, evaluation of that individual is terminated immediately. Thus, with this termination criterion, individuals that spent most of their evaluation time standing idle were terminated more quickly than would otherwise have been the case, resulting in a significant saving of simulation time. In addition, such individuals automatically received a lower fitness value, as a result of the premature termination. Furthermore, in order to favor the emergence of human-like gaits, an energy discharging function was included in the simulations. It was motivated by the fact that human bipedal locomotion is very energy efficient, compared with the gaits of humanoid robots. For instance, the state-of-the-art Honda humanoid Asimo uses at least 10 times the energy (scaled) of a typical human when walking (Collins et al., 2005). Each individual was allowed only to use a specific amount of energy as it moved. In general, the work performed by a (generalized) force in circular motion, moving from an angle φ_a to φ_b , is defined as

$$W_{ba} = \int_{\varphi_a}^{\varphi_b} |\mathbf{M}| d\varphi \quad (3)$$

where \mathbf{M} is the applied torque. The energy consumption E_{jt} of the j^{th} joint during time step t equals the work performed by that joint during the time step. In the simulations, time was discrete, and the applied torque was constant during each time step. Thus, the total energy consumption is given by:

$$E_{tot} = \sum_{j,t} E_{jt} = \sum_{j,t} (\varphi_{b,jt} - \varphi_{a,jt}) |\mathbf{M}_{ba,jt}| \quad (4)$$

When the total energy consumption E_{tot} reached some predefined value, evaluation of that individual was terminated.

3.1.4 Optimization Procedure

The optimization was carried out using a steady-state EA with tournament selection. The tournament size was set to four. Furthermore, two-point crossover and mutation, as described in Subsect. 2.2, and in (Brameier, 2003), were implemented. In the 60 independent simulation runs performed, specific parameter values were examined according to Table 3. In order to guide the evolution towards human-like gaits, much time was spent on finding an appropriate fitness function. First, in a previous study by (Wolff and Nordin, 2003) it was

Parameter	Description
P	Population size
$\langle L_i \rangle$	Initial genome length, expectation value
p_c	Crossover probability
r_{mut}	Mutation rate
E_i	Initial energy level

Table 3. Parameters examined in connection with the ODE-based simulations

assumed that including a term in the fitness function measuring the height of the robot's center of mass above the ground should be important. However, it was found that such a term did not improve the results: The robot was instead prevented from moving freely enough to improve its gait. Consequently, that term was simply skipped.

Second, another problem arose when the evolved gait controllers had reached a level of performance where they could balance the robot in an upright standing pose. In order to reach higher levels of fitness they just let the robot stand idle almost until the end of the evaluation time, and then the robot took a large leap forward. By doing so, the controllers obtained a reward for distance covered over the trial, and the fact that the robot would have fallen to the ground, had the evaluation time been slightly longer, did not affect the fitness negatively. Finally, a good fitness measure was found to be the following:

$$F = \sum_{t=1}^N (x_R + x_L) \quad (5)$$

where N is the number of time steps in the simulation and x_R and x_L are the position coordinates of the robot's right and left foot, respectively, in its initial direction of heading, along the x -axis. The motivation for this fitness measure is that it gives a small reward in

each time step. Thus, with this measure, individuals that remain idle for a large part of the evaluation time receive lower fitness. Thus, for a given distance covered, this fitness measure favors a gradual movement, rather than a quick leap towards the end of the simulation time.

3.2 EvoDyn Implementation

As mentioned earlier, in the ODE implementation described above, the user sets target speeds rather than joint torques. In order to make it possible to explicitly specify a more natural (sinusoidal) variation in the control torques, a different implementation was tried as well. In this implementation, the EvoDyn simulation library, developed at Chalmers University of Technology, was used (Pettersson, 2003).

3.2.1 Physics Simulator

Implemented in object-oriented Pascal, EvoDyn is capable of simulating tree-structured rigid-body systems and runs on both the Windows and Linux platforms. Its dynamics engine is based on a recursively formulated algorithm that scales linearly with the number of rigid bodies in the system (Featherstone, 1987). For numerical integration of the state derivatives of the simulated system, a fourth order Runge-Kutta method is used. Visualization is achieved using the OpenGL library². A fully three-dimensional bipedal robot with 14 DOFs, shown in the two rightmost panels of Fig. 3, was used in the simulations.

3.2.2 Controller model

In EvoDyn, torques are applied directly to each joint. In the EvoDyn-based simulations, the torque on joint i varied according to

$$r_i(t) = A_i \sin(k_i t + \delta_i), \quad i = 1, \dots, 14. \quad (6)$$

where, in turn, the values of the parameters A_i , k_i and δ_i were allowed to vary slowly, the rate of variation being determined by the output from a VRM. Letting z denote an arbitrary parameter (A_i , k_i or δ_i) the variation was taken as

$$\frac{dz}{dt} = c \tanh r \quad (7)$$

where c is a constant and r an output register from the VRM, corresponding to the parameter in question. The tanh function was introduced in order to limit the rate of variation to the interval $[-c, c]$. Thus, even in cases where the contents of the output registers varied strongly between time steps, the variation in the corresponding parameter would be more gentle than in the ODE implementation described above, provided, of course, that the value of c was sufficiently small.

² <http://opengl.org>

In the EvoDyn implementation, the perceptual input consisted of (1) current joint angles for the 14 joints, and (2) readings from eight touch sensors (four under each foot), filtered using a moving average with a window size of 25 time steps. The time step length was 0.002 s, and the maximum simulation time was set to 20 s.

The control loop for the simulation was quite similar to the one used in the ODE implementation: Every K^{th} time step, the perceptual input was measured, and stored in the sensor registers (see the next subsection for a description of the registers) of the VRM. Next, the VRM executed the program specified by the LGP-individual, thus modifying the contents of the calculation registers. The contents of the output registers were then used for computing the variation of the parameters A_i, k_i and δ_i , as described above. Finally, the torques were applied to the robot's joints. The interval (number of time steps) K between successive updates was set to 25. Between updates, the applied torques were constant.

3.2.3 Simulation Setup

In the EvoDyn implementation, a hybrid evolutionary algorithm was used, in which the genome of the individual consisted of two chromosomes: one that specified the sequence of instructions executed by the VRM (i.e. the LGP-individual, using the same nomenclature as for the ODE-based simulations), and one that set the initial values (for the individual in question) of the 42 parameters A_i, k_i , and δ_i as well as the 42 parameters (c , in Eq. (7)) determining the rate of variation of A_i, k_i , and δ_i . Thus, the second chromosome was used as in a standard genetic algorithm, i.e. essentially as a lookup-table.

Compared to the ODE implementation, a slightly different specification of registers (for the VRM) was used: Registers $r_1 - r_{14}$ were used as input registers, storing the joint angles. In addition, registers $r_{63} - r_{70}$ were used for storing the (filtered) readings from the eight contact sensors under the feet. Registers $r_{15} - r_{59}$ were used as calculation registers, whereas registers $r_{60} - r_{62}$ were used for storing the constant values 0.1, 0.01, and 0.001, respectively. Registers $r_{15} - r_{59}$ were initialized to zero before each execution of the LGP-individual. Once every K^{th} time step, when the execution of the LGP-individual had been completed, the contents of registers $r_{15} - r_{28}$ were used as output determining the variation in the parameters A_i , as in Eq. (7). Similarly, the contents of registers $r_{29} - r_{42}$ and $r_{43} - r_{56}$ were used for determining the variation of k_i and δ_i , respectively. The instruction set was the same as for the ODE implementation, see Table 1.

As in the ODE implementation, a combination of termination criteria was used during the evaluation of individuals. Simulations were terminated if either (1) the maximum simulation time was reached, (2) the center-of-mass of the robot dropped below a pre-specified threshold (indicating that the robot had fallen over), or (3) the center-of-mass of the upper body dropped below that of the waist, indicating that the robot was attempting to use the upper body as a third leg. In some runs, additional termination criteria were added. For example, simulations could be terminated if the robot deviated strongly from a straight-line path or if it took a very long initial step (in which case it would gain an immediate fitness increase, but would then find it difficult to retain its balance).

3.2.4 Optimization Procedure

In the EvoDyn-based simulations, an EA with population size P was used. Tournament selection was used, again with each tournament again involving four individuals. However, in the EvoDyn-based simulations, generational replacement was used instead of steady-state replacement. For the first chromosome (specifying the program executed by the VRM), two-point crossover was used whereas, for the second chromosome, a single crossover point was used.

Several different fitness functions were tried, following essentially the sequence described in Subsect. 3.1.4 above. In the end, the fitness measure was taken as in Eq. (5), but with a punishment for sideways deviation, i.e.

$$F = \sum_{t=1}^N (x_R + x_L - |y_R - y_R^0| - |y_L - y_L^0|) \quad (8)$$

where y_R^0 and y_L^0 denote the initial y-coordinates of the feet.

4. Results

In this section the results obtained with the two different implementations will be presented, starting with the results from the ODE-based simulations.

4.1 Results from the ODE implementation

The parameter values examined in the ODE-based simulations are shown in Table 4, and the simulation results are summarized in Table 5. The parameters were varied, one at a time, from their default values, resulting in 20 unique parameter combinations (thus, not all 4^5 possible parameter combinations were tested). In order to increase the reliability of the results, each parameter setting was evaluated in three separate runs. In Table 5, $\max(f_{\max})$ denotes the best fitness value obtained in any of the three separate runs for the parameter setting in question, \bar{f}_{\max} denotes the average of the best fitness values obtained in the three runs and $s(f_{\max})$ denotes the standard deviation. Finally, \bar{f}_{avg} denotes the average (over the three runs) of the average fitness values (taken over the population).

Parameter	Values
P	8, 32, 128, 512
$\langle L_i \rangle$	32, 64, 128, 256
p_c	0.0, 0.2, 0.8, 1.0
r_{mut}	0.1, 0.2, 0.4, 0.8
E_i	32, 128, 256, 512

Table 4. The different parameter settings examined in the ODE-based simulations. The default values are typeset in *italic*

The best overall fitness values were obtained for the parameter settings $P = 128$, $\langle L_i \rangle = 128$, $p_c = 0.8$, $r_{mut} = 0.2$, and $E_i = 256$ and $E_i = 256$. As is clear from Table 5, the default parameter values of P and r_{mut} produced the best fitness values. The (default) value of 0.8 for the parameter p_c also gave the best result, at least in terms of the f_{\max} and \bar{f}_{\max} fitness values. On the contrary, when considering only the best fitness value of a single individual, a p_c value of 0.0 (i.e. only mutation used) gave better results, albeit with a large standard deviation. For $\langle L_i \rangle$ and E_i , the best values turned out to be 32 and 256, respectively. It should be noted that, with a few exceptions, the difference in performance between the various parameter settings is not statistically significant. The best individual found had a fitness value of 8958. During its 36 s evaluation time (4000 time steps), the robot covered a distance of 1.93 m. The graphs of Fig. 6 show covered distances, $d(t)$, for the best individual found and for two other individuals, for comparison. As is clear from the figure, the best individual (i.e. the one labeled '8958') moved the longest distance during the evaluation time. At the end of the evaluation period, however, it fell backwards, an event indicated by the drop in the graph of $d(t)$ at the end. The other two individuals both remained on their feet for the whole evaluation period, but they received lower fitness values. The cyclic nature of the robots' movements can be seen as oscillations in the curves shown in the figure.

$\max(f_{\max})$	\bar{f}_{\max}	$s(f_{\max})$	\bar{f}_{avg}	$P(t)$	$\langle L_i \rangle$	p_c	r_{mut}	E_i
5728	4635	1777	3475	8	128	0.8	0.2	128
5839	5015	1144	4701	32	128	0.8	0.2	128
7303	6760	480	6535	128	128	0.8	0.2	128
6954	6604	486	5032	512	128	0.8	0.2	128
7449	6900	586	6546	128	32	0.8	0.2	128
5817	5065	848	4864	128	64	0.8	0.2	128
7303	6760	480	6535	128	128	0.8	0.2	128
6176	5232	1194	4007	128	256	0.8	0.2	128
7943	6054	1662	4621	128	128	0.0	0.2	128
6580	5468	973	5303	128	128	0.2	0.2	128
7303	6760	480	6535	128	128	0.8	0.2	128
7197	6687	578	6419	128	128	1.0	0.2	128
6417	5170	1109	4679	128	128	0.8	0.1	128
7303	6760	480	6535	128	128	0.8	0.2	128
6797	6292	580	5933	128	128	0.8	0.4	128
6308	6194	148	4517	128	128	0.8	0.8	128
2049	1270	581	1101	128	128	0.8	0.2	32
7303	6760	480	6535	128	128	0.8	0.2	128
8958	7598	1375	7368	128	128	0.8	0.2	256
7076	6352	660	6020	128	128	0.8	0.2	512

Table 5. Results from the parameter study using the ODE implementation. The first column shows the fitness values of the best individual, $\max(f_{\max})$ obtained for each parameter setting; The second and third columns show the averages, \bar{f}_{\max} , over the three runs (for each parameter setting) of the best fitness values as well as the standard deviations $s(f_{\max})$ (over the three runs) of the same values; The fourth

column shows the average \bar{f}_{avg} (over the three runs) of the average fitness values in the population. All values were measured after 25000 selection steps (tournaments). Each of the five partitions of the table shows the variations of a single parameter value. Numbers in bold represent the best fitness values of each partition

4.2 Results from the EvoDyn implementation

As will be further discussed below, the gaits obtained using the ODE implementation were, in fact, not very human-like. In order to try to overcome this problem, the EvoDyn implementation, allowing direct sinusoidal variation in the control torques, was tested. Several runs were carried out, using population sizes (P) in the range [30, 500], and initial lengths of the LGP programs (obtained from the first chromosome, as described in Subsect. 3.2) in the range [8, 512].

In most runs, the best evolved controller managed to keep the robot upright for the duration of the simulation (20 s, corresponding to 10000 time steps). Furthermore, the robots normally managed to take one or a few human-like steps forward, as can be seen in Fig. 7. However, continuous human-like walking was not achieved: After the first few steps, the robot normally got stuck with the back foot seemingly glued to the ground. However, in a few rare cases

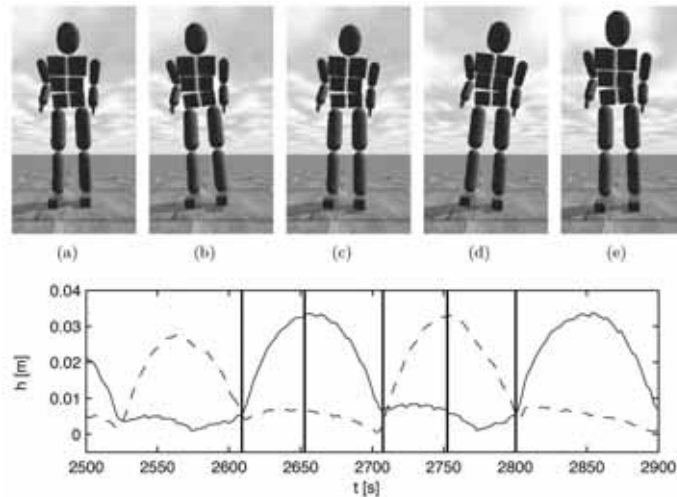


Fig. 5. Top panel: Walking scene of the bipedal robot in the ODE-based simulations. Starting from the left, the double support phase is depicted (a), followed by the single support phase with the left foot in swing motion (b). Then another double support phase is shown (c), followed by single support phase with the right foot in swing motion (d). Finally, the gait cycle is completed with a double support phase (e). Bottom panel: Plot of the depicted gait cycle. The graphs show the height above ground, $h(t)$, of the center-of-mass of the left foot (solid line) and the right foot (dashed line), respectively. The vertical lines indicate the double- and single support phases (a) through (e)

the evolved robots would walk essentially as in the ODE implementation, taking very short steps. An example of such a case is shown in Fig. 8. Here, the length of the first step was roughly equal to the length of the foot. The robot then moved the back foot in line with the front foot. All subsequent steps were significantly shorter, as indicated by the two rightmost panels of the figure. Note the somewhat peculiar, backwards-leaning posture of the robot.

5. Discussion and Conclusion

This study has been centered on essentially model-free evolution of bipedal gaits, in which the controller was not provided with any model of the bipedal robot, neither any *a priori* knowledge on how to walk. In both the ODE and EvoDyn implementations, the gait-generating controller programs were evolved starting from random sequences of basic LGP instructions (supplemented by initial values of the parameters used for specifying the torques, in the EvoDyn case).

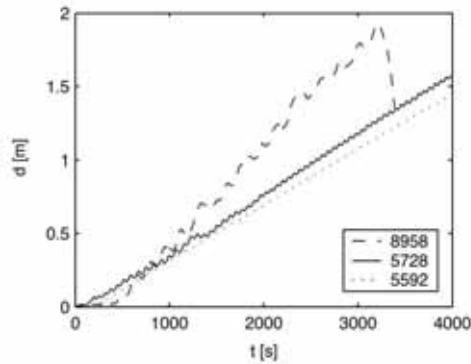


Fig. 6. Graphs of covered distances in the ODE-based simulations, $d(t)$, during 4000 evaluation time steps, for three different individuals. These individuals received fitness scores of 8958, 5728 and 5591, respectively. The individual with fitness value 8958 was actually the best individual found in any run

With the ODE implementation, evolution generated individuals that made the simulated robot walk forward almost indefinitely, albeit very slowly. In fact, some of the best individuals were actually capable of producing locomotion behavior lasting more than thirty times the evaluation time used during evolution. For example, the individual labeled '5592' was capable of keeping the robot upright and (slowly) walking for at least 20 minutes. However, no individuals obtained with the ODE implementation reached a walking speed exceeding 0.054 m/s. Considering the fact that the dimensions of the simulated robot were similar to those of a (small) human being, this is indeed a very low walking speed. Even the best individuals made the robot lift its feet only a small distance above the ground while walking, and the step length was also very small (see Fig. 5). As a result, the walking speed of the robot was very low. It appears that these individuals had difficulties in activating the knee joints very much, instead relying on the hip joints, making each step quite short.

A possible reason for these somewhat discouraging results may be derived from the manner in which joint torques (or set speeds, in the ODE case) were generated: Every K^{th} time step of a simulation, the robot must execute its LGP program, generating torque values based on current sensor readings. While an LGP program can, in principle, provide any form of variation in the registers of the VRM, it is rather unlikely to find, in a huge search space, the kind of smooth, cyclic variation generally associated with bipedal locomotion. This realization prompted the use of the second (EvoDyn) implementation, which allows direct setting of the control torques. Here, a slightly different approach was used, in which sinusoidally varying torques were applied, and the LGP program was used for determining the rate of variation of the parameters specifying the sinusoidal torques. With this implementation, the evolved individuals did indeed take larger steps or, rather, one large step. After the first step (or, in rare cases, a few steps), the evolved robots generally had difficulties proceeding: Either they simply fell over, or (more commonly) they stopped, incapable of moving the back foot forward. The obvious way of avoiding large initial steps is to alter the fitness measure so that large steps are discouraged, for example by reducing the fitness if the distance (in the x -direction) between the two feet exceeds a certain

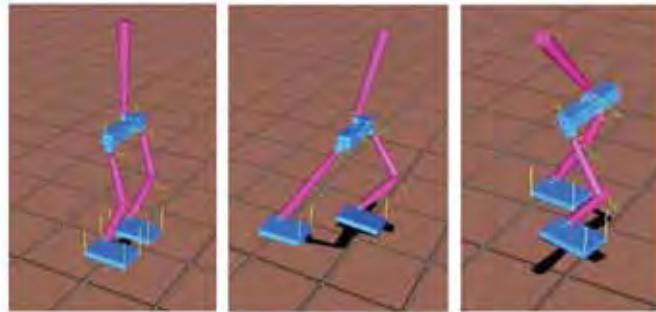


Fig. 7. The left panel shows the initial posture used in the EvoDyn-based simulations. The two panels on the right show typical first steps taken by evolved individuals. As can be seen, the first step was commonly quite long, making it difficult for the robot to maintain its posture in subsequent steps

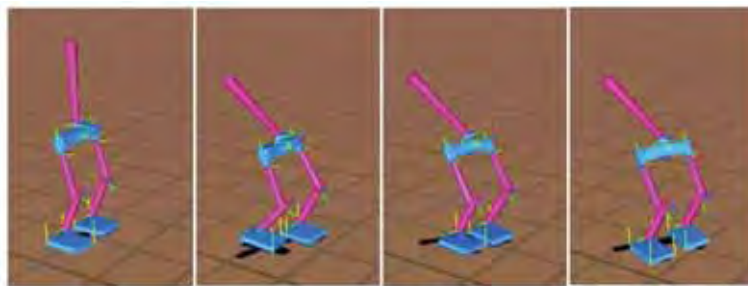


Fig. 8. An example of a successful gait obtained with the EvoDyn implementation. With the exception of the first two steps, the robot moved by taking very small steps

threshold. This approach was indeed tried and while the step length was reduced, the modification instead generated other unwanted behaviors. For example, many individuals started walking on their toes, much like a ballet dancer (but, alas, with much less skill), in order to minimize the distance between the feet in the direction of motion. Further modifications of the fitness measure, intended to remove also these adverse effects, only caused other problems to emerge.

These problems are indicative of a more general difficulty commonly present in the evolution of bipedal gaits, namely the problem of specifying a good fitness measure. As mentioned above, a significant effort was made in order to find the best possible fitness measure. Naive candidates generally give poor results. For example, if the fitness measure is taken as the distance walked (measured, for instance, by the position of the robot's center-of-mass), the robot will simply throw its body forward. Attempts at modifying the fitness measure to avoid such behaviors normally create more problems than they solve: There is always some loophole that evolution can use in order to obtain high fitness values without, at the same time, walking properly. These problems, of course, stem from the difficulty of going from a more or less random starting point to a state of walking: Even though human-like, continuous walking would generate higher fitness values than any of the behaviors that actually emerge, finding such a solution in the gigantic search space of all possible ways of specifying joint torques is very difficult indeed.

In the end, essentially the same fitness measures were used in both implementations (with an added punishment for sideways deviation in the EvoDyn case), see Eq. (8). By integrating the positions of the feet (in the direction of motion) this fitness measure allows the ODE implementation to generate careful, slow steps. The EvoDyn implementation, being forced to apply sinusoidal torque variations, had more difficulties in generating such gaits, even though they did appear in rare cases.

A further explanation for the somewhat poor results with respect to gait quality obtained in the simulations presented here compared, for example, to the results obtained in (Wolff et al., 2006), could be the choice of sensor feedback: In the implementations used here, the feedback consisted of joint angles supplemented by a balancing sense (in the ODE case) or touch sensors in the feet (in the EvoDyn case). However, unlike the simulations in (Wolff et al., 2006), which were based on a more elaborate structure involving central pattern generators (CPGs), the feedback did not include the angles of the waist, thigh, and leg *relative to the vertical axis*. Apparently, this feedback seems to be more important (and perhaps also easier for the controller to interpret and use) than the feedback signals used in the study presented here. A thorough investigation of this issue is a topic for future work. On the other hand, it is known that tactile feedback from the foot, indicating foot-to-ground contact, is essential for human locomotion (Van Wezel et al., 1997).

To summarize, the current study has shown that entirely model-free evolution of bipedal gaits (as in the ODE case) is indeed feasible, but that the generated gaits, while stable, are unlikely to be very human-like.

6. Acknowledgment

The authors wish to thank Dr. Jimmy Pettersson for providing the EvoDyn simulation library, and Mr. David Sandberg for valuable comments on the manuscript.

7. References

- Beer, R. D., Quinn, R. D., Chiel, H. J., and Ritzmann, R. E. Biologically inspired approaches to robotics: What can we learn from insects? *Communications of the ACM*, 40(3):30–38, 1997.
- Bekey, G. A. Biologically inspired control of autonomous robots. *Robotics and Autonomous Systems*, 18(1–2):21–31, 1996.
- Boeing, A., Hanham, S., and Bräunl, T. Evolving autonomous biped control from simulation to reality. In *Proceedings of the Second International Conference on Autonomous Robots and Agents*, pages 440–445, Palmerston North, New Zealand, 2004.
- Brameier, M. *On Linear Genetic Programming*. PhD thesis, Dortmund University, Dortmund, Germany, 2003.
- Collins, S. H., Ruina, A. L., Tedrake, R., and Wisse, M. Efficient bipedal robots based on passive-dynamic walkers. *Science*, 307:1082–1085, 2005.
- Featherstone, R. *Robot Dynamics Algorithms*. Kluwer Academic Publishers, 1987.
- Ficici, S., Watson, R., and Pollack, J. Embodied evolution: A response to challenges in evolutionary robotics. In *Proceedings of the Eighth European Workshop on Learning Robots*, pages 14–22, Lausanne, Switzerland, 1999.
- Fujimoto, Y., Obata, S., and Kawamura, A. Robust biped walking with active interaction control between foot and ground. In *Proceedings of the International Conference on Robotics and Automation*, volume 3, pages 2030–2035, Leuven, Belgium, 1998.
- Furusho, J. and Sano, A. Sensor-based control of a nine-link biped. *International Journal of Robotics Research*, 9(2), 1990.
- Hirai, K., Hirose, M., Haikawa, Y., and Takenaka, T. The development of Honda humanoid robot. In *Proceedings of the International Conference on Robotics and Automation*, volume 2, pages 1321–1326, 1998.
- Huang, Q. and Nakamura, Y. Sensory reflex control for humanoid walking. *IEEE Transactions on Robotics and Automation*, 21(5):977–984, 2005.
- Huang, Q., Nakamura, Y., and Inamura, T. Humanoids walk with feedforward dynamic pattern and feedback sensory reflection. In *Proceedings of the International Conference on Robotics and Automation*, pages 4220–4225, 2001.
- Huelsbergen, L. Toward simulated evolution of machine-language iteration. In *Proceedings of the First Annual Conference on Genetic Programming*, pages 315–320, Stanford University, CA, USA, 1996.
- Jakobi, N., Husbands, P., and Harvey, I. Noise and the reality gap: The use of simulation in evolutionary robotics. In *Advances in Artificial Life: 3rd European Conference on Artificial Life*, LNCS 929, pages 704–720. Springer, 1995.
- Kajita, S. and Tani, K. Adaptive gait control of a biped robot based on realtime sensing of the ground profile. In *Proceedings of the International Conference on Robotics and Automation*, pages 570–577, 1996.
- Katic, D. and Vukobratovic, M. Survey of intelligent control techniques for humanoid robots. *Intelligent and Robotic Systems*, 37(2):117–141, 2003.
- Li, Q., Takanishi, A., and Kato, I. Learning control of compensative trunk motion for biped walking robot based on ZMP stability criterion. In *Proceedings of the 1992 IEEE/RSJ International Conference on Intelligent Robots and Systems*, pages 597–603, Raleigh, NC, USA, 1992.

- Ok, S., Miyashita, K., and Hase, K. Evolving bipedal locomotion with genetic programming – a preliminary report–. In *Proceedings of the Congress on Evolutionary Computation, CEC'01*, pages 1025–1032, Seoul, South Korea, 2001.
- Park, J. and Cho, H. An on-line trajectory modifier for the base link of biped robots to enhance locomotion stability. In *Proceedings of the International Conference on Robotics and Automation*, pages 3353–3358, 2000.
- Pettersson, J. *EvoDyn: A simulation library for behavior-based robotics*. Technical report, Department of Machine and vehicle systems, Chalmers University of Technology, Göteborg, September 2003.
- Pettersson, J., Sandholt, H., and Wahde, M. A flexible evolutionary method for the generation and implementation of behaviors for humanoid robots. In *Proceedings of the 2nd International IEEE-RAS Conference on Humanoid Robots*, pages 279–286, Waseda University, Tokyo, Japan, 22-24 November 2001. Humanoid Robotics Institute.
- Quinn, R. D. and Espenschied, K. S. Control of a hexapod robot using a biologically inspired neural network. In *Proceedings of the workshop on "Locomotion Control in Legged Invertebrates" on Biological neural networks in invertebrate neuroethology and robotics*, pages 365–381, San Diego, CA, USA, 1993.
- Reil, T. and Massey, C. Biologically inspired control of physically simulated bipeds. *Theory in Biosciences*, 120(3-4):327–339, 2001.
- Taga, G. Emergence of bipedal locomotion through entrainment among the neuro-musculo-skeletal system and the environment. *Physica D Nonlinear Phenomena*, 75:190–208, 1994.
- Takanishi, A., Ishida, M., Yamazaki, Y., and Kato, I. The realization of dynamic walking by the biped walking robot WL-10RD. In *Proceedings of the International Conference on Advanced Robotics*, pages 459–466, 1985.
- Van Wezel, B. M. H., Ottenhoff, F. A. M., and Duysens, J. Dynamic control of location-specific information in tactile cutaneous reflexes from the foot during human walking. *The Journal of Neuroscience*, 17(10):3804–3814, 1997.
- Wahde, M. and Pettersson, J. A brief review of bipedal robotics research. In *Proceedings of the 8th Mechatronics Forum International Conference*, pages 480–488, Enschede, the Netherlands, 24-26 June 2002.
- Watson, R. A., Ficici, S. G., and Pollack, J. B. Embodied evolution: Embodying an evolutionary algorithm in a population of robots. In *Proceedings of the Congress on Evolutionary Computation*, volume 1, pages 335–342, Washington D.C., USA, 1999.
- Wolff, K. and Nordin, P. Evolution of efficient gait with humanoids using visual feedback. In *Proceedings of the 2nd International IEEE-RAS Conference on Humanoid Robots*, pages 99–106, Tokyo, Japan, 22-24 November 2001.
- Wolff, K. and Nordin, P. Learning biped locomotion from first principles on a simulated humanoid robot using linear genetic programming. In *Proceedings of the Genetic and Evolutionary Computation Conference*, volume 2723 of LNCS, pages 495–506, Chicago, 12-16 July 2003.
- Wolff, K., Pettersson, J., Heralic, A., and Wahde, M. Structural evolution of central pattern generators for bipedal walking in 3D simulation. In *Proceedings of the 2006 IEEE International Conference on Systems, Man, and Cybernetics*, pages 227–234, 8-11 October 2006.

- Wolff, K., Sandberg, D., and Wahde, M. Evolutionary optimization of a bipedal gait in a physical robot. Manuscript, to be submitted, 2007.
- Yamaguchi, J., Soga, E., Inoue, S., and Takanishi, A. Development of a bipedal humanoid robot-control method of whole body cooperative dynamic biped walking. In *Proceedings of the International Conference on Robotics and Automation*, pages 368–374, 1999.
- Zheng, Y. and Shen, J. Gait synthesis for the SD-2 biped robot to climb sloping surface. *IEEE Transactions on Robotics and Automation*, 6(1):86–96, 1990.
- Ziegler, J., Barnholt, J., Busch, J., and Banzhaf, W. Automatic evolution of control programs for a small humanoid walking robot. In *Proceedings of the 5th International Conference on Climbing and Walking Robots*, 2002.

Optimal Design of a New Wheeled Mobile Robot by Kinetic Analysis for the Stair-Climbing States

Chun-Kyu Woo, Hyun Do Choi, Mun Sang Kim*,
Soo Hyun Kim and Yoon Keun Kwak

Korea Advanced Institute of Science and Technology

* *Korea Institute of Science and Technology
South Korea*

1. Introduction

Many mobile robots have been developed in the various application fields, such as building inspection and security, military reconnaissance, space and undersea exploration, and warehouse services (Muir & Neuman, 1987). Mobile robots are designed with the specific locomotive mechanisms according to the environment of the application field. The various locomotive mechanisms used in mobile robots can be classified into three types: wheeled, tracked, and legged type (Kim, 1999) (Lee et al, 2000). Each locomotion type has its inherent advantages and disadvantages as described below. The wheeled mobile robots (WMRs) weigh less than robots of the other locomotive types and have other inherent advantages, such as high energy efficiency, low noise level, etc (Muir & Neuman, 1987). In comparison with legged mobile robots, the WMRs have a simpler driving part and a plain control strategy, but they have the poor adaptability to the terrain.

Tracked mobile robots have the merit of easy off-road travelling. However, they usually have a heavier driving part and need more power for turning motions, in comparison with mobile robots with other locomotive types. Additionally, tracked mobile robots are usually too noisy to be utilized for in-door applications. Legged mobile robots can easily adapt to the unstructured environments, such as off-road environments, but require more actuators to stabilize themselves than mobile robots in the other two categories. As the locomotion mechanisms are complex and need more complicated control algorithms, legged mobile robots have poor mobility on the plane surfaces.

Various types of mobile robots that are capable of climbing up stairs have been developed but, until now, most of the mobile robots developed have tracked-type locomotive mechanisms (Kohler et al., 1976) (Maeda et al., 1985) (Yoneda et al., 1997) (Iwamoto & Yamamoto, 1985) (Iwamoto & Yamamoto, 1990). For the purpose of developing a robot capable of traversing the stairs, Estier (Estier et al., 2000) proposed a WMR with three 4-bar linkage mechanisms, by applying the concept of the instantaneous centre of rotation. To explore Mars, Volpe (Volpe et al., 1997) developed a WMR named Rockey 7, which is capable of climbing up steps about 1.5 times as large as the wheel diameter.

This paper proposes a new type of locomotive mechanism for WMRs that is capable of travelling up stairs based upon two design concepts: 'adaptability' and 'passivity'. The proposed WMR has a passive linkage-type locomotive mechanism that offers extensive adaptability to rough terrain, especially stair. To fully analyze the behaviours of the proposed passive linkage mechanism during stair climbing, several states analysis was accomplished using the analytical method and the multi-body dynamic analysis software ADAMSTM. From the results of the states analysis, the optimization of the proposed WMR was performed using the multi-objective optimization method.

2. The Proposed Locomotive Mechanism

For the purpose of developing a mobile robot which has a simple structure, light weight, and good energy efficiency, we have elaborately analyzed the features of the three types of locomotive mechanism - wheeled, tracked, and legged. The tracked mobile robots have high off-road capability but usually have heavy weight; the tracked mobile robots have low energy efficiency in turning motions; and the legged mobile robots have extensive adaptability to rough terrain but usually have complex locomotive mechanisms that need complicated control algorithms. Additionally, the legged mobile robots have poor mobility on the plane surfaces. On the other hand, the wheeled mobile robots have simple structure, good mobility on the plain surfaces, and good energy efficiency in turning, but have poor adaptability to the rough terrain. Therefore, considering the indoor applications, we opted to develop a wheeled mobile robot. Our wheeled mobile robot, however, has a locomotive mechanism which enables it to adapt to rough terrain, such as the stair like the legged mobile robot.

Therefore, to develop a wheeled mobile robot that not only has adaptability to stairs but also maintains good energy efficiency, we proposed two design concepts. One is adaptability and the other is passivity (Woo et al., 2001). Based on these design concepts, we developed the first prototype of the WMR, named ROBHAZ-6W, and accomplished stair climbing experiments on several types of stairs (Woo et al., 2002). To improve the WMR's adaptability to rough terrain and its ability to climb stairs, this paper presents the modified passive linkage-type locomotive mechanism.

2.1 Adaptability

WMRs usually have been utilized in the indoor environment due to their advantages on the indoor applications. To extend the WMR's application area to the outdoor environment, the WMR must have good adaptability to the environment. In order to improve this adaptability, we proposed a simple linkage-type locomotive mechanism that makes it possible for the driving wheels to move relative to the robot body and for the wheelbases to change among the driving wheels, according to the shape of terrain.

The proposed linkage-type locomotive mechanism is a simple 4-bar linkage mechanism; the side view of the WMR with the proposed mechanism is shown in Fig. 1. As shown in Fig. 1, driving wheels 1 and 2 are interconnected with link 1, which is able to rotate about pin joint P relative to the robot body. Driving wheel 3 is attached to link 2, which is connected with link 1 by pin joint Q. To stabilize the robot body, link 3 is used to connect the robot body to link 2 by pin joints R and S. Therefore, links 1, 2, 3, and the robot body form a 4-bar linkage mechanism which has one degree-of-freedom (DOF). By using the linkage mechanism, the

wheelbases among the driving wheels of the WMR and the relative positions of the wheel axles to the center of gravity of the robot body can be changed, according to the configuration of the proposed linkage-type locomotive mechanism. The WMR has a symmetric structure with the proposed linkage-type locomotive mechanism on the right and the left.

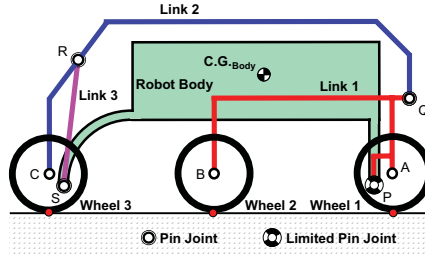


Fig. 1. Side view of the WMR with the proposed linkage-type locomotive mechanism

Fig. 2 shows the adaptability of the WMR with the proposed locomotive mechanism according to the two different types of terrain. As shown in Fig. 2, the 6-WMR with the proposed linkage-type locomotive mechanism easily adapts to the two different types of terrain profile; the concave and the convex terrain. The WMR with the proposed linkage locomotive mechanism has more extensive adaptability to the environment than conventional WMRs. The detailed locomotive method of stair-climbing will be described in the next section.



Fig. 2. Extensive adaptability of the proposed WMR

2.2 Passivity

As described in the above section, the proposed linkage-type locomotive mechanism offers extensive adaptability to the terrain. Additionally, as shown in Fig. 1, the proposed mechanism does not have any active mechanical elements, such as motors, that need active control techniques. Therefore, the proposed WMR can passively adapt to the environment, according to the linkage-type locomotive mechanism.

However, while the proposed WMR goes up the stairs, the WMR may be led into states which it cannot climb up the stairs and halts where it is. We called these unexpected states 'sticking conditions'. Some of the sticking conditions are shown in Fig. 3.

As shown in Fig. 3 (a), one of the sticking conditions may occur when driving wheels 1 and 2 of the WMR simultaneously come into contact with the wall of the stair. This sticking condition can be evaded by setting the proper wheelbase between driving wheels 1 and 2. Another sticking condition occurs when driving wheels 2 and 3 simultaneously come into contact with the wall of the stair, as shown in Fig. 3 (b). This sticking condition commonly

occurs due to excessive rotation of link 1 relative to the robot body. Not only to avoid this sticking condition and but also to maintain the design concept of ‘passivity’, we suggested a limited pin joint at point P that restricts the excessive rotation of link 1 relative to the robot body, as described in Fig. 1. The maximum allowable angle of link 1 relative to the robot body will be determined by the kinetic analysis in the next section.

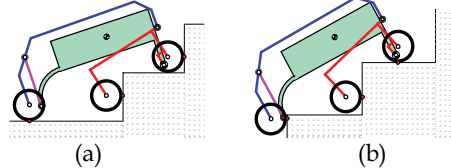


Fig. 3. Sticking Conditions

3. Kinetic Analysis

In this section, we introduce the detailed analysis of the WMR's states while the WMR with the proposed passive linkage-type locomotive mechanism climbs up the stair. The states are classified in the position of the point and the status of contact between the driving wheels and the stair. The kinetics and the dynamics of the proposed locomotive mechanism at each state are also different from each other due to the posture of the WMR and the contact forces on the driving wheels at the points of contact. The reasons for classifying the climbing motion of the WMR into the several states are to describe the contact forces acting on the driving wheels as the analytic functions and analyze the kinetics of the proposed WMR. For the whole states, the contact forces can not be expressed in the analytic function, due to the absence of contact on certain driving wheels. For each state, however, the normal forces and the corresponding friction forces acting on the driving wheels can be described in the analytic functions.

From the kinetic analysis of each state, the geometric constraints to prevent the WMR from falling into the sticking conditions are suggested and the object functions to improve the WMR's capability to climb up stairs are derived. The design variables of the proposed WMR are shown in Fig. 4.

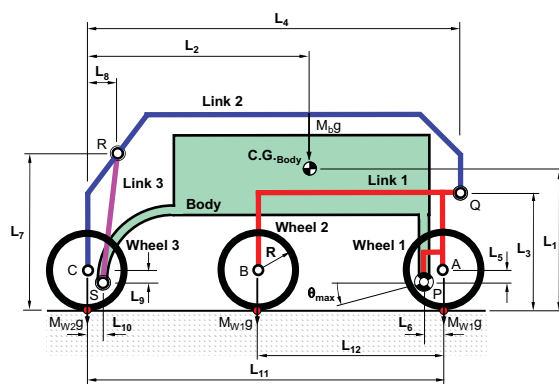


Fig. 4. Design variables of the WMR with the proposed mechanism

The schematic design in Fig. 4 shows the left side of the WMR having a symmetric structure. In Fig. 4, max indicates the maximum allowable counter-clockwise angle of the link 1 at the pin joint relative to the robot body in order to prevent the WMR from falling into the sticking condition.

Fig. 5 shows the suggested 11 states divided by considering the status of the points of contact, while the mobile robot climbs up the stair. In Fig. 5, the small dot attached around the outer circle of the driving wheels indicates the point of contact between the driving wheels and the stair. If the WMR can pass through the whole states, the WMR is able to climb the stair.

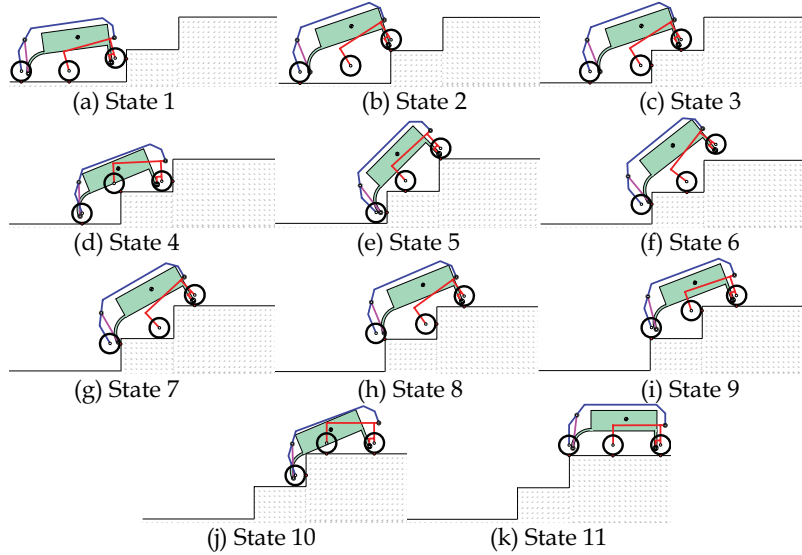


Fig. 5. Suggested 11 states while climbing up the stair

As shown in Fig. 5, the suggested 11 states can be classified into 4 groups. The first group is composed of the states which are kinetically dominant among the whole states, such as states 1, 3, 7, and 10. The capability for the WMR to climb the stair is determined by the states in this group. Therefore, to improve the WMR's ability to climb up the stair, the object functions being optimized will be obtained from the states in this group.

The second group consists of the states that are kinetically analogous to the states in the first group, such as state 4, 8, and 9. State 4 is similar to state 1 in terms of the points of contact between the driving wheels and the stair. States 8 and 9 are analogous to state 2. Therefore, if the object functions obtained from the kinetic analysis of the states in the first group are optimized, it is supposed that the WMR will automatically or easily pass through the states in this group.

The third group comprises the kinematically surmountable states, such as states 5 and 6. In these states, the WMR moves easily to the next state due to the kinematic characteristics of the proposed mechanism.

Finally, the fourth group is formed by the states in which the WMR can be automatically surmountable, such as states 2 and 11. In these states, due to the absence of forces preventing the WMR going forward, the WMR automatically passes through these states. In the next subsection, we analyze the kinetics of the WMR for the states in the first group by the analytical method. Additionally, using the multi-body dynamic analysis software ADAMS™, we will verify the validity of the kinetic analysis of the WMR. From the results of the kinetic analysis the object functions will be formulated for the purpose of optimizing the design variables of the WMR.

3.1 For State 1

As shown in Fig. 5 (a) and Fig. 6, the driving wheel 1 of the WMR comes into contact with the wall of the stair and driving wheels 2 and 3 keep in contact with the floor, because the center of rotation of the proposed linkage-type mechanism is located below the wheel axis.

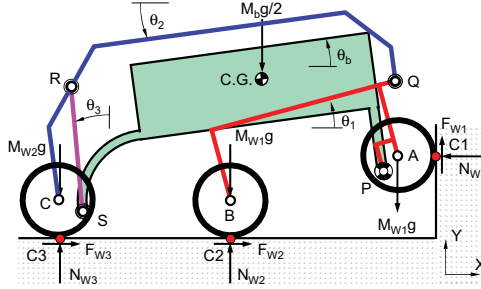


Fig. 6. Forces acting on the proposed WMR for the state 1

To find the normal reaction forces and the corresponding friction forces, we supposed that the WMR was in quasi-static equilibrium and the masses of the links composing the proposed mechanism were negligible. The dynamic friction coefficient of the coulomb friction was applied at the points of contact between the driving wheels and the stair.

If link 1 is in the quasi-static equilibrium state, the resultant forces in the x- and y-directions of the Cartesian coordinates must be zero as described in equation (1) and (2), respectively. The resultant z-direction moment of link 1 about point P also should be zero as described in the equation (3).

$$\sum F_x = 0; \Rightarrow F_{W2} - N_{W1} + P_x + Q_x = 0 \quad (1)$$

$$\sum F_y = 0; \Rightarrow F_{W1} + N_{W2} + P_y + Q_y = 2M_{W1}g \quad (2)$$

$$\begin{aligned} \sum (M_z)_p = 0; \Rightarrow & F_{W1}(L_6 \cos \theta_1 - L_5 \sin \theta_1 + R) + N_{W1}(L_6 \sin \theta_1 + L_5 \cos \theta_1) \\ & + F_{W2}\{(L_{12} - L_6)\sin \theta_1 - L_5 \cos \theta_1 + R\} - N_{W2}\{(L_{12} - L_6)\cos \theta_1 + L_5 \sin \theta_1\} \\ & - Q_x\{(L_3 + L_5 - R)\cos \theta_1 + (L_4 + L_6 - L_{11})\sin \theta_1\} \\ & + Q_y\{-(L_3 + L_5 - R)\sin \theta_1 + (L_4 + L_6 - L_{11})\cos \theta_1\} \\ & = M_{W1}g\{(2L_6 - L_{12})\cos \theta_1 - 2L_5 \sin \theta_1\} \end{aligned} \quad (3)$$

In equation (3), the forces P_x , P_y , Q_x and Q_y are x- and y-direction joint forces on the point P and Q, respectively. And θ_1 is the counter-clockwise angle of link 1 relative to the x-axis of the coordinates fixed in the ground, as shown in Fig. 6.

For link 2, the x- and y-direction resultant forces are described in equations (4) and (5), respectively. The resultant moment about the point C is expressed in equation (6).

$$\sum F_x = 0; \Rightarrow F_{W3} - Q_x + R_x = 0 \quad (4)$$

$$\sum F_y = 0; \Rightarrow N_{W3} - Q_y + R_y = M_{W2g} \quad (5)$$

$$\begin{aligned} \sum (M_z)_C = 0; \Rightarrow & F_{W3}R + Q_x \{L_4 \sin \theta_2 + (L_3 - R) \cos \theta_2\} - Q_y \{L_4 \cos \theta_2 - (L_3 - R) \sin \theta_2\} \\ & - R_x \{(L_7 - R) \cos \theta_2 + L_8 \sin \theta_2\} - R_y \{(L_7 - R) \sin \theta_2 - L_8 \cos \theta_2\} = 0 \end{aligned} \quad (6)$$

R_x and R_y are x- and y-direction joint forces on the point R, respectively. θ_2 is the counter-clockwise angle of link 2 relative to the x-axis of the coordinates fixed in the ground.

For link 3, the x- and y-direction resultant forces are described in equations (7) and (8), respectively. The resultant moment about point S is expressed in equation (9).

$$\sum F_x = 0; \Rightarrow -R_x + S_x = 0 \quad (7)$$

$$\sum F_y = 0; \Rightarrow -R_y + S_y = 0 \quad (8)$$

$$\sum (M_z)_S = 0; \Rightarrow R_x L \cos \theta_3 + R_y L \sin \theta_3 = 0 \quad (9)$$

S_x and S_y are x- and y-direction joint forces on the point S, respectively. θ_3 is the counter-clockwise angle of link 3 relative to the y-axis of the coordinates fixed in the ground, as shown in Fig. 6. L is the length of link 3 as described in equation (10).

$$L = \left[(L_7 + L_9 - R)^2 + (L_8 - L_{10})^2 \right]^{1/2} \quad (10)$$

Finally, for the robot body, the x- and y-direction resultant forces are described in equations (11) and (12), respectively. The resultant moment about point S is expressed in equation (13).

$$\sum F_x = 0; \Rightarrow -P_x - S_x = 0 \quad (11)$$

$$\sum F_y = 0; \Rightarrow -P_y - S_y = M_b g / 2 \quad (12)$$

$$\begin{aligned} \sum (M_z)_S = 0; \Rightarrow & P_x \{(L_{11} - L_6 - L_{10}) \sin \theta_b + (L_9 - L_5) \cos \theta_b\} \\ & - P_y \{(L_{11} - L_6 - L_{10}) \cos \theta_b - (L_9 - L_5) \sin \theta_b\} \\ = & \frac{1}{2} M_b g \{(L_2 - L_{10}) \cos \theta_b - (L_1 + L_9 - R) \sin \theta_b\} \end{aligned} \quad (13)$$

θ_b is the counter-clockwise angle of the robot body relative to the x-axis of the coordinates fixed in the ground.

The friction force F_{W1} can not be determined by the coulomb friction due to the kinematics of the proposed passive linkage-type locomotive mechanism, but F_{W2} and F_{W3} are determined by the coulomb friction, as in equation (14). These relationships between the normal forces and the friction forces will be shown in the simulation results as described in Fig. 7 where μ represents the dynamic friction coefficient of the coulomb friction.

$$F_{W1} \neq \mu N_{W1}, \quad F_{W2} = \mu N_{W2}, \quad F_{W3} = \mu N_{W3} \quad (14)$$

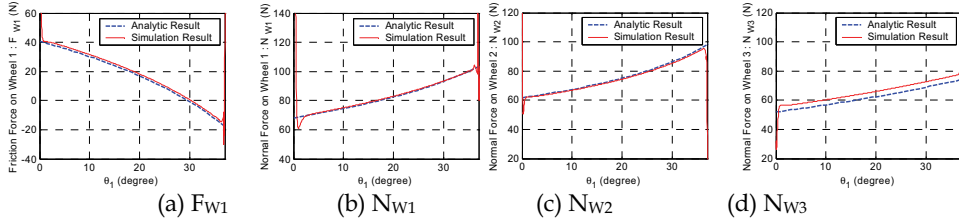


Fig. 7. Normal and friction forces on the driving wheels for the state 1

From equations (1) ~ (13), we formulate the 12×12 matrix equation as shown in equation (15) to determine the unknown contact forces F_{W1} , N_{W1} , N_{W2} and N_{W3} .

$$\begin{bmatrix} 0 & -1 & \mu & 0 & 1 & 0 & 1 & 0 & 0 & 0 & 0 & 0 \\ 1 & 0 & 1 & 0 & 0 & 1 & 0 & 1 & 0 & 0 & 0 & 0 \\ C_{31} & C_{32} & C_{33} & 0 & 0 & 0 & -C_{37} & C_{38} & 0 & 0 & 0 & 0 \\ 0 & 0 & 0 & \mu & 0 & 0 & -1 & 0 & 1 & 0 & 0 & 0 \\ 0 & 0 & 0 & 1 & 0 & 0 & 0 & -1 & 0 & 1 & 0 & 0 \\ 0 & 0 & 0 & C_{64} & 0 & 0 & C_{67} & -C_{68} & -C_{69} & -C_{610} & 0 & 0 \\ 0 & 0 & 0 & 0 & 0 & 0 & 0 & 0 & -1 & 0 & 1 & 0 \\ 0 & 0 & 0 & 0 & 0 & 0 & 0 & 0 & 0 & -1 & 0 & 1 \\ 0 & 0 & 0 & 0 & 0 & 0 & 0 & 0 & 0 & 0 & R_x & 0 \\ 0 & 0 & 0 & 0 & 0 & 0 & 0 & 0 & 0 & 0 & R_y & 0 \\ 0 & 0 & 0 & 0 & -1 & 0 & 0 & 0 & 0 & 0 & S_x & M_b g/2 \\ 0 & 0 & 0 & 0 & 0 & -1 & 0 & 0 & 0 & 0 & S_y & M_b g C_{1213}/2 \end{bmatrix} = \begin{bmatrix} F_{W1} \\ N_{W1} \\ N_{W2} \\ N_{W3} \\ P_x \\ P_y \\ Q_x \\ Q_y \\ R_x \\ R_y \\ S_x \\ S_y \end{bmatrix} \quad (15)$$

The substituted parameters are described.

$$\begin{aligned}
 C_{31} &= -L_5 \sin \theta_1 + L_6 \cos \theta_1 + R & C_{32} &= L_5 \cos \theta_1 + L_6 \sin \theta_1 \\
 C_{33} &= -L_5 (\mu \cos \theta_1 + \sin \theta_1) + (L_{12} - L_6) (\mu \sin \theta_1 - \cos \theta_1) + \mu R \\
 C_{37} &= (L_3 + L_5 - R) \cos \theta_1 + (L_4 + L_6 - L_{11}) \sin \theta_1 & C_{38} &= -(L_3 + L_5 - R) \sin \theta_1 + (L_4 + L_6 - L_{11}) \cos \theta_1 \\
 C_{313} &= -2L_5 \sin \theta_1 + (2L_6 - L_{12}) \cos \theta_1 & C_{64} &= \mu R \\
 C_{67} &= (L_3 - R) \cos \theta_2 + L_4 \sin \theta_2 & C_{68} &= -(L_3 - R) \sin \theta_2 + L_4 \cos \theta_2 \\
 C_{69} &= (L_7 - R) \cos \theta_2 + L_8 \sin \theta_2 & C_{610} &= (L_7 - R) \sin \theta_2 - L_8 \cos \theta_2 \\
 C_{99} &= L \cos \theta_3 & C_{910} &= L \sin \theta_3 \\
 C_{125} &= (L_{11} - L_6 - L_{10}) \sin \theta_b + (L_9 - L_5) \cos \theta_b & C_{126} &= (L_{11} - L_6 - L_{10}) \cos \theta_b - (L_9 - L_5) \sin \theta_b \\
 C_{1213} &= (L_2 - L_{10}) \cos \theta_b - (L_1 + L_9 - R) \sin \theta_b
 \end{aligned}$$

From the 12x12 matrix equation (15), we determined the unknown contact forces as in equations (16) ~ (19).

$$F_{W1} = \left[\frac{(4M_{W1} + M_b)(A1_1 + C_{31}) - 2M_{W1}C_{313} - 2M_{W2}(A1_1 + C_{31} - C_{38})}{2A1_1} g \right. \\
 \left. + \frac{M_{W2}C_{68}A1_4}{A1_1 A1_2} g - \frac{M_b(C_{126} - C_{1213})(C_{37}C_{910} + C_{99}C_{38})}{2A1_1 A1_3} g \right] / 10^3 \quad (16)$$

$$N_{W1} = \left[-\frac{[(4M_{W1} + M_b)C_{31} - 2M_{W1}C_{313} - 2M_{W2}(-C_{31} + C_{38})]\mu}{2A1_1} g \right. \\
 \left. - \frac{M_{W2}\mu C_{68}A1_4}{A1_1 A1_2} g + \frac{M_b\mu(C_{126} - C_{1213})(C_{910}C_{37} + C_{99}C_{38})}{2A1_1 A1_3} g \right] / 10^3 \quad (17)$$

$$N_{W2} = \left[-\frac{(4M_{W1} + M_b)C_{31} - 2M_{W1}C_{313} - 2M_{W2}(C_{38} - C_{31})}{2A1_1} g \right. \\
 \left. + \frac{M_{W2}C_{68}}{A1_2} g - \frac{M_{W2}C_{68}A1_4}{A1_1 A1_2} g + \frac{M_b(C_{126} - C_{1213})A1_5}{2A1_2 A1_3} g \right] / 10^3 \quad (18)$$

$$N_{W3} = \left[-\frac{M_{W2}C_{68}}{A1_2} g - \frac{M_b(C_{126} - C_{1213})A1_4}{2A1_2 A1_3} g \right] / 10^3 \quad (19)$$

where,

$$\begin{aligned} A1_1 &= C_{33} - C_{31} + \mu C_{32}, & A1_2 &= \mu C_{67} - C_{64} - C_{68} \\ A1_3 &= C_{126} C_{99} + C_{125} C_{910}, & A1_4 &= C_{33} + \mu C_{37} - C_{38} \\ A1_5 &= C_{99} C_{610} + C_{68} C_{99} - C_{69} C_{910} + C_{67} C_{910} \end{aligned}$$

Here, θ_1 , θ_2 , θ_3 and θ_b are determined by the kinematics of the proposed mechanism. For this state, θ_2 is a function of θ_1 as described by equation (20) and θ_3 and θ_b are functions of θ_1 and θ_2 as in equations (21) and (22), respectively.

$$\begin{aligned} \theta_2 &= \tan^{-1} \left[\frac{L_4 K_1 - (L_3 - R) \left[L_4^2 + (L_3 - R)^2 - K_1^2 \right]^{1/2}}{(L_3 - R) K_1 + L_4 \left[L_4^2 + (L_3 - R)^2 - K_1^2 \right]^{1/2}} \right] & (20) \\ \theta_3 &= \tan^{-1} \left[\frac{\left[-2(L_{11} - L_6 - L_{10}) M_x M_y + (L_9 - L_5) B_5 \right] B_2^2 + B_4 M_y}{\left[-2(L_9 - L_5) M_x M_y + (L_{11} - L_6 - L_{10}) B_6 \right] B_2^2 + B_4 M_x} \right] \\ \theta_b &= \tan^{-1} \left[\frac{B_1^2 B_2^2 B_5 + B_4 \left[M_x (L_{11} - L_6 - L_{10}) + M_y (L_9 - L_5) \right]}{B_4 \left[M_x (L_9 - L_5) - M_y (L_{11} - L_6 - L_{10}) \right]} \right] & (21) \end{aligned}$$

where,

$$\begin{aligned} K_1(\theta_1) &= (L_3 - R) \cos \theta_1 + (L_4 - L_{11} + L_{12}) \sin \theta_1 \\ M_x(\theta_1, \theta_2) &= (L_3 + L_5 - R) \sin \theta_1 - (L_4 + L_6 - L_{11}) \cos \theta_1 \\ &\quad + (L_4 - L_8) \cos \theta_2 + (L_7 - L_3) \sin \theta_2 \\ M_y(\theta_1, \theta_2) &= -(L_3 + L_5 - R) \cos \theta_1 - (L_4 + L_6 - L_{11}) \sin \theta_1 \\ &\quad + (L_4 - L_8) \sin \theta_2 - (L_7 - L_3) \cos \theta_2 \\ B_1 &= \left[(L_9 - L_5)^2 + (L_{11} - L_6 - L_{10})^2 \right]^{1/2}, & B_2 &= \left(M_x^2 + M_y^2 \right)^{1/2} \\ B_3 &= -\left(-M_x^2 - M_y^2 + L^2 + B_1^2 \right)^2 + 4L^2 B_1^2 \\ B_4 &= -\left[M_x (L_{11} - L_6 - L_{10}) + M_y (L_9 - L_5) \right] \left(-B_1^2 - B_2^2 + L^2 \right) \\ &\quad + \left[M_x (L_9 - L_5) - M_y (L_{11} - L_6 - L_{10}) \right] B_3^{1/2} \\ B_5 &= M_x^2 - M_y^2 - B_1^2 + L^2, & B_6 &= -M_x^2 + M_y^2 - B_1^2 + L^2 \end{aligned}$$

For this state, the contact forces acting on the driving wheels are described in Fig. 7. The dotted bold lines result from the kinetic analysis as expressed in equations (16) ~ (19) and the solid lines represent the simulation results computed by the multi-body dynamic analysis software ADAMS™.

As shown in Fig. 7, it is allowable to assume that the WMR are in a quasi-static equilibrium. In Fig. 7, the steep changes in the simulation results are caused by the instantaneous collision between driving wheel 1 and the wall of the stair. From Fig. 7 (a) and (b), the

normal force N_{W1} at the point of contact C1 increases as the angle θ_1 of link 1 increases, while the friction force F_{W1} on C1 decreases. Therefore, as shown in equation (14), the coulomb friction does not work between the normal force and the friction force at the point of contact C1. This is due to the kinematics of the proposed linkage-type locomotive mechanism. The other friction forces F_{W2} and F_{W3} on the points of contact C2 and C3 can be determined by the coulomb friction.

For the WMR to be in the equilibrium state, the force F_{W1} can not exceed the friction force produced by the coulomb friction as expressed in equation (22).

$$F_{W1} \leq \mu N_{W1} \quad (22)$$

Fig. 8 shows the force difference between N_{W1} and F_{W1} .

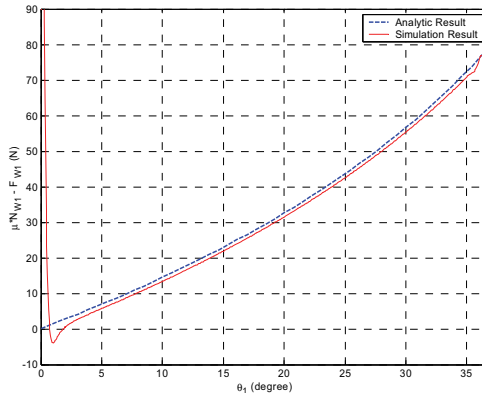


Fig. 8. Force difference between N_{W1} and F_{W1} for the state 1

As shown in Fig. 8, the force difference between N_{W1} and F_{W1} increases as the driving wheel 1 climbs up the stair, that is, as angle θ_1 increases. If the force difference has a negative value, the force F_{W1} must be higher than the coulomb friction N_{W1} that is needed for the WMR to be in the equilibrium state. As shown in equation (22), that situation can not happen absolutely. Therefore, whether the WMR can pass through the state 1 or not is determined at $\theta_1=0$. Consequently, to improve the ability for the WMR to climb up stairs, the force difference at $\theta_1=0$ will be selected as the first object function to be optimized.

The relative angle of link 1 to robot body is limited to avoid sticking conditions described in the previous section. The maximum allowable counter-clockwise angle of link 1 relative to the robot body is expressed in equation (23).

$$\theta_{1b_max} = \theta_{1_max} - \theta_b(\theta_{1_max}, \theta_2(\theta_{1_max})) , \text{ where, } \theta_{1_max} = \sin^{-1} \left[\frac{H_{S_max} - R}{L_{12}} \right] \quad (23)$$

Here, H_{S_max} is the maximum height of the stair for the WMR to climb and θ_b is determined by equations (20) and (21) at $\theta_1=\theta_{1_max}$.

3.2 For state 3

In this state, as shown in Fig. 5 (c), driving wheels 1 and 3 of the WMR contact with the floor of the stair and driving wheel 2 comes in contact with the wall of the stair. According to the characteristics of the points of contact, state 3 is divided into two sub-states as shown in Fig. 9. In Fig. 9 (a), the coulomb friction does not work on point of contact C3, while in Fig. 9 (b) the coulomb friction does not function on point of contact C2. This characteristic is due to the kinematic characteristics of the proposed passive linkage-type locomotive mechanism.

3.2.1 For state 3-1

In state 3-1, as shown in Fig. 9 (a), the relative angle of link 1 to the robot body is θ_{1_max} as expressed in equation (23). As mentioned above, the relationships between the normal forces and the friction forces are expressed in equation (24).

$$F_{W1} = \mu N_{W1}, \quad F_{W2} = \mu N_{W2}, \quad F_{W3} \neq \mu N_{W3} \quad (24)$$

In this state, the contact forces can be determined by the same manner as in section 3.1 and as described in equations (25) ~ (28).

$$N_{W1} = \left[\frac{(4M_{W1} + M_b)A2_1 - 2M_{W1}D_{313}(D_{64} + D_{67} - \mu D_{68})}{2\{(1 + \mu^2)(A2_1 + D_{32}D_{68}) - (D_{64} + D_{67})A2_2 + D_{68}A2_3\}}g \right] / 10^3 \quad (25)$$

$$- \frac{M_b(D_{126} + D_{1213})\{(\mu D_{38} - D_{32} - D_{37})(A2_5 - D_{910}D_{67}) - D_{910}D_{37}(D_{64} + D_{67} - \mu D_{68}) + D_{99}A2_1\}}{2\{(1 + \mu^2)(A2_1 + D_{32}D_{68}) - (D_{64} + D_{67})A2_2 + D_{68}A2_3\}A2_4}g$$

$$N_{W2} = \left[\frac{(4M_{W1} + M_b)\{\mu(A2_1 + D_{32}D_{68}) + D_{31}D_{68}\} - 2M_{W1}D_{313}\{\mu(D_{64} + D_{67}) + D_{68}\}}{2\{(1 + \mu^2)(A2_1 + D_{32}D_{68}) - (D_{64} + D_{67})A2_2 + D_{68}A2_3\}}g \right] / 10^3 \quad (26)$$

$$+ \frac{M_b(D_{126} + D_{1213})\{(D_{38} + \mu D_{37} - D_{31})A2_5 - D_{99}\{\mu(A2_1 + D_{32}D_{68}) + D_{31}D_{68}\} + D_{910}\{(\mu D_{64} - D_{68})D_{37} + D_{67}(D_{31} - D_{38})\}\}}{2\{(1 + \mu^2)(A2_1 + D_{32}D_{68}) - (D_{64} + D_{67})A2_2 + D_{68}A2_3\}A2_4}g$$

$$N_{W3} = \left[M_{W2}g - \frac{(4M_{W1} + M_b)A2_2(D_{64} + D_{67}) - 2M_{W1}(1 + \mu^2)D_{313}(D_{64} + D_{67})}{2\{(1 + \mu^2)(A2_1 + D_{32}D_{68}) - (D_{64} + D_{67})A2_2 + D_{68}A2_3\}}g \right] / 10^3 \quad (27)$$

$$+ \frac{M_bg(D_{126} + D_{1213})\{-(1 + \mu^2)\{(A2_5 + D_{68}D_{99} + D_{910}D_{64})D_{37}\} - D_{38}D_{99}(D_{64} + D_{67}) + A2_3(A2_5 + D_{68}D_{99} - D_{910}D_{67})\}}{2\{(1 + \mu^2)(A2_1 + D_{32}D_{68}) - (D_{64} + D_{67})A2_2 + D_{68}A2_3\}A2_4}g$$

$$F_{W3} = \left[\begin{array}{l} \frac{(4M_{W1} + M_b)D_{68}A2_2 - 2M_{W1}(1+\mu^2)D_{68}D_{313}}{2\{(1+\mu^2)(A2_1 + D_{32}D_{68}) - (D_{64} + D_{67})A2_2 + D_{68}A2_3\}}g \\ + \frac{M_bg(D_{126} + D_{1213})\left[\begin{array}{l} (1+\mu^2)\{D_{38}(A2_5 - D_{67}D_{910}) + D_{68}D_{37}D_{910}\} \\ - A2_2(A2_5 - D_{910}D_{67} + D_{68}D_{99}) \end{array}\right]}{2\{(1+\mu^2)(A2_1 + D_{32}D_{68}) - (D_{64} + D_{67})A2_2 + D_{68}A2_3\}A2_4} \end{array} \right] / 10^3 \quad (28)$$

Here, the substituted parameters are represented below.

$$\begin{aligned} D_{31} &= \mu(R - L_6 \sin \theta_1 - L_5 \cos \theta_1) + (L_6 \cos \theta_1 - L_5 \sin \theta_1) \\ D_{32} &= -(L_{12} - L_6)(\mu \cos \theta_1 + \sin \theta_1) - L_5(\mu \sin \theta_1 - \cos \theta_1) + \mu R \\ D_{37} &= -(L_3 + L_5 - R) \cos \theta_1 - (L_4 + L_6 - L_{11}) \sin \theta_1 \\ D_{38} &= -(L_3 + L_5 - R) \sin \theta_1 + (L_4 + L_6 - L_{11}) \cos \theta_1 \\ D_{313} &= (2L_6 - L_{12}) \cos \theta_1 - 2L_5 \sin \theta_1 & D_{64} &= R \\ D_{67} &= L_4 \sin \theta_2 + (L_3 - R) \cos \theta_2 & D_{68} &= -L_4 \cos \theta_2 + (L_3 - R) \sin \theta_2 \\ D_{69} &= -(L_7 - R) \cos \theta_2 - L_8 \sin \theta_2 & D_{610} &= -(L_7 - R) \sin \theta_2 + L_8 \cos \theta_2 \\ D_{99} &= L \cos \theta_3 & D_{910} &= L \sin \theta_3 \\ D_{125} &= (L_{11} - L_6 - L_{10}) \sin \theta_b + (L_9 - L_5) \cos \theta_b & D_{126} &= -(L_{11} - L_6 - L_{10}) \cos \theta_b + (L_9 - L_5) \sin \theta_b \\ D_{1213} &= (L_2 - L_{10}) \cos \theta_b - (L_1 + L_9 - R) \sin \theta_b \\ A2_1 &= D_{64}D_{38} + D_{67}D_{38} - D_{37}D_{68} - D_{32}D_{68} \\ A2_2 &= \mu D_{32} + D_{31} & A2_3 &= \mu D_{31} - D_{32} \\ A2_4 &= D_{99}D_{126} - D_{125}D_{910} & A2_5 &= D_{99}D_{610} - D_{910}D_{69} \end{aligned}$$

In this state, the angle of link 2 relative to the x-axis of the coordinates fixed in the ground is expressed in equation (29) due to the kinematics of the proposed mechanism.

$$\theta_2 = \tan^{-1} \left[\frac{L_4 K_2 - (L_3 - R) \left[L_4^2 + (L_3 - R)^2 - K_2^2 \right]^{1/2}}{(L_3 - R) K_2 + L_4 \left[L_4^2 + (L_3 - R)^2 - K_2^2 \right]^{1/2}} \right] \quad (29)$$

where, $K_2(\theta_1) = (L_3 - R) \cos \theta_1 + (L_4 - L_{11}) \sin \theta_1 + H_s$

θ_3 and θ_b are determined by equations (20) and (21), respectively. θ_1 , θ_2 , θ_3 , and θ_b are defined by the same manner described in section 3.1.

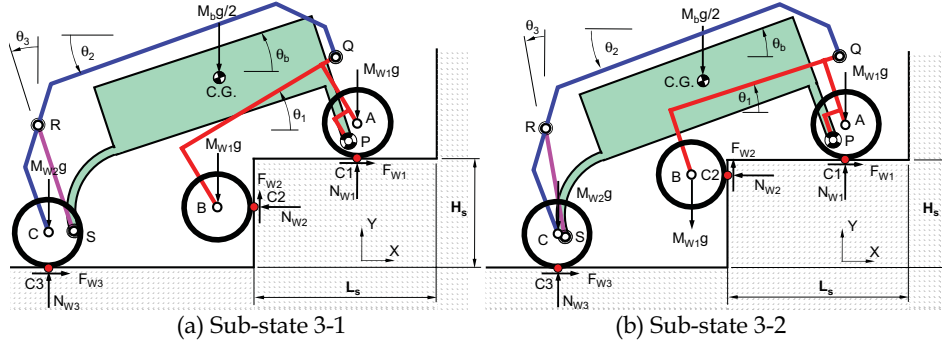


Fig. 9. Forces acting on the proposed WMR for the state 3

For this state, the contact forces acting on the driving wheels are described in Fig. 10; the dotted bold lines show the results of the kinetic analysis as expressed in equations (25) ~ (28) and the solid lines represent the simulation results obtained by ADAMSTTM.

As shown in Fig. 10, it is also allowable to assume that the WMR are in quasi-static equilibrium. In Fig. 10, the steep changes in the simulation results are also caused by the instantaneous collision between the driving wheel 2 and the wall of stair. As shown in Fig. 10 (c) and (d), the coulomb friction does not work between the normal force and the friction force at point of contact C3 as expressed in equation (24). This is also due to the kinematics of the proposed mechanism. The other friction forces F_{W1} and F_{W2} on points of contact C1 and C2 can be determined by the coulomb friction as shown in equation (24).

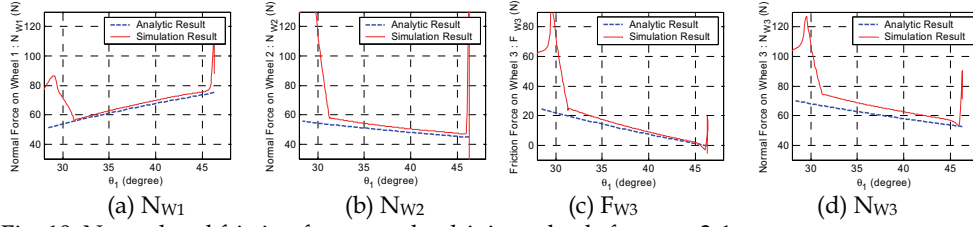


Fig. 10. Normal and friction forces on the driving wheels for state 3-1

3.2.2 For state 3-2

As link 1 rotates clockwise relative to the robot body, the WMR comes to the state 3-2, as shown in Fig. 9 (b). As mentioned above, the relationships between the normal forces and the friction forces at this state are expressed in equation (30).

$$F_{W1} = \mu N_{W1}, \quad F_{W2} \neq \mu N_{W2}, \quad F_{W3} = \mu N_{W3} \quad (30)$$

In this state, the normal forces and the friction forces can be determined in the same manner as in section 3.1 and as described in equations (31) ~ (34).

$$N_{W1} = \left[\begin{array}{l} -\frac{(4M_{W1} + M_b)E_{33}}{2A3_1}g + \frac{M_{W1}E_{313}}{A3_1}g + \frac{M_{W2}(E_{38} - E_{33})}{A3_1}g - \frac{M_{W2}E_{68}}{A3_2}g \\ -\frac{M_{W2}E_{68}A3_4}{A3_1A3_2}g - \frac{M_bE_{99}E_{38}(E_{126} + E_{1213})}{2A3_1A3_3}g + \frac{M_b(E_{126} + E_{1213})A3_5}{2A3_2A3_3}g \\ + \frac{M_b(E_{126} + E_{1213})\{A3_4(A3_5 + E_{910}E_{67}) + E_{910}A3_6\}}{2A3_2A3_2A3_3}g \end{array} \right] / 10^3 \quad (31)$$

$$N_{W2} = \left[\begin{array}{l} -\frac{(4M_{W1} + M_b)\mu E_{33}}{2A3_1}g + \frac{M_{W1}\mu E_{313}}{A3_1}g - \frac{M_{W2}\mu E_{68}A3_4}{A3_1A3_2}g \\ + \frac{M_{W2}\mu(E_{38} - E_{33})}{A3_1}g - \frac{M_b\mu E_{38}E_{99}(E_{126} + E_{1213})}{2A3_1A3_3}g \\ + \frac{M_b\mu(E_{126} + E_{1213})\{A3_4(A3_5 + E_{67}E_{910}) + E_{910}A3_6\}}{2A3_1A3_2A3_3}g \end{array} \right] / 10^3 \quad (32)$$

$$F_{W2} = \left[\begin{array}{l} \frac{(4M_{W1} + M_b)(\mu E_{32} + E_{31})}{2A3_1}g - \frac{M_{W1}E_{313}}{A3_1}g \\ + \frac{M_{W2}(\mu E_{32} + E_{31} - E_{38})}{A3_1}g + \frac{M_{W2}E_{68}A3_4}{A3_1A3_2}g + \frac{M_bgE_{38}E_{99}(E_{126} + E_{1213})}{2A3_1A3_3}g \\ - \frac{M_b(E_{126} + E_{1213})\{A3_4(A3_5 + E_{910}E_{67}) + E_{910}A3_6\}}{2A3_1A3_2A3_3}g \end{array} \right] / 10^3 \quad (33)$$

$$N_{W3} = \left[\frac{M_{W2}E_{68}}{A3_2}g - \frac{M_b(E_{126} + E_{1213})A3_5}{2A3_2A3_3}g \right] / 10^3 \quad (34)$$

Here, the substituted parameters are represented below.

$$\begin{aligned} E_{31} &= \{\mu(R - L_6 \sin \theta_1 - L_5 \cos \theta_1) + (L_6 \cos \theta_1 - L_5 \sin \theta_1)\} & E_{32} &= -(L_{12} - L_6) \sin \theta_1 - L_5 \cos \theta_1 \\ E_{33} &= -(L_{12} - L_6) \cos \theta_1 + L_5 \sin \theta_1 - R & E_{37} &= -(L_3 + L_5 - R) \cos \theta_1 + (L_4 + L_6 - L_{11}) \sin \theta_1 \\ E_{38} &= -(L_3 + L_5 - R) \sin \theta_1 - (L_4 + L_6 - L_{11}) \cos \theta_1 & E_{313} &= (2L_6 - L_{12}) \cos \theta_1 - 2L_5 \sin \theta_1 \\ E_{64} &= \mu R & E_{67} &= L_4 \sin \theta_2 + (L_3 - R) \cos \theta_2 \\ E_{68} &= -L_4 \cos \theta_2 - (L_3 - R) \sin \theta_2 & E_{69} &= -(L_7 - R) \cos \theta_2 + L_8 \sin \theta_2 \\ E_{610} &= -(L_7 - R) \sin \theta_2 - L_8 \cos \theta_2 & E_{99} &= L \cos \theta_3 & E_{910} &= L \sin \theta_3 \\ E_{125} &= -(L_{11} - L_6 - L_{10}) \sin \theta_b + (L_9 - L_5) \cos \theta_b & E_{126} &= -(L_{11} - L_6 - L_{10}) \cos \theta_b - (L_9 - L_5) \sin \theta_b \\ E_{1213} &= -(L_2 - L_{10}) \cos \theta_b - (L_1 + L_9 - R) \sin \theta_b & A3_1 &= E_{31} + \mu E_{32} - E_{33} & A3_2 &= \mu E_{67} + E_{64} + E_{68} \\ A3_3 &= -E_{99}E_{126} + E_{125}E_{910} & A3_4 &= -E_{31} + \mu E_{37} + E_{38} \\ A3_5 &= E_{68}E_{99} + E_{99}E_{610} - E_{69}E_{910} - E_{910}E_{67} & A3_6 &= E_{67}E_{31} + E_{64}E_{37} - E_{38}E_{67} + E_{68}E_{37} \end{aligned}$$

θ_1 , θ_2 , θ_3 , and θ_b are defined in the same manner described in section 3.1. θ_2 , θ_3 , and θ_b are determined from equations (29), (20) and (21), respectively.

For this state, the contact forces acting on the driving wheels are described in Fig. 11. The dotted bold lines show the results from the kinetic analysis as expressed in equations (31) ~ (34) and the solid lines represent the simulation results by ADAMSTTM.

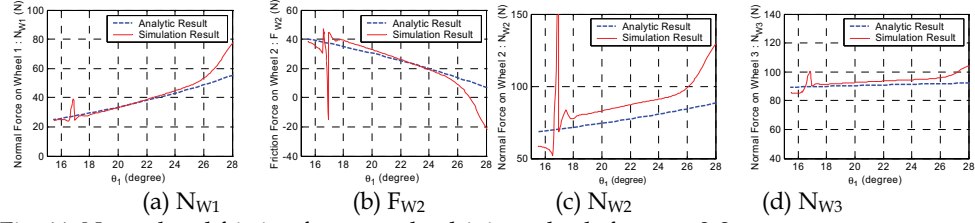


Fig. 11. Normal and friction forces on the driving wheels for state 3-2

As shown in Fig. 11, it is also allowable to assume that the WMR are in a quasi-static equilibrium. In Fig. 11, the rapid changes in the simulation results are caused by the impact between driving wheel 2 and the wall of the stair. From Fig. 11 (b) and (c), the normal force N_{W2} at point of contact C2 decreases as the angle θ_1 of link 1 decreases, while the friction force F_{W2} on C2 increases. Therefore, as shown in the equation (30), the coulomb friction does not work between the normal force and the friction force at point of contact C2. This is also due to the kinematics of the proposed linkage-type locomotive mechanism. The other friction forces F_{W1} and F_{W3} on points of contact C1 and C3 can be determined by the coulomb friction.

For state 3-1, for the WMR to be in the equilibrium state, the force F_{W3} can not exceed the friction force produced by the coulomb friction as expressed in equation (35).

$$F_{W3} \leq \mu N_{W3} \quad (35)$$

Similarly, for state 3-2, the force F_{W2} can not exceed the friction force produced by the coulomb friction as expressed in equation (36).

$$F_{W2} \leq \mu N_{W2} \quad (36)$$

Fig. 12 shows the force differences for state 3-1 and the state 3-2. As shown in Fig. 12 (a) and (b), the force difference between N_{W3} and F_{W3} and the force difference between N_{W2} and F_{W2} decrease as driving wheel 2 climbs up the wall of the stair, that is, θ_1 decreases. If equation (36) is satisfied by the design variables of the WMR, equation (35) is satisfied sufficiently for the range of θ_1 . Therefore, whether the WMR is able to pass through state 3 is determined when the driving wheel 2 comes in contact with the top-edge of the wall of the step, that is, $\theta_1 = \theta_{1_3}$ as expressed in equation (37). Consequently, to improve the ability of the WMR to climb up the stair, the force difference between N_{W2} and F_{W2} at $\theta_1 = \theta_{1_3}$ will be considered as the second object function.

$$\theta_{1_3} = \sin^{-1} \left(\frac{R}{L_{12}} \right) \quad (37)$$

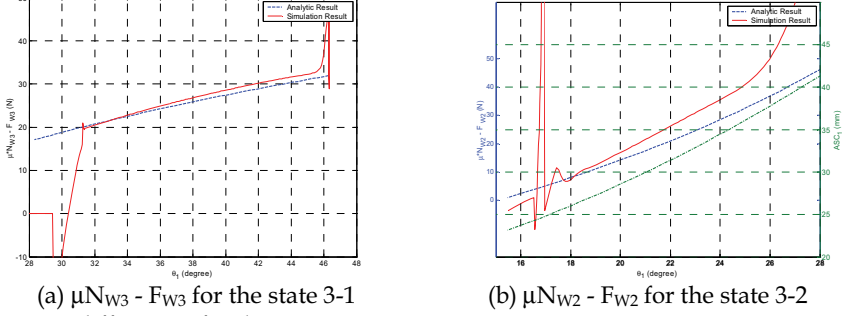


Fig. 12. Force differences for the state 3

In Fig. 12 (b), the dash-dotted line represents the distance between the outer circle of driving wheel 1 and the wall of the stair. We call this value the first 'Anti-Sticking Constraint(ASC)'. To prevent the WMR from falling into the sticking condition, the ASC_1 as expressed in equation (38) must be greater than a certain offset value at $\theta_1=\theta_{1_3}$. The offset value (ASC_{1_off}) is a fully bounded value as described in equation (39). If the ASC_{1_off} increases, the possibility of the sticking condition occurring for this state decreases, even though the WMR climbs the stair with the smaller length than the length of the step L_S .

$$ASC_1 = L_S - L_{12} \cos(\theta_1) \quad (38)$$

$$ASC_1 \geq ASC_{1_off} \quad \text{where, } 0 \leq ASC_{1_off} \leq R \quad (39)$$

3.2 For State 7

In this state, as shown in the Fig. 5 (g) and Fig. 13, driving wheel 1 comes into contact with the floor of the stair and wheel 3 comes into contact with the wall of the stair. For this state, we assumed that the proposed linkage mechanism has zero degrees-of-freedom. From this assumption, with the exception of the driving wheels, the WMR will move as a rigid body. In this state, the relationships between the normal forces and the friction forces become as found in equation (40).

$$F_{W1} = \mu N_{W1}, \quad F_{W3} = \mu N_{W3} \quad (40)$$

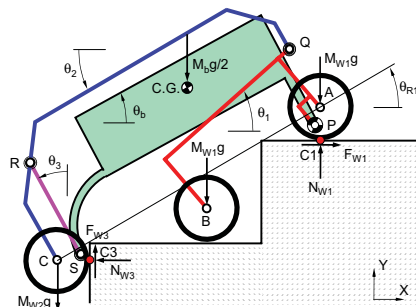


Fig. 13. Forces acting on the proposed WMR for state 7

If the WMR is in a quasi-static equilibrium state, the contact forces can be determined by Newton's 2nd law of motion. The normal forces on points of contact C1 and C3 are determined as described in equations (41) ~ (42).

$$N_{W1} = \left[\frac{(4M_{W1} + 2M_{W2} + M_b)}{2(1+\mu^2)} g \right] / 10^3 \quad (41)$$

$$N_{W3} = \left[\frac{(4M_{W1} + 2M_{W2} + M_b)\mu}{2(1+\mu^2)} g \right] / 10^3 \quad (42)$$

For this state, the contact forces acting on the driving wheels are described in Fig. 14. The dotted bold lines show the results of the kinetic analysis as expressed in equations (41) ~ (42) and the solid lines represent the results by ADAMSTM.

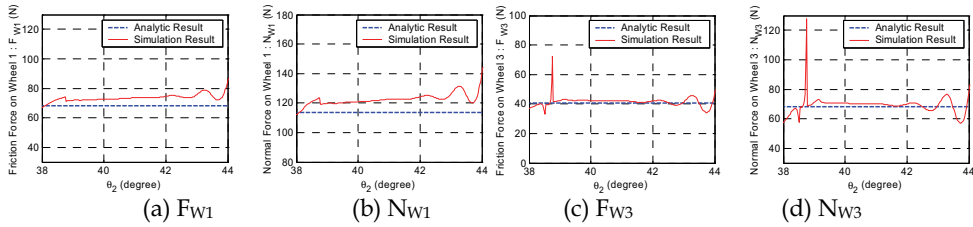


Fig. 14. Normal and friction forces on the driving wheel 1 and 3 for the state 7

In the simulation results, shown in Fig. 14, the oscillation of the forces is caused by the non-rigid body motion of the proposed linkage mechanism. However, it is allowable to assume that the WMR is in a quasi-static equilibrium and moves as a rigid body.

For the WMR to overcome this state, the z-axis moment acting on the robot about the point of contact C1 must be a negative value (Fig. 13). The z-axis moment about point of contact C1 is expressed in equation (43).

$$(M_z)_{C1} = [-N_{W3}(D_1 + \mu D_2) + M_{W2}gD_3 + M_{W1}gD_4 + M_bgD_5] / 10^3$$

where, $D_1 = -(L_3 - R)\cos\theta_1 - (L_4 - L_{11})\sin\theta_1 + (L_3 - R)\cos\theta_2 + L_4\sin\theta_2 - R$

$$D_2 = (L_3 - R)\sin\theta_1 - (L_4 - L_{11})\cos\theta_1 - (L_3 - R)\sin\theta_2 + L_4\cos\theta_2 - R \quad (43)$$

$$D_3 = (L_3 - R)\sin\theta_1 - (L_4 - L_{11})\cos\theta_1 - (L_3 - R)\sin\theta_2 + L_4\cos\theta_2, D_4 = L_{12}\cos\theta_1$$

$$D_5 = -L_5\sin\theta_1 + L_6\cos\theta_1 + (L_1 + L_5 - R)\sin\theta_b + (L_{11} - L_2 - L_{10})\cos\theta_b$$

Here, θ_1 , θ_2 , θ_3 and θ_b are described in the equation (44).

$$\begin{aligned} \theta_1' - \theta_{R1} + \theta_{R2} &\leq \theta_1 \leq \theta_1' & \theta_2' - \theta_{R1} + \theta_{R2} &\leq \theta_2 \leq \theta_2' \\ \theta_3' - \theta_{R1} + \theta_{R2} &\leq \theta_3 \leq \theta_3' & \theta_b' - \theta_{R1} + \theta_{R2} &\leq \theta_b \leq \theta_b' \end{aligned} \quad (44)$$

where, $\theta_{R1} = \sin^{-1} \left[\frac{D_1 + R}{L_R} \right]$ $\theta_{R2} = \sin^{-1} \left[\frac{H_S + R}{L_R} \right]$

Here, θ_1 , θ_2 , θ_3 and θ_b are described in equation (45) and D_1 is computed from equation (43) when $\theta_1=\theta_1'$ and $\theta_2=\theta_2'$. L_R is the axle length between driving wheels 1 and 3, when the relative angle of link 1 to the robot body is the maximum allowable angle θ_{1b_max} in equation (23), and is computed by equation (46).

$$\begin{aligned} \theta_1' &= \theta_{1\beta} & \theta_2' &= \theta_2'' + \theta_{incr} & \theta_3' &= \theta_3'' + \theta_{incr} & \theta_b' &= \theta_b'' + \theta_{mcr} \\ \text{where, } \theta_{incr} &= \theta_{1\beta} - \theta_{1\alpha} & \theta_{1\alpha} &= \sin^{-1} \left[\frac{H_{S_max} - R}{L_{12}} \right] & \theta_{1\beta} &= \sin^{-1} \left[\frac{H_S}{L_{12}} \right] \end{aligned} \quad (45)$$

$$L_R = \sqrt{\left\{ -(L_3 - R) \sin(\theta_2'') + L_4 \cos(\theta_2'') - (L_4 - L_{11}) \cos(\theta_{1\alpha}) + (L_3 - R) \sin(\theta_{1\alpha}) \right\}^2 + \left\{ (L_3 - R) \cos(\theta_2'') + L_4 \sin(\theta_2'') - (L_4 - L_{11}) \sin(\theta_{1\alpha}) - (L_3 - R) \cos(\theta_{1\alpha}) \right\}^2}^{1/2} \quad (46)$$

θ_2'' , θ_3'' and θ_b'' are computed from equations (20) and (21) at $\theta_1=\theta_{1\alpha}$ respectively.

For this state, the z-axis moment is described in Fig. 15, according to the change of θ_2 . As shown in Fig. 15, from the analytic and simulation results, the z-axis moment increases as driving wheel 3 climbs the wall of the stair, that is, θ_2 decreases. So, for the WMR to climb up the stair, the value of the z-axis moment must be sufficiently less than zero at the moment that driving wheel 3 comes in contact with the top-edge of the wall of the stair.

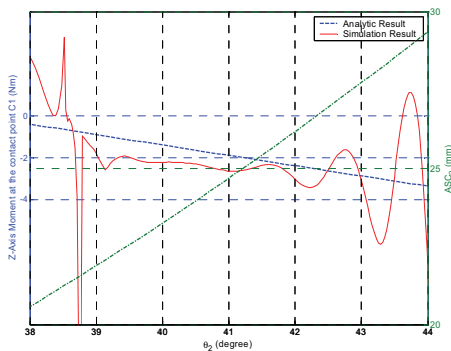


Fig. 15. Z-axis moment about the point of contact C1 for the state 7

In Fig. 15, the dash-dotted line represents the distance between the outer circle of driving wheel 2 and the wall of the stair. We call the value the second 'Anti-Sticking Constraint'. To prevent the WMR from falling into the sticking condition, the ASC_2 as expressed in equation (47) must be greater than a certain offset value (ASC_{2_off}) for all of the range of θ_2 . The

ASC_{2_off} is a fully bounded value as described in equation (48). If the ASC_{2_off} increases, the possibility of the sticking condition occurring for this state decreases, even though the WMR climbs the stair with the smaller length than L_s .

$$ASC_2 = L_s - L_4 \cos(\theta_2) + (L_3 - R) \sin(\theta_2) + (L_{12} + L_4 - L_{11}) \cos(\theta_1) - (L_3 - R) \sin(\theta_1) \quad (47)$$

$$ASC_2 \geq ASC_{2_off} \quad \text{where, } 0 \leq ASC_{2_off} \leq R \quad (48)$$

Consequently, to optimize the design variables of the proposed WMR, we designate the negative z-axis moment about point of contact C1 at $\theta_2=\theta_{2l}$ as expressed in equation (49) as the third object functions.

$$\theta_{2l} = \theta_2' - \theta_{R1} + \theta_{R2} \quad (49)$$

4. Optimization

In the previous section, we analyzed the kinetics of the WMR with the proposed passive linkage-type locomotive mechanism for several states. From the results of the kinetics, we determined the three object functions to improve the ability of the WMR to climb the stair. Additionally, to prevent the WMR from falling into the sticking conditions as described in section 2, two anti-sticking constraints (ASCs) were described.

In this section, we optimized the design variables of the proposed WMR by using three object functions. The first object function results from the kinetics for state 1 and is described in equation (50). In equation (5), N_{W1} and F_{W1} are computed by equation (16) and (17), respectively. θ_2 , θ_3 , and θ_b are determined from equations (20) and (21), respectively.

$$OF_1 = \mu N_{W1} - F_{W1}, \quad \text{when } \theta_1 = 0 \quad \text{for state 1} \quad (50)$$

The second object function results from the kinetics for state 3-2 and represents the force difference between N_{W2} and F_{W2} on point of contact C1 at the moment that driving wheel 2 comes in contact with the top-edge of the wall of the step. This object function is expressed in equation (51). The N_{W2} and F_{W2} are computed from equations (32) and (33), respectively. θ_2 , θ_3 , and θ_b are determined from equations (29) and (21), respectively.

$$OF_2 = \mu N_{W2} - F_{W2}, \quad \text{when } \theta_1 = \theta_{1_3} \quad \text{for state 3-2} \quad (51)$$

The third object function results from the kinetics for state 7 and represents the negative z-axis moment on the WMR about the point of contact C1 at the moment that the driving wheel 3 comes in contact with the top-edge of the wall of the step. This object function is described by equation (52) where the normal force N_{W3} and the substituted parameters (D_1 , D_2 , D_3 , D_4 and D_5) are computed from equations (42) and (43), respectively.

$$OF_3 = [N_{W3}(D_1 + \mu D_2) - M_{W2}gD_3 - M_{W1}gD_4 - M_bgD_5]/10^3 \quad \text{for state 7} \quad (52)$$

when $\theta_1 = \theta_1' - \theta_{R1} + \theta_{R2}$, $\theta_2 = \theta_2' - \theta_{R1} + \theta_{R2}$, $\theta_3 = \theta_3' - \theta_{R1} + \theta_{R2}$, $\theta_b = \theta_b' - \theta_{R1} + \theta_{R2}$

From the three object functions, we accomplished the optimization of the design variables with the two ASCs as described in equations (38) and (47), respectively, by using the multi-objective optimization method (Gembicki, 1974). The parameters used in the optimization method are listed in Table 1.

Object Functions & Parameters		Values	Object Functions & Parameters		Values
Goal of Object Function	OF ₁ (N)	0.3	Dimension of Stair	L _S (mm)	280.0
	OF ₂ (N)	1.0		H _S (mm)	165.0
	OF ₃ (Nm)	0.3		H _{S_max} (mm)	165.0
ASC _{1-off} (mm)		23.0	ASC _{2-off} (mm)		20.0

Table 1. Object functions and parameters used in the optimization.

The convergence of the three object functions and the optimized design variables, after the optimization process, are showed in Fig. 16 and Table 2, respectively.

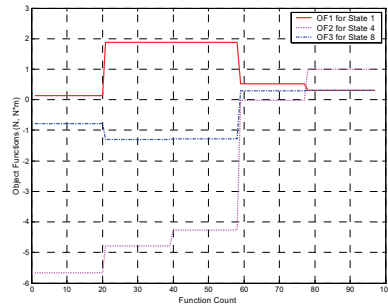


Fig. 16. Convergence of OF₁, OF₂ and OF₃ by the multi-objective optimization method

Design Parameter	Initial Value	Optimal Value	Design Parameter	Initial Value	Optimal Value
L ₁ (mm)	160.0	165.0	L ₂ (mm)	261.0	263.2
L ₃ (mm)	70.0	73.7	L ₄ (mm)	455.0	444.6
L ₅ (mm)	-40.0	-33.9	L ₆ (mm)	40.0	30.7
L ₇ (mm)	110.0	112.6	L ₈ (mm)	-50.0	-48.0
L ₉ (mm)	10.0	12.6	L ₁₀ (mm)	10.0	8.0
L ₁₁ (mm)	440.0	425.2	L ₁₂ (mm)	235.0	225.1
R (mm)	60.0		M _b (kg)	10.9	10.5
M _{w1} (kg)	3.5	3.7	M _{w2} (kg)	2.8	3.2
μ	0.6		OF ₁ (N)	0.1	0.3
OF ₂ (Nm)	-5.7	1.0	OF ₃ (N)	-0.8	0.3

Table 2. The optimal design variables of the proposed WMR

5. Fabrication

Based on the results of optimization, we fabricated the prototype of proposed mobile robot. It is composed mainly of three parts: the driving wheel assembly, the proposed passive linkage mechanism, and the robot body. A motor, a digital encoder, and a harmonic gear are assembled inside the wheel to afford a compact driving unit. The wheel-in motor is shown in Fig. 17.

50Watt Maxon EC flat motors, 500pulse USDigital optical encoders, and 160:1 HarmonicDrive® harmonic gears are used. The passive mechanism is composed of a four bar linkage and a limited pin joint. The pin joint confines the working range of the four bar linkage mechanism to avoid overturning. An electrical subsystem comprised of a single board computer (SBC), a controller area network (CAN) module, a wireless LAN, a motor controller, and Li-ion batteries are placed in the robot body. The prototype of ROBHAZ-6W has eight DOFs: six DOFs for the robot body and two DOFs for the right and left sides of the passive linkage mechanism.



Fig. 17. Wheel-in motor

The configurations of the right and left sides of the proposed linkage mechanisms are independently changed according to the environment. And the axle distance between the first and the second driving wheels is determined by considering the length of the stair and the axle distance between the 1st and the 3rd driving wheels is designed according to the height of the stairs that the mobile robot will ascend. The prototype of proposed mobile robot is shown in Fig. 18, and the design parameters are described in Table 3. It can navigate stairs and hazardous terrain areas by using the proposed four bar linkage mechanism.

Item	Parameters	Value	Parameters	Values
Dimensions (mm)	L ₁	165.0	L ₈	-48.0
	L ₂	263.2	L ₉	12.6
	L ₃	73.7	L ₁₀	8.0
	L ₄	444.6	L ₁₁	425.2
	L ₅	-33.9	L ₁₂	225.1
	L ₆	30.7	R	60.0
	L ₇	112.6		
Mass (kg)	Robot Body	10	Wheels & Linkages	18
	Batteries	3	Total	31

Table 3. Design parameters of ROBHAZ-6Wheel

Fig. 19 shows a block diagram of the control system for the robot. This control system is composed of the following: a command PC and a joystick at a remote control site, a single board computer (SBC), six motors and controller, wireless LAN equipment, and a controller. The command PC at the remote site communicates with an SBC in the ROBHAZ-6W. The command PC allows an operator to control the mobile robot movement by joystick and receives angular velocity of wheels by CAN Bus. The motor controllers each have a microprocessor and the six wheel-in motors described in the previous section can be independently controlled. These controllers are connected to the SBC by a CAN bus. This kind of control structure enables the SBC to control the six motors in real time.

All the programs are coded by MS Visual C++ on an MS-Windows 2000 Operating system. The programs are composed of three major parts: a TCP/IP server program, a robot program, and a control program. The TCP/IP server program connects the mobile robot to the remote control PC. The mobile robot program calculates the forward/inverse kinematics of the mobile robot, gives motor driving commands via a CAN bus.



Fig. 18. Prototype of the proposed stair-climbing mobile robot

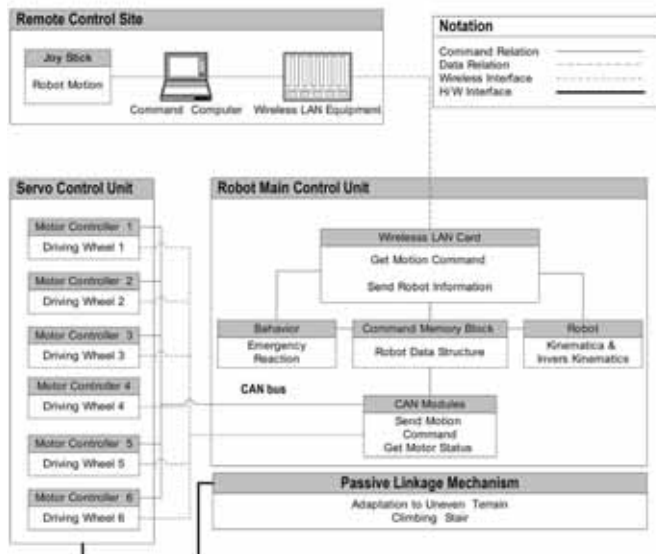


Fig. 19. The full system of proposed mobile robot

6. Experiment

Experimental investigation is performed to prove kinetic analysis and to Fig. out the characteristics of climbing states. We accomplished the experiments with the fabricated stairs of which length and height is 150 mm and 260mm and the indoor stair in KAIST of which length and height is 165 mm and 280mm, respectively. The climbing motions of the fabricated and real stairs are shown in Fig. 20 and Fig. 21, respectively.

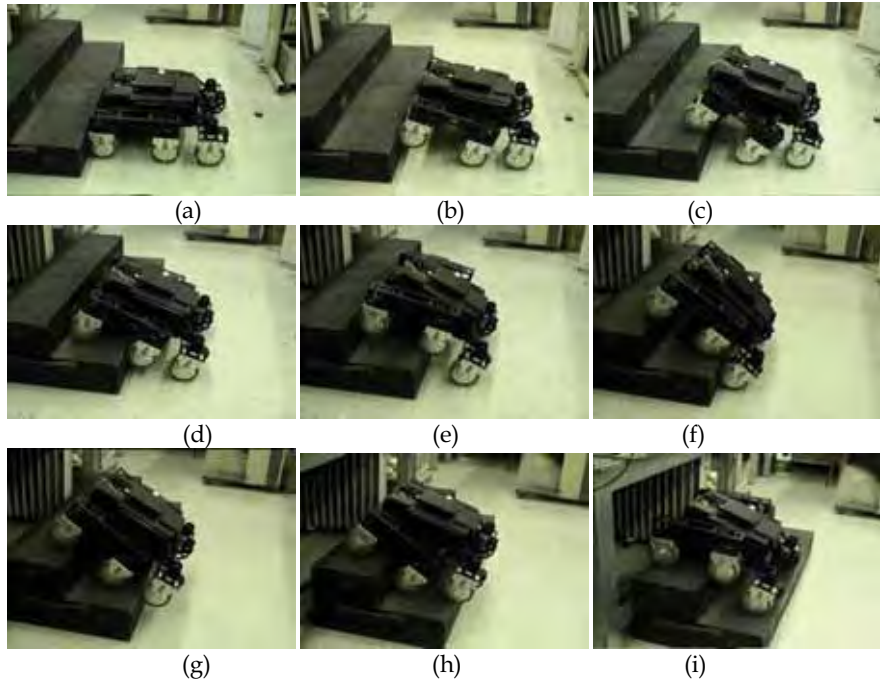


Fig. 20. Experiments for climbing the fabricated stairs

Though the mobile robot is optimized to the stair of which length and height is 165 mm and 280 mm, the proposed mobile robot can easily climb and adapt to the stairs if axle distance is adjusted not to fall in sticking condition.

Table 4 shows the result of adjustment of axle distance to climb the stairs. As L_4 and L_{12} become small, WMR overcome the state1 easily with low friction coefficient. Though WMR has a good ability to overcome state1 with small L_4 and L_{12} , they should not be smaller than specific values which are determined in state 5 and state 7. In state 5 and state 7, there are two important issues which confine minimum length of L_4 and L_{12} . At first, wheel 1 should be in contact with floor of second stair when wheel 3 start climbing up the wall of first stair not to slip on the wall of stair. Second, not to overturn in state 5, L_{12} should be long enough for the contact point of wheel 2 and floor to stay on the right side of WMR's centre of mass.

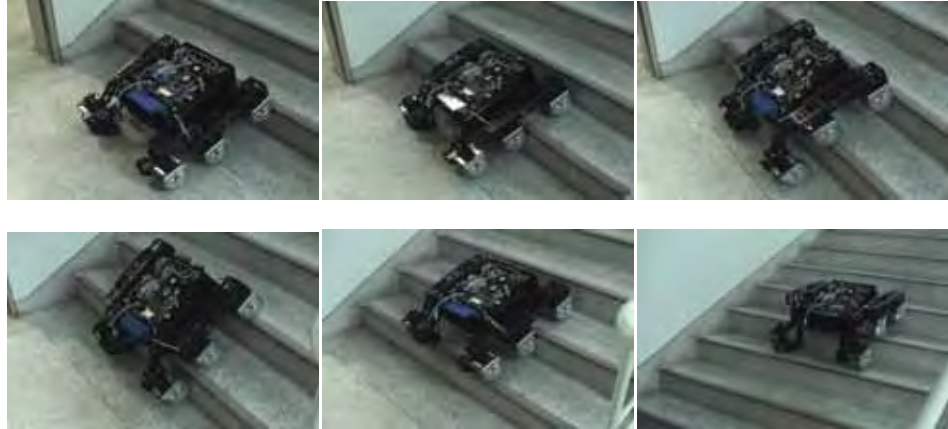


Fig. 21. Experiments for climbing the real stair

L_4	L_{12}	43.5cm	45.5cm	47.5cm
22cm		Overturn (State5)	Overturn (State5)	Overturn (State7)
25cm		Overturn(State5)	Success	Success
28cm		Slipping (State7)	Success	.

Table 4. Climb characteristics in state5 and state7

7. Conclusion

In order to be utilized in building inspection, building security, and military reconnaissance, a new type of WMR was designed with a passive linkage-type locomotive mechanism for improved adaptability to rough terrain and stair-climbing without the active control techniques. Two designed concepts, 'adaptability' and 'passivity', were considered for the design of the linkage-type locomotive mechanism of the WMR. The proposed mechanism, composed of a simple 4-bar linkage mechanism and a limited pin joint, allows the WMR to adapt passively to rough terrain and to climb stairs.

A state analysis was carried out to determine the states that primarily influence the WMR's ability to climb the stair. For the several dominant states suggested from the state analysis, a kinetic analysis was accomplished in order to improve the WMR's ability to climb the stair. The validation of the kinetic analysis was done for the states using ADAMS™. The object functions were formulated from the kinetics of the WMR and we optimized passive link mechanism using the multi-objective optimization method. The proposed WMR with the optimal design values could climb a stair with a height about three times the wheel radius.

8. References

- Estier, T.; Crausaz, Y.; Merminod, B.; Lauria, M.; Piguet, R. & Siegwart, R. (2000). *Proc. of Space and Robotics 2000*, Albuquerque, USA, Feb. 27- Mar. 2
- Estier, T.; Crausaz, Y.; Merminod, B.; Lauria, M.; Piguet, R. & Siegwart, R. (2000). An Innovative Space Rover with Extended Climbing Abilities, In : *Proc. of Space & Robotics*, the Fourth International Conference and Exposition on Robotics in Challenging Environments, New Mexico
- Gembicki, F. W. (1974). *Ph.D. Dissertation*, Case Western Reserve Univ., Cleveland, Ohio
- Iwamoto, T. & Yamamoto, H. (1985). *J. of Robotic Systems*, Vol.2 No.1, pp.125-134
- Iwamoto, T. & Yamamoto, H. (1990). *J. of Mechanical Design*, Vol.112, pp.289-294
- Kohler, G. W.; Selig, M. & Salaske, M. (1976). *Proc. of 24th Conf. on Remote Systems Technology*, pp.196-218
- Kim, H. H. (1999). *M.S. Dissertation*, KAIST, Daejeon, Korea
- Lee, C. H.; Woo, C. K.; Kim, H. H. & Kwak, Y. K. (2000). *KSAE 2000 Spring Conference*
- Maeda, Y.; Tsutani, S. & Hagihara, S. (1985). *Int. Conf. of Robotics and Automation*, pp.421-428
- Muir, P. F. & Neuman, C. P. (1987). *J. of Robotic Systems*, Vol.4, No.2, pp.281-340
- Volpe, R.; Ohm, T.; Petras, R.; Welch, R.; Balaram, J. & Ivlev, R. (1997). *Proc. of IEEE/RSJ Int. Conf. on Intelligent Robots and Systems*, Grenoble France, Sep. 7-11
- Woo, C. K.; Kim, M. S.; Kim, S. H. & Kwak, Y. K. (2001). *Proc. of Int. Conf. on Control, Automation and Systems*, Cheju, Korea, Oct. 17-21, pp.146-149
- Woo, C. K.; Cho, C. H.; Kang, S. C.; Shin, K. C.; Kim, M. S.; Kim, S. H. & Kwak, Y. K. (2002). *Proc. of ESDA2002; 6th biennial Conf. on Engineering Systems Design and Analysis*, Istanbul, Turkey, July 8-11
- Yoneda, K.; Ota, Y. & Hirose, S. (1997). *J. of Robotic Systems*, Vol.15, No.8, pp.1188-1193

City-Climber: A New Generation Wall-climbing Robots

Jizhong Xiao and Ali Sadegh

*The City College, City University of New York
USA*

1. Introduction

1.1 Motivations

An increasing interest in the development of special climbing robots has been witnessed in last decade. Motivations are typically to increase the operation efficiency in dangerous environments or difficult-to-access places, and to protect human health and safety in hazardous tasks. Climbing robots with the ability to maneuver on vertical surfaces are currently being strongly requested by various industries and military authorities in order to perform dangerous operations such as inspection of high-rise buildings, spray painting and sand blasting of gas tanks, maintenance of nuclear facilities, aircraft inspection, surveillance and reconnaissance, assistance in fire fighting and rescue operations, etc. Such capabilities of climbing robots would not only allow them to replace human workers in those dangerous duties but also eliminate costly scaffolding.

1.2 Related Work

One of the most challenging tasks in climbing robot design is to develop a proper adhesion mechanism to ensure that the robot sticks to wall surfaces reliably without sacrificing mobility. So far, four types of adhesion techniques have been investigated: 1) magnetic devices for climbing ferrous surfaces; 2) vacuum suction techniques for smooth and nonporous surfaces; 3) attraction force generators based on aerodynamic principles; 4) biomimetic approaches inspired by climbing animals.

Magnetic adhesion devices are most promising for robots moving around on steel structures. Robots using permanent magnets or electromagnets can be found in (Grieco et al., 1998), (Guo et al., 1997), (Hirose et al., 1992), (Wang et al., 1999), (Shen et al., 2005), and (Kalra et al., 2006) for climbing large steel structures and in (Kawaguchi et al., 1995), (Sun et al., 1998) for internal inspection of iron pipes. However, their applications are limited to steel walls due to the nature of magnets.

In applications for non-ferromagnetic wall surfaces, climbing robots most generally use vacuum suctions to produce the adhesion force. Examples of such robots include the ROBUG robots (Luk et al., 1996) at University of Portsmouth, UK, NINJA-1 robot (Nagakubo & Hirose, 1994) at Tokyo Institute of Technology, ROBIN (Pack 1997) at Vanderbilt University, FLIPPER & CRAWLER robots (Tummala et al., 2002) at Michigan

State University, and ALICIA robots (Longo & Muscato, 2006) developed at the Univ. of Catania, Italy. Besides those robots built in academic institutes, some robots have been put into practical use. For example, MACS robots (Backes et al., 1997) at the Jet Propulsion Laboratory (JPL) use suction cups for surface adherence when inspecting the exterior of large military aircraft; Robicen robots (Briones et al., 1994) use pneumatic actuators and suction pads for remote inspection in nuclear power plants; SADIE robots (White et al., 1998) use a sliding frame mechanism and vacuum gripper feet for weld inspection of gas duct internals at nuclear power stations. A wall climbing robot with scanning type suction cups is reported in (Yano et al., 1998). Other examples include (Rosa et al., 2002) and (Zhu et al., 2002). More recently, some robots using vacuum suction cups for glass-wall cleaning are reported in (Elkmann et al., 2002), (Zhang et al., 2004) and (Qian et al., 2006). The common defects of the suction-based climbing robots lie in the facts that the suction cup requires perfect sealing and it takes time to generate vacuum and to release the suction for locomotion. Thus they can only operate on smooth and non-porous surfaces (e.g., glass, metal walls, or painted walls) with low speed. These constraints greatly limit the application of the robots.

The third choice is to create attraction force based on aerodynamic principles including the use of propeller (Nishi & Miyagi, 1991) (Nishi & Miyagi, 1994) and recent innovative robots such as vortex climber (Illingworth & Reinfeld, 2003) and City-Climber (Xiao et al., 2005) (Elliott et al., 2007) robots. The vortex climber is based on a so-called "tornado in a cup" technology, while the City-Climber combines the suction and aerodynamic attraction to achieve good balance between strong adhesion force and high mobility. Both robots have demonstrated the capability moving on brick and concrete walls with considerable success. However, the power consumption and noise are two issues need to be addressed for some surveillance tasks.

Apart from the aforementioned adhesion mechanisms, significant progress has been made to mimic the behavior of climbing animals (e.g., geckos and cockroaches). The investigation on gecko foot (Autumn et al., 2000), (Sitti & Fearing, 2003) has resulted in many gecko inspired climbing robots including the early version of Mecho-Gecko developed by iRobot in collaboration with UC Berkeley's Poly-PEDA lab, Waalbot (Murphy & Sitti, 2007) developed at Carnegie Mellon University, and more recent work of StickyBot (Kim et al., 2007) (Santos et al., 2007) at Stanford University. These robots draw inspiration from the dry adhesive properties of gecko foot and achieved certain success in climbing applications. However, it is a challenging work to synthesize gecko foot hair which should be rugged, self-cleaning and can produce dry adhesive force strong enough for practical use, especially when large payload is desired. Other successful bio-inspired climbing robots are based on microspines observed on insects, which lead to the SpinyBot (Kim et al., 2005) (Asbeck et al., 2006) and RiSE platform (Clark et al., 2007) developed by Stanford University and other RiSE (Robotics in Scansorial Environments) consortium members. The robots are used to climb rough surfaces such as brick and concrete. A novel spider-like rock-climbing robot (Bretl et al., 2003) has been developed at Stanford University and JPL which uses claws at the end of limbs to meticulously climb cliffs. However, this robot cannot move on even surfaces without footholds.

1.3 City-Climber Features

A multi-disciplinary robotics team at the City College of New York (CCNY) has developed a new generation wall-climbing robot named as City-Climber, which has the capabilities to climb walls, walk on ceilings, and transit between different surfaces. Unlike the traditional climbing robots using magnetic devices, vacuum suction techniques, and the recent novel vortex-climber and gecko inspired robots, the City-Climber robots use aerodynamic rotor package which achieves good balance between strong adhesion force and high mobility. Since the City-Climber robots do not require perfect sealing as the vacuum suction technique does, the robots can move on virtually any kinds of smooth or rough surfaces. The other salient features of the City-Climber robots are the modular design, high-payload, and high-performance on-board processing unit. The City-Climber robots can achieve both fast motion of each module on planar surfaces and smooth transition between surfaces by a set of two modules. Experimental test showed that the City-Climber robots can carry 4.2kg (10 pound) payload in addition to 1kg self-weight, which record the highest payload capacity among climbing robots of similar size. The City-Climber robots are self-contained embedded systems carrying their own power source, sensors, control system, and associated hardware. With one 9V lithium-polymer battery, the robot can operate continuously for half hours. DSP-based control system was adopted for on-board perception and motion control. This chapter provides detailed description of City-Climber prototypes, including the adhesion mechanism, mechanical design, and control system. A video which illustrates the main areas of functionality and key experimental results (e.g., payload test, operation on brick walls, locomotion over surface gaps, and inverted operation on ceiling) can be downloaded from website <http://robotics.ccny.cuny.edu>

2. Adhesion System

2.1 Adhesion Mechanism

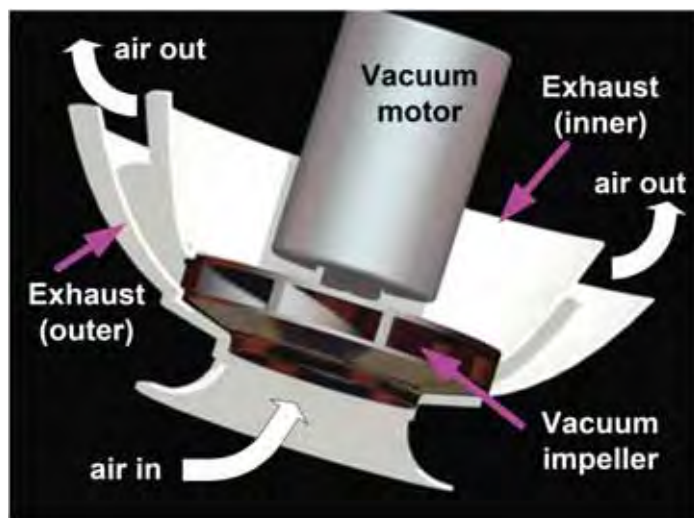


Fig. 1. Vacuum rotor package to generate aerodynamic attraction

The adhesion device we designed for City-Climber is based on the aerodynamic attraction produced by a vacuum rotor package which generates a low pressure zone enclosed by a chamber. The vacuum rotor package consists of a vacuum motor with impeller and exhaust cowling to direct air flow as shown in Fig. 1. It is essentially a radial flow device which combines two types of air flow. The high speed rotation of the impeller causes the air to be accelerated toward the outer perimeter of the rotor, away from the center radically. Air is then pulled along the spin axis toward the device creating a low-pressure region, or partial vacuum region if sealed adequately, in front of the device. With the exhaust cowling, the resultant exhaust of air is directed toward the rear of the device, actually helping to increase the adhesion force by thrusting the device forward.

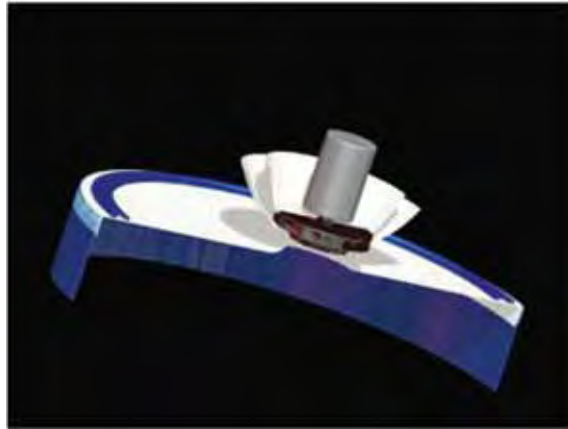


Fig. 2. Exploded view of the vacuum chamber with flexible bristle skirt seal.

In order to generate and maintain attraction force due to the pressure difference, a vacuum chamber is needed to enclose the low pressure zone. Fig. 2 shows a vacuum rotor package installed on a plate, and a vacuum chamber with flexible bristle skirt seal. When the air is evacuated through the hole on the plate by the vacuum rotor, the larger volume of the chamber, and the smaller gaps between the seal and contact surface, the lower steady state pressure we can obtain, thus increase the attraction force and load capacity. Two low pressure containment methods were investigated: inflated tube skirt seal and the flexible bristle skirt seal. The inflated tube seal is very successful, generating attraction force which is so strong that it anchored the device to wall surfaces. In order to make a trade-off between sealing and mobility, we designed a flexible bristle skirt seal, which the bristle surface is covered in a thin sheet of plastic to keep a good sealing, while the flexing of bristle allows the device to slide on rough surfaces. A novel pressure force isolation rim connecting the vacuum plate and the bristle skirt seal is designed. The rim is made of re-foam which improves the robot mobility, and also enhances sealing by reducing the deformation of the skirt as shown in Fig. 3. When the vacuum is on, the rim helps reducing the pressure force exerted directly on the skirt, thus reduce the deformation of the skirt. We select internal differential drive system which adopts two drive wheel and one castor wheel inside the chamber. Since the locomotion system and the payload are mounted on the plate, thus the

re-foam makes the skirt and the robot system flexible and adaptable to uneven surfaces such as stone walls.

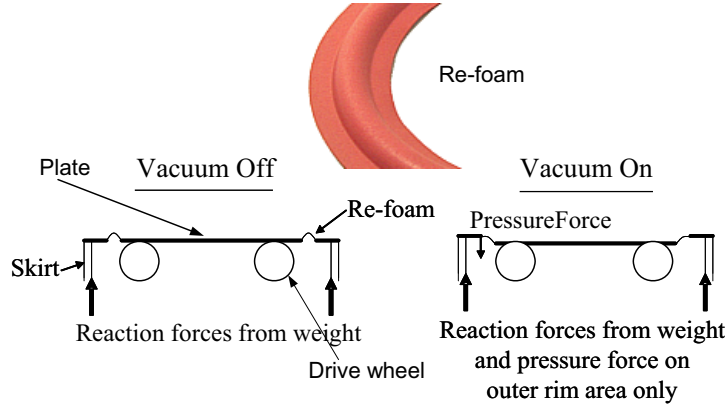


Fig. 3. The pressure force isolation rim is made of re-foam. When the vacuum is on, the rim helps reducing the pressure force exerted directly on the skirt, thus reduce the deformation of the skirt.

2.2 Aerodynamic Study

We studied the aerodynamic behavior of the adhesion mechanism by means of computational fluid dynamics (CFD) simulation using Fluent 6.2 software. The simulation results provide directions to optimize some design factors (e.g., the shape and distribution of impeller vanes, the volume of chamber, etc.) to generate stronger attraction force. Gambit 4.0 was utilized as pre-processor software for Fluent where the geometry of the rotors and the impellers were generated. In the gambit software the volume of the fluid (space within the impellers and inside the chambers) were meshed and proper boundary conditions were applied. This file was read into Fluent for the aerodynamics analysis. In Fluent, the solver was defined as "Steady State" and the type of flow was defined as a "K-Epsilon", and the material as air.

Fig. 4 and 5 (static and total pressure) show the pressure distribution inside the chamber when the impeller rotates in a constant speed of 600 rpm. It indicates that the most low-pressure region (shown in blue) is at the entrance of the curved region of the impeller which caused by the rotational flow due to the rotation velocity of the rotor. This low pressure sucks the air from the inlet and pushes it to the outlet. This has been reflected by the high-pressure region at the most outer boundary area of the rotor (shown as orange to red regions). As shown in Fig. 6, the velocity is low at the entrance and it is high at the outlet, which corresponds with the pressures at these locations. It reveals that the rotor package can generate negative pressure around the axial, and the higher the rotation speed, the lower pressure it can create inside the rotor cylinder. Note that total pressure is the sum of the static and dynamic pressure of air.

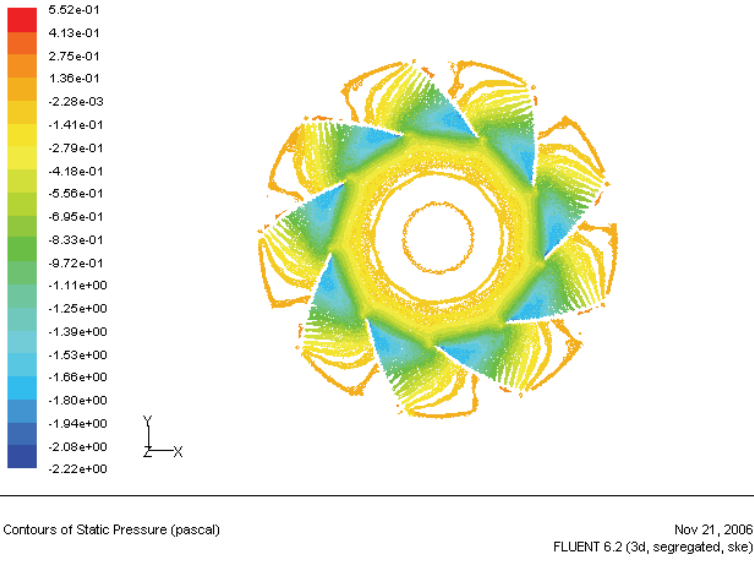


Fig. 4. Aerodynamic simulation, static pressure distribution inside the rotor cylinder (Pascal)

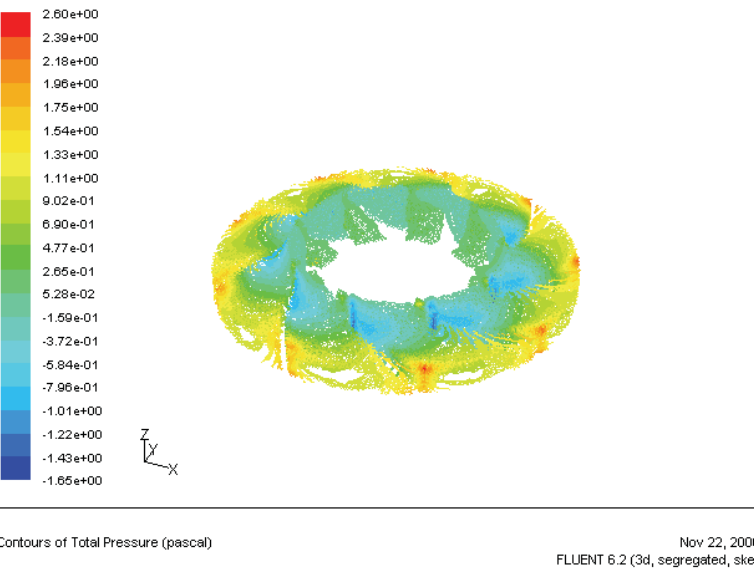


Fig. 5. Aerodynamic simulation, total pressure distribution inside the rotor cylinder (Pascal)

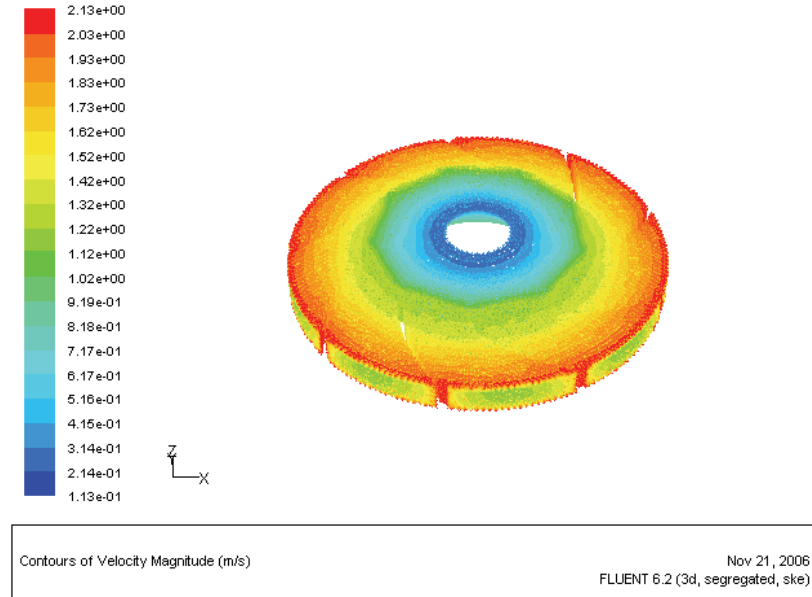


Fig. 6. Aerodynamic simulation with Fluent 6.1, velocity distribution

We compare the original design (Fig. 7, impeller diameter is 8cm) with scale two design , i.e., we left all the conditions the same and just double the size of impeller. As shown in Fig. 7 the minimum total static pressure in original design is $-2.22e^{+00}$ Pascal, but with increasing the size of impeller, Fig. 8 indicates that the minimum static pressure decreases to $-1.24e^{+03}$ Pascal.

We also compare the aerodynamic behavior with chamber diameter as 28cm in three conditions when the chamber is: 1) fully open, 2) has 1cm gap between wall and chamber, and 3) fully sealed. Simulation results show that in the case of fully open (Fig. 9) we have minimum suction pressure of $-4.54e^{+00}$ Pascal; in case 2 (Fig. 10, 1cm gap between wall and chamber) we have minimum suction pressure of $-3.80e^{+02}$ Pascal but it is not uniformly distributed; in the case of fully sealed (Fig.11) we have minimum suction pressure $-2.43e^{+02}$ Pascal and it is evenly distributed compared with case 2. The total attraction force generated by the adhesion mechanism can be calculated by integrating the pressure distribution within the the chamber. It is apparent that the attraction force will be the highest when the chamber is fully sealed because of the evenly distributed large low pressure area in Fig. 11. It also reveals that the rotor package can generate negative pressure around the axial even if there are gaps between wall and the chamber. Our simulation shows that for getting stronger suction force we need to increase the size of impeller, rotation speed, and the volume of chamber, and decrease the gaps between wall and chamber. However, these design factors have physical constraints, and balance between suction force and mobility shall be made. We use pressure sensors to monitor the pressure change inside the chamber and adjust the impeller speed to keep a constant pressure value for strong suction and smooth motion.

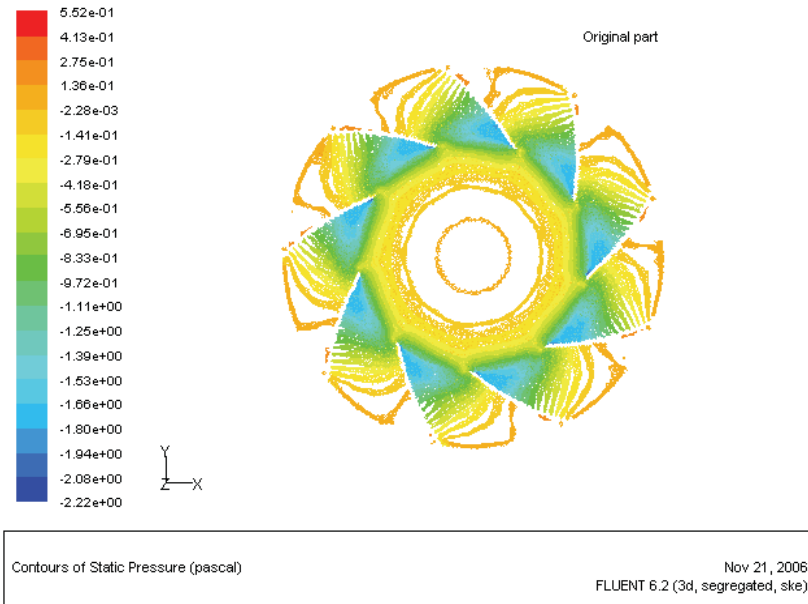


Fig. 7. Simulation of suction pressure in original design

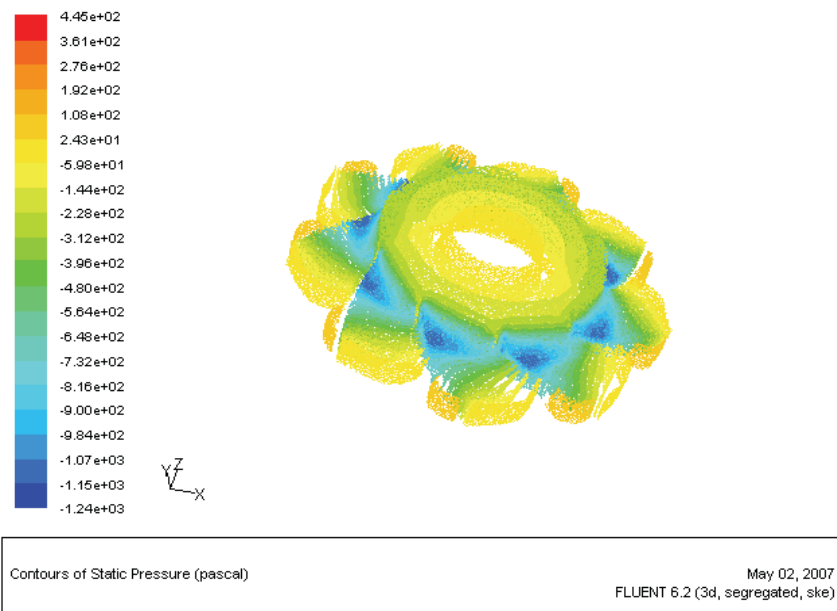


Fig. 8. Simulation of suction pressure in Scale 2

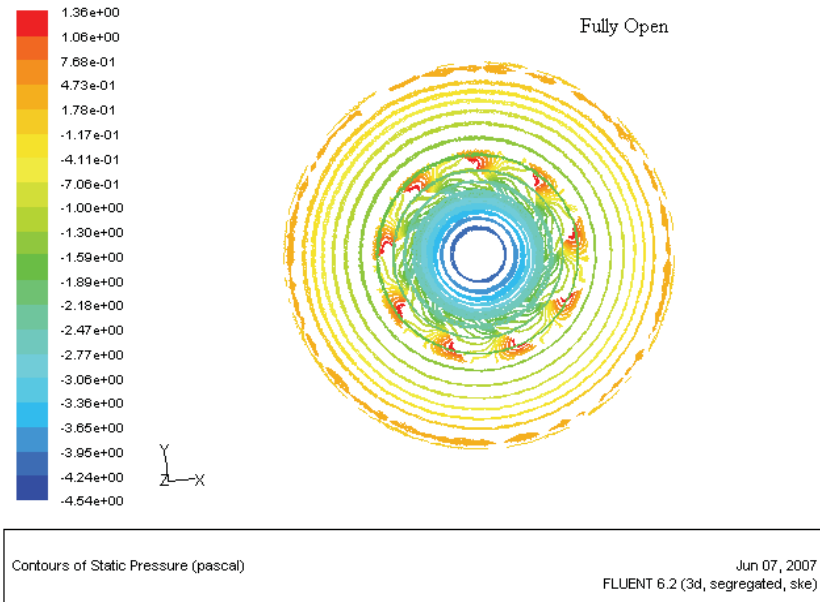


Fig. 9. Simulation of suction pressure: fully open

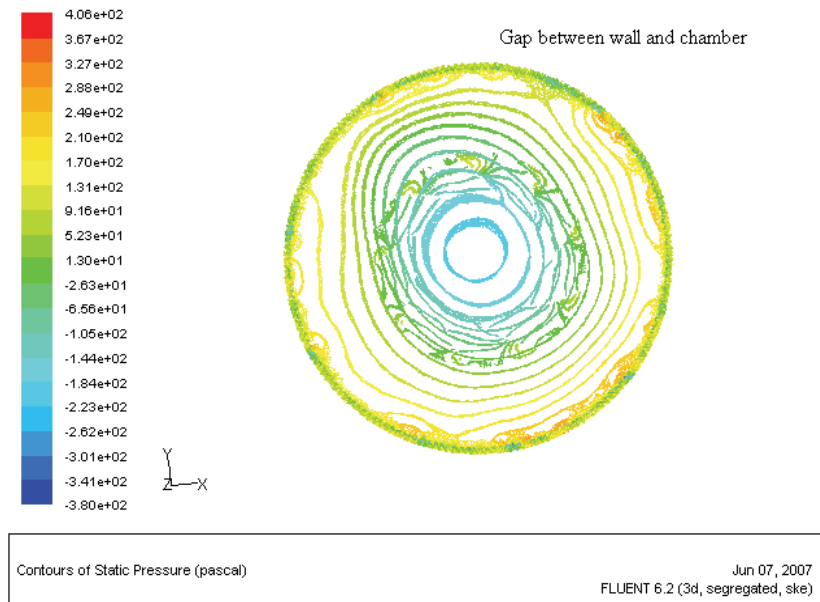


Fig. 10. Simulation of suction pressure: 1cm gap between wall and chamber

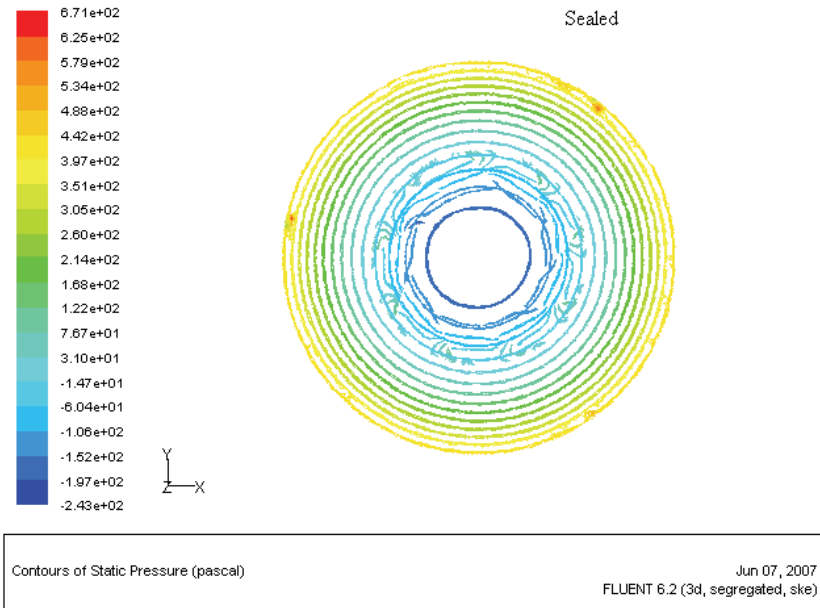


Fig. 11. Simulation of suction pressure: fully sealed

3. City-Climber Prototypes

3.1 City-Climber Prototype-I

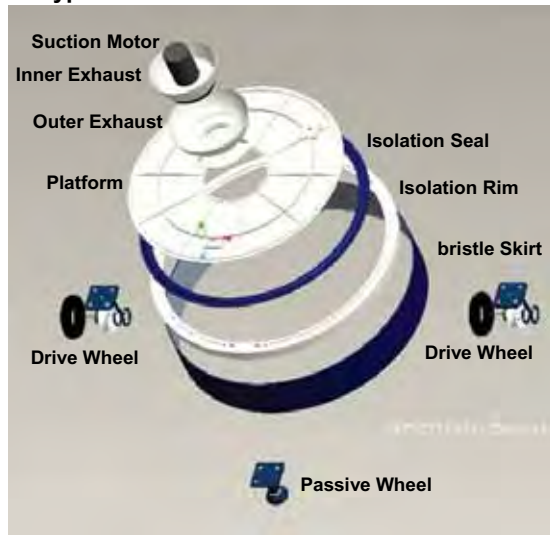


Fig. 12. Exploded view of City-Climber prototype-I.

Fig. 12 shows the exploded view of the City-Climber prototype-I that consists of the vacuum rotor package, an isolation rim, a vacuum chamber with flexible bristle skirt seal, and internal 3-wheel drive. The entire bristle surface is covered in a thin sheet of plastic to keep a good sealing, while the flexing of bristle allows the device to slide on rough surfaces. A pressure force isolation rim connecting the platform and the bristle skirt seal is made of re-foam. The rim improves the robot mobility, and also enhances sealing by reducing the deformation of the skirt. The driving system and the payload are mounted on the platform, thus the re-foam makes the skirt and the robot system adaptable to the curve of rough surfaces. Fig. 13 shows a City-Climber prototype-I operating on brick wall.



Fig. 13. City-Climber prototype-I approaching a window on brick wall, a CMU-camera is installed on a pan-tilt structure for inspection purpose.

3.2 City-Climber Prototype-II

The City-Climber prototype-II adopts the modular design which combines wheeled locomotion and articulated structure to achieve both quick motion of individual modules on planar surfaces and smooth wall-to-wall transition by a set of two modules. Fig. 14 shows the exploded view of one climbing module which can operate independently and is designed with triangle shape to reduce the torque needed by the hinge assembly to lift up the other module. To traverse between planar surfaces two climbing modules are operated in gang mode connected by a lift hinge assembly that positions one module relative to the other into three useful configurations: inline, +90°, and -90°. Responding the electronic controls, a sequence of translation and tilting actions can be executed that would result in the pair of modules navigating as a unit between two tangent planar surfaces; an example of this is going around a corner, or from a wall to the ceiling. Fig. 15 shows a conceptual drawing of two City-Climber modules operating in gang mode that allow the unit to make wall-to-wall and wall-to-ceiling transitions. Fig. 16 shows the City-Climber prototype-II resting on a brick wall and ceiling respectively. The experimental test demonstrated that the City-Climber with the module weight of 1kg, can handle 4.2kg additional payload when moving on brick walls, which double the payload capability of the commercial vortex climber.

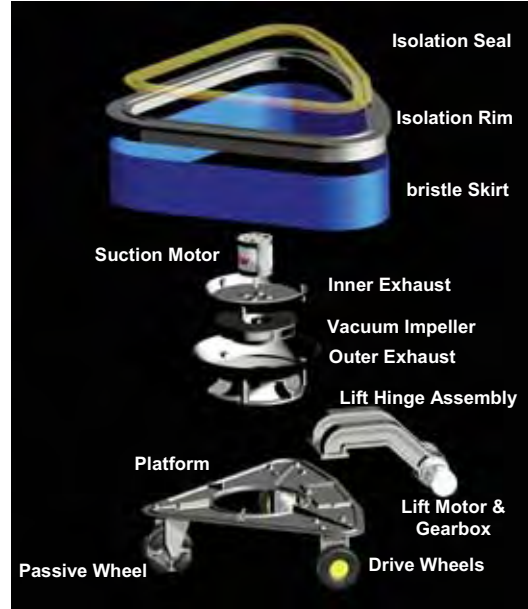


Fig. 14. Exploded view of City-Climber prototype-II



Fig. 15. Two robot modules connecting by a hinge in +90°, and -90° configurations, being able to make wall-to-wall, and wall-to-ceiling transitions



Fig. 16. The City-Climber prototype-II rests on a brick wall and sticks on a ceiling respectively

3.3 City-Climber Prototype-III

The most important improvements in City-Climber prototype-III are the redesign of transition mechanism and the adoption of 6-wheel driving system to increase the contact friction and avoid wheel slippage while climbing vertical walls. Note that the wheels are outside of the robot frame, making it possible for each module to make ground to wall transition with ease (see video demonstration on <http://robotics.ccny.cuny.edu>). The two modules are closely coupled to reduce the torque required to lift up other module, as shown in Fig. 17. Due to efficient placement of the driving system the robot is still capable of +/- 90 degree transitions, similar to prototype-II. Fig. 18 shows the robot prototype III and Fig. 19 shows the exploded view with each module consists of a vacuum rotor package and is closely coupled by shared center axel and transition motor. Same as the prototype-II, the new design still uses one motor for lift/transition and two motors for driving. The two driving motors drive the two center wheels (left and right) independently, and via the right and left belts, drive the front and rear wheels. Additional multiple modules could be linked together in the future to a form snake-like version.

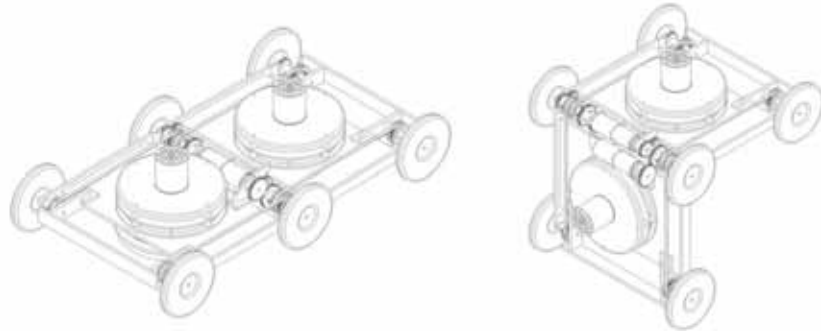


Fig. 17. City-Climber prototype-III, two modules are closely coupled with one transition motor placed in the middle and two other motors drive the two center wheels (left and right), and via the driving belts drive the front and rear wheels

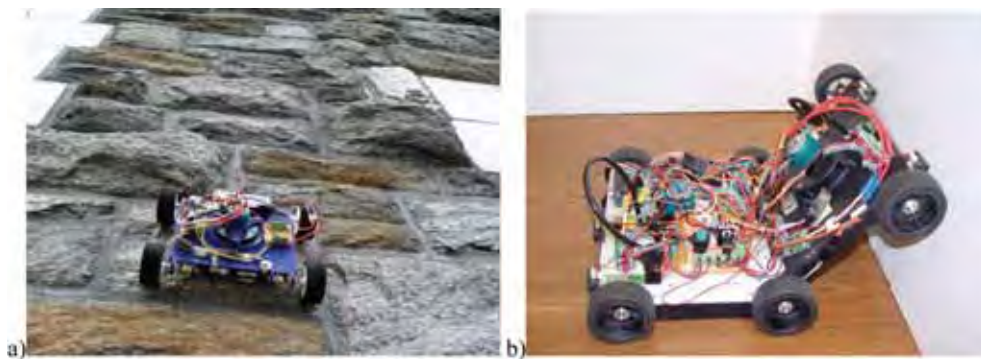


Fig. 18. City-Climber prototype-III: a) One module resting on a brick wall; b) two module

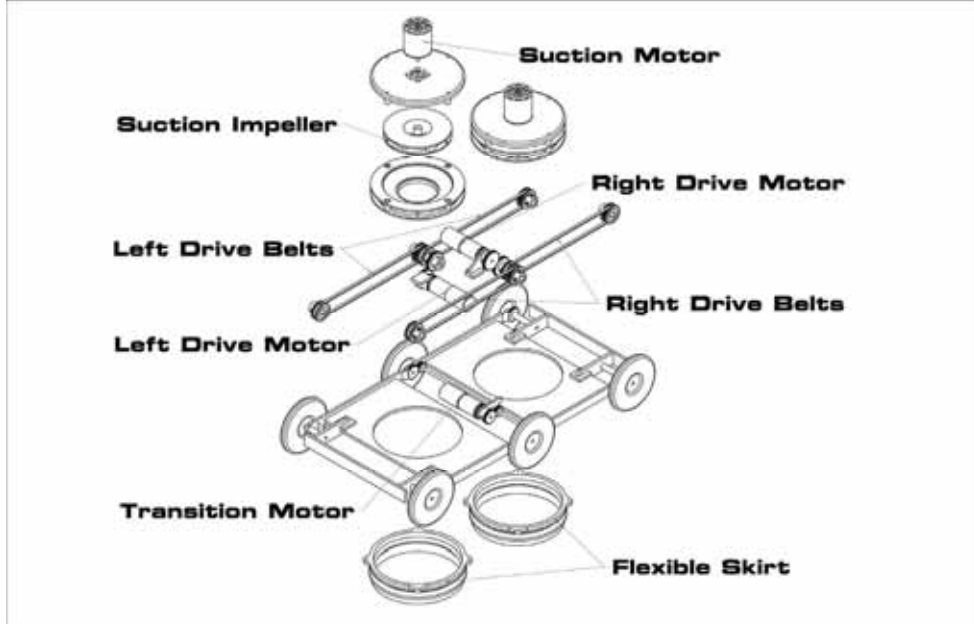


Fig. 19. Exploded view of City-Climber prototype-III

4. Control System

Good mechanical structure cannot guarantee excellent performance. It is crucial to design an effective control system to fully realize the potential of the City-Climber and empower it with intelligence superior to other robots. Resource-constrained miniature robots such as the City-Climber require small but high-performance onboard processing unit to minimize weight and power consumption for prolonged operation. The TMS320F2812 digital signal processing (DSP) chip from Texas Instruments (TI) Inc. is an ideal candidate for an embedded controller because of its high-speed performance, its support for multi-motor control and the low power consumption. This section describes the DSP-based control system design.

4.1 Actuators and Sensor Suite

To minimize weight and complexity, the City-Climber robots use limited number of actuators and sensor components. The actuators in each module include the two drive motors, one lift motor, all of them are DC servo motors with encoder feedback, and one suction motor. The primary sensor components include pressure sensors for monitoring the pressure level inside the vacuum chamber; ultrasonic sensors and infrared (IR) sensors for distance measurement and obstacle avoidance; a MARG (Magnetic, Angular Rate, and Gravity) sensor for tilt angle and orientation detection. For remote control operation the robot has a wireless receiver module, which communicates with the transmitter module in a remote controller. All the signals from those components and sensors need to be processed

and integrated into an on-board control system.

Apart from the primary sensors which are critical for operation, additional application sensors can be installed on the robot as payloads when requested by specific tasks. For reconnaissance purpose, a wireless pin-hole camera is always installed and the video images are transmitted to and processed at a host computer.

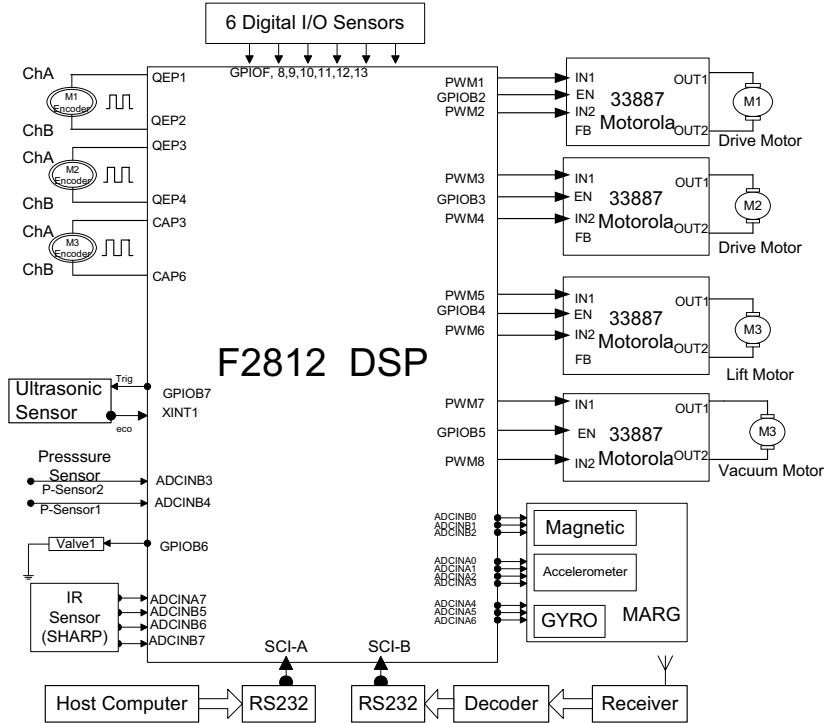


Fig. 20. Hardware design of DSP-based control system

4.2 Hardware Design

The F2812 is a 32-bit DSP controller (TI 2003) targeted to provide single chip solution for control applications. This chip provides all the resources we need to build a self-contained embedded control system. Fig. 20 illustrates the hardware connection based on F2812 DSP. The DSP controller produces pulse width modulation (PWM) signals and drives the motors via 4 Motorola H-bridge chips (Motorola 33887). F2812 DSP has two built-in quadrature encoder pulse (QEP) circuits. The encoder readings of the two drive motors are easily obtained using the QEP channels while a software solution (Xiao et al.; 2000) is implemented to get encoder reading of the lift motor using the Capture units of the DSP. With the encoder feedback, a closed-loop control is formed to generate accurate speed/position control of the drive motors and lift motor. The speed of the vacuum motor is adjusted with the feedback

from the pressure sensors. Using Analog to Digital Converter (ADC) the pressure inside the vacuum chamber is monitored continuously. If the pressure reading is higher than a threshold, the vacuum motor increases the speed to generate more suction force. If the pressure drops too low and the suction force prevent the robot from moving, the vacuum motor will slow down to restore the pressure. An ideal pressure will be maintained which keeps the robot sticking to the wall and with certain mobility.

The climbing robot can be operated both manually and semi-autonomously. Infrared sensors are installed to measure distances from close proximity objects, while ultrasonic sensors are used to measure distance from objects that are far away. The infrared sensor has a reliable reading in the range of 10 cm to 80 cm and the ultrasonic sensor has a reliable range between 4 cm to 340 cm. External interrupt (XINT) channel is connected to the ultrasonic sensor to measure the time-of-fly of sound chirp and convert the measurement to distance reading. In order for the climbing robot to understand its orientation and tilt angle, a MARG sensor is integrated into the control system. The MARG sensor (Bachmann et al., 2003) is composed of nine sensor components of three different types affixed in X-Y-Z three axes: the magnetic sensor, accelerometer, and gyro. The magnetic sensors allow the robot to know its orientation with respect to a reference point (i.e., north pole). The accelerometers measure the gravity in three axes and thus provide tilt angle information to the robot. The gyro sensors measure angular rates which are used in the associated filtering algorithm to compensate dynamic effects. The DSP controller processes the inputs from the nigh MARG sensor components via ADC and provides the robot with dynamic estimation of 3D orientation which is very important for robot navigation.

There are two ways the DSP controller communicates with external sources. Host computer can exchange data with DSP controller via serial communication interface (SCI) using RS232 protocol. Another source that can send commands to the DSP controller is a radio remote controller. This is accomplished by interfacing a receiver with a decoder and then translating the commands into a RS232 protocol compatible with SCI module.

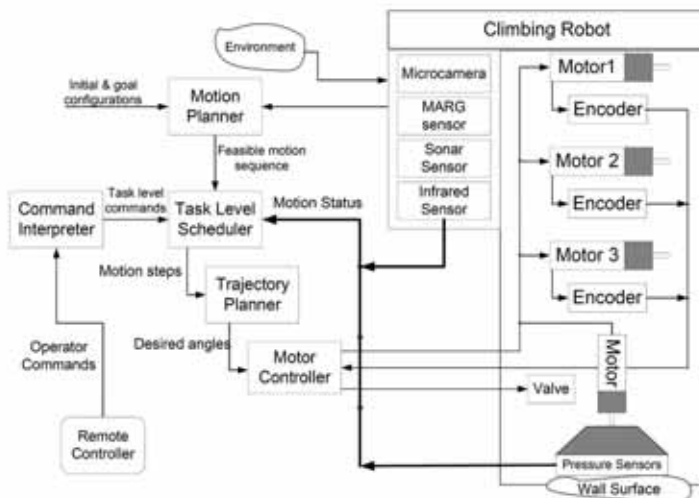


Fig. 21. Control system block diagram

4.3 Software Modules

The control system structure is illustrated in the block diagram as shown in Fig. 21. The physical actuators and sensors are represented in the right block. Other blocks represent the on-board software modules including command interpreter, task level scheduler, trajectory planner, motor controller and motion planner. The operator commands, such as “move forward”, “make left turn”, are transmitted from the remote controller held by a human operator and decoded by the on-board command interpreter. The generated task level commands are then fed into the task level scheduler. The task level scheduler uses a finite state machine to keep track of robot motion status and decompose the command into several motion steps. The trajectory planner interpolates the path to generate a set of desired joint angles. The digital motor controller then drives each motor to the desired set points so that the robot moves to the desired location. The motion planner module generates a feasible motion sequence and transmits it to the task level scheduler. After the motion sequence has been executed, the robot is able to travel from its initial configuration to its goal configuration, while avoiding the obstacles in the environment.

5. Experimental Test

Experiments were conducted to evaluate the performance of City-Climber prototypes. The main areas of functionalities and several key experimental tests are recorded in video which is downloadable from website <http://robotics.ccny.cuny.edu/>. The specifications of the City-Climber robots are listed in table 1.

Speed	Payload capacity	Step clearance	Endurance (9.5v NiCd)	Height
10m/min	4.2 kg	0.01m	30 min	0.15m

Table1. Physical specifications of the City-Climber robots

It was demonstrated that the City-Climber robots are able to move on various wall surfaces, such as brick, wood, glass, stucco, plaster, gypsum board, and metal. With the module weight of 1kg, the City-Climber can generate enough adhesion force to carry additional 4.2kg payload. The video also shows that the City-Climber can operate on real brick wall, and cross surface gaps without difficulty.

6. Conclusion and Future Work

This chapter highlights some accomplishments of CCNY robotics team in developing novel wall-climbing robots that overcome the limitations of existing technologies, and surpass them in terms of robot capability, modularity, and payload. The performance of several City-Climber prototypes are demonstrated by the experimental results recorded in video. By integrating modular design, high-performance onboard processing unit, the City-Climber robots are expected to exhibit superior intelligence to other small robot in similar caliber. The next step of the project is to optimize the adhesion mechanism to further increase suction force and robot payload, and to improve the modularity and transition mechanism to allow the robot re-configure its shape to adapt to different missions. Other directions are

to increase the robot intelligence by adding new sensors, improving on-board processing unit, and developing software algorithms for autonomous navigation.

7. Acknowledgment

This work was supported in part by the U.S. Army Research Office under grant W911NF-05-1-0011, and the U.S. National Science Foundation under grants ECS-0421159, CNS-0551598, CNS-0619577 and IIS-0644127. The authors would like to thank all the team members for their contributions to the climbing robot project, especially Matt Elliot and William Morris for mechanical design, Parisa Saboori for Fluent simulation, Angel Calle and Ravi Kaushik for control system design.

8. References

- Asbeck, A; Kim, S.; Cutkosky, M. R.; Provancher, W. R. & Lanzetta, M. (2006). Scaling Hard Vertical Surfaces with Compliant Microspine Arrays. *International Journal of Robotics Research*, Vol. 15, No. 12, pp. 1165-1180, 2006.
- Autumn, K.; Liang, Y.; Hsieh, T.; Zesch, W.; Chan, W. P.; Kenny, T.; Fearing, R. & Full R. J. (2000). Adhesive force of a single gecko foot-hair. *Nature*, 405:681-684, 2000.
- Bachmann, E. R.; Yun, X. P.; McKinney, D.; McGhee, R. B. & Zyda, M. J. (2003). Design and implementation of MARG sensors for 3-DOF orientation measurement of rigid bodies, Proceeding of 2003 IEEE International Conference on Robotics and Automation, Taipei, Taiwan, May 2003.
- Backes, P. G; Bar-Cohen, Y. & Joffe, B. (1997). The multifunction automated crawling system (MACS), *Proceedings of the 1997 IEEE International Conference on Robotics and Automation*, pp. 335-340, Albuquerque, New Mexico, USA, 1997.
- Bretl, T; Rock, S. & Latombe, J. C. (2003). Motion Planning for a Three-Limbed Climbing Robot in Vertical Natural Terrain, In Proceedings of IEEE International Conference on Robotics and Automation, Taipei, Taiwan, Sep 2003.
- Briones, L; Bustamante, P.; & Serna, M. A. (1994). Wall-climbing robot for inspection in nuclear power plants, *Proceedings of the 1994 IEEE International Conference on Robotics and Automation*, pp. 1409-1414, 1994.
- Clark, J; Goldman, D; Lin, P; Lynch, G; Chen, T; Komsuoglu, H; Full, R; Koditschek, D. (2007). Design of a Bio-inspired Dynamical Vertical Climbing Robot, *Proceedings of Robotics: Science and Systems 2007*, Atlanta, Georgia, USA, June, 2007, on line proceedings, <http://www.roboticsproceedings.org/rss03/index.html>.
- Elkmann, N; Felsch, T; Sack, M; Saenz, J. & Hortig, J. (2002). Innovative Service Robot Systems for facade cleaning of Difficult-to-access areas, *Proceedings of 2002 IEEE/RSJ International Conference on Intelligent Robots and Systems*, pp. 756 - 762, Lausanne, Switzerland, Oct. 2002.
- Elliott, M; Xiao, J; Morris, W.; Calle, A. (2007). City-Climbers at Work Video Proceeding of the 2007 IEEE International Conference on Robotics and Automation, pp2764-2765, Roma, Italy, April 2007.
- Grieco, J. C; Prieto, M; Armada, M; & Santo, P. (1998). A six-legged climbing robot for high payloads, *Proceedings of the 1998 IEEE International Conference on Control Applications*, pp. 446-450, Trieste, Italy, 1998.

- Guo, L; Roger, K & Kirkham, R (1997). A climbing robot with continuous motion, *Proceedings of the 1994 IEEE International Conference on Robotics and Automation*, pp. 2495--2500, Albuquerque, New Mexico, USA, 1997.
- Hirose, S. & Tsutsumitake, H. (1992). Disk rover: A wall-climbing robot using permanent magnet disks, *Proceedings of the 1992 IEEE/RSJ International Conference on Intelligent Robots and Systems*, pp. 2074--2079, Raleigh, NC, 1992.
- Illingworth, L. & Reinfeld, D. (2003). Vortex attractor for planar and non-planar surfaces, US Patents #6619922, Sept. 2003.
- Kalra, L. P.; Gu, J.; Max, M. (2006). Wall Climbing Robot for Oil Tank Inspection, *Proceedings of the IEEE International Conference on Robotics and Biomimetics*, pp. 1523 - 1528, Dec. 2006.
- Kawaguchi, Y; Yoshida, I; Kurumatani, H.; Kikuta, T. & Yamada, Y. (1995). Internal pipe inspection robot, *Proceedings of the 1995 IEEE International Conference on Robotics and Automation*, pp. 857--862, 1995.
- Kim, S., Asbeck, A., Provancher, W. & Cutkosky, M.R. (2005). SpinybotII: Climbing Hard Walls with Compliant Microspines, Proceedings of 12th International Conference on Advanced Robotics, pp. 601-606, July 18-20, 2005.
- Kim, S; Spenko, M; Trujillo, S.; Heyneman, B; Mattoli, V. & Cutkosky, M. R. (2007). Whole body adhesion: hierarchical, directional and distributed control of adhesive forces for a climbing robot, *Proceedings of the 2007 IEEE International Conference on Robotics and Automation*, pp. 1268-1273, Rome, Italy, April 2007.
- Longo, D. & Muscato, G. (2006). The Alicia 3 Climbing Robot, a Three-Module Robot for Automatic Wall Inspection, IEEE Robotics and Automation Magazine, Vol. 13, No. 1, March 2006.
- Luk, B; Collie, A.; Piefort, V. & Virk, G. (1996). Robug III: A tele-operated climbing and walking robot, *Proceedings of UKACC International Conference on Control*, pp. 347--352, 1996.
- Murphy, M. P. & Sitti, M. (2007). Waalbot: An Agile Small-Scale Wall-Climbing Robot Utilizing Dry Elastomer Adhesives, IEEE/ASME Transactions on Mechatronics, Vol. 12, Issue 3, pp. 330-338, June 2007.
- Nagakubo, A. & Hirose, S. (1994). Walking and running of the quadruped wall-climbing robot, *Proceedings of the 1994 IEEE International Conference on Robotics and Automation*, pp. 1005--1012, 1994.
- Nishi, A. & Miyagi, H. (1991). A wall climbing robot using propulsive force of propeller, *Proceedings of the Fifth International Conference on Advanced Robotics*, pp. 320-325, 1991.
- Nishi, A. & Miyagi, H. (1994). Mechanism and control of propeller type wall-climbing robot, *Proceedings of the IEEE/RSJ International Conference on Intelligent Robots and Systems*, pp. 1724--1729, 1994.
- Pack, R. T.; Christopher, J. L.; & Kawamura, K (1997). A rubbertuator-based structure climbing inspection robot, *Proceedings of the 1997 IEEE International Conference on Robotics and Automation*, pp 1869--1874, Albuquerque, New Mexico, USA, 1997.
- Qian, Z. Y.; Zhao, Y. Z.; Fu, Z. (2006). Development of Wall-climbing Robots with Sliding Suction Cups, *Proceedings of 2006 IEEE/RSJ International Conference on Intelligent Robots and Systems*, pp. 3417 - 3422, Beijing, China, Oct. 2006.

- Rosa, G. L; Messina, M; Muscato, G. & Sinatra, R. (2002). A low-cost lightweight climbing robot for the inspection of vertical surfaces. *Mechatronics*, 12(1):71–96, 2002.
- Santos, D.; Kim, S.; Spenko, M.; Parness, A. & Cutkosky, M. R. (2007). Directional Adhesive Structures for Controlled Climbing on Smooth Vertical Surfaces, *Proceedings of the 2007 IEEE International Conference on Robotics and Automation*, pp. 1262-1267, Rome, Italy, April 2007.
- Shen, W; Gu, J; and Shen, Yanjun. (2005). Proposed Wall Climbing Robot with Permanent Magnetic Tracks for Inspecting Oil Tanks, *Proceedings of the IEEE International Conference on Mechatronics & Automation*, pp. 2072-2078, Niagara Fall, Canada, July 2005.
- Sitti, M. & Fearing, R. S. (2003). Synthetic Gecko Foot-Hair Micro/Nanostructures for Future Wall-Climbing Robots, *Proceedings of the IEEE Robotics and Automation Conference*, pp. 1164-1170, Sept. 2003.
- Sun, L; Sun, P; Qin, X. & Wang, C. (1998). Micro robot in small pipe with electromagnetic actuator, *Proceedings of the International Symposium on Micromechatronics and Human Science*, pp. 243--248, 1998.
- TI (2003). TMS320F2812 DSP controllers reference guide, Texas Instruments Inc., January 2003.
- Tummala, R. L; Mukherjee, R.; Xi, N; Aslam, D.; Dulimarta, H.; Xiao, J. Z.; Minor, M; Dangi, G. (2002). Climbing the Walls, *IEEE Robotics and Automation Magazine*, Vol. 9, No. 4, pp. 10-19, Dec. 2002.
- Wang, Y; Liu, S; Xu, D; Zhao, Y; Shao, H. & Gao, X. (1999). Development and application of wall-climbing robots, *Proceedings of the 1999 IEEE International Conference on Robotics and Automation*, pp. 1207--1212, Detroit, Michigan, USA, 1999.
- White, T. S.; Hewer, N.; Luk, B. L. & Hazel, J. (1998). Design and operational performance of a climbing robot used for weld inspection in hazardous environments, *Proceedings of the 1998 IEEE International Conference on Control Applications*, pp. 451--455, Trieste, Italy, 1998.
- Xiao, J. Z.; Sadegh, A.; Elliot, M.; Calle, A.; Persad, A.; Chiu, H. M. (2005). Design of Mobile Robots with Wall Climbing Capability, *Proceedings of the 2005 IEEE/ASME International Conference on Advanced Intelligent Mechatronics*, pp438~443, July 2005.
- Xiao, J. Z.; Dulimarta, H.; Yu, Z.; Xi, N. & Tummala, R. L. (2000). DSP solution for wall-climber microrobot control using TMS320LF2407 chip, *Proceedings of the 43rd IEEE Midwest Symposium on Circuits and Systems*, Lansing, Michigan, USA, 2000.
- Yano, T; Numao, S. & Kitamura, Y. (1998). Development of a self-contained wall climbing robot with scanning type suction cups, *Proceedings of the 1998 IEEE/RSJ International Conference on Intelligent Robots and Systems*, pp. 249--254, Victoria, Canada, 1998.
- Zhang, H. X.; Zhang, J. W. & Zong G. H. (2004). Realization of a Service Climbing Robot for Glass-wall Cleaning, *Proceedings of the 2004 IEEE International Conference on Robotics & Biomimetics*, pp. 395 -400, Shenyang, China, Aug. 2004.
- Zhu, J; Sun, D. & Tso, S. K. (2002). Development of a tracked climbing robot. *Journal of Intelligent and Robotic Systems*, 35(4):427–444, 2002.

Connected Crawler Robot – Design and Motion Planning for Climbing a Step

Sho Yokota

School of Bionics, Tokyo University of Technology

Japan

1. Introduction

The application fields of autonomous mobile robots recently extend from indoor uses to outdoor uses. Rescue systems and planetary explorations are typical examples for such outdoor mobile robots. In such field, it is required to have both of rapid movement and adaptive function to rough terrain, while general wheel mechanisms are not suitable for such rough environment. To move in such environments, the robots need to be flexible to various environment.

There are many researches concerning rough terrain mobile robots for rescue and planetary exploration. In such field, the robots require high mobile ability on rough terrain. When we design such kinds of robot, It become very important to choose the mechanism as a mobile platform. Several types of mechanisms have been proposed as a mobile platform: Crawler type, wheel type, leg type, and their combinations.

Wheel type mechanism is the simplest mechanism and can be controlled easily, but in terms of moving on rough terrains, its performance is obviously inferior to the other two mechanisms. If we adopt wheel type and try to get enough mobility on slight obstacles, we have to utilize pretty large wheels.

The leg mechanism is able to adapt various kind of environment, but, its weak points are low energy efficiency and complicated mechanism and control, that imply high cost and product liability problems. Those might be high barrier to develop them as a consumer product.

The crawler mechanism shows the high mobile ability on various terrains; moreover it is simple mechanism and easy to control. Therefore a lot of rough terrain mobile robots adopt a crawler mechanism.

However conventional single track mechanism has also mobility limitations; the limitation is determined by attacking angle, radius of sprockets, and length of crawler. In order to improve its mobility, it is required to adjust the attack angle against the obstacles, enlarge the radius of its sprockets, and lengthen its crawler tracks. And the mobility on the area like the stairs is inferior to that of the leg (S. Hirose, 2000). Therefore, a lot of researches have been done to supplement these weak points. The main theme common to those researches is to improve the mobility performance on rough terrain. Generally, the method which

changes the form of crawler is adopted as an approach for this main theme. In order to realize these transformations, many researches proposed the connected crawler mechanism. The purpose of this chapter is also to develop a connected crawler robot for rough terrain. The connected mechanism is that; some stages with motor-driven crawler at its left and right side are serially connected by active joints. When this mechanism is adopted, it becomes problem that how many crawler stages should be connected.

Lee et al (C.H. Lee et al, 2003) designs the mechanism of two stages one joint type that uses two triangular crawlers, and shows the high mobility performance by the comparison of climb-able step height between proposed mechanism and a conventional one track type. "Souryu-III" (T. Takayama et al, 2004) is the connected crawler robot of 3 stages 2 joints type, and it shows high mobility by using some basic experiments such as climbing a step and stepping over a gap. "MOIRA" (K. Osuka & H. Kitajima, 2003) is 4 stages 3 joints type connected crawler, and it reports the maximum climb-able step height which was measured by some experiments.

As mentioned above, the mobility performance was improved by the number of stages. However this number was different in each research. The mobility performance was also evaluated by using different experiment and criterion.

Although we can observe such researches, there are no researches which show the standardized relationship between the number of stages and mobility performance. When a connected crawler mechanism is designed, there is no design guideline which indicates how many stages would be optimal. That is a big problem, because the number of stages is influenced to mobility performance strongly.

Therefore this chapter derives the each actuator's motion which conforms to the environments, and tries to demonstrate the relationship between the number of stages and mobility performance. Especially, we set the environment as one step, and derive its relationship (Fig.1). Because the climbing step ability is important factor as one of the most fundamental mobility index (T. Inoh et al, 2005), moreover a climbing step experiment is adopted by many researches as an evaluation experiment for mobility performance on rough terrain. Thus this chapter shows sub-optimal number of crawler stages for connected crawler robot which isn't cleared, through demonstrating the relationship between the number of stages and maximum climb-able step height. After that, it proposes the actual connected crawler robot, and show basic experimental result.

2. Deriving the Sub-optimal Number of Crawler Stages

In order to find sub-optimal number of crawler stages, we derive the maximum climb-able step height of n -stages crawler ($n=2\sim 10$). In this derivation, there is an optimization problem for the joint motions. Because, if the joint can't realize suitable motion for the step, it might be impossible to exercise climbing ability which the mechanism has. Therefore, the optimized joint motions for the step are required. We set the environment to one step (Fig. 1), and then we try to solve the motion planning of each joint and derive the maximum climb-able step height.

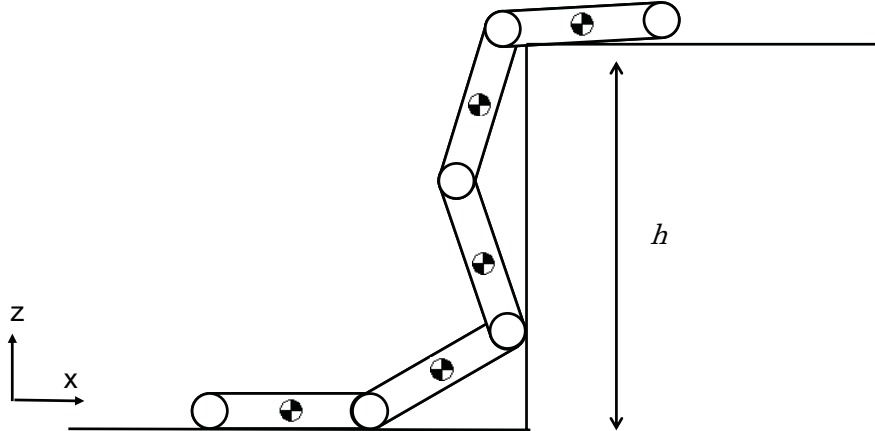


Fig. 1. The assumed case

The motions of climbing a step are divided into 2 phases which shown in Fig.2.

1. Lifting up crawlers phase
This motion is strongly influenced by friction forces, contact forces and impact forces between environments and crawlers.
2. Passing over phase
In order to generate a clockwise moment at the point of edge of the step and crawlers, the robot has to change its posture. This motion is strongly influenced by friction, balance of centre of gravity of the robot and inertia.

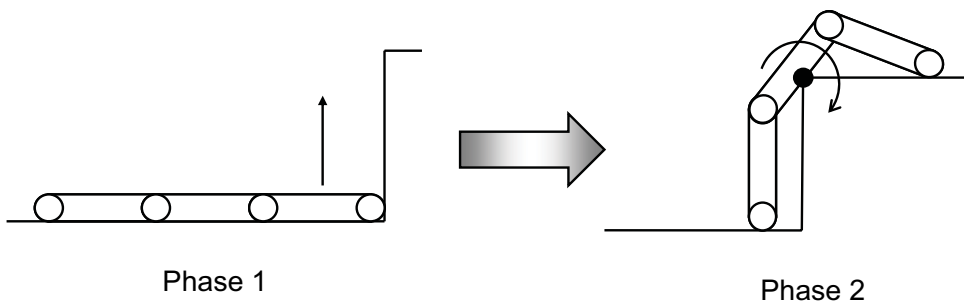


Fig. 2. The phases of climbing up a step

In each phase, changing the robot's posture is important. If the robot can not lift up the body as high as possible in Phase 1, the maximum climbable step height can not be derived. Even if the robot can lift up the body as high as possible in Phase 1, if the robot can not generate the clockwise moment at the point of step edge, the climbing up a step can not be realized. Therefore, it is need to consider not only the moment in phase 2 but also both of Phase 1 and Phase 2. The maximum climbable step height is distinguished by changes of postures. That is to say, the problem of driving the maximum climbable step height is the optimization problem of each joint motion. If the each joint can not realize suitable motion to

the environment, it is impossible to exercise the ability of step climbing of the robot as maximally as possible. Thus the each joint motion is required to realize the suitable motion to the environment. But it is almost impossible to solve this problem by using analytical methods, because the amount of patterns of changing postures (from Phase 1 to Phase 2) becomes fatness by increasing the number of crawler stages. Thus the motion of each joint is required to be derived by using a certain searching method. However, the round robin-like searching method isn't so realistic, because the amount of searching becomes fat and calculation time becomes enormous.

Therefore, we propose the following idea as one of the approach to solve this problem. If certain approximate function can express an optimal joint motion in a few parameters, the required joint motion can be derived in shorter time than a round robin-like search. Therefore we try to express each joint angle function by using approximate function and search the parameters in this function. Thus the problem of the parameter searching can be substituted for the problem of the trajectory searching.

Moreover the robot has to change its posture with taking into interactions with environment, in order to climb a maximum step height.

2.1 Proposed Method

In previous section, we described each joint motion are determined by certain approximate function, and to search parameters in this approximate function. In the following parts, we will mention the approximate function and how to search parameters, and show the method to derive maximum climb-able step height.

2.1.1 The Approximate Function

There are n-order approximation, a tailor progression, a Fourier series, a spline function, and so on, as an available approximate function. The approximate function must be possible to differentiate twice, so as to find an angular velocity and angular acceleration. It is also required that the function is periodic, and has a few parameters, and contains boundary conditions. Therefore, Fourier series is useful function to satisfy these conditions (Y. Yokose et al, 2004). Thus, Fourier series approximates a joint angle functions. And the equation (1) is Fourier series for this approximation,

$$\theta_n(t) = \sum_{i=0}^j \alpha_i \cos \frac{i}{T} 2\pi t + \sum_{i=0}^j \beta_i \sin \frac{i}{T} 2\pi t \quad (1)$$

Here, n means the number of joints, j refers to the number of order of Fourier series, T means the period. α_i , β_i , T are parameters which are searched.

2.1.2 Searching for Parameters in the Fourier Series

Searching for each coefficient and period in the Fourier series corresponds to the problem which is to derive the optimized answer in a wide area. There are many approaches to solve such optimization problems. Many researches proposed to use GA for such a problem (Mohammed, 1997) ~ (S. Kawaji et al, 2001). Because, GA is able to find comparatively an excellent answer in the utility time, and fit various problems. Therefore this chapter also

adopts GA to search unknown coefficients in the Fourier series. We use simple GA (S. Kobayashi et al, 1995), and set following parameters (Table. 1).

Number of chromosomes	10
Gene Length for one coefficient[bit]	10
Crossover rate [%]	25
Mutation rate[%]	1

Table 1. Parameters of GA

We also set the equation (2) to evaluate the chromosomes.

$$E = h + \frac{1}{t} + \frac{\sum_{i=1}^n x_i + \sum_{i=1}^n z_i}{1000} \quad (2)$$

Here, h is the step height which the robot could climb up, t is the time for climbing up a step. Then, it is understood that the evaluation is high when the robot could higher step in shorter time. On the other hand, when the robot couldn't climb a step, we set $h=0$, $t=100$ as a penalty. However, in these conditions, the evaluation of gene which couldn't climb up a step becomes equal, and it makes difficult to execute crossover. Therefore the third clause of the equation (1.2) exists as the valuation item. Here, x_n , z_n are the centre of gravity coordinates of each stage. Thousand in the denominator is numerical value to scale it 1000 down .

2.1.3 The Method to Derive the Maximum Climbable Step Height

In order to evaluate gene, we have to acquire appropriate position of centre of gravity in each stage and distinguish whether the robot could climb or not. Because mobility performance of the mobile mechanism concerns with topography characteristic closely, the consideration of the interaction with the environment is very important. Therefore we must consider dynamics and an interaction between robot and environment, for appropriate acquisition of centre of gravity position and distinction of climbing. Thus we adopt ODE(Open Dynamics Engine)(R. Smith) to calculate these values. ODE is open source software, and is adopted by many robotic simulators to calculate dynamics. We derived maximum climbable step height by integrating ODE and GA. The calculation System is shown in Fig.3.

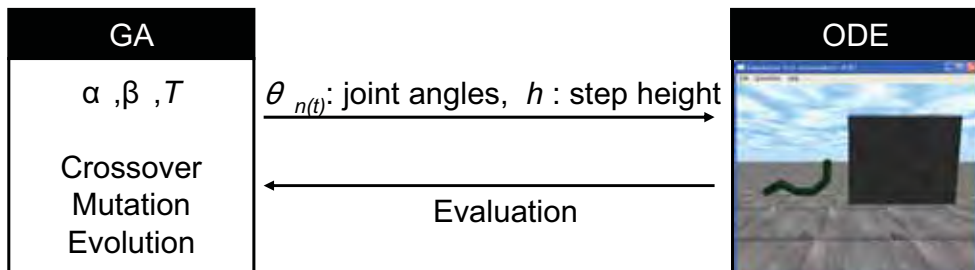


Fig. 3. Proposed simulation system

GA gives joint angles and step height, and ODE calculate dynamics. After that, ODE distinguishes whether the robot could climb or not, and returns the evaluation to GA. GA makes a gene evolve, and optimizes joint angle function. Then the robot can climb higher step in shorter time. A robot is considered to climb a step, when all centres of gravity in each stage are higher than the height of the step h and it is on the right of A in Fig1.

2.2 Deriving the Maximum Climbable Step Height of n -Stages

In this part, we derive maximum step height of n -stages based on the above mentioned method. We set the conditions and assumption as follows.

Each initial joint angle is set 0.0[rad], and the range is -2.0 ~ 2.0[rad]. The range of Fourier coefficients is -2.0 ~ 2.0. The range of Fourier series period T is 10 ~ 60[sec], and the order of Fourier Series is 5. The initial genes are determined randomly. The specifications of the connected crawler robots are shown in Table. 2 and Fig. 4. Other conditions are as follows.

Total length L [m]	2
Total mass M [kg]	2
Radius of the sprocket [m]	0.1

Table. 2. Parameters of the connected crawler robot

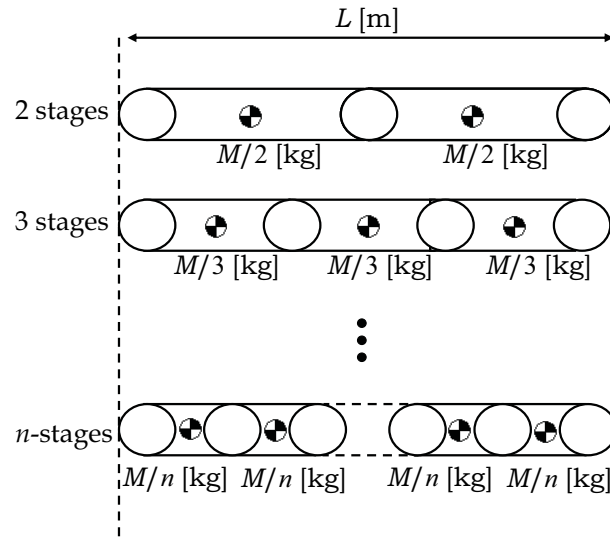


Fig. 4. The dividing definition of the robot

- Each stage is divided in constant total length L by corresponding to the number of links.
- The crawler velocity is constant 0.1[m/s].
- The actuators have enough torque for driving joints.

The range of step height h is $0.5 \sim 2.0[\text{m}]$, because the total length of connected crawler is $L=2.0[\text{m}]$. By using above conditions, the simulation is done which is 4 stages and the number of generations is 500. Then the maximum climbable step height is derived.

2.3 Results

The results are shown in Fig.5 ~ Fig. 7.

In the Fig. 5, we can confirm that the robot could climb higher step when the number of generations is increased, and time for climbing was shorten.

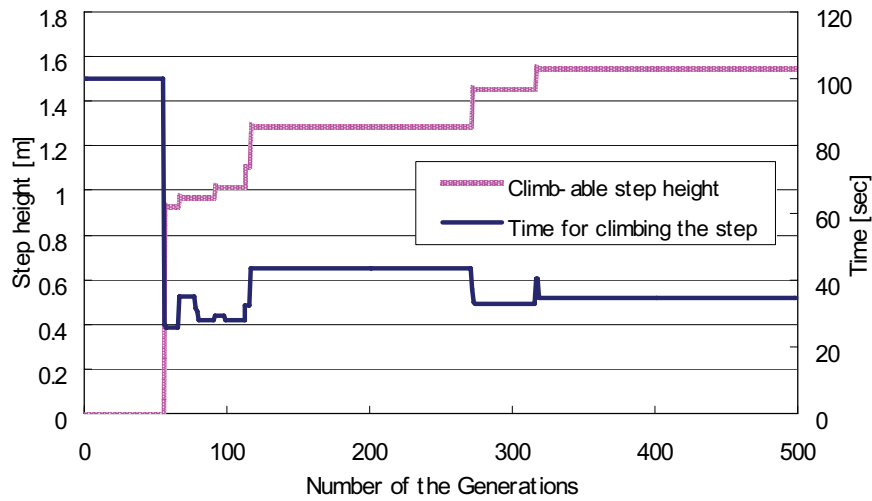


Fig. 5. Transition of the climbable step height derived by GA (4 stages)

Fig.6 and Fig. 7 are snapshot when the robot is climbing up a step. In Fig.6, the height of step is $0.9[\text{m}]$ and the number of generations is 56. In Fig.7, the height of step is $1.544[\text{m}]$ (this is the maximum climbable step height of 4 stages). From these figures, the climbable step height becomes higher and the motions of the joints are changed when the number of generations is increased.

We also derive the maximum climbable step height of $2 \sim 10$ stages by using same method. The results are shown in Fig.7. It is confirmed that the robot can climb higher step when the number of generations is increased as well as the case of 4 stages, and maximum climbable step height of each link is derived.

Since the maximum climbable step height of each stage has been shown in Fig.8, the relationship between the number of stages and mobility performance of connected crawler is demonstrated in Fig.9.

By this figure, it is able to be derived that the sub-optimal number of stages for connected crawler is 5. Because it is turned out that the mobility performance is saturated more than 5 stages. Thus we can get the answer against the question that how many crawler stages should be connected, namely that is 5 stages.

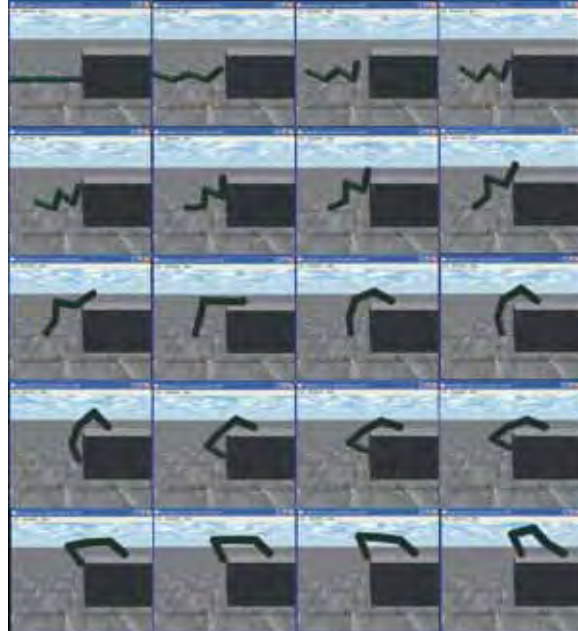


Fig. 6. Connected Crawler robot climb the step by using sub-optimized joint motion by GA
(4 stages, $h=0.9$ m, 56 generations)

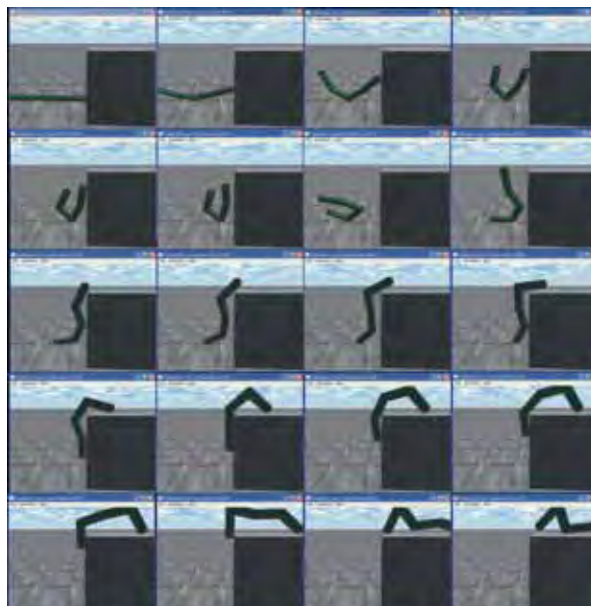


Fig. 7. Connected Crawler robot climb the step by using sub-optimized joint motion by GA
(4 stages, $h=1.544$ m, 500 generations)

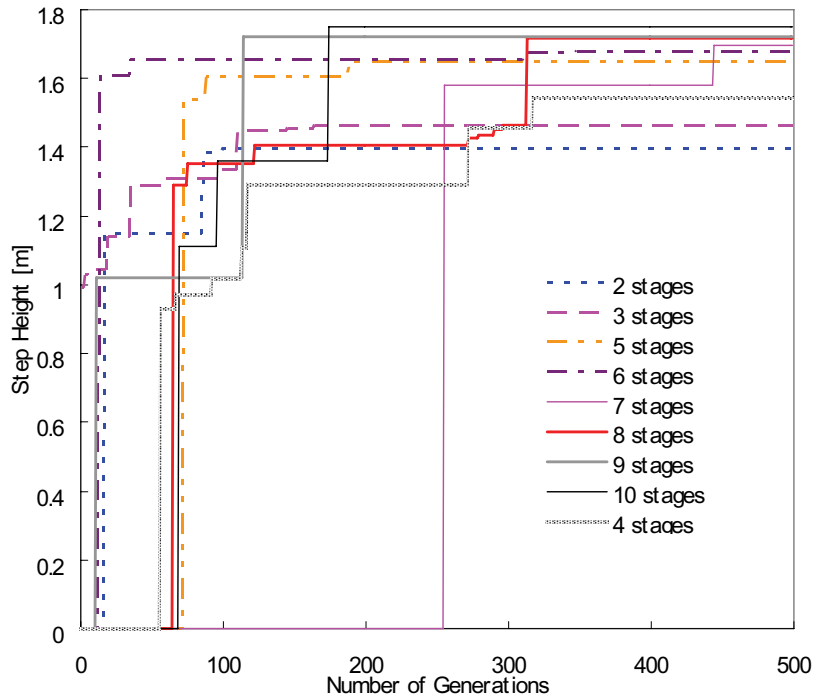


Fig. 8. Transition of the climbable step height derived by GA (2 ~ 10 stages)

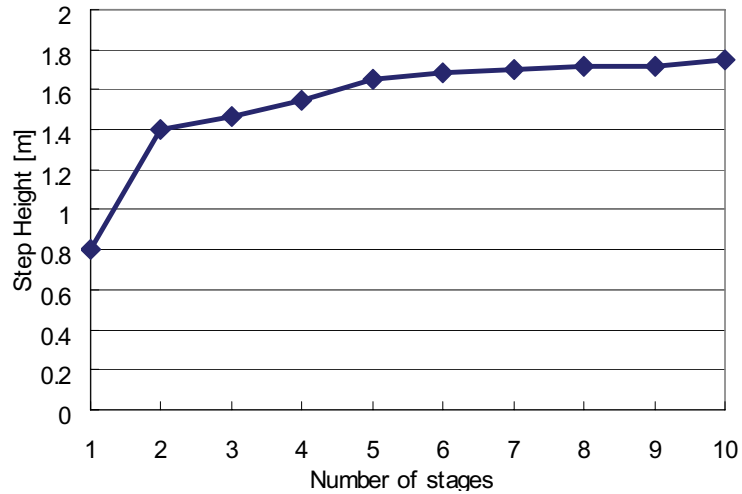


Fig. 9. Relationship between the number of stages and climbable step height

3. Constructing the Prototype

In the previous section, we have been able to obtain the sub-optimal number of crawler stages, that is 5. Based on this conclusion, we have designed and developed the prototype of connected crawler robot. It is shown in Fig. 10. The length is 0.59 m, width is 0.130 m, mass is 1.28 kg.

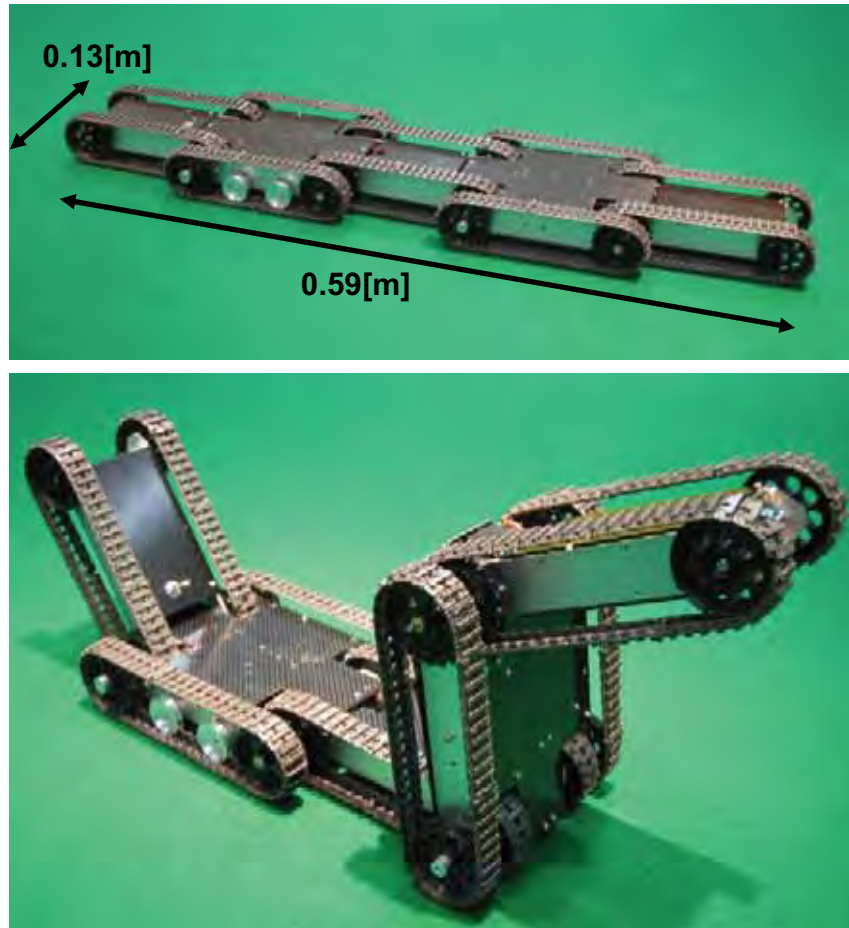


Fig. 10. Prototype of connected crawler robot

3.1 Mechanical Structure

Our mechanism has 5 connected stages with the motor-driven crawler tracks on each side (Fig. 11). RC-servo motors are used for driving joints between the stages. The left and right crawlers are driven by 4 DC motors independently, while the 5 crawlers on each side are driven by a motor simultaneously. The output of each motor is transmitted to the sprockets of the three or two crawlers through several gears (Fig.12).

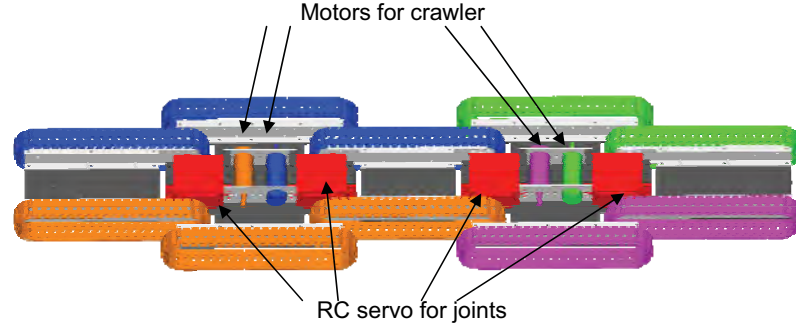


Fig. 11. The driving structure (Color indicates driving relationship between motors and crawlers)

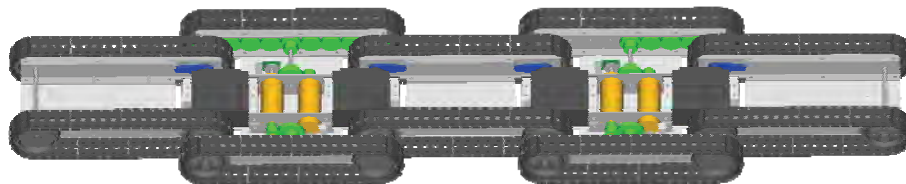


Fig. 12. Transmission of motor outputs to the crawlers

3.2 Control Structure

The control architecture is hierarchical structure by connecting master controller and servo unit (Fig. 13, and Fig. 14).

The servo units control low level task: crawler velocity and joint angle by PID control law. Each servo unit consists of one microcontroller (PIC16F873) and 2 DC motor drivers (TA8440H). One microcontroller is installed to control two RC-servo units for the joint control, where RC-servo is controlled only by PWM signal. Master controller controls high level task: such as calculating robot trajectory. Table.3 shows the communication data format. The command sent by master controller consists of 3 bytes. First byte indicates mode ID and motor ID. The mode ID distinguishes 2 kinds of control modes: position control and velocity control. The motor ID is used for selecting motor to control.

Second byte shows the data depends on control modes. The third byte is checksum.

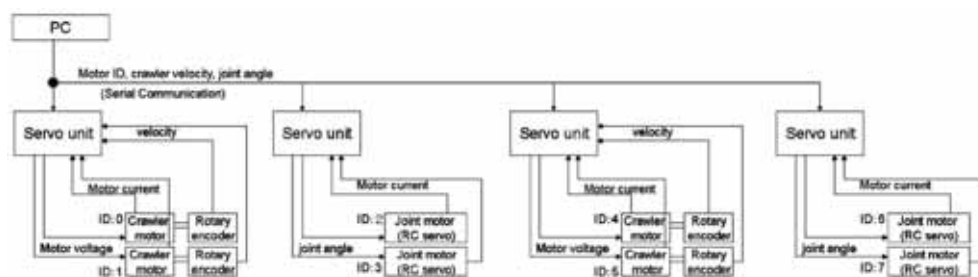


Fig. 13. The control system

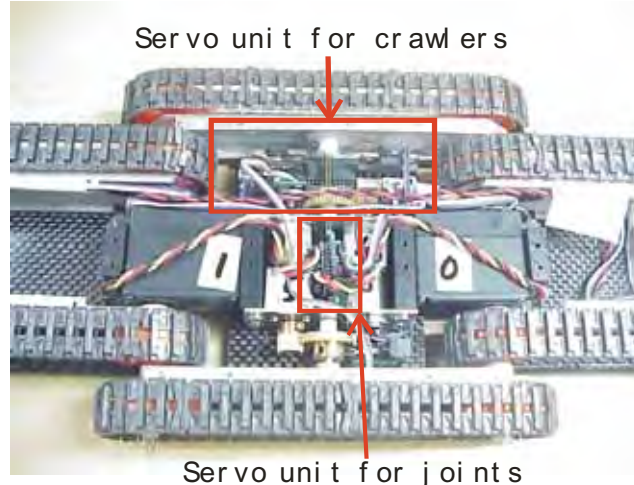


Fig. 14. The servo units

1 byte								2 byte	3 byte
Data 1								Data 2	Check Sum
7	6	5	4	3	2	1	0	0~254	Data1 Data2
Mode=0~2	ID=0~7								

Table. 3. Communication data format

4. Experiments

The climbing step experiment is conducted to verify the performance of our prototype. The height of step is 0.23 m. The master controller sends instructions to each actuator through servo units. Li-Polimer battery (1320mAh, 11.1V) is embedded to the robot for supplying electric power. In this experiment, PC is used as master controller. The USB cable is used for connecting robot to PC. The result is shown in Fig. 15. As we can observe, the robot can climb up a step. Therefore the mobility of this robot is confirmed.

5. Conclusion

This chapter showed sub-optimal number of crawler stages for connected crawler robot, through demonstrating the relationship between the number of stages and maximum climbable step height. After that, it proposed the actual connected crawler robot, and indicated basic experimental result. The conclusions of this chapter are as follows.

- A joint angle function was approximated by Fourier series and parameters were searched by GA.

- Due to fusion of GA and ODE, it has been possible to consider the interactions between robot and environment.
- The relationship between the number of crawler stages and mobility performance was cleared.
- Though mobility performance was raised by increasing the number of stages. However its increasing rate was small in comparison between before 5 stages and after 6 stages.
- Therefore the sub-optimal number of crawler stages is Five.
- By basic experimental results, the mobility of the prototype was confirmed.

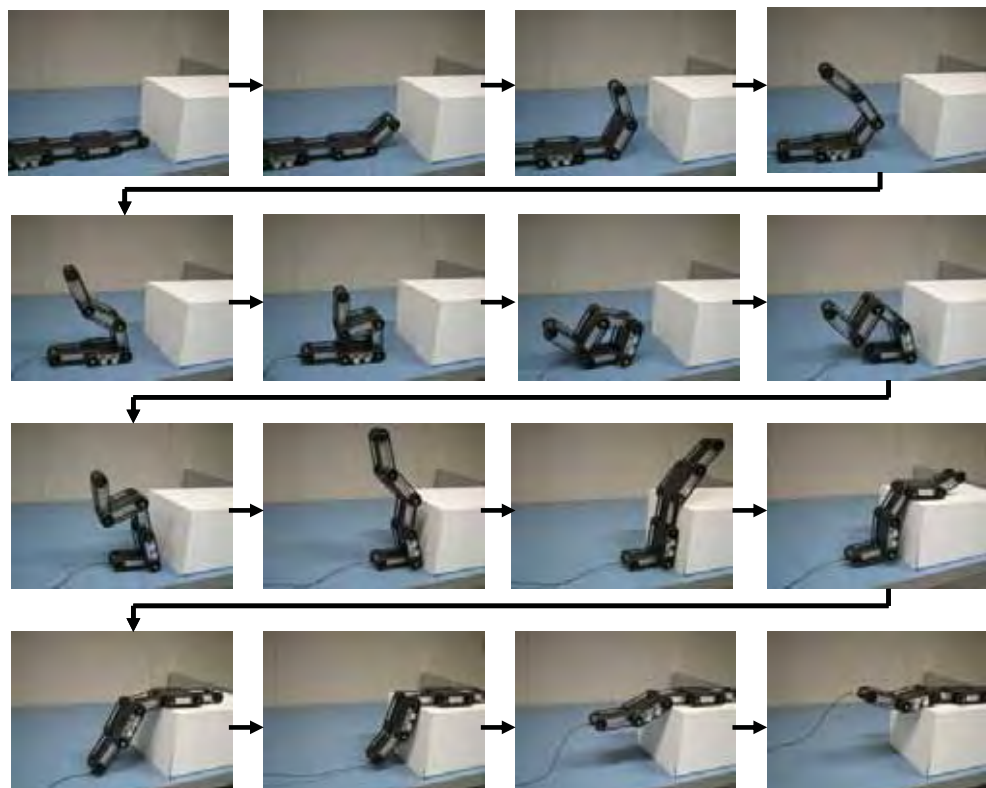


Fig. 15. Experimental results

References

- C.H. Lee, S. H. Kim, S. C Kang, M.S.Kim, Y.K. Kwak (2003). "Double -track mobile robot for hazardous environment applications", *Advanced Robotics*, Vol. 17, No. 5, pp 447-495, 2003
- K. Osuka, H. Kitajima (2003). "Development of Mobile Inspection Robot for Rescue Activities:MOIRA", *Proceedings of the 2003 IEEE/RSJ Int'l. Conference on Intelligent Robots and Systems*, pp3373-3377, 2003

- Mohammed , G.F.Uler (1997). "A Hybrid Technique for the Optimal Design of Electromagnetic Devices Usign Direct Search and Genetic Algorithms" , *IEEE Trans. on Magnetics*, 33-2, pp1931-1937, 1997
- R. Smith, "Open Dynamics Engine", <http://ode.org/>
- S. Hirose (2000). "Mechanical Designe of Mobile Robot for External Environments", *Journal of Robotics Society of Japan*, Robotics Society of Japan, vol.18, No.7, pp904-908, 2000 (*in Japanese*)
- S. Kawaji et al, (2001). "Optimal Trajectory Planning for Biped Robots" , *The Transactions of the Institute of Electrical Engineers of Japan. C*, vol.121, No.1, pp282-289, 2001 (*in Japanese*)
- S. Kobayashi et al, (1995). "Serach and Learning by Genetic Algorithms" , *Journal of Robotics Society of Japan*, vol.13, No.1, pp57-62, 1995 (*in Japanese*)
- T. Inoh et al (2005). "Mobility of the irregular terrain for resucue robots" , 10th Robotics symposia , pp 39-44, 2005 (*in Japanese*)
- T. Takayama, et al (2004). Name of paper. "Development of Connected Crawler Vehicle "Souryu-III" for Rescue Application " , *Proc. of 22nd conference of Robotics Society of Japan CD-ROM*, 3A16, 2004 (*in Japanese*)
- Y. Yokose et al (2004). "Minimization of Dissipated Energy of a Manipulator with Coulomb Friction using GA Increasing the Calculated Genetic Information Dynamically" , *Transaction of JSCES*, Paper No.20040024, 2004 (*in Japanese*)
- Y.Yokose , V.Cingosaki, H.Yamashita (2000). "Genetic Algorithms with Assistant Chromosomes for Inverse Shape Optimization of Electromagnetic devices" , *IEEE Trans. on Magnetics*, 36-4, pp1052-1056, 2000

A PAWL for Enhancing Strength and Endurance during Walking Using Interaction Force and Dynamical Information

Feng Chen^{1,3}, Yong Yu², Yunjian Ge¹, Jian Sun¹ and Xiaohong Deng¹

¹ Dept. of Automation, University Science and Technology of China
China

² Dept. of Mechanical Engineering, Kagoshima University
Japan

³ Institute of Intelligent Machines, Chinese Academy of Sciences
China

1. Introduction

PAWL (power assist walking leg) represents a high integration of robotics, information technology, communication, control engineering, signal processing and etc. Today, trends in robotics research are changing from industrial applications to non-industrial applications, such as service robots, medical robots, humanoid robots, personal robots and so on. Human ability to perform physical tasks is limited not only by intelligence, but also by physical strength (Kazerooni, 1990). Our research on robot is using mechanism to augment human muscle and capability of sense during walking; synchronously, it can hold human agility and sense of direct operation. The primary task of this project is to develop a power assist walking support leg (shown in Fig.1) which not only amplifies strength of human legs and enhances endurance during walking, but also reduces user inner force. Power assist system has many potential applications. It can be designed for care-worker, elderly people, nurse,

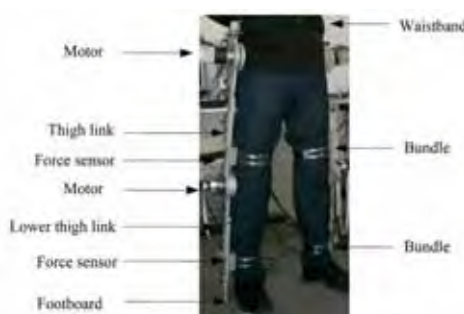


Fig. 1. Power Assist Walking Leg

Source: Climbing & Walking Robots, Towards New Applications, Book edited by Houxiang Zhang, ISBN 978-3-902613-16-5, pp.546, October 2007, Itech Education and Publishing, Vienna, Austria

soldier, fireman, even for a person with gait disorder (medical rehabilitation system). And it is also expected to have powerful impacts on many applications in the manufacturing, service, and construction industries. In order to utilize PAWL as human locomotion assist apparatus, the PAWL must comply with the locomotion of human legs, i.e. the system in this study is supposed to generate flexible human-like motion without delay. So, the PAWL kinematics must be close to users'. Here, we propose a power assist method using human-robot interaction force. And, the ability of the walking support leg to perform a task depends on the available actuator torque. The direction of the motor rotation is made certain by the user motion based on sensors information, especially the interaction force (between the user and the exoskeleton) and the floor reaction force (FRF). And, the motor rotation actuated by periodic signals should be flexible because the user is in physical contact with the mechanism.

2. Related Works of Wearable Power Assist Device

Many projects about a wearable power assist device are developed or developing. Their power assist is distributed to arm, leg, back, and so on. Some representative power assist systems are summarized in this section.

A study of power assist robot was started in 1960s. Hardiman (Makinson, 1971) was the first power assist system. The main purpose of the project is to be used by soldiers, who have to move long-distance with heavy loads. The Hardiman project was a large, full-body exoskeleton weighing 680 kg and controlled using a master-slave system. BLEEX (the Berkeley Lower Extremity Exoskeleton) (Kazerooni et al., 2005; Steger et al., 2006) project has developed an energetically autonomous exoskeleton capable of carrying its own weight plus an external payload. BLEEX has more than 40 sensors and hydraulic actuators, and helps lighten the load for soldier or worker. Currently BLEEX has been demonstrated to support up to 75kg, walk at speeds up to 1.3m/s, and shadow the operator through numerous maneuvers without any human sensing or pre-programmed motions.

In Japan, several universities are developing the power assist system. Kanagawa Institute of Technology has designed a wearable power assist suit (Keijiro et al., 2002; Keijiro et al., 2004) for nurses. The target load is about 60kgf, powered by unique pneumatic actuators controlled by measuring the hardness of the corresponding human muscles. HAL (Kasaoka & Sankai, 2001; Lee & Sankai, 2002; Kawamoto & Kanbe, 2003; Kawamotio & Sankai, 2004; Hayashi et al., 2005) of Tsukuba University was a lightweight power assist device. Its actuators are DC motors at the knee and hip. They use EMG electrodes on human's leg muscles and ground reaction force sensors to estimate a human inner force and motion information. Tohoku University developed a wearable antigravity muscles support system for supporting physically weak person's daily activities (W.W.H-KH2) (Nakamura et al., 2005). The joint support moments are designed based on a part of the gravity term of the necessary joint moment derived by human approximated model.

The robot that we proposed is for assisting activities of daily life through decreasing human inner force / increasing human strength. So, the system must have many DOFs like humans. And, the PAWL DOFs are all purely rotary joints. To make the system work smoothly and toted easily, the control scheme must be effective and the weight of the whole system should be light. Aluminium alloy are used as the main material for the exoskeletal frame in consideration of lightness.

3. Conceptual Design and Calculation of Necessary Joint Torques

PAWL is composed of five main parts: lower exoskeletons, actuators, controllers, sensors, and power unit. By matching human degrees of freedom and limb lengths, PAWL must have the necessary degrees of freedom and its segments length equal human legs' in order to satisfy human normal walking. This means that for different operators to wear the exoskeleton, almost all the exoskeleton limbs must be highly adjustable, even for the waistband. In order to make the exoskeleton work smoothly and safety, the PAWL must have the kinematics which is similar to man. The PAWL is to be attached directly to the bilateral side of human legs. Fig.1 shows the hybrid system of human-PAWL. It can be said that PAWL will become a part of human body or human body is a part of PAWL.

The PAWL that we proposed is for assisting activities of daily life without affecting the user to walk normally. So, the system has many DOFs like humans, however, it is impossible to include all the DOFs of human legs in consideration of design and control complexities. Here, our mechanical structure consists of a 12 DOFs mechanism (6 DOFs for each leg). And, all joints of PAWL are rotary structure. The hip structure has 3 DOFs in total. They perform function of flexion/extension, abduction/adduction and internal rotation /external rotation. At the knee joint, there is 1 DOF, which perform the flexion/extension. 1 DOF at the ankle permits dorsiflexion/planter flexion and 1 DOF at the metatarsophalangeal joint for flexion/extension.

Comparing to other joint motion, the flexion/extension of hip and knee is the most important to normal walking and its energy consumption is also most. So, only the motion of flexion/extension at hip and knee is currently powered. To make the system work smoothly and move easily, besides the validity of the control strategy, the weight of the whole system should be light. Here, aluminium alloy are mainly used as the material for the exoskeletal frame in consideration of lightness. To avoid the motion collision between the WPAL exoskeleton and the user, the designed joint axes and human joint axes must be on an identical axis. So, the length of PAWL exoskeleton is designed to be changed according to the real length of user thigh and lower leg as shown Fig.2.

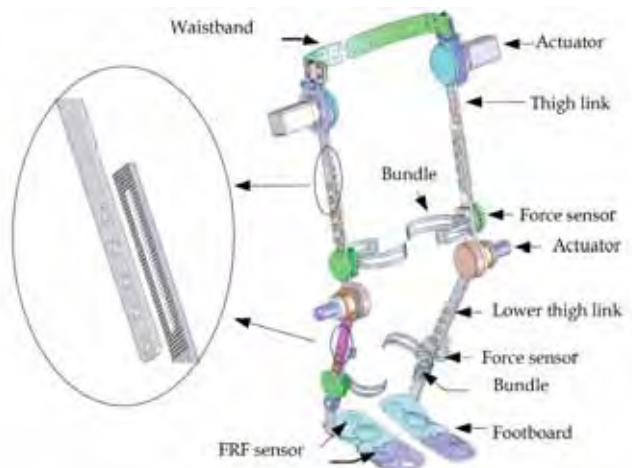


Fig. 2. Configuration of the robot suit

Fig.1 and Fig.2 also show the fundamental configuration of PAWL. The actuator used in PAWL is DC servomotor attached with a harmonic drive gear, which provide assist force for knee and hip joints. Here, MAXON DC servomotor and reducer are selected for PAWL actuators by analysing the dynamic model of human body and the exoskeleton. The direction of the interaction force decides the rotation direction of the manipulator. And the motor clockwise/anti-clockwise rotation achieves the flexion/extension of human leg. According to (Zheng, 2002), we can obtain the relative weight of human body segments, especially lower limb. Aluminium alloy is mainly used as the material for the exoskeleton frame in consideration of lightness. Table 1 shows the weight of the main links. Considering the safety to user, the motion range of the exoskeleton joint must be restricted according with human each joint's (shown in Table 2). That is, the joint range of PAWL should not go over the corresponding range of human. So, we restrict the joint motion range of PAWL during mechanical design. And, it is also insured against maximum by pre-programmed software. The maximum velocity of actuator is limited by software, too. Furthermore, there is a close-at-hand emergency switch to shut off the motor power in order to avoid the unexpected accident.

Objects(unilateral)	Weight [g]	Material
Waistband	390.69	Stainless steel
Thigh Link (m_1)	769.97	Duralumin
Lower Thigh Link (m_2)	371.42	Duralumin
Foot Board (m_3)	755.55	Duralumin

Table 1. Weight of each link

Hip Joint	Flexion	120°
	Extension	10°
	Abduction	45°
	Adduction	30°
	Internal rotation	45°
	External rotation	45°
Knee Joint	Extension to flexion	135°
Ankle Joint	Dorsiflexion	20°
	Planter flexion	50°
Metatarsophalangeal Joint	Flexion	45°
	Extension	70°

Table 2. Human joint ranges of motion

Many sensors are used to detect the conditions of the PAWL and user. The two two-dimension force sensors are equipped on thigh and lower thigh respectively per exoskeleton leg, which detect the interaction force caused from the motion difference between PAWL and the user. And they contact directly with human leg through bundles. FRF (Floor reaction force) sensors are developed to measure FRF which are generated in front and rear parts of the footboard. Rotary encoders are used to measure the hip and knee joint angles. The multi-sensors information is used to understand human motion intent. So, the sensors

must have the properties of high stability, sensitivity and accuracy. Furthermore, the PAWL motion should be prompt and smooth. Otherwise, the PAWL will be a payload to the user. Using Lagrange method, we can work out the necessary joint torque for lifting up the user leg and the exoskeleton itself. The simplified model is shown in Fig.3. In this simplified model, we assumed that all links and segments of human lower limbs are rigid and the mass distribution of each link or limb is uniform. The lengths of the links are indicated by the symbol d_i , m_i denotes mass of links, M_i denotes mass of human lower limbs and θ_i denotes the angle of joints, m_f denotes the total mass of user foot and the aluminum alloy footboard, i.e. $m_f = m_3 + M_3$. Besides, the motors mounted on the hip and knee joint respectively have masses (include the mass of harmonic gear reducer) m_{c1} and m_{c2} , and the friction of joint and gearing is ignored.

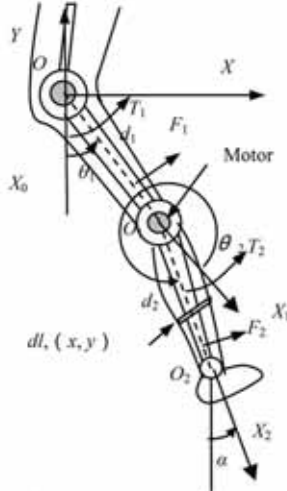


Fig. 3. Simplified model of the human-robot system

Using the derivative and the partial derivative knowledge, we can derive the hip torque T_1 and the knee torque T_2 .

$$\begin{bmatrix} T_1 \\ T_2 \end{bmatrix} = \begin{bmatrix} D_{11} & D_{12} \\ D_{21} & D_{22} \end{bmatrix} \begin{bmatrix} \ddot{\theta}_1 \\ \ddot{\theta}_2 \end{bmatrix} + \begin{bmatrix} 0 & D_{212} \\ D_{221} & 0 \end{bmatrix} \begin{bmatrix} \dot{\theta}_1^2 \\ \dot{\theta}_2^2 \end{bmatrix} + \begin{bmatrix} D_{311} & D_{312} \\ 0 & 0 \end{bmatrix} \begin{bmatrix} \dot{\theta}_1 \dot{\theta}_2 \\ \dot{\theta}_2 \dot{\theta}_1 \end{bmatrix} + \begin{bmatrix} D_1 \\ D_2 \end{bmatrix} \quad (1)$$

Where

$$\begin{aligned} D_{11} &= \left(\frac{1}{3}m_1 + \frac{1}{3}M_1 + m_{c2} + m_2 + M_2 + m_f \right) d_1^2 + \left(\frac{1}{3}m_2 + \frac{1}{3}M_2 + m_f \right) d_2^2 \\ &\quad + 2 \left(\frac{1}{2}m_2 + \frac{1}{2}M_2 + m_f \right) d_1 d_2 \cos \theta_2 \dot{\theta}_1 \\ D_{12} &= \left(\frac{1}{3}m_2 + \frac{1}{3}M_2 + m_f \right) d_2^2 + \left(\frac{1}{2}m_2 + \frac{1}{2}M_2 + m_f \right) d_1 d_2 \cos \theta_2 \end{aligned}$$

$$\begin{aligned}
D_{21} &= \left(\frac{1}{3}m_2 + \frac{1}{3}M_2 + m_f \right) d_2^2 + \left(\frac{1}{2}m_2 + \frac{1}{2}M_2 + m_f \right) d_1 d_2 \cos \theta_2 \\
D_{22} &= \left(\frac{1}{3}m_2 + \frac{1}{3}M_2 + m_f \right) d_2^2 \\
D_{212} &= -\left(\frac{1}{2}m_2 + \frac{1}{2}M_2 + m_f \right) d_1 d_2 \sin \theta_2 \\
D_{221} &= \left(\frac{1}{2}m_2 + \frac{1}{2}M_2 + m_f \right) d_1 d_2 \sin \theta_2 \\
D_{311} &= -\left(\frac{1}{2}m_2 + \frac{1}{2}M_2 + m_f \right) d_1 d_2 \sin \theta_2 \\
D_{312} &= -\left(\frac{1}{2}m_2 + \frac{1}{2}M_2 + m_f \right) d_1 d_2 \sin \theta_2 \\
D_1 &= \left(\frac{1}{2}m_1 + \frac{1}{2}M_1 + m_{c2} + m_2 + M_2 + m_f \right) gd_1 \sin \theta_1 \\
&\quad + \left(\frac{1}{2}m_2 + \frac{1}{2}M_2 + m_f \right) gd_2 \sin (\theta_1 + \theta_2) \\
D_2 &= \left(\frac{1}{2}m_2 + \frac{1}{2}M_2 + m_f \right) gd_2 \sin (\theta_1 + \theta_2)
\end{aligned}$$

We can also simplify the Eq. (1) to static body mechanics. Based on the Eq. (1), we can estimate the necessary output torque of the motors. It is well known that the torque is important to motors decided. Here, the weight of force sensors is not taken into account in the above model.

4. Dynamic Model and Control Strategy

4.1 Dynamic behavior of the PAWL and human

The behavior of walking support machines must be simple for user. So, the system should be worn easily; and, its sensors should not be placed directly on the user body.

In order to use PAWL as a human power assistant, we should consider when and how to make the power assist leg to provide assist to user. The analyses focus on the dynamics and control of human-robot interaction in the sense of the transfer of power and information. Sensor systems are equipped on PAWL to detect the motion information of the PAWL and user. Force sensors are used to measure the interaction force between the PAWL and user (the force caused from the motion difference between the walking support robot and human, all feedback forces are assumed to be on the sagittal plane). Encoders provide the pose of the low limbs (angle of the hip joint and knee joint). According to the information of the encoder, we can obtain the velocity of the joint. Motion intention may be rightly made certain by sensors fusion and calculated joint torque, and has to be directly transmitted to the control system.

It's well known that interaction force is produced between two or more objects when they are in contact. Contact force is an important piece of information that shows their interaction

state to some extent. Because the user is in physical contact with the exoskeleton, the power assist walking support leg kinematics must be close to human leg kinematics.

Using a simplified model, we can establish a model named mass-spring-viscosity system (shown in Fig. 4 (a)), which can be used as the interaction description. A simplified configuration of user's lower leg equipped with PAWL is shown in Fig. 4 (b). In order to found effective control strategy, firstly, we analyze the dynamic characteristics of the bone-muscle model. At the fore, we assume that the mechanism system is rigid, m denotes the mass of lower thigh; k and c denote the coefficient of muscle spring and viscosity respectively.

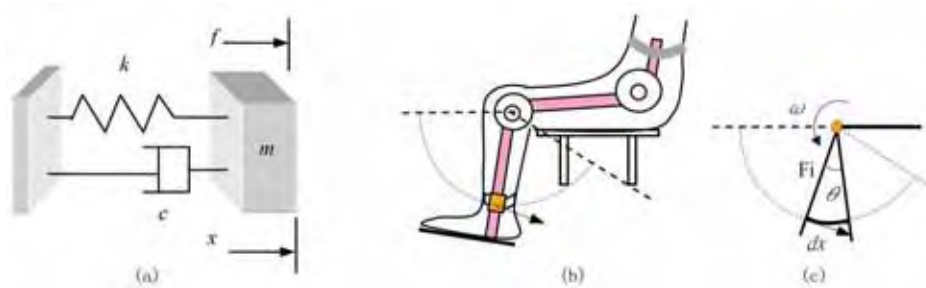


Fig. 4. Simplified model hybrid system

In the above simplified model, we ignore the disturbance which maybe caused by the friction of bearings and gears. It is described with the following differential equation

$$f = m\ddot{x} + c\dot{x} + kx \quad (2)$$

where

- f composition of forces, [N],
- m mass of exoskeleton, [kg],
- x position of exoskeleton, [m],
- \dot{x} velocity of exoskeleton, [m/s],
- \ddot{x} acceleration of exoskeleton, [m/s²],
- c viscosity coefficient of interface,
- k stiffness coefficient of interface.

Acceleration and velocity have another expression:

$$\ddot{x} = \frac{v_{n+1} - v_n}{dt} \quad , \quad \dot{x} = v_n \quad (3)$$

Substituting Eqs. (3) for (2), we obtain

$$v_{n+1} = \frac{dt}{m}(f_n - cv_n - kdx_n) + v_n \quad (4)$$

From Fig. 4 (c), we can obtain

$$v_n = \omega_n \cdot r \quad , \quad dx_n \doteq r \cdot d\theta_n = r\omega_n \cdot dt \quad (5)$$

$d\theta_n$ and w_n can be obtained by the information of encoder.

Considering the system controlled by PC periodically (control cycle time is indicated by the symbol T), dt can be approximately described with time T . That is

$$dt \doteq T \quad (6)$$

On inserting Eqs. (5), (6) into Eq. (4), we can obtain

$$\omega_{n+1} = \frac{T}{mr} (f_n - c\omega_n r - kr\omega_n T) + \omega_n = \frac{T}{mr} f_n + \left(1 - \frac{cT}{m} - \frac{kT^2}{m}\right) w_n \quad (7)$$

Because PAWL is a part of human body or human body is a part of PAWL, we must amend the Eq. (7). Here, except for the weight of the exoskeleton link, the weight of the user lower thigh must be included in the Eq. (7), i.e. the weight of the user thigh should be regarded as a part of the PAWL. Therefore, the user limb is not only the subject-body of force giving out but object-body of load to PAWL. Referring to (Zheng, 2002), we can obtain the segments relative weight of human body. Now a revised equation is given as follows:

$$\begin{aligned} \omega_{n+1} &= \frac{T}{(m + M)r} (f_n - c\omega_n r - kr\omega_n T) + \omega_n \\ &= \frac{T}{(m + M)r} f_n + \left(1 - \frac{cT}{(m + M)} - \frac{kT^2}{(m + M)}\right) \omega_n = \alpha f_n + \beta \omega_n \end{aligned} \quad (8)$$

Where

$$\alpha = \frac{T}{(m + M)r}, \quad \beta = 1 - \frac{cT}{(m + M)} - \frac{kT^2}{(m + M)}$$

The operator ω_{n+1} and ω_n are the output angular speed of reducer in the equations mentioned above.

Eq. (8) shows an approach that stands on the interaction force. In fact, it is difficult to obtain the exact value of α and β . The main reason is that the weight of segments of the human lower limb can not be measured accurately, and the coefficient k and c are not obtained accurately. We also found the thigh model according to the same rules as before. The Eq. (8) is very important to found the control strategy of the system. Here, each individual motor is controlled by a local controller with the velocity control scheme illustrated in Fig.5. The velocity is controlled by a simple PID feedback controller on all joints.

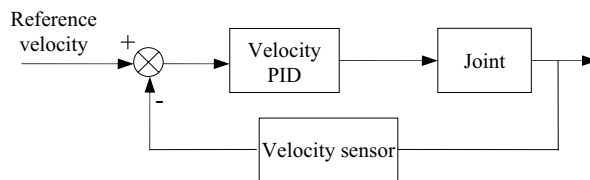


Fig. 5. PID velocity control Scheme

4.2 Control strategy

Fig.6 shows the dynamical control scheme of PAWL. The basic control demand of the PAWL rests on the notion that the control strategy must make the user comfortable, and ensure that the PAWL can provide power assist for the user. Based on Eq. (8), a pseudo-compliance control scheme was proposed to provide the exoskeleton with mechanisms to coordinate with human operator.

It is important that the system has ability to adapt itself to the gait of many human. And the system must have fine sensitivity in response to all movements.

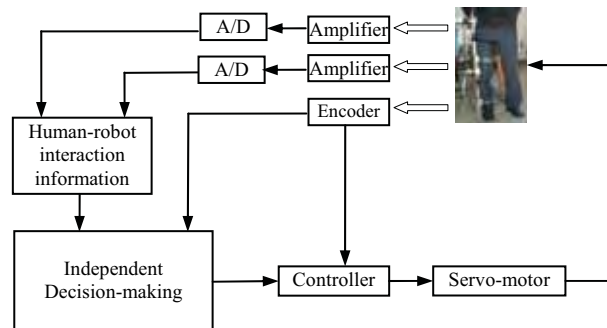


Fig. 6. PAWL dynamical control scheme

5. Experiments Result and Future Work

We have conducted experiments to demonstrate and verify the pseudo-compliance control method. Fig.6 shows the right side of PAWL. We use this experimental platform to permit human-robot walking. And we also obtain the interaction information between human lower limb and PAWL.

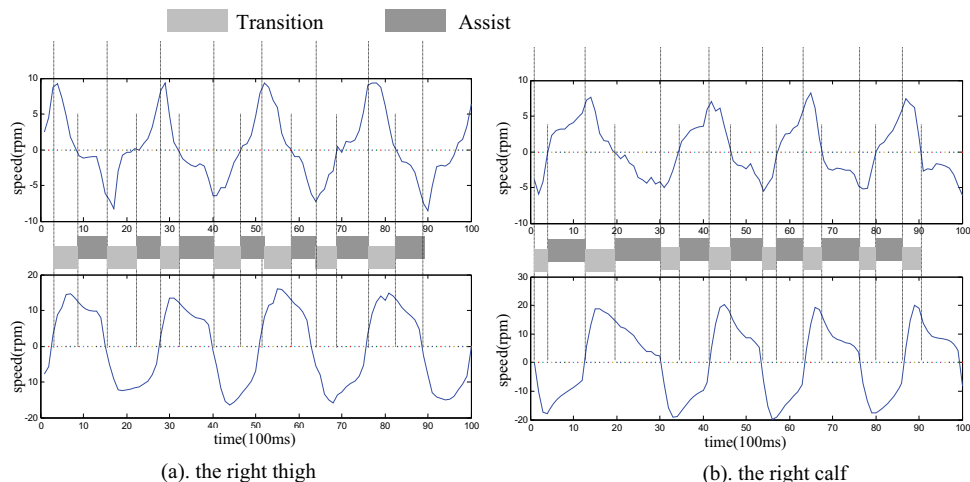


Fig. 7. Output response to experiment

In our experiments, the force sensors and dextral PAWL are used to verify the proposed control strategy. Force sensor fixed on the links is used to measure the interaction force between the experimental exoskeleton and human leg. Here, the sensors of FRF are not used in this experiment because the FRF sensor still processing. And, the software is designed especially for the experiment PAWL.

The work presented is developing a mechanism with the main goal of decreasing human inner force/increasing human strength. And human is in physical contact with PAWL in the sense of transfer mechanical power and information signals. Because of this unique interface, control of PAWL can be accomplished without any type of keyboard, switch and joystick. The final goal of our research is to develop a smart system which can support power for user without any accident.

Fig.7 shows the result of the single hybrid leg experiment. Two phases are in the each motion process of flexion/extension. In fact, we hope that the mechanism should provide much more power for user, so we should shorten the time of transition phase, and lengthen the time of assist. The judgement of user motion intention will be very important to improve the performance of power assist. The percentage of assist can be changed through regulating the coefficient of m , k and c . And, the coefficient of m , k and c (i.e. α , β) can also make the output velocity smoothness as shown in Fig. 8 (b).

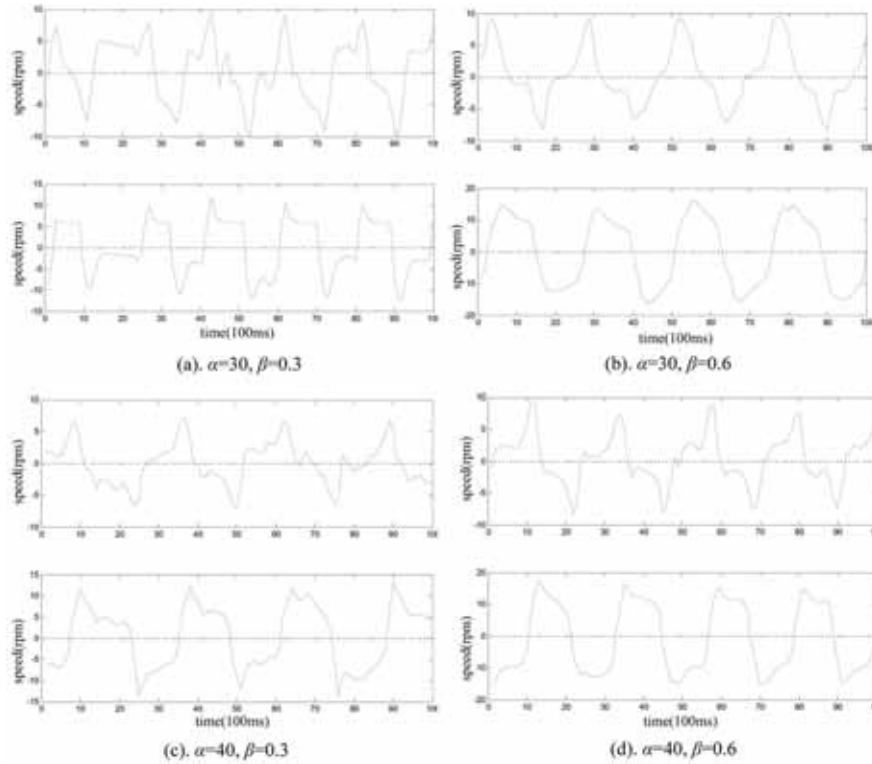


Fig. 8. Response to different coefficient

There is still significant work remaining. Through the calculation of the process of transition and assist, we may get the percentage of power assist from PAWL, and furthermore, we may found a certain relationship between the value of power assist support for user and the coefficient of m , k and c .

Current works on PAWL include developing FRF sensors, increasing sensor stability and sensitivity, improving the system control and sensing system and developing evaluation method of power assist supply. PAWL robot represents a high integration of robotics, information technology, communication, control engineering, signal processing and etc. Hopefully with continued improvement to the system performance, the PAWL will become a practical system for human power augmentation.

6. Acknowledgment

We like to thank the support from the National Science Foundation of China (Grant No. 60575054).

7. References

- H.Kazerooni (1990), Human-Robot Interaction via the Transfer of Power and Information Signals. *IEEE TRANSACTIONS ON SYSTEMS, MAN, AND CYBERNETICS*, VOL. 20, NO. 2, pp. 450-463.
- B.J. Makinson (1971), General Electric CO., Research and Development Prototype for Machine Augmentation of Human Strength and Endurance, Hardiman I Project, General Electric Report S-71-1056, Schenectady, NY.
- H.Kazerooni (2005), Exoskeletons for Human Power Augmentation. *Proc. IEEE/RSJ International Conference on intelligent Robots and Systems*, pp.3120-3125.
- Adam Zoss, H.Kazerooni, Andrew Chu (2005), On the Mechanical Design of the Berkeley Lower Extremity Exoskeleton (BLEEX). *Proc. IEEE/RSJ International Conference on intelligent Robots and Systems*, pp. 3132-3139.
- Ryan Steger, Sung Hoon Kim, H. Kazerooni (2006), Control Scheme and Networked Control Architecture of for the Berkeley Lower Extremity Exoskeleton (BLEEX), Proc. Of IEEE International Conference on Robotics and Automation, pp. 3469-3476.
- Yamamoto, Keijiyo; Hyodo, Kazuhito; Ishi, Mineo; Matsuo Takashi, T (2002). Development of power assisting suit for assisting nurse labor, *JSME International Journal, Series C: Mechanical Systems, Machine Elements and Manufacturing*, v 45, n 3, September, pp. 703-711.
- Keijiyo Yamamoto, Mineo Ishi, Hirokazu Noborisaka, Kazuhito Hyodo (2004), Stand Alone Wearable Power Assisting Suit-Sensing and Control Systems-, *Proc. IEEE International Workshop on Robot and Human Interactive Communication*, pp. 661-666.
- Kota Kasaoka, Yoshiyuki Sankai (2001), Predictive Control Estimating Operator's Intention for Stepping-up Motion by Exo-Skeleton Type Power Assist System HAL, *Proc. IEEE/RSJ International Conference on Intelligent Robots and Systems*, pp. 1578-1583.
- S. Lee, Y. Sankai (2002), Power Assist Control for Walking Aid with HAL-3 Based on EMG and Impedance Adjustment around Knee Joint, *Pro. IEEE/RSJ Intl. Conference on Intelligent Robots and Systems*, pp. 1499-1504.

- Hiroaki Kawamoto, Shigehiro Kanbe (2003), Power Assist Method for HAL-3 Estimating Operator's Intention Based on Motion Information, *Proc. IEEE International Workshop on Robots and Human Interactive Communication*, pp. 67-72.
- Hiroaki Kawamoto, Yoshiyuki Sankai (2004), Power Assist Method Based on Phase Sequence Driven by Interaction between Human and Robot Suit, *Proc. IEEE International Workshop on Robot and Human Interactive Communication*, pp. 491-496.
- Tomohiro Hayashi, Hiroaki Kawamoto, Yoshiyuki Sankai (2005), Control Method of Robot Suit HAL working as Operator's Muscle using Biological and Dynamical Information, *Proc. IEEE/RSJ International Conference on Intelligent Robots and Systems*, pp. 3455-3460.
- Takahiko Nakamura, Kazunari Saito, ZhiDong Wang and Kazuhiro Kosuge (2005), Control of Model-based Wearable Anti-Gravity Muscles Support System for Standing up Motion, *Proc. IEEE/ASME International Conference on Advanced Intelligent Mechatronics Monterey*, pp. 564-569.
- Xiuyuan Zheng (2002), *MODERN SPORTS BIOMECHANICS*, Beijing: National Defence Industry Press.
- Youlun Xiong (1992), *Robotics*, Beijing: Mechanical Industry Press.
- Takeshi Muto, Yoshihiro Miyake (2003), Co-emergence Process on the Humans' Cooperation for Walk-Support, *Proc. IEEE International Symposium on Computational Intelligence in Robotics and Automation*, pp. 324-329.
- Kiyoshi Nagai, Isao Nakanishi (2004), Force Analysis of Exoskeletal Robotic Orthoses and its Application to Mechanical Design, *Proc. IEEE/RSJ International Conference on Intelligent Robots and Systems*, pp. 1648-1655.
- Jaydeep Roy, Louis L. Whitcomb (2002), Adaptive Force Control of Position/Velocity Controlled Robots: Theory and Experiment, *IEEE TRANSACTION ON ROBOTICS AND AUTOMATION*, VOL. 18, NO. 2, pp. 121-137.
- Jerry E. Pratt, Benjamin T. Krupp, Christopher J. Morse (2004), The RoboKnee: An Exoskeleton for Enhancing Strength and Endurance During Walking, *Proc. IEEE International Conference on Robotics & Automation*, pp. 2430-2435.
- K.H.Low, Xiaopeng Liu, Haoyong Yu (2005), Development of NTU Wearable Exoskeleton System for Assistive Technologies, *Proc. IEEE International Conference on Mechatronics & Automation*, pp. 1099-1106.
- Kyoungchul Kong, Doyoung Jeon (2005), Fuzzy Control of a New Tendon-Driven Exoskeletal Power Assistive Device, *Proc. Of IEEE/ASME International Conference on Advanced Intelligent Mechatronics*, pp. 146-151.

Worm-like Locomotion Systems (WLLS) – Theory, Control and Prototypes

Klaus Zimmermann¹, Igor Zeidis¹, Joachim Steigenberger¹, Carsten Behn¹,
Valter Böhm¹, Jana Popp¹, Emil Kolev¹ and Vera A. Naletova²

¹*Technische Universität Ilmenau, ²Moscow State University*

¹*Germany/*²*Russia*

1. Introduction

Most of biologically inspired locomotion systems are dominated by walking machines - *pedal locomotion*. A lot of biological models (bipedal up to octopodal) are studied in the literature and their constructions were transferred by engineers in different forms of realization. *Non-pedal* forms of locomotion show their advantages in inspection techniques or in applications to medical technology for diagnostic systems and minimally invasive surgery (endoscopy). These areas of application were considered by (Choi et al., 2002), (Mangan et al., 2002), (Menciassi & Dario, 2003). Hence, this type of locomotion and its drive mechanisms are current topics of main focus.

In this chapter we discuss the problem of developing worm-like locomotion systems, which have the earthworm as a living prototype, from two points of view:

- modelling and controlling in various levels of abstraction,
- designing of prototypes with classical and non-classical forms of drive.

2. Motion and Control of WLLS

2.1 General Approach to WLLS

The following is taken as the basis of our theory:

- i. A worm is a terrestrial locomotion system of one dominant linear dimension with no active legs nor wheels.
- ii. Global displacement is achieved by (periodic) change of shape (such as local strain) and interaction with the environment.
- iii. The model body of a worm is a 1-dimensional continuum that serves as the support of various fields.

The continuum in (iii) is just an interval of a body-fixed coordinate. Most important fields are: mass, continuously distributed (with a density function) or in discrete distribution (chain of point masses), actuators, i.e., devices which produce internal displacements or forces thus mimicking muscles, surface structure causing the interaction with the environment.

Source: Climbing & Walking Robots, Towards New Applications, Book edited by Houxiang Zhang,
ISBN 978-3-902613-16-5, pp.546, October 2007, Itech Education and Publishing, Vienna, Austria

Observing the locomotion of worms one recognizes first a surface contact with the ground. It is well known, that, if there is contact between two bodies (worm and ground), there is some kind of friction, which depends on the physical properties of the surfaces of the bodies. In particular, the friction may be anisotropic (depends on the orientation of the relative displacement). This interaction (mentioned in (ii)) could emerge from a surface texture as asymmetric Coulomb friction or from a surface endowed with scales or bristles (we shall speak of spikes for short) preventing backward displacements. It is responsible for the conversion of (mostly periodic) internal and internally driven motions into a change of external position (undulatory locomotion (Ostrowski et al., 2006)), see (Steigenberger, 1999) and (Zimmermann et al., 2003).

One of the first works in the context of worms, snakes and scales is the paper of (Miller, 1988). The author considers, in a computer graphics context, mass-spring systems with scales aiming at modelling virtual worms and snakes and their animations.

Summarizing, we consider a WLLS in form of a chain of point masses in a common straight line (**a discrete straight worm**), which are connected consecutively by linear visco-elastic elements, see (Behn, 2005), (Behn & Zimmermann, 2006), (Zimmermann et al., 2002), (Zimmermann et al., 2003) for instance and Fig. 1.

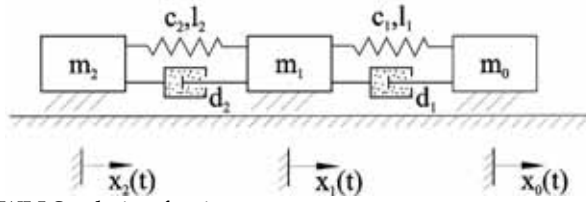


Fig. 1. Model of a WLLS - chain of point masses

In the next Subsection 2.2 we consider the case, where the point masses are endowed with scales, which make the friction orientation dependent (in sliding forward the frictional forces are minimal while in opposite direction the spikes dig in and cause large friction), see (Steigenberger, 1999) and (Steigenberger, 2004). In Subsection 2.3, due to (Behn, 2005) and (Behn & Zimmermann, 2006), we do not want to deal with reactive forces as before, instead we model this ground interaction as impressed forces - asymmetric (anisotropic) dry friction as a Coulomb sliding friction force, see (Blekhman, 2000).

2.2 Kinematic Theory of WLLS

In this subsection we focus on interaction via *spikes*.

The *kinematics* of this $DOF = n + 1$ system formulates as follows.

The spikes entail the differential constraint

$$\dot{x}_i(t) \geq 0, i = 0, \dots, n, \forall t \quad (1)$$

whence with $S_i = x_0 - x_i$ there holds $\dot{x}_0 \geq \dot{S}_i$ for all i and thus

$$\dot{x}_0 = V_0 + w, V_0 := \max\{\dot{S}_i, i = 0, \dots, n\}, w \geq 0. \quad (2)$$

w is a common part of the velocities, it describes a rigid motion of the system. The value w remains undetermined in kinematics, it only follows from dynamics.

The dynamics of the WLLS are governed by the momentum laws of the point masses,

$$m\ddot{x}_i = g_i + \mu_i - \mu_{i+1} + \lambda_i, \quad i = 0, \dots, n, \quad (3)$$

where the g_i are external physically given forces, μ_i are internal forces ($\mu_0 = \mu_{n+1} := 0$), whereas λ_i are the *reaction forces* corresponding to the *one-sided* constraint (1), so there hold the *complementary slackness conditions*

$$\dot{x}_i \geq 0, \quad \lambda_i \geq 0, \quad \dot{x}_i \cdot \lambda_i = 0. \quad (4)$$

Let $g_i + \mu_i - \mu_{i+1} =: f_i$, then for any motion (4) will be satisfied by the 'controller'

$$\lambda_i = -\frac{1}{2}(1 - \text{sign}(\dot{x}_i))(1 - \text{sign}(f_i))f_i. \quad (5)$$

Now let us suppose a *kinematic drive*, i.e., the actuators are assumed to precisely prescribe the mutual distances l_j as functions of time, see Fig. 2.

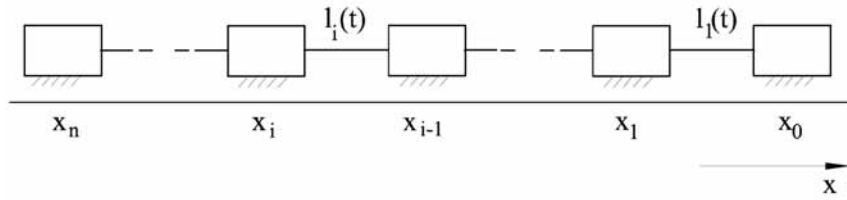


Fig. 2. WLLS with kinematic drive

The kinematic drive implies the *holonomic constraint*

$$x_{j-1} - x_j - l_j(t) = 0, \quad j = 1, \dots, n \quad (6)$$

with μ_j as respective reactions. \dot{S}_i and V_0 are now given functions of time, the *DOF* of the system shrinks to 1.

We confine the external forces to $g_i = -k\dot{x}_i - \Gamma$ then, summing up all the momentum laws

(3) while observing $\dot{x}_i = V_0 - \dot{S}_i + w$ there follows a *bimodal ADE* for w and $\lambda := \frac{1}{n+1} \sum_0^n \lambda_i$,

$$\begin{aligned} m\dot{w} + k w + \sigma(t) &= \lambda, & w \geq 0, \lambda \geq 0, w\lambda = 0, \\ \sigma &:= m\dot{W}_0 + kW_0 + \Gamma, \quad W_0 := V_0 - \frac{1}{n+1} \sum_0^n \dot{S}_i. \end{aligned} \quad (7)$$

In mode 1 $\{w > 0; \lambda = 0\}$ no point mass is at rest whereas in mode 2 $\{w = 0, \lambda > 0\}$ at least one does not move (active spike). If we set $w = 0$ then all what follows is called *kinematic theory*.

It is easy to deduce: *If $\sigma(t) > 0$ for all t then the motion is always in mode 2, at any time at least one spike is active, the motion is well-determined by kinematics.*

We consider an example with $n = 2$. The actuators are chosen so as to generate l_1 and l_2 as T-periodic piecewise cosine functions. This given gait will be reconsidered in Subsection 2.3. Fig. 3 shows l_1, l_2 vs. t/T (left), and with some system data m, k, Γ chosen the corresponding worm motion (right, t -axis upward).

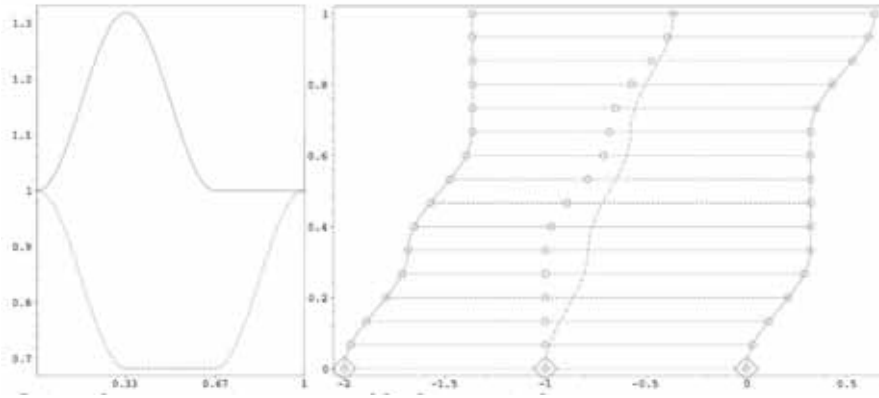


Fig. 3. Gait and worm motion governed by kinematic theory

Mind that one spike is active (resting point mass) at any time. So this gait might be suitable for motion 'in the plane'. An uphill gait (two resting point masses at any time) could easily be constructed, too (Steigenberger, 2004). To ensure $w = 0$ and sufficiently small λ (to prevent the spikes from breakdown) certain restrictions for T and Γ must be obeyed, see (Steigenberger, 2004).

Two items deserve particular observation.

- i. Using common actuators the proper control variable u is not l_i or \dot{l}_i but rather an electrical voltage or a pressure applied to some piezo or hydraulic device that in turn acts to the point masses via some visco-elastic coupling. In this case there remains $DOF = n+1$ and the internal forces μ_j follow a law of the form
$$\mu_j = c(x_{j+1} - x_j) + d(\dot{x}_{j+1} - \dot{x}_j) + u_j(t). \quad (8)$$
- ii. By chance it could practically be promising to consider asymmetric dry friction instead of spikes (though the simple kinematical theory then is passé). In a rough terrain, unknown or changing friction coefficients lead to uncertain systems and require adaptive control to track a kinematic gait, that has been discovered as a favourable one. This objective will be addressed in the next section.

2.3 WLLS as a Dynamical Control System

In this subsection we model the ground interaction as an **asymmetric Coulomb dry friction force** F (see above), which is taken to be different in the magnitude depending on the direction of each point mass motion:

$$\dot{x} \mapsto F(\dot{x}) = \begin{cases} -F^+, & \dot{x} > 0 \\ F^0, & \dot{x} = 0 \\ F^-, & \dot{x} < 0 \end{cases} \quad (9)$$

where $F^+, F^- > 0$ are fixed with $F^- \gg F^+$ and F^0 is arbitrary, $F^0 \in (F^-, -F^+)$.

For later simulation we restrict the number of point masses to $n = 2$, but we point out that our theory is valid for fixed but arbitrary $n \in N$, see (Behn & Zimmermann, 2006).

Mathematical model

Firstly, we derive the differential equations of motion of the WLLS by using Newton's second law:

$$\begin{aligned} m_0 \ddot{x}_0 &= -c_1(x_0 - x_1) - d_1(\dot{x}_0 - \dot{x}_1) + F_0(\dot{x}_0) + u_1(t) \\ m_1 \ddot{x}_1 &= \begin{cases} -c_1(x_1 - x_2) + c_2(x_0 - x_1) - d_1(\dot{x}_1 - \dot{x}_2) + d_2(\dot{x}_0 - \dot{x}_1) \\ \quad + F_1(\dot{x}_1) + u_2(t) - u_1(t) \end{cases} \\ m_2 \ddot{x}_2 &= c_2(x_1 - x_2) + d_2(\dot{x}_1 - \dot{x}_2) + F_2(\dot{x}_2) - u_2(t) \end{aligned} \quad (10)$$

with $x_0(0) = x_{00}$, $x_1(0) = x_{10}$, $x_2(0) = x_{20}$, $\dot{x}_0(0) = x_{01}$, $\dot{x}_1(0) = x_{11}$, $\dot{x}_2(0) = x_{21}$ (all initial values are real numbers) and $g_i = 0$. Putting

$$u_1 := c_1 l_1 \text{ and } u_2 := c_2 l_2 \quad (11)$$

then u_{ij} is in fact a control of the original spring length. Therefore, we have *internal* inputs and no longer external force inputs, as in (Behn, 2005). New outputs of this system could be the actual distances of the point masses

$$y_1 := x_0 - x_1 \text{ and } y_2 := x_1 - x_2. \quad (12)$$

Therefore, this system (10), (12) is described by a mathematical model that falls into the category of quadratic, nonlinearly perturbed, minimum phase, multi-input $u(\cdot)$, multi-output $y(\cdot)$ systems with strict relative degree two. In a normalized form (after elaborate transformations) the zero dynamics of the system are decoupled from the controlled part of the system.

Control Objective

For the further analysis of this system we suppose that the masses are all equal, but unknown, also the damping factors and spring stiffnesses, and the friction magnitudes as well (**uncertain systems**).

The consideration of uncertain systems leads to the use of adaptive control. The aim is to design universal adaptive controllers, which learn from the behavior of the system, so automatically adjust their parameters and achieve a pre-specified control objective. Simple adaptive mechanisms, which achieve tracking of a given reference signal within any pre-specified accuracy λ , will be introduced. $\lambda > 0$ denotes the size of the feasible tracking error (we do not focus on exact tracking).

Precisely, given an arbitrarily small $\lambda > 0$, a control strategy $y \mapsto u$ is sought which, when applied to the system, achieves λ -tracking (λ -tracking control objective) for every reference signal $y_{ref}(\cdot)$ (belonging to a certain function class, for instance a given favoured kinematic gait presented in the previous subsection), i.e., the following:

- i. every solution of the closed-loop system is defined and bounded on $R_{\geq 0}$, and
- ii. the output $y(\cdot)$ tracks $y_{ref}(\cdot)$ with asymptotic accuracy quantified by $\lambda > 0$ in the sense that $\max\{0, \|y(t) - y_{ref}(t)\| - \lambda\} \rightarrow 0$ as $t \rightarrow +\infty$.

The last condition means that the error $e(t) := y(t) - y_{ref}(t)$ is forced, via the adaptive feedback mechanism (controllers (13) and (14)), towards a ball around zero radius $\lambda > 0$, see Fig. 4.

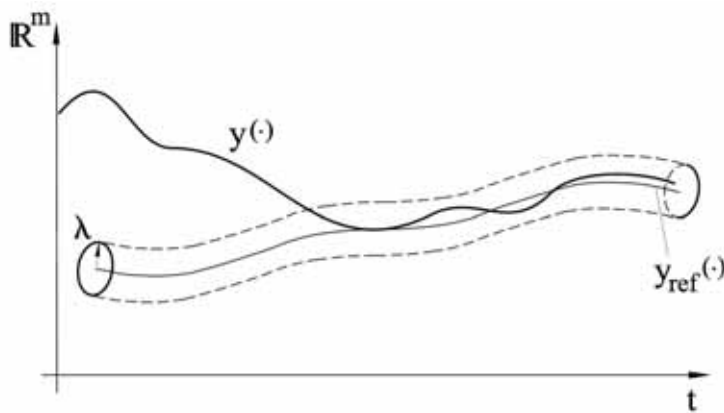


Fig. 4. The λ -radius around the reference signal

Controllers

Let us consider the following two λ -trackers, see also (Behn, 2005).

$$\left. \begin{array}{l} e(t) := y(t) - y_{ref}(t) \\ u(t) = -\left(k(t) e(t) + \frac{d}{dt}[k(t) e(t)] \right) \\ \dot{k}(t) = (\max\{0, \|e(t)\| - \lambda\})^2 \end{array} \right\} \quad (13)$$

with $k(0) = k_0 \in R$, $\lambda > 0$, $y_{ref}(\cdot) \in W^{2,\infty}$ (a Sobolev-Space), $u(t), e(t) \in R^2$ and $k(t) \in R$.

The second one includes a dynamic compensator due to a controller of (Miller & Davison, 1991). This controller allows us to avoid the drawback of using the derivative of the output, mentioned above, in the following way:

$$\left. \begin{array}{l} e(t) := y(t) - y_{ref}(t) \\ u(t) = -\left(k(t) \vartheta(t) + \frac{d}{dt}[k(t) \vartheta(t)] \right) \\ \dot{\vartheta}(t) = -k(t)^2 \vartheta(t) + k(t)^2 e(t) \\ \dot{k}(t) = (\max\{0, \|e(t)\| - \lambda\})^2 \end{array} \right\} \quad (14)$$

with $\vartheta(0) = \vartheta_0$, $k(0) = k_0 > 0$, $\lambda > 0$, $y_{ref}(\cdot) \in W^{2,\infty}$, $u(t), e(t), \vartheta(t) \in R^2$ and $k(t) \in R$.

We stress, that the controller (14) does not invoke any derivatives.

The structure of the feedback law and the simple adaptation law of the controllers in this subsection already exist in the literature, but they were only applied to systems with relative degree one. The considered WLLS has relative degree two. Therefore, the novelty is the application of the controller to systems with relative degree two. There are only a few papers which focus the adaptive λ -tracking problem for system with relative degree two, but the feedback law here is simpler than the introduced ones in (Dragan & Halanay, 1999), (Ye, 1999), (Miller & Davison, 1991).

These controllers achieve λ -tracking (for the proofs the reader's attention is invited to (Behn, 2005)) as presented in the following simulations. We apply both controllers (13) and (14) to system (10), (12) to track the given gaits.

2.4 Simulations

In this subsection we apply the presented simple adaptive λ -tracking control strategies to our WLLS (dynamical control system) in order to track given reference signals. Firstly, we try to track a time-shift $\sin(\cdot)$ -signal, and, second, a kinematic gait developed in (Steigenberger, 2004) to achieve a certain movement of the WLLS. The numerical simulations will demonstrate and illustrate that the adaptive controllers work successfully and effectively. We point out, that the adaptive nature of the controllers is expressed by the arbitrary choice of the system parameters. It is obvious that for numerical simulation the system data have to be chosen fixed and known, but the controllers are able to adjust their gain parameter to each set of system data.

The tracking results when applying controller (13) to our WLLS are already presented in (Behn & Zimmermann, 2006). Therefore, we choose the same parameters (dimensionless) as there to obtain comparable simulations in using the second controller (14). Then we have:

- system: $m_0 = m_1 = m_2 = 1$, $c_1 = c_2 = 10$, $d_1 = d_2 = 5$, $x_{00} = 0$, $x_{10} = 2$, $x_{20} = 4$, $x_{01} = 0$, $x_{11} = 0$, $x_{21} = 0$;
- Coulomb friction forces: $F^+ = 1$, $F^- = 10$, hence we have by an approximation $v_i \mapsto 5.5 \tanh(40v_i) - 4.5$, $i = 0, \dots, 2$;
- λ -tracker (controller): $\lambda = 0.2$, $k_0 = 1$, $\vartheta_1(0) = 1$, $\vartheta_2(0) = 1$.

In order to detect differences we present the simulation results with the λ -trackers (14) and (13), respectively, side by side.

Tracking of a Gait Presented in Fig. 3, left

This gait is derived from the theory of a chain of point masses with spikes and links of given t -dependent lengths. Such a theory is essentially kinematical and does not require dynamics from the very beginning, see Subsection 2.2. In (Steigenberger, 2004) two paradigmatic gaits for a three point system were derived such that at any time during motion the same (prescribed) number of spikes is active: one in a fast ‘in-plane gait’, two in a slow ‘up-hill gait’. We try to track this fast gait in our dynamical theory, it is for $t \in [0,1]$:

$$t \mapsto y_{ref}(t) = \begin{cases} l_0[1 - \varepsilon(-1 + \cos(3\pi t))] & , t \in [0, 2/3) \\ l_0 & , t \in [2/3, 1] \\ l_0[1 - \varepsilon(1 - \cos(3\pi t))] & , t \in [0, 1/3) \\ l_0[1 - 2\varepsilon] & , t \in [1/3, 2/3) \\ l_0[1 - \varepsilon(1 + \cos(3\pi t))] & , t \in [2/3, 1] \end{cases}, \quad (15)$$

where l_0 is the original length (dimensionless chosen as 2 units) and $2\varepsilon = 0.3$ is the elongation. This gait is periodically repeated. We obtain the following simulations.

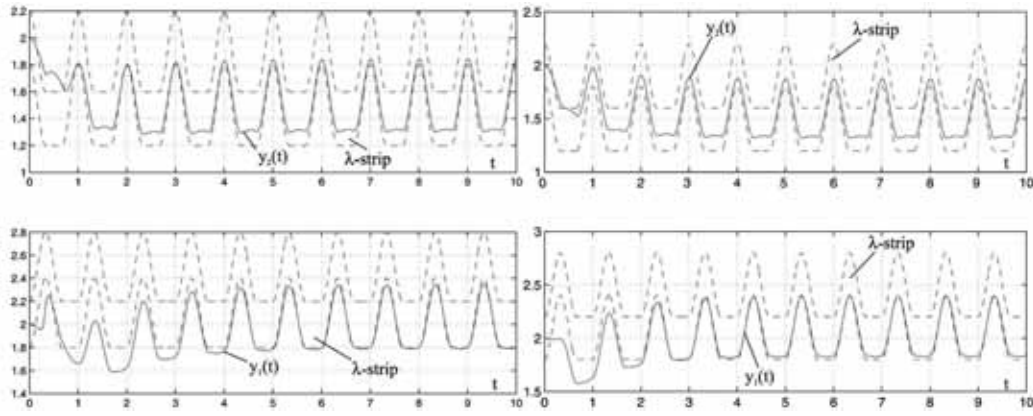


Fig. 5. Outputs and λ -strips – left: for (14), right: for (13)

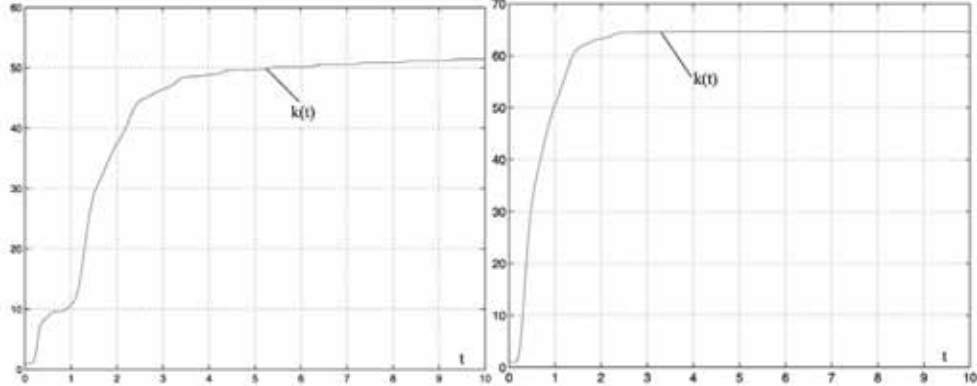


Fig. 6. The gain parameters - left: for (14), right: for (13)

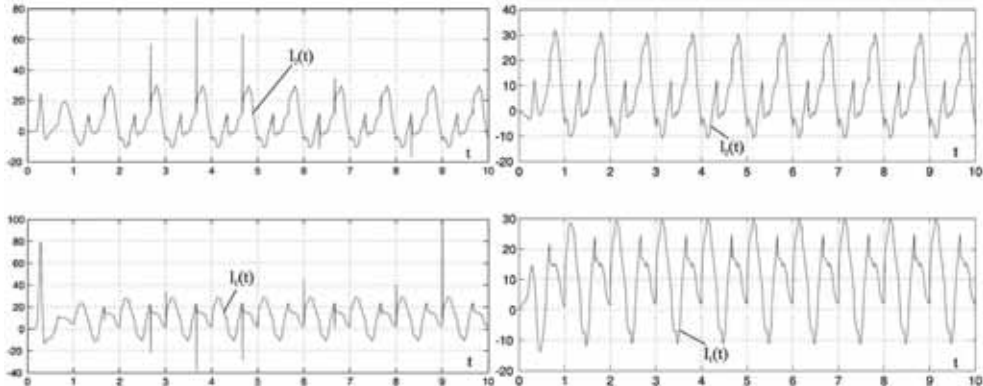


Fig. 7. The control inputs - left: for (14), right: for (13)

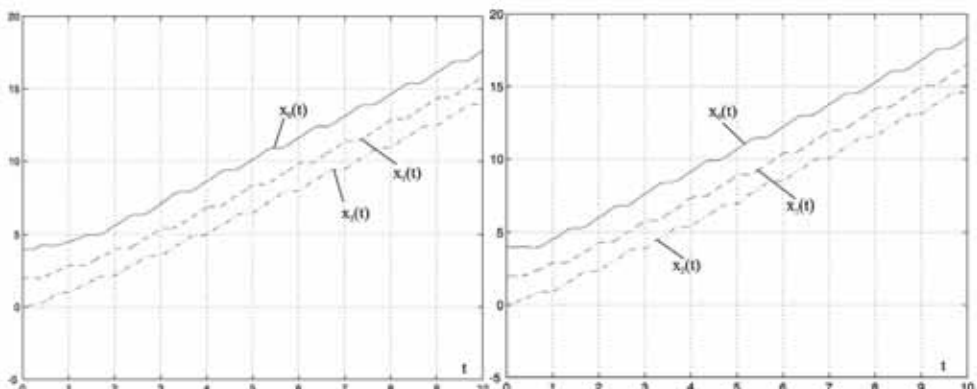


Fig. 8. The motions of the worm - left: with (14), right: with (13)

Fig. 5 shows the outputs of the systems and the according λ -strips. The reference signal is tracked very quickly with controller (13) in comparison to controller (14). In Fig. 5, left, the

outputs are not captured yet. The gain parameters, shown in Fig. 6, increase as long as the outputs are outside the λ -strips. Fig. 7 shows the necessary control inputs, and Fig. 8 the corresponding motions of the worm.

It can be seen that controller (13) works more effectively than controller (14) because we feed back more information about the output derivative than (14), which has to estimate the derivative. Hence, in the simulation with controller (14), the outputs are not captured on the considered time interval and the gain parameter is still increasing. Fig. 6, right, clearly shows the convergence of the gain parameter in the simulation with controller (13).

2.5 Electromechanical Prototype

A prototype was designed in order to check the above-mentioned theory (Abaza, 2006). It consists of two stepping motors and a dummy to produce a three point mass worm system (Fig. 9). Each stepping motor can separately travel along a threaded rod in both directions with different controllable speeds to generate \dot{l}_i .



Fig. 9. Three point mass worm system

Additionally, a special bristle-structure had been integrated (Fig. 10) to prevent the point masses from slipping backwards. Experiments justified the results of the theory.



Fig. 10. The bristle-structure

2.6 Open Problems

The following problems should be considered for future work:

- algorithms to construct preferable kinematic gaits;

- to include a suitable friction law allowing for stiction;
- revised control objectives
 - keep spikes (improved Coulomb friction with a big stiction coefficient for negative velocities F_0^-);
 - prescribe $y_{ref}(\cdot)$ as a kinematic gait;
 - let c_i and d_i be random (possibly t -dependent).

3. WLLS Using Deformable Magnetizable Media

3.1 Introductional Remarks

The realization of locomotion systems using the deformation of magnetizable materials (a magnetic fluid or a magnetizable polymer) in a magnetic field is an actual problem. The initiator of motion in such devices is an alternate magnetic field, which forms to exterior sources (electromagnetic system or motion permanent magnets). In (Zimmermann et al., 2004a, b) the theory of a flow of layers of magnetizable fluids in a travelling magnetic field is considered. It is shown, that the travelling magnetic field can create a flux in the fluid layers. This effect can be applied for the realization of locomotion. A micro-robot with individual cells corresponding to the earthworm's segment and sealed with water-based magnetic fluid is developed by (Saga & Nakamura, 2002, 2004).

In the present chapter theoretical and experimental possibilities of using deformable magnetizable media as actuators for mobile robots are investigated.

In the subsection 2.5 a classical electromechanical drive was used for controlling the distance between the two masses of the WLLS. In (Zimmermann et al. 2003) we considered a system of two masses connected by a piezo element. In the following second subsection we used a magneto-elastic element as an internal drive. The undulatory locomotion of an biological inspired artificial worm is based on travelling waves on its surface. Therefore the expression for the magnetic field strength creating a sinusoidal wave on the surface of a viscous magnetic fluid as a function of the characteristics of the fluid (viscosity, surface tension, and magnetic permeability) and the parameters of the wave are obtained in the third also theoretically oriented subsection of this section. In the fourth subsection the motions of three samples of a magnetizable body (magnetizable worm) in an alternate magnetic field are studied experimentally for large diapason of the electromagnetic system frequency. The prolate bodies of the magnetizable composites (an elastic polymer and solid magnetizable particles) and a capsule with a magnetic fluid are used. The analytical estimation and numerical calculation of the deformation of the bodies in applied magnetic field and of the velocity of the bodies are done. A deformable magnetizable worm in a magnetic field is a prototype of a mobile crawling robot. Such devices have some characteristics, which allow to use them in medicine and biology. For example, it does not contain solid details contacting with a surrounding medium and it moves autonomously.

The fives subsection deals with fundamental investigations necessary for the design and the application of segmented artificial worms, which have the earthworm as living prototype, and of new passive locomotion systems. A important question in this interconnection is the estimation of the pressure distribution in the magnetic fluid under the influence of a controlled magnetic field.

3.2 Modelling of WLLS with Magneto-Elastic Elements

In (Turkov, 2002) a deformation of the elastic composite body, when a magnetic field is applied, is considered. A formula, which allows to calculate the deformation of a parallelepiped in noninductive approximation was obtained. If the Lame coefficients λ and η satisfy the condition $\lambda >> \eta$ then relative lengthening in the direction of the axis OX (for small strains), when magnetic field $\mathbf{H} = \mathbf{H}_0$ in orthogonal direction is applied, is given by expression $u = \frac{p}{E_y^{eff}} + u_0$ (Fig. 11). Here p is the density of surface force, u_0 is the deformation of

the sample, produced by the action of the magnetic field only in absence of force ($p = 0$), E_y^{eff} is the effective value of the Young modulus

$$u_0 = \frac{\mu_0 [2(\mu^0 - 1) - a_1] H^2}{12\eta \left(1 + \frac{2}{3}G\right)} > 0, \quad E_y^{eff} = 3\eta \frac{\left(1 + \frac{2}{3}G\right)}{\left(1 + \frac{1}{2}G\right)}, \quad G = \frac{\mu_0 a_1 H_0^2}{2\eta}.$$

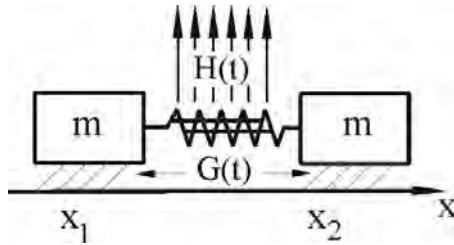


Fig. 11. Model of a WLLS with two mass points, non-symmetric Coulomb friction and a periodic internal force $G(t)$ produced by an external magnetic field H

The value $\mu_0 = 4\pi \times 10^{-7} N/A^2$ is the permeability of free space, μ^0 is the permeability of the unstrained material, $a_1 = -\frac{2}{5}(\mu^0 - 1)^2$. By the action of a magnetic field the sample of the composite with a drop of a magnetic fluid lengthens, and the value modulus E_y^{eff} in a magnetic field has to become less than without a magnetic field. The experimental dependencies between the stress and the strain without influence of field ($H = 0$) and with influence of a field ($H = 1.5 \cdot 10^5$ A/m) for a sample with the length $l_0 = 29$ mm and the area of cross section $S_0 = 5.5$ mm² is shown in Fig. 12.

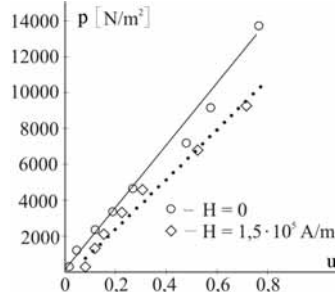


Fig. 12. Stress p vs. strain u

The size of the ferromagnetic particles in the magnetic fluid is about 110 Å. The experiment allowed us to define $u_0 = u(0) = 0,071$.

The motion of a system of two material points x_1 and x_2 with the masses m , connected by a spring of stiffness $c = E_y^{eff} \cdot S_0 / l_0$ ($\omega^2 = c/m$) along an axis x is considered (Fig. 11). It is supposed that the points are under the action of a small non-symmetric Coulomb dry frictional force $mF(\dot{x})$, depending on velocities $\dot{x} = \dot{x}_i$ ($i=1,2$), where $F(\dot{x}) = F^+$ if $\dot{x} > 0$, $F(\dot{x}) = -F^-$ if $\dot{x} < 0$, $F(\dot{x}) = F_0$ if $\dot{x} = 0$; $-F^- < F_0 < F^+$, $F^- \geq F^+ \geq 0$. By influence of an external harmonic magnetic field a small harmonic internal forces is produced: $G(t) = \frac{1}{2}u_0 c l_0 (1 + \cos \psi)$, $\psi = \nu t$. We introduce the dimensionless variables (the dimensional variables are denoted here with the asterisk): $x_1, x_2 = x_1^*, x_2^* / l_0$, $t = t^* \omega$, $v = v^* / \omega$, $F = F^* / (\frac{1}{2}u_0 l_0 \omega^2)$, $\varepsilon = \frac{1}{2}u_0 \ll 1$. The dimensionless equations of the motion are:

$$\begin{aligned} \ddot{x}_1 + x_1 - x_2 &= -\varepsilon [F(\dot{x}_1) + (1 + \cos \psi)], \\ \ddot{x}_2 + x_2 - x_1 &= -\varepsilon [F(\dot{x}_2) - (1 + \cos \psi)]. \end{aligned} \quad (16)$$

To the system (16) we apply the procedure of averaging. For this purpose we introduce new variables: the velocity of the center of mass $V = (\dot{x}_1 + \dot{x}_2)/2$ and the deviation relatively to the center of mass $z = (x_2 - x_1)/2$. Replacing $z = a \cos \varphi$, $\dot{z} = -a \Omega \sin \varphi$, $\varphi = \Omega t + \vartheta$, $\Omega = \sqrt{2}$ where V, a, ϑ - slow variables, we receive system (16) in a standard form:

$$\begin{aligned} \dot{V} &= -\frac{\varepsilon}{2} [F(V + a \Omega \sin \varphi) + F(V - a \Omega \sin \varphi)], \\ \dot{a} &= -\frac{\varepsilon}{2\Omega} \sin \varphi [F(V + a \Omega \sin \varphi) - F(V - a \Omega \sin \varphi) + 2(1 + \cos \psi)], \\ \dot{\varphi} &= \Omega - \frac{\varepsilon}{2a\Omega} \cos \varphi [F(V + a \Omega \sin \varphi) - F(V - a \Omega \sin \varphi) + 2(1 + \cos \psi)], \\ \dot{\psi} &= \nu. \end{aligned} \quad (17)$$

We investigate the system (17) in a vicinity of the main resonance $\nu = \Omega + \varepsilon \Delta$ ($\Delta \neq 0$), introducing a new slow variable $\xi = \psi - \varphi$. After averaging on a fast variable φ we obtain:

$$\begin{aligned} \dot{V} &= \begin{cases} -\varepsilon \left(\frac{F^- + F^+}{\pi} \arcsin \frac{V}{a\Omega} - \frac{F^- - F^+}{2} \right) & \text{if } 0 \leq V < a\Omega, \\ -\varepsilon F^+ & \text{if } V \geq a\Omega, \end{cases} \\ \dot{a} &= \begin{cases} -\frac{\varepsilon}{\Omega} \left(\frac{F^- + F^+}{\pi} \sqrt{1 - \frac{V^2}{a^2 \Omega^2}} + \frac{a}{2} \sin \xi \right) & \text{if } 0 \leq V < a\Omega, \\ -\varepsilon \frac{a}{2\Omega} \sin \xi & \text{if } V \geq a\Omega, \end{cases} \\ \dot{\xi} &= \varepsilon \left(-\frac{1}{2\Omega} \cos \xi + \Delta \right). \end{aligned} \quad (18)$$

We are interested in an approximately steady motion as a single whole, therefore we seek for the solution $\dot{V} = 0$. Then from system (18) we have $\dot{a} = \dot{\xi} = 0$ and

$$\begin{aligned} V &= \frac{\sin \Phi}{|\Delta|} \sqrt{\frac{1}{4} - E^2 \cos^2 \Phi}, \quad a = \frac{1}{\Omega |\Delta|} \sqrt{\frac{1}{4} - E^2 \cos^2 \Phi}, \quad E \cos \Phi \leq \frac{1}{2}, \\ \xi &= \arccos \left[-\frac{2\Delta}{|\Delta|} \sqrt{\frac{1}{4} - E^2 \cos^2 \Phi} \right], \quad E = \frac{F^- + F^+}{\pi}, \quad \Phi = \frac{\pi}{2} \cdot \frac{F^- - F^+}{F^- + F^+}. \end{aligned} \quad (19)$$

The result of the numerical integration of the exact system (1) is given in Figure 13.

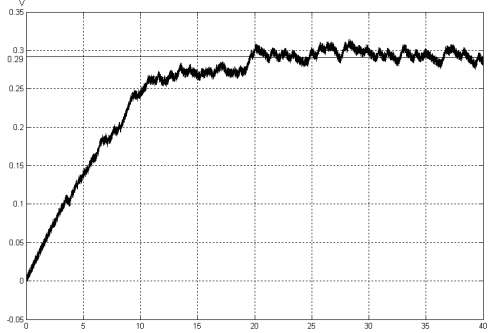


Fig. 13. Velocity V vs. time t

The following values of parameters for a magneto-elastic sample as described in Section 1 are taken: $m = 3 \times 10^{-3} \text{ kg}$, $E_y^{eff} = 1.6 \times 10^4 \text{ N/m}^2$, $u_0 = 0.071$, $l_0 = 29 \text{ mm}$, $S_0 = 5.5 \text{ mm}^2$, $\omega = 32 \text{ s}^{-1}$. So, the values of the parameters are: $\varepsilon = 0.036$, $F_+ = 0.5$, $F_- = 1$, $\Delta = 0.5$. The

formula (4) gives the value for the dimension velocity of center of mass $V = 0.29 \text{ m/s}$. The average velocity of such locomotion systems depends on the difference of the friction coefficients between the system and the substrate, which depends on the directions of motion.

3.3 Locomotion Using a Magnetic Fluid in a Traveling Magnetic Field

We consider a plane flow of an incompressible viscous magnetic fluid layer along a horizontal surface in a non uniform magnetic field (see Fig. 14). The magnetic permeability of the fluid μ is assumed to be constant. The pressure on the free fluid surface is constant. In the case of a constant magnetic permeability, the body magnetic force is absent and the magnetic field manifests itself in a surface force acting on the free surface (Rosenweig, 1985).

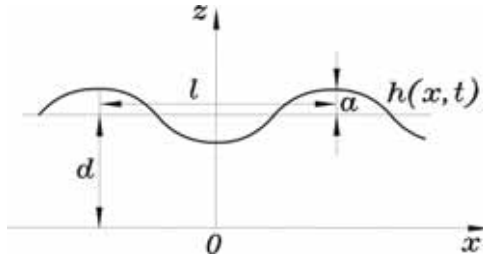


Fig. 14. Magnetic fluid layer

The gravity is not taken into account. In this case, the system of equations consists of the continuity and Navier-Stokes equations:

$$\operatorname{div} \mathbf{V} = 0, \quad \frac{\partial \mathbf{V}}{\partial t} + (\mathbf{V} \nabla) \mathbf{V} = -\frac{1}{\rho} \operatorname{grad} p + \frac{\eta}{\rho} \Delta \mathbf{V}. \quad (20)$$

Here, \mathbf{V} is the velocity vector (u and w are the horizontal and vertical coordinates), p is the fluid pressure, η is the dynamic fluid viscosity coefficient, ρ is the fluid density, and t is time.

On the rigid substrate $z=0$, the no-slip condition is satisfied:

$$\mathbf{V}(z=0) = \mathbf{0} \quad (21)$$

On the free surface $z=h(x, t)$, conditions of two types, kinematic and dynamic ones, should be satisfied. The kinematic condition is of the form:

$$\frac{dh}{dt} = \frac{\partial h}{\partial t} + u \frac{\partial h}{\partial x} = w \quad (22)$$

The dynamic conditions of continuity of the normal and tangential stresses on the free surface $z=h(x, t)$ take the form (neglecting the influence of the environment)

$$\left[-p + \gamma \frac{1}{R} + \frac{B_n^2}{8\pi} \left(\frac{1}{\mu} - 1 \right) - \frac{H_t^2}{8\pi} (\mu - 1) \right] \mathbf{n} + \tau_{ij} n^j \mathbf{e}^i = \mathbf{0}. \quad (23)$$

Here, τ_{ij} are the viscous stress tensor components, R is the radius of curvature of the surface $z=h(x,t)$, \mathbf{n} is the vector of outward normal to the surface, \mathbf{e}^j are the basis vectors, γ is the film surface tension coefficient, $B_n = \mu H_n$ is the normal component of the magnetic field strength vector. The magnetic field \mathbf{H} is assumed to be fixed, since the non-inductive approximation implies $\mu - 1 \ll 1$.

We will assume that the magnetic field creates the periodic travelling wave on the surface of a sufficiently thin layer (we denote the dimensional variables with the asterisk *):

$$h^*(x,t) = d + a \cos(\omega t^* - kx^*), \quad \varepsilon = d \cdot k \ll 1. \quad (24)$$

We introduce the dimensionless variables

$$\begin{aligned} x &= x^* \cdot k, \quad z = z^*/d, \quad h = h^*/d, \quad \delta = a/d, \quad u = u^*/U_c, \quad w = w^* U_c / \varepsilon, \quad U_c = \omega/k, \\ t &= t^* \cdot \omega, \quad p = p^*/P, \quad P = \eta \omega / \varepsilon^2, \quad H^2 = H^{*2}/P, \quad Re = \rho U_c d / \eta, \quad W = \gamma d k^2 / P. \end{aligned} \quad (25)$$

For $\varepsilon \ll 1$, we will seek for a solution in the form of a power series in ε ($A \equiv h, u, w, p$):

$$A(x, z, t) = A_0(x, z, t) + \varepsilon \cdot A_1(x, z, t) + \dots \quad (26)$$

In the zeroth approximation in ε , for $Re < 1$ and $W = O(1)$, using the equations (20) and the condition (21) – (23), we obtain an expression for the velocity components (subscript “0” is omitted):

$$u(x, z, t) = F(x, t) \left(\frac{z^2}{2} - h z \right), \quad w(x, z, t) = F(x, t) \frac{\partial h}{\partial x} \cdot \frac{z^2}{2} + \frac{\partial F}{\partial x} \left(\frac{h}{2} \cdot \frac{z^2}{2} - \frac{z^3}{6} \right), \quad (27)$$

where $F(x, t) = \frac{\partial p}{\partial x}$.

The mass conservation law (20), condition (22), expression (24), and the assumption that $h(x, t) = h(\xi)$, $\xi = t - x$ imply the following equation for the flow rate Q :

$$\frac{\partial h}{\partial t} + \frac{\partial Q}{\partial x} = 0, \quad Q(x, t) = -F h^3 / 3 = h + C. \quad (28)$$

If the flow is T -periodic, we can introduce the average flow rate: $\bar{Q}(x) = \frac{1}{T} \int_0^T Q(x, t) dt$. For

$h(\xi) = 1 + \delta \cos(\xi)$, the dimensionless average flow rate is $\bar{Q} = 1 + C$.

Relation (23), with respect to (24), implies

$$W \frac{\partial^3 h}{\partial \xi^3} + \frac{(\mu - 1)}{8\pi} \frac{\partial H^2}{\partial \xi} = -\frac{3}{h^2} - \frac{3C}{h^2}. \quad (29)$$

Using equation (29) it is possible to find the magnetic field creating the prescribed film shape:

$$H^2 = H_0^2 + \frac{8\pi}{\mu-1} \left[-W \frac{\partial^2 h}{\partial \xi^2} - 3 \int_h^1 d\xi - 3C \int_h^1 \frac{1}{d\xi^3} d\xi \right], \quad h(\xi) = 1 + \delta \cos(\xi), \quad \delta < 1. \quad (30)$$

The requirement for the magnetic field magnitude to change periodically leads to the expression $C = -2(1 - \delta^2)/(2 + \delta^2)$. The dependence of the average volume flow rate $\bar{Q} = 1 + C$ on the surface oscillation amplitude δ is shown in Fig. 15. The expression for the magnetic field (26) takes the form

$$H^2 = H_0^2 - D, \quad D = \frac{8\pi}{\mu-1} \left[-W \delta \cos(\xi) + \frac{3\delta \sin(\xi)(2 + \delta \cos(\xi))}{(2 + \delta^2)(1 + \delta \cos(\xi))^2} \right]. \quad (31)$$

The constant H_0^2 can be chosen arbitrarily. However, this constant must not be less than the maximum value, $D_{\max} > 0$, of the function D in order not to violate the condition $H^2 \geq 0$. Thus we can assume $H_0^2 = D_{\max}$.

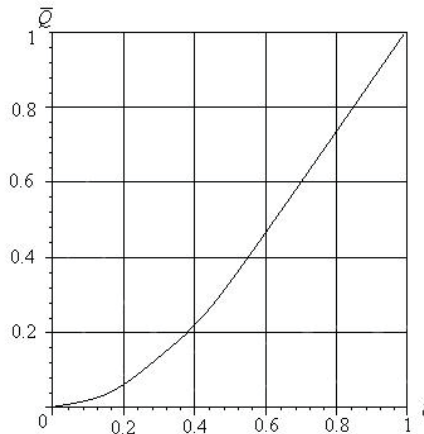


Fig. 15. Average volume flow rate \bar{Q} vs. surface oscillation amplitude δ

3.4 Magnetizable Bodies in an Alternate Magnetic Field

In the experiments we use cylindrically-shaped bodies located in a cylindrical channel. The channel diameter d exceeds that d_w of the body. We denote the length of the body as l_w . The magnetic field is created by coils. The axes of the coils are in the horizontal plane, L is the distance between the axes of the coils and I is the current in the coils (see Fig. 16). The coils are placed at the left and right hand sides of the channel. Magnetic field is created by three coils simultaneously (for example, coils numbers 6 - 8 in Fig. 16), the axis of the middle coil is the symmetry axis of the magnetic field.

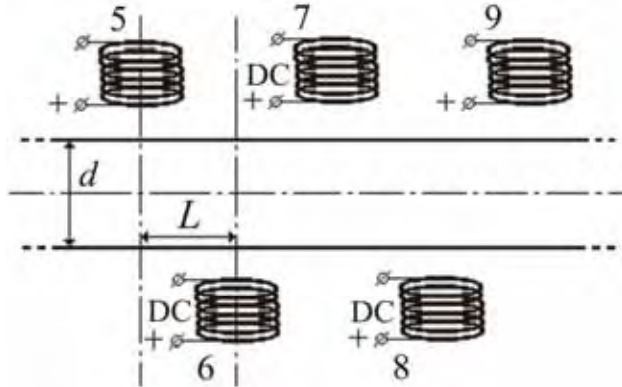


Fig. 16. Arrangement of coils of the electromagnetic system

Periodically, the left coil is switched off and the next coil is switched on, n is the number of the coil switches per second (the frequency), so $T = 1/n$ is the period between change-over of the coils. Currents flowing through the coils are unidirectional. Such an electromagnetic system forms a travelling magnetic field \mathbf{H} , which is a complex function of x, y, z, t (x is the coordinate along the channel, z is parallel to axis of the coils, y is orthogonal to x and z).

It is shown experimentally that in such periodic magnetic field the cylindrical magnetizable bodies move along the channel. The direction of the body motion is opposite to the direction of the travelling magnetic field.

The Bodies from a Magnetizable Polymer

In the first experiment $I = 4.6\text{A}$, $L = 10\text{mm}$, $d = 11\text{mm}$ and the parameters of the "worm" (sample 1) are as follows: Young's modulus $E_y = 50000\text{Pa}$, length $l_w = 48\text{mm}$, diameter $d_w = 4\text{mm}$. The frequency n changes from 5s^{-1} to 1000s^{-1} in this experiment. In the second experiment the parameters are $I = 4.6\text{A}$, $L = 10\text{mm}$, $d = 10\text{mm}$, $l_w = 75\text{mm}$, $d_w = 4.5\text{mm}$ and the sample 2 consists of a polymer with Young's modulus $E_y = 22000\text{Pa}$. The frequency n changes from 5s^{-1} to 1000s^{-1} . A cycle of body deformation by the travelling magnetic field is the process when the travelling magnetic field covers the body (see Fig. 17). At the end and beginning of this process the body is not deformed.



Fig. 17. Magnetizable elastic body (sample 1) in the travelling magnetic field

Elastic Capsule Filled with a Magnetic Fluid

In a third experiment an elastic cylindrical capsule filled with a magnetic fluid is in-side a cylindrical channel. The channel and capsule diameters (d , d_c) are 10mm and 4mm. The length of the capsule filled with a magnetic fluid l_c is 75mm.

In our experiments the frequency n changes from 5s^{-1} to 1000s^{-1} . The phases of deformation of the capsule are shown in Fig. 18. The direction of the worm motion is opposite to the direction of the travelling magnetic field.

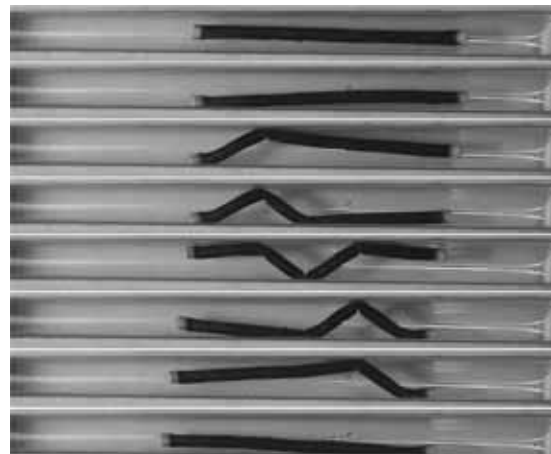


Fig. 18. The form of the capsule at different moments in the travelling magnetic field

The body velocity depends on the geometrical shape of the deformed body and that of the channel. If n is small enough and the body inertia does not affect the body velocity, the following formula is valid:

$$v = k_s(l_s - L)/t_c, \quad t_c = (k_s + 3)T, \quad k_s = [l_w/l_s]. \quad (32)$$

Here l_s is the segment length (a segment is a part of deformed body between two neighbouring coils), k_s is number of the segments, The symbol $[...]$ denotes the integral part of the number, t_c is the time of a cycle. The length of the segment may be determined under assumption about it's form. A segment form is determined by the elastic and magnetic properties of the body material, and the value of the magnetic field.

The problem of determination of the body form is very complex and here we consider three assumptions about the segment form.

Sinusoidal Form

Let us assume that the segment of the body between two coils has sinusoidal form. In this case the equation of the central line of the segment is as follows:

$$y_S = 0.5(d - d_w)\sin(\pi x/L). \quad (33)$$

For parameters $L = 10\text{mm}$, $d = 11\text{mm}$, $l_w = 48\text{mm}$, $d_w = 4\text{mm}$ the length of the sinusoidal segment is $l_s = 12.6\text{mm}$, $k_s = 4$. The analytical estimation of the body velocity is determined as $v = 1.46 \cdot n \text{ mm s}^{-1}$.

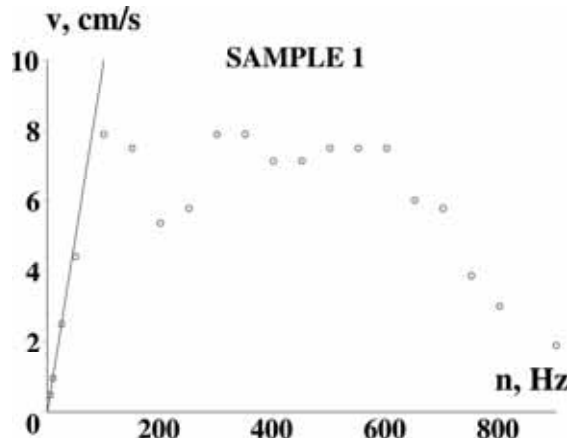


Fig. 19. Body velocity $v = v(n)$ (sample 1)

Body Form is Determined by the Model of Elastic Beam

Let us assume that the form of the segment of the body between two coils is determined by the model of the elastic beam without extension (the bending moment is due to the magnetic forces, assuming that magnetic forces act on the ends of the segment). In this case the equation of the central line of the segment is as follows:

$$y_E = ax^3 + bx^2 + d_w/2, \quad (34)$$

where $a = -2(d - d_w)/L^3$, $b = 3(d - d_w)/L^2$. For this assumption and for parameters as above the length of the segment is equal to 12.5mm, $k_s = 4$ and the analytical estimation of the body velocity is $v = 1.43 \cdot n \text{ mms}^{-1}$.

Body Form is a Broken Line

Let us assume that the form of the body segment between two coils is a straight line. The equation of the central line of the segment is as follows:

$$y_R = (d - d_w)x/L. \quad (35)$$

In this case for parameters as above the length of the segment is 12.2mm, $k_s = 4$ and the analytical estimation of the body velocity is $v = 1.26 \cdot n \text{ mms}^{-1}$. From Fig. 19 we can see that for $n < 100 \text{ s}^{-1}$ the theoretical result (the body form is determined by the model of an elastic beam) matches with the experimental data for the sample 1 for the first experiment. The maximal obtained body velocity is $v = 7.89 \text{ cms}^{-1}$ for $n = 100 \text{ s}^{-1}$. For $n > 950 \text{ s}^{-1}$ in the first experiment sample 1 does not move.

From the second experiment it follows that the segment form of the capsule is a straight line. The length of the segment is determined by the formula

$$l_s = \sqrt{L^2 + (d - d_c)^2} = 11.66 \text{ mm}, \quad k_s = 6. \quad (36)$$

From (20) we find dependency of the velocity of the body on n : $v = 1.1 \cdot n \text{ mms}^{-1}$. The theoretical dependency of the velocity of the body v on n and experimental data are shown in Fig. 20.

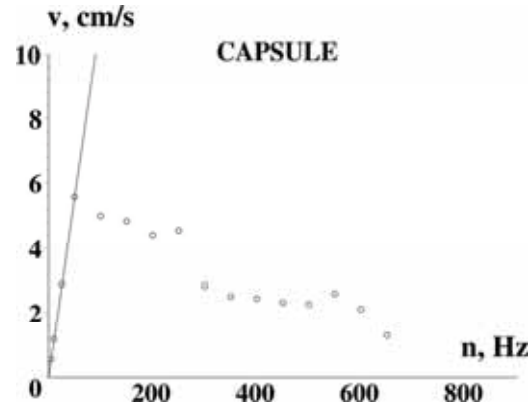


Fig. 20. Body velocity $v = v(n)$ (a capsule with a magnetic fluid)

For the frequency $n < 50\text{s}^{-1}$ the theoretical estimation of the velocity of the capsule matches with the experiments. In our experiment for $n > 700\text{s}^{-1}$ the capsule does not move. The maximal obtained capsule velocity is $v = 5.56 \text{ cm/s}$ for $n = 50\text{s}^{-1}$. The body velocity depends on the geometrical shape of the deformed body and that of the channel. Only if n is small enough the body inertia does not affect the body velocity and the formula (32) is valid. A simulation of the dynamic behavior of the elastic body was made by Finite-Element-Method (Fig. 21). For $n < 100\text{Hz}$ the numerical results coincide with experimental data.

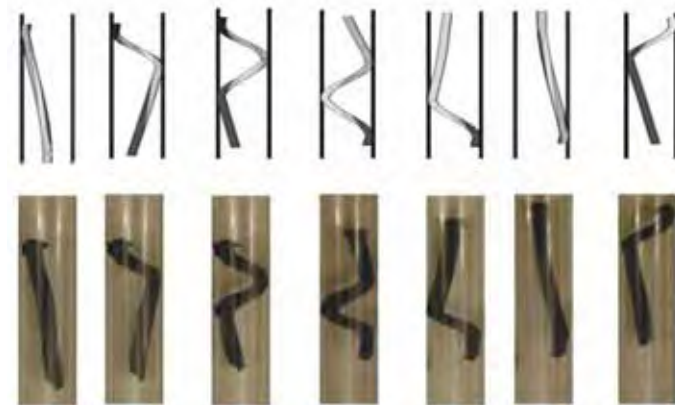


Fig. 21. Analysis of the locomotion (sample 1) for $n < 100\text{Hz}$ using Finite-Element- Method

The Finite-Element-Method is also a useful tool to define optimal control frequencies for the cascaded system of the coils (switching frequencies). As it is shown in Fig. 22 there exists a correlation between the measured velocity of the worm, the switching frequencies of the coils and the eigenfrequencies of the worm respectively.

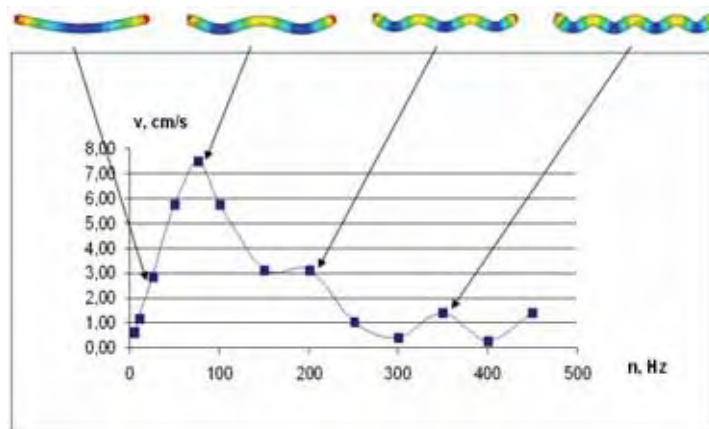


Fig. 22. The velocity of the worm vs. eigenfrequencies (switching frequencies of the coils)

Finally, we should remark that the type of locomotion realized with the magnetic elastomer or the elastic capsule filled with ferrofluid is a snake-like motion called *concertina motion*.

3.5 Design of Active and Passive Locomotion Systems and the Interaction between a Controlled Magnetic Field and a Magnetic Fluid

A moving magnetic field can generate a travelling wave on the surface of magnetic fluids. This travelling wave can be useful as a drive for locomotion systems. Therefore, peristaltically moving active locomotion systems could be realized with an integrated electromagnetic drive (see Fig. 23, left (A)). Also passive locomotion systems can be taken into account. Objects, which are on the surface of the fluid or are lying in the fluid, could be carried floating and/or shifting (see Fig. 23, left (B) and Fig. 26, 27).

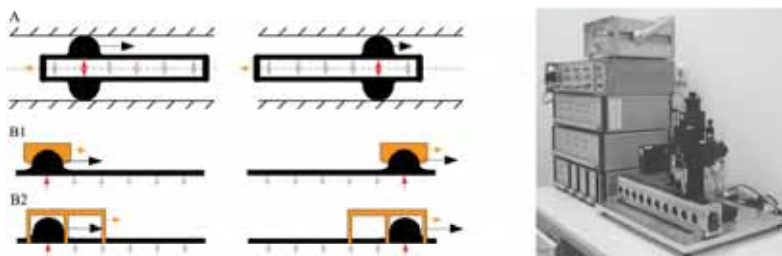


Fig. 23. Schema of possible locomotion systems (left), and the experimental setup (right)

The following properties are important for the locomotion: (i) mass and geometry of the moving or moved object, (ii) the change of the shape and the position of the magnetic fluid, and (iii) the pressure distribution of the magnetic fluid with respect to the action of the moving magnetic field.

To analyse the behavior of the magnetic fluids (under the described action of the magnetic field) and such locomotion systems, the experimental setup consists of 20 consecutively arranged cascaded electromagnets (1 coil generates 3000 ampere turns).

The measurement system to detect the pressure of the fluid and the optical system to analyse the shape of the fluid are connected to a 3 axis-positioning unit (see Fig. 23, right). Fig. 24 shows a travelling wave in a magnetic fluid.

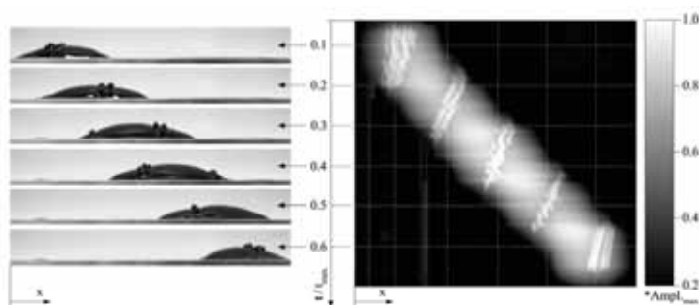


Fig. 24. Travelling wave generated by a moving magnetic field

Fig. 25 shows schematically the magnetic field, which emerges from an electromagnet, the shape of the fluid and the pressure distribution.

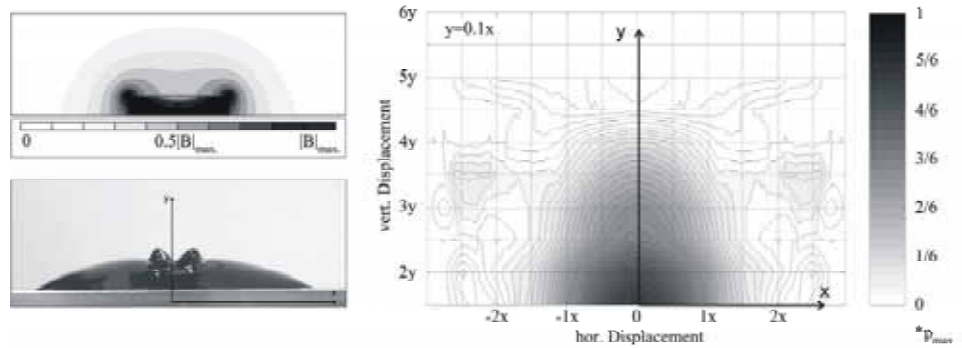


Fig. 25. Schematic presentation of the electric induction density of an excited coil (left top), the emerged shape of the magnetic fluid surface (left bottom), and the pressure distribution of the magnetic fluid (right)



Fig. 26. Example of a passive locomotion by means of travelling waves in a magnetic fluid

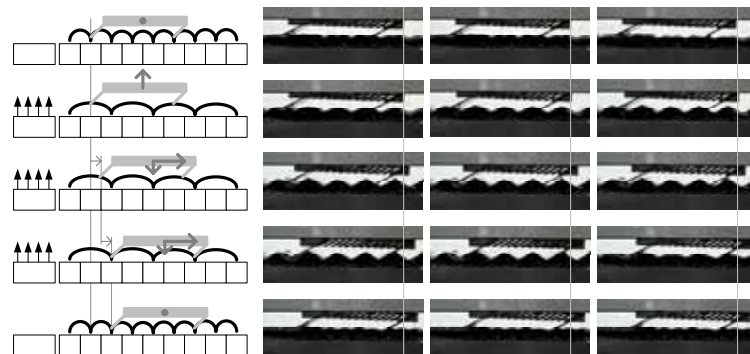


Fig. 27. Functional principal of a passive locomotion system (form of the magnetic field (l.) and the corresponding video sequences (r.))

In the experimental setup using a water-based ferrofluid a maximal change of the fluid pressure about 2200 MPa was measured in the origin (see Fig. 25, right) after applying the magnetic field. Thus, it could be a realistic scenario to construct a cascaded structure of cylindrical membranes filled with a magnetic fluid ("worm") and to get the necessary interaction between "worm" and the environment for peristaltic locomotion.

3.6 Conclusional Remarks

The expression for the magnetic field strength creating a sinusoidal wave on the surface of a viscous magnetic fluid as a function of the characteristics of the fluid (viscosity, surface tension, and magnetic permeability) and the parameters of the wave are obtained.

It is experimentally shown that in a specially structured periodic travelling magnetic field a cylindrical magnetizable elastic body moves along the channel. The direction of the body motion is opposite to the direction of the travelling magnetic field.

The maximal obtained body velocity is $v=10 \text{ cms}^{-1}$ for $n=250 \text{ s}^{-1}$. For the frequency $n < 100 \text{ s}^{-1}$ (samples 1) and for $n < 50 \text{ s}^{-1}$ (the capsule with the magnetic fluid) the theoretical (analytical and numerical) estimations of the velocity of the elastic body (the capsule with the magnetic fluid) coincide with the experimental data.

The creation of active biologically inspired locomotion systems and new principle for a passive motion is possible using the deformation deformable magnetizable media in controlled magnetic fields.

4. Summary and Outlook

At the beginning of the chapter it was mentioned that the motion of an earthworm was the inspiration for a technical solution of an artificial worm. A theory is developed for the peristaltic motion of such systems, which to a large extent allows to characterize these motions already on a kinematic level. The advantage of adaptive control for the dynamical realization of these motions is shown. Experiments using a simple prototype checked the results of the theory.

Using magnetizable materials in compliant structures rather snake-like motion (concertina movement) has been realized until now. Since the peristaltic crawling of the earthworm has many advantages for the locomotion in difficult environments the realization of such a motion remains a challenge in theory and control as well as in experiments (Fig. 28).

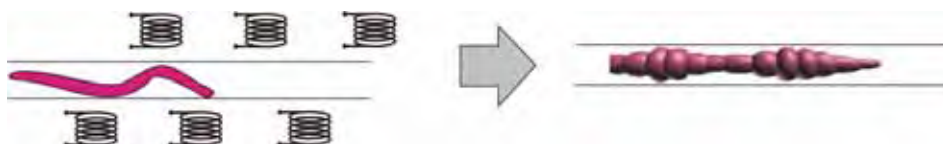


Fig. 28. From the snake-like concertina motion to worm-like peristaltic crawling

This also applies to the technological realization of an enveloping membrane structure for the artificial worm.

Here two problems (and actually opposite demands) are to be solved:

- ☞ membrane thickness as small as possible, to achieve a big force extraction and a very flexible worm structure and
- ☞ membrane thickness as big as possible, to avoid diffusion processes of the ferrofluid through the membrane and to keep environmental influences away from the ferrofluid to improve the long-term stability of the worm system.

The objective is to find optimal parameters and to verify these experimentally.

Another challenge for future research is to realize two-dimensional (planar) motions using ferrofluids.

5. References

- Abaza, K. (2006). Ein Beitrag zur Anwendung der Theorie undulatorischer Lokomotion auf mobile Roboter – Evaluierung theoretischer Ergebnisse an Prototypen, *PhD thesis*, Faculty of Mechanical Engineering, TU Ilmenau
- Behn, C. (2005). *Ein Beitrag zur adaptiven Regelung technischer Systeme nach biologischem Vorbild*, Cuvillier, Göttingen
- Behn, C. & Zimmermann, K. (2006). Adaptive lambda-tracking for locomotion systems, *Robotics and Autonomous Systems*, 54, pp. 529-545
- Blekhman, I.I. (2000). *Vibrational Mechanics: Nonlinear Dynamic Effects, General Approach, Applications*, World-Scientific, Singapore
- Choi, H.R.; Ryew, S.M.; Jung, K.M., Kim, H.M.; Jeon, J.W., Nam, J.D.; Maeda, R. & Tanie, K. (2002). Microrobot actuated by soft actuators based on dielectric elastomer, *Proceedings of IEEE/RSJ International Conference on Intelligence Robots and System*, 2, pp. 1730-1735
- Dragan, V. & Halanay, A. (1999). *Stabilization of Linear Systems*, Birkhäuser, Boston
- Kato, T.; Nakamura, T.; Iwanaga, T. & Muranaka, Y. (2006). Peristaltic Crawling Robot Based on the Locomotion Mechanism of Earthworms. *Proc. of the 4th IFAC Symposium on Mechatronics*, Heidelberg, September 12-14, 2006, pp. 139-144
- Mangan, E.V.; Kingsley, D.A.; Quinn, R.D. & Chiel, H.J. (2002). Development of a peristaltic endoscopies, *Proceedings of IEEE International Conference on Robotics and Automation*, 1, pp. 347-352
- Menciassi, A. & Dario, P. (2003). Bio-inspired solutions for locomotion in the gastrointestinal tract: background and perspectives, *Phil. Trans. R. Soc. London, A* 361, pp. 2287-2298
- Miller, G. (1988). The motion dynamics of snakes and worms, *Computer Graphics*, 22, pp. 169-173
- Miller, D.E. & Davison, E.J. (1991). An adaptive controller which provides an arbitrary good transient and steady-state response, *IEEE Transaction on Automatic Control*, 36, pp. 68-81
- Ostrowski, J.P.; Burdick, J.W., Lewis, A.D. & Murray, R.M. (1995). The mechanics of undulatory locomotion: the mixed kinematic and dynamic case, *Proceedings of IEEE International Conference on Robotics and Automation*, pp. 1945-1951, Nagoya, May, 1995, Japan

- Naletova, V.A., Kviantsev, A.S. & Turkov, V.A. (2003). Movement of a magnet and a paramagnetic body inside a vessel with a magnetic fluid. *J. Magn. Magn. Mater.*, 258-259, pp. 439-442
- Naletova, V.A., Turkov, V.A. & Tyatyushkin, A.N. (2005). Spherical body in a magnetic fluid in uniform electric and magnetic fields. *J. Magn. Magn. Mater.*, 289, pp. 370-372
- Naletova, V.A., Kviantsev, A.S. (2005). Thermomagnetic force acting on a spheroidal body in a magnetic fluid. *J. Magn. Magn. Mater.*, 289, pp. 250-252
- Popp, J. (2006). Ferrofluide und Ferrogele – Neue Materialien in der Anwendung für Lokomotions- und Manipulationssysteme. *Diploma Thesis*, Faculty of Mechanical Engineering, TU Ilmenau
- Rosensweig, R.E. (1985). *Ferrohydrodynamics*, Cambridge University Press, Cambridge
- Raj K. , Moskowitz B. (1990). Commercial applications of ferrofluids, *J. Magn. Magn. Mater.*, 85, pp. 233-245.
- Raj K. , Moskowitz B. , Casciari R.(1995). Advances in ferrofluid technology, *J. Magn. Magn. Mater.*, 149 (1-2), pp.174-180.
- Saga, N. & Nakamura, T. (2002). Elucidation of propulsive force of micro-robot using magnetic fluid, *J. Appl. Phys.*, 91, pp. 7003-7005
- Saga, N. & Nakamura, T. (2004). Development of a peristaltic crawling robot using magnetic fluid on the basis of locomotion mechanism of the earthworm, *Smart Mater. Struct.*, 13, pp. 566-569
- Steigenberger, J. (1999). On a class of biomorphic motion systems, *Preprint No. M12/99*, Faculty of Mathematics and Natural Sciences, TU Ilmenau, Germany
- Steigenberger, J. (2004). Modelling artificial worms, *Preprint No. M02/04*, Faculty of Mathematics and Natural Sciences, TU Ilmenau, Germany
- Steigenberger, J. (2003). Contribution to the mechanics of worm-like motion systems and artificial muscles, *Biomech. and Modeling in Mechanobiology*, 2, pp. 37-57
- Turkov, V.A. (2002). Deformation of an elastic composite involving a magnetic fluid, *J. Magn. Magn. Mater.*, 252, pp. 156-158
- Weiting, L.; Menciassi, A.; Scapellato, S.; Dario, P.; Yuquan Chen (2006). A biomimetic sensor for crawling. *Robotics and Autonomous Systems*. 54, pp. 513-528
- Ye, X. (1999). Universal lambda-tracking for nonlinearly-perturbed systems without restrictions pn the relative degree, *Automatica*, 35, pp. 109-119
- Zimmermann, K.; Steigenberger, J. & Zeidis, I. (2002). Mathematical model of worm-like motion systems with finite and infinite degree of freedom, *Proceedings of 14th CISM-IFTOMM Symposium on Theory and Practice of Robots and Manipulators (ROMANSY)*, pp. 507-515, Udine, July, 2002, Italy
- Zimmermann, K.; Steigenberger, J. & Zeidis, I. (2003). On artificial worms as a chain of mass points, *Proceedings of 6th International Conference on Climbing and Walking Robots (CLAWAR)*, pp. 11-18, Catania, September, 2003, Italy
- Zimmermann, K.; Zeidis, I.; Naletova, V.A. & Turkov, V.A. (2004). Waves on the surface of a magnetic fluid layer in a travelling magnetic field, *J. Magn. Magn. Mater.*, 268, pp. 227-231
- Zimmermann, K.; Zeidis, I.; Naletova, V.A. & Turkov, V.A. (2004). Travelling waves on a free surface of a magnetic fluid layer, *J. Magn. Magn. Mater.*, 272-276, pp. 2343-2344
- Zimmermann, K.; Zeidis, I.; Naletova, V.A. & Turkov, V.A. (2004). Modelling of worm-like motion systems with magneto-elastic elements, *Phys. Stat. Solid.*, 1, pp. 3706-3709

- Zimmermann K.; Naletova V.A., Zeidis I.; Böhm, V.; Kolev, E. (2006). Modelling of locomotion systems using deformable magnetizable media. *J. of Physics: Cond. Matter*, 18, pp. 2973–2983
- Zimmermann, K.; Zeidis, I.; Naletova, V.A.; Turkov, V.A.; Bachurin, V.E. (2004). Locomotion Based on a Two-layers Flow of Magnetizable Nanosuspensions. *Proceedings of the JEMS'04, Joint European Magnetic Symposia*, September, 5-10, Dresden, Germany, pp. 134
- Zimmermann, K.; Naletova, V.A.; Zeidis, I.; Turkov, V.A.; Kolev, E.; Lukashevich, M.V.; Stepanov, G.V. (2007). A deformable magnetizable worm in a magnetic field – a prototype of a mobile crawling robot. *J. Magn. Magn. Mater.* 311, pp. 450-453